expert›

Ignition Systems
for Gasoline Engines

4th International Conference
Michael Günther, Marc Sens (eds.)
and 98 Co-Authors

Michael Günther,
Marc Sens (eds.)
and 98 Co-Authors

Ignition Systems
for Gasoline Engines

Ignition Systems for Gasoline Engines

4th International Conference,
December 6 -7, 2018, Berlin, Germany

Michael Günther, Marc Sens (eds.)
and 98 Co-Authors

With 369 Figures and 48 Tables

expert›

automotive
engineering **iaʋ**

FSC
www.fsc.org
MIX
Papier aus ver-
antwortungsvollen
Quellen
FSC® C016368

Bei der Erstellung des Buches wurde mit großer Sorgfalt vorgegangen; trotzdem lassen sich Fehler
nie vollständig ausschließen. Verlag und Autoren können für fehlerhafte Angaben und deren Folgen
weder eine juristische Verantwortung noch irgendeine Haftung übernehmen.
Für Verbesserungsvorschläge und Hinweise auf Fehler sind Verlag und Autoren dankbar.

Preface

In addition to increasing electrification, forecasts show a worldwide increase in the number of gasoline engines being produced. Rising industrialization will likely lead to 120 million new registrations, at least 75% of them for vehicles based on combustion engines, by the year 2030. Ambitious climate targets will remain a chimera as long as the gasoline engine is not adapted to help significantly reduce carbon emissions. In addition to the requirements of the established markets, we must be prepared for new challenges in emerging economic regions in particular. Engines require greater optimization while remaining sufficiently robust to meet the demands of use all around the world. In addition to the Miller combustion cycle, the industry needs engines that employ strongly charge-diluted combustion to achieve efficiencies significantly above 40%. Instrumental in this will be ignition processes with great potential to shift ignition limits.

The question we have to ask ourselves is how can ignition systems help further boost the efficiency of the combustion engine?

Together with the participants we discussed this key question during the 4th International Conference on Ignition Systems for Gasoline Engines.

Michael Günther, IAV GmbH
Department Manager Advanced Development
Thermodynamics SI Engines Gas Exchange/Combustion

Marc Sens, IAV GmbH
Senior Vice President Advanced Development
Thermodynamic/Powertrain Concepts

Contents

Preface

Contents

Contents

1 New Ignition Systems

1.1 Spark-based Advanced Ignition Control for Future Diluted Gasoline Engines

Ming Zheng, Guangyun Chen, Jimi Tjong, Liguang Li, Shui Yu, Xiao Yu, Zhenyi Yang

Abstract

To meet the mandatory CO_2 emissions regulations in the future, current gasoline engines require significant work for efficiency improvement. One critical part of combustion optimization is to improve the spark ignition process, especially for the engines that utilize charge dilution concept incorporated with strong cylinder flow. Such high efficiency combustion process requires the ignition systems to effectively ignite the mixture and secure the flame kernel until developing to self-sustainable propagation. In this paper, the extent of spark stretching and the ability to withhold from restrike in high-speed flow are investigated for various sparking strategies. A thick plasma channel that is generated by boosted glow current is less prone to be blown off by the strong flow, consequently, the restrike frequency is lowered. In comparison with a low current long lasting spark generated by the dual-coil continuous discharge strategy, the boosted current strategy can lead to a faster flame kernel growth. Single-cylinder engine experiments indicate that the combustion phasing controllability and the stability of lean/diluted engine operation can be improved by using the boosted current ignition strategies with conventional spark plug. Extensive engine test results indicate that the multi-core ignition can better control the gasoline combustion and extend the operable limits of lean/diluted engine combustion, compared with single-pole ignition for low to medium engine loads. Experimental results indicate that the multi-core ignition strategy, even with lower current on each pole, have clear advantages over the high current single-pole strategies such as the multi-coil ignition and the boosted current ignition, with respect to the combustion phasing controllability of super lean gasoline combustion. Multiple-cylinder production gasoline engine test results show that the multi-core ignition can improve the stability of gasoline engine at high levels of dilution, thereby leading to improvement of indicated specific fuel consumption.

1 Introduction

Presently, internal combustion engines (ICEs) power over 99% automotive vehicles in the world. New generations of ICEs will continuously power the majority automotive vehicles including hybrids for the foreseeable future, despite that renewed emphasis

on electric and plug-in hybrid vehicles gains ground recently. Worldwide research programs are targeting to raise the ICE brake thermal efficiency (BTE) to 55~60% for heavy-duty engines, and 40~45% for light-duty engines, while to lower the exhaust pollutants by 70~90% from current standards. The BTE will be increased through engine technology innovations and combustion control advances, in addition to friction reduction and waste heat recovery etcetera; the emissions will be reduced with advanced combustion control and exhaust after-treatment.

As the CO_2 emission regulations become mandatory, meeting the standards requires significant work to improve the efficiency of gasoline engines. The current trend is to utilize the vehicle and powertrain downsizing to improve the fuel efficiency and thus reduce CO_2 production while applying forced air induction, usually via turbocharging techniques, to compensate the otherwise reduced torque and power performance due to downsized engine displacement. Under the boosted engine conditions, especially in part load operation, the diluted combustion concepts through internal or external exhaust gas recirculation (EGR) provide further improvements in fuel efficiency and NOx emission reduction[1,2]. Moreover, instead of running conventional stoichiometric combustion, the gasoline lean burn operation also draws increasing attention in the research field. The charge dilution increases the fuel efficiency of gasoline engines primarily due to (1) reduction in pumping loss at partial loads, (2) mitigation in combustion knock to allow better combustion phasing, (3) decrease in heat loss because of lower combustion temperature [3-5]. Furthermore, an adequately lean and/or diluted cylinder charge potentially allows the use of a higher compression ratio for additional improvements in thermal efficiency. At the same time, a diluted cylinder charge also presents challenges to combustion stability, because the dilution tends to prolong the ignition delay and slowdown the burn rate; in extreme cases, it can result in engine misfire. In addition, it is desired to attain the combustion phasing within a crank angle window close to the top dead center (TDC) in order to achieve the optimal thermal efficiency. For instance, the crank angle of 50% mass fraction burned (CA50) should be located at 6~8 °CA after the top dead center (aTDC) [6]. However, the slow flame kernel growth and burn rate of a highly diluted cylinder charge make it challenging to achieve the optimal combustion phasing. The degree of dilution is generally limited by late combustion phasing, severe cyclic variation, and declined mixture ignitability.

In order to secure ignition and accelerate flame propagation, substantial efforts have been spent in the mixture aspect, such as mixture preparation, intensification of cylinder flow, and the geometry matching of the combustion chamber especially in the flow field near the spark electrodes. In another aspect, the enhancement of the ignition source can extend the tolerance of worsened mixture ignitability and thus allows higher levels of mixture dilution. The impacts of a more robust ignition source include reducing ignition delay, allowing closer to TDC spark timing, and accommodating variations in charge motion and mixture homogeneity. The enhancement of the conventional single-spot ignition sparkplugs normally seeks a high discharge power [6-10] or a prolonged duration of spark glow [11, 12]. Advanced ignition techniques such as non-equilibrium plasma discharge can produce multiple-spot ignition in the proximity of the igniter. Volume-type ignition is achieved through the discharge of transient plasma [13-15] or radio-frequency corona [16]. Research in microwave ignition [17] and laser ignition [18] also shows promising potential of improving the ignition control of diluted mixtures by distributed and multiple ignition sites. Multiple-spot ignition via these advanced ignition techniques are effective to secure ignition and accelerate combustion for spark ignition

engines under diluted conditions. However, the hardware complexity and compatibility to common engine designs remain a major concern.

In this paper, the authors present an innovative three-core igniter system as a drop-in technology to improve the ignition and combustion for gasoline engines under diluted conditions [19-22]. While having the same dimensions as a regular sparkplug, the new igniter is capable of delivering three spark arches simultaneously in the perimeter of the igniter, resulting in multiple-spot ignition sites and a larger ignition volume. The three-core igniter is tested in optical combustion vessels to visualize its effects on the ignition process, and on a production gasoline engine to examine its impact on engine combustion characteristics. This novel igniter architecture also unfolds multiple possibilities to apply advanced control strategies for efficient utilization of the ignition energy, such as sequential arcing among the three HV electrodes and real-time ignition current modulation. This paper primarily focuses on the three-core igniter in lieu of a conventional spark plug running with the ignition coil drivers in current production.

2   Experimental Setups

2.1   Advanced Ignition Systems

A range of ignition technologies were developed in the clean combustion engine laboratory (CCEL) in the past decade. The effective ones are listed in table 1. The ignition improvement is realized either to enhance the transient power or modulate the energy delivery profile after the spark breakdown. One technique is to utilize direct capacitor discharge to enhance the breakdown power or deploy high ignition energy. The high intensity of plasma offers high temperatures that enhance the chemical reactions of the gas mixture in the spark gap. The fast deposition of a large amount of energy is effective to expand the plasma beyond the constraint of electrodes, which can significantly affect the flame kernel development, especially under moderate flow conditions.

Table 1: Advanced Ignition Technologies Development at CCEL

Technology	Principle	Impact
Multi-core Ignition System [19]	Spark spatial distribution	Multiple site, large ignition volume
Boosted Current Ignition [23]	Spark glow-current control	Long duration continuous discharge, current boosting on demand
High-power Ignition [24, 25]	Direct capacitor discharge	Breakdown enhancement
High-energy Ignition	Direct capacitor discharge	High energy plasma
Active Control Resonant Ignition [26]	RF corona discharge	Non-thermal plasma, large ignition volume, continuous discharge
Multi-coil Ignition [22]	Increase spark energy	High peak glow current
Pre-chamber ignition	Flame jet	Fast burning
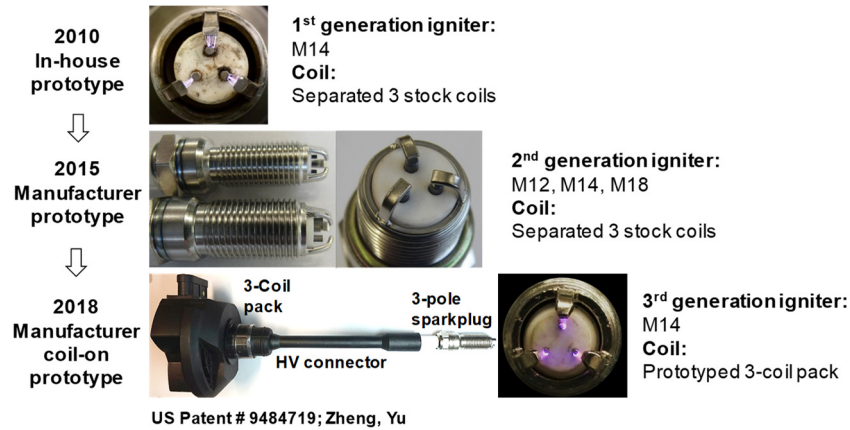
Figure 1: Multi-core ignition technology and prototypes development

The pursuit for multiple ignition sites has moved from the traditional multiple spark plug technique, which employs more than one spark plug per cylinder, to seek multiple ignition kernels with a single igniter, due to the tight space on the cylinder head. This technology has been developed and extensively evaluated in CCEL in the past ten years. The technology development pathway is given in figure 1. The three-core igniter prototyping started from in-house made igniters with sintered ceramic core. Two generations of manufacturer prototypes are developed in collaboration with the sparkplug manufacturers. The latest system-level prototype consists of a 3-coil pack, high voltage connector, and a fine-electrode three-core igniter.
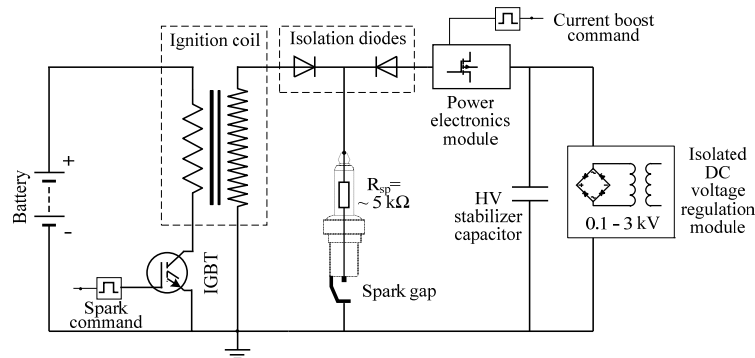
Figure 2: Sketch diagram of single-channel boosted current ignition control system

The enhancement of spark glow current is considered an effective way to secure the ignition kernel development in high-speed flow. A sketch diagram of the boosted current ignition control system developed in the CCEL is illustrated in figure 2. The spark-plug used is a conventional resistor spark plug. A traditional inductive ignition coil is used to energize the spark breakdown, while an auxiliary power control module is used to enhance the glow current after the spark breakdown. The glow current boosting is realized through constant-voltage control. A power electronics module is used to modulate the glow current amplitude and duration. Multi-coil ignition is the other technique used to enhance the spark current. In this paper, three identical ignition coils are connected in parallel to supply spark energy to a single spark plug. The spark current profile is still following the traditional triangular delaying shape, while the peak of the spark current is increased significantly.

2.2   Optical Constant Volume Combustion Vessel System

A schematic diagram of the combustion vessel platform is illustrated in figure 3. The optical chamber has a working volume of about 1.2L with a Ø80mm view port. High-speed shadowgraph imaging tests are conducted to visualize the ignition flame kernel development and flame propagation processes. The high-speed imaging setup includes two identical parabolic mirrors with a diameter of 6 inches and a focal length of 48 inches, a cold white LED light source, a 0.4 mm pinhole, and a knife-edge. Images are recorded by a Phantom v7.3 digital high-speed camera.

An Environics 4040 gas divider is employed to provide accurate concentration control on the methane (CH_4), Carbon dioxide (CO_2) and air. The combustion vessel3s are fitted with dynamic pressure transducers for combustion pressure measurement. The combustion pressure is recorded by a data acquisition system which is externally triggered by the spark energizing command signal.
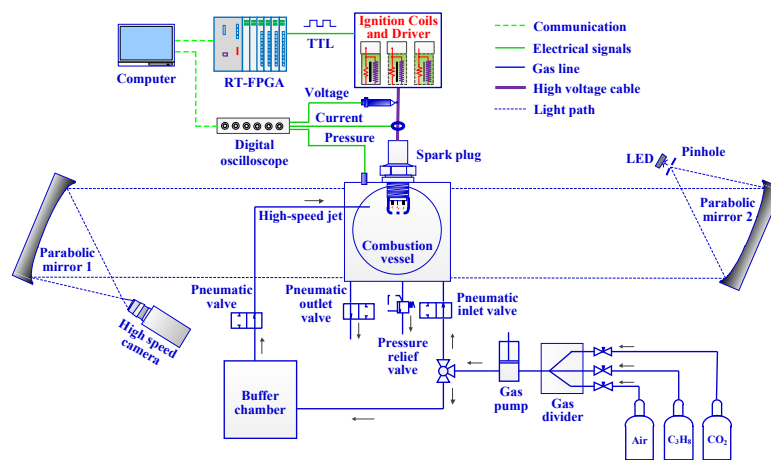
Figure 3: Schematic of optical combustion vessel test platform

For the 3-core ignition power drive, three identical ignition coils are connected in parallel to energize the three spark gaps of the igniter. Each ignition coil is independently controlled by an individual insulated gate bipolar transistor (IGBT) chip which is driven by a specifically designed gate-drive circuit. The electronics driver circuit is packaged in-house. The ignition command signal for each spark event is generated from a National Instruments real-time computer and field programmable gate array (FPGA) setup. In order to characterize the spark discharge process, three identical wide-band current probes (Pearson 411) are employed to measure the discharge current. For the spark discharge high voltage measurement, two Tektronix P6015a probes and one Northstar PVM-6 are used. Good measurement fidelity between three high voltage probes is observed during the validation tests. The discharge voltage and current waveforms are recorded in a digital oscilloscope. The recording of the waveforms of the discharge voltage and current are triggered by the rising edge of the spark command signal at the start of the ignition coil charging. The waveforms are recorded by the digital oscilloscope with a sampling rate up to 40 MHz.

2.3   Single-cylinder Research Engine

The ignition systems are evaluated on a single-cylinder engine. The engine is modified to locate a centrally-mounted spark plug. A diagram of the spark plug location, the orientation of the three electrodes is shown in figure 4. The key engine parameters are shown in Table 2. The piston shape and the intake system of the engine are modified

to operate the spark ignition diluted gasoline combustion mode. The compression ratio was modified to 13:1 and 9.2:1 by removing material to form a shallow bowl across approximately 80% of the piston top surface. The spark plugs installation aligns the spark gap protrusion and the gap orientation comparable in all the engine tests for various ignition strategies.
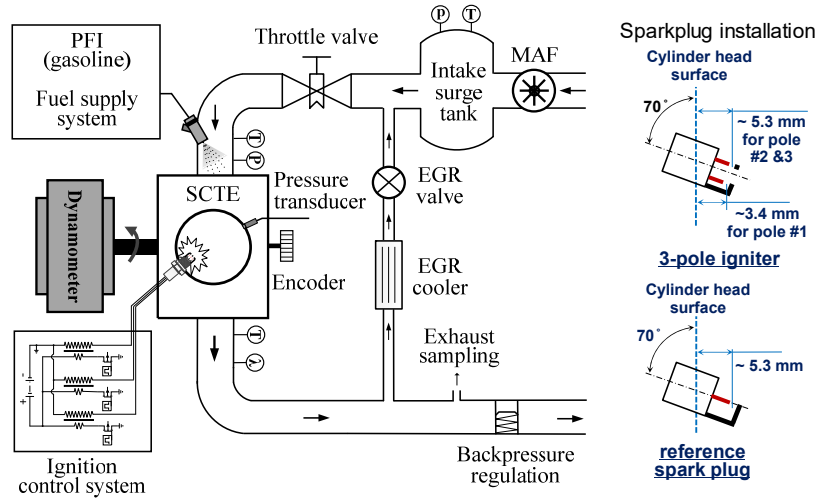
Figure 4: Single-cylinder engine setup and spark plug adaption

Table 2: Engine specifications

Engine parameter	Value
Displacement	0.84 L
Bore	101 mm
Stroke	105 mm
Compression ratio	13:1, 9.2:1
Fuel	#87 gasoline

An intake manifold is fabricated to integrate a low-pressure port fuel injector. The engine is coupled with a direct current dynamometer. The in-cylinder pressure is acquired with a pressure transducer at 0.1°CA in synchronization with a crank-mounted optical encoder. The manifold pressure is acquired with a piezo-resistive absolute pressure transducer. Data recording of the pressures at each condition consists of 200 consecutive engine cycles. The fresh engine air intake is provided by a dry, clean compressed-air compressor system and controlled with electronic pressure regulation. A manual ball valve is used to throttle the engine intake. The fresh air flow rate is measured by a mass air flow rate meter (Roots Meter 5M175). No exhaust gas recirculation is used for these tests. The fuel flow rate is measured by a piston-type flow meter (Ono Sokki FP-213). The engine coolant circulation and temperature control is carried out by an external coolant conditioning unit and maintained to 80 °C. The fuel used in the engine test is pump-octane #87 gasoline, with estimated research octane and motoring octane number of 91, and 83, respectively

2.4   Multiple-cylinder Development Engine

A production development engine is instrumented with cylinder pressure acquisition and exhaust gas sampling for the three-core igniter study(figure 5). The engine specifications are given in table 3. Each bank of the engine has an overhead camshaft, and

the dual-equal VCT technology controls the cam retard of both intake and exhaust valves simultaneously. By design, a retard of the intake and exhaust valve events results in a greater amount of exhaust gas trapped in the cylinder, thereby increasing the internal EGR dilution.

	Test 1					
	Speed (rpm)	BMEP (bar)	VCT (°CA)	λ	Spark timing (°CA BTDC)	Tested cylinder
	1500	2.6	1.3 - 50.5	1.0	32.3 – 49.4	#2
	Test 2					
	Speed (rpm)	BMEP (bar)	VCT (°CA)	λ	Spark timing (°CA BTDC)	Tested cylinder
	1500	2.6	1.5 - 50.5	1.0	32.3 – 49.4	#4
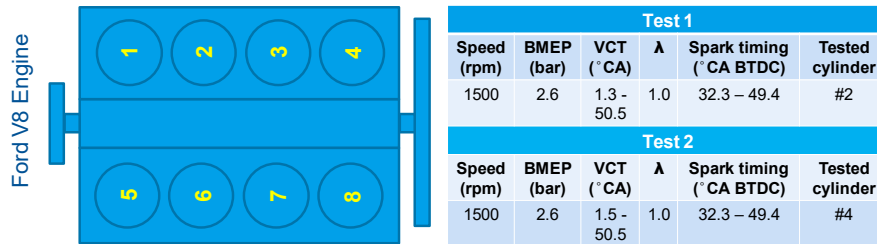
Figure 5: Multiple-cylinder development engine testing conditions

Table 3: Test engine specifications

Engine Type	Naturally Aspirated V8 4-stroke
Displacement [L]	6.2
Bore [mm]	102
Stroke [mm]	95
Compression Ratio	9.8:1
Valve-train	Single Overhead Cam (SOHC)
Ignition system	Individual Coil on Plug

A fully open powertrain control module (PCM) is set up to allow flexible control over the engine operating parameters, such as the spark advance and VCT retard. The engine torque and power are measured by an AC dynamometer. The engine cylinder pressure and other operating parameters are recorded through the data acquisition system.

3   RESULTS AND DISCUSSIONS

3.1   Spark glow current boosting to improve plasma stretching in high-speed flow

The effects of gas flow on the spark discharge process are investigated under controlled flow conditions with nitrogen as the background gas first. The discharge voltage and current are measured simultaneously with high speed imaging recording of the spark plasma. The current boosting strategy is adopted to study the performance of elevated discharge current under flow conditions. The spark plasma is stretched by the gas flow as illustrated in Figure 6. The background pressure is varied from 1 bar to 23 bar and the selected photos represent the cases with and without boosted current. The flow velocity is approximately 40 m/s. The spark plasma is stretched by the flow, and the maximum stretched length is affected by both discharge current level, and the background pressure. When the discharge current is low, the spark plasma is stretched to a shorter extent, and with a thinner plasma profile. Restrikes are observed under both background pressure conditions with the low current. While when the current level is boosted, the stretched plasma is significantly longer and thicker. Restrikes are only observed when a higher background pressure is applied.
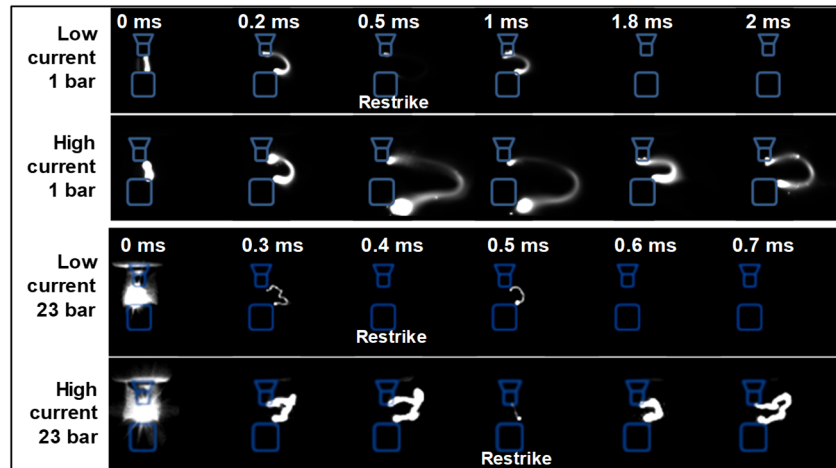
Figure 6: Spark stretching behavior under a cross-flow speed of ~40m/s

The discharge duration and restrike numbers are summarized in Figure 7 for the four experiments. The velocity increases from 0 m/s up to 50 m/s. For the baseline spark discharge with a low discharge current level, the spark duration decreases when the flow velocity increases, with a more drastic decrease under the high background pressure of 23 bar. Whereas for the boosted current discharge, the discharge duration is maintained in the flow velocity range of 0 to 50 m/s under the low background pressure, although the duration is shortened when the background pressure is increased to 23 bar. In these experiments the spark charging duration and boosted current duration are controlled separately. The commanded boosted current duration is 2 ms which can be increased on demand. This comparison suggests that the boosted current strategy is beneficial for maintaining the discharge duration under flow conditions, especially when the background pressure is comparatively low.

The restrike numbers are plotted in the bottom plot of Figure 7. Corresponding to the shortened spark duration under flow conditions, there are also more frequent restrikes under flow conditions. Under low background pressure of 1 bar, the restrike numbers of the baseline low current discharge is strongly related to the flow velocity, an almost linear trend of increase is observed when the velocity is increasing from 10 m/s to 45 m/s. In contrast, there are no restrikes for boosted current discharge under 1 bar background pressure when the velocity is increasing up to 50 m/s. Under a higher background pressure of 23 bar, restrikes are observed with both the baseline and the boosted current discharge. The restrike number of the boosted current discharge is still lower compared to the baseline, but the difference is not as significant as in the low-pressure cases.

The restrike numbers under 23 bar background pressure is substantially lower than the restrike numbers when the low background pressure of 1 bar is used. To better explain this, the spark plasma lengths under different flow velocity are plotted in Figure 8 to show the history of the stretching and restrike of the plasma under 23 bar background pressure. It can be seen that the main reason for the reduced restrike number is probably due to the shortened discharge duration. Under a higher background pressure, a higher voltage is required to form the plasma channel so that the energy consumption is faster, and the duration is shorter. Within the shortened discharge duration, the restrike numbers are decreased. Overall the boosted current discharge can be

stretched longer. In addition, the boosted current discharge can be stretched to a similar length after restriking, in contrast to the baseline case where initially the plasma can be stretched long, but the similar length cannot be reached after the restrikes.

The two extreme background pressure cases are compared to show the spark discharge under flow conditions in a detailed manner. Then two medium background pressure conditions are selected to demonstrate the general trend of flow effects on spark process as shown in Figure 9. The flow velocity is in the similar range of 50-55
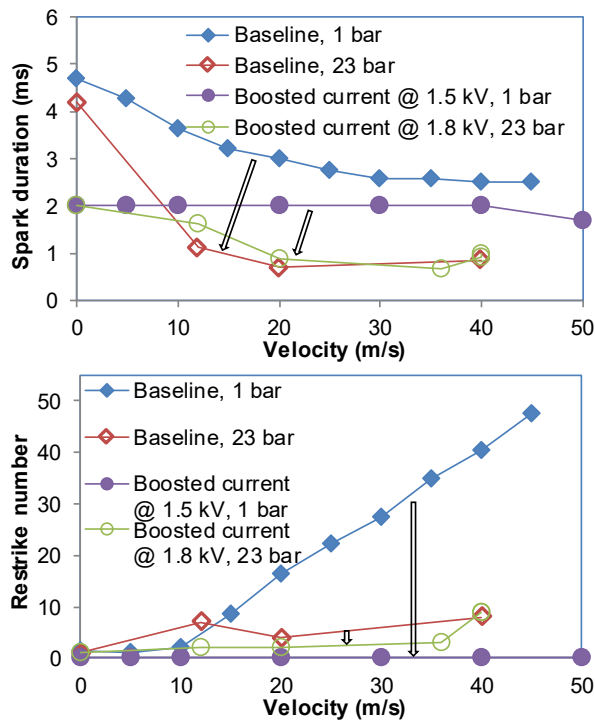
Figure 7: Effect of background pressure on discharge duration and restrike number
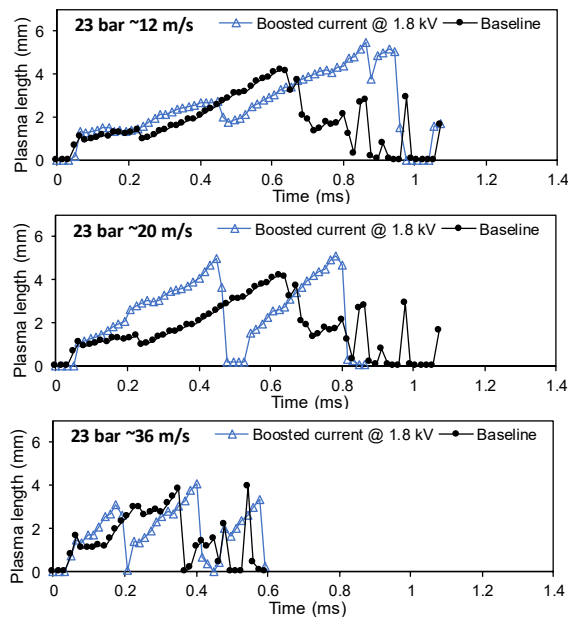
Figure 8: Effect of flow velocity on plasma length
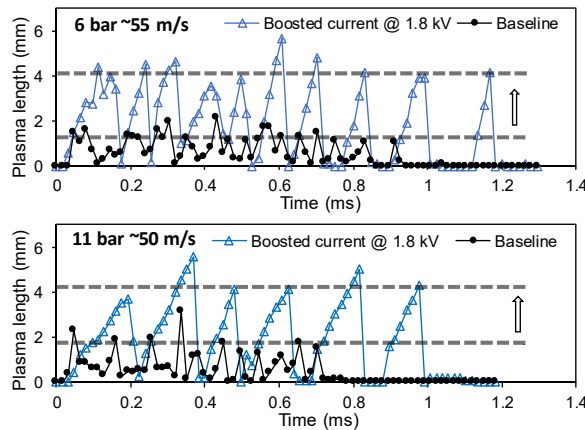
Figure 9: Effect of boosted current on the spark plasma length

m/s with a background pressure of 6 bar and 11 bar respectively. Under both background pressure conditions, the boosted current spark discharge is able to maintain longer stretched spark plasma channels and longer spark durations.

3.2 Improvement of ignition flame kernel development in high-speed flow

3.2.1 High energy plasma vs. long glow on single-pole spark plug

Combustion tests are carried out in the constant volume combustion chamber to investigate the impacts of different spark discharge on the ignition process under flow conditions. Three ignition strategies are used as shown in Figure 10. The three strategies include a low current discharge (80 mA) but with a long discharge duration (~13 ms); a boosted current discharge (~200 mA) with a shorter discharge duration (~3 ms); and a capacitor discharge with an extremely high transient current (~800 A) in a very short discharge duration (~15 μs). The background gas in these tests are stoichiometric methane-air mixture with CO_2 dilution of 8% volume ratio. The background pressure is 4 bar absolute pressure. The gas flow velocity is controlled at about 30 m/s. The flowing gas is with the same composition as the background gas.

The flame kernel development of the three spark strategies is recorded by the high-speed shadowgraph imaging system and the images are shown in Figure 11. The flame kernel is initiated at the spark gap and keeping attached to the spark plug during the discharge period. The dual coil discharge has the longest discharge duration of about 13 ms, so that an attached flame kernel is observed 10 ms after the break-down. The capacitor discharge is initiated with a very bright spark. The transient high current discharge release high energy in a very short period of time and a "micro explosion" is observed. This high transient energy generates a larger flame kernel compared to the previous two spark discharge strategies, as can be seen from the images recorded at 0.6 ms after breakdown.

However, due to the very limited duration, this initial advance is not carried to the later phase of flame kernel development. The flame areas of the three tests are shown in Figure 12. The results from these three tests suggest that both the discharge current level and discharge duration are important factors in the flame kernel develop ment under flow conditions. The flame kernel development is impaired when the spark current is too low or the discharge duration is too short.

10
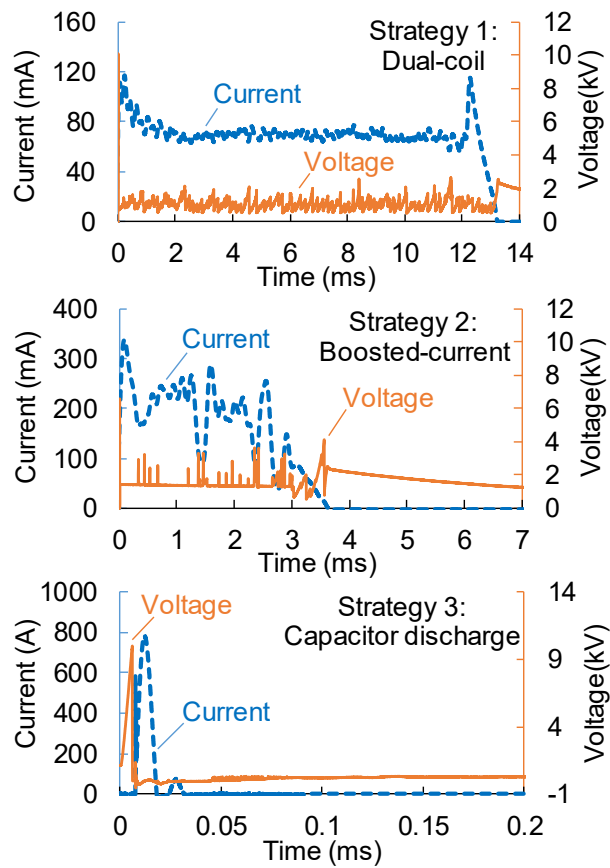
Figure 10: Voltage and current waveforms for dual-coil, boosted-current, and high energy capacitor discharge methods
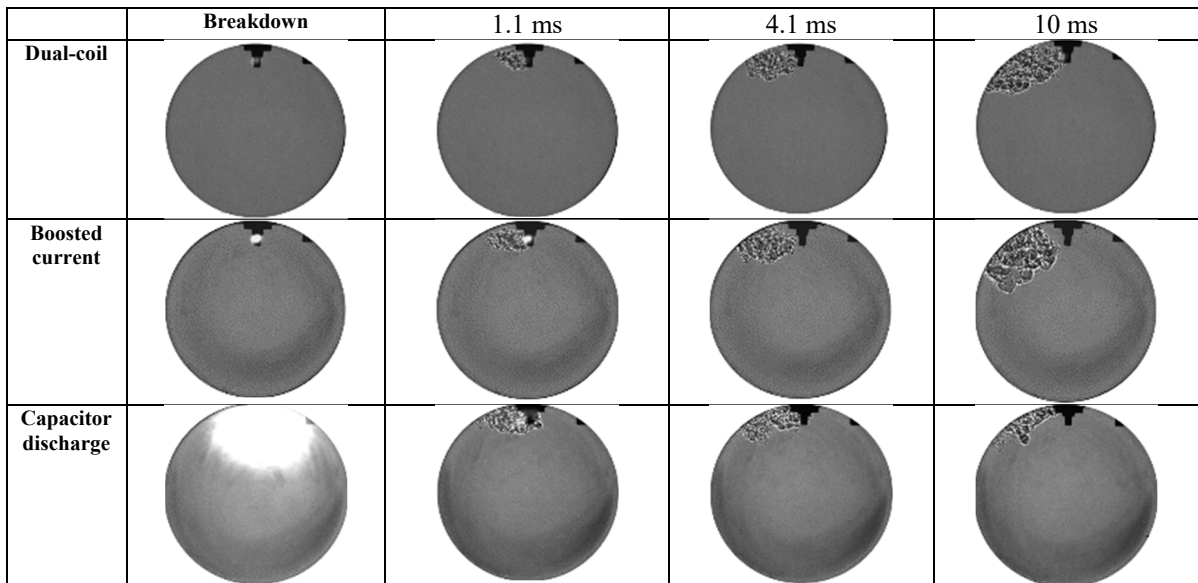
Methane-air mixture initial conditions: 4 bar pressure, 25 °C temperature; lambda 1.0; CO_2: 8%; Flow speed: 30m/s.

Figure 11: Comparison of the flame kernel images for different ignition strategies
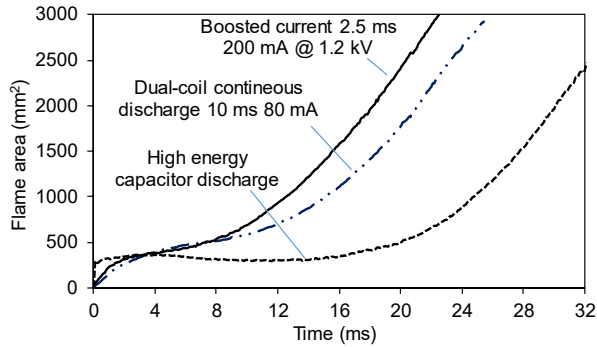
Figure 12: Comparison of flame area between three ignition methods in high-speed flow

3.2.2 Single-pole vs. Multi-core

In addition to the modulation of the spark discharge current and duration of a conventional spark ignition system, a patented three-core ignition system is used to increase the spark volume. The three-core configuration can increase the ignition volume to three times of the conventional ignition system. Moreover, the multiple ignition sites can also increase the tolerance of the ignition system to the variation in the stochastic in-cylinder charge conditions.

The combustion tests using the conventional spark ignition system and the patented three-core ignition system are performed in the same constant volume combustion chamber. The methane-air mixture with an excess air ratio of 1.6 is used as both the background gas and the flowing gas. The velocity is controlled at about 30 m/s and the background pressure is 4 bar absolute pressure. The discharge current and voltage waveforms of the two discharge processes are shown in Figure 13. The commanded duration for both spark systems are 3 ms. The discharge duration of the conventional spark system is about 0.7 ms. However, the discharge durations of each pole of the three-core spark plug are not the same, varying from 1 ms to 2.2 ms. This variation is because of the different flow conditions at the location of each pole.

The shadowgraph images of the combustion process are shown in Figure 14. The three-core spark plug has significantly larger flame kernel compared to the single pole spark plug. The flame kernel form the single-pole spark plug is small and the flame propagation is largely affected by the flow conditions. The flame survives in areas behind the spark plug due to the lower flow velocity. In this case, higher
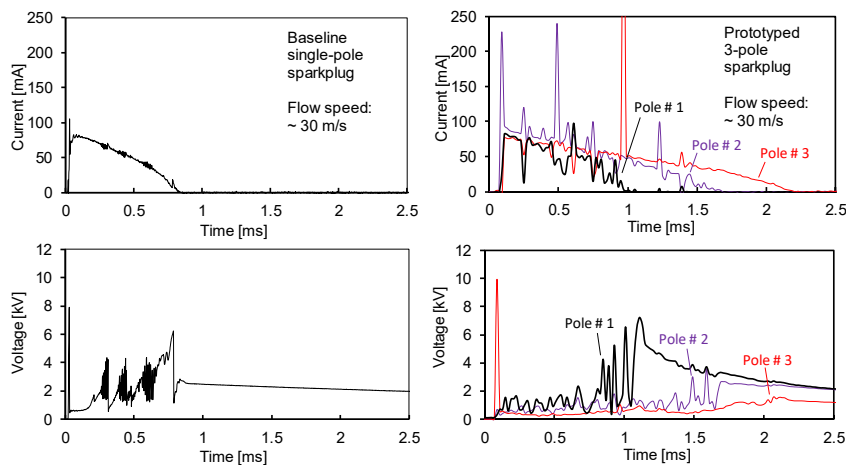
Figure 13: Discharge waveforms of single-core and three-core sparkplug

Variations are expected compared to the three-pole case where a larger flame kernel survives even in the pathway of the gas flow.

The three-core technology can also be combined with various ignition strategies mentioned in section 3.2.1, therefore, triple the amount of energy wants to be transferred into the combustion chamber to help establishing the flame kernel. Figure 15 and figure 16 demonstrate two cases applying boosted current strategy and high-energy capacitor discharge strategy to all three spark gaps, respectively. Detailed investigation still needs to be done to pin point the effectiveness of these strategies

Methane-air mixture initial conditions: 4 bar pressure, 25 °C temperature; lambda 1.6; CO_2: 0%; Flow speed: ~30m/s.
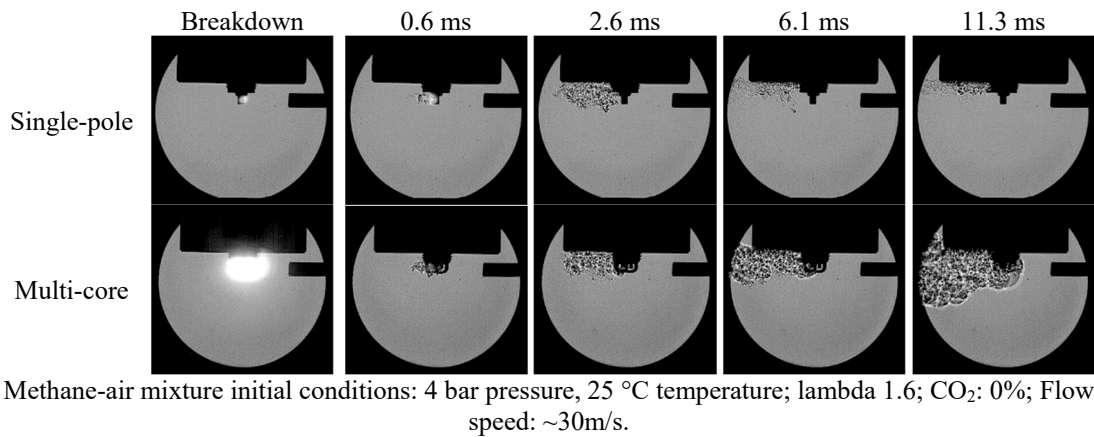
Figure 14: Flame kernel images of single pole and multi-core strategy

Methane-air mixture initial conditions: 4 bar pressure, 25 °C temperature; lambda 1.6; CO_2: 0%; Flow speed: ~30m/s.
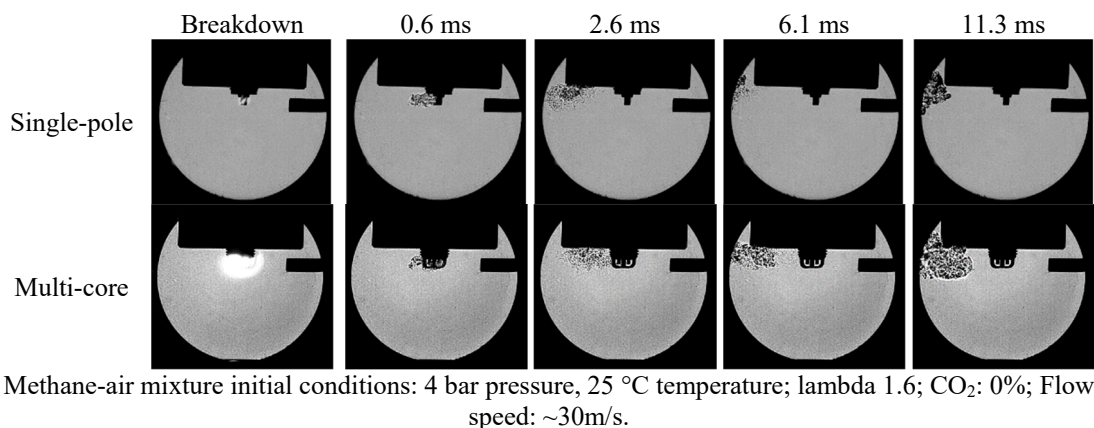
Figure 15: Boosted current strategy via single pole and multi-core sparkplug

Methane-air mixture initial conditions: 4 bar pressure, 25 °C temperature; lambda 1.6; CO_2: 0%; Flow speed: ~30m/s.
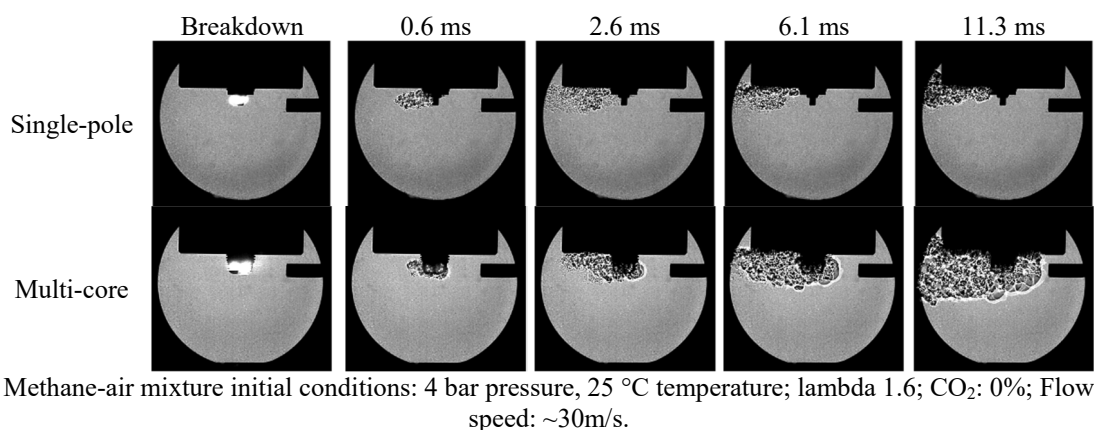
Figure 16: High energy strategy via single pole and multi-core sparkplug

under different energy level as well as background conditions (cross flow speed, pressure, temperature), but the figures shows a clear advantage when energy delivery amount is tripled. When in-cylinder air movement is intense, the size of the initial flame kernel is essential for flame to propagate. The three flame kernels generated by the three independent spark gaps can merge with each other and form a flame kernel in larger, therefore, shorten the transition period from initial flame kernel to a self-sustained flame kernel.

3.3   Effect of advanced ignition strategies on lean/diluted gasoline combustion – evaluation on single-cylinder research engine

3.3.1 Effect of boosted current on lean-burn engine control

The boosted current ignition device can generate a strong spark channel with a current level up to 500 mA and an extended glow duration up to 10 ms. The current boosting command is triggered by the falling edge of the ignition coil charging control signal. The current level is adjusted by the regulation of the voltage applied onto the spark gap after the breakdown. To understand the effect of the current level on the lean burn operation, tests were conducted with different sparking current profiles. The parameter settings of different ignition strategies are given in table 4. The engine was operated at lambda 1.4. Five different ignition strategies were tested. The strategy 1 and strategy 2 utilize conventional ignition energy control methods. The rest ones are boosted current ignition strategies with the current level changing from 200 mA to 500 mA. The current waveforms of the five different ignition strategies are given in figure 17.

Spark timing sweep tests are conducted for all five ignition strategies under same engine operating conditions. The engine IMEP, COV of IMEP, and the misfire rates during the spark timing sweep tests are shown in figure 18. It is observed that the boosted current is able to obtain higher IMEP and lower cycle to cycle variation. The 500 mA boosted current case has stronger ability to stabilize the combustion process consistently compared with the 200 mA case. It is obvious that the impacts of boosted current on the combustion phasing is more significant when the spark timing is between 305 °CA ~315 °CA. The ignition delay and the CA50 under different spark timing are shown in figure 19. The boosted current ignition strategy can reduce the ignition delay and improve the controllability over the CA50.

Table 4. Test conditions for baseline and boosted current ignition strategies

	Peak current (mA)	Charging duration (ms)	Current boost	Spark plug
Strategy 1	30 mA	2	NA	Stock Iridium
Strategy 2	100 mA	5	NA	Stock Iridium
Strategy 3	200 mA	2	2 ms @ 200 mA	Stock Iridium
Strategy 4	500 mA	2	2 ms @ 500 mA	Stock Iridium
Strategy 5	500 mA	5	2 ms @ 500 mA	Stock Iridium
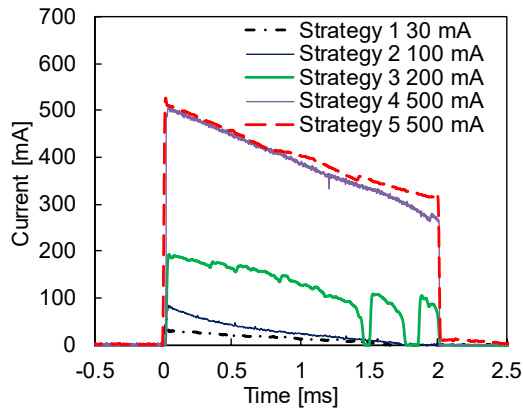
Figure 17. Current waveforms for various ignition strategies
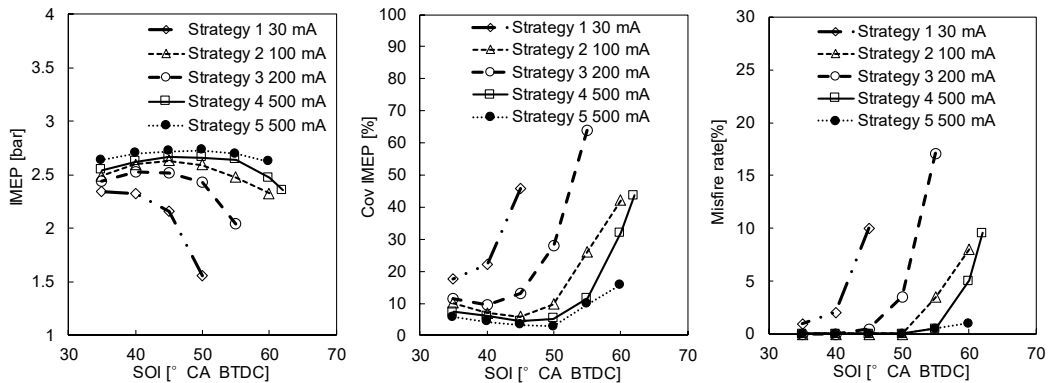
Figure 18: Effect of boosted current ignition strategies on lean burn stability (CR 9.2, λ= 1.4)
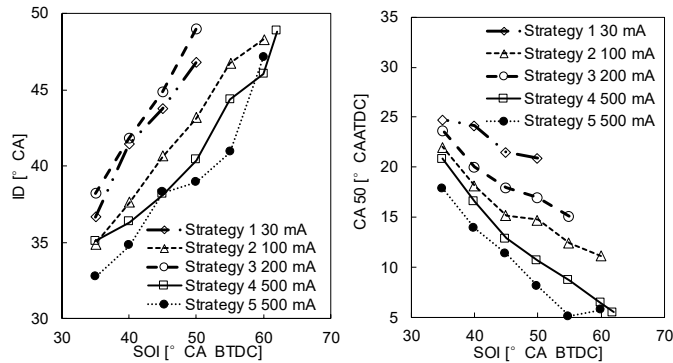
Figure 19: Effect of boosted current ignition strategies on ignition delay and CA50 (CR 9.2, λ= 1.4)

3.3.2 Effect of multi-core on lean-burn control

Previous investigations indicate that the three-core ignition can improve the lean-burn gasoline combustion thus achieve fuel efficiency gain because of the extension of lean limits. The three-core ignition can improve the combustion phasing control for the low load ultra-lean operation. The results were collected at the compression ratio of 13:1. Because of the high compression ratio, the engine load was limited up to 6 bar IMEP because of the severe knocking. The newer results were collected from the single-cylinder engine with a lowered compression ratio of 9.2:1. The engine load was extended to 10 bar IMEP. Test results of the spark timing sweep with lambda 1.5 and 1.66 are given in figure 20. At lambda 1.5, the three-core behaves very similar to the single-pole baseline ignition, while the difference was much bigger at lambda 1.66.

With the spark timing advanced, the baseline single-pole ignition cannot maintian the target IMEP. Severe cyclic variations are also observed. Cylinder pressure and heat release rate curves of example cases at spark timing of -40 °CA ATDC are shown in figure 21. The three-core ignition can noticeably advance the heat release rate thereby leading to higher cylinder pressure, for both lambda 1.5 and 1.66 cases.
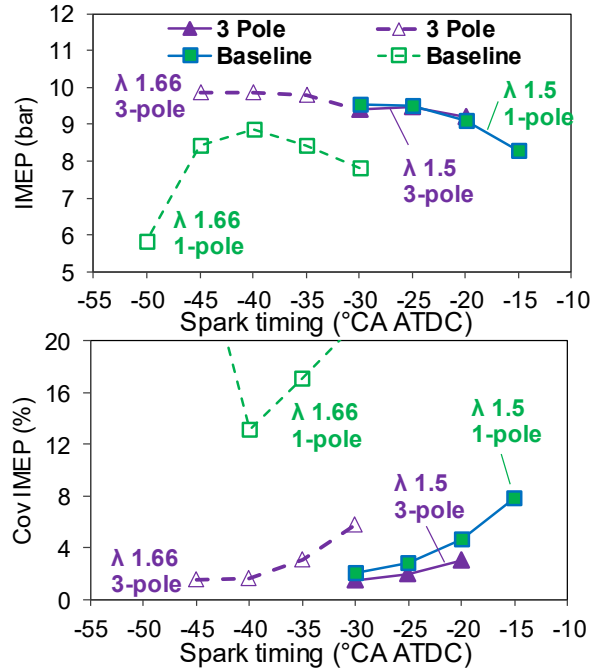
Figure 20: Effect of three-core ignition strategies on lean burn engine stability

Target IMEP: 10 bar; λ =1.5;
Spark timing: -40 °CA ATDC
P_int. : 2.2 bar; 1300 rpm; CR: 9.2 :1

Target IMEP: 10 bar; λ =1.66;
Spark timing: -40 °CA ATDC
P_int. : 2.2 bar; 1300 rpm; CR: 9.2 :1
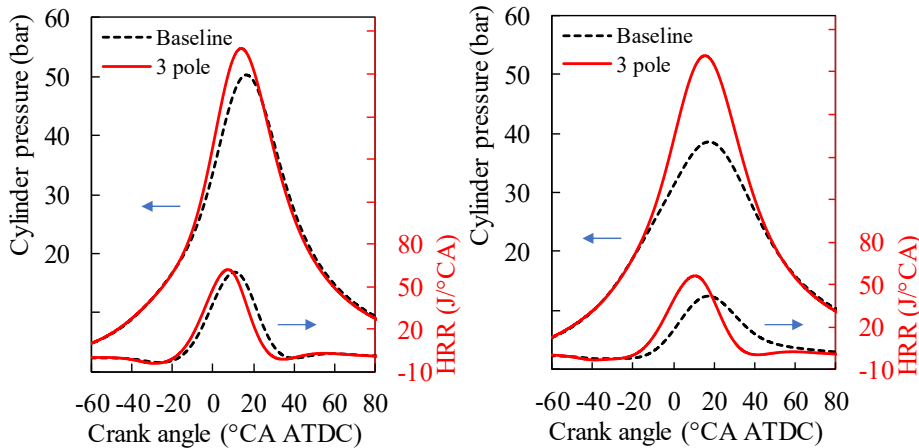
Figure 21: Effect of three-core ignition strategies on cylinder pressure and heat release rate

The combustion and emissions parameters for lean burn operation are given in figure 22, comparing the effects of three-core ignition and single-pole baseline ignition strategies. The three-core ignition exhibits better controllability over the CA50 for both lambda 1.5 and 1.66 cases. The standard deviation of CA50 is also improved by the three-core ignition. When the spark timing is advanced under the lean burn condition,

the engine is achieving maximum IMEP without knocking. Therefore, an increasing trend of the indicated thermal efficiency is observed, except for the baseline ignition at lambda 1.66. The three-core ignition leads to a higher level of NOx emissions that means a stronger combustion, compared with the baseline single-pole ignition strategy. The HC and CO emissions are reduced by the three-core ignition, which suggests improved combustion efficiency of the lean-burn operation.
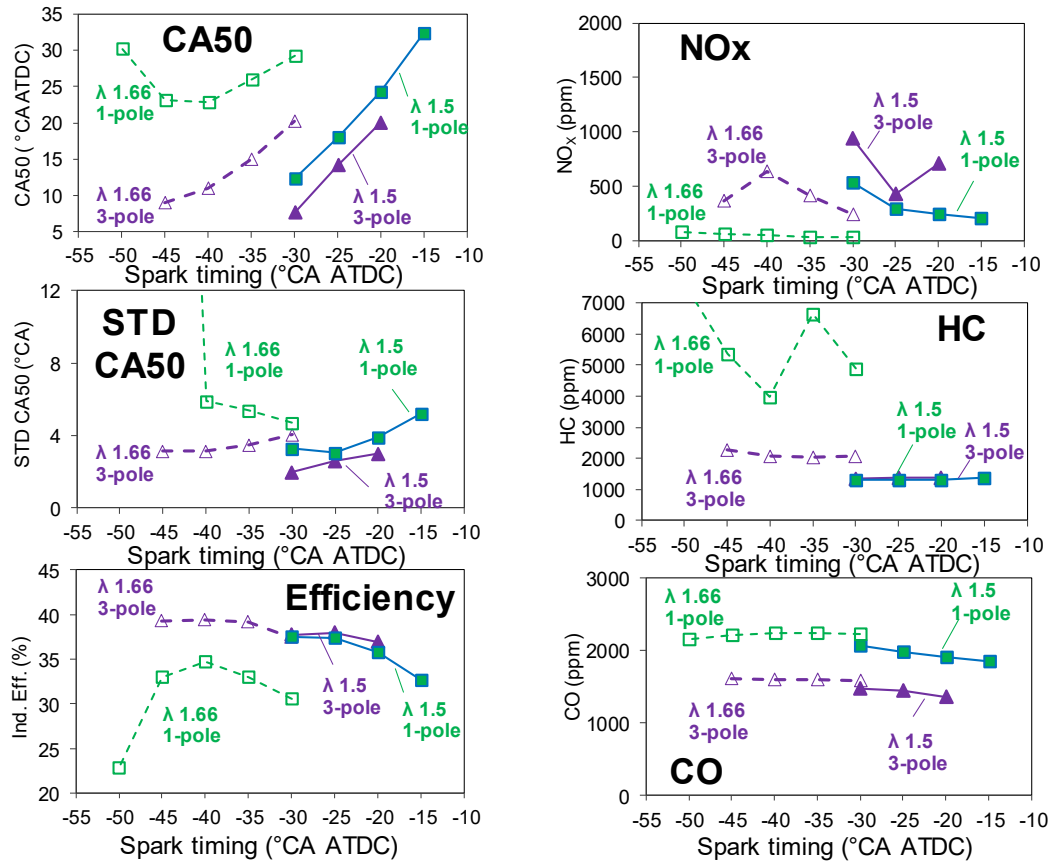
Figure 22: Effect of three-core ignition strategies on combustion and emissions of lean burn

3.3.3 Comparison between multi-core and multi-coil single-pole ignition strategies

The three-core igniter uses three independent ignition coils for ignition energy distribution control. The output of the three ignition coils can also be bundled together to deliver the ignition energy to single spark gap. Bundling the output of the three coils can significantly enhance the spark current of the single-pole iridium spark plug. Three spark discharge cases are compared in figure 23. Case 1 uses the three-core igniter with each pole energized by one of the three independent ignition coils. The peak spark current in case 1 is about 50 mA. Case 2 uses the reference iridium spark plug connecting to one of the ignition coils. A peak current of about 110mA is achieved for case 2. Case 3 discharge three coils simultaneously onto the single-pole iridium spark plug, producing a peak spark current of about 280 mA. The charging duration for case 2 and case 3 are kept the same, meaning that the stored energy in the primary winding of the ignition coils for case 3 should be about 3 times of that for case 2. Case 1 uses a charging duration shorter than those for case 2 and case 3.
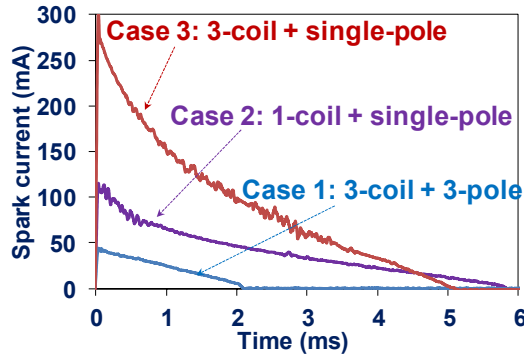
Figure 23: Spark current waveforms for three-core and 3-coil ignition strategies
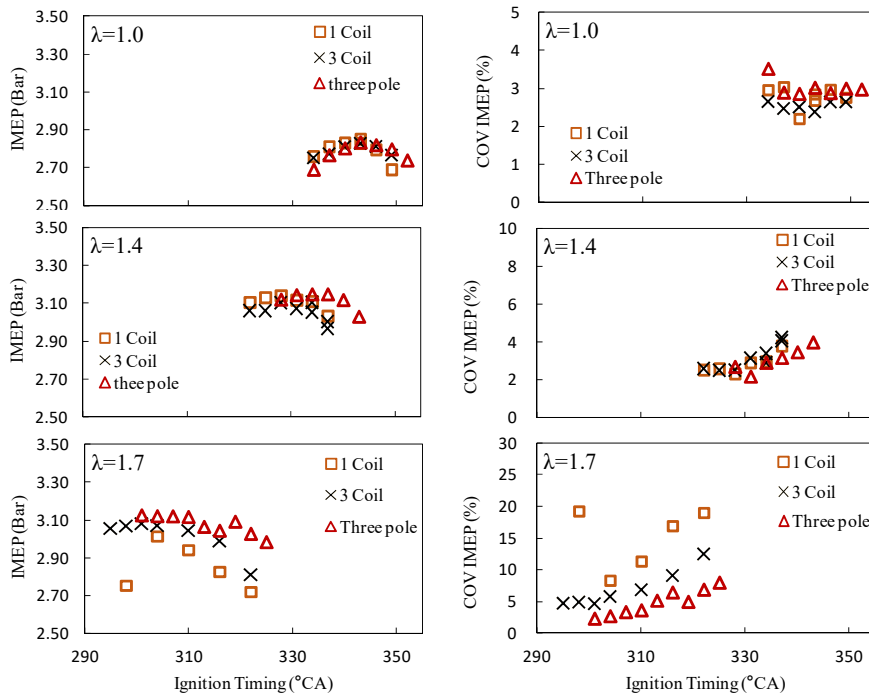
Figure 24: Effect of three-core strategy on lean burn engine stability
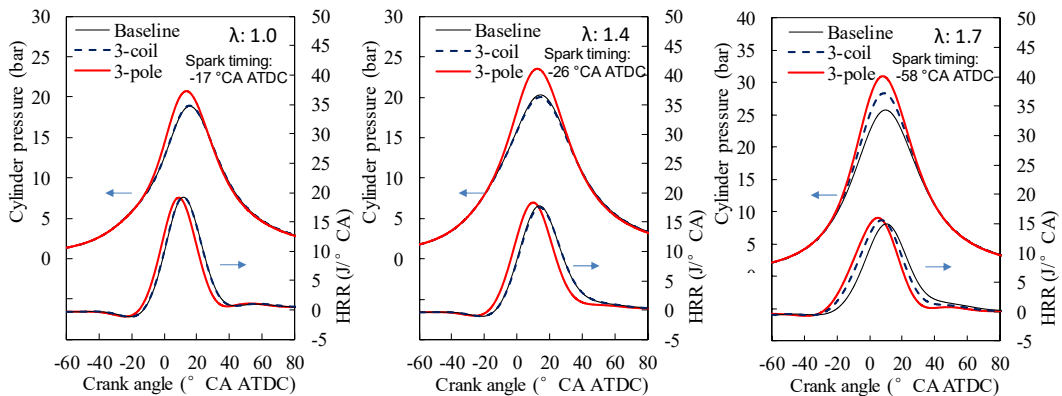
Figure 25: Effect of three-core strategy on cylinder pressure and heat release rate

Experiments are conducted to evaluate the three ignition strategies given in figure 23 for lambda of 1.0, 1.4, and 1.7. The engine IMEP and the COV of IMEP against the spark timing are plotted in figure 24. For engine operations with near stoichiometric and moderate lean mixtures, the ignition behaviors are very similar for different ignition strategies. For the very lean mixture with λ of about 1.7, the three-core ignition energy distribution strategy exhibits lower COV of IMEP, shorter ignition delay and less varying CA50. The cylinder pressure and heat release rate for the three ignition strategies at different lambda are given in figure 25. The enhancement of spark current by bundling the outputs of three coils does improve the ignition for the single-pole sparkplug, whereas the benefits are less prominent than that of using three-core igniter with a lower peak current for each spark.

3.3.4 Comparison between multi-core and boosted current single-pole strategies

Three ignition strategies are compared at 10 bar IMEP with lambda 1.5 and 1.66. The parameter settings of three ignition strategies are given in table 5. The purpose of this test is to compare the effect of the boosted current single-pole strategy with the three-core ignition strategy for lean-burn combustion control. The baseline ignition strategy generates a spark with a peak current of 100 mA. The boosted current strategy supplies a 2 ms pulse with 500 mA over the baseline spark. For the three-core ignition strategy, each of the poles has a discharge current level the same as that of the baseline ignition strategy. Spark timing sweep experiments are performed for each ignition strategy at lambda 1.5 and 1.66 respectively. The engine load target is 10 bar IMEP.

The combustion parameters are compared in figure 26 for the different ignition strategies. During the spark timing sweep, the three-core performs the best among the three ignition strategies, in terms of the combustion phasing control sensitivity and the engine stability. The boosted current strategy can also improve the lean-burn combustion control, but the effect is less prominent compared with the three-core ignition strategy under the selected test conditions. The cylinder pressure and the heat release rate curves are compared in figure 27. The spark timing is set at -40 °CA ATDC for the three cases and the lambda was 1.66. For the same spark timing, the three-core ignition generates the earliest heat release and the highest cylinder pressure. On the scattering plot of IMEP vs CA50 (figure 28), the three-core ignition exhibits the earliest CA50 and the least scattering of both IMEP and CA50, compared to the boosted-current and the baseline ignition strategies.

Table 5: Test conditions for baseline, boosted current and three-core comparison

	Peak current (mA)	Charging duration (ms)	Current boost	Energy to sparkplug (mJ)	Spark plug
Baseline	100 mA	5	NA	150 mJ	Stock Iridium
Boosted current	500 mA	5	2 ms @ 500 mA	~2 J	Stock Iridium
three-core	100 mA	5	NA	450 mJ	Three-core
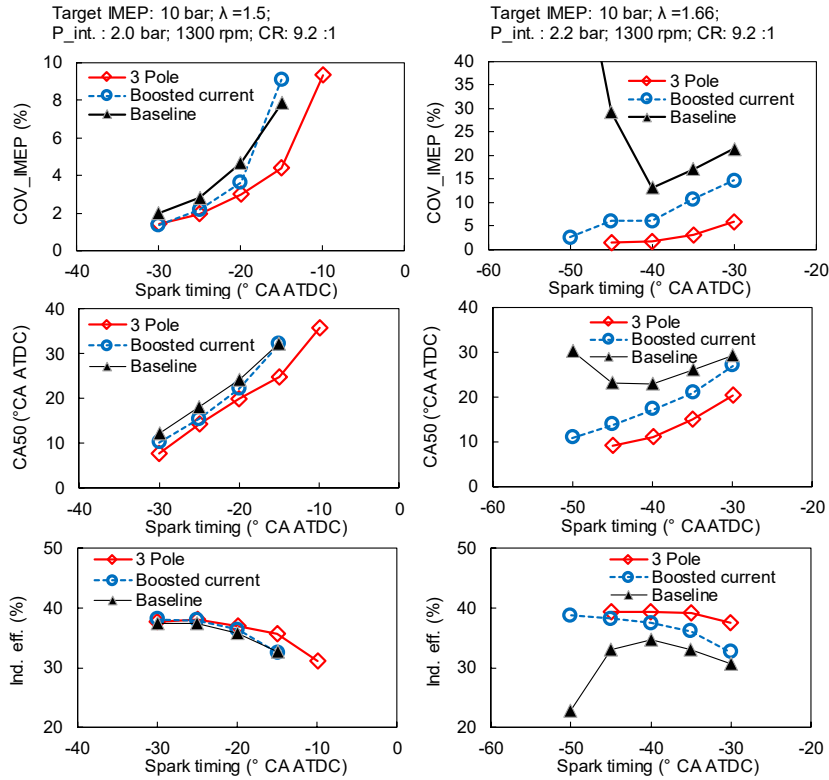
Figure 26: Combustion parameters for the various ignition strategies
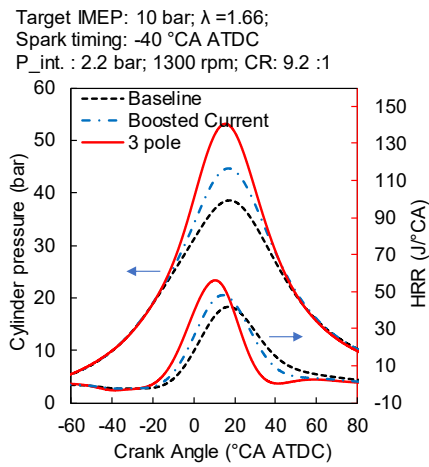
Figure 27: Cylinder pressure and HRR for various ignition strategies
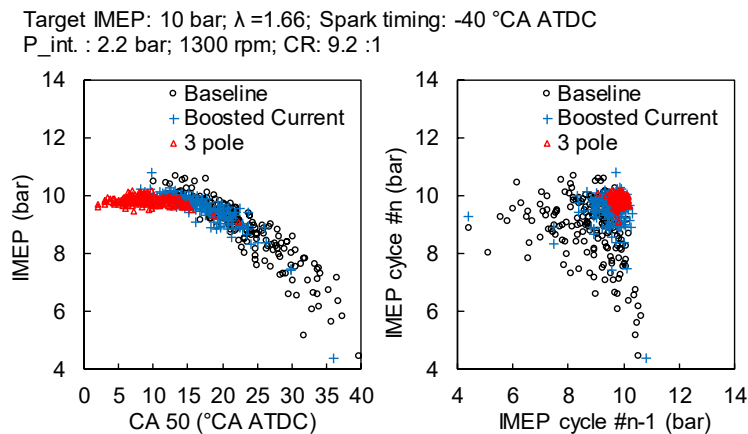
Figure 28: IMEP scattering plots for various ignition strategies

3.4   Evaluation of multi-core ignition on multiple-cylinder production engine under high dilution

Comparison tests have been conducted on a production gasoline engine for the three-core igniter and the original single-pole spark plug. The comparison comprises a baseline test with the production ignition system and a repeat test with a three-core igniter installed in cylinder 1 under the same test conditions. In both tests, the engine runs at 1500 rpm and 2.62 bar BMEP, the Ford World Wide Mapping Point (WWMP); cam timing retard is employed to increase the trapped exhaust gas and thus to achieve higher internal EGR dilution. The retarded cam timing and diluted combustion can improve the engine fuel economy at the tested engine speed/load conditions. As the dilution gradually increases, an overall trend of reduced BSFC is observed with the greatest improvement reaching ~5%. However, the BSFC trended to decrease at the highest dilution level when the cam retard is set to 50 degrees. The primary cause is the late combustion phasing and incomplete combustion. A large portion of the fuel consumption improvement comes from the reduction of pumping loss. At a constant engine load of 2.62 bar BMEP, the engine MAP increases; therefore, the reduced vacuum in the intake manifold ultimately results in less pumping work. Since the engine runs at a better brake efficiency, it requires less air and fuel to achieve 2.62 bar BMEP. As the cam phasing retarded, the ISFC remains nearly unchanged until the cam retard approaches 45 and 50 degrees. Combustion phasing and combustion duration of three-core and the baseline ignition strategies are compared in figure 29. As can be seen, the 3-core ignition can shorten the combustion duration and move forward the combustion phasing, with the same spark timing of the baseline single-pole ignition. In figure 30, comparisons of the cylinder pressure and the mass fraction burnt are made between three-core igniter and the baseline spark plug, for the low and high dilution cases respectively. In both cases, three-core igniter leads to an earlier start of combustion and a faster burn rate. The three-core igniter results in a higher peak cylinder pressure compared with the baseline spark plug with the same spark timing. The difference is more noticeable for the high dilution level associated with the large VCT retard angle.
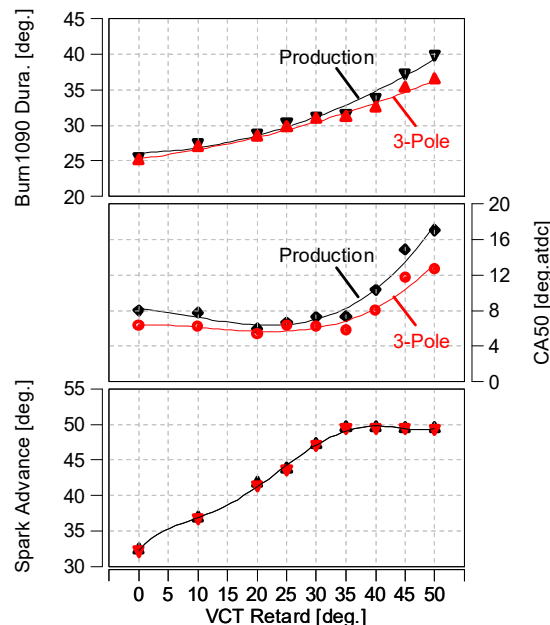
Figure 29: Effect of three-core ignition strategies on burning duration and combustion phasing
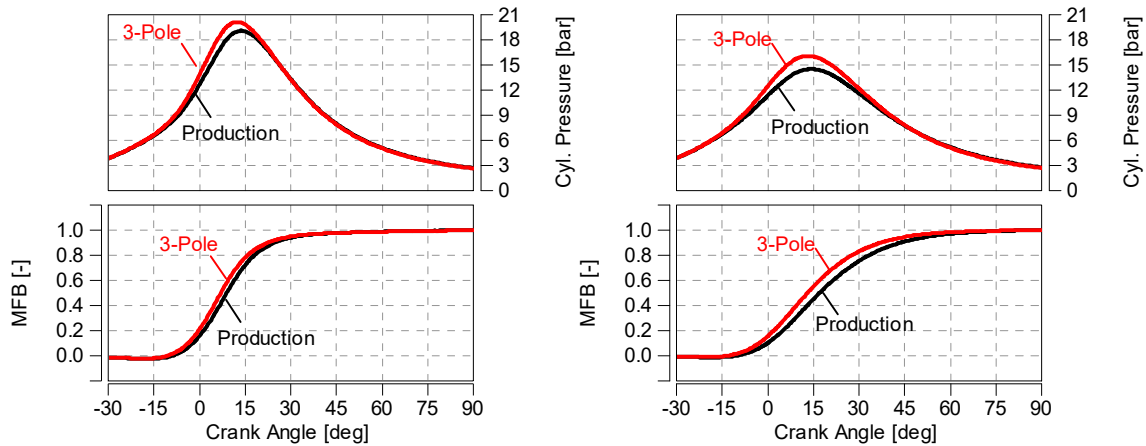
Figure 30: Effect of three-core ignition strategies on the cylinder pressure and MFB under low and high dilution levels
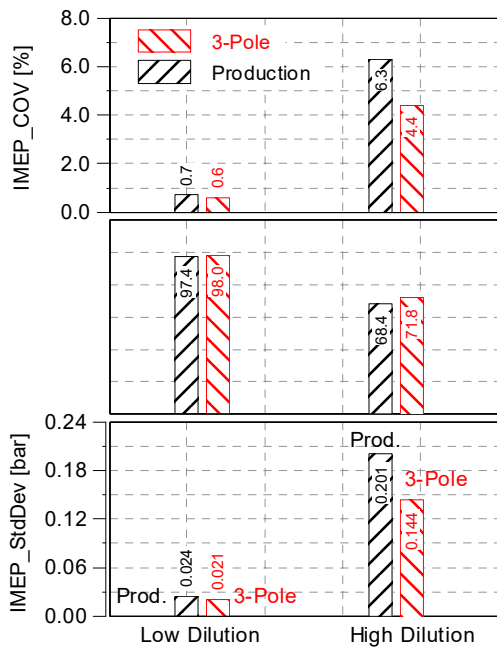
Figure 31: Effect of three-core ignition strategies on the engine stability under low and high dilution levels
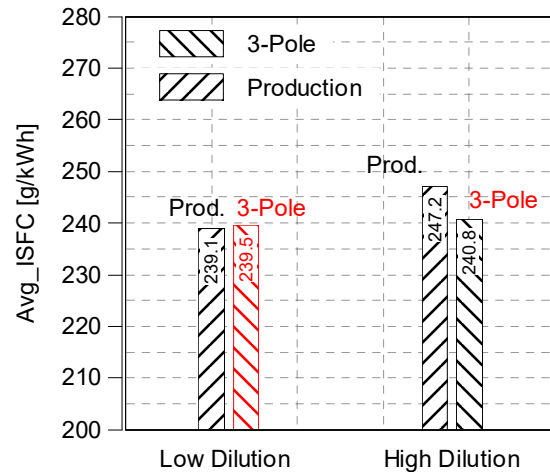
Figure 32: Effect of three-core ignition strategies on ISFC under low and high dilution levels

Figure 31~32 indicate the variability of the IMEP of cycle #1. The COV, LNV, and Std of IMEP at the low dilution level has marginal change between the tests with the three-core igniter and the baseline spark plug. At the high dilution level, the three-core igniter decreases the COV and the Std of IMEP, while the LNV of IMEP is increased slightly. For a given combustion system, the ISFC of a gasoline engine combustion cycle is affected by the phasing, duration and completeness of the combustion process. At a low dilution level, the three-core igniter has insignificant impact on the ISFC, because of the favorable mixture for a fast ignition, flame propagation and complete combustion in relatively short periods. However, at the high dilution level, the three-core igniter improves the combustion phasing more prominently, thereby reducing the ISFC compared with the baseline ignition. The use of three-core igniter leads to a reduction of 2.5% in ISFC at the high dilution level, compared with the baseline spark plug ignition. The ultimate benefit of using the three-core igniter on the multiple cylinders remains in the future work.

Conclusions

Ignition technologies with enhanced ignition capability including discharge energy profiling as well as multi-core ignition system are introduced in this paper, and their effects on ignition improvements are investigated on both constant volume combustion vessels and research engines. Conclusions can be drawn as below.

(1)   Under flow condition, boosted discharge current can significantly increase the length of the plasma channel, and reduce the frequency of the blow-off event.

(2)   A longer glow phase, boosted discharge current, and transient high ignition energy can all enhance the ignition ability of the plasma channel; the boosted discharge current strategy appears to be most effective under CO_2 diluted conditions through test on the constant volume combustion chamber.

(3)   Engine test results show that the ignition technologies are most effective when intake charge is at the boundary of lean/dilution limit; single cylinder engine test under 10 bar IMEP shows a indicated thermal efficiency improvement of 6% when engine is running under 1.66 using three-core ignition system; while ISFC is improved by 5% on a Ford multi-cylinder engine at 2.6 bar IMEP, 1500 rpm when using a multi-core ignition system under high EGR dilution condition.

4   Acknowledgements

5   References

1. Wei, H., Zhu, T., Shu, G., Tan, L., et al. "Gasoline Engine Exhaust Gas Recirculation–A Review," *Applied Energy.* 99:534–44, 2012, doi:10.1016/ j.apenergy. 2012.05.011.

2. Gallon, E., Fontana, G., Palmaccio, R., "Effects of Exhaust Gas Recycle in a Downsized Gasoline Engine," *Applied Energy.* 105:99–107, 2013, doi: 10.1016/j.apenergy.2012.12.046.

3. Takahashi, D., Nakata, K., Yoshihara, Y., Ohta, Y. et al., "Combustion Development to Achieve Engine Thermal Efficiency of 40% for Hybrid Vehicles," SAE Technical Paper 2015-01-1254, 2015, doi: 10.4271/2015-01-1254.

4. Zheng, M., Tan, Y., Mulenga, M., and Wang, M., "Thermal Efficiency Analyses of Diesel Low Temperature Combustion Cycles," SAE Technical Paper 2007-01-4019, 2007, doi:10.4271/2007-01-4019.

5. Gukelberger, R., Alger, T., Gingrich, J., and Mangold, B., "Impact of Operating Parameters on Ignition System Energy Consumption," SAE Technical Paper 2014-01-1233, 2014, doi:10.4271/2014-01-1233.

6. Hampe, C., Kubach, H., Spicher, U., et al. "Investigations of Ignition Processes Using High Frequency Ignition," SAE Tech Paper, 2013-01-1633, 2013; doi: 10.4271/2013-01-1633.

7. Shiraishi, T., Urushihara, T., Gundersen, M., "A Trial of Ignition Innovation of Gasoline Engine by Nanosecond Pulsed Low Temperature Plasma Ignition," Journal of Physics D: Applied Physics, 2009, 42: 135208; doi: 10.1088/00223727/42/13/135208.

8. Sjöberg, M., Zeng, W., Singleton, D., Sanders, J., et al. "Combined Effects of Multipulse Transient Plasma Ignition and Intake Heating on Lean Limits of Well-mixed E85

DISI Engine Operation," SAE Int J Engines, 2014, 7(4):1781-1801; doi: 10.4271/2014-01-2615.

9. Rohwein, G. J., "An Efficient Power-Enhanced Ignition System," *IEEE Transactions on Plasma Science,* 25(2): 306-310, 1997, doi:10.1109/27.602504.

10. Rohwein, G. and Camilli, L., "Automotive Ignition Transfer Efficiency," SAE Technical Paper 2002-01-2839, 2002, doi:10.4271/2002-01-2839.

11. Yoshida, K., Shoji, H., and Tanaka, H., "Performance of Newly Developed Plasma Jet Igniter," SAE Technical Paper 1999-01-3327, 1999, doi:10.4271/1999-01-3327.

12. Dale, J.D., Checkel, M.D., Smy, P.R., "Application of High Energy Ignition Systems to Engines," *Progress in Energy and Combustion Science*, 23(5-6): 379-398, 1997, doi:10.1016/S0360-1285(97)00011-7.

13. Heise, V., Farah, P., Husted, H., and Wolf, E., "High Frequency Ignition System for Gasoline Direct Injection Engines," SAE Technical Paper 2011-01-1223, 2011, doi:10.4271/2011-01-1223.

14. Alger, T., Gingrich, J., Mangold, B., and Roberts, C., "A Continuous Discharge Ignition System for EGR Limit Extension in SI Engines," SAE Int. J. Engines 4(1):677-692, 2011, doi:10.4271/2011-01-0661.

15. Hall, M., Matthews, R., and Ezekoye, O., "Railplug Ignition Operating Characteristics and Performance: A Review," SAE Technical Paper 2007-01-1832, 2007, doi:10.4271/2007-01-1832.

16. Suess, M, Guenthner, M, Schenk, M, et al., "Investigation of the Potential of Corona Ignition to Control Gasoline Homogeneous Charge Compression Ignition Combustion," P I MECH ENG D-J AUT, 2011, 226(2): 275-286, doi: 10.1177/0954407011416905.

17. Stevens, C. A., Pertl, F. A., Hoke, J. L., et al. "Comparative Testing of a Novel Microwave Ignition Source, the Quarter Wave Coaxial Cavity Igniter," J Phys D: Appl Phys, 2011, 225(12): 1633-1640, doi: 10.1177/0954407011411389.

18. Ryu, S. K., Won, S.H., Chung, S. H., "Laser-Induced Multi-point Ignition with Single-Shot Laser Using Conical Cavities and Prechamber with Jet Holes," Proc Combustion Inst, 2009, 32(2): 3189–3196, doi:10.1016/j.proci.2008.05.080.

19. US Patent 9.441.604, "Multi-coil Spark Ignition System", M Zheng, S Yu, K Xie.

20. Xie, K., Yu, S., Zheng, M., "Investigation of Multi-pole Spark Ignition on Flame Kernel Development and in Engine Operation," Proceedings of the ASME 2016 Internal Combustion Fall Technical Conference, Oct 9-12, 2016, Greenville, SC, USA, ICEF2016-9474

21. Yu, S., Xie, K., Tan, Q., Wang, M. et al., "Ignition Improvement of Premixed Methane-Air Mixtures by Distributed Spark Discharge," SAE Technical Paper 2015-01-1889, 2015, doi:10.4271/2015-01-1889.

22. Yu, S., Wang, M., and Zheng, M., "Distributed Electrical Discharge to Improve the Ignition of Premixed Quiescent and Turbulent Mixtures," SAE Technical Paper 2016-01-0706, 2016, doi:10.4271/2016-01-0706.

23. Yu, X., Yang, Z., Yu, S., et al., "Boosted Current Spark Strategy for Lean Burn Spark Ignition Engines," SAE Technical Paper 2018-01-1133, 2018.

24. US Patent Application 15/162,473, "High Power Breakdown Spark Plug", Inventors: M Zheng, S Yu, L Li, M Liu.

25. Yu, S., Xie, K., Yu, X., et al. The Effect of High-Power Capacitive Spark Discharge on the Ignition and Flame Propagation in a Lean and Diluted Cylinder Charge," SAE Technical Paper 2016-01-0707, 2016.

26. US Patent 9.484.719, "Active Control Resonant Ignition System", Inventors: M Zheng, S Yu, M Wang.

6   Definitions/Abbreviations

EGR	Exhaust Gas Recirculation
SI	Spark Ignition
CA	Crank Angle
MFB	Mass Fraction Burnt
CA5	Crank Angle of 5% MFB
CA50	Crank Angle of 50% MFB
TDC	Top Dead Center
ATDC	After Top Dead Center
BTDC	Before Top Dead Center
CO_2	Carbon Dioxide
CH_4	Methane
AWG	American Wire Gauge
IGBT	Insulated Gate Bipolar Transistor
FPGA	Field Programmable Gate Array
IMEP	Indicated Mean Effective Pressure
$t_{5\%}$	Time to 5% mass burn fraction
$t_{50\%}$	Time to 50% mass burn fraction

1.2 Ignition by Capacitance Sparks and Non-Thermal Plasmas

Johann-Robert Kummer, Stefan Essmann, Detlev Markus,
Holger Grosshans, Ulrich Maas

Abstract

For optimization of combustion engines understanding the ignition of combustible mixtures by electrical discharges is of crucial importance. A combined experimental-numerical approach is employed to gain deeper insight into the related physicochemical processes during the ignition by thermal and non-thermal plasmas. In both applications energies near the minimum energy necessary for ignition have been imposed. The temporal development of the plasma kernel and the shock wave measured using a schlieren method in combination with numerical simulations were used to quantify the ignition efficiency of a capacitance sparks. Radial profiles of OH radicals measured by laser induced fluorescence (LIF) were compared with numerical results to validate the numerical tools which now can be used to model ignition of advanced biofuels. Volumetric ignition by non-thermal plasmas has been investigated through numerical simulations which were used to examine the temporal development of temperature and radicals inside the plasma channel in detail.

Kurzfassung

Für die Optimierung von Verbrennungsmotoren ist das Verständnis der Zündung von brennbaren Gemischen durch elektrische Entladungen von entscheidender Bedeutung. Ein kombinierter experimentell-numerischer Ansatz wird verwendet, um tiefere Einblicke in die physikalisch-chemischen Prozesse während der Zündung durch thermische und nicht-thermische Plasmen zu erhalten. Bei beiden Anwendungsbeispielen wurden Energien im Bereich der mindestens zur Zündung notwendigen Energie untersucht. Die zeitliche Entwicklung des Plasmakerns und der Stoßwelle mittels einer Schlieren-Methode zusammen mit numerischen Simulationen wurde verwendet, um die Effizienz einer Funkenzündung zu quantifizieren. Radiale Profile von OH-Radikalen, die durch laserinduzierte Fluoreszenz (LIF) gemessen wurden, werden mit numerischen Ergebnissen verglichen, um die numerischen Werkzeuge zu validieren, die nun zur Modellierung der Zündung nachhaltig erzeugter Biokraftstoffe verwendet werden können. Eine volumetrische Zündung kann mit nichtthermischen Plasmen erreicht werden. Hier wurden numerische Simulationen verwendet, um die zeitliche Entwicklung von Temperatur und Radikalen im Plasmakanal im Detail zu untersuchen.

1   Introduction

The need for clean combustion engines has grown in scope and importance over the years due to increasing shortage of energy resources and growing future environmental concerns. The transportation sector of the developed world depends mainly on energy released during the burning of fossil fuels, such as coal, oil, and natural gas. However, the release of greenhouse gases contributes to global climate change. In 2014, transport was responsible for 20 % of the direct CO_2 emissions in Germany [1], mainly due to road traffic. To meet transport demands of the future, there is a need to find alternative energy sources and alternative combustion engines especially with respect to the growing need for energy from the emerging countries. The EU's renewable energy directive 2009/28/EC demands a reduction of greenhouse gas emissions by at least 20 % and an increase of the share of renewable energy to at least 20 % of consumption by 2020 [2]. All EU countries are also required to have at least a 10 % share of renewable energy in their transportation sector. In can be expected that the EU will increase its climate, renewable energy and energy savings targets in order to achieve the Paris climate conference (COP21) commitments. Just recently, the European environment ministers agreed on a 35 % car emission cut of CO_2 by 2030 from recorded levels in 2020 [3]. Here, further trends are of particular interest. First, biofuels as high-density energy storage media for use in conventional combustion engines offer a significant reduction of greenhouse emissions using the current fossil fuels infrastructure. Second, innovative ignition systems to achieve ultra-lean combustion in spark ignited (SI) engines will result in better fuel economy and reduced NOx emissions.

Advanced biofuels use as feedstock non-food biomass and are of increasing interest concerning the replacement of fossil energy carriers for use in conventional combustion engines as they offer a significant reduction of greenhouse emissions using the current fossil fuels infrastructure. Different types of biofuels exist including oxygen-containing and nitrogenated species [4]. Energy stored in the fuel is converted to kinetic energy in the combustion process. Therefore, the combustion chemistry of advanced biofuels is of particular interest and a detailed knowledge of the combustion process can be used to improve the efficiency of SI engines. The knock behavior of advanced biofuels for example can be optimized with proper chemical synthesis i.e. future fuels can be designed for future cars to increase engine efficiency and reduce the emission [5].   Hence, it is of crucial importance to understand the ignition of future fuels in detail. In SI engines the use of spark plugs producing thermal plasmas has a long history [6]. However, a larger ignition volume can be obtained using specific non-thermal plasmas, which facilitates combustion in high exhaust gas recirculation engines or under ultra-lean combustion conditions. Here, in conjunction with an appropriate electrode design, a transient non-thermal plasma can take advantage of specific non-equilibrium chemistry to boost a more reliable ignition [7].

For the evaluation of the combustion of advanced biofuels and the efficiency of volumetric ignition systems it is necessary to understand the ignition process in detail. In this work, a combined experimental-numerical approach provides insight to the related physicochemical processes during the ignition by thermal and non-thermal plasmas to evaluate two different mechanisms by which an electrical discharge can affect the ignition of a combustible/air mixture. Typically, there are two necessary conditions for a successful ignition, namely the actual ignition event (short enough time for the formation of the radical pool) and the survival of the initially formed flame kernel (which is governed by the interaction of chemical kinetics and transport). The temporal development of the hot gas kernel and the subsequent flame propagation after ignition were

examined using a Schlieren method and laser induced fluorescence (LIF) of OH radicals. The ignition energy was varied to examine the interaction of convection, molecular transport and chemical reactions.

In case of non-equilibrium plasma, the dissociation and excitation of molecules by electron impact reactions can produce a significant number of active radicals and, therefore, can promote the ignition and initiate a chain reaction already at relatively low temperatures [8, 9]. High voltage alternating currents result in the formation and propagation of cathode-directed repetitive streamer discharges with a duration of several nanoseconds. The influence of mixture composition, applied voltage and number of streamer discharges on the ignition process and ignition volume was examined using chemiluminescence and OH-LIF. The experimental results are compared with numerical simulations in which the electron impact reactions are considered properly. Chemical pathway analysis shows more robust ignition and faster flame development in case of the repetitive streamer discharges compared to the capacitance sparks. This demonstrates the potential of non-thermal plasmas for volumetric ignition in SI engines.

2   Numerical simulation

Concerning the ignition by capacitance sparks the electrical discharge was modeled with a cylindrical shape by adding a source term to energy conservation equation [10]. The parameters describing the source term are set according to the experimental results [11]. The one-dimensional simulations were carried out using the program INSFLA for unsteady flames in laminar flow [12]. It does not consider the discharge in detail but is capable of solving the gas-dynamic equations and comprises a detailed transport model and detailed chemical kinetics. The conservation equations for mass, momentum, energy and species mass are solved using the method of lines. This results in a time-integration for the differential-algebraic equations which are obtained by spatial discretization using finite differences. The propane mechanism consists of 53 species and 592 elementary reactions [13].

For the numerical simulation of the ignition of H_2/air mixtures by non-thermal plasmas using INSFLA also a cylindrical configuration of the streamer is assumed. The ignition source in [12] is represented using a source term in the energy conservation equation. For non-thermal plasmas an additional energy source term resulting from the non-equilibrium plasma has to be regarded [14]. The energy deposition as a result of inelastic collisions leading to excitation and dissociation of gas molecules takes place due to an accompanying change in enthalpy exciting or dissociating molecules due to electron impact reactions. The additional source term, therefore, takes into account this additional energy coupling into the system during the time a reduced electric field is accounted for in the calculation [15]. The reaction mechanism incorporates the plasma chemistry of a high-current discharge in hydrogen/air mixtures [16] and a kinetic scheme of the non-equilibrium discharge in nitrogen/oxygen mixtures [17] resulting in a mechanism consisting of 29 species and 182 elementary reactions [18, 19]. The rate coefficients of the electron impact reactions are determined by solving the electron Boltzmann equation in the classical two-term approximation for reduced electric fields between 1 Td and 1000 Td using the BOLSIG+ software and database [20, 21].

For a numerical examination of the ignition by non-thermal plasma a conventional electric spark ignition was used as a basis for comparison. In order to check the influence of the chemical mechanism we calculated ignition delay times. In Figure 1 calculated

ignition delay times of a stoichiometric H_2/air mixture as a function of temperature using three different reaction mechanisms are shown. The mechanism of Bowman [18] shows good agreement with the well-known mechanisms of Maas [12] and Ó Conaire [22]. Therefore, we use the mechanism of Bowman et al. [18], which accounts for electron impact reactions for the computation of both ignition scenarios (streamer discharge and conventional spark ignition).
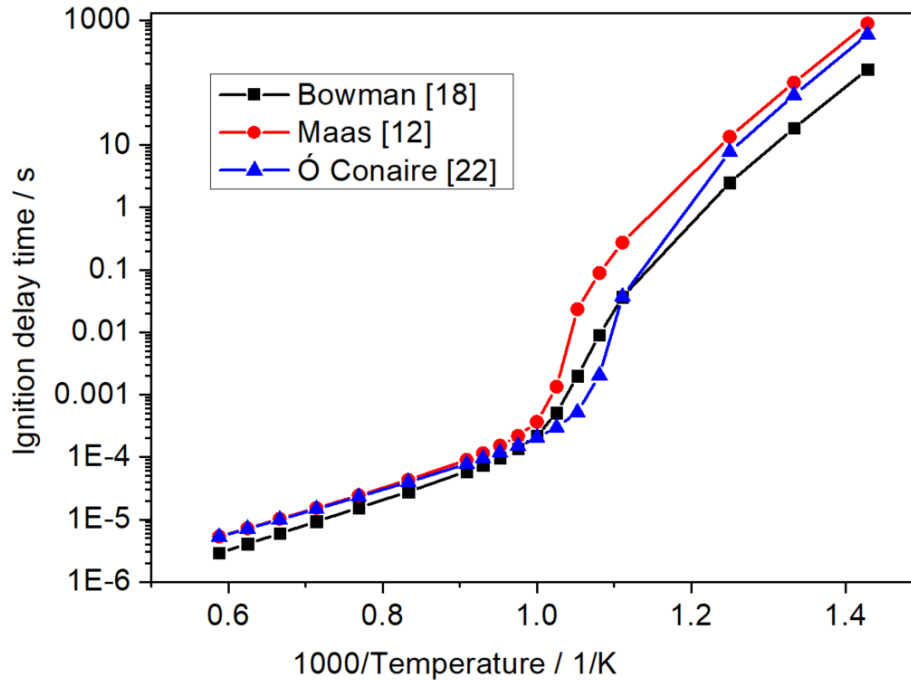
Figure 1: Ignition delay times of stoichiometric H_2/air mixture at 1 bar, calculated with different reaction mechanisms

3   Results

3.1   Ignition by capacitive sparks

In a capacitive discharge, a high voltage U is applied to a capacitor and the stray capacitances of the electrical circuit, C. When this voltage exceeds the breakdown voltage for a sufficiently long time, the energy stored in the system, $E = 1/2\ CU^2$, is released within a short time interval on the order of 1 µs. A plasma channel forms between the electrodes of the ignition system due to the Townsend or the streamer mechanism [23]. This channel rapidly expands radially, and its electric resistance decreases, allowing strong currents to flow across the formerly non-conductive gas gap. Eckhoff [24] gave a comprehensive overview of energy balance of the processes following the electrical discharge which may lead to the ignition of a burnable mixture. In the following, we illustrate the most important sub-processes that govern the ignition by capacitive discharges. While a repeatable and secure ignition in an engine usually calls for high discharge energy, the consideration of much smaller discharge energies is useful to gain a detailed understanding of the ignition process. Also, some processes may be covered by very high discharge energies but may still deserve consideration e.g. in a numerical model for the prediction of the ignition and flame propagation. Therefore, we illustrate the processes using the example of a 5.2 vol. % propane/air mixture with discharge energies of several hundred µJ. The tungsten electrodes with rounded tips

have a diameter of 2.4 mm and the electrode distance is 1.7 mm. The energy is close to the minimum amount needed to ignite this mixture in an optimized setup [25].

3.1.1 Expansion of the hot gas channel and the pressure wave

The deposition of the discharge energy in a short amount of time in a small volume results in high gas temperatures and pressures. This leads to the rapid expansion of a hot gas channel. Also, a shock wave forms at the perimeter of the hot channel. The shock wave will separate from the channel and travel outwards at supersonic speed, slightly heating the gas in the surrounding as it passes. Depending on the discharge energy, the shock wave decays rather quickly to a sound wave with velocity $Ma = 1$. In the following, the term pressure wave will be used as it includes both the shock and the sound wave.

Figure 2 shows the expansion of the hot gas channel and the pressure wave for propane. The data was obtained via schlieren measurements at different times after the discharge. From the single-shot images, the respective radii were extracted [11]. The data shows that the expansion of the gas channel occurs in distinct phases. Within the first microsecond following the discharge, the channel grows rapidly due to high temperature and pressure. A plasma induced pressure wave is distinguishable from the channel after 0.5 µs. In this particular case, its speed is $Ma = 1.4$ but quickly reduces to $Ma = 1$ after around 30 µs. After the detachment of the pressure wave, the hot channel expansion slows considerably. A second stage of expansion follows, starting after around 10 µs, which is governed mainly by the flow field induced by the discharge and the geometry of the electrodes [26, 27]. This second expansion phase is orders of magnitude slower than the first one.
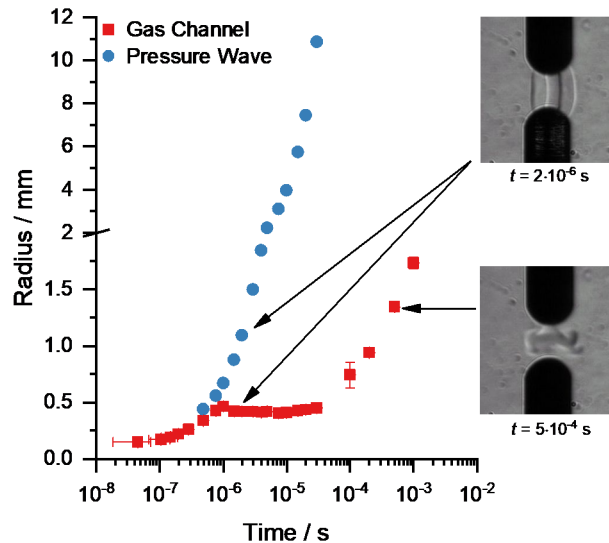
Figure 2: Temporal evolution of the hot gas channel and the pressure wave following a capacitive discharge in a 5.2 vol. % propane/air mixture. The discharge energy was 240 µJ. Each data point corresponds to the average of at least five experiments; the error bars indicate their standard deviation. The insets show a typical schlieren image 2 µs and 500 µs after the discharge. The hot gas channel and the pressure wave are clearly visible.

Numerical models allow the simulation of this expansion process. We introduced an efficiency factor in the source term of our model and simulated the expansion of the channel and the pressure wave for several efficiencies. The best agreement between

the results from this numerical model with the experimental data allowed us to determine the efficiency of the discharge. For a 249 µJ discharge in air we found that the efficiency was approximately 40 % [28].

3.1.2 Early phase of flame propagation

The temperature increase due to the capacitive discharge starts chemical reactions in the burnable mixture. When the energy input is finished (50 to 100 ns in the case considered here), the energy balance between heat released by the combustion reactions and heat transfer to the electrodes and the surrounding cold gas is the deciding factor as to whether an ignition will occur or not. If the discharge energy is sufficiently large, loss processes are irrelevant and need not be modelled. However, a detailed analysis of these processes may aid in designing improved ignition systems. Their proper investigation demands that the discharge energy is at a level where ignition is equally or even less likely than non-ignition.

We investigated the early phase of flame propagation using high-speed schlieren videography [29] and single-shot laser-induced fluorescence of the OH radical (OH-LIF) [30]. Typical results for the ignition phase in the propane/air mixture are shown in Figure 3. Experiments for two energies are compared, a low energy (E = 480 µJ) where the ignition probability is only 1 % and a higher energy (E = 960 µJ) with an ignition probability of 75 %. The ignition probabilities were calculated using a logistic regression model [31]. For each energy, the top row shows four frames extracted from a high speed schlieren video while in the bottom row single-shot planar OH-LIF images are shown. In the examples shown, the lower energy does not lead to an ignition while the higher energy discharge successfully ignites the mixture. The schlieren images indicate the region where the temperature is significantly higher than in the unperturbed surrounding. It needs to be kept in mind that this technique integrates the changes of the refractive index over the depth of the interrogation volume. Thus, the images do not show the flame directly but allow for an interpretation of the fluid dynamics that influence the ignition process. The OH-LIF images, on the other hand, present a 2D cut through the center of the flame and, as OH is an intermediate species of the combustion reaction, indicate the regions where combustion reactions are taking place.
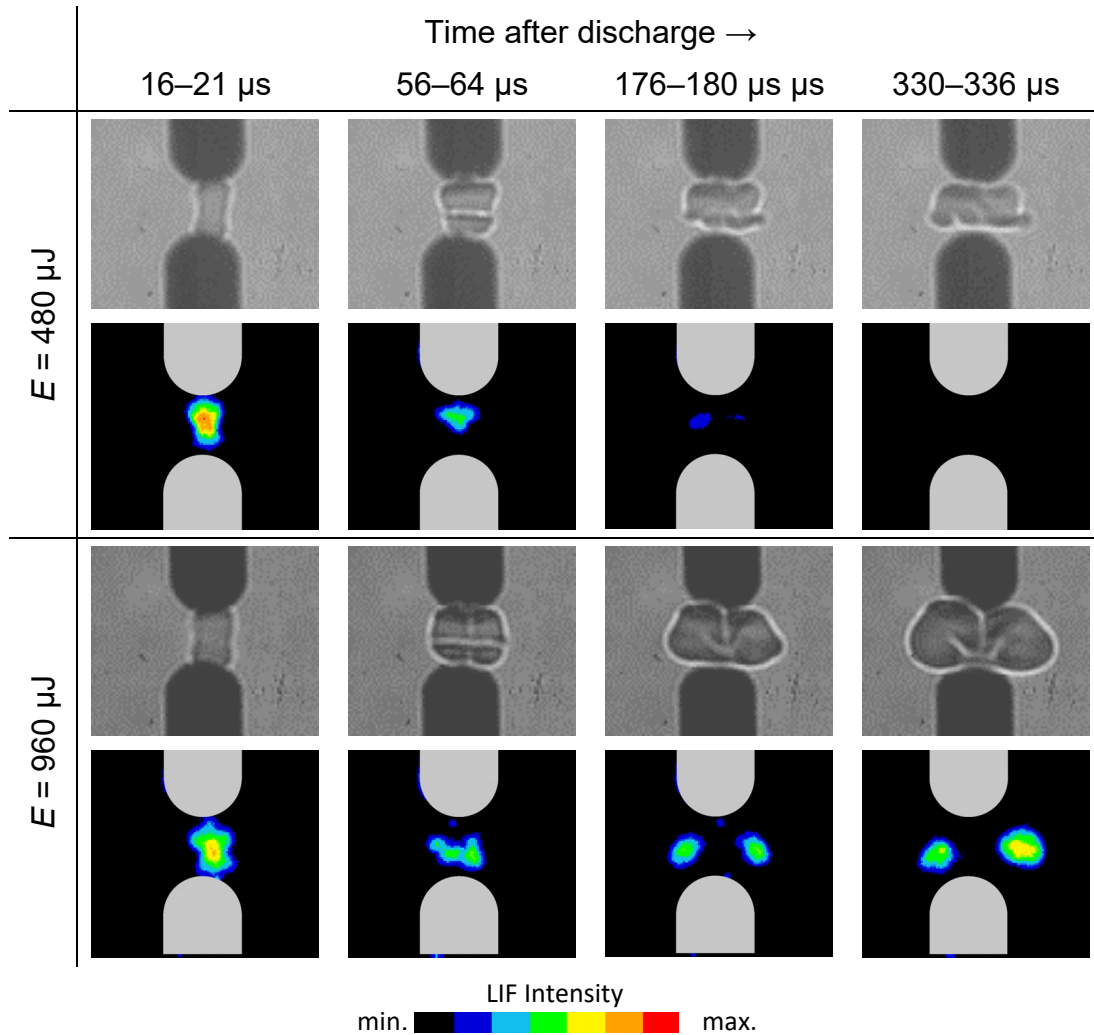
Figure 3: Evolution of the early flame kernel in a 5.2 vol. % propane/air mixture after a capacitive discharge at two energies. For each energy, single frames from a high-speed schlieren video and single-shot OH-LIF images are given in the top and bottom row, respectively. In the LIF images, the electrodes were added as grey shapes for better orientation.

The schlieren images reveal that starting from a near-cylindrical channel in the first frame, a complex three-dimensional shape of the flame kernel develops within 50 μs. As was seen in the previous section, the growth of the kernel due to the gas-dynamic expansion is slow for times greater than 1 μs after the discharge. The further expansion is a superposition of the flow field induced by the discharge and the combustion. It is faster when the energy is increased. The last two schlieren frames of the higher-energy case show how a non-spherical flame develops and expands outwards. In the lower-energy case, no ignition occurs and the hot kernel cools down. It is no longer detectable after some milliseconds (not shown here).

The OH-LIF images also illustrate the complex change of shape of the reaction zone. Between frames two and three, it splits into two distinct regions, indicating a toroidal flame. At both discharge energies, the intensity and therefore the OH concentration decrease significantly up to about 180 μs. However, in the high-energy case, the temperature in the kernel is still high enough to allow for a self-sustained flame propagation, seen in the last frame. In the lower-energy case, the cooling due to the electrodes

and the surrounding cold gas draws more energy from the reaction zone than what is produced by the chemical reaction. Therefore, the OH signal decays to zero and the reaction stops.

In Figure 4 the calculated temporal evolution of maximum temperature and maximum OH mole fraction is displayed for the same two ignition energies. In the higher energy case, there is a large temperature rise up to 6300 K due to the energy deposition by the source term. This goes along with a significant formation of OH radicals. The temperature and formation of OH is high enough to form a self-sustaining flame. For the lower energy level, the temperature rise up to 50 ns is much lower, it does not exceed 2500 K. A significant formation of OH starts only after the energy deposit has ended due to beginning combustion reactions. However, much less OH is formed compared to the higher energy level and cooling in addition prevents an ignition of the mixture.
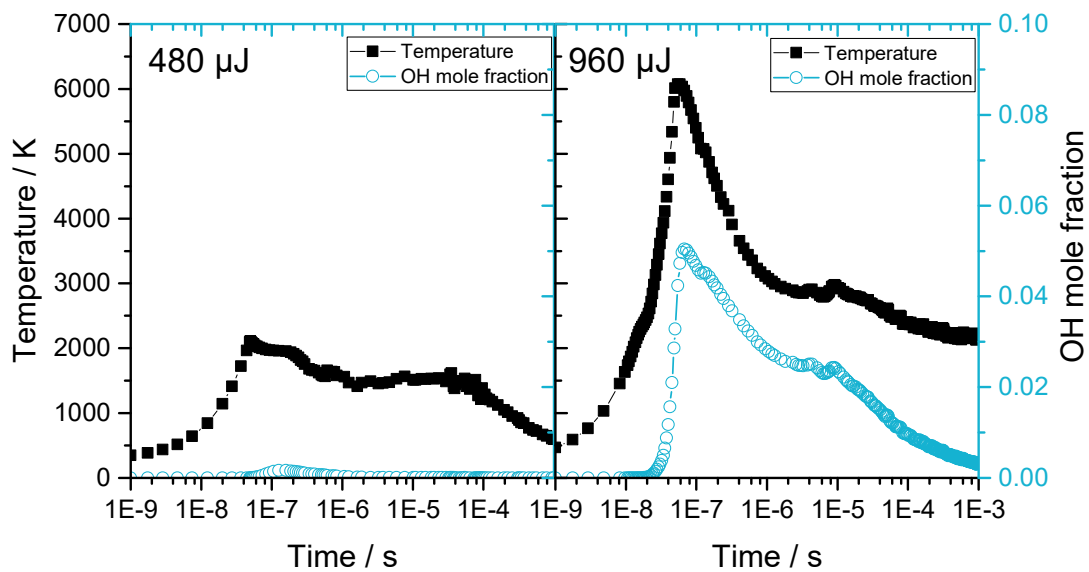
Figure 4: The temporal profiles of maximal temperature and OH mole fraction for two different energy levels. The left column shows results of a non-ignition (source radius 200 µm) and the right column calculation of ignition (source radius 150 µm).

Figure 5 compares experimental and numerical results regarding the radial profiles of the OH radical. In the left column, the normalized LIF intensity from the experiment is shown on the vertical axis. The different results for repeated experiments illustrate the stochastic variability of the ignition process. In the right column, the OH mole fraction extracted from numerical simulations is plotted. The top row shows an early time instant corresponding to the first time step in Figure 3. A comparison of the experimental results at the two energies shows that the flame kernel is larger in diameter when the energy is higher. Also, the intensity of the signal is stronger. These trends are well captured in the numerical simulation. The approximately Gaussian shape of the LIF profiles at this early time step is reproduced. In the bottom row, a time step during the evolution of the flame kernel is shown, corresponding to the third time step in Figure 3. Here, the differences between the two ignition energies are obvious. At the higher energy, the center of the flame kernel has travelled 1 mm from the electrode axis and the measured LIF intensity is still strong. However, for the lower-energy discharge the flame kernel has travelled a significantly shorter distance away from the electrodes and the LIF intensity is reduced significantly. In the simulation, the higher ignition energy

correctly leads to a larger flame diameter at this point. While the flame front position is given correctly by the numerical simulation, there is a discrepancy between the radial OH profiles near the center of the former plasma channel. Mainly due to cooling by the electrodes the OH radicals vanish in the experiment. This effect was not considered in the numerical simulations. While they have no influence on the subsequent flame propagation, they may disturb the ignition of combustible mixtures with longer ignition delay time and have to be considered then using 2D models e.g. as in [26].
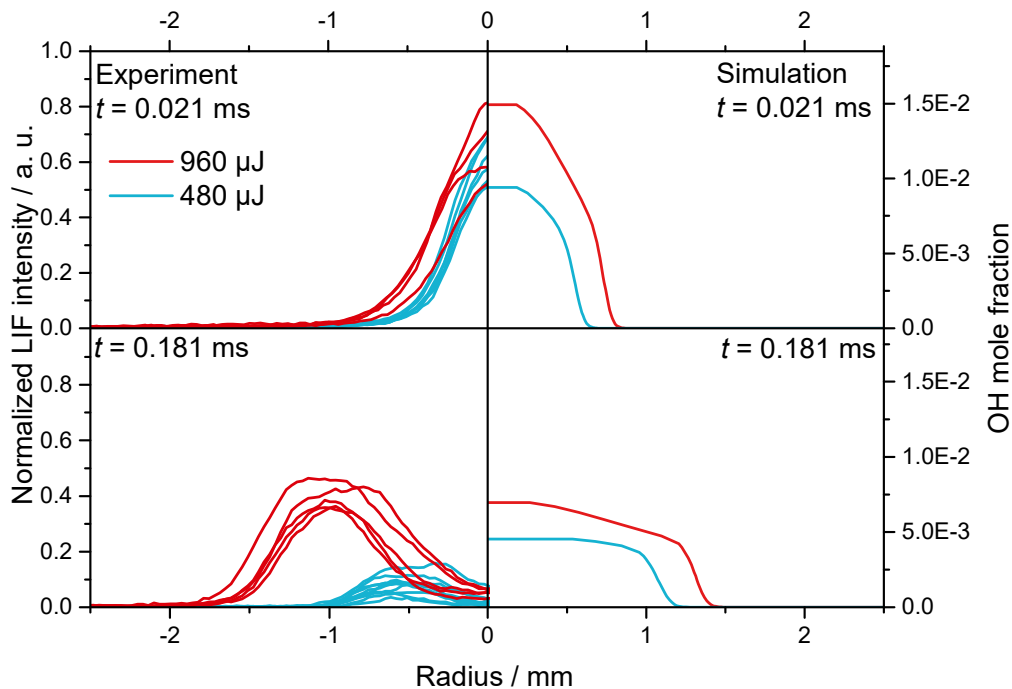
Figure 5: Radial profiles of the normalized LIF intensity measured in the experiment (left column) and of the OH mole fraction from the numerical simulation (right column). Two time steps are shown (top and bottom row). For each time step, two energies are depicted. Several realizations of the experiment are shown to illustrate the stochastic variability of the ignition process

As these results show, complex interactions between chemistry, fluid dynamics and transport processes such as heat transfer overlap each other even in this simple and initially quiescent setup. The conditions in an engine add further difficulty to the problem: inhomogeneous, multi-phase mixtures including exhaust gas from the previous stroke, turbulent flow fields, more complicated geometries and temperature fields need to be accounted for. Nevertheless, the aforementioned aspects should not be neglected. In particular, detailed chemical kinetics and transport processed are needed to properly describe ignition processes.

3.2   Ignition by streamer discharges

A high voltage pulse leads to a streamer discharge and if the pulse is too short in time to result in a spark breakdown the energy deposition takes place mainly in the streamer head [32]. Currents between 0.1 and 1 mA can be measured in the voltage range of 10 to 100 kV and only negligible heating occurs during one single streamer discharge. Repetitive streamer discharges, however, can be used to achieve a volumetric ignition

of combustible/air mixtures. Using an alternating voltage in a rod/plane configuration in which the plane is grounded, an intensive streamer discharge occurs for approximately 100 ns as can be seen in Figure 6 if positive voltage is supplied to the rod [15]. While at 9 kV only one streamer channel is visible after 100 voltage cycles, several plasma channels are visible using 11 kV. Due to the long exposure time of 140 µs the light emission of several hundred streamer discharges is shown in Figure 6.
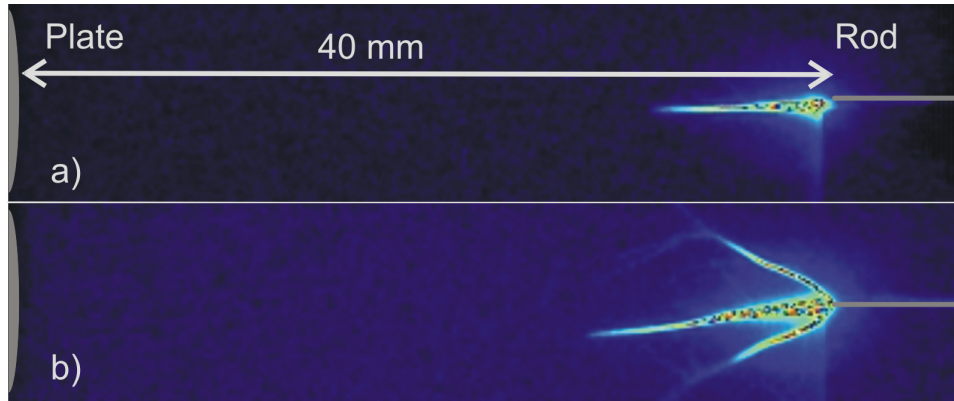
Figure 6: Streamer discharges after 100 voltage cycles at 740 kHz, exposure time 140 µs a) $\widehat{U}$ = 9 kV, b) $\widehat{U}$ = 11 kV

The physical and chemical processes of plasma-assisted ignition and plasma-assisted combustion have been in the focus of research for several years now [8, 9, 33]. It is well known that using non-thermal plasmas as an ignition source the overall energy necessary for ignition is approximately the same or less than that required for conventional spark ignition [28, 34]. The mean electron energy here is determined by a reduced electric field *E/N*, where *E* is the electric field and *N* is the gas density [8]. A comparison of the temporal development considering either a reduced electrical field of 0 Td (spark ignition) or 300 Td (non-thermal plasma) reveals that a lower temperature is necessary for ignition (Figure 7a). For both reduced electrical fields the minimum amount of energy necessary for ignition was used, i.e. using lower energies would result in non-ignition in both cases. Even though additional energy deposition occurs due to electron impact reaction using non-thermal plasmas, they are more efficient concerning the energy necessary for ignition [15]. Due to electron impact reactions the dissociation of O_2 and H_2 results in a great number of radicals even at low temperatures. As shown in Figure 7b directly after the first streamer discharges in the numerical simulation a strong increase of O, H and OH radicals occurs. The formation of these radicals via Arrhenius-type elementary reactions in case of the thermal plasma takes much longer to produce a similar number of radicals.
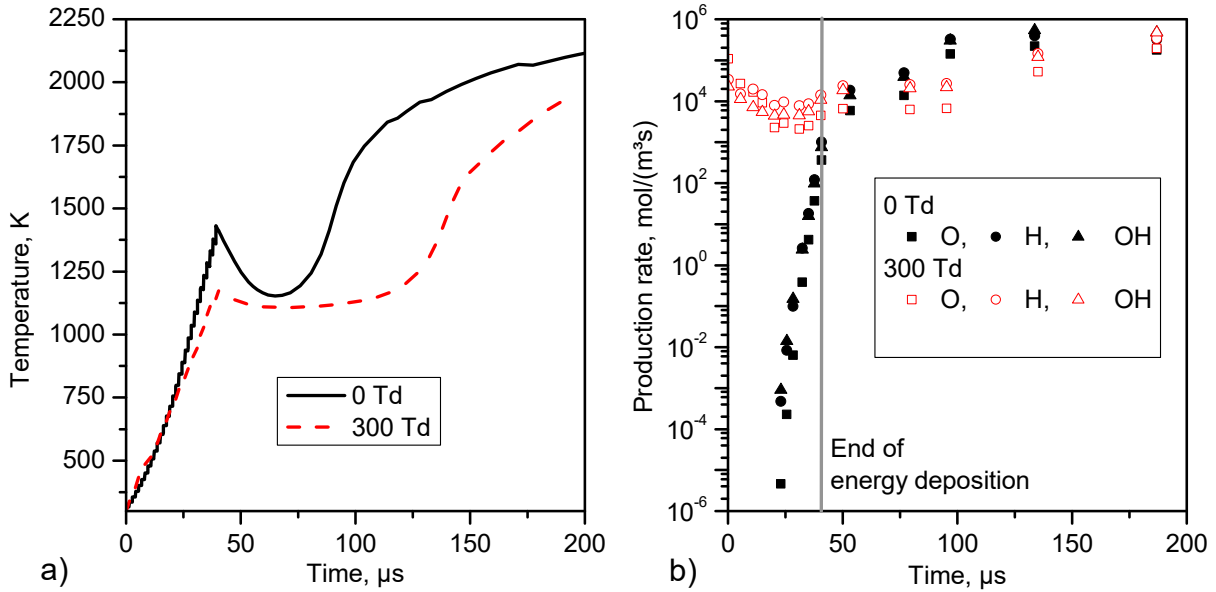
Figure 7: Comparison of the ignition of a 25 vol.% H₂ in air mixture by a thermal plasma (0 Td) and a non-equilibrium plasma (300 Td); a) maximum temperature in the computational domain, b) production rate of O, H and OH (reprint from [35]).

As was shown in Figure 6 a distance of 40 mm between rod and plate was used to examine the ignition of H_2/air mixtures by streamer discharges experimentally. A sequence of OH images using a peak voltage of 14 kV and 100 voltage cycles corresponding to an energy deposition time of 140 µs is shown in Figure 8. From numerical simulations it is known that there is a temperature gradient along the plasma channel [36]. Starting with a maximum temperature near the tip of the rod the temperature inside the plasma channel decreases towards the end of the channel. As is visible in Figure 8 the ignition starts around 110 µs near the tip of the rod. However, after 160 µs the whole plasma channel has led to ignition and afterwards the subsequent flame propagation perpendicular to the plasma channel can be seen. A further increase of energy would shorten the ignition delay time. Additionally, using higher energies results in additional plasma channels which would enlarge the volume of ignition.
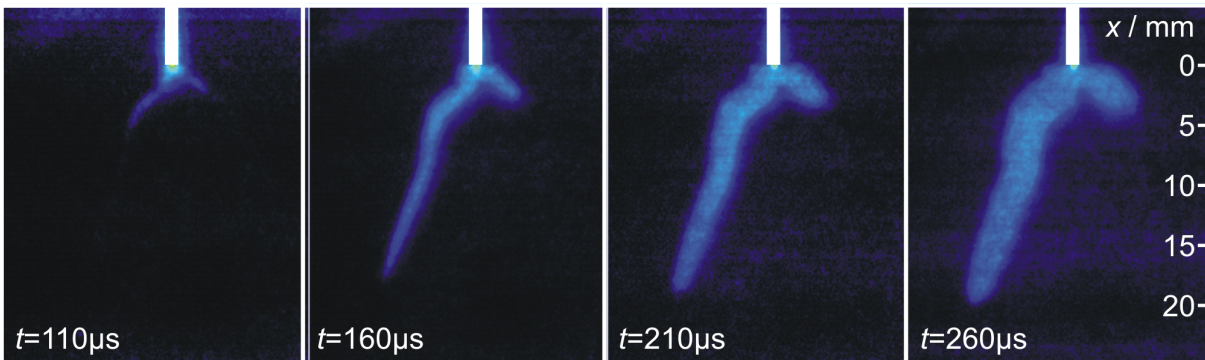
Figure 8: Sequence of OH-LIF images of an ignition along the whole streamer channel (25 vol.-% H2, $\widehat{U}$ = 14 kV, 100 voltage cycles)

4   Conclusions

Alternative fuels like advanced biofuels and more efficient combustion engines can promote further reduction of CO_2 and pollutant emissions in the road transportation sector. For both topics a detailed understanding of the ignition process will help to support these developments using numerical simulations. Fundamental work on the probability of ignition and the dominating factors considering spark ignition of quiescent mixtures helps to improve numerical tools like INSFLA used in this work. The comparison of experimental and numerical results considering spark ignitions using detailed chemical kinetics demonstrates qualitatively good agreement despite the restriction to a one-dimensional (cylindrical) model. This offers the opportunity to examine the ignition of advanced biofuels in depth which will support the development of detailed reaction mechanisms.

The ignition by non-thermal plasmas like repetitive streamer discharges of up to 100 ns as examined in this work have shown significant advantages compared to the ignition by conventional spark ignition. The proper use of non-thermals plasmas may help to reduce ignition delay time compared to conventional spark ignition and enables volumetric ignition which would support the development of high exhaust gas recirculation engines or ultra-lean combustion engines. A deeper knowledge of the non-thermal plasma processes like electron impact reactions is necessary to understand the ignition by non-thermal plasmas more in detail. Again, numerical tools like INSFLA can be used to examine the fundamental physical and chemical processes and will, therefore, support the development of modern engine concepts.

References

[1] Umweltbundesamt, Kohlendioxid-Emissionen, http://www.umweltbundes-amt.de/daten/klimawandel/treibhausgas-emissionen-in-deutschland/kohlendi-oxid-emissionen. Accessed 11 Oct 2018.

[2] Directive 2009/28/EC, Directive 2009/28/EC of the European Parliament and of the Council of 23 April 2009 on the promotion of the use of energy from renewable sources and amending and subsequently repealing Directives 2001/77/EC and 2003/30/EC.

[3] The European council, CO_2 emission standards for cars and vans: Council agrees its position, https://www.consilium.europa.eu/en/press/press-re-leases/2018/10/10/co2-emission-standards-for-cars-and-vans-council-agrees-its-position/. Accessed 11 Oct 2018.

[4] K. Kohse-Höinghaus, P. Oßwald, Terrill A. Cool and Tina Kasper, N. Hansen, F. Qi, C. K. Westbrook, P. R. Westmoreland, Angew. Chem., Int. Ed. 2010, 49, 3572 – 3597. DOI: 10.1002/ange.200905335.

[5] W. Leitner, J. Klankermayer, S. Pischinger, H. Pitsch, K. Kohse-Höinghaus, Angew. Chem., Int. Ed. 2017, 56 (20), 5412 – 5452. DOI: 10.1002/anie.201607257.

[6] R.R. Maly, Symp. (Int.) Combust. 1994, 25 (1), 111 – 124. DOI: 10.1016/S0082-0784(06)80635-1.

[7] T. Shiraishi, A. Kakuho, T. Urushihara, C. Cathey, T. Tang, M. Gundersen, SAE Int. J. Engines 2009, 1 (1), 399 – 408. DOI: 10.4271/2008-01-0466.

[8] S. Starikovskaia, J. Phys. D: Appl. Phys. 2006, 39, R265-R299. DOI: 10.1088/0022-3727/39/16/R01.

[9] S. M. Starikovskaia, J. Phys. D: Appl. Phys. 2014, 47 (35), 353001. DOI: 10.1088/0022-3727/47/35/353001.

[10] A. Dreizler, S. Lindenmaier, U. Maas, J. Hult, M. Aldén, C. F. Kaminski, Appl. Phys. B 2000, 70, 287 – 294. DOI: 10.1007/s003400050047.

[11] S. Essmann, Plasma Phys.Technol. 2016, 3 (3), 116 – 121.

[12] U. Maas, J. Warnatz, Combust. Flame 1988, 74, 53 – 69. DOI: 10.1016/0010-2180(88)90086-7.

[13] C. Chevalier, Entwicklung eines detaillierten Reaktionsmechanismus zur Modellierung der Verbrennungsprozesse von Kohlenwasserstoffen bei Hoch- und Niedertemperaturbedingungen, Dissertation, University of Stuttgart 1993

[14] T. Langer, D. Markus, U. Maas, in 42nd AIAA Plasmadynamics and Lasers Conference 2011. DOI: 10.2514/6.2011-3450.

[15] T. Langer, Zündung von Wasserstoff/Luft-Gemischen durch repetierende Teilentladungen, Dissertation, Karlsruhe Institute of Technology 2013.

[16] N. A. Popov, Plasma Phys. Rep. 2008, 34, 376 – 391. DOI: 10.1134/S1063780X08050048.

[17] I. A. Kossyi, A. Y. Kostinsky, A. A. Matveyev, V. P. Silakov, Plasma Sources Sci. Technol 1992, 1, 207 – 220. DOI: 10.1088/0963-0252/1/3/011.

[18] S. Bowman, I. Choi, K. Takashima, I. V. Adamovich, W. R. Lempert, in 48th AIAA Aerospace Sciences Meeting 2010.

[19] M. Uddi, N. Jiang, I. V. Adamovich, W. R. Lempert, J. Phys. D: Appl. Phys. 2009, 42, 75205. DOI: 10.1088/0022-3727/42/7/075205.

[20] G J M Hagelaar, L. C. Pitchford, Plasma Sources Sci. Technol 2005, 14 (4), 722 – 733.

[21] BOLSIG+, https://www.bolsig.laplace.univ-tlse.fr/. Accessed 11 Oct 2018.

[22] M. Conaire, H. Curran, J. Simmie, W. Pitz, C. Westbrook, International Journal of Chemical Kinetics 2004, 36, 603 – 622. DOI: 10.1002/kin.20036.

[23] A. Küchler, High Voltage Engineering: Fundamentals - Technology - Applications, VDI-Buch, Springer Berlin Heidelberg; Imprint; Springer Vieweg, Berlin, Heidelberg 2018.

[24] R. K. Eckhoff, W. Olsen, J. Electrostat. 2010, 68 (1), 73 – 78. DOI: 10.1016/j.elstat.2009.11.001.

[25] E27 Committee, Test Method for Minimum Ignition Energy and Quenching Distance in Gaseous Mixtures, ASTM International, West Conshohocken, PA.

[26] S. P. M. Bane, J. L. Ziegler, J. E. Shepherd, Combust. Flame 2014 (0). DOI: 10.1016/j.combustflame.2014.07.017.

[27] M. Thiele, J. Warnatz, U. Maas, Combust. Theor. Model. 2000, 4 (4), 413 – 434. DOI: 10.1088/1364-7830/4/4/303.

[28] D. Markus, S. Essmann, J.-R. Kummer, R. Shekhar, C. Uber, U. Gerlach, U. Maas, Z. Phys. Chem. 2017, 231 (10), 1655 – 1682. DOI: 10.1515/zpch-2016-0903.

[29] S. Essman, D. Markus, U. Maas, in 26th International Colloquium on the Dynamics of Explosion and Reactive Systems. Boston 2017.

[30] S. Essmann, J. R. Kummer, D. Markus, U. Maas, in Proceedings of the twelfth International Symposium of Hazards, Prevention, and Mitigation of Industrial Explosions. Kansas City 2018.

[31] A. Wähner, G. Gramse, T. Langer, M. Beyer, J. Loss Prevent. Proc. 2013, 26 (6), 1655 – 1660. DOI: 10.1016/j.jlp.2013.06.002.

[32] T. Langer, D. Markus, F. Lienesch, U. Maas, Combust. Sci. Technol. 2010, 182, 1718 – 1734. DOI: 10.1080/00102202.2010.497374.

[33] A. Y. Starikovskii, N. B. Anikin, I. N. Kosarev, E. I. Mintoussov, S. M. Starikovskaia, V. P. Zhukov, *Pure Appl. Chem* **2006**, *78*, 1265 – 1298. DOI: 10.1351/pac200678061265.

[34] D. Singleton, S. J. Pendleton, M. A. Gundersen, *J. Phys. D: Appl. Phys.* **2011**, *44 (2)*, 22001. DOI: 10.1088/0022-3727/44/2/022001.

[35] D. Markus, T. Langer, U. Maas, in: *44th AIAA Plasmadynamics and Lasers Conference*. San Diego **2013**. DOI: 10.2514/6.2013-3006.

[36] D. Markus, T. Langer, U. Maas, in *24th International Colloquium on the dynamics of explosions and reactive systems*. Taipeh **2013**.

1.3 An Advanced Ignition System for High Efficiency Engines

Cherian A. Idicheria, Hanho Yun, Paul M. Najt

Abstract

A pragmatic approach to meeting future CO_2 regulations while delivering vehicles that customers want and can afford will require the synergistic integration of advanced tech-nologies that enhance engine efficiency by minimizing loss mechanisms and maximi-zing work recovery. Aggressive downsizing, higher compression ratios, increased le-vels of charge dilution, and homogeneous stoichiometric operation at wide open throttle with acceptable peak pressure levels are essential technologies to meet these challenging objectives. Many of these enabling technologies pose significant challen-ges for the conventional spark ignition system. To maximize gasoline engine efficiency, the ignition system should enhance early flame kernel development to support robust spark ignition combustion, should be able to enhance mixture reactivity to support part-load lean low-temperature combustion, and should tolerate high heat fluxes to support high speed and load operation without compromise. In this paper, we demonstrate a single, passive, low-temperature plasma ignition concept that simultaneously addres-ses all these challenges. The groundless barrier discharge igniter (GBDI) can enhance early flame kernel development through the local deposition of high energy reactants, enable lean low-temperature combustion control through the generation of pre-com-bustion ozone, enhance knock tolerance by reducing early flame kernel variability, and enhance overall engine robustness through the elimination of ground straps, spark gaps, and heat ranges.

1 Introduction

In the pursuit of high efficiency gasoline engines, conventional inductive ignition sys-tems face severe challenges. As engines are downsized and boosted, to maximize engine efficiency we must focus on minimizing loss mechanisms and maximizing work recovery. In these next-generation engines, the ignition system must handle multiple operating conditions. Future high efficiency engines will aim to have compression ra-tios between 13 & 14 to maximize work extraction without incurring major parasitic losses. These engines will also utilize elevated levels of charge dilution at part-load to minimize heat losses and maximize work extraction. This implies that the ignition sys-tem must enable increased EGR tolerance and/or enable lean low- temperature com-bustion (LTC) with robust phasing control. Also, the engine must support homogene-ous stoichiometric operation at higher loads and wide-open-throttle (WOT) operation with rated speed above 6000 rpm while maintaining modest peak pressure levels. At such operation, ignition systems must not only handle increased breakdown voltages but also withstand significant thermal loading and avoid overheating.

The higher in-cylinder pressure with downsizing and boosting demands higher break-down voltages and one way to overcome the problem is to reduce the spark gap size on conventional inductive spark ignition systems. The smaller gap size can worsen

combustion stability, especially with EGR dilution and/or lean operation. Advanced ignition systems are being investigated as an enabling technology for downsize boost dilute combustion engines [1-3]. Among these advanced ignition systems, low-temperature plasma based systems are gaining in importance. Several alternatives to conventional spark plug systems are considered and the most prominent among them are the radio frequency based systems like the corona ignition system and the barrier discharge ignition system. Other technologies include multi-charge ignition, dual-coil offset/ignition system, passive and active jet ignition systems, microwave high-frequency ignition system and laser ignition. While many of these systems were evaluated for dilute stoichiometric combustion and lean homogeneous applications, low-temperature plasma systems were explored for achieving advanced combustion strategies like lean stratified-charge combustion and lean homogeneous charge compression ignition (HCCI) [4-6].

Figure 1 shows a schematic of engine speed and load operating regimes for a lean LTC high-efficiency engine. As shown in the schematic, the engine operation is differentiated by low- mid- and high-load operating regimes that support different combustion modes. In the low-load regime, negative valve overlap (NVO) may be utilized to trap hot-residuals that is necessary to support flameless and flame-assisted controlled lean LTC. In the mid-load regime, positive valve overlap (PVO) operation and advanced injection strategies may be utilized to achieve flame-assisted controlled lean LTC. At even higher speed and load operation, the engine is required to support stoichiometric combustion with significant dilution and knock tolerance. There are several advanced technologies that need to be synergistically integrated to achieve these objectives and the ignition system plays a key role. For example, the capability of the ignition system to enable robust control of lean LTC, as well as increase dilution and knock tolerance at high-load stoichiometric operation are critical. An advanced ignition system may outperform a conventional inductive ignition system while taking into consideration the desired engine operation. Table 1 shows a comparison between different ignition systems and their pros and cons while considering its capability to meet the desired results. In this paper, we present results for a groundless barrier discharge ignition (GBDI) system that enables all the challenges to be addressed.
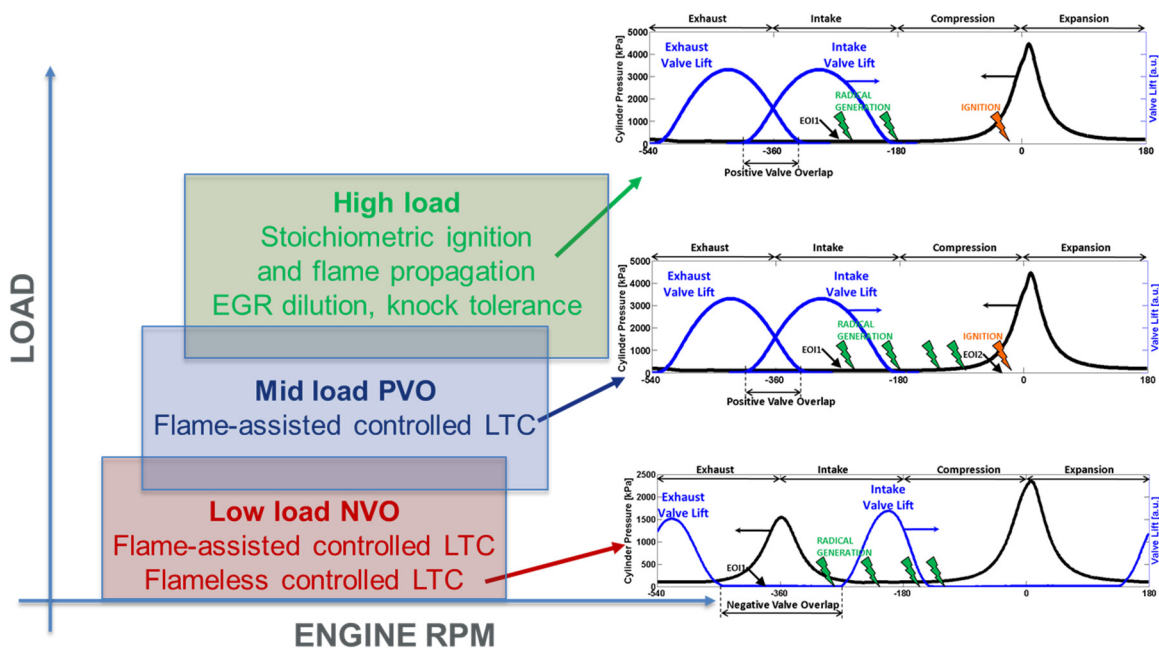
Figure 1: Schematic show engine speed load operating regimes and different combustion modes that needs to be supported by the ignition system

Table 1: Alternate ignition systems and their pros and cons.

Ignition Concept	Low Temperature Plasma	Low Temperature Plasma	Low Temperature Plasma	Capacitive Discharge	Inductive Discharge	Inductive Discharge
Type	Corona	GBDI	Passive Jet ignition	Passive Jet ignition	Passive jet ignition	Active Jet ignition
Pros						
	Supports lean combustion	Supports lean combustion	Potential to support lean combustion			Supports lean combustion
	Supports high EGR	Supports high EGR	Supports high EGR			Supports high EGR
	Increases knock tolerance	Increases knock tolerance	Increases knock tolerance	Increases knock tolerance	Increases knock tolerance	Increases knock tolerance
	Reduced erosion concerns	Eliminates erosion concerns	Eliminates erosion concerns			
	Reduced fouling concerns	Eliminates fouling concerns	Reduces fouling concerns	Reduces fouling concerns		
		Simplified control strategy				
Cons						
	Arc detection and control necessary		Poor light load combustion stability	Poor light load combustion stability	Poor light load combustion stability	Complexity with additional injector
			Poor cold performance	Poor cold performance	Poor cold performance	Poor cold performance
				Gap erosion	Fouling/heat range issues	Fouling/heat range issues
Cost	+++	++	++	+	+	++

1.1   Low-temperature plasma ignition system

From Table 1 it is evident that low-temperature plasma based ignition systems offer significant advantages when compared to alternate ignition systems. Figure 2 shows a comparison between two radio frequency low-temperature plasma ignition systems. On the left column is the corona discharge based plug and the right column is the GBDI plug. It is important to illustrate the difference between the two systems and understand why one may be preferred over the other. The more traditional corona system has a power electrode (the example in Figure 2 has four prongs), from which multiple low-

temperature plasma streamers emanate. The propensity for these streamers to transition to a single high-temperature plasma (arc) discharge is well understood and is dependent primarily on the driving voltage, duration, the proximity of the power electrode prongs to any ground surface (e.g. opening valves, piston surface, cylinder head), and the in-cylinder conditions (e.g. pressure at time of ignition). The advantage of the corona system is its capability to promote near-simultaneous and closely located multiple ignition points, thereby reducing the 0-10 burn duration (ignition delay). Also, the absence of a prominent ground electrode reduces potential heat losses suffered by the early flame kernel. This is in addition to the widely accepted difference in the underlying ignition process between low-temperature plasma and high-temperature plasma (e.g. inductive spark plug) ignition systems. In contrast, the barrier discharge system has a power electrode that is fully enclosed in the dielectric casing and does not have a prominent ground electrode. As shown in Figure 2, multiple streamers propagate on the surface of the dielectric. The streamers originate at the base of the plug shell and reach the tip of the dielectric, depending on the ambient pressure, voltage and duration settings. The images in the bottom row of Figure 2 shows multiple events in a single exposure. It shows that while the corona streamer discharges emanate from the prongs, they largely seem to repeat their spatial location from discharge to discharge, in this quiescent environment. On the other hand, for the barrier discharge, in a similar environment, the streamers move and form all around the dielectric surface.
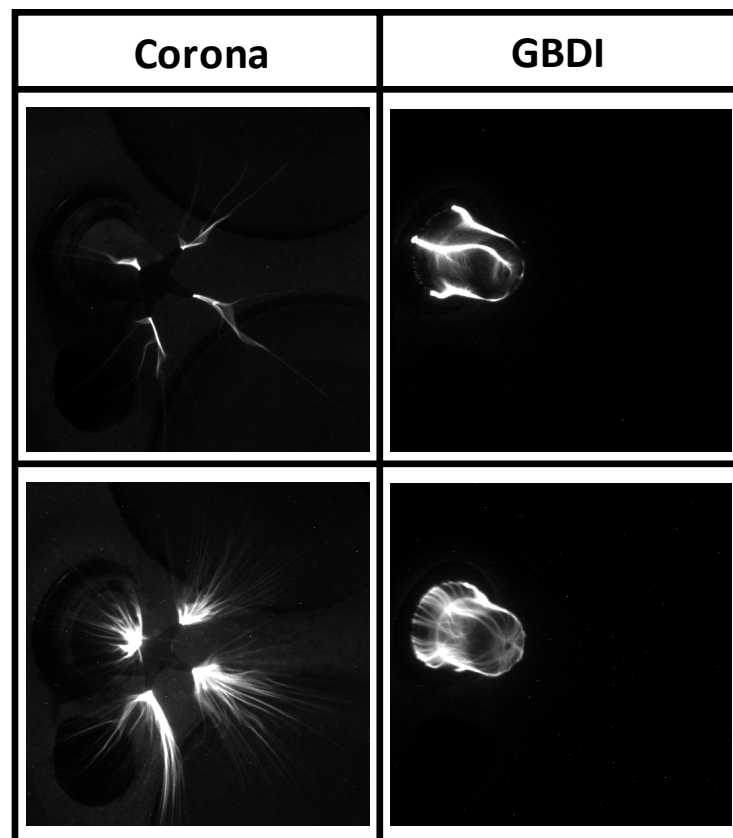
Figure 2: Visualization of corona ignition system and GBDI system. The top row shows a single discharge event and the bottom row shows multiple discharge events visualized in the same exposure.

2   Results

In this section, we will present results from single- and multi-cylinder engine testing. Results are presented for engine operating regimes and combustion modes as illustrated in Figure 1.

2.1   Lean LTC NVO operation

This section presents the voltage based reactivity control achieved by using a barrier discharge ignition system for NVO operation. The engine speed is 1000 rpm and the fueling rate for the single-cylinder engine experiment is approximately 9 mg/cycle with an NVO duration of 156 CAD and intake temperature set to 125 C. As shown in Figure 1, for this flameless controlled LTC mode, the fuel is injected after TDC of the recompression process, thereby limiting the amount of fuel reforming. The plasma igniter is actuated multiple times after fuel injection to generate radicals that assist with the combustion. For this example, an additional plasma igniter was also added in the intake plenum and actuated multiple times. Figure 3 shows the cycle averaged (200 cycles) heat release rate for multiple operating strategies. When the igniter in the intake and cylinder are turned off, the heat release rate is delayed and combustion is unstable and unacceptable. However, activating the intake and in-cylinder igniters and increasing the driving voltage, the combustion phasing is advanced and the combustion stability is improved as well. In Figure 3, the effect of increasing the driving voltage from 30 V to 40 V to 50 V is evident as COV of IMEP improves to 2% and combustion is phased more favorably. It should be emphasized that there is no propagating flame in this combustion mode, and the plasma igniter is enhancing the flameless low-temperature combustion. For this lean operating condition, the low-temperature plasma igniter supports generation of ozone that enhances the reactivity of the fuel-ambient mixture and supports controlled low-temperature combustion.

The corona based system can also support generation of ozone to enhance LTC as shown for the barrier discharge system. However, active control of the voltage and duration of the corona discharge is required to ensure that the discharge is in low-temperature plasma mode. For example, for these light-load operating conditions, when the discharge events are occurring at ambient pressure conditions, the sensitivity for the corona discharge to transition to a high-temperature plasma that does not produce any ozone is increased. On the other hand, the barrier discharge system never transitions to a high-temperature plasma with increasing voltage and therefore the voltage is the most important control parameter to achieve distinct levels of combustion enhancement and phasing control by varying the amount of ozone that is generated.
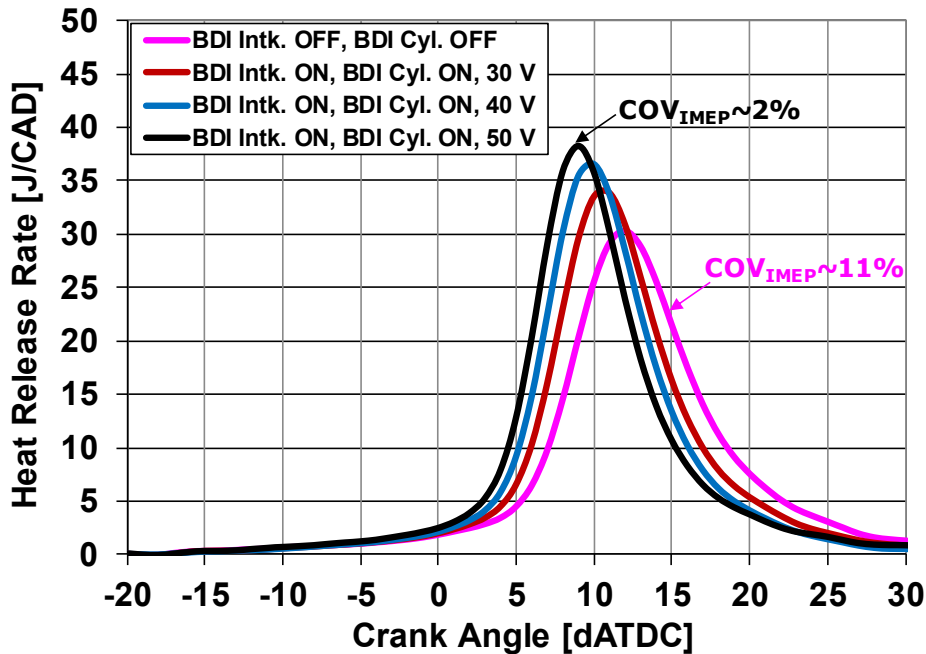
Figure 3: Voltage based reactivity control achieved by using barrier discharge ignition system for flameless low-temperature combustion at NVO operation.

Figure 4 shows results from cylinder #1 of multi-cylinder engine testing depicting the lean operation limit with different ignition systems. For these tests, a single GBDI igniter is used per cylinder and only a single ignition event was utilized, unlike the results obtained in Figure 3. The engine is operated at 2000 rpm with a fueling rate of 10 mg/cycle/cylinder (nominally 250 kPa IMEP) and intake temperature of 40 C. The change in air-fuel ratio (AF ratio) was achieved by changing the amount of NVO, while maintaining the injection timing and spark timing. As the mixture gets leaner, the combustion phasing is delayed and combustion instability increases as indicated in Figure 4 by the COV of IMEP. This flameless combustion mode can be achieved without any ignition and the maximum achievable AF ratio is a little over 21 with COV of IMEP < 3%. If a traditional high energy spark ignition system is used, the lean limit can be extended to a little over 22. Further enhancement of the lean limit to 23.5 can be achieved by using the GBDI system. It is the unique voltage based reactivity enhancement of the GBDI system that enables reliable combustion performance at lean condition. The higher voltage that is required for the GBDI system at the leaner condition is labeled in Figure 4. The system that was evaluated in this study was limited to peak voltage setting of 70 V. Beyond this voltage, the potential for dielectric puncture failures was high for the GBDI system.
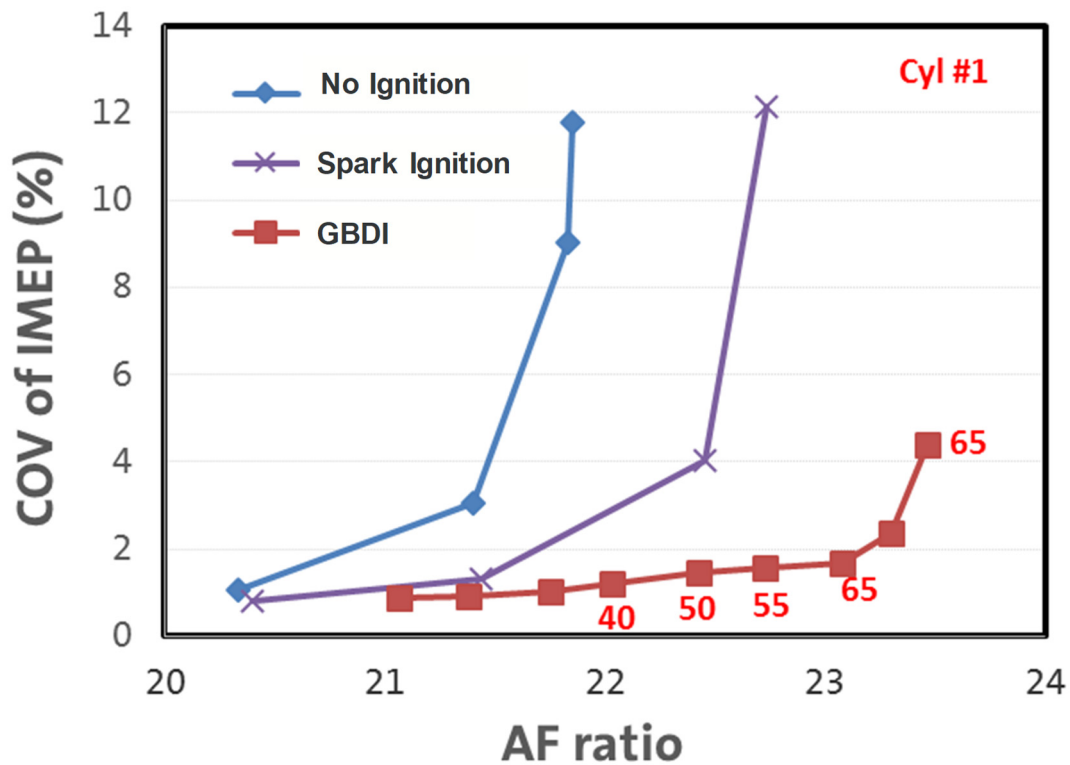
Figure 4: Voltage based reactivity control achieved by using GBDI system for flame-less low-temperature combustion at NVO operation.

2.2   Lean LTC PVO operation

This section presents the voltage and number of events based reactivity control achieved by using a GBDI system for PVO operation. The combustion mode in this operating regime is flame-assisted controlled LTC. The engine speed is 1000 rpm and the fueling rate for the single-cylinder engine experiment is approximately 12 mg/cycle with a PVO duration of 100 CAD and intake temperature set to 40 C. As shown in Figure 1, the fuel is injected in two parts with an early injection event that delivers majority of the fuel (10 mg) during the intake stroke, and a second smaller quantity of fuel (2 mg) during the compression stroke that is ignited with a closely coupled ignition event. Also, there are multiple actuations of the igniter (referred to as radical generation in Figure 1 or pre-strikes in Figure 5 and 6) during the intake and early compression stroke, to generate ozone or reactants that enhance the reactivity of the mixture. The small quantity second injection is ignited (referred to as ignition in Figure 1) that initiates the combustion of the stratified mixture with a turbulent flame propagation. This is followed by a controlled LTC (autoignition) of the remaining mixture. This mixed mode of combustion is clearly shown in Figure 5 and Figure 6. The unique capability of the GBDI igniter to enable controllability of LTC with voltage and number of pre-strikes is shown in Figure 5 and Figure 6, respectively.

Figure 5 presents cycle averaged (200 cycles) heat release rates for flame-assisted controlled LTC at PVO operation. Three different cases are shown, with radical generation or pre-strikes turned off or two pre-strikes events at 40 V and 50 V. With the pre-strikes turned off, the heat release shows a robust flame initiation event of the stratified mixture, followed by a weak low-temperature combustion that leads to combustion instability and poor COV of IMEP. For the same condition, when the pre-strikes are

turned on with a setting of 40 V, the flame initiation portion remains relatively the same, but significant enhancement of low-temperature combustion and improvement in combustion stability is achieved. As the voltage is increased further to 50 V, continued enhancement of LTC and combustion stability is obtained.
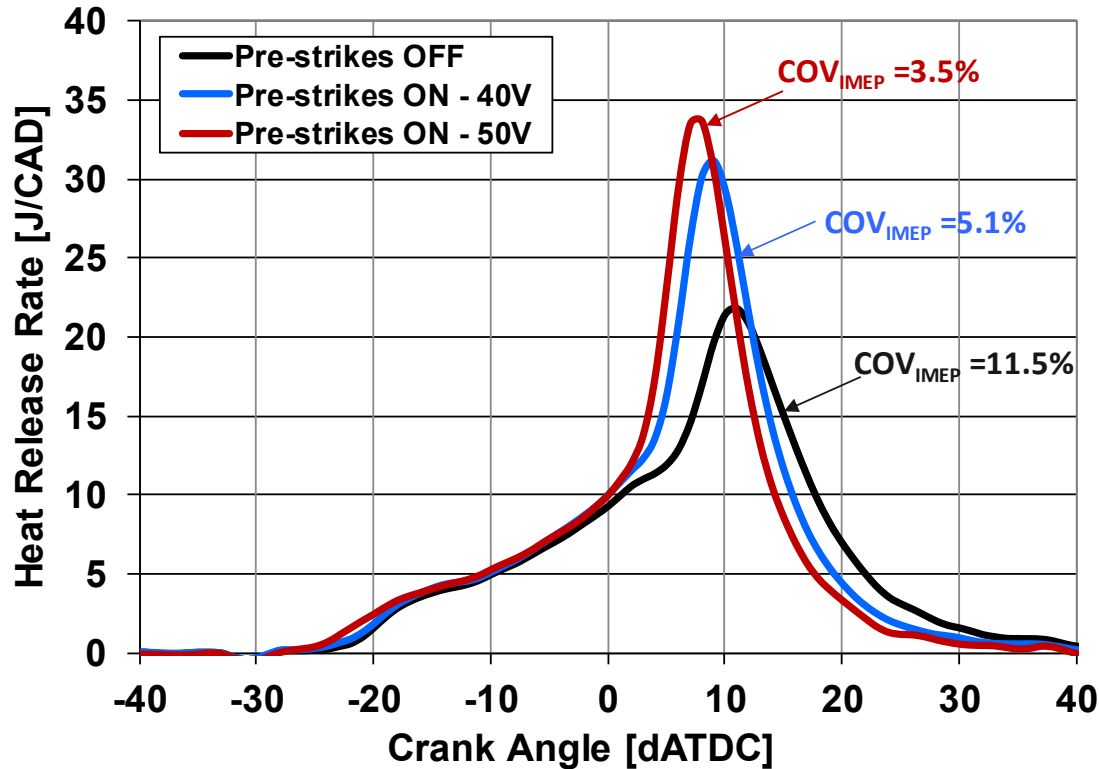
Figure 5: Robust ignition and voltage based control achieved by using GBDI system for flame-assisted LTC at PVO operation.

Figure 6 presents cycle averaged (200 cycles) heat release rates for a similar condition as in Figure 5. Four different cases are shown, with radical generation or pre-strikes turned off and varying the number of pre-strikes at a fixed 50 V. With the pre-strikes turned off, the heat release shows a robust flame initiation event, followed by a weak low-temperature combustion that leads to combustion instability and poor COV of IMEP. As the number of pre-strikes is increased from 2 to 3 to 4, increasing levels of low-temperature combustion enhancement is achieved with improving combustion stability. The results shown in Figure 5 and Figure 6 together indicates that the applied voltage and number of pre-strikes are effective controls for enhancing and controlling low-temperature combustion for flame-assisted LTC with PVO.
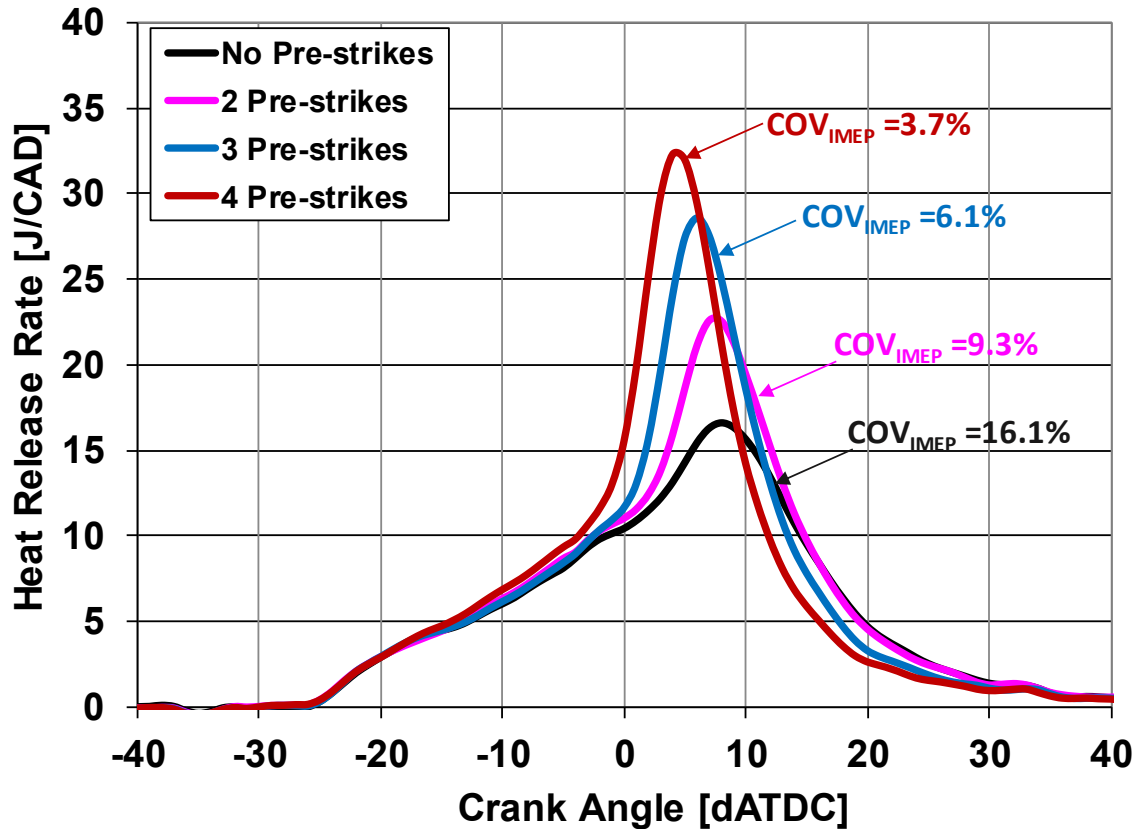
Figure 6: Robust ignition and number of pre-strikes based control achieved by using GBDI system for flame-assisted LTC at PVO operation.

2.3   Stoichiometric part-load operation (dilution tolerance)

This section presents the unique capability of GBDI system for dilute stoichiometric part-load operation. As shown in Figure 1, the impact of using pre-strikes to improve exhaust gas residual (EGR) dilution tolerance is demonstrated, followed by EGR dilution tolerance improvement by using only a single ignition event.

Figure 7 shows indicated mean effective pressure (IMEP) plotted for 200 cycles from single-cylinder engine tests with an engine speed of 1000 rpm and fueling of 12 mg/cycle (nominally 325 kPa IMEP) at stoichiometric condition. The EGR is simulated in this operating condition by adding excess nitrogen to the intake air, and is estimated to be at 32%. Minimal amount of trapped internal residuals is present at this condition and the dilution is primarily due to simulated EGR. In the absence of pre-strikes, the best attainable COV of IMEP is 9% with a spark advance of -34 aTDC, and misfire and partial burn cycles are present. Adding one pre-strike while maintaining the same spark timing improves the combustion stability with COV of IMEP of 3%, but there are several cycles with less than optimal IMEP. With two pre-strikes added during the early part of compression stroke, the combustion stability is further improved and COV of IMEP is less than 2%. This clearly shows that by adding pre-strikes the EGR tolerance for this engine can be enhanced with the unique capability of GBDI. It should also be empha-

sized that for this operating regime, the combustion is purely ignition and flame propagation dominated with no LTC. The improvement in combustion with the pre-strikes is therefore because of enhancement of the propagating flame speed.
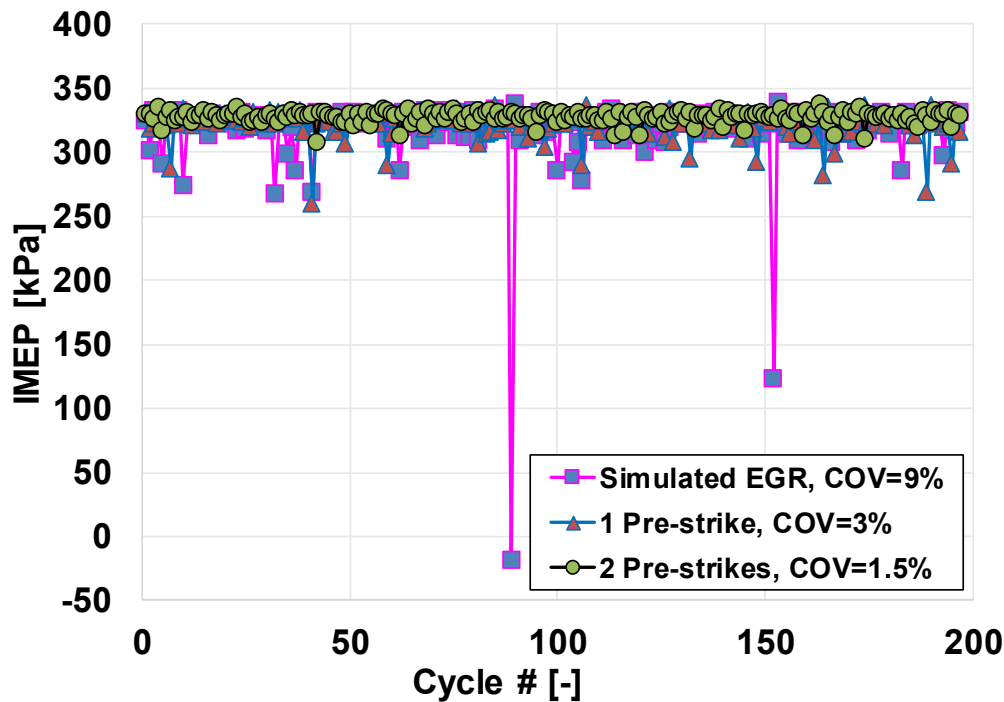
Figure 7: Improvement in simulated external EGR tolerance with GBDI by implementing pre-strikes.

The results shown in Figure 8 and Figure 9 are from a single-cylinder metal engine testing with an engine speed of 2000 rpm and fueling rate of 12 mg/cycle at stoichiometric condition. The sensitivity of the ignition system to real EGR dilution is presented in this section. It should be noted that the relative improvement in EGR rate between ignition systems is of most significance than the absolute dilution rate achieved.

Figure 8 shows the COV of IMEP as a function of EGR rate for three different ignition systems. For these EGR sweeps, the spark timing was chosen such that the combustion phasing was matched between the ignition systems (CA50 ~ 8° aTDC). For the spark plug system, two different energy levels are examined (60 mJ and 100 mJ) and compared to corona ignition and GBDI. The target COV of IMEP is 3% and is shown as a red dashed line. Figure 8 shows that at this operating condition, the GBDI system has the maximum tolerance to EGR dilution with rates of up to 25% with COV of IMEP < 3%. The unique capability of the GBDI system is its potential to deliver a wide range of ignition energy while maintaining its discharge in low-temperature plasma mode. The loss in combustion stability at the high EGR rates is also more gradual for the GDBI when compared to the other ignition system, thereby allowing for a more effective calibration.

From Figure 8, corona ignition is shown to be least tolerant to EGR dilution with onset of combustion instability as EGR is increased from 20% to 21%. For corona ignition, as EGR is increased, an advanced spark timing is demanded for achieving the target combustion phasing, to compensate for the slower combustion burn rates with increasing EGR. However, the advanced spark timing decreases the pressure at time of corona discharge and requires a reduction in driving voltage to prevent the transition to

arcing. Also, an increased duration of the discharge event is desired as EGR dilution is increased, which is a further challenge for the corona ignition system to prevent a transition to arcing. Therefore, the corona ignition system is more constrained by transition from low-temperature plasma discharge mode to high-temperature plasma discharge mode (arcing) at this part-load stoichiometric operation with EGR dilution.

For the spark plug system, the increase in ignition energy supports an improvement in EGR dilution tolerance by 1% for an acceptable combustion stability.
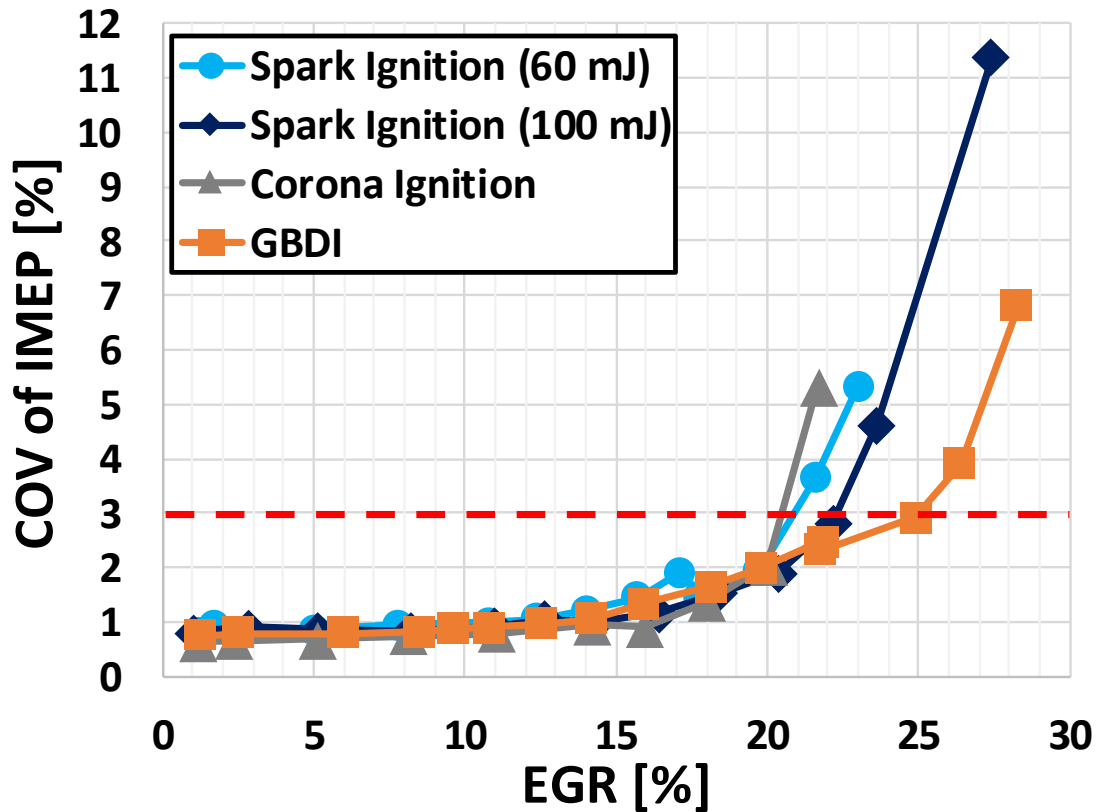
Figure 8: Improvement in external EGR tolerance with different ignition systems.

Figure 9 shows the improvement in net specific fuel consumption (NSFC) for the same operating condition as Figure 8. The data in Figure 9 is plotted as a relative improvement (negative values) in NSFC as a function of EGR rate. For the data shown in Figure 9, the NSFC at the lowest EGR rate for the 60 mJ spark plug case is chosen as the baseline and relative difference is shown for the different ignition systems. From Figure 9, adding EGR lowers the NSFC, implying an improvement in fuel consumption, and most of this benefit is from reducing pumping losses and improving thermodynamic properties. The data also shows that as the ignition energy is increased for the spark plug, there is no significant improvement in NSFC. However, for the corona ignition and GBDI, there is improvement in NSFC for the same EGR rate when compared to the spark ignition system. The most benefit is seen for the corona ignition system (~1%-2% improvement) and the GBDI system in between the spark ignition and corona ignition systems. As mentioned previously, the tendency for the corona ignition system to transition to arcing is a challenge at lighter load conditions. Therefore, the GBDI system is a good alternate that offers a much simpler and passive control of maintaining the low-temperature plasma discharge, while delivering efficiency benefits.

The improvement in NSFC for the same EGR level can be attributed to several reasons. The low-temperature plasma ignition systems provide consistent ignition from cycle to cycle and reduces the 0-10 burn duration significantly when compared to the spark ignition system. The overall reduction in burn duration these systems offer over the spark ignition system translates to an improvement in combustion efficiency as well as less cumulative heat release prior to TDC of firing, which may support reduced heat losses. Additionally, the GBDI system has demonstrated an impact on the later burn (50-90 burn duration), but the reason for this improvement is not well understood. Taken together, the low-temperature plasma ignition systems improve the combustion performance, potentially reduce heat losses and hence provide efficiency improvement.
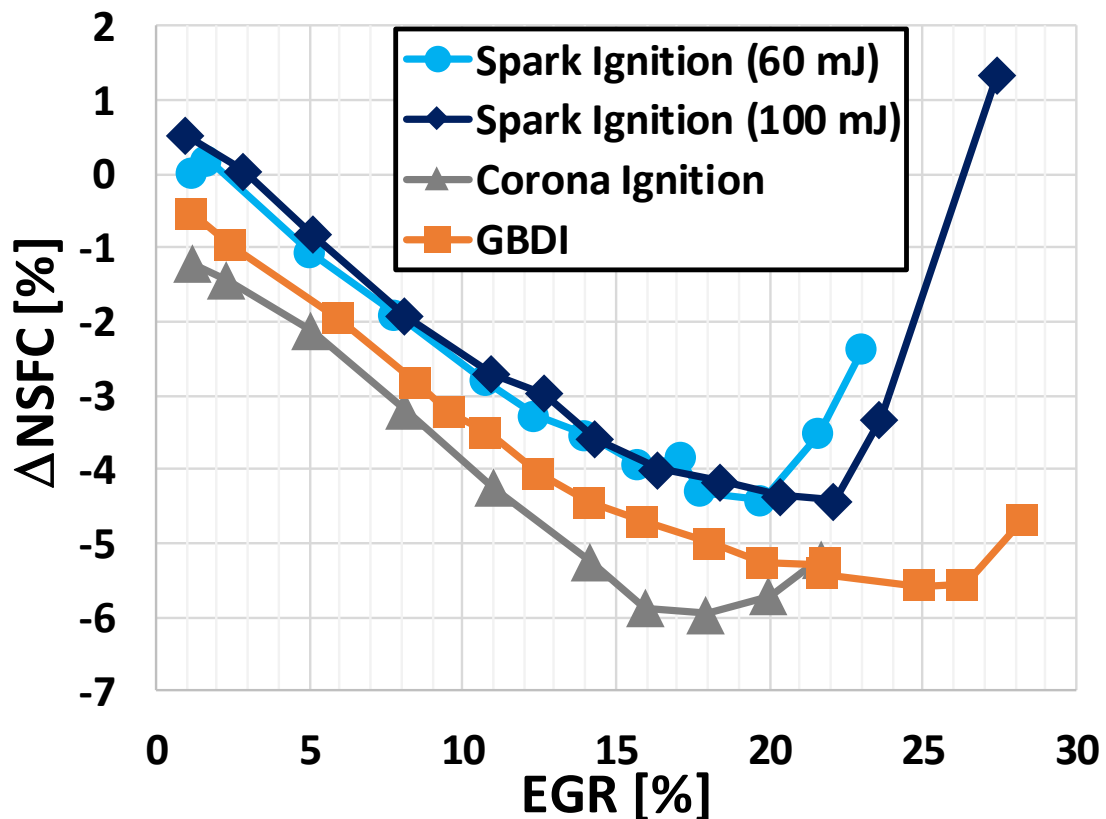
Figure 9: Improvement in net specific fuel consumption with different ignition systems for part-load stoichiometric operation with EGR dilution.
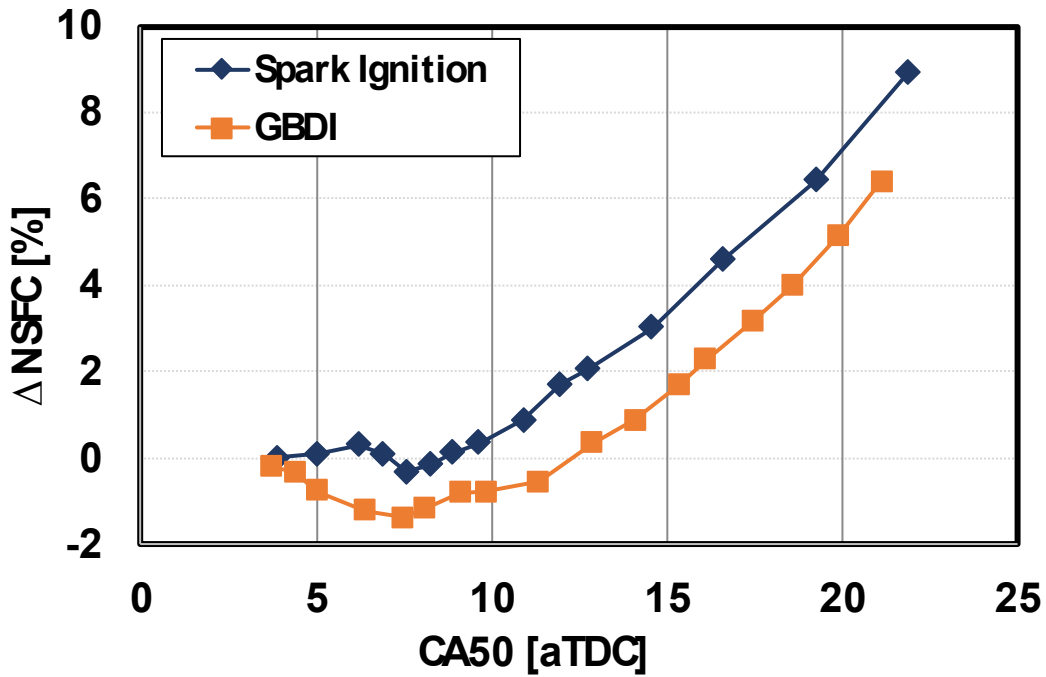
Figure 10:   Comparison of net specific fuel consumption between spark ignition and GBDI for higher load stoichiometric operation.

Figure 10 shows multi-cylinder engine data for stoichiometric operation at 2000 rpm, 26 mg/cycle/cylinder fueling rate (nominally 800 kPa IMEP) with a fixed EGR of 10%. A spark advance sweep is conducted for this operating condition and the relative improvement in NSFC is shown for spark ignition and GBDI. For the data shown in Figure 10, the NSFC value at the most advanced combustion phasing for the spark ignition system is the baseline. At the most advanced combustion phasing, the NSFC of the GBDI is very similar to the spark ignition. As the combustion phasing is delayed, the spark ignition system does not show any significant improvement in NSFC, but the GBDI system shows an improvement by 1.5% as the phasing is more optimally placed at 7° CAD aTDC. When comparing spark ignition and GBDI, it is also evident that there is a wider range of combustion phasing where the GBDI can operate without significant loss in efficiency. NSFC increase with further delay of combustion phasing for both ignition systems, but the 1%-2% efficiency gain with the GBDI continues even with the delayed phasing.

2.4   Wide open throttle operation (knock tolerance)

This section presents the capability of improving the knock tolerance with GBDI for wide open throttle operation in a multi-cylinder engine. The results are from a 1.0 L, 3-cylinder turbocharged engine opearting at wide open throttle at 4000 RPM. Figure 11 presents the crank angle at mass burned fraction of 5% (MBF5%) plotted against mass burned fraction of 50% (MBF50%) for three different ignition systems. The corona igntion system and GBDI were operated at a voltage and duration of 50 V and 150 µs, respectively. The scatter plot includes data from all the three cylinders. The engine is knock limited at this opearting condition and the maximum combustion advance that can be achieved for the spark ignition system is at an average of 26° aTDC. It is also noticable that there are several late burning cycles and several early burning cycles for the spark ignition system that largely limits the average combustion phasing. With the corona ignition system, the scatter plot indicates a tighter spread than spark ignition,

but the average combustion phasing is the same or marginally better by 0.5°. In contrast, the GBDI system shows a tighter grouping of the individual cycles and offer an improvement in combustion phasing advance by almost 3°.

The advantage of the GBDI system to mitigate knock is in its ability to provide consistent and reliable igntion and combustion from cycle to cycle while reducing the overall burn duration. The tigther scatter of individual cycles in Figure 11 is indicative of such consistency and is an important feature of the GBDI system.
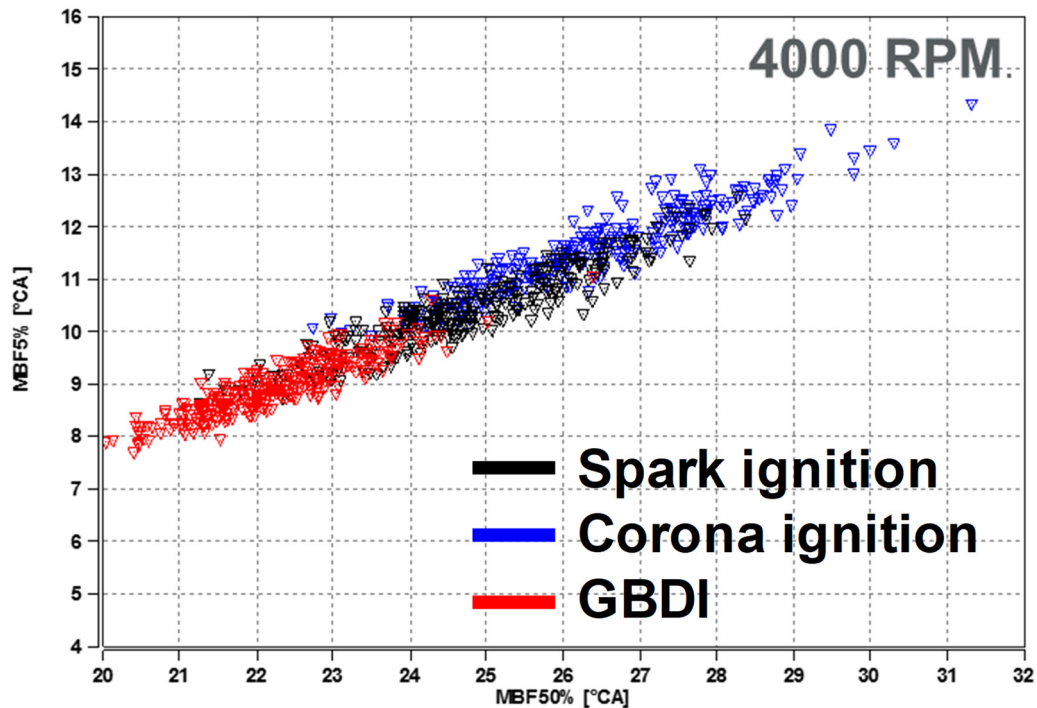
Figure 11: Improvement in knock tolerance for GBDI system at WOT operation.

3   Summary

The paper demonstrates the potential of low-temperature plasma ignition system, specifically groundless barrier discharge ignition (GBDI) system in enabling multiple combustion modes that are of importance for future high efficiency engines. To summarize, GBDI offers unique capabilities that make it a very compelling alternative to conventional inductive spark ignition systems.

- GBDI can enable flameless and flame-assisted controlled LTC in part-load lean operation and offers a simple and passive control with voltage, duration and number of pre-strikes as the primary control parameters.
- GBDI can enable significant improvement in dilution tolerance for part-load stoichiometric operation with and without the use of pre-strikes. The GBDI system also provides efficiency improvement potential due to better combustion performance and potential reduction in heat losses.
- At WOT operation, GBDI demonstrates the potential to improve knock tolerance when compared to corona and spark ignition systems, primarily due to shorter burn duration and reduced cycle to cycle variability.

- The inherent design of the GBDI lacks a ground electrode that helps with reducing heat losses and removes a potential hot-spot for pre-ignition.
- The GBDI is also not dependent on a gap and thus gap erosion is not a concern. It has the potential to be a plug for the life of the engine.
- The GBDI is in an active state of development with plug to plug variability and dielectric issues to be addressed. The primary failure mode of the plug is through puncture of the dielectric. These concerns need to be addressed as future development of this promising system continues.

4 Acknowledgements

References

[1] Proceedings of First International Conference: Advanced Ignition Systems for Gasoline Engines, Nov. 12 – Nov. 13, 2012, Berlin, Germany.

[2] Proceedings of Second International Conference: Advanced Ignition Systems for Gasoline Engines, Nov. 24 – Nov. 25, 2014, Berlin, Germany.

[3] Proceedings of Third International Conference: Advanced Ignition Systems for Gasoline Engines, Nov. 3 – Nov. 4, 2016, Berlin, Germany.

[4] Shiraishi, T., Possibility of the new ignition system using the low temperature plasma having dual functions of strengthening ignition for SI combustion and promoting and controlling autoignition of HCCI combustion, Proceedings of First International Conference: Advanced Ignition Systems for Gasoline Engines, Nov. 12 – Nov. 13, 2012, Berlin, Germany.

[5] Schenk, M., Fessler, M., Wolf, T., Klaus, B., Fischer, H., Comparison of the thermodynamic Potential of alternative Ignition Systems for SI-Engines, Proceedings of First International Conference: Advanced Ignition Systems for Gasoline Engines, Nov. 12 – Nov. 13, 2012, Berlin, Germany.

[6] Suess, M., Guenthner, M., Schenk, M., Rottengruber, H-S., Investigation of the potential of corona ignition to control gasoline homogeneous charge compression ignition combustion, Proc. IMechE, Part D: J. Automobile Engg., Vol 226, pp. 275 – 286, 2011.

2 Design

2.1 High-fidelity Numerical Modelling of Spark Plug Erosion

Douglas Breden, Anand Karpatne, Kenta Suzuki, Laxminarayan Raja

Abstract

Spark plug erosion is critical in determining the overall efficiency of a spark ignition engine. Over its lifetime, a spark plug is subject to millions of firings. Each spark event results in material erosion due to several mechanisms such as melting, vaporization, sputtering and oxidation. With electrode wear, the inter-electrode spacing increases and a larger voltage difference is required to initiate the spark. The probability of engine misfires also increases with electrode erosion. Once a critical gap is reached, the energy in the ignition coil is not enough to cause a spark breakdown, and the spark plug must be replaced. Due to the long relevant time scales over which erosion occurs, and the difficulty of analyzing the spark plug environment during operation, determining spark plug lifetime typically requires extensive field testing. A high fidelity commercial thermal plasma solver, *VizSpark* is used simulate electrode erosion due to spark events. The model preserves key arc physics such as current conservation, conjugate heat transfer, fluid flow and electrode ablation. The solution framework includes the capability of coupling high fidelity arc physics with a dynamically deforming spark-plug electrode. A phenomenological model for electrode erosion based on energy is derived from prior experimental work on single-pulse electrode erosion. The energy based electrode erodion model is validated against experimental results, and 3-D electrode erosion simulations in stationary and cross-flow were performed.

1 Introduction

The maximum lifetime of a spark plug is limited by electrode erosion. Over the course of 10's to 100's of millions of repeated sparking events, the electrode material ablates and the electrode gap increases. Eventually a point is reached where the spark-plug driving circuit is unable to provide the threshold voltage necessary to breakdown the gap and strike an arc. Essentially, the spark-plug is no longer operable and must be replaced. The issue of spark plug erosion has been investigated experimentally for many years now [1] [2] [3]. Spark plug erosion is a major issue in the long-term maintenance-free operation of a natural gas engine [4] [5]. Due to the long relevant time scales over which erosion occurs, and the difficulty of analyzing the spark plug environment during operation, determining spark plug lifetime typically requires extensive field testing.

The objective of this work is to develop a computational model that can accurately simulate the electrode erosion process and make predictions on the effective lifetime of a spark plug. The problem is challenging in that there are a vast range of time scales, all of which must be resolved to model the erosion. Time scales range from milliseconds needed to resolve arc physics up to weeks/months for timescales of electrode deformation due to ablation.

Previous numerical studies on spark igniters have focused predominantly on simulation of the arc itself [6] [7] [8] [9] [10] [11]. For predicting electrode erosion and lifetime, dynamic coupling between arc physics and an eroding electrode must be developed. In this study, a high-fidelity thermal arc solver is used to model the arc physics which determines the net heat and electrical energy fluxes to the electrodes. The solid electrodes themselves are modelled using an immersed object method, which allows for a dynamic change in shape of the electrode as the simulation progresses. Ablated mass flux from the electrodes is modelled using an energy dependent ablation model derived from experimental and numerical work performed by [1] [2]. As mass is removed from the electrode-gas interface, the immersed object dynamically deforms, which in turn modifies the gap voltage and the arc physics.

2   Model Description

Our general purpose commercial thermal plasma modeling solver *VizSpark*® [12] is used in this study. This high-fidelity computational tool has been utilized previously in the context of modeling arc formation, stretch and re-strike phenomena in a spark-plug gap [13] [14]. The physics represented in this tool involve solving compressible fluid flow physics coupled with the electromagnetic equations. The gas composition, thermal, electrical, and transport properties are solved by assuming chemical equilibrium. The thermal plasma model has been validated on a component basis to test the individual flow (viscous, inviscid), gas property thermodynamic and transport generation, and electromagnetic physics. Validation of the full arc physical has been performed for a spark channel in crossflow (see [14]) and for a stationary free-burning arc.

Arc Model

Governing differential equations for the coupled fluid and electromagnetic physics are solved in a coupled manner.

Navier-Stokes Equations

The compressible Navier-Stokes equations are solved to describe the mean-mass flow velocities, the gas pressure, mass density, and the arc (gas) temperature. The mass conservation equation can be written as

$$\frac{\partial \rho}{\partial t} + \vec{\nabla}.\left(\rho \vec{V}\right) = 0$$

(1)

where ρ is gas density, and $\vec{V}$ denotes flow velocity. The momentum equation in conservative form can be expressed as

$$\frac{\partial(\rho \vec{V})}{\partial t} + \vec{\nabla}.\left(\rho \vec{V} \vec{V}\right) = -\vec{\nabla}P + \vec{\nabla}.\bar{\bar{\tau}} + \vec{S}_M$$

(2)

Here P denotes gas pressure, $\bar{\bar{\tau}}$ corresponds to the viscous stress tensor and $\vec{S}_M$ is the volumetric external force vector acting on the fluid. Finally, the energy equation can be written as

$$\frac{\partial(\rho E)}{\partial t} + \vec{\nabla}.\left((\rho E + P)\vec{V}\right) = (\bar{\bar{\tau}}.\vec{\nabla})\vec{V} + \vec{\nabla}.(k\nabla T) + S_E$$

(3)

where E is specific internal energy (kinetic plus potential energy per unit volume of the fluid), 'k' corresponds to thermal conductivity and S_E is the external energy source. These governing equations are written in vector form as

$$\frac{\partial \vec{U}_{flow}}{\partial t} + \vec{\nabla} \cdot \left(\vec{F}_{\text{inv}} + \vec{F}_{\text{vis}} \right) = \vec{S}_{flow}$$

(4)

Here, the vector of conserved variables $\vec{U}_{flow}$ are listed below as

$$\vec{U}_{flow} = \begin{bmatrix} \rho \\ \rho u \\ \rho v \\ \rho E \end{bmatrix}$$

(5)

where 'u' and 'v' are the 'x' and 'y' components of velocity.
The flow convective/inviscid flux $\vec{F}_{inv}$ is given as

$$\vec{F}_{inv} = \begin{bmatrix} \rho u \\ \rho u^2 + P \\ \rho u v \\ (\rho E + P)u \end{bmatrix} \hat{x} + \begin{bmatrix} \rho v \\ \rho v u \\ \rho v^2 + P \\ (\rho E + P)v \end{bmatrix} \hat{y} \quad ,$$

(6)

and the flow diffusive/viscous flux $\vec{F}_{vis}$ is written as

$$\vec{F}_{vis} = \begin{bmatrix} 0 \\ \tau_{xx} \\ \tau_{xy} \\ u\tau_{xx} + v\tau_{xy} + k\dfrac{\partial T}{\partial x} \end{bmatrix} \hat{x} + \begin{bmatrix} 0 \\ \tau_{yx} \\ \tau_{yy} \\ u\tau_{yx} + v\tau_{yy} + k\dfrac{\partial T}{\partial y} \end{bmatrix} \hat{y}$$

(7)

Note that the energy diffusive flux consists of energy diffusion due to viscosity and heat conduction represented by Fourier's law. The viscous stresses can be found using the formula $\tau_{x_i x_j} = \mu \left(\dfrac{\partial x_i}{\partial x_j} + \dfrac{\partial x_j}{\partial x_i} \right) + \lambda \delta_{ij} \vec{\nabla}.\vec{V}$ where μ is the coefficient of viscosity and λ is the bulk coefficient of viscosity. Stokes hypothesis is used to express the bulk viscosity term as $\lambda = -\dfrac{2}{3}\mu$. The last term in the coupled Navier-Stokes system of equations is the source term $\vec{s}$ given as

$$\vec{S}_{flow} = \begin{bmatrix} 0 \\ (\vec{J} \times \vec{B})_x \\ (\vec{J} \times \vec{B})_y \\ \vec{J} \cdot \vec{E} - \dot{Q}_{rad} \end{bmatrix}$$

(8)

Here, Joule heating due to the electric field is modeled by the inclusion of $\vec{J} \cdot \vec{E}$ source term on the fluid energy equation. Lorentz effects on the arc are modeled by including $(\vec{J} \times \vec{B})$ forcing terms in the fluid momentum equations. The conduction current density

is $\vec{J}$, the electric field is $\vec{E}$, and $\vec{B}$ is the local magnetic field. Cooling of the arc due to radiation is treated using a source term $\dot{Q}_{rad}$ and a net emission coefficient model.

Electromagnetic Equations

The governing equation to solve is the current continuity equation

$$\nabla \cdot J = \vec{0} \tag{9}$$

Where the current density $\vec{J}$, is expressed using Ohm's Law

$$\vec{J} = \sigma(T,P)\vec{E} \tag{10}$$

Assuming that $\vec{A}$ is the magnetic vector potential, such that $\vec{B} = \vec{\nabla} \times \vec{A}$, the expression for the electric field $\vec{E}$ is modified to account for magnetic fields

$$\vec{E} = -\vec{\nabla}\phi - \frac{\partial \vec{A}}{\partial t} \tag{11}$$

Equations (9), (10) and (11) in turn lead to the governing equation in the form of a second-order elliptic equation for electrostatic potential ϕ

$$\nabla \cdot \sigma \nabla \phi = 0 \tag{12}$$

For magnetic vector potential, the following time evolution equation is solved

$$\sigma \frac{\partial \vec{A}}{\partial t} + \sigma \nabla \varphi - \frac{1}{\mu} \nabla^2 \vec{A} - \nabla(\frac{1}{\mu}) \times \nabla \times \vec{A} = 0 \tag{13}$$

Immersed Boundary for Electrodes

Electrode (cathode) motion is accounted for by modeling the solid electrodes using an immersed boundary formulation [15]. The same governing equations for fluid flow and electric field are solved in the gas region and in the parts of the mesh that are tracked as immersed boundary electrodes.

The presence of the solid material is imposed by applying large numerical forcing terms on the 'x' and 'y'-momentum equations, essentially forcing the fluid velocity in the immersed object regions to zero [16]. Material properties of the solid are imposed in the regions of the immersed anode and cathode.

Removal and deformation of electrode surface cells is done by tracking the electrode mass in each cell, set at the start of the simulation using the material density and the cell volume. As ablation occurs at electrode-gas interfaces, tracked solid material mass is removed from the electrode and converted into vapor mass in the gas region. Once most of a cell's mass has been removed in this manner, the immersed object cell is converted into a gas cell indicating that it has ablated away. The new gas cell properties and variables are set using a cell clearing method (see [15]) where variables from neighboring gas cells are used to interpolate the newly cleared cell variables.

Governing Equations in Immersed Electrodes

In the immersed electrode regions, the Navier-Stokes equations are modified with the addition of forcing terms that act to force the fluid velocity in the gas to go to zero. For the case of zero velocity, one can effectively ignore the x and y-direction momentum equations.

Diffusive heat transfer within the immersed objects and between the gas-solid interface is accounted for by the energy equation of the Navier-Stokes equations. The fifth row corresponding to the energy equation in the Navier-Stokes system reduces to the unsteady heat transfer equation

$$\frac{\partial \rho C_p}{\partial t} + \vec{\nabla} \cdot (\kappa \vec{\nabla} T) = 0 \tag{14}$$

To correctly model heat transfer within the immersed object, the effective density, thermal conductivity and specific heat of the immersed object cells are overridden with those of the metal being modeled (in this study copper is used).

For obtaining the electric fields, no modification to the governing equation for current continuity is necessary. The only requirement is to set the electrical conductivity of the immersed object electrodes to that of the electrode metal. Consequently, electric current can flow seamlessly through the electrodes, through the electrode-gas interface, and through the arc channel.

Gas Properties

Closure of the governing equations requires specification of gas thermodynamic properties: the density and specific heats of the mixture; as well as transport properties: viscosity, thermal conductivity, and electrical conductivity. The approach with this model is to solve for all properties as a function of temperature and pressure and store the results in lookup tables.

Air thermodynamic and transport properties were obtained by assuming thermal and chemical equilibrium and applying Gibb's free energy minimization. First, the specific heats of the individual constituent species of air (NASA polynomials were used in this study), were provided as inputs. By solving Gibb's Free energy minimization problem, the species compositions as a function of temperature and pressure are obtained. Once the mixture composition is known, the mixture thermodynamic and transport properties can also be computed.

Radiation Model

Arc radiation cooling is modeled using a net emission coefficient model, which acts as a cooling volumetric source term. Net emission coefficients are tabulated as a function of temperature and assumed to vary linearly with pressure. The net emission coefficient data for air was taken from [17].

Energy Dependent Erosion Model

The mechanism of mass removal of material from a metal electrode surface is due to a multitude of complex physical phenomena that are not completely understood. Spark erosion occurs at length scales on the order of the arc root (tens of microns) and timescales of the order of nanoseconds to microseconds. Attempting to model all the

physical phenomena that can occur at the arc root such as sputtering, melting, vaporization, mass ejection, surface Joule heating and oxidation simultaneously with a simulation on the time and length scales required to resolve the spark is numerically infeasible. Therefore, developing a model that can accurately capture ablation yet avoid the numerical cost of modeling the arc root erosion process at full fidelity is imperative. Three mechanisms that have been investigated include sputtering of the surface due to ion bombardment, ejection of molten material due to an imbalance in the surface tension of the melt pool and an ion pressure force from the arc, and melting and vaporization of the material due to heat addition from the arc. The authors of [1] performed an experimental study of single spark ablation in an attempt to understand which of the proposed mechanisms (sputtering, melting/vaporization, or mass ejection) is the dominant ablation mechanism. They found that material ablation was strongly correlated to the energy required to melt the material. Furthermore, the ratio of ablated volume to input energy (V/E) to the inverse of melting enthalpy (energy input required to melt the material per unit mass) ΔH_{melt} for different pure metals (platinum, iridium, nickel, gold, silver, aluminum, nickel, tungsten, tin, lead, ruthenium, and copper) was calculated and plotted for pure air and nitrogen. The ratio or constant, herein referred to as the K-factor was found to be relatively close for all the pure metals [1].

$$K = \frac{V/E_{input}}{1/\Delta H_{melt}} \tag{15}$$

From the insights provided by the experimental and numerical work in [1] [18] [19], a phenomenological model for mass flux from a surface due to an input energy has been determined. Using the K-factor defined above, the erosion mass flux rate $\vec{\Gamma}_{eroded}$ at a surface can be modelled as

$$\vec{\Gamma}_{eroded} = K \frac{\rho \dot{E}_{input}}{\Delta H_{melt}} \tag{16}$$

$\dot{E}_{input}$ is an input power flux (W/m2-s), ρ is the density of the bulk metal, and ΔH_{melt} is the energy per kg mass required to melt the material from a reference temperature. What this equation essentially says is that erosion is strongly correlated to the input energy, the amount of mass (density) that can absorb the energy, and the energy required to melt that mass. The K-factor is relatively insensitive to the material type and accounts for the detailed physics such as radiation, surface Joule heating/ that this model tries to abstract away.

The chief advantage of this model is its simplicity: the surface ablation which involves complex interaction between the arc root and the metal is simplified to a function of three material dependent constants (K, ΔH_{melt}, and), ρ) and an input energy. The input power for the model at the surface can either be electrical energy (the surface voltage times the surface current) or the net incident heat flux, both of which are obtainable from an arc solver.

3   Arc Root Scale Erosion Modelling

The energy dependent erosion model utilized in this study depends on obtaining the material dependent K-factor. The input energy can be specified as either the electrical or incident heat flux energy. This factor can be calculated either from experiments [18] or through high-fidelity thermal modeling near the arc root [19]. The amount of eroded

volume is correlated with the amount of melt pool for a given arc energy and electrode material. In this section, an estimate of the melting and heating of the arc spot for a given input energy at the arc time scale is performed. Note that the current study is an essential first step in numerically determining K-factor. The eventual goal is to develop a computational tool can be used to perform high fidelity modelling of the heating and melting of the metal surface near the arc root to obtain the K-factors. Once K-factors are known, the same computational tool can be used to simulate the full spark-plug erosion problem. This work is similar to and mostly follows that done in the simulation work of [19].

The same domain and input energy profiles from [19] are used here. A key requirement is the ability to predict material erosion is to track the material phase transition. One approach is to explicitly track the phase of the material using a phase variable as was done in [19]. In this work, instead of explicitly tracking the material phase, the material properties of the metal across all phases over a range of temperatures are tabulated and the phase change is accounted for in the specification of the material's temperature dependent thermodynamic and transport properties. The energy required to change phase (latent heat of fusion for solid to liquid and latent heat of vaporization for liquid to gas) is accounted for in the specification of the specific heat of the material.

Solid Material Properties and Phases

Temperature dependent material properties are specified for each metal. Thermodynamic properties include temperature dependent density and specific heat and the transport properties include temperature dependent thermal conductivity. A sample of the thermodynamic and transport properties for nickel over a temperature ranging from 1000 K to 4000 K are shown in Figure 1.
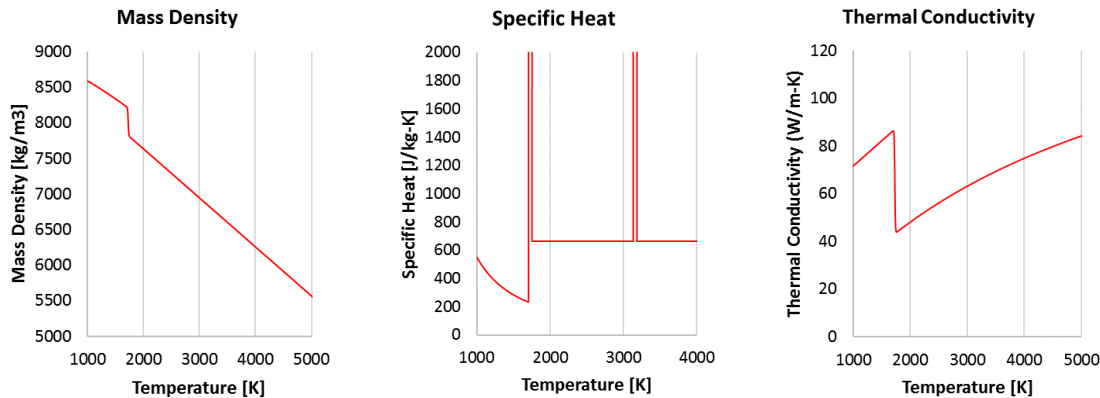
Figure 1: Temperature dependent thermodynamic and transport properties for nickel. The energy of phase transition is accounted for in the material specific heat

The phase change of the material is accounted for by modifying the specific heat with the energy required to undergo the phase change from the formula for the enthalpy of fusion/vaporization

$$\Delta H_{vap} = \int_{T_0}^{T_{melt}} C_p(T)dT + L_{fusion} + \int_{T_{melt}}^{T_{boil}} C_p(T)dT + L_{vaporization} + \int_{T_{boil}}^{T} C_p(T)dT \ (17)$$

The total energy required to heat a material from a referenced temperature T_0 to T is obtained by integrating the specific heat over the temperature range. When the temperature reaches the melting and boiling points of the material, the latent heat of fusion

and vaporization respectively, are added to account for energy required for the phase transformation.

The formula for enthalpy of fusion/vaporization can be used to derive a modified specific heat function. We assume that phase transformation occurs over a small but finite temperature interval ΔT_{ph} (10 K) and that the heat of fusion/vaporization can be re-expressed as a constant specific heat times the finite interval temperature.

$$L_{fusion} = C_{p,fusion}\Delta T_{ph} \tag{18}$$

$$L_{vaporization} = C_{p,vaporization}\Delta T_{ph} \tag{19}$$

Hence the total energy required to undergo phase change from solid, to liquid, to gas is conserved and can be expressed purely as a function of a piecewise continuous specific heat function

$$\Delta H_{vap} = \int_{T_0}^{T_{melt}} C_p(T)dT + C_{p,fusion}\Delta T_{ph} + \int_{T_{melt}}^{T_{boil}} C_p(T)dT +$$

$$C_{p,vaporization}\Delta T_{ph} + \int_{T_{boil}}^{T} C_p(T)dT \tag{20}$$

Simulation Configuration

A two-dimensional 40 x 40 micron axisymmetric quad mesh is used for all simulations.
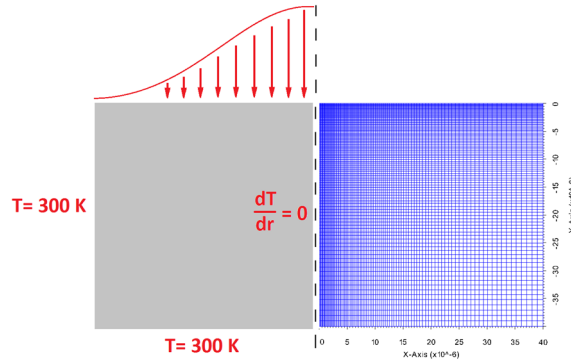
Figure 2: Axisymmetric configuration with boundary conditions (left) and numerical mesh (right)

Fixed temperature boundary conditions are applied at the bottom and side, and a zero-temperature gradient boundary condition is applied along the axis. For comparison with [19], the same energy deposition profile (gaussian in space and gaussian in time) was chosen, as shown in Figure 2. A quad mesh with a size of 0.1 micron was chosen (close to the axis boundary).

Results

Simulations were completed for the following metals: tungsten (W), iridium (Ir), nickel (Ni), platinum (Pt), copper (Cu), gold (Ag), and aluminum (Al). The specific heat and temperature profiles for nickel at the end of 1 microsecond are shown in Figure 3. The specific heat profile spikes at phase transitions due to the addition of the latent heat of fusion and vaporization, and acts as an indirect marker of the location of phase transition. For nickel, the phase transition region along the region where specific heat spiked (undergoing phase transition) from solid to molten nickel is indicated at the top of Figure 3. The temperature of the nickel melt pool reaches a peak of approximately 3000 K with a depth of approximately 3 microns. The melt pool radius is about 15 microns compared to the imposed arc root radius (radius where heat was applied) of 10 microns.
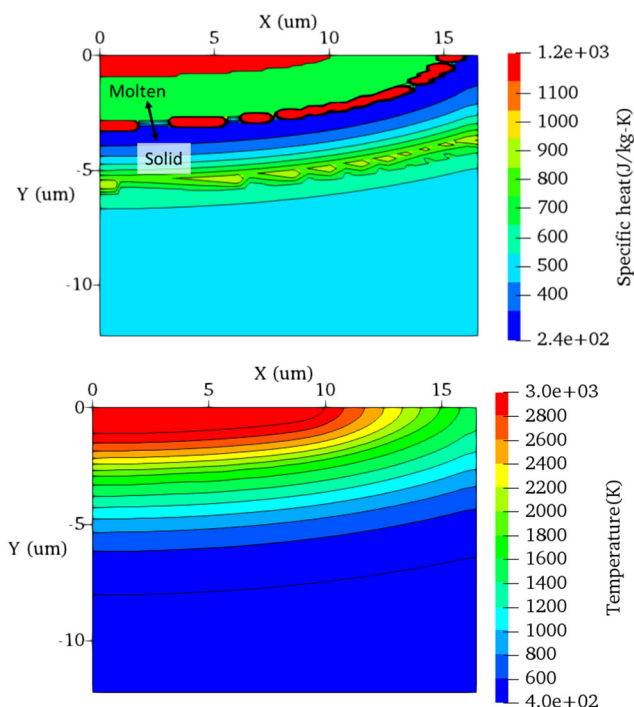
Figure 3: Specific heat (top) and temperature (bottom) profiles for nickel after 1 millisecond of simulation time. The solid-molten transition region can be identified by the large spike in specific heat and is indicated with arrows.

Figure 4 shows a comparison between melt pool volume prediction from the arc solver and numerical results from Lasagni et al. [19] for different ratios of eroded volume to spark energy. The data points correspond to different materials. It can be observed that the molten pool volume prediction from the arc modelling tool agrees well with previous results from [19].
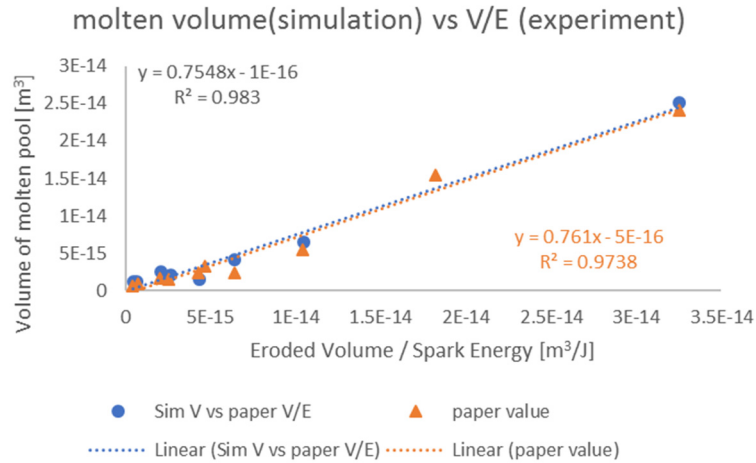
Figure 4: Comparison of volume of molten volume pool vs V/E of current simulations with simulations of [19].

The molten pool volume prediction is only the first step in determining the K-factor. Materials with larger molten pool volume are susceptible to more erosion due to vaporization, oxidation, and ejection of melt pool volume due to an imbalance of surface tension forces on the electrode surface. Therefore, Figure 4 can be used to quantify erosion trends for different materials. More work is necessary to accurately determine eroded volume for every electrode material/spark energy combination. Therefore, for the rest of this study, the electrical energy depenedent K-factor based on previous experimental data [2] is used.

4   Validation of Energy Dependent Erosion Model

Given an energy dependent K-factor for electrode erosion, the above described model is validated against prior experiments [2] [1] for tungsten (W), iridium (Ir), nickel (Ni), platinum (Pt), tin (Sn) and silver (Ag) . The inputs to the model are geometry, electrical parameters and the predicted outputs are volume of eroded electrode and the total spark discharge energy. The surface electrical energy dependent K-factor for air are taken from [1].

Simulation Configuration

The geometry (Figure 5) consists of an axisymmetric pin-to-plane spark plug, with a cylindrical cathode (diameter 1 mm), and a conical anode (max diameter 0.6 mm). The mesh consists of variable sized triangles across the entire domain. At the cathode boundary, a fixed current profile is applied (Figure 6) with a peak amplitude of 0.9 A that decreases linearly to 0 over 1.1 milliseconds. The anode boundary is treated as electrically grounded. For the outer boundaries, a symmetry condition is applied such that there are no far-field gradients in flow or electric field variables.
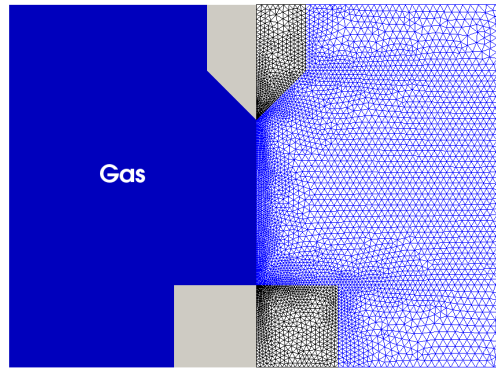
Figure 5: Domain and mesh for the pin to plane arc simulation. The mesh consists of 9,664 cells. The anode (top electrode) is conical in shape with base diameter of 0.6 mm, and the cathode (bottom electrode) is cylindrical (diameter 1 mm).

Figure 6 shows the applied cathode current as a function of time and the predicted boundary voltages. Initially, as a large current is applied, the cathode voltage increases self-consistently to allow for the passage of current. This high voltage (~ 1000 V) causes significant local joule heating and an arc channel forms with increased conductivity. Once this channel is established, the cathode potential drops down to ~50 V. Finally, when the applied current approaches zero (after ~1ms), the cathode voltage again increases due to a drop in the channel temperature and conductivity. Finally, when the applied current drops down to zero, the electrode voltage also reduces to zero as no current flows between the spark-gap.
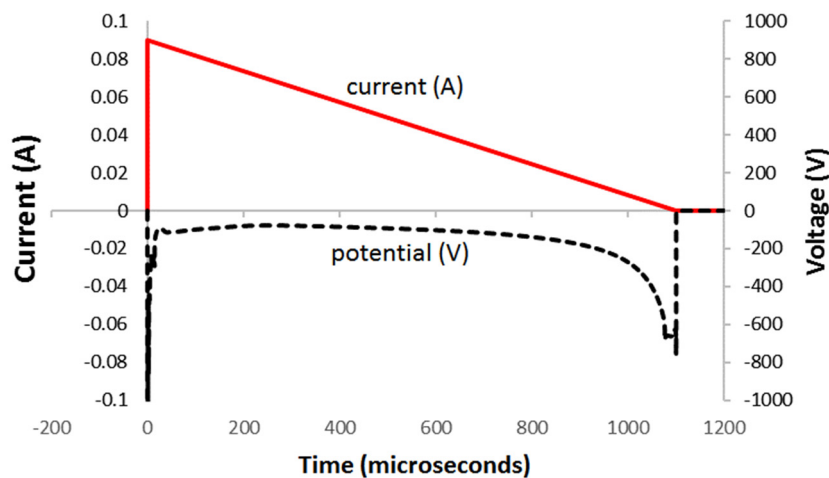
Figure 6: Current and Voltage as function of time for the pin-plane simulation using platinum as the cathode material. Current is the applied (input) boundary condition and the voltage is obtained by the arc solver self-consistently.

The volumetric current density and temperature snapshots are shown in Figure 7. Initially, when the arc forms (0.05 milliseconds), the current density is maximum (~10^8 A/m^2) and concentrated along the axis. The arc temperature is also maximum along the centerline (~6000 K). With time, as the total applied current diminishes, the current density magnitude reduces to ~10^6 A/m^2.
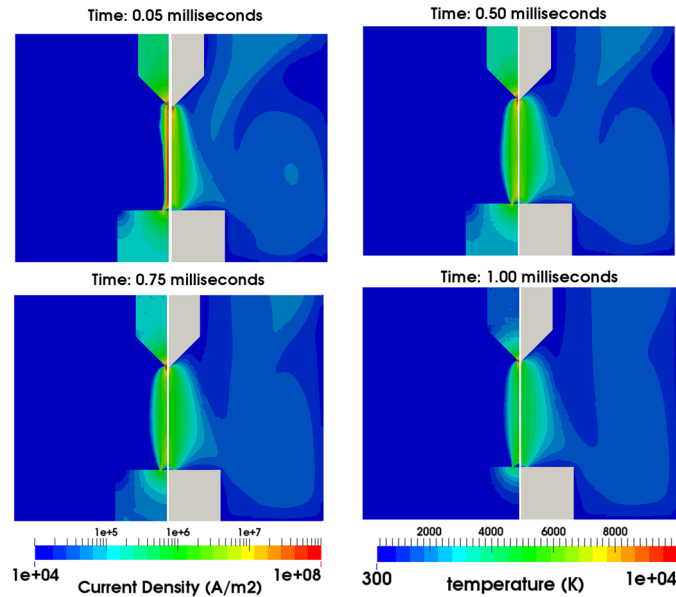
Figure 7: Time snapshots of the current density (left half) vs temperature (right half) in the arc channel for 0.25, 0.5, 0.75 and 1 milliseconds. Note that the current density through the metal electrodes is also included.

The comparison between experiments and predicted results is shown in Figure 8. The x-axis corresponds to the inverse of material melting enthalpy (varies with material type), and the y-axis denotes the ratio of volume eroded to input spark energy. The spark energy is obtained by integrating cathode electrical power (product of electrode voltage and current from Figure 6) over the entire spark duration. Given an instantaneous electrical power, eroded volume flux is computed using Eq. 16. Finally, the ratio of total eroded volume to spark energy is obtained for different material types. Good correlation with experimental data is observed, and all data points lie along a straight line with a slope of $K = 2.095811 \times 10^{-5}$.
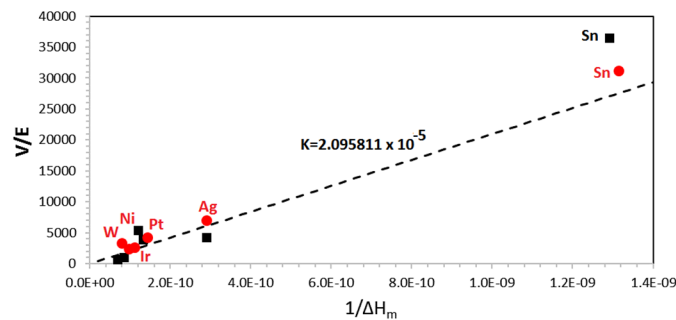
Figure 8: Comparison of calculated eroded volume/energy vs the reciprocal of material melting enthalpy ($1/\Delta H_m$) from simulations (red circles) to experimental values (black squares) from [1].

5   3-D Spark Plug Erosion Prediction

Spark erosion occurs over many millions of spark events. Simulating millions of sparking events at high fidelity is numerically infeasible with current computing power. We utilize several approximations and techniques to approximately capture the erosion

that occurs over long time scales and millions of firings with only a few high-fidelity simulations.

A typical spark duration for a car ignition system is of the order of 1 millisecond and for inductive ignition systems the current profile will often have a sawtooth waveform [13]. In this work the electrical input boundary condition is specified as a sequence of sawtooth current wave form pulses with an initial peak of 50 mA which then decrease linearly to zero (see Figure 11 and Figure 14).

The rate at which ablation takes place along the electrode surface can be accelerated beyond the timescale of the arc event by applying a multiplicative factor to the surface erosion rate calculated by the surface erosion model. For example, if a single spark event is simulated and an erosion rate multiplier of 100,000 is used, that single sparking event would remove roughly the equivalent mass to 100,000 spark events.

Another acceleration technique used to reduce simulation time is to use shorter pulses in tandem with the surface erosion rate multiplicative factor. Because the erosion model is energy dependent, a multiplicative factor on the input energy can be used to approximate energy input from a longer pulse.

Simulation Configuration

A 3-D domain for the sparkplug consisting of a prong cathode and an L-jacket grounded anode similar to the spark plug geometry from [13] is specified and shown in Figure 9. Two ablation prediction simulations are performed: one with an air cross-flow of 8 m/s and another in stationary air. The pressure is 5 bar and the ambient temperature at the start of simulation is 300 K. For the case with 8 m/s cross-flow, the inflow direction is indicated in Figure 9 and the other boundaries are outflowfar-field boundaries. An electrical current is specified on the cathode bottom boundary as a function of time and a zero voltage (grounded) boundary condition is specified for the anode L-jacket.
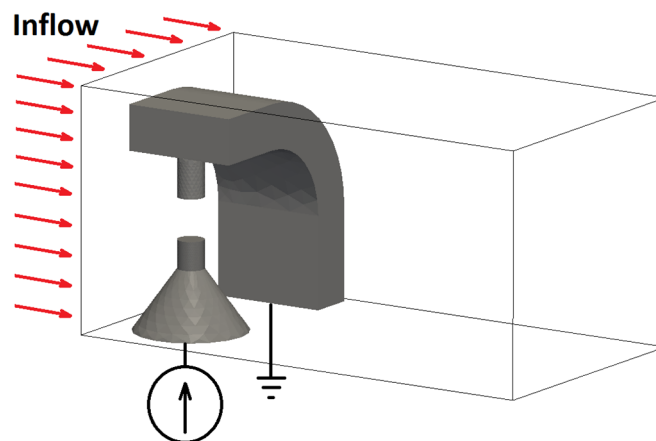
Figure 9: Domain for 3-D sparkplug with constant current power source and grounded L-jacket. The boundary where inflow is applied is shown with red arrows.

A numerical mesh consisting of 328,287 tetrahedral cells is imposed on the problem domain and shown in Figure 10. A domain decomposition approach is utilized, where

the numerical mesh is split equally amongst multiple processors and solved in parallel to reduce the computational solve time.
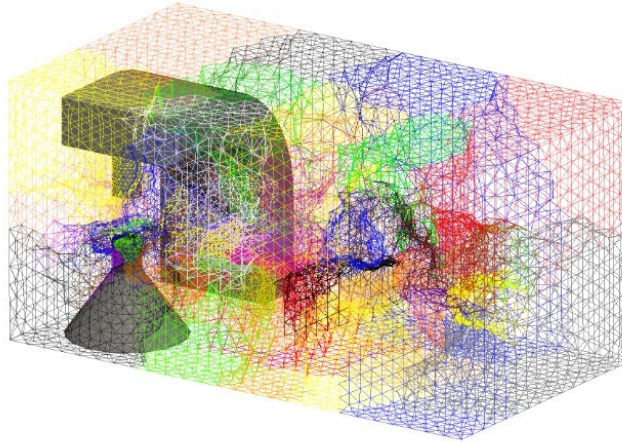
Figure 10: The numerical mesh consisting of 328,287 cells split amongst 40 computing processors.

For both flow and no-flow simulations, 10 numerical pulses of 0.1 milliseconds are applied. Each pulse consists of applying an input current with peak current of 50 mA which then decreases linearly to zero (sawtooth pulsing).

In this work, the simulated pulses are 0.1 milliseconds in duration with an input energy multiplier of 10 such that the effective pulse duration is 1 millisecond. In addition to pulse energy multiplier, we apply an erosion multiplicative factor of 100,000 such that each simulated pulse removes the mass that approximately 100,000 real pulses would remove.

Each simulated pulse is separated by 20 microseconds of zero-current off time. During the pulse off-time, an artificially large energy source term is applied to quench the arc temperature channel such that each simulated pulse is applied to fresh gas and ensuring that each simulated spark is independent of the prior simulated arc.

The cross-flow and no cross-flow simulations were each simulated using parallel domain decomposition on 40 processors. The total run time required to complete each simulation is approximately 3-4 days.

Results

Cross-Flow (8 m/s):

The results for the simulation with an 8 m/s cross-flow are presented first. Figure 11 presents time snapshots of the arc temperature and the electrode surface topology at the end of each simulated pulse. One can see the arc stretch due to the cross-flow in each of the images and the steady removal of cells on the powered cathode as the simulation evolves with time.
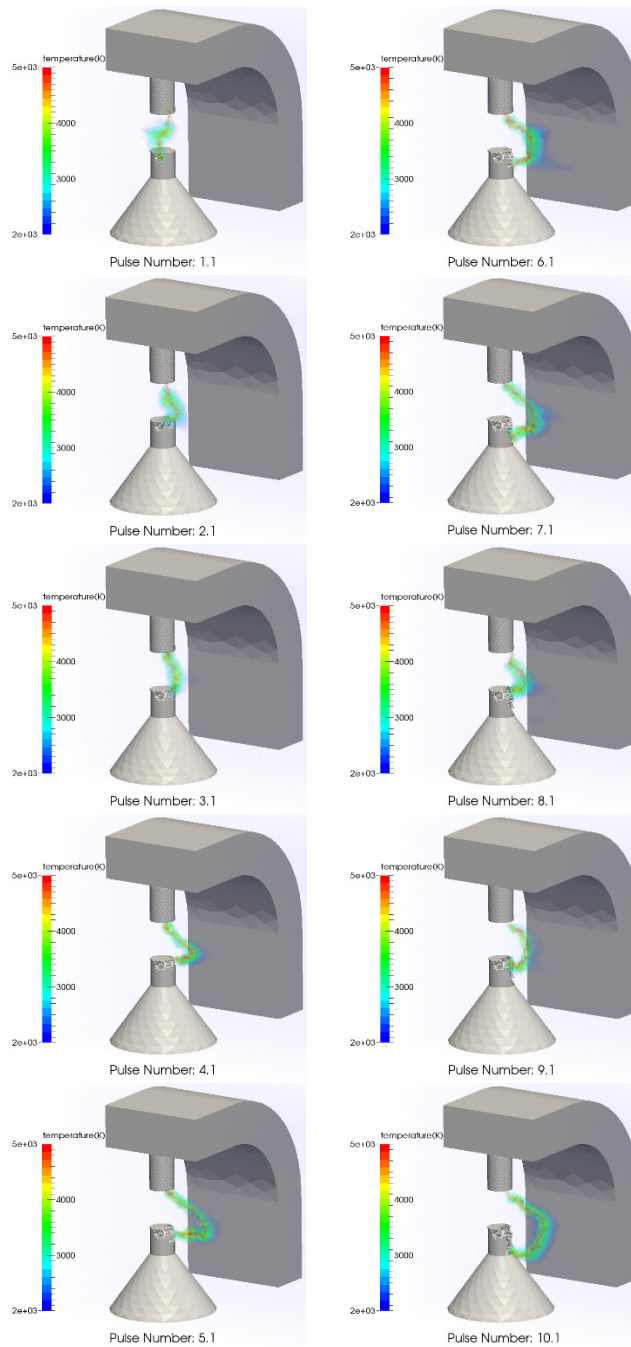
Figure 11: Time transients of the arc channel and electrodes for the sparkplug in 8 m/s crossflow at start of each simulated pulse (10 pulses total).

Figure 12 presents the current applied and voltage measured at the base (bottom side) of the powered electrode as function of pulse. The current was applied in a series of saw-tooth pulses and the voltage on the electrode is obtained self-consistently by the solver. Note the initially high voltage spike at the start of each current pulse indicating gas breakdown. Note also, the increase in voltage as the arc stretches with the cross-flow.
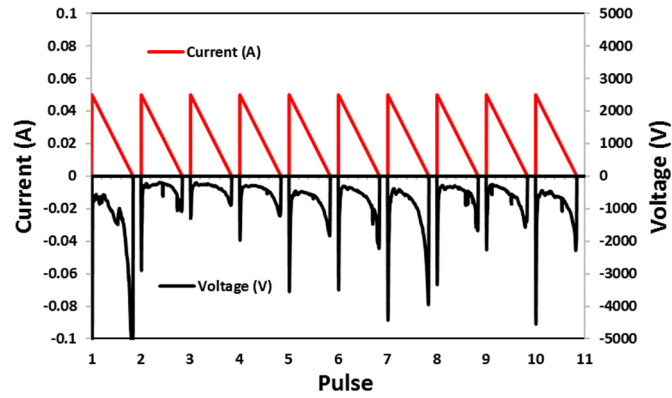
Figure 12: Electric current (top) and voltage (bottom) transients as function of applied pulse for the simulation with cross-flow.

Stationary (No Cross-Flow):

The same simulation configuration is repeated with no-crossflow to determine the impact of flow on spark life time.
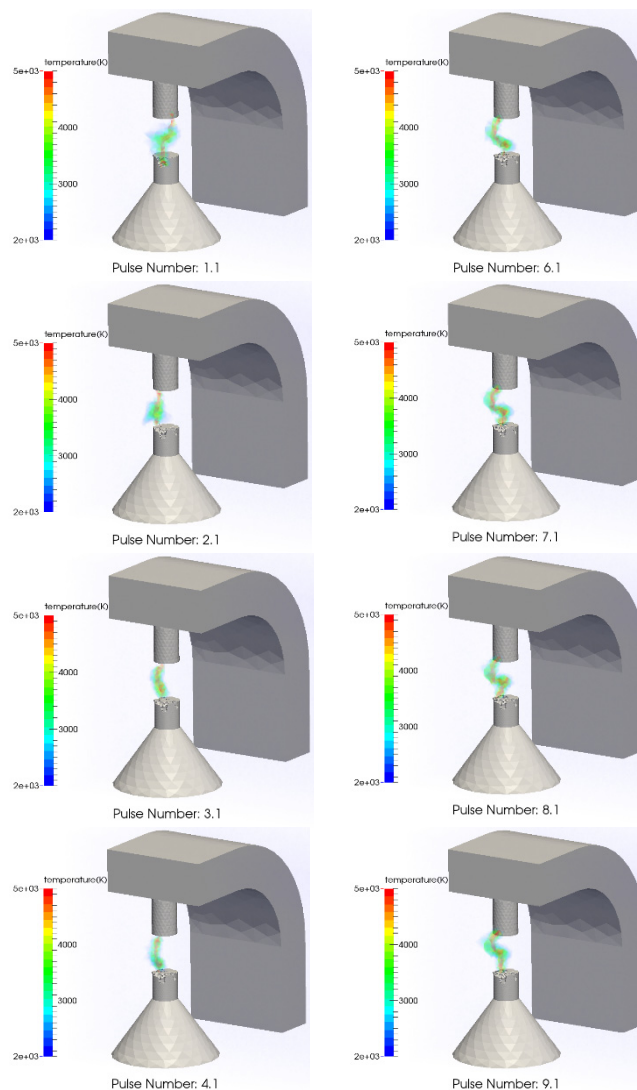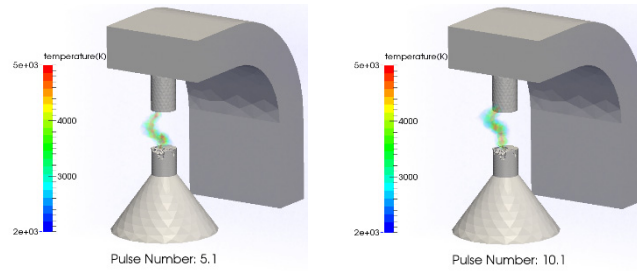
Figure 13: Time transients of the arc channel and electrodes for the sparkplug in stationary flow at start of each simulated pulse (10 pulses total).

The voltage and current transients as a function of individual pulses are shown in Figure 14. The same saw-tooth current profile that was used for the cross-flow case is used as a boundary condition input to the cathode. The voltage profile displays voltage peaks during breakdown and a slow increase in the voltage. Compared to the case with cross-flow (Figure 12), the peak voltages are lower and the magnitude of voltage increase over each pulse duration is lower. The lower voltages indicate that the spark channel resistance in the no-flow case is lower compared to the cross-flow case. This makes sense intuitively as the channel length and hence channel resistance is lower when there is now cross-flow compared to the case when there is cross-flow and arc stretch.
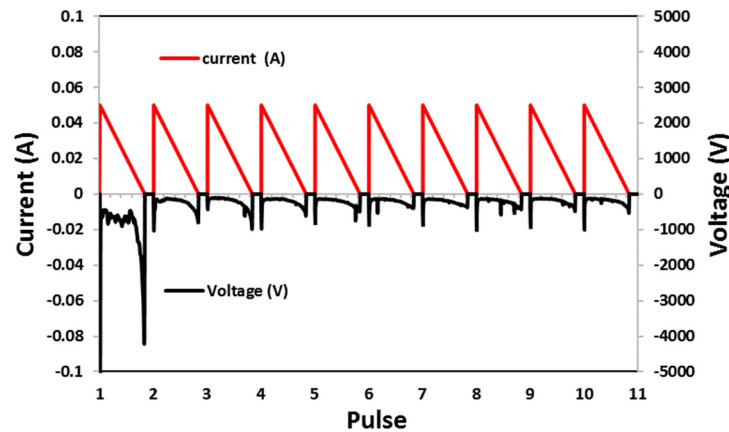
Figure 14: Electric current (top) and voltage (bottom) transients as function of applied pulse for the simulation with no cross-flow.

The erosion profile of the powered electrode (cathode) for the case with and without cross-flow are compared in Figure 15. The cross-flow case shows preferential wear on the downwind side of the electrode.

Pulse Number: 11.0   Pulse Number: 11.0
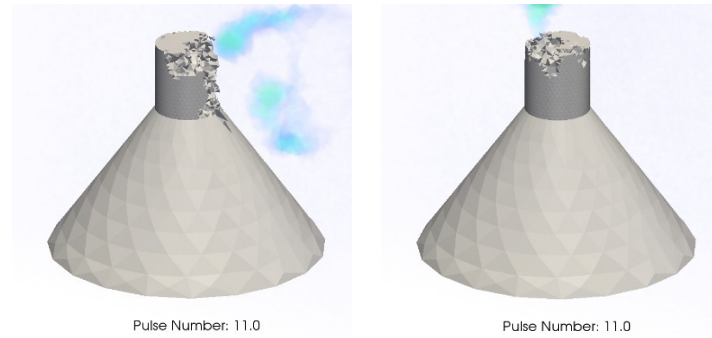
Figure 15: Erosion profiles for sparkplug cathode after 10 simulated pulses for the case with 8 m/s crossflow (left) and case with no cross-flow (right).

The eroded mass of the powered electrode (cathode) for 8 m/s cross-flow and stationary flow compared in Figure 16. Two trends are noticeable: the first is that during breakdown at the start of each pulse there is more mass removal then during the arc phase. The second is that the net eroded mass is higher for the case of cross-flow. The observation that increased material erosion is observed for the case of cross-flow can be explained through the following argument. The supplied current for both simulations is the same yet cross-flow stretches the arc. The arc channel can be thought of as a resistive element, hence a longer stretched arc will have more electrical resistance then a non-stretched arc. More energy is required to maintain a stretched arc compared to a stationary arc and because electrode erosion is a function of electrical energy deposition, more energy will also go into the electrodes which leads to more erosion.
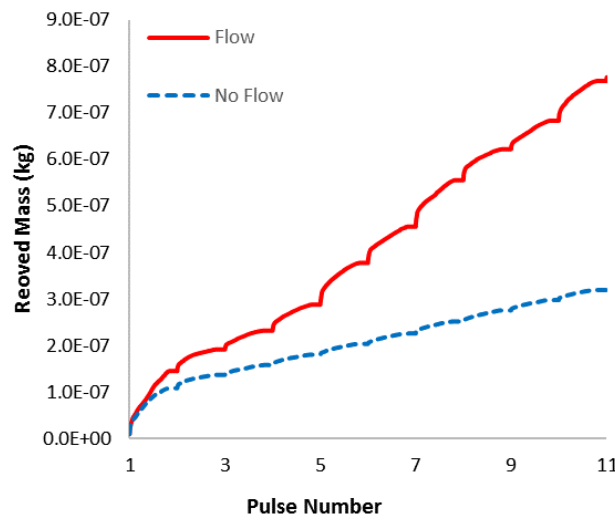
Figure 16: Eroded electrode (cathode) mass as a function of simulated pulses. The eroded mass for stationary flow is shown with the dashed line (blue). Eroded mass for the cross-flow case is shown with the solid line (red).

6   Summary and Conclusions

In summary, a roadmap for simulating erosion of spark plug electrodes has been presented. Based on experimental studies of single spark electrode erosion, an energy dependent phenomenological model for electrode erosion based on the strong correlation between input energy and the energy required to melt the material is formulated.

The energy dependent model for electrode erosion is validated by comparing single-pulse simulated electrode erosion rates with experimentally determined erosion rates. Using the energy dependent erosion model, simulations of electrode erosion from a sample spark plug were performed for stationary and cross-flow configurations. It was found that cross-flow induced arc stretch increases the arc resistivity and hence the energy deposition into the arc channel and the electrodes. This resulted in an increased net electrode erosion for cross-flow compared to no cross-flow when input current was the same for the two cases.

References

[1] F. A. Soldera, F. T. Mucklich, K. Hrastnik and T. Kaiser, "Description of the discharge process in spark plugs and its correlation with the electrode erosion patterns," *IEEE Transaction on Vehicular Technology,* vol. 53, no. 4, 2004.

[2] A. Lasagni, F. Soldera and F. Mucklich, "Quantitative investigation of material erosion caused by high-pressure discharges in air and nitrogen," *Zeitschrift für Metallkunde,* vol. 95, no. 2, pp. 102-108.

[3] R. Maly, "Spark ignition: its physics and effect on the internal combustion engine," in *Fuel Economy*, 1984, pp. 91-148.

[4] H. Lin, M. P. Brady, R. K. Richards and D. M. Layton, "Characterization of erosion and failure processes of spark plugs after field service in natural gas engines," *Wear,* vol. 259, pp. 1063-1067, 2005.

[5] S. Javan, S. V. Housseini, S. S. Alaviyoun and F. Ommi, "Effect of electrode erosion on the required ignition voltage of spark plug in CNG spark ignition engine," *The Journal of Engine Research,* vol. 26, pp. 31-39, 2012.

[6] M. Akram and E. Lundgren, "The evolution of spark discharges in gases: I. Macroscopic models," *J.Phys. D: Appl. Phys.,* vol. 29, pp. 2129-2136, 1996.

[7] M. Arkam, "The evolution of spark discharges in gases: II. Numerical solution of one-dimensional models," *J. Phys. D: Appl. Phys.,* vol. 29, pp. 2137-2147, 1996.

[8] R. Reinmann and M. Akram, "Temporal investigation of a fast spark discharge in chemically inert gases," *J. Phys. D: Appl. Phys.,* vol. 30, pp. 1125-1134, 1997.

[9] M. Thiele, S. Selle, U. Riedel, J. Warnatz, R. Schießl and U. Maas, "A detailed two-dimensional numerical study of spark ignition including ionization," *SAE Technical Paper,* 2002-01-1110.

[10] R. Dahms, T. D. Fansler, M. C. Drake, T. W. Kuo, A. M. Lippert and N. Peters, "Modeling ignition phenomena in spray-guided spark-ignited engines," *Proceedings of the Combustion Institute,* vol. 32, pp. 2743-2750, 2009.

[11] O. Ekici, O. A. Ezekoye, M. J. Hall and R. D. Matthews, "Thermal and flow fields modelig of fast spark discharges in air," *Journal of Fluids Engineering,* vol. 129, no. 55, 2007.

[12] VizSpark Manual, Esgee Technologies, 2016.

[13] T. Shiraishi, A. Teraji and Y. Moriyoshi, "The Effects of Ignition Environment and Discharge Waveform Characteristics on Spark Channel Formation and Relationship between the Discharge Parameters and the EGR Combustion Limit," *SAE International,* 2015.

[14] D. Breden, A. Karpatne and L. Raja, "Modelling of Electrode Erosion for Prediction of Spark Plug Lifetime," in *WCX World Congress Experience* , Detroit, 2018.

[15] R. Mittal and G. Iaccarino, "Immersed Boundary Methods," *Annu. Rev. Fluid Mechanics,* vol. 37, pp. 239-61, 2005.

[16] S. Patnakar, Numerical Heat Transfer and Fluid Flow, New York: Mcgraw-Hill, 1980.

[17] T. Billoux, T. Cressault, P. Teulet and A. Gleizes, "Calculation of the net emission coefficient of an air thermal plasma at very high pressure," *Journal of Physics: Conferene Series,* vol. 406, 2012.

[18] F. Soldera, A. Lasagni, F. Mucklich, T. Kaiser and K. Hrastnik, "Determination of the Cathode Erosion and Temperature for the High Voltage Discharges using FEM Simulations," *Computational Materials Science,* vol. 32, pp. 123-139, 2005.

[19] A. Lasagni, F. Soldera and F. Mucklich, "FEM Simulation of Local Heating and Melting During Electrical Discharge Plasma Impact," *Modelling Simul. Mater. Sci. Eng.,* vol. 12, pp. 835-844, 2004.

2.2 Test Rig for Fundamental Investigations of Ignition System Characteristics under Severe Flow Conditions

Anton Tilz, Georg Meyer, Constantin Kiesling, Gerhard Pirker,
Sebastian Salbrechter, Andreas Wimmer

Abstract

Stationary spark ignited (SI) gas engines play an important role in decentralized energy supply concepts. To achieve further improvements in efficiency and to decrease emissions, engine operating strategies with very lean air-fuel mixtures and high turbulence levels are required. However, these severe conditions have a significant impact on the inflammability of the mixture and compromise combustion stability. Reliably igniting the mixture and keeping cycle-to-cycle variation of the combustion process at a low level is challenging and requires deeper understanding of the fundamentals of the ignition process. The electric arc, which transfers the electric energy to the air-fuel mixture and initiates the inflammation, plays a central role in the ignition process. Thus, the paper at hand presents a test rig that was developed for detailed investigations of electric arc behavior under flow conditions similar to those in spark ignited large gas engines.

The test rig consists of a closed loop flow circuit. Flow velocities at the spark plug up to 30 m/s, pressures up to 60 bar and temperatures up to 80 °C can be achieved under non-combustible conditions. The centerpiece of the test rig is the test cell, which provides excellent optical access from three sides for high-speed imaging of the arc without disturbing the flow field at the spark plug. A sufficiently long stabilizing path upstream of the test cell guarantees defined and fully developed turbulent pipe flow conditions at the spark plug. Sophisticated post-processing algorithms were developed that automatically extract relevant data from the high-speed images (e.g., arc length) and compare the information with electrical signals such as current and voltage on both the primary and secondary sides of the electronic ignition system. The results provide a deeper understanding of the ignition process and serve as basis for model validation. Finally, measurement results of a pressure variation are presented and discussed. The results show greater arc stretching and increased cycle-to-cycle variation in arc length at higher pressures.

Kurzfassung

Stationäre Großgasmotoren mit elektrischer Funkenzündung stellen eine wichtige Säule für die dezentrale Energieversorgung dar. Zur Steigerung des Wirkungsgrads sowie zur Absenkung der Emissionen kommen dabei immer höhere Luftverhältnisse bei gleichzeitig gesteigerten Turbulenzniveaus im Brennraum zum Einsatz. Diese Betriebsbedingungen beeinflussen jedoch die Entflammbarkeit des Gas-Luft-Gemisches und beeinträchtigen die Verbrennungsstabilität. Die zuverlässige Entflammung des Gemisches und die Erreichung geringer zyklischer Schwankungen beim Verbrennungsprozess stellen somit eine Herausforderung dar und setzen ein tiefgehendes Verständnis des Zündprozesses voraus. Eine zentrale Rolle spielt dabei der elektrische Funke, der die elektrische Energie an das Gas-Luft-Gemisch überträgt und den Zündprozess einleitet. Zur detaillierten Untersuchung des Funkenverhaltens unter motornahen Bedingungen wurde daher ein spezieller Prüfstand entwickelt, der in der vorliegenden Publikation vorgestellt wird.

Der Prüfstand besteht aus einem geschlossenen Kreislauf, in dem Strömungsgeschwindigkeiten an der Zündkerze von bis zu 30 m/s, Drücke bis zu 60 bar und Temperaturen bis zu 80 °C unter Verwendung nicht brennbarer Gase realisiert werden können. Kernstück des Prüfstandes bildet eine Testzelle, welche zur Aufzeichnung des Funkenverhaltens mittels Hochgeschwindigkeitskamera exzellente optische Zugänglichkeit von drei Seiten her bietet, ohne dabei die Strömung an der Zündkerze zu beeinflussen. Eine ausreichend lang dimensionierte Einlaufstrecke stromaufwärts der Testzelle sorgt dabei für eine definierte und voll ausgebildete turbulente Rohrströmung an der Zündkerze. Eigens entwickelte Auswertealgorithmen dienen zur Quantifizierung der Messdaten aus den Hochgeschwindigkeitsaufnahmen und zur Einbeziehung der elektrischen Signale von der Primär- und der Sekundärseite des Zündsystems. Die Messergebnisse erlauben ein tiefgehendes Verständnis des Zündprozesses und dienen überdies zur Validierung eines Zündungsmodells.

In der vorliegenden Publikation wird anhand einer Parameterstudie gezeigt, dass die Anhebung des Drucks an der Zündkerze bei konstanter Strömungsgeschwindigkeit zu einer größeren Funkenstreckung sowie zu höheren zyklischen Schwankungen der Funkenlänge führt.

1   Introduction

Spark ignited (SI) large gas engines are important for decentralized energy supply concepts and will continue to be so in the future, cf. [1] [2]. Increasingly stringent emission regulations along with the quest for greater engine efficiency present challenges in the design of the combustion process. To meet these requirements with gas engines, there is a trend towards leaner air-fuel mixtures and higher mean effective pressures, cf. [1] [2] [3]. Consequently, the range for stable engine operation between knocking and misfiring is significantly reduced, cf. [4]. Since robust engine operation under these difficult boundary conditions must be ensured, a central topic of research is combustion stability, cf. [2] [5]. The ignition system is a key component in reducing cycle-to-cycle variations because it initiates combustion with an infant flame kernel that turns into a stable flame front, cf. [4] [5]. Research focuses on improving the ignition process and developing alternative ignition systems, cf. [2] [4] [6] [7] [8] [9]. Despite the availability of alternative ignition concepts, the concept with electric gas discharge at a spark plug remains the standard in production engines thanks to its robustness and reliability as well as its cost-effective design, cf. [2] [10].

The ignition system transfers electrical energy to an ignitable mixture and initiates combustion with the help of an electric arc, which raises the local gas temperature above a level favorable for the formation of an infant flame kernel, cf. [11] [12] [13]. Flow and thermodynamic conditions at the spark plug greatly vary depending on the engine design as well as on the operating conditions, e.g., lean or rich, homogenous or stratified air-fuel mixture, low or high charge motion and low or high pressures. Since the electric arc is a conducting region between the electrodes and part of the electric circuit, these local conditions at the spark plug have a significant impact on electric arc behavior and on ignition system performance, cf. [12] [13] [14]. Reliable ignition of the air-fuel mixture under all conditions is very challenging. Since the ignition process is one possible cause of irregular combustion, e.g., misfire and large cycle-to-cycle variability, it is important to investigate the effect of electric arc behavior on the combustion process, cf. [5] [15].

There are two main advantages to conducting detailed research into electric arc behavior at spark plugs. First, the ignition process in large spark ignited gas engines can be better understood by analyzing the details of spark discharge at extreme conditions comparable to those in large gas engines. Second, it enables the improvement and validation of the capabilities and accuracy of ignition and combustion simulation models that assess SI engine concepts without engine test beds. LEC GmbH is in the process of developing a detailed ignition model for 3D CFD simulation that consists of several submodels including an electric network model and an arc model, cf. [16]. Arc behavior and flow-feedback on the ignition system are thus an important part of the model that needs to be validated over wide operating ranges.

The innovative test rig presented in this paper is designed to facilitate a detailed investigation of electric arc behavior under cross-flows at a spark plug typically used in gas engines. The following two sections provide a short summary of the fundamentals of the arc test rig, the arc test rig requirements and the methodology; for more detailed information, see [13].

2   Arc Test Rig Fundamentals and Requirements

This section provides a brief introduction into the fundamentals of electric gas discharge. Based on these fundamentals, requirements for a test rig suitable for addressing key research topics are deduced.

2.1   Fundamentals

Figure 1 presents a schematic circuit model of a modulated capacitive discharge ignition (MCDI) system, cf. [2] [12] [13], an ignition system common in large gas engines. This system was installed on the arc test rig described in this paper. Activation of the ignition system transfers the energy stored in a capacitor on the primary side to the secondary side via an ignition coil. As long as the gap between the spark plug electrodes is insulating, the voltage across the electrode gap rapidly increases until breakdown occurs. In the first short phase of breakdown, the energy stored in the capacitors on the secondary side is released at time scales on the order of microseconds. In the glow or arc phase that follows, electric discharge occurs as a result of the transfer of energy from the primary capacitor through the ignition coil; a distinct arc column is established at time scales on the order of several microseconds and is sustained up to one millisecond by the energy transferred from the primary side.
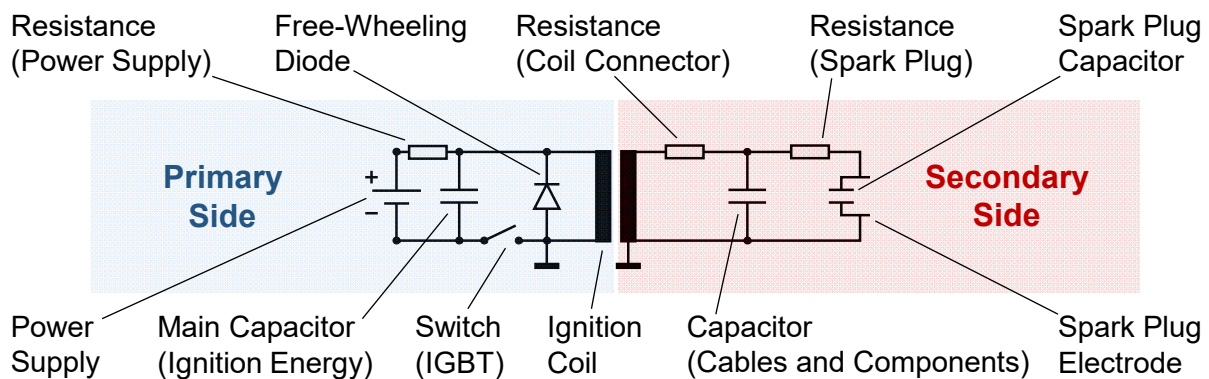
Figure 1: Schematic circuit model of a MCDI system

In this phase, the spark power is influenced by modulating a switch on the primary side; this is the core principle of MCDI technology. The flow field at the spark plug has approximately one millisecond during which it interacts with the arc column. Therefore, the state of the arc that acts as electric impedance in the secondary circuit greatly depends on the prevailing thermodynamic conditions and flow situation at the spark plug.

2.2   Requirements

An investigation of arc behavior and its impact on the transfer of energy from the electronic ignition system to the gas necessitates a study of the electric arc under well-defined, stable oncoming flow conditions at pressures and flow velocities similar to those in an engine and in an otherwise inert gas atmosphere. Three main parameters must be examined in a test rig:

- Flow velocity at the spark plug
- Ambient pressure
- Ambient temperature

Any observation of the influence of flow motion requires a well-defined, directed and steady oncoming flow. The velocities at the spark plug electrodes should be able to be adjusted from 0 – 30 m/s; this upper limit was derived from engine simulation results. The spark plug orientation should be as flexible as possible in order to ascertain the influence of the main flow direction on the arc behavior. Since load changes in the engine result in a wide variety of pressures at ignition timing, the pressure should be variable over a large range during experiments, cf. [16]; the target is a pressure range of 1 – 60 bar. It is expected that the sensitivity of the electric properties of the arc column to changes in ambient temperatures (in contrast to breakdown properties) is less than to changes in pressure, cf. [13] [25]. Thus, a temperature range of 25 – 100 °C is envisioned in order to avoid disproportionate effort with respect to the test rig design.

The test rig must make it possible for different non-combustible gas atmospheres to be obtained in order to isolate electric arc behavior from the actual combustion. The focus is placed on air, a main component of inflammable mixtures in gas engines, yet it should be possible to use other non-combustible atmospheres as well. Equally important is the proper integration of the ignition system and the types of spark plugs used in real engines into the test rig. Furthermore, specialized spark plug geometries such as spark plugs with two separate electrodes must be accommodated. High-speed optical evaluation of the electric arc behavior requires good optical access to the spark plug electrodes. Optical access from multiple angles is desirable to obtain an impression of the three-dimensionality of the arc evolution. Since this optical information has to be linked to the electronic feedback of the electric arc in the ignition system of the same spark event, a sophisticated measurement setup is necessary that can record fast measurement signals such as current and voltage on both the primary and secondary sides.

2.3   State-of-the-Art

Prior to the development of the arc test rig, a detailed literature study was carried out to determine the characteristics of existing test rig designs and their limitations in arc behavior investigations. The state-of-the-art systems are summarized briefly below.

Several studies described investigations of arc behavior in optically accessible constant volume pressure chambers, some of which were able to achieve comparatively high pressures and/or temperatures but under quiescent flow conditions, cf. [17] [18] [19] [20]. Research engines with side chambers facilitate high flow velocities but do not obtain defined steady-state flow conditions at the spark plug, cf. [21] [22] [23]. In test rigs where spark plugs lack a housing or in specific open chamber concepts (gas flows through the chamber), the flow velocities are achieved with a nozzle or a connection to inlet piping upstream of the spark plug. However, these systems do not provide high temperatures and high pressures, cf. [17] [24] [25] [26] [27] [28]. A setup described in [29] can obtain high gas temperatures up to 1200 °C at mass flow rates up to 2.15 kg/s but at pressures up to only 5 bar. A test rig consisting of a closed loop flow circuit with an integrated chamber for the spark plug is described in [30] and [31]. Because of its compact design, the length of the inlet before the spark plug is comparatively small, which may impede the achievement of defined flow conditions at the spark plug due to induced secondary flow. All test rigs except [18] [19] [20] [21] [22] [23] [24] [26] use non-inflammable atmospheres.
Because none of the test rigs available in the literature meet these requirements, a completely new test rig was designed; the methodology is outlined in the following section.

3   Methodology

This section introduces the newly developed, innovative test rig system that meets the requirements for investigating spark discharge from the previous section. It also presents the measuring techniques as well as the methodology for evaluating the measurement data.

3.1   Arc Test Rig Setup

Figure 2 shows a CAD mock-up of the test rig and its key components. The rig consists of a closed-loop flow circuit that is filled with the desired medium and pressurized to the target pressure through a filling valve. A blower, which consists of a radial compressor with a hermetically sealed casing, a magnetic coupling and an electric motor allows the setting of the required flow velocity at the spark plug. A heat exchanger maintains a constant gas temperature in the system. A mass flow meter based on the Coriolis principle is located downstream of the heat exchanger and measures the mass flow in the piping circuit; in this manner, the flow velocity at the spark plug is derived.
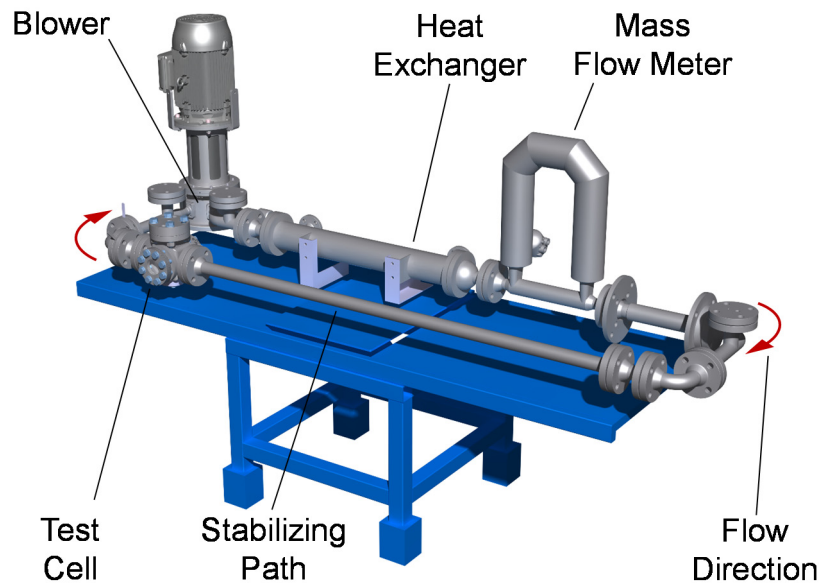
Figure 2: CAD mock-up of the arc test rig

The centerpiece of the test rig is the test cell with optical access, upstream of which is a stabilizing path that provides a hydrodynamic entrance length so that a defined and fully developed flow pattern is set before the medium reaches the spark plug in the test cell. A turbulence grid may be inserted to influence the turbulence of the flow at the spark plug. The test cell has three large optical accesses through which spark dis-charge can be recorded with a high-speed camera from different angles. Downstream of the test cell is an outlet section that is long enough that flow from the spark plug is not negatively influenced by any flow deflection in the bends. Before the flowing me-dium enters the radial compressor, a filter protects the turbomachine from damage due to debris transported by the gas.

This setup allows the boundary conditions in the system to be varied over a wide range according to the requirements described in section 2. Table 1 provides an overview of the targeted ranges for the basic operating parameters pressure, temperature and flow velocity at the spark plug. The test rig was specially designed to obtain the values in Table 1 with an atmosphere of air, nitrogen or carbon dioxide.

Table 1: Technical data of the arc test rig [13]

Parameter	Minimum Value	Maximum Value
Pressure	1 bar	60 bar (at 80 °C) 100 bar (at 20 °C)
Temperature	20 °C	80 °C
Velocity	0 m/s	30 m/s

The integration of the optical accesses in the area of the spark plug is particularly chal-lenging in the design of the test cell; these accesses must not disturb the defined flow pattern at the spark plug. At the same time, the test cell must be able to withstand the

conditions in Table 1. The solution was provided by the double-walled design shown in Figure 3. A thin-walled inner pipe with a square cross-section facilitates the desired flow geometry while a solid outer pipe safeguards the pressure resistance of the system. The flow passes from the stabilization path through the test cell and to the outlet section completely via the inner pipe, which is sealed off from the outer pipe. A small hole in the stabilization path guarantees pressure compensation between the inner and outer pipes.
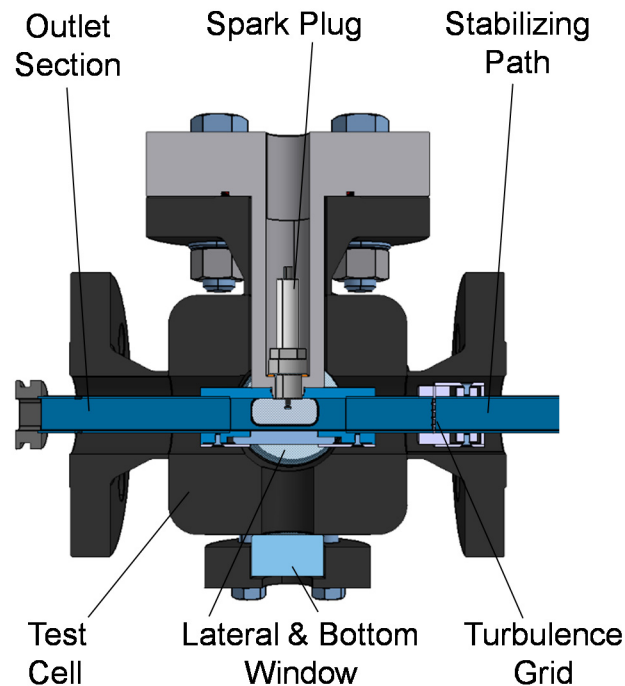
Figure 3: Double-walled design and optical access of the test cell

A hydrodynamic entrance length (stabilizing path) more than eighty times the hydraulic diameter [32] upstream of the test cell yields a fully developed turbulent pipe flow is achieved at the spark plug. To influence the turbulence level in the flow at the spark plug, an optional turbulence grid can be inserted into a slot in the inner pipe upstream of the spark plug.

The electric arc behavior is captured with a high-speed camera from three different angles through two optical accesses parallel to the spark plug axis and the flow direction and one access orthogonal to the spark plug axis. The borosilicate glasses are flush with the inner surface of the rectangular pipe so that flow is not disturbed by the optical access. Spark plugs with a thread diameter of up to 18 mm can be used and the orientation of the spark plug to the flow direction is adjustable. Prior to the measurements, the spark plug was replaced by a constant temperature anemometry probe that recorded the flow velocity at the spark plug electrode as a function of mass flow, pressure, temperature and atmosphere. Knowledge of this relationship is required to set the desired flow velocity at the spark plug without having to measure it directly during the arc behavior investigations.

To sum up, the test rig has several important features that distinguish it from previous setups for investigating spark behavior.

- Option to investigate spark behavior with a high flow velocity (up to 30 m/s), high pressure (up to 60 bar) and temperatures of 20 – 80 °C at the spark plug
- Defined flow condition at the spark plug obtained with a stabilizing path that ensures fully developed turbulent flow in the pipe
- Option to vary turbulence at the spark plug by inserting a turbulence grid upstream of the spark plug
- Option to view the spark plug through optical accesses on three sides simultaneously
- Measurement of flow velocity at the position of the spark plug with a constant temperature anemometry system

3.2   Measuring Instruments

Standard measuring instruments and optical measuring instruments are used to record all relevant measurands on the test rig. Standard measuring instruments are further divided into slow measuring instruments, with sampling rates up to 50 samples per second (S/s), and fast measuring instruments, with sampling rates up to 10 megasamples per second (MS/s).

Slow measurands include pressure, temperature and mass flow. Fast measurands include primary current, secondary current and voltage in the ignition system as well as the flow velocity at the spark plug. The flow velocity is measured with a highly accurate constant temperature anemometry system. As described above, the probe of this system replaces the spark plug. The recorded data revealed a correlation between the local flow velocity and mass flow, pressure, temperature and atmosphere.

A Fastcam SA-X2 high-speed camera from Photron, inc. that has a lens with a focal length of 100 mm recorded the processes in the test cell. The camera has a maximum frame rate of 600,000 frames per second at a spatial resolution of 128 x 24 pixels.

3.3   Post-processing

One direct consequence that the flow field has on the arc at the spark plug is spark stretching, i.e. the increase in the overall arc length due to flow motion. As a result, arc length is considered to be an indicator for the influence of flow velocity. To quantify the arc length, LEC GmbH developed an algorithm that automatically extracts numerical values from the high-speed images.

The arc length is computed starting with the raw image, which is transformed into a binary black and white image, cf. Figure 4a) and b). The algorithm starts with a high threshold value of 90%. After binarization, the algorithm checks whether any disjunct areas appear in the white region as a result of binarization. The threshold value is iteratively reduced until a simply connected region is obtained, cf. Figure 4c). In the following step, the interior is removed so that only the outer contour remains of the

formerly white region of the binarized image, cf. Figure 4d). The arc length is computed as half the length of the outer contour. In addition, another algorithm verifies the validity of an image by checking whether the arc roots are in close proximity to the electrode surfaces.
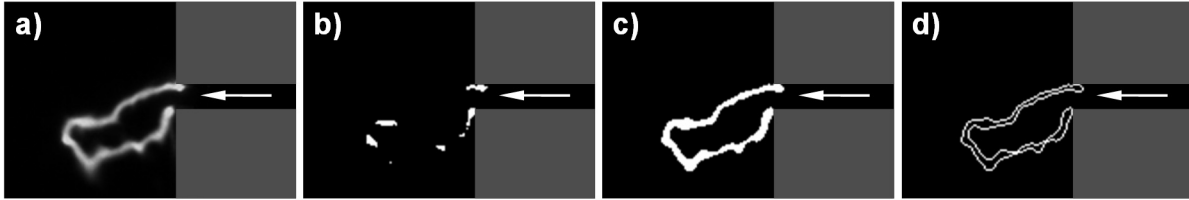
Figure 4: Image processing to determine arc length [4]

It must be emphasized that the value of the arc length is generated from two-dimensional images; the algorithm does not consider arc deflection in the third dimension.

4   Selected Results

Applying the methodology explained above, this section presents sample results that illustrate the possibilities with the arc test rig. The influence of pressure at the spark plug is examined in detail. The measurements were performed with an air atmosphere, a flow velocity of 30 m/s at the spark plug, a spark current duration of 900 µs, a spark current level 50% of the maximum possible current and a system temperature of 25 °C. The J-shaped ground electrode of the spark plug was located opposite the camera, enabling good optical access to the electrode gap and minimal disturbance of the flow pattern at the electrode gap. The ignition system is a MCDI system as described in section 2, which facilitates a comparison between the results from the arc test rig and those from analogous engine test beds.

Figure 5 provides samples of high-speed recordings of arc behavior at different pressures. The time scale and flow advance from right to left. The first row illustrates the results at a system pressure of 35 bar, the second row at 10 bar and the last row at 0 bar (gauge). The time step between each image is constant. Each picture shows the spark plug electrodes and the arc at the specific time step in one single measurement cycle.

It can be seen that as the pressure goes up, arc illumination as well as arc deflection increase. As arc length grows, the folding of the arc increases. The bright flash in the first image with the 10 bar system pressure coincides with arc breakdown, illustrating the initial plasma expansion due to the blast wave that results from the fast energy release during breakdown. At all illustrated pressures and time steps, the arc roots are already located downstream of the electrodes as they move with the flow. In the last three images with a system pressure of 35 bar, the lower arc root is not on the electrode but on the electrode holder (bright rectangular shape in the image). Due to short circuits of the arc column caused by turbulent motion (cf. [33]), a pronounced shortening of the arc length is observed, such as in the last three images at a system pressure

of 10 bar. It is assumed that the increasing illumination of the arc as the system pressure increases is related to the rise in dissipation of secondary energy that occurs as the system pressure increases (cf. Figure 6). The greater arc deflection with increasing system pressure is assumed to be due to the reduced influence of inhomogeneous arc heating at higher pressure, cf. [2] [16].
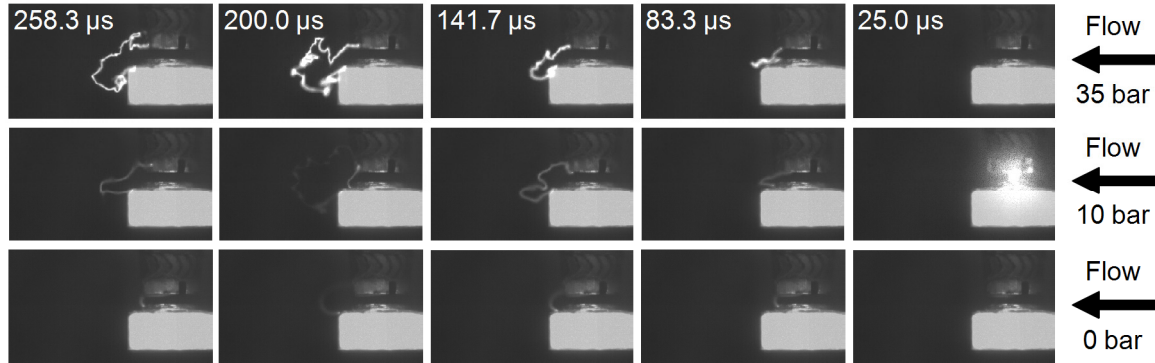
Figure 5: Influence of pressure on electric arc behavior

To better understand arc behavior, the measurement points shown in Figure 5 are analyzed using the image post-processing algorithm. The results are shown in Figure 6. The first diagram of Figure 6 plots the arc length, the second diagram the secondary voltage and the third diagram the dissipated secondary energy over time. Each pressure is indicated by a different color. The thick lines represent the mean curves calculated from 50 consecutive cycles and the thin lines represent single cycles. The more a single cycle differs from the mean curve, the lighter its color. The dashed lines represent one standard deviation.

The qualitative statements from Figure 5 can be evaluated quantitatively based on the analysis of the arc length traces in Figure 6. The results confirm that the arc stretches more when the pressure is increased as indicated by its greater arc length. At all pressures, a certain level of arc length is not exceeded, which is a result of arc shortening effects during the arc burning phase.

As the pressure increases, the absolute value of the arc breakdown voltage (first distinct minimum in the secondary voltage curve) also increases and is reached at a later time. This effect is also visible in the first images at 25 µs in Figure 5; at 0 bar, the arc is already burning (yet is hardly visible due to the low illumination). At 10 bar, the arc breakdown is just starting to occur and at 35 bar, the breakdown voltage has not yet been reached.
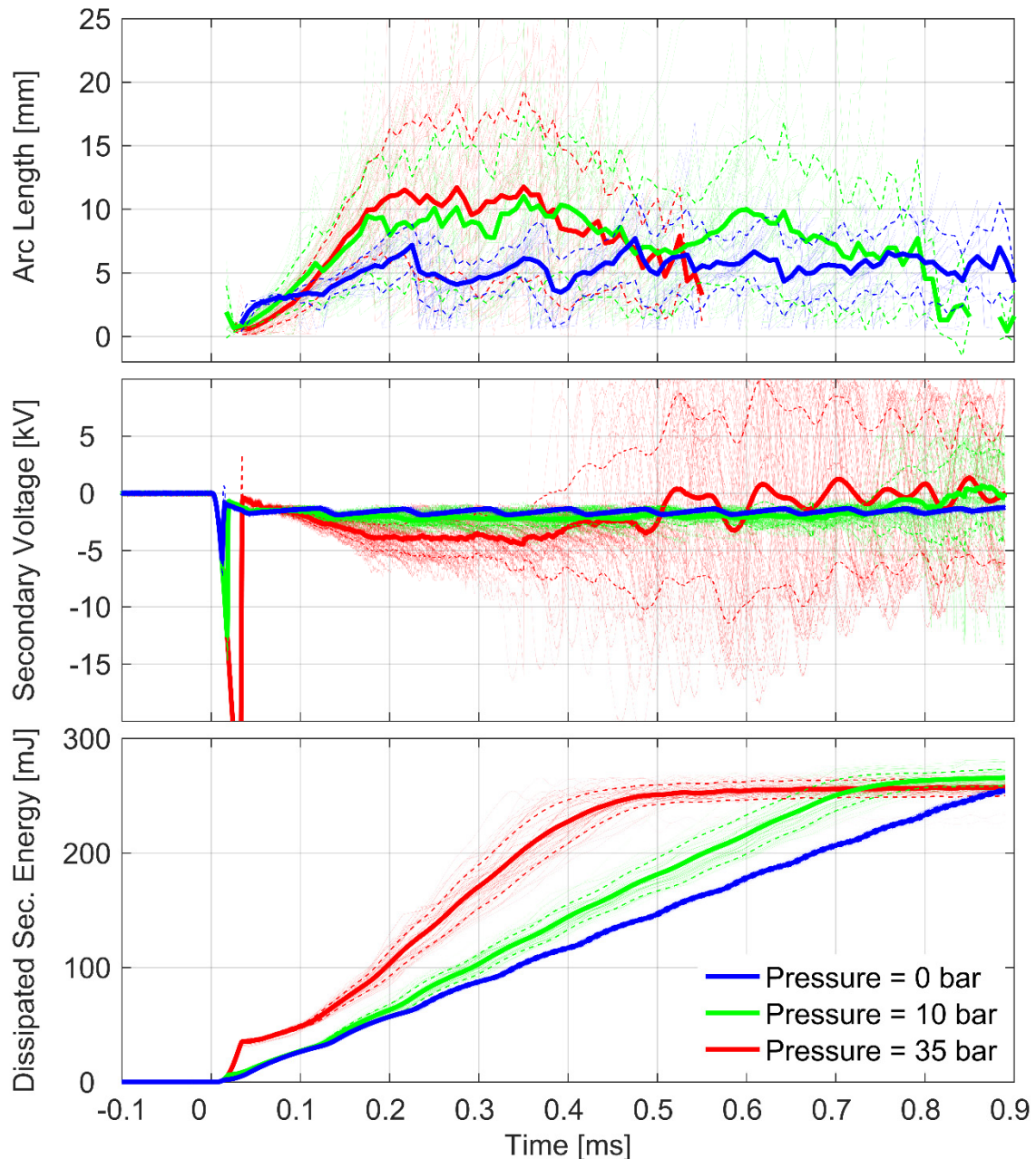
Figure 6: Influence of pressure on arc length, secondary voltage and dissipated secondary energy

In addition, it is evident that despite the controlled boundary conditions upstream of the spark plug (steady-state mean flow velocity and a defined flow profile), the cycle-to-cycle variation in arc length increases at high pressures. While the secondary current from the ignition system is controlled so it remains as constant as possible during the entire spark duration, the secondary voltage history and its cycle-to-cycle variation are strongly influenced by arc length. This is reflected in the cycle-to-cycle variation in the dissipated secondary energy that directly causes cycle-to-cycle variations in the spark energy input to the flowing gas, cf. Figure 6. As the arc length increases, the secondary voltage goes up, leading to a steeper rise in the total spark energy that is introduced. Even though the spark current duration is set to a constant target value of 900 µs, the arc burning time at 35 bar is significantly shorter because the energy limit of the ignition

system has been reached, which is indicated by a plateau in the dissipated secondary energy.

These measurement results have resulted in a deeper understanding of the influence of system pressure on electric arc behavior. The measurement data can also be used to improve and validate the electric arc model currently under development at LEC GmbH.

5   Summary and Outlook

This paper presented a test rig on which electric arc behavior can be investigated under engine-like flow conditions at the spark plug in non-combustible atmospheres in order to better understand and optimize the ignition process in internal combustion engines. The setup allows investigations of the influences of the ignition system, the flow conditions and the electric arc behavior on each other and provides a large database for validating arc models. The requirements for the test rig were derived from a description of the fundamentals of electric gas discharge. The geometric design for excellent optical access, defined flow and flexible spark plug installations was determined and the variation ranges for important parameters were defined: flow velocities at the spark plug electrodes (0 – 30 m/s), pressure (1 – 60 bar) and temperature (25 – 80 °C).

A methodology for consistent experimental investigations of electric arc behavior on an arc test rig was elaborated and presented. The setup of an innovative test rig as well as the corresponding measurement techniques and the post-processing methodology were explained in detail. The test rig was set up as a closed circuit for non-inflammable gases that consists of a blower and an optically accessible test cell connected to a stabilizing path located upstream that allows a defined and fully developed flow. A wide variety of standard measuring instruments for pressure, temperature, mass flow, current and voltage were applied along with optical measuring techniques that use a high-speed camera. Image processing algorithms were developed to generate quantitative values from qualitative measurements and thus facilitate the interpretation of the results.

Based on the sample results obtained by varying system pressure at the spark plug, the methodology was applied in spark investigations and conclusions regarding electric arc behavior were presented. The key findings are that the stretching of the electric arc increases as the system pressure increases; this is apparent from the greater arc length. The cycle-to-cycle variation in arc length also increases as pressure increases. The arc length in turn influences the secondary voltage and its cycle-to-cycle variation. Consequently, the spark energy input to the flowing gas also depends on the cycle-to-cycle variation.

To make further progress in the two main areas of emphasis of the research presented in this paper, i.e. a better understanding of the ignition process in large spark ignited gas engines and improved and validated ignition and combustion simulation models,

the methodology described above will be applied in future research. Potential topics include evaluations of various spark plug geometries in combination with different turbulence levels at the spark plug and the testing of different ignition systems and ignition parameter setups.

6 Acknowledgement

Literature

[1] Warnecke, W.; Karanikas, J.; Levell, B.; Mesters, C.; Schreckenberg, J.; Adolf, J.: "Gas – A Bridging Technology for Future Mobility?", contribution at: "34th International Vienna Motor Symposium", Vienna, 2013.

[2] Meyer, G.; Gschirr, A.; Lindner-Silwester, T.; Stadlbauer, K.: "Recent Advances in Modeling Modulated Capacitive High- Energy Ignition Systems and Application of the Findings in a New Generation of Ignition Systems," in: Eichlseder, H. (Ed.): "14th Symposium The Working Process of the Internal Combustion Engine," Graz, 2013.

[3] Wimmer, A.; Pirker, G.; Engelmayer, M.; Schnessl, E.: "Gas Engine Versus Diesel Engine: A Comparison of Efficiency", in: "MTZ Industrial" Volume 1, November 2011, pp. 2-6.

[4] Pirker, G; Wimmer, A.; Meyer, G.; Kiesling, C; Nickl, A; Tilz, A: "Diagnostic Methods for Investigating the Ignition Process in Large Gas Engines" in "Proceedings of 13th International AVL Symposium on Propulsion Diagnostics", Baden Baden, June 2018, p.5f.

[5] Poggiani, C.; Battistoni, M.; Grimaldi, C. N.; Magherini, A.: "Experimental Characterization of a Multiple Spark Ignition System," in: "Energy Procedia," Volume 82, December 2015, pp. 89–95.

[6] Brüggeman, D.; Hüttl, C.: "Stand der Entwicklung bei der Laserzündung", in: "Motortechnische Zeitschrift", in "MTZ - Motortechnische Zeitschrift", Volume 70, 2009, Issue 3, pp. 228-231.

[7] Herdin, G.; Klausner, J.; Weinrotter, M.; Graf, J.; Wimmer, A.: "GE Jenbacher's Update on Laser Ignited Engines" in: "Proceedings of ICEF 2006, Fall Technical Conference of the ASME Internal Combustion Engine Division", 2006.

[8]   Burrows, J.; Lykowski, J.; Mixell, K.: "Corona Ignition System for Highly Efficient Gasoline Engines", in: "Motortechnische Zeitschrift, MTZ worldwide Edition" Volume 74, 2013, Issue 6, pp. 38-41.

[9]   Rixecker, G.; Bohne S.; Adolf, M; Becker, M; Trump, M; Bargende, M.: "The High Frequency Ignition System Eco Flash", in: Kratzsch, M.; Günther, M. (Eds.): "1st International Conference: Advanced Ignition Systems for Gasoline Engines", Renningen, 2012.

[10] Lepley, J .; Brooks, K.; Bell, D.: "A New Technology Electronic Ignition Which Eliminates the Limitations of Traditional Ignition Systems," Paper No. 173, CIMAC Congress 2010, Bergen.

[11] Franke, A.; Reinmann, R.: "Calorimetric Characterization of Commercial Ignition Systems", SAE technical paper 2000-01-0548, 2000.

[12] Maly R.; Herweg R.: "Spark Ignition and Combustion in Four-Stroke Gasoline Engines", in: Arcoumanis, C.; Kamimoto, T. (Eds.): "Flow and Combustion in Reciprocating Engines", Berlin, Heidelberg, 2009, pp. 1-67.

[13] Tilz, A.; Meyer, G.; Kiesling, C.; Pirker, G.; Salbrechter, S.; Wimmer, A.: "Design of a Test Rig of Fundamental Investigations of Spark Characteristics", in: "International Journal of Engine Research", submitted 2018.

[14] Edels, H.: "Properties and theory of the electric arc. A review of progress", in: "Proceedings of the IEE - Part A: Power Engineering", Volume 108, 1961, Issue 37, 1961, pp. 55-69.

[15] Liu, K.; Burluka, A. A.; Sheppard, C. G. W.: "Turbulent flame and mass burning rate in a spark ignition engine", in: "Fuel" Volume 107, 2013, pp. 202-208.

[16] Meyer G.; Salbrechter S.; Tilz A.; Wimmer A.: "Assessment of Electric ARC Models Used in Recent Spark Ignition Models" in: "Digital Proceedings of the 8th European Combustion Meeting", Dubrovnik, 2017, pp. 644–648.

[17] Meyer, G.; Stadlbauer, K.; Gschirr, A.; Lindner-Silwester, T.; Puttinger, S.: "Modeling of Modulated Capacity Discharge Ignition Systems", in: "Proceedings of the 8th Dessau Gas Engine Conference", Dessau Roßlau, 2013.

[18] Ast, G.: "Vergleich Laserzündung mit Zündkerzenzündung", Diploma thesis, Vienna University of Technology, 2004.

[19] Ko, Y.; Anderson, R. W.; Arpaci V. S.: "Spark Ignition of Propane-Air Mixtures Near the Minimum Ignition Energy: Part I. An Experimental Study", in: "Combustion and Flame", Volume 83, 1991, Issue 1-2, pp: 75-87.

[20] Lim, M.; Anderson, R.; Arpaci, V.: "Prediction of Spark Kernel Development in Constant Volume Combustion", in: "Combustion and Flame", Volume 69, 1987, Issue 3, pp. 303-316.

[21] Herweg, R.; Maly, R.: "A Fundamental Model for Flame Kernel Formation in S. I. Engines", SAE technical paper 922243, 1992.

[22] Herweg, R.; Begleris, P; Zettlitz, A.; Ziegler, G. F. W.: "Flow Field Effects on Flame Kernel Formation in a Spark-Ignition Engine", SAE technical paper 881639, 1988.

[23] Sayama S.; Kinoshita M.; Mandokoro Y.; Fuyuto T.: "Spark ignition and early flame development of lean mixtures under high-velocity flow conditions: An experimental study", in: "International Journal of Engine Research", 2017.

[24] Schneider, A.; Leick, P.; Hettinger, A.; Rottengruber H.: "Experimental studies on spark stability in an optical combustion vessel under flowing conditions", in: Liebl, J.; Beidl, C. (Eds.): "Internationaler Motorenkongress 2016, Mit Konferenz NFZ-Motorenentwicklung, Proceedings", 1st edition, Wiesbaden, 2016, pp. 327-348.

[25] Gardiner, D. P.; Wang, G.; Bardon, M. F.; LaViolette, M.; Allan W. D.: "An Experimental Study of Spark Anemometry for In-Cylinder Velocity Measurements", in: "Journal of Engineering for Gas Turbines and Power", Volume 130, Issue 4, 2008.

[26] Verhoeven, D.: "Spark Heat Transfer Measurements in Flowing Gases", contribution at: "SAE Fuels and Lubricants Meeting and Exposition", Toronto, 1995.

[27] Yu, S.; Xie, K.; Han, X.; Jeftic, M.; Gao, T.; Zheng, M.: "A Preliminary Study of the Spark Characteristics for Unconventional Cylinder Charge with Strong Air Movement", in: "Proceedings of the ASME 2011, Internal Combustion Engine Division Fall Technical Conference, ICEF", West Virginia, 2011.

[28] Pashley, N.; Stone, R.; Roberts, G.: "Ignition System Measurement Techniques and Correlations for Breakdown and Arc Voltages and Currents", SAE 2000 World Congress, technical paper 2000-01-0245, Detroit, 2000.

[29] Universitat Politècnica de València, CMT-Motores Termicos: "Flow test rigs: Hot and high flow rig", online: http://www.cmt.upv.es/EF02_03.aspx, accessed on: 2017-02-01.

[30] Günther, M.: "Ignition Sparks in Slow Motion", in: "auto motion, IAV's Customer Magazine", Issue 01/2015, Berlin, pp. 30-32.

[31] Günther, M.; Nicklitzsch, S.; Tröger, R.; Adolf, M.: "Optimizing the Spark Position While Allowing for the Effect of In Cylinder Flow", contribution at: "IAV International Conference on Ignition Systems for Gasoline Engines 2012", Berlin, 2012.

[32] Zanoun, E. S.; Kito, M.; Egbers, C.: "A Study on Flow Transition and Development in Circular and Rectangular Ducts", in: "Journal of Fluids Engineering", Volume 131, 2009.

[33] Sayama S.; Kinoshita M.; Mandokoro Y.; Fuyuto T.: "Spark ignition and early flame development of lean mixtures under high-velocity flow conditions: An experimental study", in: "International Journal of Engine Research", 2018.

2.3 Investigation on Ignition Coil Specification for Dilution Combustion System

Kazuhiro Oryoji, Kengo Kumano, Shogo Namba, Yoshihiko Akagi, Yoshifumi Uchise, Tatsuya Kuboyama, Yasuo Moriyoshi

Abstract

To improve thermal efficiency of internal combustion engine, dilution combustion system, such as lean burn and Exhaust Gas Recirculation (EGR) system, have been developed with spark ignition coils generating large discharge current and energy. Several researches have clarified that large discharge current increases discharge channel stretch and decreases possibility of discharge channel blow-off and misfire. However, these investigations don't mention effect of discharge current profile on combustion speed and discharge channel behaviour enough. Purpose of this research is to investigate relation among dilution rate, combustion speed, discharge channel behaviour and discharge current. To achieve this purpose, five coils having different current profiles were evaluated by combustion test and in-cylinder optical measurement test with research single cylinder engine. The combustion test results showed a correlation between dilution limit and initial combustion period. And optical measurement test results showed a correlation of initial combustion period with discharge channel stretch. Moreover, saturation of discharge channel stretch were observed from a certain discharge current value on up. Based on these results, adequate coil for dilution system was selected. Finally, the coil was equipped on a vehicle and performance test was conducted. The vehicle with LP-EGR system was stably driven with 18% of EGR rate, and 2.3% of fuel reduction rate were verified in the WLTC mode. The selected high energy ignition coil was contributing reduction of misfire during EGR operation.

1   Introduction

In order to prevent from global warming, regulations of CO2 emission of automotive are going to be stricter. In order to comply with future CO2 regulation, dilution combustion systems, such as lean burn and EGR (Exhaust Gas Recirculation) system, for reducing pumping loss and cooling loss, have been developed. Since air-fuel mixtures are diluted by air or EGR gas under dilution combustion condition, ignition of mixture gas by spark ignition is harder than conventional stoichiometric condition. Though conventional stoichiometric mixture is successfully ignited by tens mJ of ignition coil secondary energy, hundreds mJ of its secondary energy might be required for dilution combustion. Therefore, to clarify required coil specifications, several studies have been investigating relation between flame kernel formation and coil specifications, such as secondary current or relation between dilution limit stretch and coil specifications[1].

Shiraishi et al investigated relation between discharge channel stretch and flow velocity around spark plug or discharge current, or relation between EGR combustion limit and discharge current, and they disclosed that large discharge current increases EGR rate limit. Brandtor et al proposed ignition coil which is able to keep discharge current value at certain range for a while, and they disclosed that air-fuel ratio of stable combustion condition is increased by long duration of discharge current keep [2]. Suzuki et al clarified that flame kernel formation is prevented by shortage of energy supply due to discharge blow-off under high velocity condition and by slow laminar flame speed at discharge blow-off area[3]. These investigations, however, mentioned relation between coil specification and discharge channel behavior and relation between coil specification and EGR rate limit or air-fuel ratio limit, these have not mentioned relation between coil specification and combustion status or discharge channel behavior of each combustion cycle. With accepting this background, the purpose of this investigation is to clarify combustion status index having correlation with dilution limit of stable combustion and relation between the index and coil specification or discharge channel stretch. To achieve this purpose, five kinds of ignition coils are evaluated with optical single cylinder engine and relation among combustion status, discharge channel stretch and discharge energy were investigated. Finally, selected ignition coil was equipped on a demo vehicle and the performance was evaluated.

2   Experimental setup

In this study, combustion performance test and in-cylinder optical measurement test were conducted by using a single cylinder engine. Fig. 1 shows schematic of the single cylinder engine and table 1 shows single cylinder engine specifications. The engine works as a single cylinder engine by occurring combustion in one cylinder only. Combustion chamber type is pent roof and compression ratio is 12.2.Furthermore, a tumble adapter was equipped at intake port to increase turbulent energy as shown on left figure of fig.2.The right figure of fig.2 shows estimated value of turbulent energy by three dimensional fluid dynamics As shown on fig.2, in-cylinder turbulent energy is expected to achieve five times larger value than normal setting. To suppress variation of in-cylinder mixture distribution, fuel is supplied by port injection. Fuel is supplied by 0.26g/s and air flow rate is adjusted to achieve target air-fuel ratio. Air-fuel ratio was calculated by Brettschneider/Spridndt method [4] based on density of emission species such as HC, CO2, CO O2 and NOx measured by emission analyzer (MEXA-7100Fx). RON99.8 fuel is applied. The H/C ratio of fuel is 1.708 and stoichiometric air-fuel ratio is 14.37. Spark plug has 0.9mm gap between center electrode and ground electrode and the internal resistance is 5kΩ.
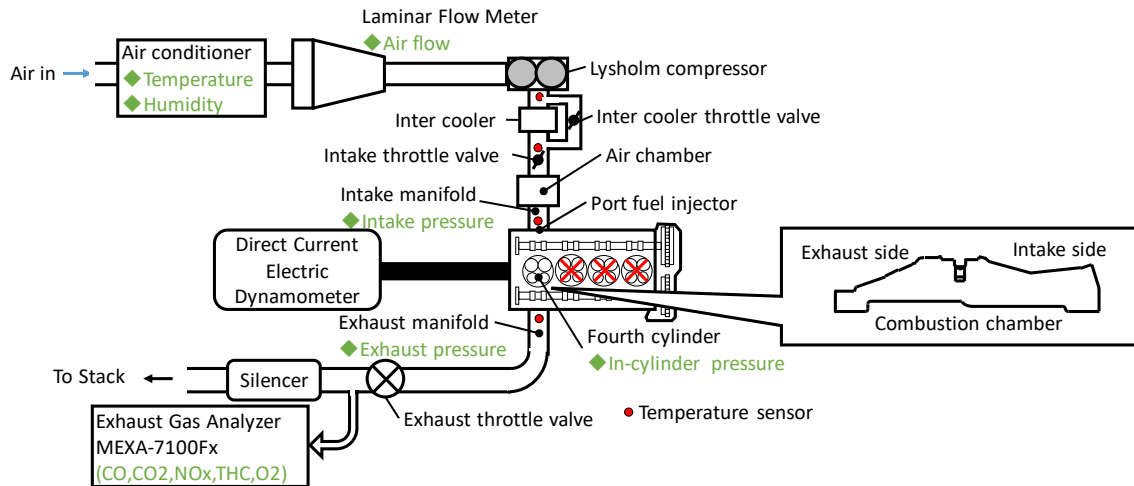
Figure 1: Schematic of the engine system for coil evaluation.

Table 1: Engine specification

Engine type	4 stroke engine
Bore x Stroke	79.7 mm x 81.3 mm
Displacement	404 cc
Compression ratio	12.2
Fuel supply system	Port fuel injection
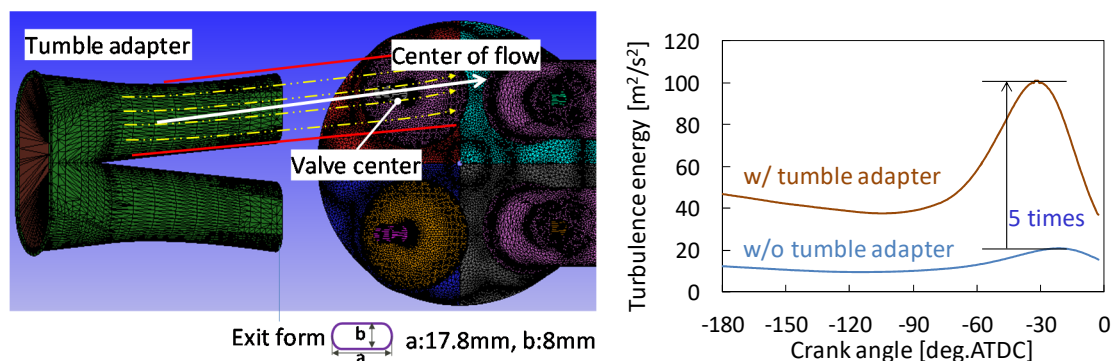
Figure 2: Schematic of tumble adapter (left) and estimation result of turbulent energy by using three-dimensional computational fluid dynamics simulation (right).

The engine equips optical window, and area around spark plug were taken by high speed camera (Photron: FASTCAM SA-X2) through an endoscope (KARLSTORZ:88370A).View angle of the endoscope is about 67degree and wide area from spark plug electrode to piston crown around top dead center can be observed. Fig. 3 is photo of in-cylinder and schematic of view area with description. Images were taken by a high speed camera with 40000 FPS (Frame Per Second) shutter speed and 23.4 µs exposure time. In this study, outer electrode of spark plug is located on center plane between intake valve and exhaust valve to prevent from disturbing tumble flow.
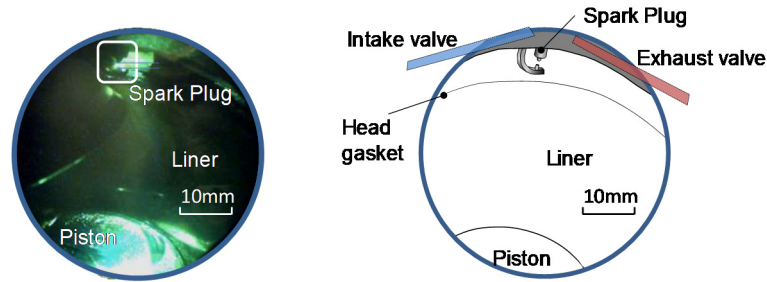
Figure 3: In-cylinder optical measurement area taken with high-speed camera through endoscope.

In order to measure discharge characteristics, both voltage of secondary coil (secondary voltage) and its current (secondary current) were measured. Fig.4 shows schematic of secondary voltage and current measurement system. Secondary current was measured by AC current prove (Person; Model 110A, reaction time 20ns), and secondary voltage was measured by high voltage prove (Tektronix; P6015A, reaction time up to 4.67ns). Sampling frequency of both current and voltage measurement are 1MHz. Output signal of both probes were measured by oscilloscope and data were transferred to PC through Ethernet. To reduce measurement noise, data were measured with Box Averaged model by the oscilloscope.
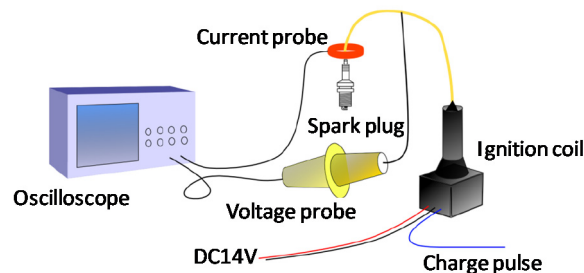
Figure 4: Secondary voltage and current measurement system.

In this study, five kinds of ignition coil were evaluated. As table 2 shows, though secondary energy of coil A, coil B and coil C is equivalent, maximum current of coil B and coil C are larger than coil A. Secondary energy of coil D is about twice of secondary energy of coil A. Coil E consists of two coil D which are parallel-connected and simultaneously discharged. Fig. 5 shows secondary current wave form of 5 coils. The secondary current waves on Fig. 5 were measured during engine test under 2000rpm engine speed and 0.6MPa NMEP. Maximum current value appears just after discharge start and current gradually reduces over time. Furthermore, secondary current oscillation due to restrike appears around end of discharge during engine test.

Table 2: Coil specification

No.	A	B	C	D	E
Secondary energy	86mJ	91mJ	97mJ	153mJ	274mJ
Peak secondary current	73mA	171mA	136mA	195mA	356mA
Spark duration	3.10ms	1.45ms	1.60ms	2.60ms	2.70ms
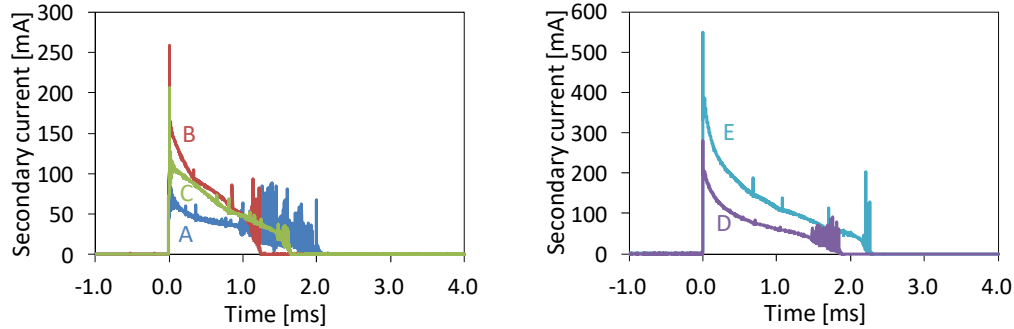
Figure 5: Secondary current form of each coil.

As coil evaluation test, two types of measurement test were conducted, one is combustion test which measures in-cylinder pressure, and another is optical measurement which conducts in-cylinder pressure measurement and optical access measurement simultaneously. Table 3 shows test conditions of combustion test and optical measurement. Engine speed is 2000rpm and fuel flow rate which achieves 0.6 MPa NMEP under stoichiometric combustion condition were applied to all test condition. Under combustion test, maximum air-fuel ratio realising stable engine combustion as dilution limit were investigated by increasing air-fuel ratio.

Table 3: Experimental conditions for combustion test and optical measurement

Control parameter	Combustion test	Optical measurement
Engine speed	2000 rpm	←
NMEP under stoic. condition	0.6 MPa	←
Coolant temperature	85 deg.C	←
Oil temperature	85 deg.C	←
Intake gas temperature	30 deg.C	←
Air Fuel ratio	14.7 ~ lean limit	23

Optical measurement were conducted under air-fuel ratio 23. In optical measurement, image recording by high-speed camera, measurement of secondary current, secondary voltage and in-cylinder pressure were conducted synchronously. Regarding in-cylinder optical measurement, discharge channel located between center electrode and grand electrode were recorded by taking visible light. According to recorded images, data relating with discharge channel behavior were measured. Fig. 6 shows discharge channel by visible light image taken by the camera. High voltage generated by ignition coil caused breakdown, and then discharge channel at spark plug gap emits visible light as shown on Fig. 6. Discharge channel was deformed by convection. In

this engine, flow direction at spark timing is from intake valve to exhaust valve, therefore the discharge channel stretchs to right hand side. Though flow direction around spark plug is not only horizontal direction of visualized plane but also vertical direction of the plane, the stretch of vertical direction were not acquired because the measurement was done from one observation point. Therefore, channel stretch to vertical direction of the plane was ignored. In this study, channel stretch is defined as distance from the line connecting electrodes to edge of the channel. Furthermore, channel stretch rate was calculated by ratio of channel stretch until 1st restrike and period from discharge start to 1st restrike occurrence.
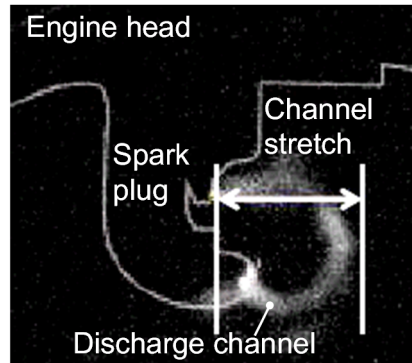
Figure 6: Definition of channel stretch.

3   Discussion

3.1   Dilution limit based on combustion test

In this section, air-fuel ratio limit of each coil, combustion index correlating with air-fuel ratio limit and relation between the index and coil specifications were investigated. Fig.7 shows air-fuel limit of each coil. Air-fuel ratio limit was defined as air-fuel ratio at coefficient of variation of NMEP by 3%. Fig.7 shows that the maximum air-fuel ratio limit of coil E is 24.6 and that of coil A is 23.1. Fig.8 shows relation between air-fuel limit and initial combustion period. Initial combustion period was defined as the period from spark timing until 10% of heat release was done. The initial combustion period of each coil were measured under air-fuel ratio 23 and spark timing 30 deg.BTDC. On fig.8, the dot shows average value of each coil and error bar shows standard deviation. As shown on fig. 8, it was confirmed that coil achieving shorter initial combustion period tends to lead larger air-fuel ratio. According to this result, initial combustion period under same conditions was clarified as a combustion index correlating with air-fuel ratio limit.
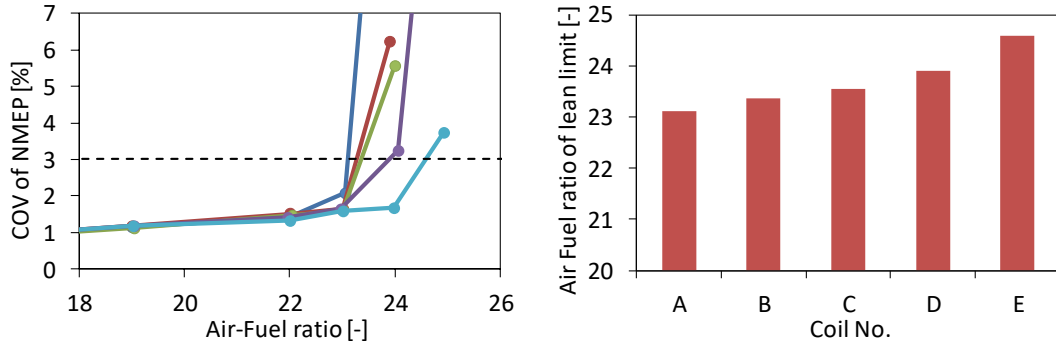
Figure 7: Coefficient of variance of NMEP over air-fuel ratio of lean limit (left) and air-fuel ratio of lean limit of each coil (right).
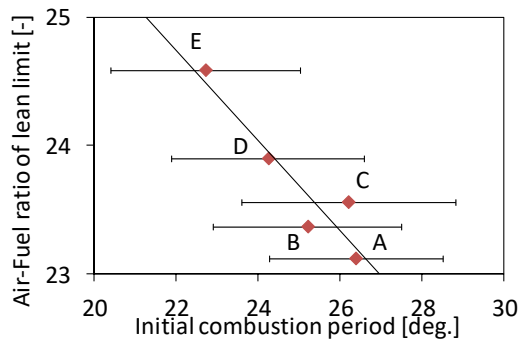
Figure 8: Air-fuel ratio of lean limit over initial combustion period. Diamond shows average value of each coil and error bar shows standard deviation.

As next step, coil specification to realize shorter initial combustion period was investigated. As a coil specification, secondary energy, average secondary power and average secondary current were selected.

$$E_{\mathrm{S}} = \int_0^{t_{\mathrm{D}}} I_{\mathrm{S}} V_{\mathrm{S}} dt$$

$$P_{\mathrm{ave}} = \frac{1}{t_{\mathrm{D}}} \int_0^{t_{\mathrm{D}}} I_{\mathrm{S}} V_{\mathrm{S}} dt$$

$$I_{\mathrm{ave}} = \frac{1}{10^{-3}} \int_0^{10^{-3}} I_{\mathrm{S}} dt$$

Here, P_{ave} is average secondary power [W], t_{D} is discharge period [s], I_{s} is secondary current [A], V_{s} is secondary voltage [V], E_{s} is secondary energy, I_{ave} is average secondary current [A]. Average secondary power is average power from spark timing to end of discharge. Average secondary current is average secondary current during 1ms from spark timing. Secondary power and secondary current were selected as index relating coil generating power. Fig. 9 shows initial combustion period over secondary energy, Fig. 10 shows initial combustion period over average secondary current. All values on these figures are average value of 20 combustion cycles and error bar shows

standard deviation. Furthermore, linear interpolate line and determination coefficient were shown on figures. According to figure, larger secondary energy, average secondary power and average secondary current leads shorter initial combustion period. Among these three paramters, average secondary current shows the strongest correlation with initial combustion period.
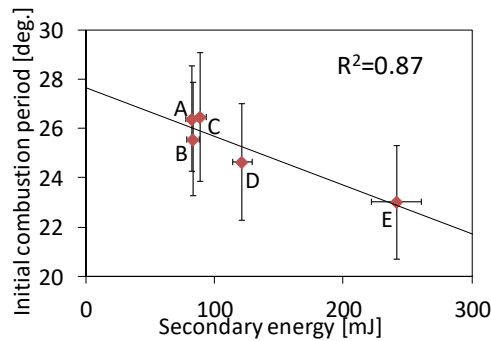
Figure 9: Initial combustion period over secondary energy.
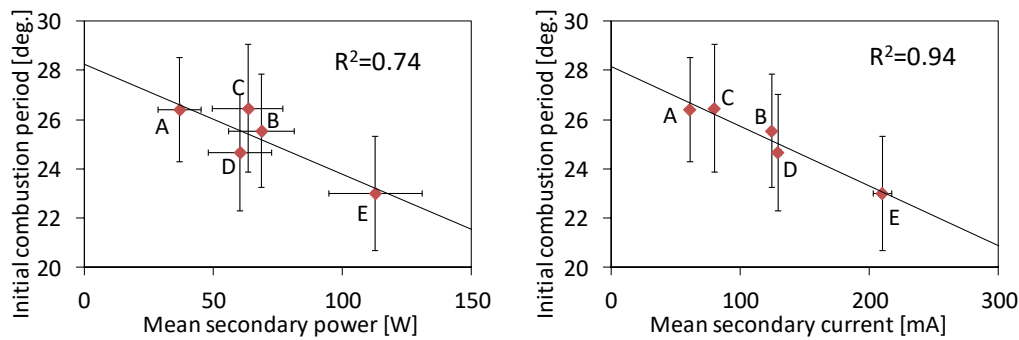
Figure 10/11: Initial combustion period over power related parameters, mean secondary power (left) and mean secondary current (right).

3.2   Analysis of combustion control factor based on optical measurement

Other index correlating with initial combustion period limit was investigated by analyzing discharge channel behavior taken by high-speed camera. In optical measurement, in-cylinder pressure at spark timing was 8.6 bar. According to a literature [1], discharge channel stretch rate might be close to flow velocity, therefore zero relative velocity between flow velocity and channel stretch rate was assumed in this study. With this assumption, mixture in discharge channel is assumed to be continuously heated from break down to restrike occurrence.

Since energy supply with mixture from discharge, mixture ignition, flame kernel formation and burning of a part of mixture by turbulent flame propagation might occur during initial combustion period, not only energy supply amount from discharge but also other physical parameters, such as flow velocity around spark plug, turbulence, mixture distribution and temperature distribution, might effect on initial combustion period [5]. Therefore, secondary energy from break down to 1st restrike occurrence and discharge channel stretch rate as index of flow velocity are selected as initial combustion period related parameters, and relation between initial combustion peri-od and these parameters were investigated.

Fig. 12 shows initial combustion period over channel stretch until 1st restrike. The left figure of fig. 12 shows average data classified by channel stretch and the right figure of fig.12 shows each cycle data. Though initial combustion period tend to decrease by increase of channel stretch until 1st restrike on Fig. 12, causal association among these are not clear and further investigation is required. .It was confirmed that variation of initial combustion period under same channel stretch condition is 8deg. Channel stretch is one of initial combustion period related index.
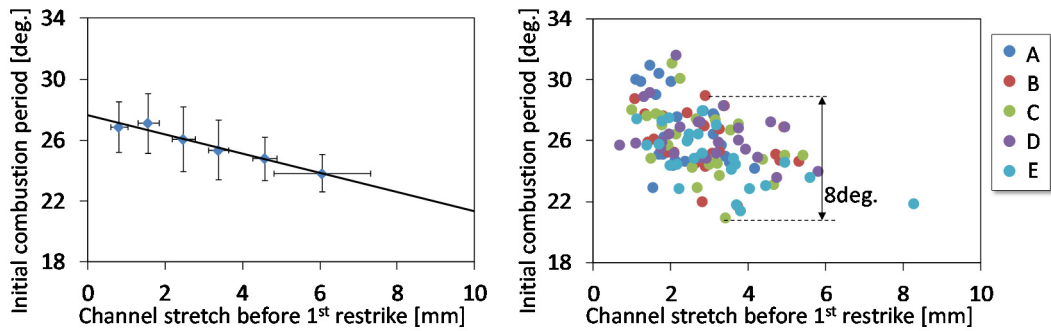
Figure 12: Initial combustion period over channel stretch until 1st restrike, mean value (left) and each cycle value (right).

Fig.13 shows initial combustion period over secondary energy until 1st restrike. The left figure of fig. 13 shows average data classified by channel stretch and the right figure of Fig.13 shows each cycle data. The left figure of Fig.13 shows initial combustion period tends to decrease by increase of secondary energy up to 50mJ. Furthermore, initial combustion period is saturated above 50 mJ. This result shows that increase of secondary energy until 1st restrike is effective to reduce initial combustion period reduction and upper limit of initial combustion period reduction by secondary energy increase exists. Since secondary energy until 1st restrike by coil E exceeds 50mJ every cycle, secondary energy and secondary current of coil E are sufficient enough, therefore initial combustion period is not reduced by further increase of secondary parameters. Fig.13 shows that variation of initial combustion period under same secondary energy until 1st restrike can be 8deg.
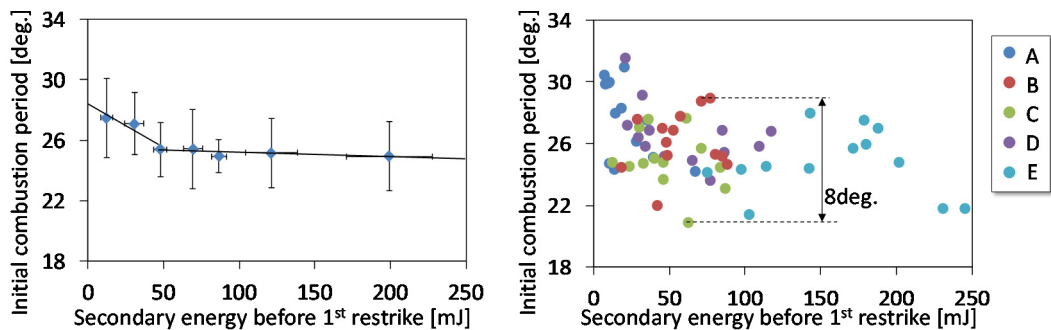
Figure 13: Initial combustion period over secondary energy until 1st restrike, mean value (left) and each cycle value (right).

Fig.14 shows initial combustion period over discharge channel stretch rate. The left figure of fig. 14 shows average data classified by channel stretch and the right figure of fig.14 shows each cycle data. The left figure on fig.14 shows initial combustion period tend to decrease by increase of channel stretch rate up to 20m/s. This result indicates larger flow velocity from intake valve side to exhaust valve side generates faster initial combustion period and consistent with investigation result by Furui et al [6]. Fig.14 shows that variation of initial combustion period under same channel stretch rate can be 9deg.
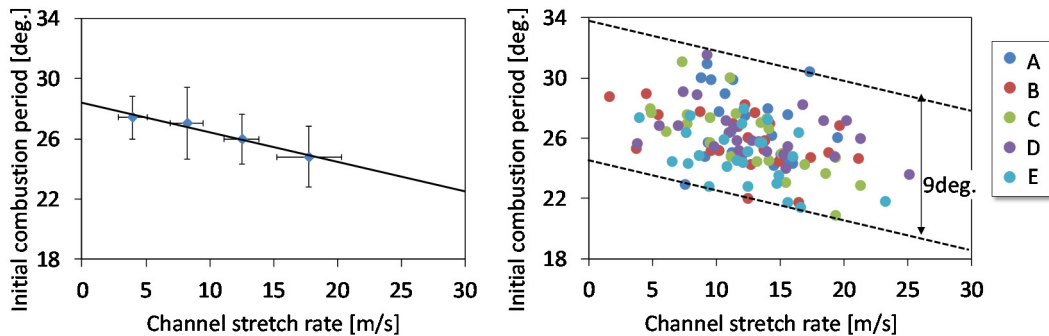
Figure 14: Initial combustion period over channel stretch rate, mean value (right) and each cycle value (left).

Further investigation was done by using Fig.15. Fig.15 shows initial combustion period distribution on a plane of channel stretch rate and secondary energy until 1st restrike. Fig.15 shows totally 18 data abstracted from measurement data of coil A, coil D and coil E. The three largest initial combustion period cycles and the three smallest initial combustion period cycles were selected. The circle size indicates initial combustion period. As discussed above, channel stretch rate affects initial combustion period, therefore data under a certain range of channel stretch rate was selected and was compared with each other.

Difference between maximum initial combustion period and minimum value of each coils are 6.8 by Coil A, 6.4 by Coil D and 6.5 by Coil E. Difference of these three coils are equivalent and it means that increase of secondary energy or secondary current does not affect to reduce variance of initial combustion period are not affected by under relatively stable control condition which coefficient of variation of NMEP is less than 3%.

Moreover, Fig.16 shows initial combustion period over channel stretch rate and initial combustion period over secondary energy until first restrike. The left figure on fig.16 shows data under secondary energy 10mJ, 21mJ and 64mJ. The right figure on fig.16 shows data under channel stretch rate 8.9m/s and 15.5m/s. Horizontal axis value are normalized by 66mJ for left figure and 18m/s for right figure. Initial combustion period change over channel stretch rate is steeper than that over secondary energy until first restrike. According to this result, flow around spark plug affects more on initial combustion period variation under this evaluation condition.

According to discussion of test under small variation of NMEP, increase of secondary energy or secondary current affects reduction of initial combustion period. Variation of initial combustion period, however, is not suppressed by increase of secondary energy

or secondary current. Moreover variation of the initial combustion period depends on in-cylinder flow condition.
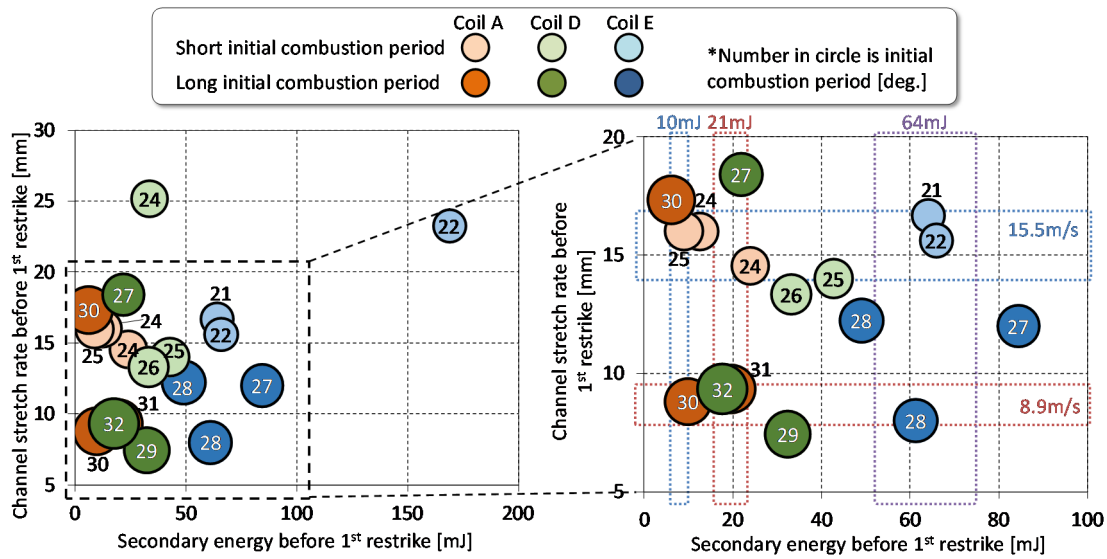
Figure 15: Initial combustion period on a plane of channel stretch rate and secondary energy until 1st restrike.
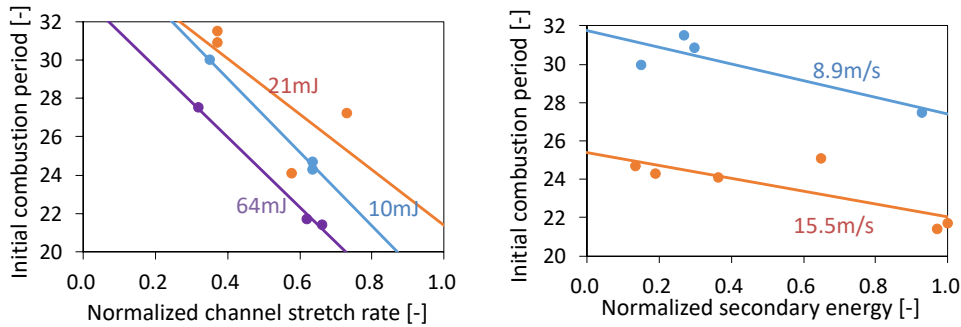
Figure 16: Initial combustion period over normalized channel stretch (left) and initial combustion period over normalized secondary energy until 1st restrike (right).

3.3   Vehicle test of selected coil

As discussed in section 3.2, channel stretch until 1st restrike is one of parameters correlating with initial combustion period correlating. Adequate coil specification for dilute combustion system was selected based on channel stretch. Fig.17 shows relation between channel stretch and secondary energy listed on table 2. As shown on Fig.17, channel stretch until 1st restrike seems to be saturated above 100mJ secondary energy. Then finally ignition coil generating 120mJ was selected including margin, and evaluated dilution combustion performance with vehicle which is 1.6liter turbo-charged direct injection engine.

EGR rate were calibrated for vehicle for demonstration. Fig. 18 shows EGR map above middle load conditions. The maximum EGR rate is more than 20% by mounting selected ignition coil. Finally, we drove the car on WLTC driving cycle and confirm fuel

consumption benefit. Fig. 19 shows history of fuel consumption and EGR rate over time. The test clarified that fuel consumption was reduced by 2.3% than original setting.
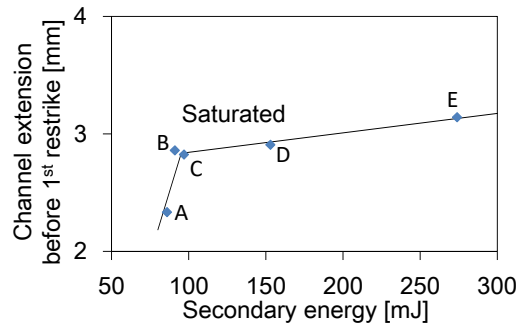
Figure 17: Channel stretch until 1ˢᵗ restrike over secondary energy
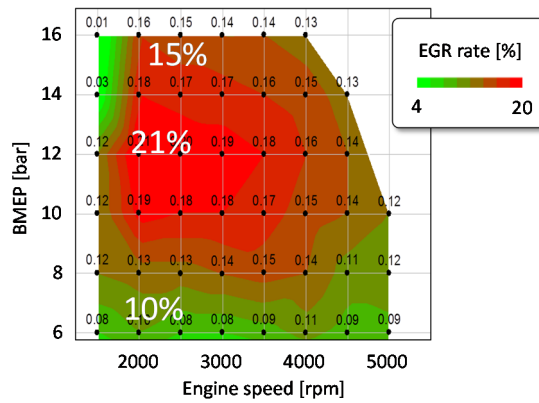
Figure 18: EGR rate map
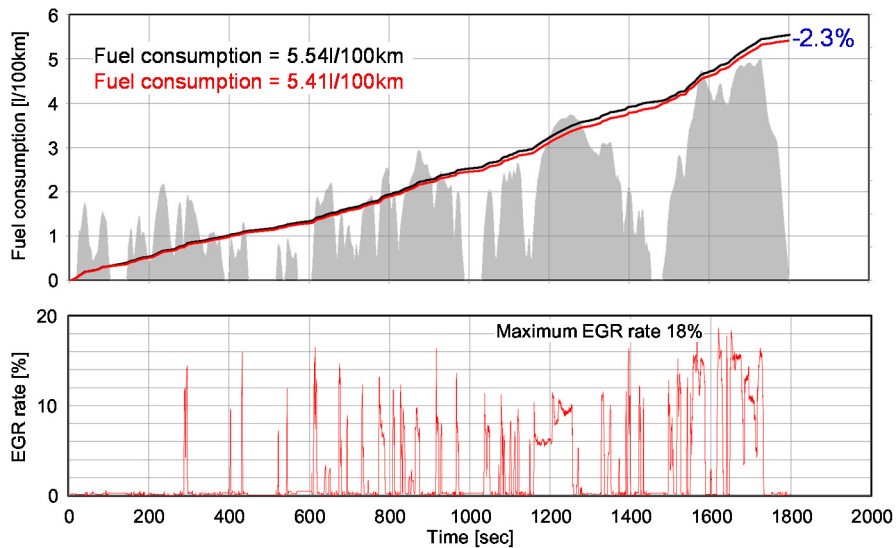
Figure 19: Fuel consumption and EGR rate profile on WLTC

102

4   Conclusion

In order to clarify effects of ignition specifications on combustion status and factors affecting on dilution limit, five coils generating different current profile were evaluated with combustion test and optical measurement by using a single cylinder engine. Finally, one opacification was selected based on channel stretch result and evaluated it on demonstration vehicle. Based on these investigation, followings were obtained.

- Initial combustion period measured under equivalent condition has correlation with dilution limit. It means that coils achieving shorter initial combustion period can extend dilution limit.
- Initial combustion period has correlation with coil secondary energy, average secondary power and average secondary current until 1ms. The average secondary current showed the largest correlation with initial combustion, average current until 1ms is adequate value for coil evaluation.
- Optical measurement test results showed a correlation of initial combustion period with discharge channel stretch.
- Under small variation of NMEP, increase of secondary energy or secondary current affects reduction of initial combustion period. Variation of initial combustion period, however, is not suppressed by increase of secondary energy or secondary current. Moreover variation of the initial combustion period depends on in-cylinder flow condition.
- Ignition coil generating 120mJ was selected and equipped on a test vehicle. The vehicle achieved maximum EGR rate more than 20% and 2.3% of fuel consumption reduction was confirmed by WLTC driving cycle test.

Literature

[1] Shiraishi, T., Teraji, A. and Moriyoshi, Y., The effects of ignition environment and discharge waveform characteristics on spark channel formation and relationship between the discharge parameters and the EGR combustion limit, JSAE 20159179, SAE 2015-01-1895 (2015).

[2] Brandt, M., Hettinger, A., Schneider, A., Senftleben, H. and Skowronek, T., Extension of operating window for modern combustion systems by high performance ignition, Ignition Systems for Gasoline Engines 3rd International Conference (2016), pp.26-51.

[3] Suzuki., K., Uehara, E. and Nogawa, S., Study of ignitability in strong flow field, Ignition Systems for Gasoline Engines 3rd International Conference (2016), pp.69-84.

[4] William, M. S., The algorithmic structure of the air/fuel ratio calculation, Readout HORIBA Technical Reports, No.15 (1997), pp.17-24.

[5] Johansson, B., Cycle to cylce variation in S.I engines – the effects of fluid flow and gas composition in the vicinity of the spark plug on early combustion, SAE Technical Paper 962084 (1996).

[6] Furui, T., Nishiyama, A., Minh, K., L., and Ikeda, Y., Analysis of in-cylinder flow and flame propagation in a gasoline engine using PIV, proceeding of JSAE meeting (spring) (2017), pp.1021-1026 (in Japanese).

3 Simulation

3.1 Advanced Ignition Modelling for Pre-chamber Combustion in Lean Burn Gas Engines

Evgeniy Shapiro, Irufan Ahmed and Nick Tiney

Abstract

Lean burn combustion systems present a viable route to emissions reductions. However, sustainable and conrolled combustion of lean mixtures can be challenging. Scavenged pre-chamber ignition systems aim to address this challenge by creating favourable ignition conditions close to stoichiometry in the spark region. The main lean charge ignition is then delivered by flame jets propagating through the nozzles connecting the pre-chamber to the cylinder.

Accurate and fast CFD modelling of the mixture formation and early flame kernel development in the pre-chamber are essential for the design of such systems. The initial stages of ignition in spark-ignited engines typically occur at time scales, temperatures and length scales falling outside of the remit of conventional CFD techniques prompting development of specialised ignition models.

A review of the models currently available highlighted a gap in the technology currently available in commercial CFD codes. Simplistic models based on direct energy transfer or fixed temperature kernel development are readily available but these models to not provide an accurate representation of the spark growth. More complex models are also available which are based on complex chemistry/turbulence interaction. While these models can provide accurate solutions they require standalone chemistry solvers or spatial temperature distribution calculations. These can be time consuming to solve, making the models less than ideal for simulations in a production environment.

A novel spark model has been developed by Ricardo and implimented into the CFD software VECTIS, allowing for an accurate specification of the spark-ignition process. The model covers all stages of spark discharge from breakdown and the formation of the initial kernel and includes a predictive model for the initial flame kernel size. The flame kernel evolution is computed via a 1D variable temperature model incorporating plasma physics with two-way coupling with 3D CFD. The detailed chemistry effects are included through flame speed and mixture properties tabulation.

This paper illustrates the principles and applications of the developed model. The model is then applied to the analysis of a novel pre-chamber ignition system and the results are compared with measurement data. A study is performed to investigate the sensitivity of the results to the input parameters within the spark ignition model.

1   Introduction

Road transport in Europe is required to be substantially more efficient by 2020+ with the target of obtaining sustainable mobility, reducing global green-house gas (GHG) emissions such as carbon dioxide (CO2) and reducing local impact emissions such as soot, NOx and unburnt hydrocarbons.

Electrification is at the forefront of the carbon emissions reduction effort and while this technology can provide vehicles which do not emit CO2 from the vehicle themselves, there are other challenges such as battery range vs charging infrastructure/time to contend with. In the short to medium term, a large amount of the targeted improved efficiency will still need to come from the improvement of the energy efficiency of the internal combustion engine.

One approach to reduce the CO2 emissions is to look at alternative low carbon fuels. Natural gas and Compressed Natural Gas (CNG) can be used reduce the carbon emissions compared to traditional gasoline engines but still provide comparable performance.

CNG has several advantages. CNG reserves are greater than oil and on a like for like comparison it is significantly less expensive than gasoline at today's prices. Of all the fossil-based fuels, CNG has the greatest potential for reducing GHG emissions [1]. It is more resistant to knock which makes it ideal for boosting and downsizing. Higher compression ratios can be used to improve efficiency and further reduce CO2 emissions. Additionally, a renewable version of CNG, biogas or biomethane, can achieve carbon neutral fuel classification if produced by biomass or liquid manure [2].

In addition to its natural tendency to reduce CO2 emissions, further efficiencies can be gained when lean burn combustion is employed. By running the engine lean, significant efficiency improvements can be achieved due to reduce heat losses, reduced exhaust losses and a higher compression specific heat ratio.

However, there are also drawbacks to running the engine lean which must be overcome. High cycle to cycle variations and high unburnt hydrocarbons can occur due to the lean flammability limit. These problems have been shown to be functions of the ignition system and combustion speed/duration. One method to avoid these issues is to use a pre-chamber ignition system which can provide large ignition energy into the main combustion chamber via distributed ignition points which ignite the main lean premixed charge more efficiently.

The pre-chamber approach allows for the generation of near stoichiometric conditions and enables control over the turbulence generation close to the spark plug, improving initial combustion and thus cycle to cycle variation. Once the spark ignites the prechamber, the main combustion chamber is then ignited by the flame jets as they exit the pre-chamber nozzles.

While there has been lots of research into pre-chamber design for large, heavy duty applications, comparatively little has been done for smaller automotive applications at high compression ratios.

The research and development of such a system is one of the objectives of the Horizon 2020 GasOn project. The GasOn target is to extend the lean limit of operation in natural gas engines to Diesel-like compression ratios [3]. The full GasOn project investigates numerous pre-chamber designs and operating conditions but the initial requirement was the development of a new ignition model to prediction of the initial spark ignition and its growth and propagation through the pre-chamber. This paper looks at the modelling of this spark ignition using the computation fluid dynamics software VECTIS and investigates the sensitivity of the model implemented to modelling parameters.

Accurate modelling of the initial stages of spark ignition is essential for the overall accuracy of the simulations. The Dynamic Discrete Particle Model (DDPIK) developed at Ricardo [5,13] covers all stages of the spark from the point the power is supplied by the ignition coil to the transition of the flame kernel supported by the discharge to a fully developed turbulent flame.

The model for the spark discharge stage in isolation has been previously validated against academic experiments [5]. The complete simulation methodology reported in this paper combining the spark model and the RANS combustion model within Ricardo VECTIS CFD solver has been validated against Rapid Expansion Compression Machine (RCEM) measurements [13] and Large Eddy Simulation combustion models [14]. Furthermore, the complete model has demonstrated good accuracy when applied to the pre-chamber lean operation natural gas engine development with high compression ratio within Horizon 2020 GasOn project [4, 6].

However, in the absence of a detailed spark characterisation under precise conditions of interest and optical access measurements close to spark position, which in the case of pre-chamber engine development remains quite challenging, a number of model parameters remain uncertain. These uncertainties are not fully resolved by the extrapolation of information obtained from validation using stand-alone spark measurements under low pressure quiescent conditions and optical access measurements in different applications. In the present paper the modelling uncertainties are discussed and the effects of the modelling parameters and discretisation approach onto predictions obtained for flame propagation in a pre-chamber mounted on an RCEM are investigated using a validated set-up reported in [13] as a starting point.

2   Validation case description

To validate the spark ignition model, experimental data has been obtained from an optical Rapid Compression Expansion Machine (RCEM). This experiment and methodology is fully described in [13]

This base engine geometry is used throughout, with a single pre-chamber design used in the work presented here. The geometry has an 84mm bore with a stroke length of 249mm. An optical access piston is used with a top hat profile. The top hat shape has a diameter of 52mm and a depth of 2.2mm.

The model of RCEM has then been constructed in VECTIS CFD. The geometry of the RCEM is illustrated in Figure 1.
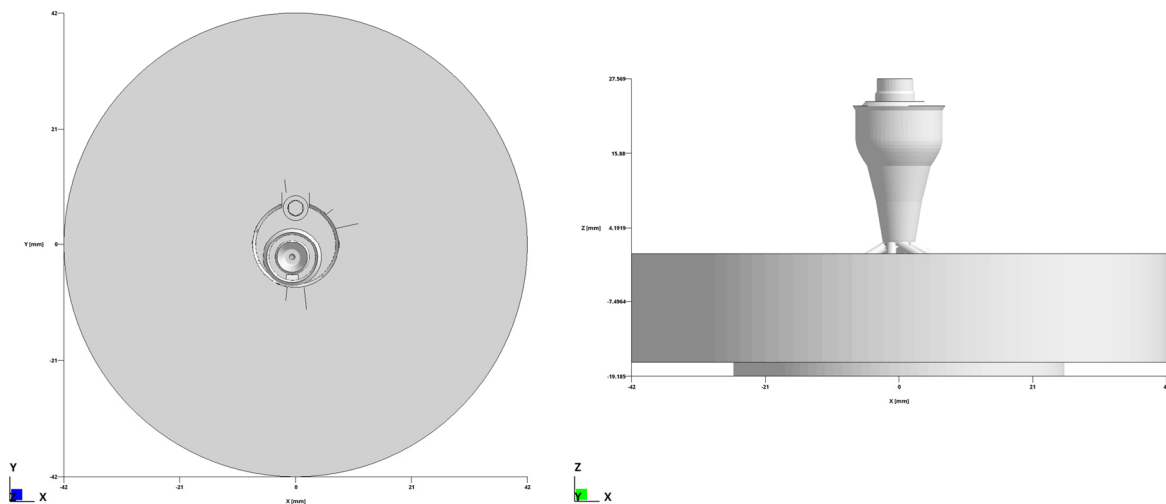
Figure 1: RCEM Geometry

The pre-chamber investigated is shown in Figure 2. The geometry has an effective volume of 1.7e-6. The effective volume is not including the volume of the nozzles but just the volume of the chamber itself. It has 7 nozzles which join the pre-chamber at a tangent. Each nozzle has a diameter of 1.5mm. The nozzle angle with respect to the bore axis is 64.5deg. The shape has been developed at VW through numerical optimisation focussing on mixture homogeneity and ignitability using VECTIS CFD tool within the GasOn project [4,13].
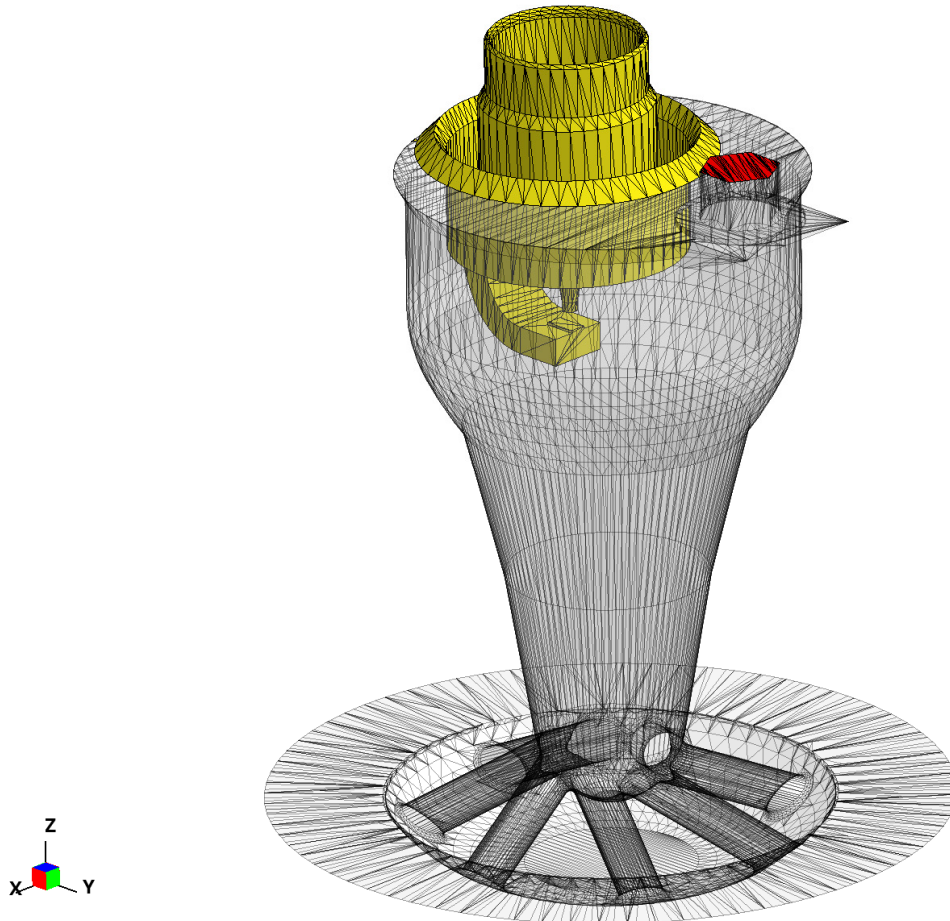
Figure 2: Pre-chamber PC-A Geometry

The RCEM operation is assigned a nominal RPM of 600 which maps bottom dead centre of the RCEM stroke to 540 degrees CA. The simulations are started from quiescent flow conditions with pressure, temperature and composition initialised based on the experimental data at 37 ms bTDC (-133.2 deg CA).

Four combinations of air-fuel mixing are simulated. For each case the mass of fuel injected and the injection duration is varied. The fueling and spark timings of the simulations are given in Table 1

Table 1: Fueling and spark timing

Case	Mass	Start of injection	Injection duration	Spark timing
	mg	CA. deg.		
1	0.9	645.7	18.0	708.8
2	1.2	646.5	23.4	708.8
3	1.5	647.1	28.8	708.7
4	1.7	647.3	34.2	708.7

Initial conditions for the simulations for temperature and pressure are also taken from experiment. The initial conditions used are shown in Table 2.

Table 2: Simulation initial conditions

Case	Temperature	Pressure
	K	Pa
1	380.2	136978
2	389.2	141551
3	396.2	139407
4	392.0	142369

The models and parameters used for combustion modelling in all cases are given in Table 3.

Table 3: Base Simulation models and parameters

Model/parameter	Value
Combustion model	G-equation/RTZF
Laminar flame speed	Metghachi & Keck modified
Turbulent flame speed	Herweg and Maly
G-equation re-initialisation	Geometric with smoothing

For the spark ignition, there are five base inputs which are listed in Table 4.

Table 4: Spark model and parameters

Model/parameter	Value
Spark model	Dynamic DPIK
Breakdown energy	0.1mJ
Effective power	210W
Kernel particles	20000
Spark duration	1.8ms
Burnout radius	1.1mm

The spark duration is defined based on measurement data and is fixed to 1.8ms based on a study of similar spark [25]. The remaining spark parameters will be investigated for model sensitivity.

3   Model formulation and investigated parameters

Accurate modelling of the initial stages of spark ignition is essential for the overall accuracy of the simulation. The Dynamic Discrete Particle Model (DDPIK) developed at Ricardo [5,13] covers all stages of the spark from the point the power is supplied by the ignition coil to the transition of the flame kernel supported by the discharge to a fully developed turbulent flame. To detail the uncertainties inherent in the modelling, it is essential to consider the inputs required for every part of the model.

Firstly, consider the predictive model for the initial radius and temperature of the flame kernel. The estimate of radius at the end of the breakdown of the spark discharge is critical for the correct initial state of the energy balance.

The model employed in DDPIK is an extension of the two-stage breakdown model proposed in [7,8]. The breakdown occurs over the first ~10ns since the initiation of the discharge. At this point a cylindrical plasma channel is formed between the electrodes with the pressure $P_{bd} \sim 20 - 30 MPa$ and temperature corresponding to completely dissociated and ionised plasma in a state approaching thermal equilibrium [8, 15, 11]. Due to the extremely rapid nature of this process, the approach proposed in [8] considers that the breakdown energy E_{bd} is supplied instantaneously, followed by an expansion of the activated volume of the plasma to equilibrate the pressure with the surrounding ambient in a shock wave process. Applying energy conservation over the two stages of the breakdown process results in the following expression of the breakdown radius [8,5]:

$$r_{bd} = \sqrt{\frac{\gamma - 1}{\gamma} \frac{E_{bd}}{P \pi l \left(1 - \frac{T + LHV/c_p}{\left(\frac{1}{\gamma} (T_{bd} - T) + T \right)} \right)}} \quad (1)$$

The above expression builds on the theory of [8] by including the chemical energy released in the oxidation of fuel present in the activated volume through the lower heating value (LHV) term. In this expression, the parameters of the ambient are the result of a 3D CFD simulation with a low uncertainty level. The break-down temperature, T_{bd}, is well defined. It has been observed that it has the upper limit in the range of $T_{bd} \sim 60000K$, due to the high energy barrier of the third ionisation level of nitrogen [12], which does not change with the flow conditions or mixture composition as long as nitrogen remains the dominant component. The definition of the breakdown energy is more uncertain. This value depends on the ambient conditions and in practice it is not known a-priori. Measurements reported by Rivin et. al. [9] indicate energy less than 1mJ with a spark plug gap of 0.8mm for premixed air/methane at 0.25MPa. The theoretical model of [7] points to breakdown energies <1mJ for the activated plasma channel diameter of 40μm. Maly and Herweg [16] refer to levels of 0.3-1mJ in commercial ignition systems with a minimum energy of 0.3mJ required for breakdown in a 1mm spark gap at 1bar.

After the breakdown, the arc and glow discharge stages follow. In the arc stage, temperatures are in the range 4,000-10,000K, and are dominated by dissociation processes. The glow discharge rate is characterised by temperatures just above the adiabatic flame temperature [11].
After the breakdown stage, a complete simplified 1D model can be formulated in terms of the conservation of mass and energy as follows [5,13]:

$$\begin{cases} \dfrac{dr_k}{dt} = \dfrac{\rho_k}{\rho_u} S_b + \dfrac{r_k}{3} \left(\dfrac{1}{R_k T_k} \dfrac{d(R_k T_k)}{dt} - \dfrac{1}{P_u} \dfrac{dP_u}{dt} \right) \\ \dfrac{dT_k}{dt} = \dfrac{Q}{\frac{4}{3} \pi r_k^3 \rho_u} \dfrac{\gamma_k - 1}{\gamma_k} \dfrac{T_k}{R_u T_u} + \dfrac{3}{c_{p,k} r_k} \left(LHV - \left(c_{p,k} T_k - c_{p,u} T_u \right) \right) \dfrac{\rho_k}{\rho_u} S_b + \dfrac{\gamma_k - 1}{\gamma_k} \dfrac{T_k}{P_u} \dfrac{dP_u}{dt} \end{cases} \quad (2)$$

Where subscripts „k" and „u" refer to kernel and unburnt side of the flame front respectively and in the usual notation R is the gas constant, ρ is the gas density, c_p is the specific heat capacity and γ is the adiabatic index. P represents ambient pressure, Q

is the effective spark power and Sb is the cumulative burn rate comprising turbulent flame speed S_T and the plasma expansion speed:

$$S_b = S_T + \frac{Q}{4\pi r_k^2 \rho_u \left(c_{p,k} T_k - c_{p,u} T_u \right)} \quad (3)$$

S_T is modified to account for curvature of the flame:

$$S_T^* = S_T - \frac{2}{r_k} \left(\frac{\nu}{Pr} + 0.28 l_{ft} u' \right) \quad (4)$$

where Pr and ν are laminar Prandtl number and dynamic viscosity and u' is the turbulent velocity. The flame brush thickness of the spark flame front l_{ft} is approximated based on the time since ignition and the local turbulent properties ([5]).

The basic turbulent flame speed uses the expression proposed by [11]:

$$\frac{S_T}{S_L} = 1 + A \left(\frac{u'}{u' + S_L} \left(1 - exp\left(-\frac{r_k}{l_I} \right) \right) \left(1 - exp\left(-\frac{(u' + S_L)t}{l_I} \right) \right) \right)^{\frac{1}{2}} \left(\frac{u'}{S_L} \right)^{\frac{5}{6}} \quad (5)$$

Where $l_I = u'^3/\epsilon$ is the integral time scale and S_L is the laminar flame speed.
The 1D model is coupled to 3D CFD using an approach similar to the one proposed in [10] with the kernel front discretised using individual particles randomly distributed on the surface of the spherical flame kernel which is allowed to move with local flow velocity. The particle positions are used to sample the 3D solution for the unburnt quantities required for the 1D model and at the same time particle density is used to distribute the reaction rate source to 3D computational cells.
It is important to note that the kernel radius and temperature are tightly coupled through the system of Equations 2 and temperature must be appropriate for the radius of the kernel. Models which do not take the variation of temperature with time into account (e.g. [10, 20]) should select the kernel temperature carefully to avoid unphysical values of the plasma velocity. For example, using adiabatic flame temperature as the kernel temperature (e.g. [20]) in Equation 2, clearly results in plasma speed increasing away from stoichiometry, where the adiabatic flame temperature decreases.
The 1D model is computed in a coupled manner until either the spark discharge completes, or the kernel reaches the sustainable flame length scale. The sustainability of the kernel has two criteria. Firstly, its radius must exceed the integral length scale of turbulence l_I. Secondly, it should be self-sustained at this stage, i.e. the diffusion of the turbulent flame front should not exceed the flame propagation speed at the kernel surface. The latter criterion can be expressed [19] as:

$$R_c > \frac{2}{S_T} \left(\frac{\nu}{Pr} + 0.28 l_{ft} u' \right) \quad (6)$$

Some of the uncertainties in the 1D flame kernel model are familiar from other aspects of modelling methodology for the internal combustion engine. For example, both the turbulent flame speed and the flame brush thickness depend on the integral length

scale, which can be challenging to predict in simulations using Reynolds-Averaged Navier Stokes (RANS) turbulence modelling (e.g. [17]).

The expression for the turbulent flame speed in its fully turbulent form introduced substantial modelling assumptions (e.g. [18]). The main modelling parameters which are a subject of uncertainty in Equation 2 are the effective spark power and the critical radius of transition.
The power transferred to the plasma is a function of time and rapidly varies from $O(10^5)$ to $O(10)$W over the time interval between end of the breakdown stage and end of the glow stage of the discharge. In the absence of detailed measurement data the effective average spark power can be considered as a model tuning parameter.

Note, that there are in effect two critical parameters for the kernel radius. R_c given by Equation 6 corresponds to flame diffusion driven by turbulence generated by the flame front itself. At the same time, the kernel is embedded in the external inhomogeneous turbulent field. For the kernel to be sustainable, it's size should exceed the integral length scale of this turbulent field. This critical radius R_b is subject to uncertainty in terms of the turbulence modelling. Furthermore, the definition. $R_b \sim l_I = u'^3 / \epsilon$ provides a correct functional dependence, but the uncertainty in the coefficient of proportionality means that the actual value can be treated as a tuning parameter as well. For example, Tan and Reitz suggest the following definition of the critical radius:

$$R_b = C_T C_\mu^{0.75} k^{1.5} / \epsilon \ (7)$$

[10], with the tuning constant $C_T = 1 - 5$. The length scale definition used in the DDPIK model corresponds to a constant $C_T = 3.3$ in the formulation of [10].
Errors in the solution can also be introduced by the discretisation of the 1D problem. The implementation in VECTIS employs a 1st order accurate discretisation of Equation 2 based on the local Courant number. The space discretisation is given by the number of particles used to sample the 3D solution.

The remaining parts of the CFD set-up follow VECTIS default approach. The realisable k-e model [21] is used with a first order in time, second order in space pressure-correction solver. Based on a grid sensitivity study, a uniform mesh size of Δx=0.18mm was used in the pre-chamber with 0.94mm mesh in the cylinder. The G-equation combustion model is used with a constant A=2.75 in the fully turbulent form of Equation 5.

The baseline case employed 20000 particles with the first 0.2 degrees of the simulation conducted with a Courant number of 0.1, increasing to 1 thereafter. The effective power was set to 210W, with a break-down energy of 0.1mJ and a breakdown temperature of 60000K [5, 13]. The transition radius was estimated a-priori to be 1.1mm based on experience with previous simulations.

The range of the parameters which have been investigated are summarised in Table 5.

Table 5: Simulated cases

Parameter	Minimal value	Maximum value
Effective Power (W)	1	210
Number of particles	1000	20000
Breakdown energy (mJ)	0.1	1
Transition radius (mm)	0.8	1.4
Courant number	0.1/1	0.1/4

To simplify the comparison of the RCEM set-up with engine cases, where appropriate the timings of the RCEM operation have been converted to degrees of crank angle using 600 rpm speed based on the RCEM compression cycle time. The averaging of reported quantities is performed in the volume of the pre-chamber and the spark volume comprised of a sphere centred on the spark plug gap with a 3mm radius.

4   Results and discussion

Figure 3 illustrates the flow and turbulence quantities in the spark region for 0.9mg injection, just before the ignition at -11.15deg. Here the length scale is evaluated using $C_T = 1$ in Equation 7. The velocity and turbulent velocity distributions illustrate the flow structure driven by the inclined nozzles of the pre-chamber which result in a wall-attached spiral jet flow. The spark gap is shielded by the electrodes and features low velocities and moderate turbulence levels creating conditions beneficial for ignition. The local mixture is close to stoichiometry. Note that the turbulent length scale is very close to the initial radius typically assumed in the models which do not cover breakdown conditions (e.g. 0.5mm in [10]).
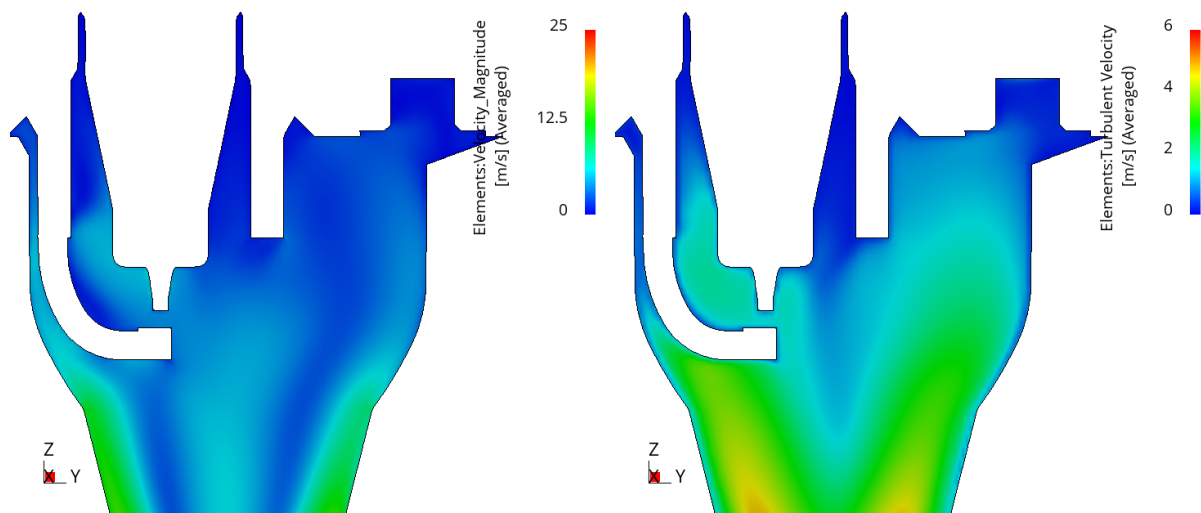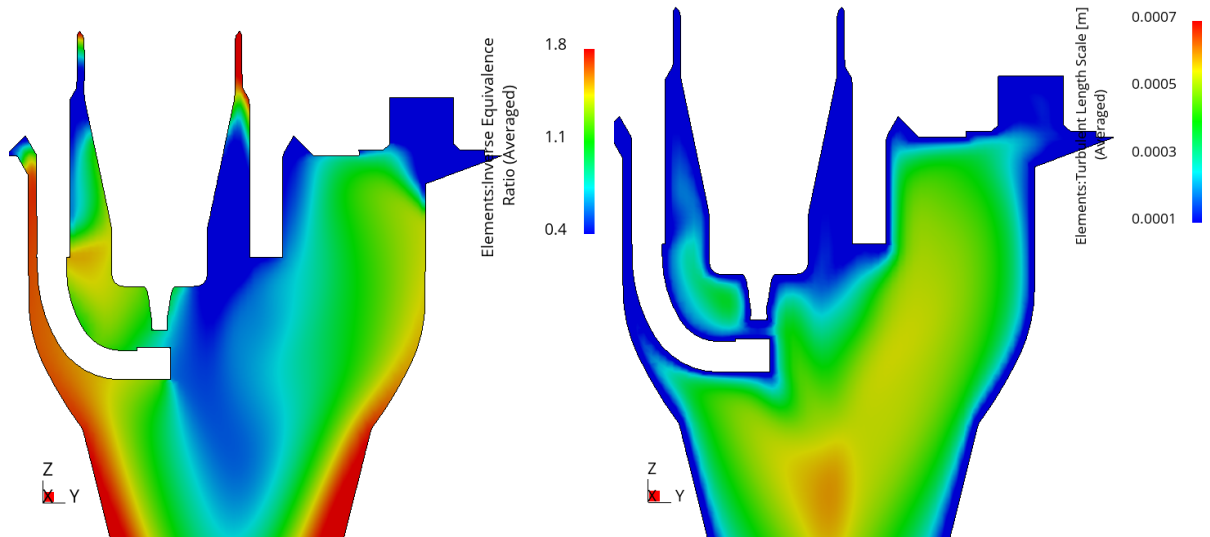
Figure 3: Velocity, turbulent velocity, inverse equivalence ratio and turbulent length-scale near spark plug gap for m=0.9mg injection, at -11.15deg
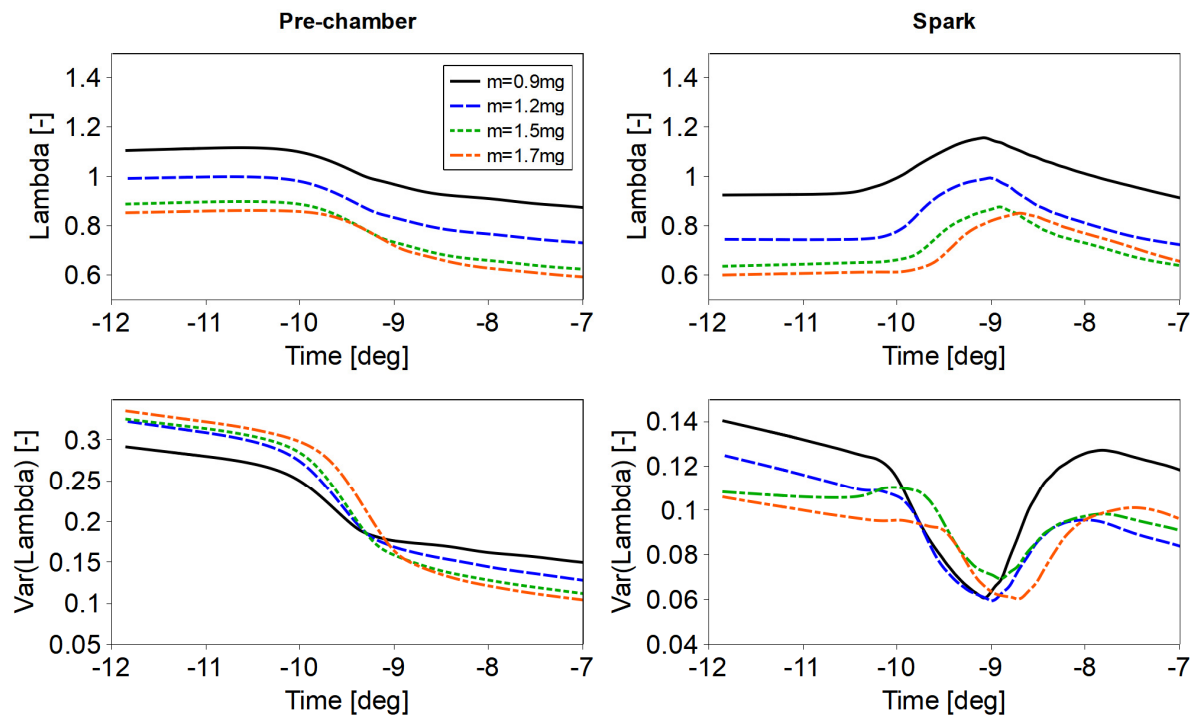
Figure 4: Pre-chamber and spark region mixture composition

Figure 4 illustrates the composition of mixture and its homogeneity in terms of the average values of λ within the pre-chamber and the spark volumes. As could be expected, an increase in the injection mass leads to an increase in the equivalence ratio in both control volumes. Longer injection timings increase inhomogeneity levels in the pre-chamber. However, the effect on the spark volume is opposite. The results indicate that when controlling the total injected mass, it is beneficial to target values slightly leaner (~10% in the investigated case) than estimated stoichiometry based on the pre-chamber volume and density.

An interesting observation is that while the spark volume is always richer than the pre-chamber on average, the actual difference of the average λ between the two volumes at the point of ignition does not change significantly with the injected mass (Figure 5).
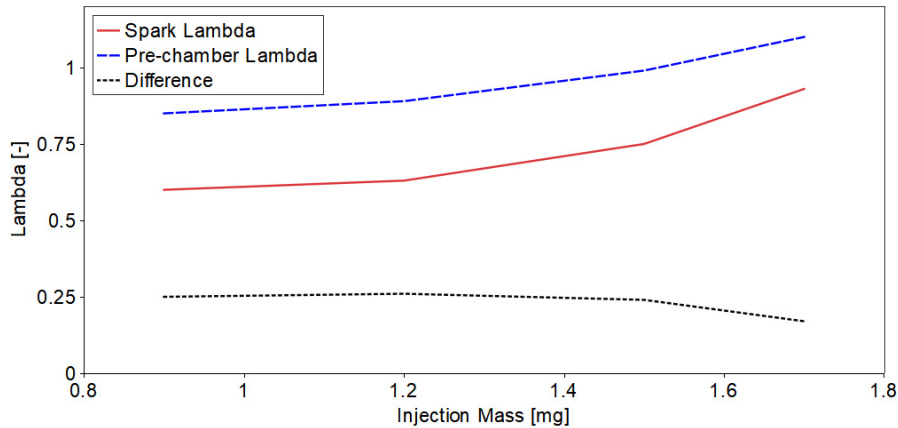
Figure 5: Pre-chamber and spark region mixture composition at ignition point

The integral length scale and turbulence levels at the spark location and in the pre-chamber up to the ignition time are illustrated in Figure 6 for a representative injection case with baseline model parameters. The spark region is less turbulent due to the sheltering by the spark body. The actual integral length-scale is lower than the a-priori estimation.
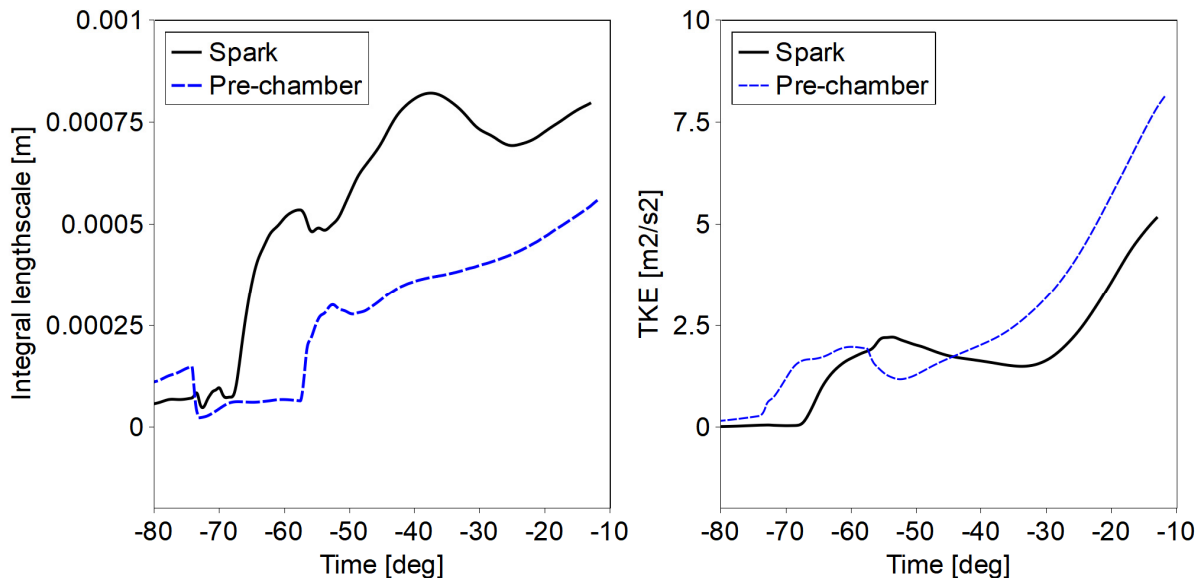
Figure 6: Integral lengthscale evolution (injected mass m=0.9mg, injection timing: -74.3- -56.3deg)

Figure 7 shows the evolution of the kernel radius, critical parameters and the kernel temperature. As the kernel grows, the turbulent component of the flame speed becomes much greater than the laminar component and the turbulent flame brush thickness l_{ft} and the critical radius R_c become identical. The kernel radius for this case grows much faster than the flame brush thickness and as a result, no quenching is

observed. The temperature relaxes over the first ~20µs and becomes close to the ad-iabatic flame temperature, which is in line with the behavior reported in other studies (e.g. [11]).

The kernel radius at this point is ~0.5mm, which is the appropriate initial kernel radius for models neglecting the evolution of the kernel temperature. The final critical radius, based on the flame front thickening R_c, is much smaller than the critical radius based on the turbulent length scale of the external turbulence R_b, illustrated in Figures 3 and 6, indicating that the limiting factor for the quenching is the external turbulent field, and not the turbulence generated by the flame front.
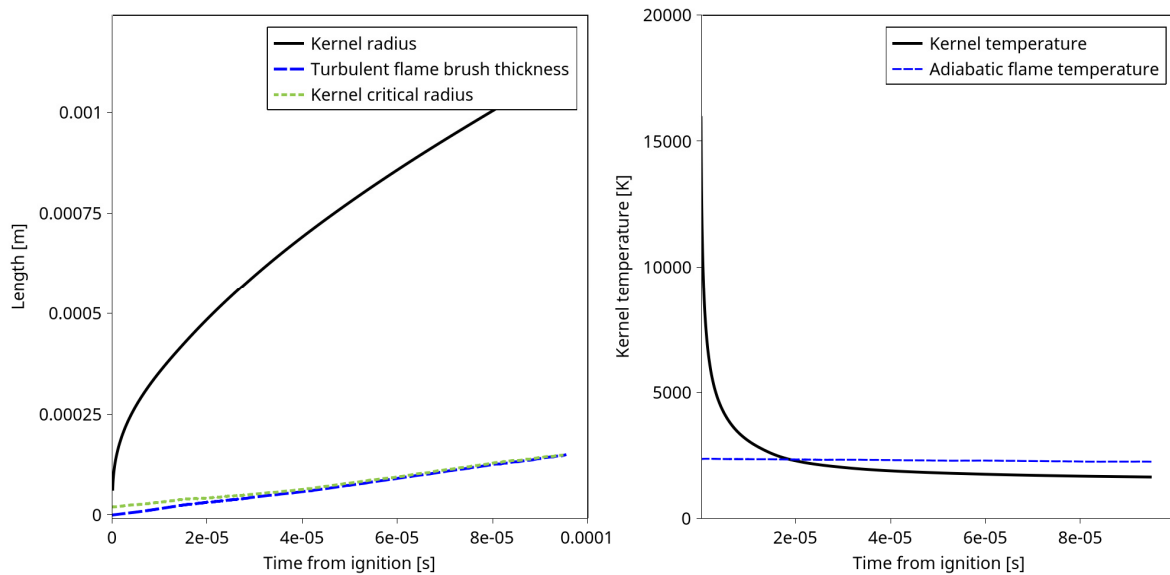
Figure 7: Kernel evolution for the baseline model parameters, (injected mass m=0.9mg)

The speed of the flame kernel growth follows the composition of the mixture in the spark region as shown in Figure 8.
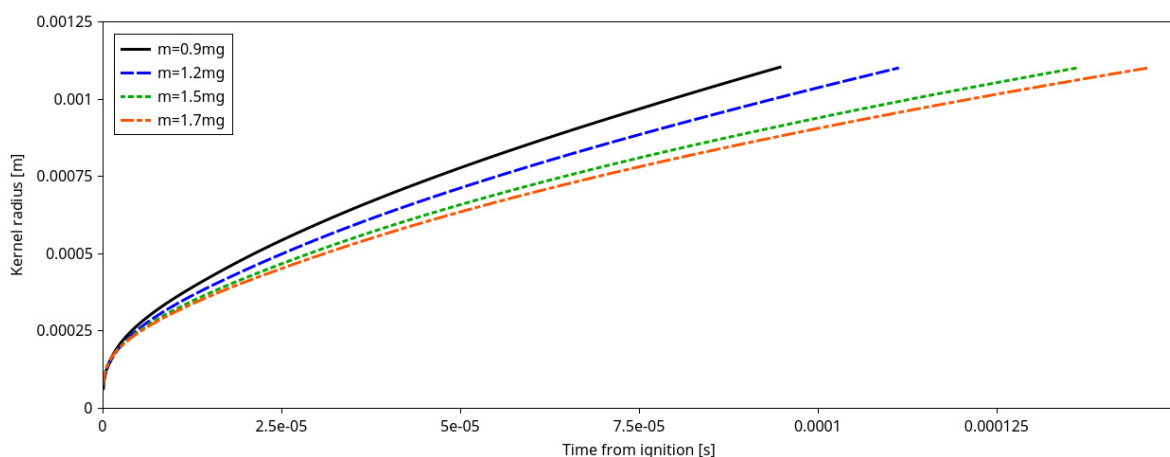
Figure 8: Kernel evolution for the baseline model parameters, (injected mass m=0.9mg)

The flame jet exit time obtained in the simulations and the comparison with the exper-imental data are summarized in Table 6. The jet exit times were determined in the

simulation by calculating the time at which the concentration of the burnt fuel in the mass flow rate through the outlets of pre-chamber nozzles reaches 4.5%.
The time was then averaged between the nozzles. Tests with various thresholds showed low sensitivity to the threshold value (see [13] for more detail). Experimental jet exit times are determined by the threshold in OH* chemiluminescence levels. It is difficult to compare the two levels directly. However, the indication of the agreement is the offset between the two values, which is constant apart from the outlier 1.5mg injection, which also shows a local maximum in the standard deviation of the experimental results.

Table 6: Flame jet exit timings for baseline set-up

Injected mass (mg)	Experiment		Simulation	
	Flame jet exit time (ms)	Standard deviation (%)	Flame jet exit time (ms)	Difference vs experiment (%)
0.9	0.75	11.3	0.58	22.6
1.2	0.81	12.5	0.60	23.5
1.5	0.94	15.5	0.66	30.0
1.7	0.88	9.8	0.68	22.7

The results reported in Table 6 show higher deviation from the experimental data than the results reported in [22], where a different experimental set-up was considered with a much shorter injection duration. Note that results reported in [22] were obtained with the effective spark power of 180W and transition radius of 4mm, in effect delaying the flame development.

Simulation of cases with varying number of particles demonstrated that the flame jet exit times exhibit no sensitivity to kernel. For example, the variation of the maximum of recorded flame jet exit time between the nozzles, when changing the number density from 20000 to 1000 particles was equal to 0.06% for the baseline case with 0.9 injected mass. The critical gas phase Courant number for the initial stage of the kernel growth comprising the first ~20μs during which the temperature relaxes to adiabatic flame temperature was found to be equal to 0.1. While the model would still converge, increasing time step beyond this value resulted in a sharp unphysical decrease of the kernel temperature. After this initial stage, the model was found to be stable with the gas phase Courant number of up to 2.

The increase in the breakdown energy leads to the increase in the initial flame kernel size, which results in faster cooling of the kernel due to a higher initial surface area. The current implementation of the model explicitly restricts the contraction of the kernel, hence this slower initial growth still leads to the same values of the kernel radius at later times (Figure 9).
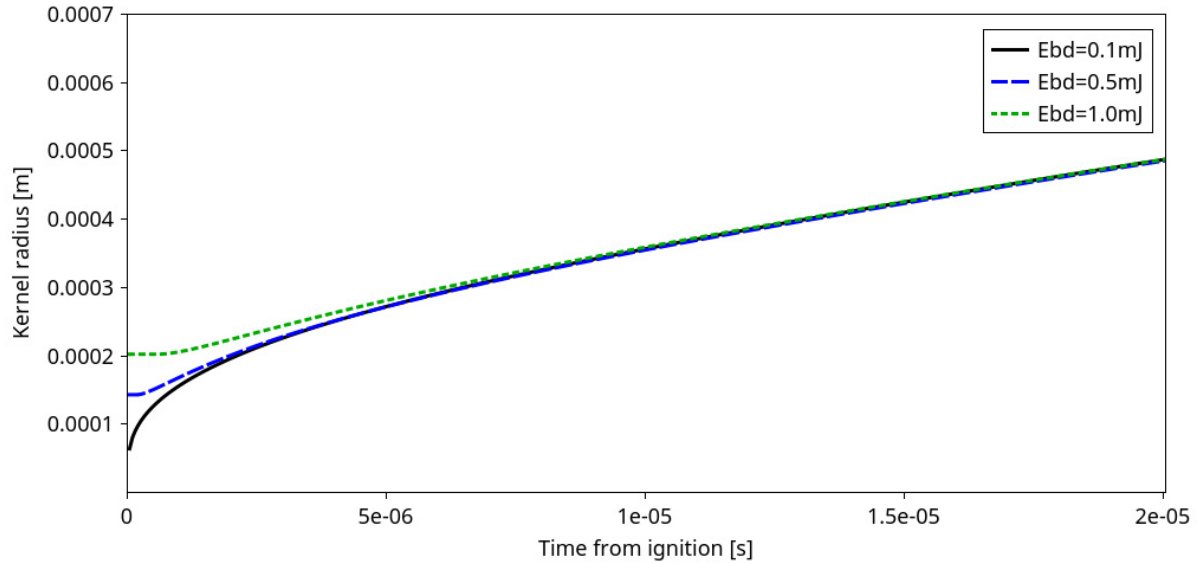
Figure 9: Effect of the breakdown energy on the kernel growth (injected mass m=0.9mg)

Within the 1D model context, increase of the transition radius is equivalent to an extension of the duration of the 1D stage. Extended duration of the 1D model slows down the development of the flame and increases the flame jet exit time. The decrease of the effective power has the same effect; hence it is useful to consider the two together. Figure 10 shows the burned fuel mass fraction in the mass flow rate through one of pre-chamber nozzles (there was no substantial asymmetry observed between the nozzles). The variation of the transition radius for the same spark within the limits suggested in [10] does not have a strong effect on the flame jet exit time. However, the effective spark power change within the 210W-1W range changes the jet exit time by 0.31ms (1.1deg).
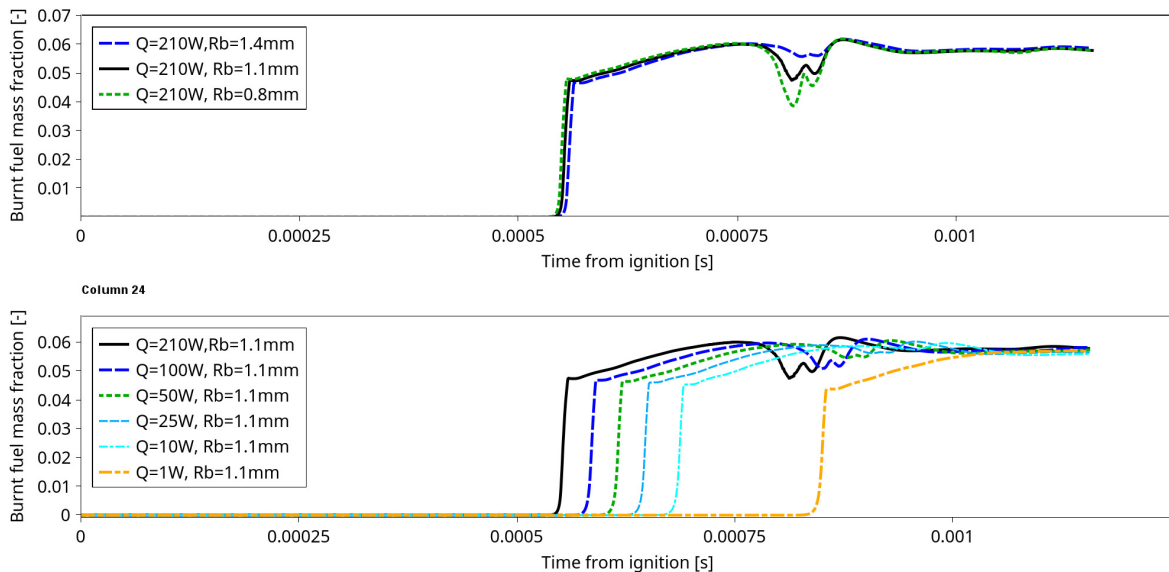
Figure 10: Effect of the effective power and transition radius on flame propagation (injected mass m=0.9mg)

The effective spark power in the range 180-210W, has been shown to produce correct results when compared with the experiments of Maly [15] ([5, 13]), with a different coil. The same set-up also showed good results when compared with the measurements done in the optical engine for a similar coil/spark combination [5]. While some variation in the effective power depending on ambient pressure, density and spark coil properties can be expected, the values of the effective power ~5W required to close the gap with the experimentally observed flame jet exit times are not realistic.

5   Conclusions

The Dynamic Discrete Particle Ignition Kernel has been designed and implemented within the VECTIS software product as part of the Horizon 2020 GasOn project. This model has been successfully validated against academic test cases in other published works and here the model is used within a Rapid Expansion Compression Machine environment.

The results have shown that there can be some variation between simulation results and those from measurements when comparing the time taken for an ignition event to travel from the spark through the pre-chamber and into the main combustion chamber. The implemented ignition model has several input parameters which are subject to uncertainty. Here these parameters have been investigated to examine the effect that they have on this discrepancy between the flame jet timings.

The sensitivity to the number of particles used in the DDPIK model is slight, with a reduction from 20000 to 1000 producing only a 0.06% change in the results. The reduction in the number of particles being tracked also results in a reduction in computational cost, improving the model for industrial applications and time frames. Variation of the transition timing for the same spark energy also produces small variations and does not produce as strong effect on the flame jet exit timing. The results are sensitive to the effective spark power input parameter. However the variation of the effective spark power input within reasonable limits does not allow closing the gap with the experimentally observed flame jet timings.

The dynamic discrete particle ignition model shows good robustness and accuracy over a range of air-fuel ratios. The sensitivity analysis of model parameters conducted here indicates that the uncertainties in the spark model alone cannot account for the faster flame propagation apparently observed by comparison with the experiment. The model is robust and can be used with the default settings established in [5.13].

The only remaining factor which can affect the flame jet exit time is the turbulent flame speed closure used in the G-equation part of the combustion model. In particular, the value of the coefficient A used in Equation 5 has been reported to be sensitive to flow conditions and turbulence levels [13, 23, 24].

The effect of the turbulent flame speed on the simulations of the RCEM experiment are explored in detail in the following publication [13].

Acknowledgements

Bibliography

[1]   Christof Schernus, RD., Knut Habermann, BGP. "Potentials of gas mobility in road transport", BDEW-Fachkongress 2016. Berlin 2016-03-02

[2]   Möhring, L., Andersen, J.: "CNG Mobility - Scalable, Affordable and Readily Available Solution for Environmental and Climate Challenges" 38. Internationales Wiener Motorensymposium 2017

[3]   Ferrera, M., "Gas-Only Internal Combustion Engines, H2020GV-3-2014 Future natural gas powertrains and components for cars and vans". NGVA – Clean future with g-mobility. Paris. 25 May 2018,

[4]   Lucas, G., Tallu, G. and Weißner, M., "CFD-based Development of an Ignition Chamber for a lean and highly efficient CNG Combustion", Proc. THIESEL 2018 Conference on Thermo- and Fluid Dynamic Processes in Direct Injection Engines, 2018.

[5]   Tallu, G., Beck, L. M., Prouvier, M., Winkler, A. and Shapiro, E., "3D CFD Modelling and Simulation of Spark Ignition Inclusive of Turbulence Effects and Detailed Chemical Kinetics", Proc. 3rd International Conference on Ignition Systems for Gasoline Engines, November 3–4, 2016, Berlin

[6]   Tallu G., Frambourg M., Prouvier M., Weißner M., Winkler A., "Numerical Investigation of Spark Ignition Processes in Natural Gas Engines with the Advanced Spark Ignition Model", Proc. 4th International Conference on Ignition Systems for Gasoline Engines, Berlin, December 2018

[7]   Sher, E., Ben-YaIsh, J. and Kravchik, T., "On the birth of spark channels", Combustion and Flame, 89:168-194, 1992.

[8]   Refael S. and Sher E., "A theoretical study of the ignition of a reactive medium by means of an electrical discharge", Combustion and Flame, 59:17-30, 1985.

[9]   Rivin B., Dulger M. and Sher E., "Extending Lean Misfire Limit of Methane-Air Mixtures by Means of an Enhanced Spark Discharge", SAE - 1999-01-0573

[10] Tan, Z. and Reitz, R. "Modeling ignition and combustion in spark-ignition engines using a level set method", SAE Technical Paper 2003-01-0722, 2003.

[11] Herweg R. and Maly, R. R. "A fundamental model for flame kernel formation in S.I. engines". In SAE International, 922243, 1992.

[12] Maly R.R., "Spark Ignition, its Physics and Effect on the Internal Combustion Process", in Fuel Economy: Road Vehicles Powered by Spark Ignition Engines, ed. by J.C. Hilliard, G.S. Springer, Plenum Press, New York 91–148 (1984).

[13] Shapiro E., Kyrtatos P., Kotzagianni M., Bolla M., Tiney N., Boulouchos K., "Experimental and numerical analysis of pre-chamber combustion systems for lean

burn gas engines", Submitted to SAE World Congress and Exhibition, Manuscript no: 19PFL-0579

[14] Bolla M., Shapiro E., Tiney N., Kyrtatos P., Kotzagianni M., Boulouchos K., "Numerical study of turbulence and fuel-air mixing within a scavenged pre-chamber using RANS and LES", Submitted to SAE World Congress and Exhibition, Manuscript no: 19PFL-0664

[15] Maly, R. and Vogel, M., "Initiation and propagation of flame front in lean ch4-air mixture by the three modes of the ignition spark", Proceedings of the 17th Symposium (international) on Combustion, The Combustion Institute, 17, pp. 821-831, 1978.

[16] Maly R.R., Herweg R. "Spark Ignition and Combustion in Four-Stroke Gasoline Engines". In: Arcoumanis C., Kamimoto T. (eds) Flow and Combustion in Reciprocating Engines. Experimental Fluid Mechanics. Springer, Berlin, Heidelberg, 2008

[17] Miles P. C., RempelEwert B. H., Reitz R. D., "Experimental Assessment of Reynolds-Averaged Dissipation Modeling in Engine Flows", SAE-2007-24-0046

[18] Lipatnikov, A.N. and Chomiak, J. "Turbulent Flame Speed and Thickness: Phenomenology, Evaluation, and Application in Multi-Dimensional Simulations", Progress in Energy and Combustion Science, 28, No. 1, pp. 1-73, 2002

[19] Ewald, J. and Peters, N., "On unsteady premixed turbulent burning velocity prediction in internal combustion engines.", Proceedings of the Combustion Institute, 31:3051–3058, 2007.

[20] Stiesch G, Merker GP, "A Simplified Model for Description of Triple Flames in Stratified Charge Gasoline Engines", in: Proc 12th Int. Multidim. Engine Modeling, Users Group Meeting, Detroit, MI, 2002.

[21] Przulj, V., Tiney, N., Shapiro, E., Penning, R. and Shala, M., "The time scale bounded k-e turbulence model and its assessment for automotive applications", Proc. 7th Int. Symp. Turbulence, Heat and Mass Transfer, Palermo, Italy, 2012

[22] Hernández, I., Shapiro, E., Tiney, N., Kotzagianni, M., Kyrtatos, P. and Boulouchos, K., "Flame-wall interaction modelling for pre-chamber combustion in lean burn gas engines", Proceedings of 34th International CAE Conference and Exhibition, 2018, Vicenza, Italy

[23] Schmitt M., Hu, R., Wright, Y. M., Soltic P. and Boulouchos K. "Multiple Cycle LES Simulations of a Direct Injection Methane Engine," Flow, Turbulence and Combustion (95):645–668, 2015

[24] Xu, G., Hanauer, C., Wright, Y., and Boulouchos, K., "CFD-Simulation of Ignition and Combustion in Lean Burn Gas Engines", SAE Technical Paper 2016-01-0800, 2016, doi:10.4271/2016-01-0800

[25] Kammermann T., Kreutner W., Trottmann M., Merotto L., Soltic P., Bleinera D., "Spark-induced breakdown spectroscopy of methane/air and hydrogenenriched methane/air mixtures at engine relevant conditions", Spectrochimica Acta Part B 148, pp. 52–164, 2018

3.2 Towards a Thermally Robust Automotive Pre-Chamber Spark Plug for Turbocharged Direct Injection Gasoline Engines

Peter Janas, Werner Niessner

Abstract

This study presents a first step towards a thermally robust passive pre-chamber spark plug for boosted direct injection gasoline engines, where the pre-chamber spark plug is used to precisely control the start of combustion, increase the engine efficiency, while decreasing pollutant emissions and providing a more stable combustion, compared to conventionally initiated combustion with a j-gap spark plug. The here presented passive pre-chamber spark plug can be integrated into an existing cylinder head design without introducing additional components.

A new passive pre-chamber spark plug is proposed based on a surface discharge electrode configuration, in order to extend the operating range of a previously developed pre-chamber spark plug using a two pin ground electrode configuration. The new passive pre-chamber spark plug is based on a patented surface discharge concept (GB 2 361 264 A), which allowed us to create a barrier-free pre-chamber working volume, to better control the residual gas distribution, turbulence and flame front propagation inside the pre-chamber. The key parameters of the pre-chamber, such as pre-chamber volume and hole diameter were estimated in a first step by using a simple gas displacement model and by 3D heat transfer simulations, using thermal boundary conditions under typical full-load operating conditions. Furthermore, in order to better understand the inner physical phenomena of our passive pre-chamber spark plugs, additional 3D CFD simulations of the turbulent mixing and subsequent combustion were carried out by means of large eddy simulations (LES). The LES simulations only considered the pre-chamber volume and were solely applied for the compression stroke. The influence of the engine was modelled as time depended boundary conditions coming from 0D simulations. Combustion was modelled by a flame surface density approach and ignition initiated by an increase of the flame surface density in a spherical volume in the vicinity of the spark plug. The 3D CFD simulation revealed a strong sensitivity of the residual gas distribution and turbulent flow field to the pre-chamber orifice and inner volume geometry, which influenced the combustion progress inside the pre-chamber significantly. First promising experiments on an engine test bench with the new barrier-free concept were conducted, where the working envelop could have been extended compared to our previously developed two-pin pre-chamber spark plug design.

1   Scope and Motivation

In order to cope with the more stringent emission regulation of today's passenger car vehicles, OEMs have to increase the efficiency, while reducing the pollutant emissions of the already highly sophisticated thermal combustion engines. The window for improvements can only be extended by the introduction of new key technologies. A promising technology for passenger car sized engines is the pre-chamber spark plug, which is in turn not a brand new invention and known for 100 years (US patent 1365143). It never reached the maturity for mass production, except for Honda's CVCC engine [35] in 1975. A review on pre-chamber spark plugs for automotive applications can be found in the work of Alvarez et al [4]. Its reconsideration for automotive application was recently triggered by MAHLE's torch ignition system [28] and by some successfully applied pre-chamber spark plugs for racing engines.
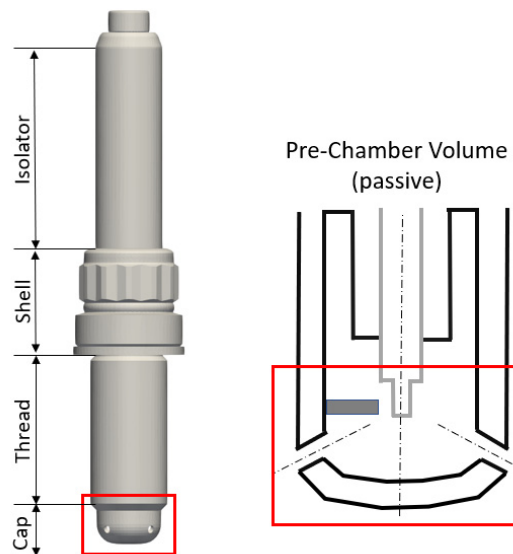
Figure 1: Passive Pre-chamber spark plug (left) and cut through the symmetry plane showing a simplified inner-geometry of the pre-chamber volume, including ground and center electrode (right).

Also very recently in a feasibility study on pre-chamber plugs by Sens et al. [22], emphasis was put on its potential for the future of highly efficient spark ignition engines, where they have operated an in-house developed pre-chamber spark plug system under varies engine operating conditions with promising results on fuel efficiency and the reduction of pollutant emissions.

A pre-chamber spark plug is composed of an ordinary spark plug with electrodes, on which a cap, also known as pre-chamber, is put. An example of a passive pre-chamber spark plug is shown in figure 1. The encapsulated volume represents a second combustion chamber, which is connected to the main chamber by orifices. Different kinds of pre-chamber spark plug systems exist, which can be classified into active [29] and passive systems. The active pre-chamber system is equipped with an additional fuel and/or air injector inside the pre-chamber, which allows to precondition the mixture, whereas a passive pre-chamber realizes its gas exchange solely by the pressure difference between pre- and main-chamber and of course by the local flow field in the vicinity of the orifices. In the scope of completeness, results based on both systems, active and passive, will be discussed in the following, due to similar working principles

and physical phenomena. No clear distinction between passive and active is made for the ongoing discussion in this chapter.

The benefits that a pre-chamber spark plug can deliver are the following:
- Ignition of lean main combustion mixtures → Reduction of NOx emissions by lower overall combustion temperatures.
- Faster combustion progress → Knock mitigation by competing with the auto ignition delay time of the cylinder end gas.
- Reduced turbulence inside engines with a low tumble flow can be compensated by the turbulence created by the flame/hot burned gas jets.
- Diluted mixtures with a high amount of residual gasses can be faster burned → Reduction of the laminar flame speed due to residual gasses are compensated by multiple ignition sources initiated by the hot gas/active radial jet and turbulence produced by the emitted jets.
- Igniting at multiple locations increases the probability of the main combustion chamber charge ignition → Reduction in cycle-to-cycle variations (CCV).
- Shorter flame travel time towards the piston top-land crevice → Reduction in unburnt hydrocarbon emissions (UHC).
- Active control of the turbulence in specific areas inside the main combustion chamber → Complementing technology to Miller/Atkinson cycle.
- Similar performance as HCCI, which lacks of control due to high sensitivity to temperature stratification.

It has to be mentioned that the aforementioned benefits may not be all achieved together for one particular application, hence the design of the pre-chamber will be highly dependent on the motivation of the OEM. Nowadays, pre-chamber spark plugs, active or passive, are successfully used in big bore stationary gas engines. One can easily understand that a bigger engine will have less packaging constraints as a passenger car-sized engine, in first place, and secondly the calibration for a single operating point reduces the design tremendously, compared to high transients, as one can find in modern downsized gasoline engines.

Within this study, we propose a new barrier free passive pre-chamber system for modern gasoline passenger car sized engines and compare it to a previously developed two-pin passive pre-chamber design. Emphasis is put on an efficient development workflow, which should allow to quickly assess many operating conditions and different pre-chamber geometrical parameters. Therefore, 0D simulations, 3D thermal analysis and "pre-chamber-only" CFD simulations by means of large eddy simulations were developed and applied exemplarily for a fictive engine. Finally, first experimental results of our pre-chamber systems are presented.

1.1   State of the art

In the past a lot studies were conducted to find the optimal design parameter of a pre-chamber spark plug. The majority of the literature sees the pre-chamber orifices as a key-parameter, and performed experimental and numerical analysis on the orifice size ([18] [14] [11] [16] [22] [26] [28] [31] [32] [33]), using orifice diameters from 0.8 mm [22] up to 4.5 mm [33]. There is no clear consensus on an orifice diameter, since it depends on many parameters such as the fuel properties, thermodynamic conditions inside the pre- and main chamber, governed by the local flow conditions inside the pre-chamber

during the compression stroke and the jet velocity of the hot burned gas and/or active radical stream towards the main combustion chamber. Most of the studies used methane as fuel ([16] [15] [18] [26] [10] [11] [31] [33]), but also experiments with propane ([12] [14]) ethylene [18], CNG for direct injection [22], gasoline ([21] [22] [28]) and H_2 ([17] [33] [34]) can be found. For example Roethlisberger, R. P. et al. studied numerically [8] and experimentally [9] an unscavenged pre-chamber system inside a modified Liebherr type 926 engine powered with natural gas. They revealed that, on the one hand, by decreasing the orifice diameter, the velocity/turbulence intensity inside the pre-chamber will increase, which can cause misfire by too high flow velocities in the vicinity of the spark gap. On the other hand, they experimentally demonstrated, that not only the flow velocity into the pre-chamber increases, but also the velocity of the flame torch jets coming out of the pre-chamber, leading to an earlier flame arrival at the piston top-land crevice, which reduces the unburnt hydrocarbon emissions (UHC). The orifice diameter is of key importance, because it has to work, literally, in two senses, (a) towards the pre-chamber as an induction device and flow field preconditioner and (b) as an exhaust nozzle, which creates an ignition jet that leads to a multiple ignition source (ideally with low wall contact, to reduce heat losses). Therefore, not only the size of the hole is important, but also its orientation inside the cap, where different orientations have been examined in the literature, such as by Baumgartner et al. [31], who used a 45° and 70° hole orientation relative to the spark plug vertical axis and demonstrated that an orientation towards the top-land crevice region, decreases the UHC emissions.

Another influencing parameter for the inner aerodynamics of the pre-chamber and jet pattern inside the main chamber is the number of orifices. Orifice numbers from one up to eight can be found in the literature ([22] [26] [14] [16] [28] [11] [31] [32]), where it was found that the probability of ignition inside the main chamber increased with the number of orifices, hence ignition locations. The number of holes, however, is limited by the total effective area, which will govern the pressure drop, hence the filling and scavenging of the pre-chamber volume. This leads us to the next important global design parameter of the pre-chamber, which is the volume of the pre-chamber itself. Also here, different volumes have been investigated in the literature. The volume of the pre-chamber is usually given in % relative to the clearance volume of the main chamber volume at top-dead-center (TDC). The values found in the literature range from 1.9% to 3.5%, where the majority use 2% ([12] [28] [21] [22]). Nakazano et al. [3], for example, studied experimentally in 1994 the effect of the volume (2% - 3% of the engine's clearance volume) and orifice diameter of an actively scavenged and water cooled pre-chamber. They discovered that an increase of the pre-chamber volume led to an increase in combustion speed and the NOx emissions. Experiments done by Roethlisberger, R. P. [9] with different pre-chamber volumes showed, that the cycle-to-cycle variations (CCV) decreased by decreasing the pre-chamber volume, but the UHC emissions increased. The reduction of CCV was attributed to smaller turbulence intensities inside the pre-chamber volume and the higher UHC due to shorter flame torches, which will later arrive at the crevice regions.

Another critical dimension is the length of the orifice, which is usually expressed relative to the orifice diameter. This value is, to the best of the authors' knowledge, not so extensively studied, since the orifice channel is experimentally unavailable and by means of CFD extremely difficult to account for (a) the heat transfer, (b) flow restriction by boundary layer development (if any) and (c) flame quenching effects. Akhtar et al.

[16] did not change the length of the orifices, but did study experimentally the influence of the orifice geometry inside a constant volume chamber with optical access. They revealed that slit holes produced a deeper flame torch penetration compared to conventional round holes. They claimed that the slit type orifice produced more turbulence and longer jets.

In order to get a feeling of the interaction of the aforementioned geometrical features of the pre-chamber spark plug (pre-chamber volume, orifice diameter, length and number of orifice) a 0D model was developed by Bardis et al. [24], which allows to calculate the turbulence intensity and length scales during the compression stroke inside the pre-chamber prior to ignition. This approach requires the calibration of many model constants with CFD and experimental data. Obviously, the identification of the model constants will be restricted to a particular engine and pre-chamber design, but once calibrated, it delivers very quickly a global overview about the inner flow and thermodynamic conditions over the entire operating range of the engine, which is in particular very interesting for pre-chamber applications of passenger car sized engines. Also Sens et al. [22] used a 0D model to investigate the boundaries of their pre-chamber design and the importance of the global heat losses during the combustion phase. Another 0D model for the pre-chamber combustion and torch ignition was developed by Kenji et al. [25]. They treated the ejected hot gass as a classical free jet with air entrainment. They compared their model to experimental evidence of a single cylinder gas engine (170 mm bore and 220 mm) and obtained a good qualitative and quantitative agreement.

Also the material of the cap plays an important role, since the cap is projected into the main chamber and exposed from both sides to temperature over 2000 K. For example Sens et al. [22] used steel and copper caps and Yoshitane et al. [11] steel, aluminum and even ceramic. Yoshitane et al. observed that the bulk flow temperature inside the pre-chamber was 100 °C cooler for a pre-chamber made out of aluminum than out of stainless steel over a lambda range of 1.0-1.6. On the one hand, reducing the thermal conductivity of the pre-chamber material increases the gas temperature in the pre-camber volume, but on the other hand, it stabilizes the jets, shortens the early-phase of combustion and extends the lean limit.
Koji et al. [10] studied experimentally the heat range of a passive pre-chamber spark plug with thermocouples inside the pre-chamber cap, ground electrode and center electrode. They measured the hottest temperatures (>800 °C) at the ground electrode, which was based on a Rhodium Iridium alloy. They showed that by retarding the spark timing (from 35°CA bTDC to 18°CA bTDC), the outer cap component temperature decreased from 850°C to 600°C.

In many experimentally studies, hypothesis on the jet dynamics have been made based on the tail end pipe emissions and in-cylinder pressure curve, which is not sufficient. Transparent engines would be perfect means to shed light on the jet dynamics, however, conclusions drawn from them might be biased from the particular engine flow conditions and not generically applicable. The already wide scatter on different compression ratios used for the engine experiments, makes the comparison even more difficult (10:1 [21],14:1 [22], 11.2:1 [10], 9.7:1 [31]). Therefore, research on the outflowing jet dynamics is conducted in rapid compression machines (RCM) in the vast majority of literature ([19] [13] [15] [14] [12]). Due to its easier optical accessibility, Schlieren images and OH* chemiluminescence measurement techniques can be applied,

which can show the morphology of the jet, jet penetration length, and position of active radicals, which is an indication of an actively burning flame front. However, high speed images of the hot jets can also be obtained in real engines, as shown by Sens et al. [22]. Another interesting test vessel and widely used in academia is a constant volume chamber, which allows the application of optical diagnostics, too ([33] [34] [17] [16]). Allison et al [18] even used a complete transparent pre-chamber, having the unique feature to study the flame propagation inside the pre-chamber. Using the aforementioned devices allowed them to make more fundamental studies on the flame torch species concentration ([21] [17]), the jet velocity coming out of the pre-chamber ([21], [18] [26] [17]), vorticity in the main chamber [17] and jet-to-jet interaction [34]. A strong correlation of the ignition position inside the pre-chamber to the jet penetration could be found by many authors ([18] [14] [22] [10] [11] [33] [34]), saying spark location has a deterministic effect on the jet penetration length and strength. For example Thelen et al. [14] studied the spark location inside the pre-chamber in regards to the flame torch development, where the furthest possible position away from the orifices yielded the strongest jet into the main chamber, hence the best combustion performance. The slowest onset of pre-chamber combustion was observed while igniting in the middle of the pre-chamber. The highest amount of cold unburnt mixture is ejected for the spark locations the furthest away from the orifices. The slowest onset of combustion inside the main chamber was observed for the case, where combustion was triggered close to the orifices.

During the last years the picture of the jet shape, structure and its sensitivity to the global pre-chamber parameters became more complete. It is now understood that depending on the spark location and orifice diameter the content of the ejected jet out of the pre-chamber will change. In the beginning of the ejection phase, residual gases lying ahead of the flame front will be expelled, followed by the flame front, which (a) can be quenched depending on the orifice diameter or (b) passing through. Hereby, two different ignition mechanisms are identified by Bisawis et al. [33], depending whether the flame is quenched or not. Bisawis et al. [33] proposed a global Damköhler number to distinguish jet and flame ignition and introduced a critical limit, under which ignition inside the main chamber was not possible anymore. In an extension to this work, Bisawis et al. [17] studied the ignition mechanism inside the main chamber with different orifice geometries. By introducing a Laval nozzle type orifice, they were able to introduce jets with higher overall temperature, but also higher velocities along the jet axis. They revealed that a high temperature is not sufficient to initiate combustion in the main chamber, but also a not too high turbulent jet intensity.

2   Pre-Chamber concepts

Within this work two different pre-chamber concepts are tested; a concept which uses two pins as ground electrode and one which is based on a surface discharge working principle. The two pin electrode pre-chamber spark plug will be denoted for the sake of simplicity as "2Pin" and the surface discharge spark plug as "SD". Figure 2 shows a sketch of the two concepts, where for the SD concept, two different hole orientations are considered.
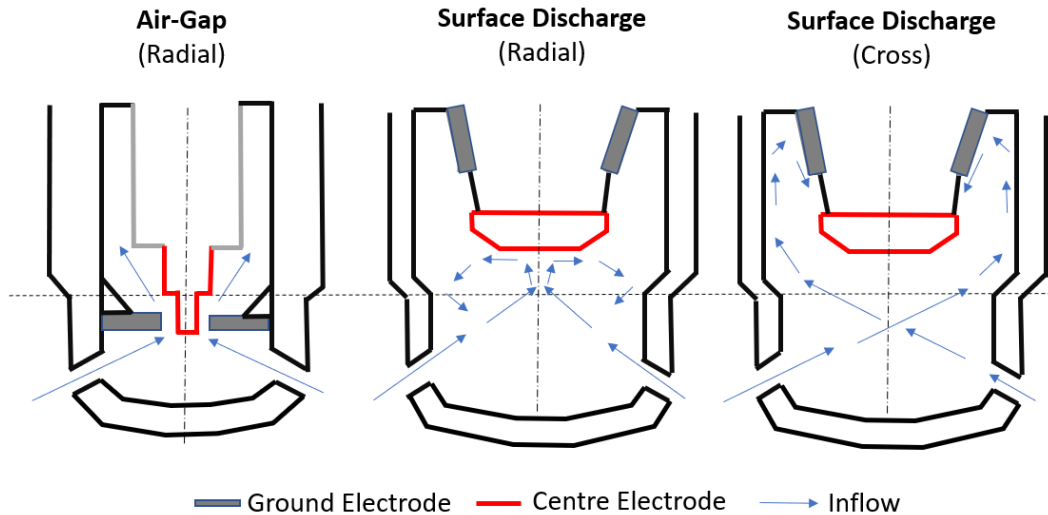
Figure 2: Sketch of the pre-chamber spark plug with 2Pin ground electrode (left) and of the pre-chamber spark plug with the surface discharge electrode configuration with radial orifices (middle) and radial-tangential orifices (right).

The 2Pin and SD pre-chamber spark plugs have very similar pre-chamber volumes and differ mainly in the spark location. The 2Pin electrode version (Figure 2, left picture) has two spark locations, which are positioned close to the orifices, where the SD version has four different spark location in the circumferential region of the insulator. The spark discharge will not happen in the air-gap, as for the 2Pin plug, but literally slide on the surface of the insulator from the center electrode to the ground electrode. As a discharge over a surface requires lower voltage, a longer spark becomes possible.

The reasons for using a surface discharge ignition concept are as follows:
- Combustion chamber was desired without any obstacles to the flow, in order to better control the inner aerodynamics.
- Reduction of the overall thermal behavior of the bulk flow and surface temperatures.
- Spark location, which is at the upper position inside the pre-chamber (away from the orifices), which should be beneficial for the flame propagation and sub-sequential pressure build-up in the pre-chamber (see discussion chapter 1.1).
- Better mixing of the residual gases in the core nose region.
- All has to fit in a conventional M12 spark plug.

As mentioned above in the literature review, typical pre-chamber volumes are in the range of 1.9%-3.5% of the engine clearance volume. Since, one of the pre-chamber target is to exploit higher compression ratios (assumed 14:1) it was started with a rather small pre-chamber volume V_{pc}/V_{clear} of roughly 1.3% compared to the literature. It has to be stressed that none of the literature (to the best of the authors' knowledge) provides a generic explanation of the "right" volume, they only show trends derived from a baseline volume. It was also not the intention of the authors' to optimize the breakdown voltage demand at this state.

The pre-chamber volume is fixed and its influence only discussed based on 0D simulations. Table 1 summarizes the main differences of the two concepts.

Table 1: Specification of the two pre-chamber spark plug concepts for the 0D simulation. For the engine tests, the hole diameter in parenthesis are applied.

	2Pin	**SD – Radial**	**SD - Cross**
Volume	375 mm³	399 mm³	399 mm³
Spark location	2 sparks location within cap volume	4 spark locations at core nose region	4 spark locations at core nose region
# holes	4	4	4
Ø holes [mm]	1.0 (1.2)	1.2 (1.0)	1.0 (1.0)
Orientation	Radial	Radial	Radial-Tangential
Cap material	Nickel alloy	Nickel alloy	Nickel alloy

3   Numerical investigation

In order to access the performance of the inflow conditions during a wide range of operating conditions, simple 0D simulations are performed within the compression stroke for two different engine configurations. In a next step, the thermal behavior is investigated based on a typical full load operation and the flow inside the pre-chamber by means of large eddy simulation during the compression stroke studied. The flow fields are then used to initialize the combustion simulations.
The individual development steps are now discussed in detail.

3.1   0D analysis

Inspired by the work of Bardis et al. [24], a 0D model is developed, which describes the flow and thermodynamic properties inside an un-scavenged pre-chamber during the compression stroke. The pre-chamber and cylinder volume are treated as two separated open systems, which are communicating via an orifice. The mass, which is transported out from one volume is equal to the mass, which is flowing in the other, hence the total mass of the system must be constant. (Neglecting for the moment the gas exchange phase – Intake and Exhaust stroke). The subscript Pc denotes pre-chamber and Mc main-chamber.
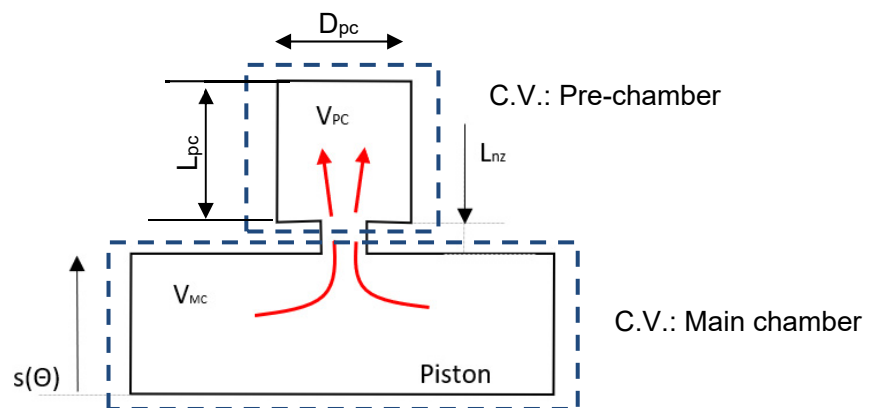

Figure 3: Pre-chamber and main-chamber system illustration for the 0D model.

Figure 3 shows a sketch of the two control volumes (C.V.) For the sake of completeness the governing equations (1-4) will be shown, which read in differential form:

$$m_{\mathrm{MC}}\, c_{v,\mathrm{MC}}\, \frac{\partial T_{\mathrm{MC}}}{\partial t} = \frac{\partial Q_{\mathrm{MC}}}{\partial t} - p_{\mathrm{MC}} \frac{\partial V_{\mathrm{MC}}}{\partial t} - \frac{\partial m_{\mathrm{MC}}}{\partial t}(h_{out} - e_{in}) \tag{1}$$

$$p_{\mathrm{MC}} \frac{\partial V_{\mathrm{MC}}}{\partial t} + V_{\mathrm{MC}} \frac{\partial p_{\mathrm{MC}}}{\partial t} = m_{\mathrm{MC}}\, R\, \frac{\partial T_{\mathrm{MC}}}{\partial t} - T_{\mathrm{MC}}\, R\, \frac{\partial m_{\mathrm{MC}}}{\partial t} \tag{2}$$

$$m_{\mathrm{PC}}\, c_{v,\mathrm{PC}}\, \frac{\partial T_{\mathrm{PC}}}{\partial t} = \frac{\partial Q_{\mathrm{PC}}}{\partial t} + \frac{\partial m_{\mathrm{PC}}}{\partial t}(h_{out} - e_{in}) \tag{3}$$

$$p_{\mathrm{PC}} \frac{\partial V_{\mathrm{PC}}}{\partial t} + V_{\mathrm{PC}} \frac{\partial p_{\mathrm{PC}}}{\partial t} = m_{\mathrm{PC}}\, R\, \frac{\partial T_{\mathrm{PC}}}{\partial t} + T_{\mathrm{PC}}\, R\, \frac{\partial m_{\mathrm{PC}}}{\partial t} \tag{4}$$

In the governing equations (1-4), p denotes the pressure, T the temperature, m the mass, c_v the specific enthalpy under constant volume, R the universal gas constant, h the enthalpy, e the internal energy and Q the heat losses.

The heat transfer coefficients for the convective heat losses inside the pre-chamber are modelled by the Bargende correlation [45] and inside the engine with the Woschni correlation [46]. A simplified model for the turbulent kinetic energy k, which takes into account the generation of turbulence created by the incoming jet, is used. A detailed description can be found in the work by Bardis et al. [24] and Hiraoka et al. [44]. The here used turbulence model reads:

$$\frac{\partial (m_{\mathrm{PC}}k)}{\partial t} = \left(\eta_{jet} \dot{m}_{\mathrm{Pc}} \frac{u_{jet}^2}{2} \right)_{P_{jet}} - \left(m_{\mathrm{Pc}} \frac{(2k/3)^{3/2}}{l_I} \right)_{P_{diss}} \tag{5}$$

With u_{jet} being the incoming jet velocity, η_{jet} describing the fraction of how much turbulence is produced by the jet (assumed 0.5 % of the kinetic energy is converted into turbulence) and l_I the integral length scales according to Hiraoka et al. [44].

3.1.1 Assumptions and boundary conditions

Two fictive engines are used for the 0D analysis to investigate the influence of the global pre-chamber parameters. The two engine configurations only differ in the compression ratio, where engine 1 exhibits a compression ratio of 10:1 and engine 2, a compression ratio of 14:1. A detailed description of the engine configuration and the corresponding pre-chamber set-up is shown in table 2.

Table 2: Specification of two fictive engines used for the 0D simulations and operating conditions.

	Engine 1	Engine 2
Bore [m]	0.07	0.07
Stroke [m]	0.09	0.09
Conrod length [m]	0.13	0.13
Compression ratio [-]	10:1	14:1
PC-Volume [mm³]	395	395
V$_{pc}$/V$_{clear}$ [%]	1.0	1.4
No. Holes	4	4
Ø Holes [mm]	1	1
Engine Speed [rpm]	1500/3500/6500	1500/3500/6500
In-cylinder pressure at BDC [bar]	1.0	1.0
PC Wall temperature [K]	600	600

An in-cylinder pressure of 1 bar is chosen as initial condition for the 0D simulation and an in-cylinder temperature of 300 K at BDC. The same initial conditions are used for the pre-chamber. The pre-chamber wall temperature is assumed to be 600 K. Three different engine speeds are considered: low (1500 rpm), medium (3500 rpm) and high (6500 rpm) engine speed. Standard model constants from the literature are used for all models and no calibration of the model constants carried out. Three consecutive compression and expansion strokes are calculated to ensure a statistically converged solution.

A sensitivity analysis of the model constants and its calibration is not intendent in first place, rather to observe first qualitative trends. However, a recalibration of the model can be considered, once the pre-chamber design has been fixed and 3D CFD simulation and experimental data are available.

3.1.2 Results 0D: Influence of the compression ratio

Figure 4 shows 0D simulation results of the pre-chamber within the compression stroke for the two engines presented in table 2 and comprises (a) the pressure difference between pre- and main-chamber, (b) the inflow velocity into the pre-chamber, (c) the pre-chamber temperature, and (d) the turbulent kinetic energy (TKE) inside the pre-chamber. The results of engine 2 (CR 14:1) are presented with thin lines and symbols and the results of engine 1 (CR 10:1) with thick bold lines. The different engine speeds are illustrated by different colors.
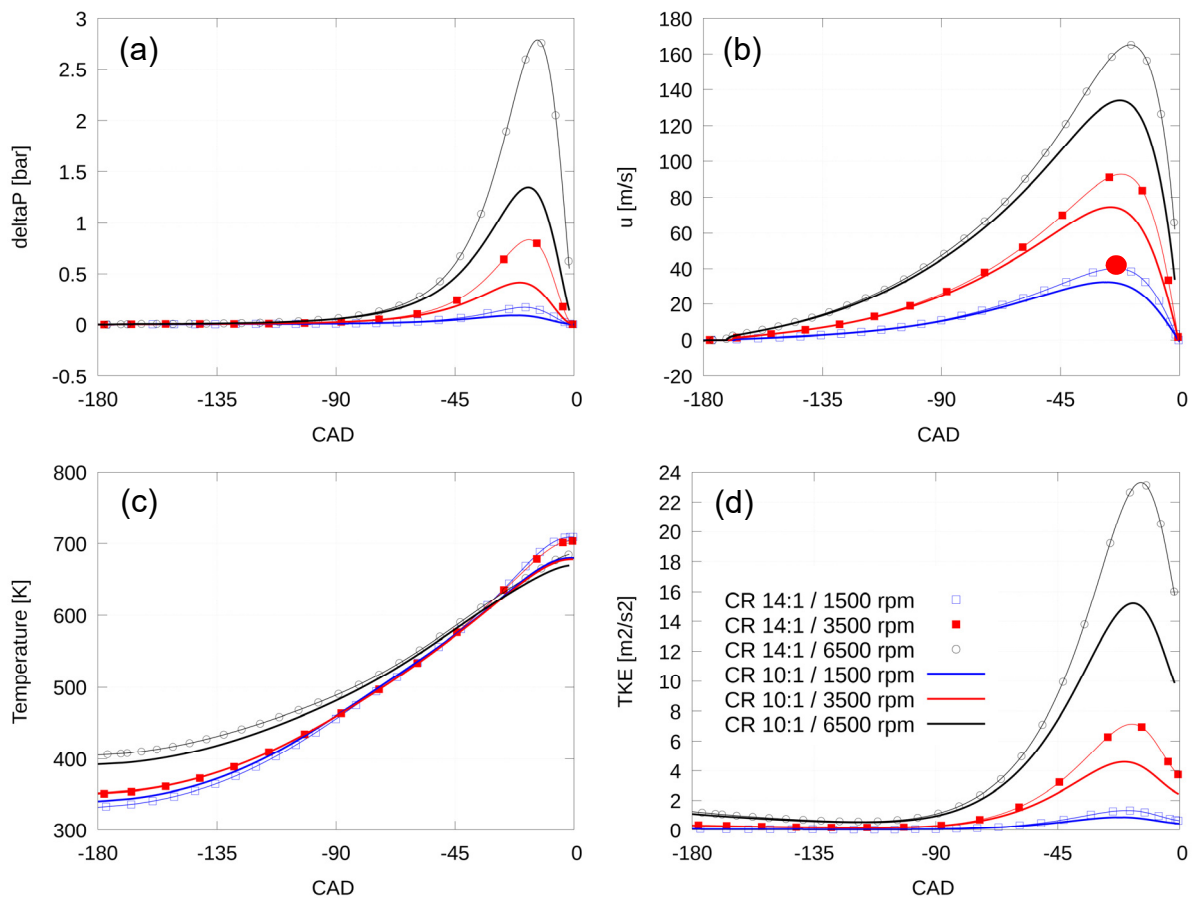

Figure 4: 0D results for a fictive engine with 10:1 and 14:1 compression ratio. Red dot shows example for max. velocity taken for study in figure 5.

It is observed, that with higher compression ratio, also a higher pressure difference between main- and pre-chamber is obtained. The same holds true for the engine speed, where an increase of the engine speed also leads to a higher pressure difference, where its peak value is roughly at 20°bTDC for all simulated points. The pressure difference is the main driving force for the flow, hence it will govern the flow direction and its magnitude. Also here, the flow velocity gradually rises and peaks at ~20°bTDC, from where it decreases to 0 m/s at TDC. The same trend is found for the turbulent kinetic energy, because the inflow jet is assumed to be the main turbulence generator. The function of the turbulence is obviously to enhance the combustion progress inside the pre-chamber, however, it influences also the heat transfer, which manifests in a cooler gas temperature at the end of compression, as seen for the cases with 6500 rpm.

So far, the 0D study is only valid for one particular pre-chamber design, which must not necessarily be the (local or global) optimum. The 0D tool is well suited to perform parametric studies with different pre-chamber geometrical details, such as volume and orifice diameter. A parametric study for different orifice diameters and pre-chamber volumes (constant inner surface) is conducted for the low rpm point (1500 rpm at CR:14:1), which is seen to be a critical operating point, due to the lower inflow velocities and overall hotter bulk gas temperature. Figure 5 shows the maximum inflow velocity and bulk gas temperature for different pre-chamber volumes and orifice diameter. The red dot denotes the pre-chamber configuration of the 0D study presented in figure 4 at 1500 rpm (blue thin line). Increasing the diameter and keeping the pre-chamber volume fixed leads to lower flow velocities, which comes along with a reduction of the convective heat transfer coefficient, hence lowering the heat flux through the wall. The scenario with a fixed pre-chamber volume and a variation of the orifice diameter is highlighted with white arrows. The effect of a different pre-chamber volume is annotated by the orange arrow. Here, for small orifice diameter, an increase of the pre-chamber volume yields an increase of the gas temperature, where for orifices bigger than 1.4 mm the bulk temperature decreases with increasing volume (reversed trend).
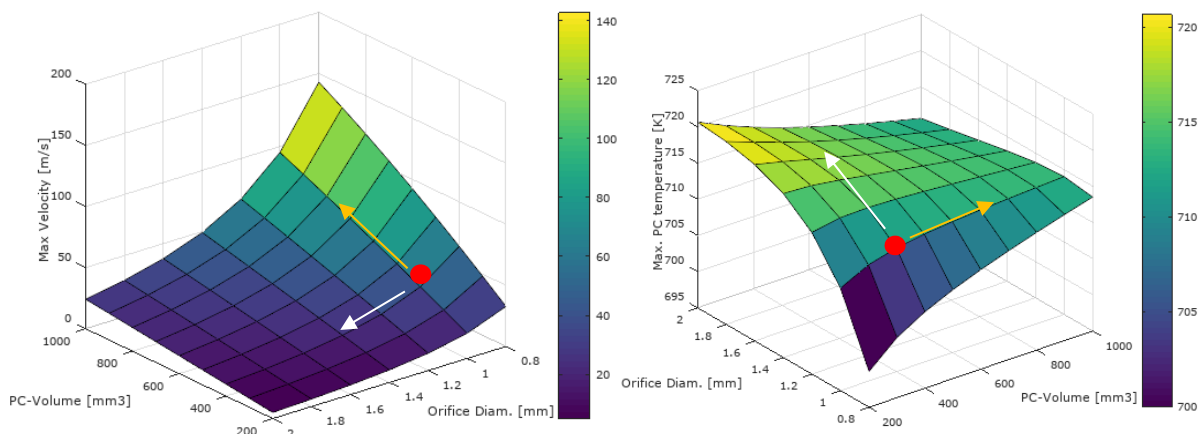
Figure 5: Max. velocity (left) and max. temperature (right) for different pre-chamber volumes and orifice diameters at 1500 rpm and 1 bar operating point for an engine with CR 14:1 during the compression stroke. Constant inner surface 0.0005 m².

Based on this picture, one can draw conclusions about the global thermodynamic conditions at ignition timing. Knowing globally the thermodynamic and turbulent flow con-

ditions may help to estimate the combustion progress, however, it will not allow to predict the ignitability of the pre-chamber charge, which is highly dependent on the local flow conditions in the vicinity of the spark plug. Here, 3D CFD simulations can be used to better understand the likelihood of ignition and the flame propagation path. 3D simulation can also be used to calculate the component temperature, which is up to now a global parameter and will be discussed in the next subchapter.

3.2   Thermal investigation

Due to the complex shape of the inner volume, leading to locally different turbulent flow conditions, the heat transfer inside the pre-chamber is far too complicated to be easily calculated with a 0D model without thorough calibration.

3.2.1 Assumptions and boundary conditions

In order to have a better representation of the component temperature, 3D thermal simulations are performed under typical high load operating conditions. A convection boundary condition at an average gas temperature of 1200°C is applied on all walls and the influence of radiation taken into account.

3.2.2 Thermal results

Figure 7 shows the component temperature of the 2Pin and surface discharge spark plug. For the 2Pin spark plug, the hottest temperatures are found at the edge of the insulator and center electrode. The surface discharge spark-plug is overall cooler than the two-pin design. The insulator and center electrode are around 200 K and the cap temperature 90 K lower than the 2Pin design.
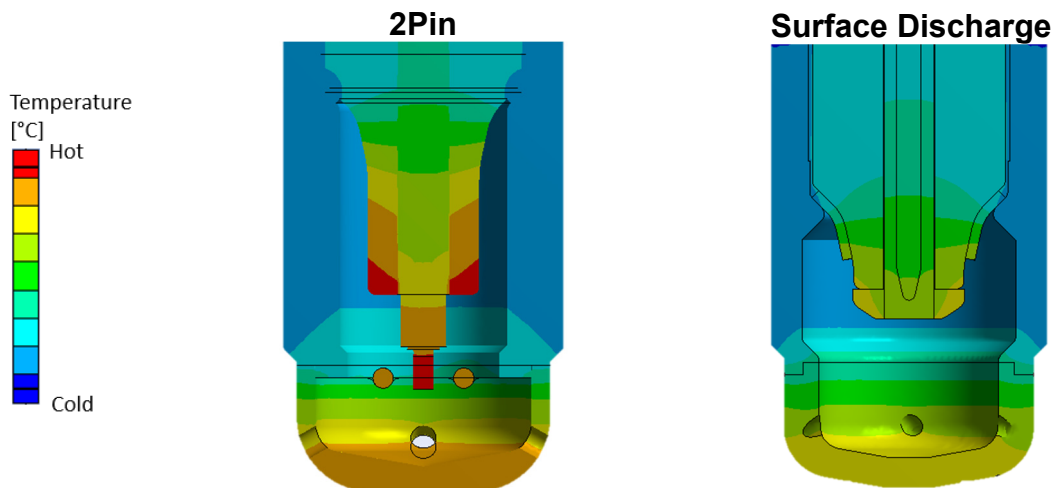

Figure 7: Thermal simulation results of the component temperature of the 2Pin (left) and surface discharge spark plug (right).

In the next step the aerodynamic performance, which will govern the residual gas distribution and combustion is assessed.

3.3   Cold flow analysis

Among the literature most of the numerical investigations are based on the RANS (Reynolds Average Navier-Stokes) approach, which gives an ensemble average of the flow field and completely relies on turbulence closure models, such as the two equation k-epsilon turbulence model. The RANS simulation approach can yield results within a few days, covering the complete engine cycle, including the gas exchange phase, spray formation, mixture preparation and pre- and main chamber combustion. These methods, however, require a tremendous effort in the tuning of varies model constants. A less model dependent approach, which can also predict the unsteadiness of the flow correctly, is the large eddy simulation (LES). Pre-chamber simulations using LES can be found in recent works of Allison et al. [18] and Gholamisheeri et al. [15]. Both LES simulations are not performed for an engine, where Allison et al. [18] studied the pre-chamber combustion inside a constant vessel and Gholamisheeri et al. [15] inside a rapid compression machine. Gholamisheeri et al. compared RANS and LES to chemiluminescence images of the outflowing hot jet, where they obtained a better agreement with LES. Unlike the RANS approach, LES is based on a spatial filtering technique, where the biggest scales, up to the size of the computational grid (cut-off length), are directly resolved. Only flow structures, which are smaller than the cut-off length, have to be modelled, where smaller scales are easier to model due to their isotropic character. LES requires high quality grids, accurate high-order numerical discretization schemes and relative small time steps (ideally, CFL < 1), which make the simulation computationally more demanding compared to RANS. Furthermore, in order to calculate turbulence depending properties, mean and fluctuating values need to be calculated from a sufficient large number of statistical points. Within an engine this becomes even more complicated, because the computational domain is changing with time, which requires a phase-locked averaging method.

3.3.1 Assumptions and boundary conditions

In order to benefit from the accuracy of the LES approach, while bearing in mind the higher computational effort and numerical accuracy compared to RANS, only the pre-chamber will be considered. Pressure and temperature boundary conditions are derived from the 0D analysis of fictive engine 2 (see section 3.1.2) and directly imposed on the orifice entrance surface. It has to be mentioned that the development of the turbulent flow field is not discussed within this work nor velocity fields are shown. The flow development inside the pre-chamber is seen as a crucial parameter for the working principle in regards of different engine speeds.

The following assumptions are made for the cold flow analysis:
- Pressure and temperature boundary conditions are taken from 0D modelling (Engine 2, CR 14:1) for 1500 rpm and 6500 rpm at 1 bar pressure at start of compression.
- Turbulence is mainly generated by in-coming flow through the small orifices (assumed that turbulent length scales inside the engine are bigger than the orifice) → No turbulence inlet generator used.
- All walls have a fixed temperature of 600 K
- Pre-chamber is filled with 100% burnt gas of stoichiometric gasoline combustion at the start of the simulation.
- Fresh mixture without residual burnt gasses is flowing into the pre-chamber.
- Only one compression stroke will be simulated (no mean values calculated).

The Favre-filtered governing equation for mass, momentum and energy are solved using the finite volume method (FVM) with the open source software OpenFOAM [39], [40], [41]. The time is discretized by an implicit second order backward Euler scheme. The convective scalar-fluxes are discretized with a total variation diminishing scheme (TVD) using the Sweby limiter, where the convective fluxes of the momentum equation are calculated by a central differencing scheme (CDS). The compressibility of the flow is taken into consideration by a pressure-velocity-density approach proposed by Demirdžic [36] and a compressible version of the standard Smagorinsky model is used for the turbulent sub-grid scales fluxes [37] [38].
The computational grids are based on equidistant cubic cells with a cell size of 0.1 mm leading to 0.39 million cells for the SD- and 0.37 million for the 2Pin pre-chamber spark plug.

3.3.2 Results: Pre-chamber gas temperature

The three different variants, shown in table 1, are simulated at low and high engine speed conditions. Figure 9 shows the LES simulation results of the volumetric aver-aged bulk gas temperature inside the pre-chamber during the last 45°CA of the com-pression stroke. For all three variants the high engine speed cases (6500 rpm) result in a higher peak pre-chamber temperature compared to the 1500 rpm cases.
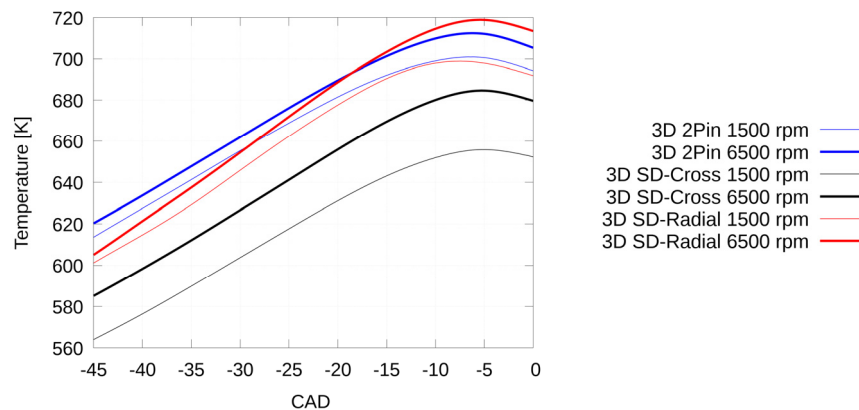
Figure 8: 3D LES results of the bulk gas temperature for the 2Pin-Radial, SD-Radial and SD-Cross variants during the compression stroke.

The highest overall temperature is obtained for the SD-Radial (4 x 1.2mm orifices) variant with a peak temperature of 720 K and about 710 K for the 2Pin-Radial (4 x 1 mm) variant. A reduction of the peak temperature by 40 K is achieved with the SD-Cross variant, which is attributed to the rather swirly flow conditions, with higher veloc-ities at the pre-chamber walls. It is evident that the temperature of the bulk flow is highly influenced by the aerodynamic performance, which is governed by the orifice diameter, pre-chamber volume and orifice angle.

3.3.3 Results: Residual gas distribution

Since the window for flushing out the residual burnt gases after combustion is very small (mainly during the expansion phase) some residual gasses will always remain inside the pre-chamber. It is of paramount importance to deliver at the spark location an ignitable mixture and to transport the residual gasses away from it.
Figure 9 shows contour plots of the residual gas mass fraction at 20°bTDC for the 2Pin-Radial, SD-Radial and SD-Cross variants at 1500 rpm and 6500 rpm in a cut through

the vertical center plane (SD-Cross uses a different cutting face). A very low residual gas mass fraction is obtained (<5%) for the 2Pin-Radial variant at the electrode gap, from where the fresh gas is redirected towards the core nose region. For the SD-Radial variant, however, spots of 30 % residual gas mass fraction appear in the core nose region close to the ignition region for the 1500 rpm operating point. Due to the radial orientation of the 4 orifices, the 4 jets impinge at the insulator tip and form a recirculation zone, which hinders the fresh gasses reaching the spark location. Fortunately, for higher engine speeds, the unsteadiness of the impingement of the 4 radial jets (not shown here) allow the flow to reach the core nose region occasionally, yielding to a lower residual gas mass fraction. The SD-Cross variant has for 1500 rpm and 6500 rpm a low residual gas fraction in the vicinity of the 4 spark locations, since the jets are directly streaming towards the core nose zone and creating there a swirl motion.
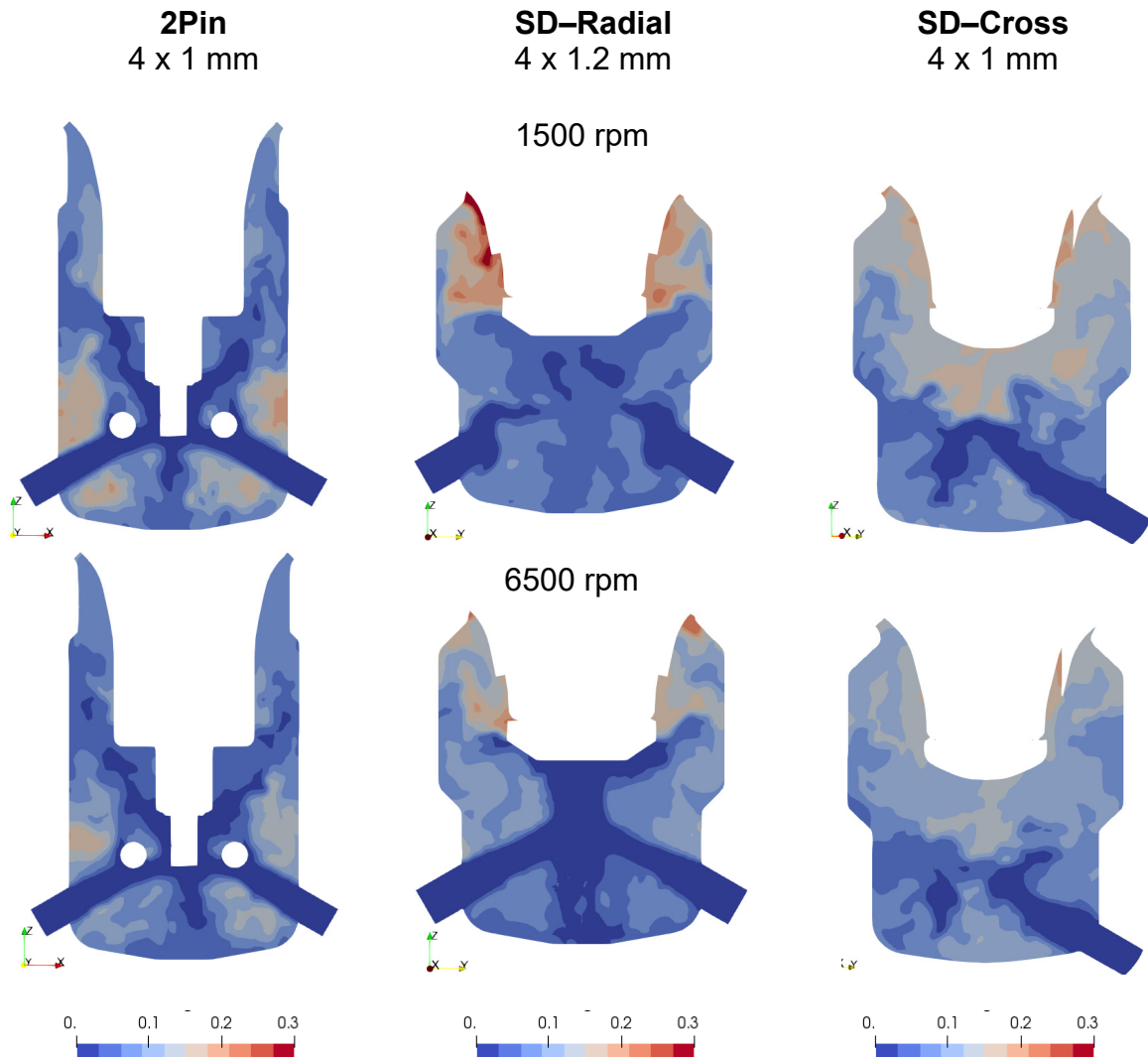
Figure 9: Residual gas distribution in a cut through the symmetry plane at 20°bTDC at 1500 rpm and at 6500 rpm for the 2Pin-Radial (left), SD-Radial (middle) and SD-Cross (right) variant. SD-Cross variant uses a different cutting face.

For a better visualization of the residual gas distribution at 20°bTDC, figure 10 shows only cells with a residual gas fraction higher than 20% in a 3D transparent version of the corresponding pre-chamber variants.
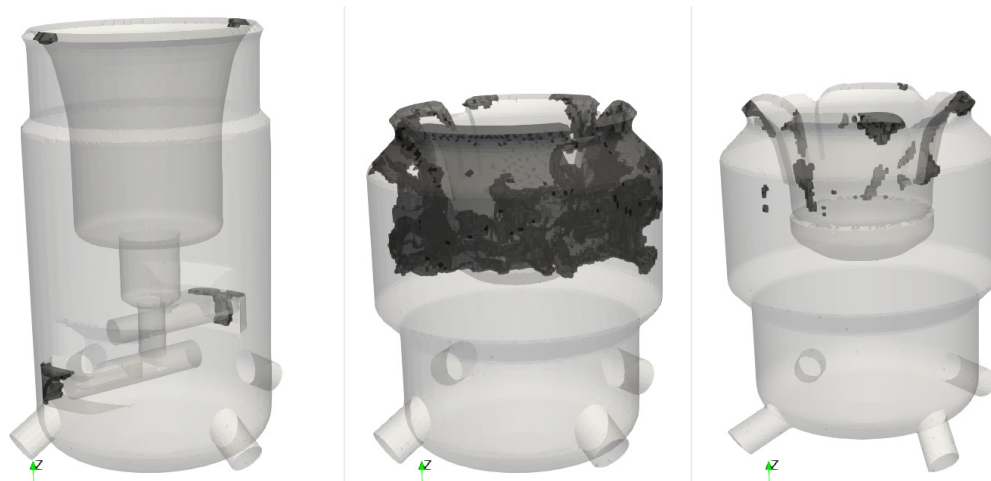
Figure 10: Residual gas distribution in a cut through the symmetry plane at 20°bTDC for 1500 rpm showing only region with a residual gas fraction higher than 20%.

3.4   Pre-chamber combustion

Different modelling approaches can be found to describe pre-chamber combustion and ignition in the literature. For example Chinnathambi et al. [21], Thelen et al. [14] and Gholamisheeri et al. [15] used a well stirred reactor based model and coupled it with a skeletal reaction mechanism, emphasizing on the importance of the chemistry for the "jet ignition" inside the main combustion chamber. Turbulence chemistry interaction is not taken into account and only the mean quantities are taken. Ignition is triggered by increasing the energy inside a spherical volume in-between the spark plug gap. Bisawis et al. [17] used a similar approach, where a detailed chemistry model was used (9 species and 21 reactions,) but the turbulence-chemistry interaction taken into account by the eddy dissipation concept (EDC). Kotzagianni et al. [19] used the G-equation to describe the flame front propagation, where the thermodynamic properties for the burnt mixture were obtained from a chemical equilibrium assumption. The laminar flame velocity was calculated by the Gülder formulation [42] and the turbulent flame velocity by the Damköhler closure. They have tracked the flame propagation of the pre-chamber in the Borghi-Peters diagram, where it fell in the thin reaction zone regime. Allison et al. [18] used an LES flame surface density (FSD) approach, where the flame wrinkling is described by an algebraic expression proposed by Weller [43].

According to a non-dimensional estimation of the Damköhler-number (Da>1), we assume that the flame can be put into the thin reaction region (according to the Peters-Borghi diagram), where the flame propagation is rather dominated by the turbulent flow. Here, the reaction layer is thin and the reaction time fast. Similar findings have made Kotzagianni et al. [19]. Therefore, we neglect the details of the chemistry for an investigation of the flame propagation inside the pre-chamber. However, it has to be mentioned that this assumptions may not be true outside of the pre-chamber and in the orifices region, thinking about quenching and later the reignition process of the main combustion chamber charge.

3.4.1 Assumptions and boundary conditions

In order to keep the complexity of the modelling as low as possible, it was decided against a detailed chemistry driven combustion model and focused on the flame turbulence interaction. The influence of a later ignition of the main chamber charge and the corresponding pressure rise at the inlet/outlet of the pre-chamber will also not be considered. Our assumptions and boundary conditions for the combustion simulations are the following:

- The simulation will be initialized with the fields of the cold flow simulations at 20°bTDC.
- The pressure and temperature boundary conditions are taken from the 0D modelling of engine 2.
- Ignition will be triggered at 20°bTDC by an increase of the source term of the progress variable for a duration of 2 °CA inside a spherical volume with a diameter of 0.4 mm → No physical ignition model.
- Laminar flame velocity calculated by the Gülder formula [42].
- The flame front propagation will be calculated by a flame surface density model, using the Weller algebraic flame wrinkling model [43].
- The wall temperature is fixed at 600 K.
- A fuel mass fraction of 0.062 is assumed (lambda 1) diluted with an initial residual gas distribution given by the previous cold flow analysis.

3.4.2 Results: Pre-Chamber Combustion

Figure 11 (a) shows the combustion progress inside the pre-chamber for all three variants at 1500 rpm and 6500 rpm. For the low engine speed operating condition, the mixture of the 2Pin-Radial variant is almost completely burned (~90 %) in less than 3°CA, followed by the SD-Radial variant with twice of the time (6°CA). The slowest pre-chamber combustion at 1500 rpm is obtained with the SD-Cross variant with a duration of 10°CA to reach a combustion progress of ~90%. Since the 2Pin-radial variant uses an air gap discharge concept, the spherical flame kernel is less constrained by walls and can easier expand. Furthermore, the inflowing jet of the 2Pin-Radial variant is directly pointing towards the spark position, which literally pushes the kernel away from the narrow electrode region, where it has more space to expand. For the SD-Radial variant the flame kernel needs more time to develop, because the ignition is triggered close to the insulator surface. Here, the flame kernel is completely constraint from one side and only little flow velocities available for supporting a faster flame kernel growth.

For the SD-Cross variant, the flame kernel starts growing at a similar °CA as for the SD-Radial variant for 1500 rpm, but then the flame starts propagating slower until it reaches the 45% combustion progress point. Beyond the 45% combustion progress point, the combustion speed inside the SD-Cross variant is very similar to the other 2 variants at 1500 rpm. The reason for the slower onset of combustion for the SD-Cross variant can be explained by the cross-jets itself (schematically shown in figure 2), which are forcing the flame to propagate down the core nose wall towards the center of the pre-chamber volume.
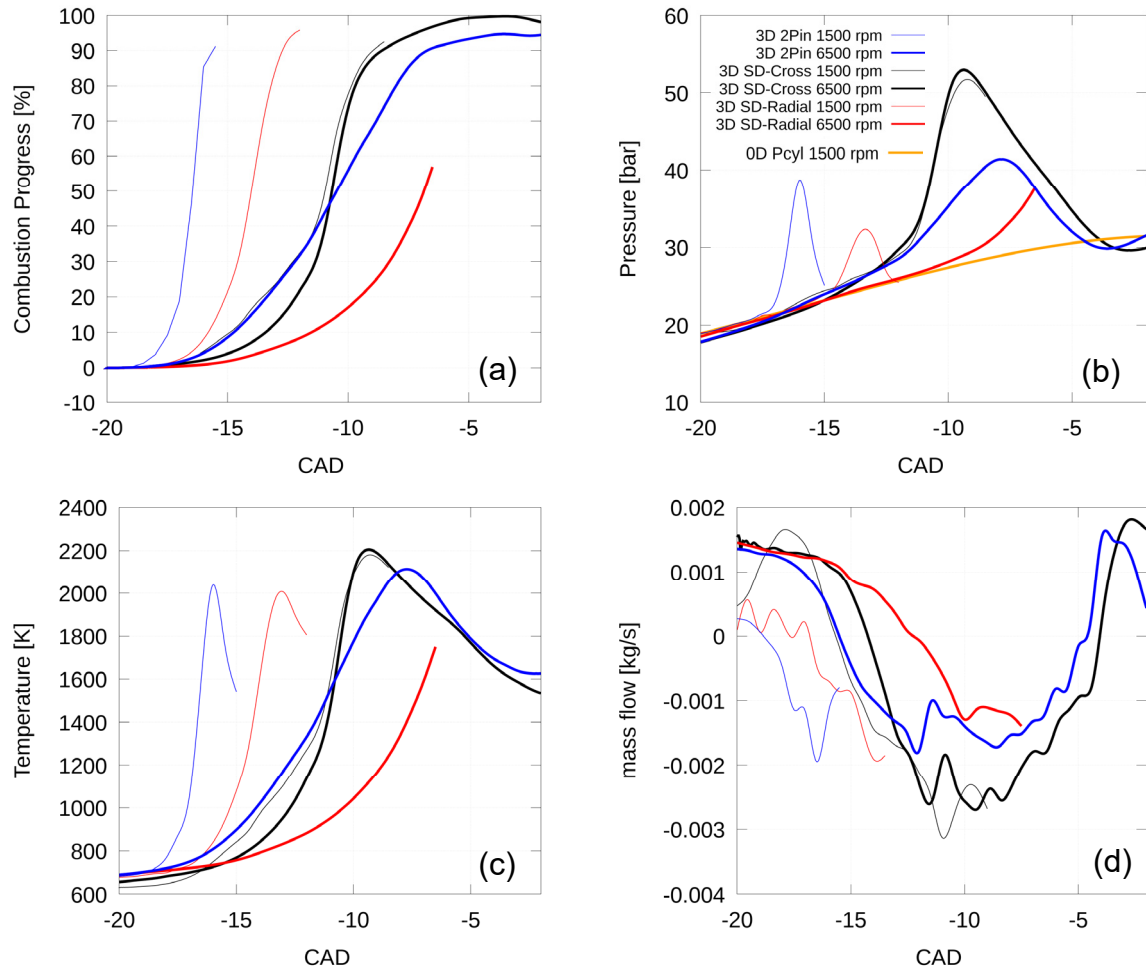
Figure 11: LES Results: Combustion progress inside the pre-chamber (a) (open system), pre-chamber pressure (b), temperature (c) and mass flow (d) for one orifice of the 2Pin-Radial, SD-Radial and SD-Cross Variant for engine 2 at 6500 rpm and 1500 rpm.

The same effect of the flow-driven flame along the core nose region is obtained for the SD-Cross variant at 6500 rpm, where the higher engine speed, hence higher flow velocities inside the pre-chamber, supports a faster transport of the flame to the center, where (a) the flame has a lot of space to propagate in all direction and (b) a highly turbulent flow field is present, due to high shear stresses generated by the "crossing jets". The 2Pin-Radial variant has a rather smooth combustion progress gradient at 6500 rpm, but it has again the shortest ignition delay time (time to reach 10% combustion progress) among all three variants, which can be attributed to the air-gap electrode configuration. Surprisingly, the SD-Radial variant has the slowest combustion progress for the high rpm point. Here, the flame is literally entrained by the big vortices (see schematic of the flow in figure 2) and cannot easily reach the center of the pre-chamber volume. The discussed flame travel paths are illustrated in figure 12, which shows the iso-contour surface of the progress variable for all three variants. The yellow surface presents the 6500 rpm cases and the red surface the 1500 rpm cases. Since we are showing the history of the flame travel path in °CA and not physical time per second, only one flame front scenario for the 1500 rpm case is presented at 15.5°bTDC.

The trend of the combustion progresses manifests also in the pressure curve traces for all three variants for both engine rpm conditions, where the peak pressures are obtained at the moment where roughly 80 % to 90 % of the mixture is consumed. The highest pressure is build up for the SD-Cross variant for both operating conditions. The smallest peak pressure is obtained for the SD-Radial variant, which has also the biggest holes among the three variants. Even though, no engine is present in our study, trends on the performance of the ignition of the main chamber charge can be constructed based on the mass flow rates (figure 11,d) and temperature profiles (figure 11,c). All of the three variants will have a different outflowing jet characteristic, where the biggest difference is found in the duration of the mass ejection and its temperature.

2Pin-Radial

SD-Radial

SD-Cross

| -17.5 °CA | -15.5 °CA | -12.5 °CA | -10 °CA |

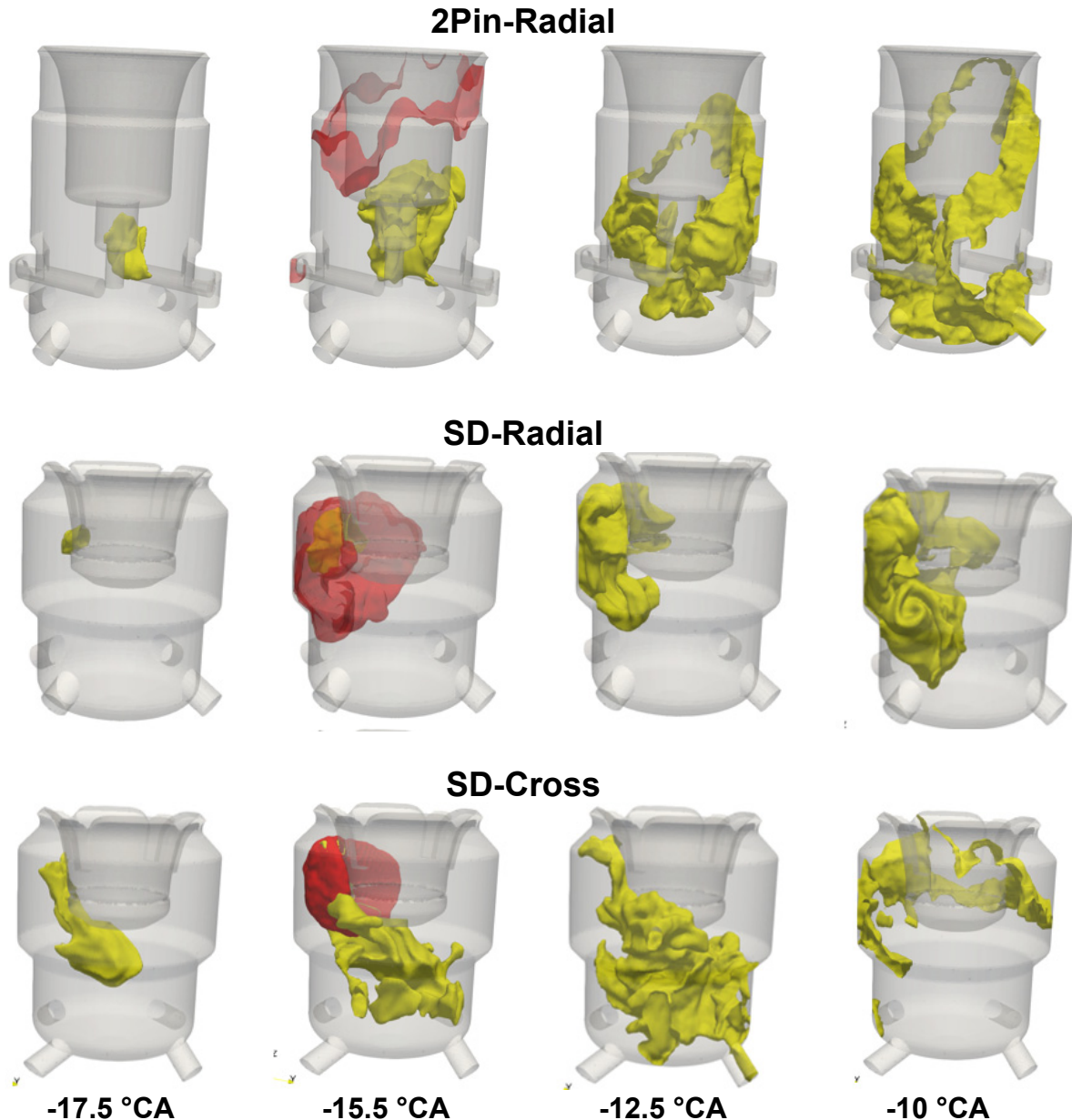

Figure 12: Iso-contour of the progress variable ($\tilde{c} = 0.5$), representing the flame front at -17.5°, -15.5°, -12.5° and -10°bTDC for the 2Pin-Radial, SD-Radial and SD-Cross Variant using engine 2 (table 2) at 6500 rpm (yellow) and one flame surface at 1500 rpm (red).

4   Experimental investigation

In order to evaluate our concept of a thermally robust passive pre-chamber spark plug, we have run experiments on an engine test bench equipped with the 2Pin, SD-Radial and SD-Cross variants. Therefore, a three cylinder gasoline engine with typical passenger car engine dimension and a compression ratio of 12:1 was used. It has to be mentioned, that it was beyond the scope of the current study to investigate all different engine operating characteristics and conditions, but rather to have a first assessment based on a "plug-and-play" approach without any engine calibration or modifications to it. Only the engine speed and load is set for a few operating points. Minimum and maximum reached operating conditions, which are shown here, will therefore not necessarily represent the edges of the experimental envelop. We also do not use the recently proposed knock criterion by Sens et al. [22], which distinguishes conventional knocking induced by occasional ignition of the unburnt air/fuel mixture and between in-cylinder pressure fluctuations triggered/amplified by pressure waves emitted from the pre-chamber. A "standard" knock detection system of an engine will not necessarily be able to separate both phenomena, thus will misleadingly not allow to run the engine at some operating points. Furthermore, it has to be stressed that the tested variants for the 2Pin-Radial and SD-Radial spark plugs use a different orifice diameter compared to our numerical investigation shown in section 3.3 and 3.4 (due to engine and prototypes availability). Therefore, the imposed boundary conditions of our numerical study are not fully comparable to the test engine, which were derived for a fictive engine with a compression ratio of 14:1. However, the results can be already used to derive global trends.

4.1.1 Combustion inside the main-chamber

Figure 13 shows the center of combustion and the corresponding exhaust gas temperature for different engine loads for the 2Pin-Radial (4x1.2mm), SD-Cross (4x1mm) and SD-Radial (4x1mm) variants at 1500 rpm, 3000/3500 rpm and 6000 rpm. The lowest engine speed and load was achieved with the SD-Radial variant, with an indicated mean effective pressure (IMEP) of 3 bar at 1500 rpm. By increasing the load at fixed engine speed (solid lines), the center of combustion shifted towards later °CA after TDC for all variants, where the SD-Cross variant (4x1mm) showed the most retarded center of combustion at IMEP=10 bar for 1500 rpm (square symbols in figure 13).
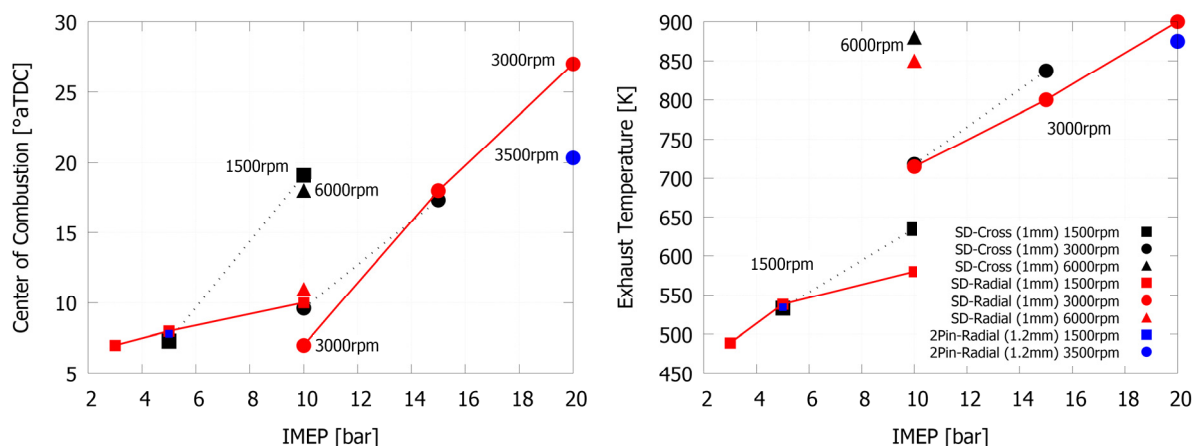

Figure 13: Center of combustion (left) and exhaust temperature (right) for the 2Pin-Radial (4x1.2mm), SD-Radial (4x1mm) and SD-Cross (4x1mm) variants at 1500 rpm, 3000 rpm and 6000 rpm. Preliminary tests of a few operating points.

A reason for the rather late center of combustion for 1500 rpm at IMEP=10 bar using the SD-Cross variant, might be found in the already slower combustion progress inside the pre-chamber as seen in figure 11 (SD-Cross, 1500 rpm), which manifests also in a later jet formation inside the main-chamber. A similar trend is obtained for 6000 rpm (triangle symbols in figure 13) at IMEP=10bar, where the center of combustion is obtained at 10°aTDC for the SD-Radial variant and 8°CA later for the SD-Cross variant. Unfortunately, for the SD-Cross (4x1mm) variant the knock detection system hindered the engine to operate above an IMEP of 16 bar. Here, a "jet-shock" amplification during the first stage of combustion might be present, as Sens et al. [22] has experimentally proven inside a similar engine. Also, we do see in our simulations of the SD-Cross variant the biggest pressure built-up inside the pre-chamber, which could yield bigger pressure fluctuations inside the main-chamber. Further experiments and simulations are required to verify this statement.

Figure 13 also shows the corresponding exhaust gas temperatures measured before the turbo charger, which are correlating with the center of combustion. The exhaust gas temperature is increasing with load, but also with the engine speed, where at higher engine speed less time is available for heat transfer inside the main combustion chamber. The highest exhaust gas temperatures are achieved with the SD-variants, where no pre-ignition caused by hot pre-chamber components were detected, which is the first evidence for a thermally robust design of the SD variants. Differences of the exhaust gas temperatures using the SD-Radial (4x1mm) and SD-Cross variant (4x1mm) might be also explained by the different emitted jet angles, where the SD-Radial variant will have very likely a longer and closer to the wall hot jet penetration than the SD-Cross variant. Radial jets will have a shorter travel path towards the cylinder liner, and therefore increasing the heat losses to the wall. Higher heat losses to the wall caused by hot turbulent jets are a notorious weakness of the pre-chamber spark plugs.

Figure 14 shows the cyclic variations of the operating points shown in figure 13. In the sake of completeness the ignition timing is shown next to the points in °bTDC. In general we have obtained a more stable combustion inside the main-chamber for the SD-Cross variant for all measured operating conditions. Here, the bigger and overall longer duration for the pressure built-up, as seen in figure 11, might be favorable for the development of the jets and subsequent ignition and combustion event in the cylinder volume. The higher cyclic variations of the SD-Radial variant might be triggered by the unsteady behavior of the big vortices underneath the isolator cap (see figure 2). In addition to the more unsteady flow field close to the spark location inside the SD-Radial variant, the higher residual gas amount at spark location could be also a reason for higher CCV. In particular for the low load and low engine speed point (1500 rpm/3 bar), the relative residual gas content inside the pre-chamber will be high. A similar phenomena is observed in our CFD simulation (see figure 10), where the relative residual gas amount was the highest for the SD-Radial variant at spark location, especially below 20°bTDC at 1500 rpm.
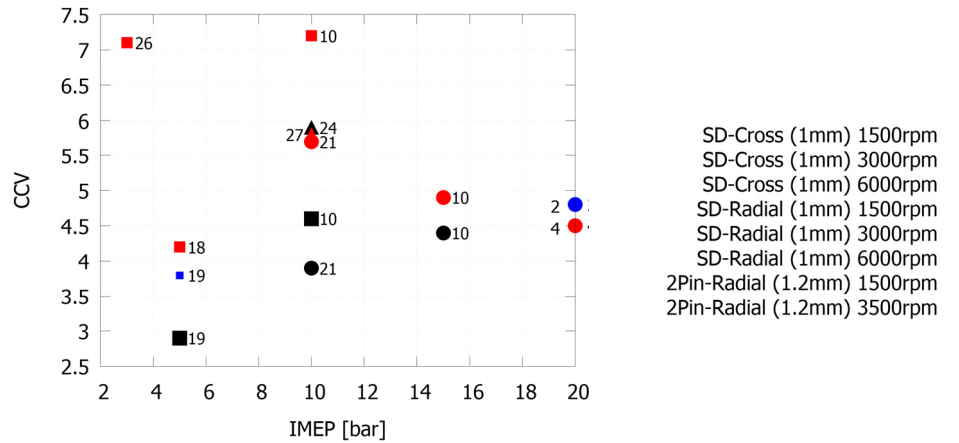
Figure 14: CCV for the 2Pin-Radial (4x1.2mm), SD-Radial (4x1mm) and SD-Cross (4x1mm) variants at 1500 rpm, 3000 rpm and 6000 rpm. Preliminary tests of a few operating points. Next to the points is the ignition timing indicated in °bTDC.

It is clear that the discussed experimental data does not show a fair comparison for all variants, and is only used to show to the reader first trends. However, the data is sufficient to conclude that the aerodynamic performance and spark location inside the pre-chamber is of paramount importance, because they will govern the start, duration and strength of the emitted jets, hence the combustion performance in the main-chamber. Also, we have obtained in our CFD simulation different pre-chamber combustion progresses and mass flow rates, which support our understanding of our experimental findings.

In order to have a more representative and fair comparison among the variants, we have fixed the ignition angle at 20°bTDC and varied only the engine speed. Figure 15 shows the engine speed variation at constant ignition angle for the 2Pin-Radial (4x1.2mm), SD-Radial (4x1mm) and SD-Cross (4x1mm) variants. At 1500 rpm, the center of combustion is shortly obtained before TDC for the SD-Cross variant and 1°CA after TDC for the SD-Radial variant (IMEP=6 bar). At 3500 rpm, however, using the SD-Cross variant led to a slightly later center of combustion compared to the SD-Radial. One explanation to this inversed trend with increasing engine speed can be the aerodynamic performance inside the pre-chamber, which probably differently scales with engine speed for the SD-variants. Further experiments and simulations are needed to confirm it. Increasing the load from 6 bar to 10 bar at 3500 rpm, has led to a 7°CA earlier center of combustion for the SD-Radial variant. A higher load will also increase the turbulence inside the pre-chamber and air/fuel charge, which in turn will favor a stronger and faster pre-chamber combustion, thus turbulent jet formation inside the main-chamber.

The center of combustion for the 2Pin-Radial variant is reached 4°CA earlier compared to the SD-Cross and SD-Radial variants for 3500 rpm. The faster combustion may also be here attributed to the earlier start of the jet formation, as generally seen in our numerical simulation for the 2Pin-Radial variant. For the sake of completeness, figure 15 also shows the exhaust gas temperature, where the exhaust temperature increases with increasing engine speed and load.
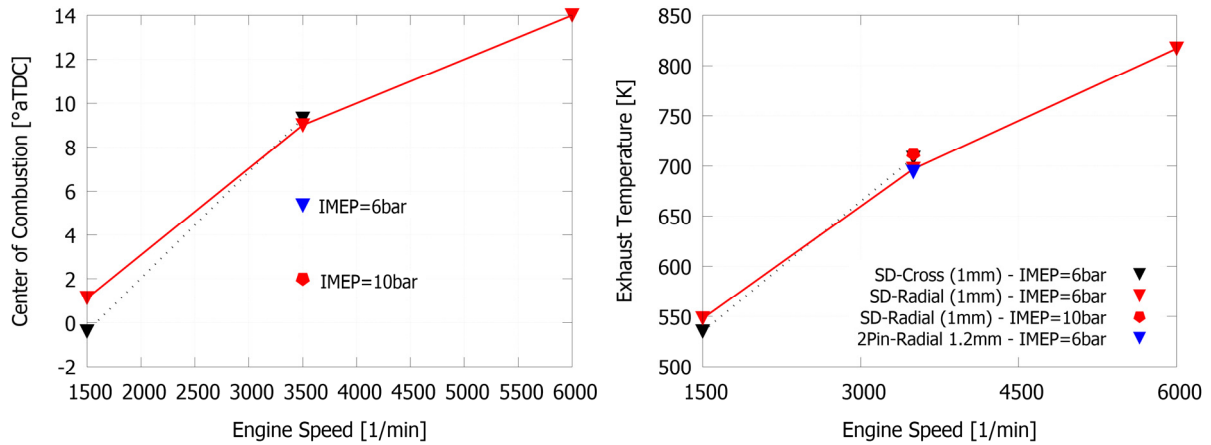
Figure 15: Center of combustion for a fixed ignition angle of 20°bTDC and exhaust gas temperatures for the 2Pin-Radial (4x1.2mm), SD-Radial (4x1mm) and SD-Cross (4x1mm) variants at 1500 rpm, 3500 rpm and 6000 rpm.

4.1.2 Voltage demand

Figure 16 shows the voltage demand of the different investigated points shown in figure 13. The surface discharge spark plug shows a higher voltage demand at lower loads compared to the air-gap discharge spark plug, but then only slowly increases with load and engine speed. The SD-Radial variant might have a lower voltage demand compared to the SD-Cross variant, because the spark location is exposed to lower flow velocities. For the SD-Cross variant, the incoming jets are redirected towards the spark location and might further stretch the spark, which manifests in a higher voltage demand. The 2Pin-Radial variant has at IMEP=5 bar and 1500 rpm engine speed a lower voltage demand than the surface discharge type plugs, but requires at higher load (IMEP=20) and engine speed (3500 rpm), 5 kV more than the SD-Radial variant. The high voltage demand of the 2Pin-Radial variant might also be here a consequence of the high velocities in the spark gap region, where the flow, immediately after entering the pre-chamber, streams towards the electrode gap (see figure 2).
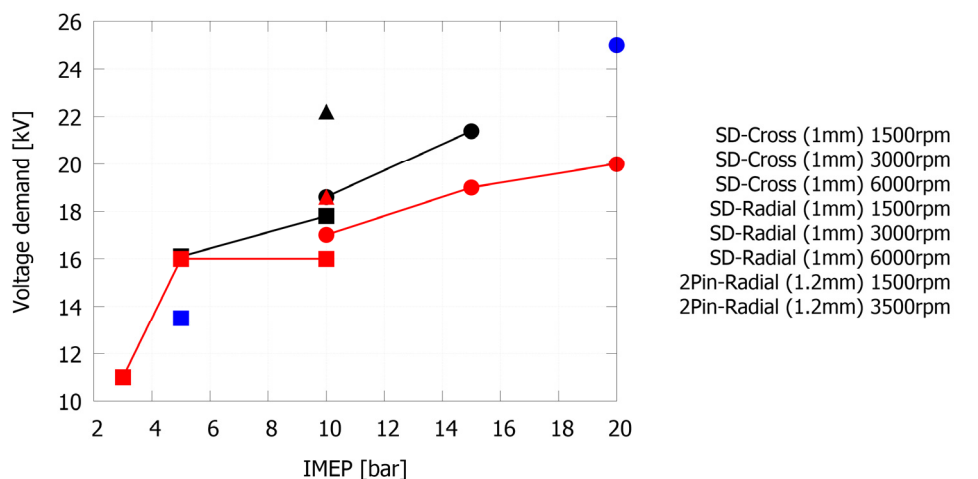
Figure 16: Voltage demand for the 2Pin, SD-Radial (4x1.2mm) and SD-Cross (4x1mm) variants at 1500 rpm, 3000 rpm and 6000 rpm

5   Conclusions / Outlook

A barrier-free pre-chamber concept with a surface discharge working principle is proposed, with the goal to (a) lower the components temperatures compared to a previously developed pre-chamber design with 2 side electrodes (2Pin), (b) to have more control over the residual gas distribution and (c) over the turbulence generation inside the pre-chamber volume. In order to assess the performance of the barrier-free pre-chamber spark plug, CFD simulations of the inflow and combustion are performed without physically considering the engine geometry inside the computational domain. In order to mimic the engine influence to the pre-chamber, boundary conditions were derived from an in-house 0D simulation tool and directly imposed on the pre-chamber orifices. The 0D approach is also discussed and presented within this work, which allowed us to calculate relevant pre-chamber quantities during the compression stroke for different pre-chamber geometrical parameters, such as pre-chamber volume and orifice diameter.

Neglecting the engine and focusing on the pre-chamber only, allowed us to apply large eddy simulations, with which it is possible to resolve the highly unsteady and turbulent flow field on our computational grid – smaller scales are still modelled. With the LES "pre-chamber-only" approach, we have calculated the residual gas distribution during the compression stroke for the surface discharge and 2Pin concepts for low and high engine speeds. The flow fields from the cold flow analysis were then used for combustion simulations, which were based on a flame surface density type LES model, using a simple algebraic wrinkling model proposed by Weller. All variants had different flame path characteristics, where only minor differences (hole orientation) for the SD-type plugs existed, which puts emphasis on the importance of the turbulent flow field to the flame propagation inside the pre-chamber. Even though, we did not have any experimental evidence to validate the combustion inside the pre-chamber, the simulated combustion progress and mass flow rates already helped us to better understand some experimental data of our plugs inside a typical passenger car sized engine. Those engine tests showed, that the barrier-free concept enabled a larger and more stable operating window compared to the 2Pin design, where even low load and low engine speed operating conditions were possible to operate, which are regarded for passive pre-chamber plugs as critical. Exhaust gas temperatures of ~900 K were reached with no pre-ignition events triggered by hot pre-chamber components, which is a first indication of the high thermal tolerance of the barrier-free pre-chamber surface discharge spark plug.

It is clear that the here proposed development approach can only work together with engine experiments and is rather used as a sorting tool. By using this approach, the development cycle time can be speed-up, which allows (a) to test more pre-chamber variants and (b), more importantly, to focus on the pre-chamber relevant physics in detail. At a later stage RANS full cycle simulations with engine are considered, which then allow us to fully exploit the gas-exchange between pre- and main-chamber (including IGR and EGR), which was up to now neglected and only the compression stroke considered.

The residual gas tolerance of the three variants is currently work in progress and the origin of pre-chamber combustion induced pressure fluctuation inside the main-chamber under investigation.

Literature

[1]   Heywood, John B. "Internal combustion engine fundamentals." (1988).

[2]   Colin, O., and A. Benkenida. "The 3-zones extended coherent flame model (ECFM3Z) for computing premixed/diffusion combustion." Oil & Gas Science and Technology 59.6 (2004): 593-609.

[3]   Nakazono, Tohru, and Yoshihiro Natsume. "Effect of dimensions of prechamber on lean burn gas engine." JSME International Journal Series B Fluids and Thermal Engineering 37.4 (1994): 951-956.

[4]   Alvarez, Carlos Eduardo Castilla, et al. "A review of prechamber ignition systems as lean combustion technology for SI engines." Applied Thermal Engineering (2017).

[5]   Schumacher, Moritz, and Michael Wensing. A gasoline fuelled pre-chamber ignition system for homogeneous lean combustion processes. No. 2016-01-2176. SAE Technical Paper, 2016.

[6]   Rivin, Boris, Mark Dulger, and Eran Sher. Extending lean misfire limit of methane-air mixtures by means of an enhanced spark discharge. No. 1999-01-0573. SAE Technical Paper, 1999.

[7]   Pashley, Nick, Richard Stone, and Graham Roberts. Ignition system measurement techniques and correlations for breakdown and arc voltages and currents. No. 2000-01-0245. SAE Technical Paper, 2000.

[8]   Roethlisberger, R. P., and Daniel Favrat. "Comparison between direct and indirect (prechamber) spark ignition in the case of a cogeneration natural gas engine, part I: engine geometrical parameters." Applied Thermal Engineering 22.11 (2002): 1217-1229.

[9]   Roethlisberger, R. P., and Daniel Favrat. "Comparison between direct and indirect (prechamber) spark ignition in the case of a cogeneration natural gas engine: Part II: Engine operating parameters and turbocharger characteristics." Applied Thermal Engineering 22.11 (2002): 1231-1243.

[10]   Yamanaka, Koji, Yosuke Shiraga, and Shunsaku Nakai. Development of Pre-chamber Sparkplug for Gas Engine. No. 2011-01-1870. SAE Technical Paper, 2011.

[11]   Takashima, Yoshitane, et al. "Evaluation of engine performance and combustion in natural gas engine with pre-chamber plug under lean burn conditions." SAE International Journal of Engines 8.1 (2015): 221-229.

[12]   Thelen, Bryce Charles, Gerald Gentz, and Elisa Toulson. Computational study of a turbulent jet ignition system for lean burn operation in a rapid compression machine. No. 2015-01-0396. SAE Technical Paper, 2015.

[13]   Gholamisheeri, Masumeh, et al. CFD modeling of an auxiliary fueled turbulent jet ignition system in a rapid compression machine. No. 2016-01-0599. SAE Technical Paper, 2016.

[14]   Thelen, Bryce Charles, and Elisa Toulson. A computational study of the effects of spark location on the performance of a turbulent jet ignition system. No. 2016-01-0608. SAE Technical Paper, 2016.

[15]   Gholamisheeri, Masumeh, Bryce Thelen, and Elisa Toulson. CFD modeling and experimental analysis of a homogeneously charged turbulent jet ignition system in a rapid compression machine. No. 2017-01-0557. SAE Technical Paper, 2017.

[16]   Akhtar, Muhammad Saqib, et al. Effect of the Pre-Chamber Orifice Geometry on Ignition and Flame Propagation with a Natural Gas Spark Plug. No. 2017-01-2338. SAE Technical Paper, 2017.

[17]   Biswas, Sayan, and Li Qiao. "A Numerical Investigation of Ignition of Ultra-Lean Premixed H 2/Air Mixtures by Pre-Chamber Supersonic Hot Jet." SAE International Journal of Engines 10.2017-01-9284 (2017): 2231-2247.

[18]   Allison, P. M., et al. "Pre-chamber ignition mechanism: Experiments and simulations on turbulent jet flame structure." Fuel 230 (2018): 274-281.

[19]   M. Kotzagianni*, D. Sakellarakis*, P. Kyrtatos*, Y.M. Wright* and K. Boulouchos* Experimental and computational investigations of prechamber jet ignition in a rapid compression expansion machine, Naples, MCS 10, 2017

[20]   Wang, Zhi, Hui Liu, and Rolf D. Reitz. "Knocking combustion in spark-ignition engines." Progress in Energy and Combustion Science 61 (2017): 78-112.

[21]   Chinnathambi, Prasanna, Michael Bunce, and Luke Cruff. RANS based multidimensional modeling of an ultra-lean burn pre-chamber combustion system with auxiliary liquid gasoline injection. No. 2015-01-0386. SAE Technical Paper, 2015.

[22]   Marc Sens, Emanuel Binder, Andreas Benz, Lutz Krämer, Kurt Blumenröder, Matthias Schultalbers, Pre-Chamber Ignition as a Key Technology for Highly Efficient SI Engines – New Approaches and Operating Strategies, Conference Paper, 39. Internationales Wiener Motorensymposium 2018

[23]   Guoqing, X. U., et al. "Experimental and Numerical Investigation of the Engine Operational Conditions' Influences on a Small Un-Scavenged Pre-Chamber's Behavior." SAE International Journal of Engines 10.2017-24-0094 (2017): 2414-2428.

[24]   Bardis, Konstantinos, et al. "A Zero Dimensional Turbulence and Heat Transfer Phenomenological Model for Pre-Chamber Gas Engines." SAE Technical Papers (2018).

[25]   Hiraoka, Kenji, et al. Phenomenological 0-Dimensional Combustion Model for Spark-Ignition Natural Gas Engine Equipped with Pre-Chamber. No. 2016-01-0556. SAE Technical Paper, 2016.

[26]   Roethlisbeger, R.P and Favrat, D, Investigation of the prechamber geometrical configuration of a natural gas spark ignition engine for cogeneration: part I. Numerical simulation, International Journal of Thermal Sciences 42, 2003

[27]   Roethlisbeger, R.P and Favrat, D, Investigation of the prechamber geometrical configuration of a natural gas spark ignition engine for cogeneration: part II. Experimentation, International Journal of Thermal Sciences 42, 2003

[28]   Attard, William P., et al. A new combustion system achieving high drive cycle fuel economy improvements in a modern vehicle powertrain. No. 2011-01-0664. SAE Technical Paper, 2011.

[29]   Schumacher, Moritz, and Michael Wensing. A gasoline fuelled pre-chamber ignition system for homogeneous lean combustion processes. No. 2016-01-2176. SAE Technical Paper, 2016.

[30] Shah, Ashish, Per Tunestal, and Bengt Johansson. Applicability of Ionization Current Sensing Technique with Plasma Jet Ignition Using Pre-Chamber Spark Plug in a Heavy Duty Natural Gas Engine. No. 2012-01-1632. SAE Technical Paper, 2012.

[31] Baumgartner, Laura Sophie, et al. Experimental Investigation of Orifice Design Effects on a Methane Fuelled Prechamber Gas Engine for Automotive Applications. No. 2017-24-0096. SAE Technical Paper, 2017.

[32] Chiodi, M., Kaechele, A., Bargende, M., Wichelhaus, D. et al., "Development of an Innovative Combustion Process: Spark-Assisted Compression Ignition," 10(5):2486-2499, 2017

[33] Biswas, Sayan, et al. "On ignition mechanisms of premixed CH4/air and H2/air using a hot turbulent jet generated by pre-chamber combustion." Applied Thermal Engineering 106 (2016): 925-937.

[34] Biswas, Sayan, and Li Qiao. "Ignition of ultra-lean premixed H2/air using multiple hot turbulent jets generated by pre-chamber combustion." Applied Thermal Engineering 132 (2018): 102-114.

[35] https://world.honda.com/history/challenge/1972introducingthecvcc/page07.html

[36] Demirdžic, I., Lilek, Ž., Peric, M.: A collocated finite volume method for predicting flows at all speeds. International Journal for Numerical Methods in Fluids 16(12), 1029–1050 (1993). DOI 10.1002/fld.1650161202

[37] Smagorinsky, J.: General circulation experiments with the primitive equations: I. the basic experiment*. Monthly weather review 91(3), 99–164 (1963)

[38] Yoshizawa, A.: Statistical theory for compressible turbulent shear flows, with the application to su grid modeling. Physics of Fluids 29(7), 2152–2164. DOI 10.1063/ 1.865552

[39] https://openfoam.org/

[40] Janas, Peter, et al. "On the evolution of the flow field in a spark ignition engine." Flow, Turbulence and Combustion 98.1 (2017): 237-264.

[41] Janas, Peter. Large Eddy Simulation of In-cylinder Phenomena in Spark Ignition Engines. Diss. Universitätsbibliothek Duisburg-Essen, 2017.

[42] Gülder, O.L.: Correlations of Laminar Combustion Data for Alternative S.I. Engine Fuels. In: SAE Technical Paper. SAE International (1984). DOI 10.4271/841000

[43] Weller, H., Tabor, G., Gosman, A., Fureby, C.: Application of a flame-wrinkling LES combustion model to a turbulent mixing layer. In: Proc. Combust. Inst, vol. 27, pp. 899–907. Elsevier (1998). DOI 10.1016/S0082-0784(98)80487-6

[44] Hiraoka, Kenji, et al. Phenomenological 0-Dimensional Combustion Model for Spark-Ignition Natural Gas Engine Equipped with Pre-Chamber. No. 2016-01-0556. SAE Technical Paper, 2016.

[45] Bargende, Michael. Ein Gleichungsansatz zur Berechnung der instationären Wandwärmeverluste im Hochdruckteil von Ottomotoren. na, 1990.

[46] Woschni, G.: A universally applicable equation for the instantaneous heat transfer coefficient in the internal combustion engine. Tech. rep., SAE Technical paper (1967). DOI 10.4271/670931

3.3 Passive Pre-Chamber Spark Plug for Future Gasoline Combustion Systems with Direct Injection

Matthias Blankmeister, Muhammed Alp, Eriko Shimizu

Abstract

The challenge of using a pre-chamber spark plug for future gasoline combustion processes with direct injection is, on the one hand, to realize an ignitable mixture in the pre-chamber at low load and speed. On the other hand, at high speed and high load, keeping component temperatures have to be kept low in order to prevent irregular combustions (pre-ignition, glow ignition).

With increasing requirements regarding fuel consumption and emissions, the challenges to modern combustion strategies are growing steadily. Measures to further increase the efficiency of the combustion engine are required for this purpose. There are different approaches to increase efficiency. These include increasing the compression ratio and diluting the air-fuel mixture. The latter can be generally classified into two broad categories: Dilution with air and dilution with residual gas. In both cases, it turns out that the highest possible dilution is to be preferred with respect to combustion efficiency. Increasing dilution, however, leads in both cases to a deterioration in flammability and a decrease in the flame velocity of combustion. In the resulting requirements for the ignition system, the passive pre-chamber spark plug is an interesting alternative to the conventional spark plug. Due to its functional principle, it can simultaneously improve the ignition and shorten the burn duration. In the present work, the focus is on the behavior of the pre-chamber spark plug while diluting the cylinder charge with air.

A particular challenge for the passive pre-chamber spark plug is to safely ignite the mixture at idling and in the low to medium part load with a correspondingly high internal residual gas content. Dilution of the cylinder charge with air also complicates the possibility to have a good air-fuel mixture within the pre-chamber. In order to ensure a reliably ignitable mixture in the pre-chamber even under these boundary conditions, it is necessary to design a suitable pre-chamber geometry in conjunction with the direct injection.

This work describes the behavior of different passive pre-chamber spark plugs when using lean mixtures at low and medium part load with CFD simulation. Criteria such as residual gas content and air-fuel ratio at start of ignition at the ignition point as well as other flow parameters such as temperature, velocity and turbulent kinetic energy are examined in detail. The effect of the torch coming out of the pre-chamber is finally assessed by combustion simulation.

Kurzfassung

Die Herausforderung bei dem Einsatz einer Vorkammerzündkerze für zukünftige Otto-Brennverfahren mit Direkteinspritzung ist es, zum einen bei niedriger Last und Drehzahl ein zündfähiges Gemisch in der Vorkammer zu realisieren. Zum anderen bei hoher Drehzahl und hoher Last die Bauteiltemperaturen niedrig zu halten, um eine irreguläre Verbrennung (Vorentflammung, Glühzündung) zu verhindern.

Mit stetig steigenden Anforderungen an den PKW-Motor hinsichtlich Verbrauch und Emissionen, wachsen auch die Herausforderungen an die modernen Verbrennungsstrategien. Maßnahmen zur weiteren Wirkungsgradsteigerung der Verbrennungskraftmaschine sind hierzu erforderlich. Es existieren verschiedene Ansätze zur Erhöhung der Effizienz. Hierzu zählen unter anderen die Erhöhung des Verdichtungsverhältnisses und die Verdünnung des Luft-Kraftstoff-Gemisches. Letzteres lässt sich im Allgemeinen in zwei Kategorien unterteilen: Die Verdünnung mit Luft und die Verdünnung mit Restgas. In beiden Fällen zeigt sich, dass eine möglichst hohe Verdünnung zielführend für einen hohen thermischen Wirkungsgrad ist. Steigende Verdünnung führt jedoch in beiden Fällen zur Verschlechterung der Entflammbarkeit und zur Abnahme der Brenngeschwindigkeit. Bei den hierdurch entstehenden Anforderungen an das Zündsystem stellt die passive Vorkammerkerze eine interessante Alternative zur Standard Hakenkerze dar. Aufgrund ihres Funktionsprinzips kann sie gleichzeitig zur Verbesserung der Entflammung und der Beschleunigung des Durchbrandes führen. In der vorliegenden Arbeit wurde der Fokus auf das Verhalten der Vorkammer bei Verdünnung der Zylinderladung mit Luft untersucht.

Eine besondere Herausforderung für die passive Vorkammerkerze besteht darin, das Gemisch bei Leerlauf und in der unteren bis mittleren Teillast bei entsprechend hohem, internen Restgasgehalt, sicher zu entflammen. Eine Verdünnung der Zylinderladung mit Luft erschwert ebenfalls die Darstellung eines gut brennbaren Luft-Kraftstoff-Gemisches innerhalb der Vorkammer. Damit auch unter diesen Randbedingungen das Gemisch in der Vorkammer sicher zündfähig ist, gilt es eine geeignete Vorkammergeometrie in Verbindung mit der Direkteinspritzung zu gestalten.

Im Beitrag wird das Verhalten unterschiedlicher passiver Vorkammerkerzen beim Einsatz von mageren Gemischen bei niedriger und mittlerer Teillast mittels CFD Simulation beschrieben. Kriterien wie Restgasgehalt und Lambda zum Zündzeitpunkt am Zündort sowie weitere Strömungsgrößen wie Temperatur, Geschwindigkeit und turbulente kinetische Energie werden detailliert untersucht. Die Wirkung der Fackelaustrittsbohrungen wird anschließend mittels Verbrennungssimulation bewertet.

1   Introduction

The advantages of pre-chamber ignition systems for spark ignited engine concepts are well known. The main differences to a conventional spark plug ignition system are illustrated in Figure 1.

The passive pre-chamber spark plugs are standard in many stationary gas engines, mainly for block heating power plants. In such applications lean limit is extended up to lambda = 1.8 (lambda λ corresponds to the reciprocal value of the equivalence ratio Φ) due to higher combustion stability and faster combustion compared to conventional spark plugs. These latest developments were referring to the Clean Air Act (TA Luft) [1] and power ratings of 0.8 to 2.5 MW, suitable for use with natural and other special gases [2].

Another area in which the passive pre-chamber spark plug is used is motorsports. Similar to stationary gas engines, the main focus in motorsports is the operation of the engine at high load. The functional design on a quasi-singular operating point is readily implementable, and therefore the use of the pre-chamber spark plug in these two areas is now state of the art.

The use of the passive pre-chamber spark plug in a mobile application, e.g. a passenger car is currently not possible. The reason for this is the operation from cold start, idle over part load to full load. All operating points must be ensured and up to now this has not been proven with a single pre-chamber spark plug. At the two extreme operating points, low part load (idle) and full load, there are different challenges towards the pre-chamber spark plug. At low load, despite low pressure sufficient fuel in the pre-chamber is required to ignite the mixture reliably. At high speed and high load, the challenge for the pre-chamber spark plug is to keep component temperatures low to prevent irregular combustion (pre-ignition, glow ignition).

This article focusses on the first part, the analysis of the behavior of different passive pre-chamber spark plug when using lean mixtures at low and medium part load by means of CFD simulation with and without combustion and also at the test bench.
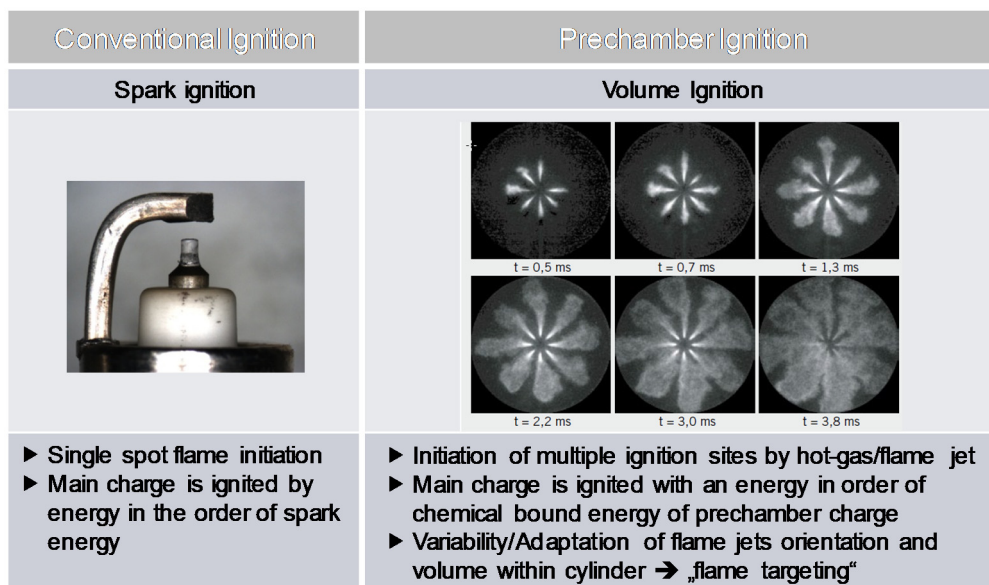

Figure 1: Comparison of conventional spark ignition and pre-chamber ignition with picture of OH-Chemiluminescence measurement combustion of a pre-chamber ignition system [3]
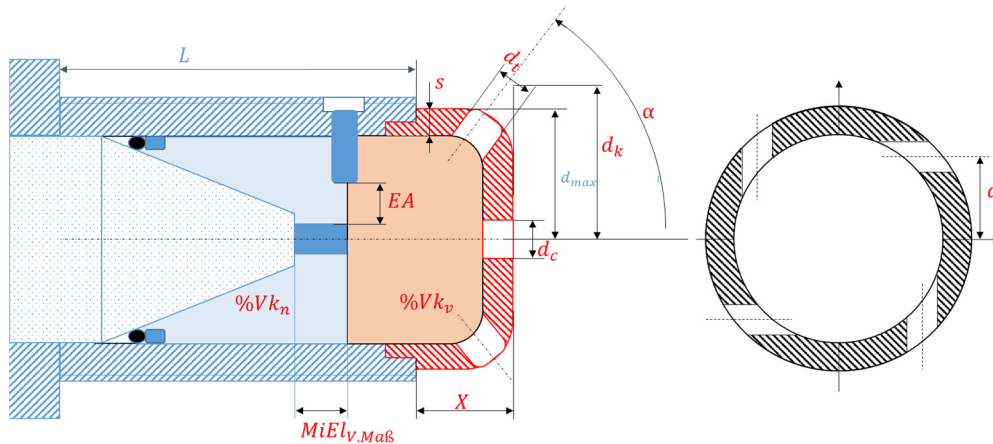
2   Design

Figure 2: Schematic drawing and example of a pre-chamber spark plug

There are many different approaches belonging to the design of a passive pre-chamber spark plug. The idea of the Bosch approach was to accomplish a design suitable as a plug-and-play solution for an existing cylinder head with a conventional spark plug design. This approach is shown in Figure 2. The design philosophy has some characteristic elements. Besides the insulator, center electrode and the housing it includes a ground electrode with a special implementation and the pre-chamber cap mounted directly onto the housing of the pre-chamber. As can be seen, there are many geometrical parameters that theoretically can be varied.

To reduce the amount of variants for the planned CFD simulation study to a convenient level, two things were done. Firstly, it was decided only on a certain set of parameters to be varied. Secondly, the number of increments in each parameter dimension was reduced by using a simple two step approach based on the idea of a reference geometry. The design of the reference geometry was derived from empirical values and values from literature, such as for example pre-chamber volume, hole diameters and hole angles.

Figure 3 shows the seven parameters, which were chosen to be varied, as shown in the left hand box. All parameter variations which led to the other pre-chamber geometries to be investigated were derived on bases of the aforementioned two step approach.
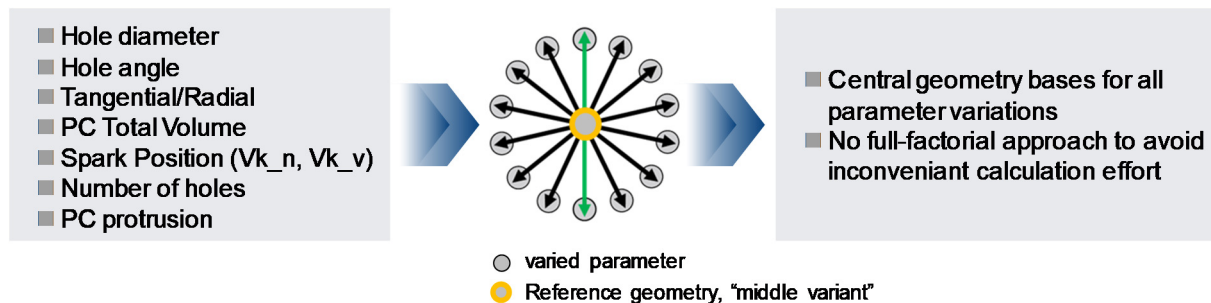
Figure 3: Investigation approach for CFD investigations

This means each change was made based on the reference geometry in such a way that a change to a parameter's value was made into one direction and another to the opposite direction referring to the mentioned reference geometry. For example the hole

diameter was increased by 0.3 mm for one variant and decreased by 0.3 mm for another variant. This manner of variations helps understand sensitivities of system on a basic level with reasonable effort. The symbol in the middle of Figure 3 is representing this scheme. Eventually this approach leads to a non full-factorial approach, reducing the simulation effort significantly.
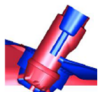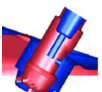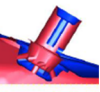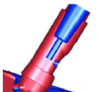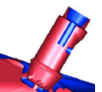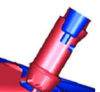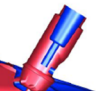
An overview of the designs which were derived based on the described approach can be found in Figure 4. The illustrated pictures of the different variants represent the inner gas volume of the pre-chamber spark plug including the holes connecting the pre-chamber volume to the main chamber volume. In other words, these are the fluid domains used by the CFD model for the simulation.

	V1	V2	V3	V4	V5	V6	V7
d_t [mm]	1	1.3	0.7	1	1	1	1
d_c [mm]	1	1	1	0	2	1	1
a [mm]	2	2	2	2	2	0	1.5
a [°]	base	base	base	base	base	base	base
Nr. of holes	9	9	9	8	9	9	9

	V8	V9	V17	V18
d_t [mm]	1	1	1	1
d_c [mm]	1	1	1	1
a [mm]	2	2	2	2
a [°]	low	high	base	base
Nr. of holes	9	9	5	7

Reference Geometry "middle variant"

	V10	V11	V12	V13	V14	V15	V16
Protrusion	step 1	step 2	base	base	base	base	base
PC Volume	base	base	small	big	base	base	base
Vk_v	base	base	base	base	high	highest	low
Vk_n	base	base	base	base	low	lowest	high
Nr. of holes	9	9	9	9	9	9	9

Figure 4: Overview investigated pre-chamber Variants

Variants V10 to V16 have the same hole designs (hole diameter etc.). Changes are made regarding V1 so that parameters can be clustered into a pair of geometries, for which a certain geometrical parameter was changed.

3   CFD Simulation

To establish a better understanding of the dominating physics within the pre-chamber spark plug 3D CFD simulations were conducted.

In this study the different pre-chamber variants were compared amongst each other based on residual gas mass fraction, tke and equivalence ratio at ignition timing. These CFD results were then used to derive a ranking of pre-chamber spark plugs and consequently to help decide for samples to be used on the engine test-bench.

Due to the importance of the gas exchange for the evaluation of the pre-chamber scavenging the simulations comprise the full 720 °CA cycle.

The residual gas mass fraction will be denoted as "EGR" in this paper, even though this word is usually used for external gas recirculation.

3.1   CFD Model Setup

Simulations were done using an in-cylinder geometry, including intake and export ports, a DI injector and the spark plug. The illustration Figure 5 shows the CFD model with the base pre-chamber variant integrated.

All 3D CFD calculations were conducted with the commercial Software AVL Fire, using the RANS approach. Furthermore, the k-zeta-f turbulence model was used. For the liquid phase n-heptane was used as reference species. For the spray the wave break-up model was used and the spray temperature was set to 343.15 K. Constant wall temperatures were used for all wall boundaries.

The geometrical model for the in-cylinder simulation is based on an engine combustion chamber containing complete intake and exhaust ports and a central DI injector.

As depicted in Table 1, two operation points were chosen to be investigated via the CFD simulation. The nomenclature b. IDTC means "before ignition top dead center".

Table 1: Simulated operation points

Operation Point	Engine Speed [rpm]	Imep [bar]	SOI [°CA b. ITDC]	$\lambda = 1/\Phi$ [-]
OP1	1500	3	330	~ 1.6
OP2	2000	8	330	~ 1.5

OP1 with low engine speed and low load was chosen to address a pre-chamber operation at relatively high residual gas mass level, small in-cylinder charge and low charge motion level. OP2 represents higher part-load with mid-range engine speeds, which was intensively investigated and optimized on preliminary studies on homogeneous lean combustion.

In Figure 5 the geometrical setup of the pre-chamber within the combustion chamber is illustrated. In this study predominantly two volumes have been used for the CFD evaluation: the total pre-chamber volume and the main chamber. As also can be seen in the illustration, the chosen spray pattern (blue) of the multi-hole injector does not involve any beam which directly points to the pre-chamber spark plug.
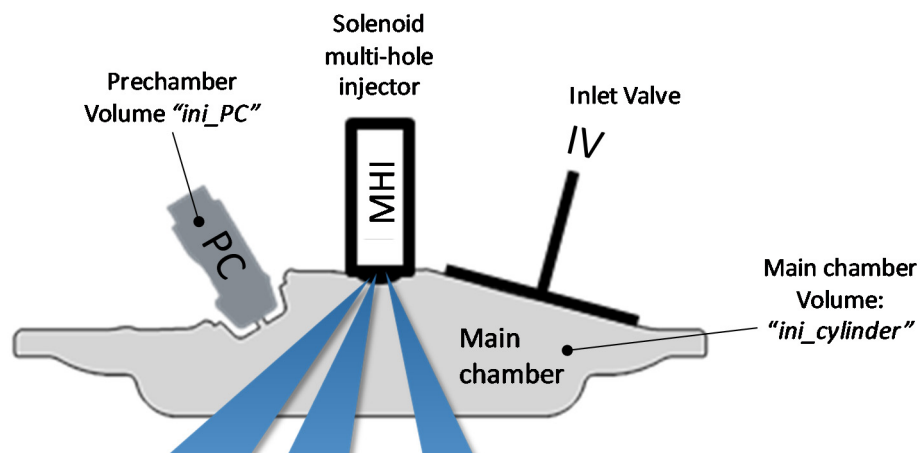
Figure 5: CFD in-cylinder model cut plane

3.2   Results

The results of the gas exchange and mixture preparation simulations will be illustrated and explained in two steps: first a qualitative analysis of the flow field and mixture condition based on 3D and 2D evaluation will be shown. Secondly the results will be quantified in chosen volumes by integrating the values in all of its cells and then averaging them, so that the development of the mixture within the pre-chamber over crank angle can be analysed.

Eventually the condition of the mixture at ignition timing will be analysed and representative values will be plotted against each other to evaluate if and what kind of correlations can be found.

3.2.1   Comparison of Operation Points

In Figure 6 residual gas mass fraction ("EGR"), lambda λ and the turbulent kinetic energy ("tke") are illustrated for operation points OP1 and OP2. The blue coloured circles symbolize the mean value over all pre-chamber variants simulations at 695 °CA (25 °CA bITDC) for the ini_PC volume for OP1 and respectively OP2. The grey coloured circles show the mean value of all simulations for the ini_cylinder volume.

The ignition timing was assumed to be within the relevant region at the beginning of the CFD study.

Comparing the two evaluated volumes, the pre-chamber volume shows higer EGR values, higher lambda values and lower tke values compared to the main chamber, as can be expected. It is worth noting, that the discrepancy for the lambda value between pre-chamber volume and main chamber volume has the tendency to decrease for higher load and engine speed operation points. In other words, a richer lambda can be reached within pre-chamber volume for increasing load and engine speed at the same main chamber lambda value.
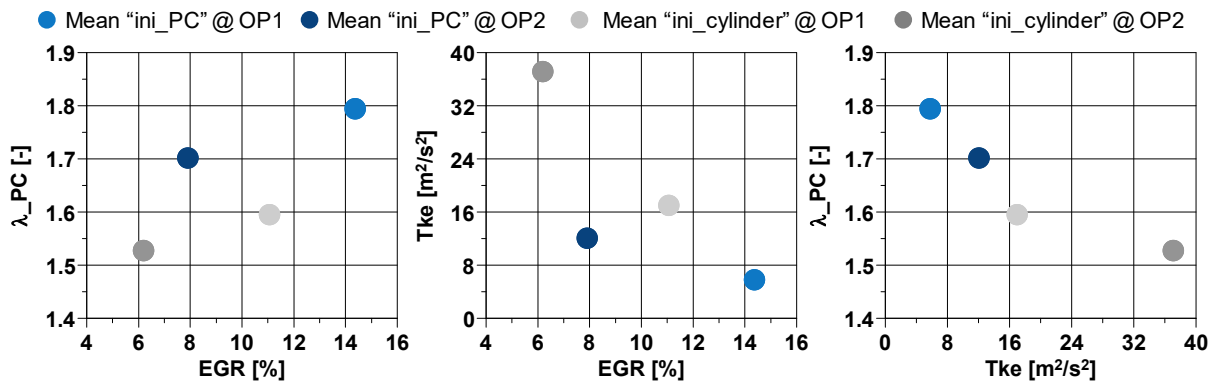
Figure 6: Mean values of egr, lambda, tke at OP1 & OP2

3.2.2   Crank Angle Based Analysis of EGR, Tke & Equivalence Ratio

In this section a more detailed analysis of the EGR, tke and lambda within the pre-chamber will be discussed. In the following illustrations the dotted black lines describe the integrated mean values for the main chamber volume ("ini_cylinder"), while the grey solid lines denote the behaviour within the pre-chamber volumes ("ini_PC"). The vertical blue lines represent inlet valve opening and respectively closing. The orange vertical line represents fuel injection timing. Furthermore contour plots of variant V1 are used to indicate the spatial distribution of the values at 695 °CA (25 °CA bITDC).

For easy comparison the same timing was used to evaluate the pre-chamber variants at OP1.

In Figure 7 the trends for EGR over crank angle degree for all pre-chamber variants are illustrated. For almost all variants the EGR level in the pre-chamber volume is higher than the main chamber level independent from the operation point. For both OP the highest EGR level can be found for the variant V3, where the total flow cross section is the smallest which describes the sum of each hole cross section area. The variant V12, which has the smallest total pre-chamber volume on the other hand has the lowest EGR level in both operation point cases. In fact, for the OP2 it even reaches a slightly lower EGR level than the main chamber charge already at the end of the intake stroke. Obviously, total residual gas mass at the beginning of scavenging is less for variant V12 than all the other variants with bigger volume.

The EGR distribution plots show a tendency of EGR to accumulate around the pre-chamber axis. This is due to the swirl induced by the tangentially arranged radial bores.
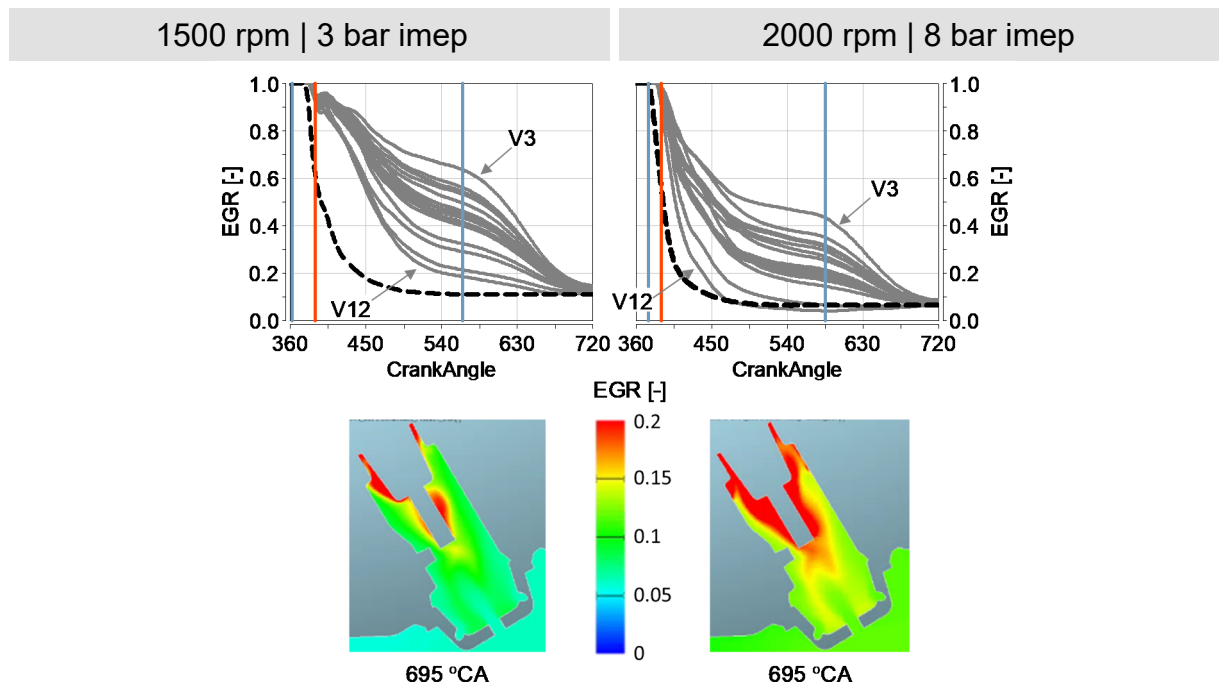
Figure 7: Comparison pre-chamber variants, EGR trends and distribution

The main chamber EGR level after inlet valve closing determines the minimum EGR level within the pre-chamber volume which can only be reached asymptotically. Much of the change in EGR is already happening within gas exchange phase. During compression EGR values further decrease rapidly. The upward movement of the piston causes a pressure difference between the main chamber and the pre-chamber volume. This in consequence feeds the pre-chamber volume with the main chamber air-fuel mixture with its main chamber EGR level.

On basis of this observation one can conclude that, without the consideration of the scavenging in the gas exchange phase, the mean EGR level of the total pre-chamber volume at the end of compression will almost exclusively depend on the ratio between pre-chamber volume and main chamber volume. Additionally, it can be concluded, that the actual residual gas mass within the pre-chamber is determined by the gas exchange phase from inlet valve opening up to the point when main chamber pressure

exceeds the pressure in the pre-chamber volume. After this EGR level only changes by displacing the resident residual gas mass of the pre-chamber volume by the main chamber mixture with lower EGR level.

Analysing the tke levels and trends illustrated in Figure 8 the results show, that the tke values reached within the pre-chamber variants are always lower than within the main chamber. Furthermore it can be observed that the positions of tke peaks close to ITDC are very similar comparing between main chamber and pre-chamber volumes.
The variant V3 reaches for both variants high tke levels.
Contrary to V3 the variant V12 shows the lowest tke values. This can be explained by the fact that when the piston moves up and the condition $\Delta p = p\_pc - p\_mc < 0$ is met, the mass flow into the pre-chamber volume to equalize the pressure difference is the lowest compared to the other variants.
The contour plots show that tke is mainly generated at the holes. The increased load and engine speed at OP2 push up regions of high tke towards the spark position.
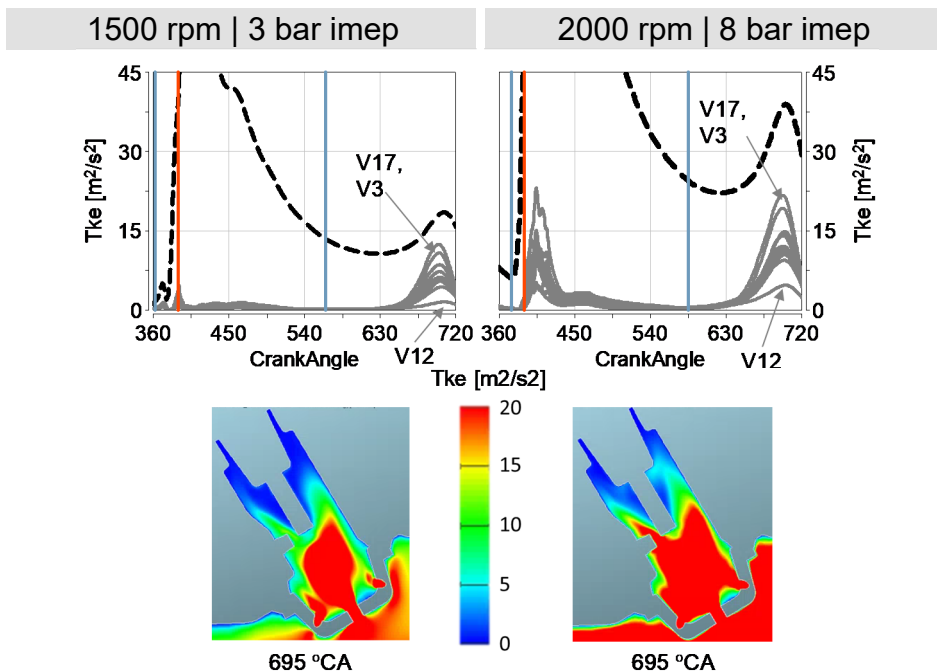
Figure 8: Comparison pre-chamber variants, Tke trends and distribution

Another important aspect of the passive pre-chamber spark plug is the equivalence ratio Φ within the pre-chamber, which is illustrated in Figure 9.
In both operation point cases, the main chamber mixture is already settled to a constant value at bottom dead center (540 °CA), which it keeps unchanged until the end of compression. However, in the pre-chamber volumes Φ change significantly after inlet valve closing.
In compression phase, mixture with a Φ ratio of the main chamber level is pushed into the pre-chamber volume, causing an asymptotic approximation to main chamber level, quite similarly as for the behaviour of the EGR values shown before.
Especially for OP1 the pre-chamber variants show a significant increase in Φ within the gas exchange phase. This phenomenon in principle can also be seen for OP2 but in a much more moderate level.

The low load case OP1 will have less fuel injected leading to lower penetration of the fuel into the main chamber. This in return leads to a rich zone closer to the holes during scavenging phase than compared to OP2.

The highest Φ values at ignition relevant timings is reached by the variant V6 for OP1 and Variant V3 for OP2.

For OP1 the pre-chamber volume can reach a value of Φ very close to that in the main chamber volume. For OP2 this is not the case.

The contour plots, showing an accumulation of leaner reagions around the pre-chamber axis, representing a very similar structure like the EGR distributions.
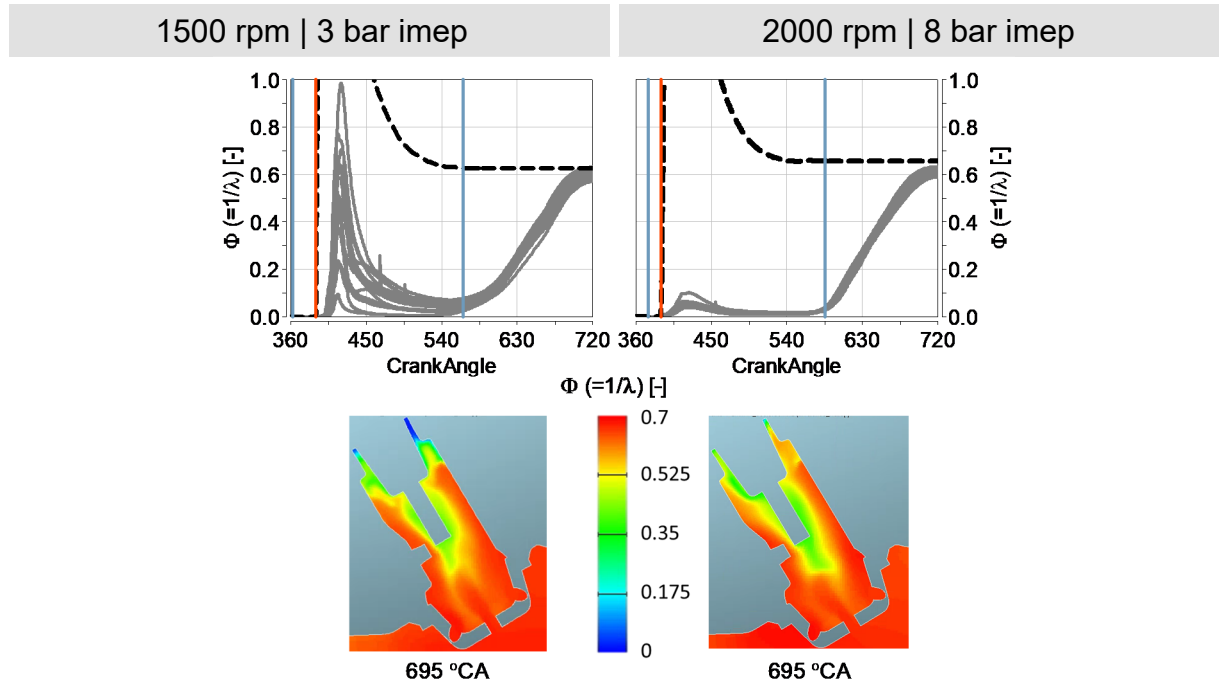
Figure 9: Comparison pre-chamber variants, A/F trends and distribution

As described before there are similarities to the EGR behaviour. However, a big difference is the Φ distribution within the main chamber. The inhomogeneities with respect to Φ will be much higher than for EGR. Therefor timing of the injection as well as the geometries will have an influence on the trend within the pre-chamber volume.

3.2.3 Scavenging Mechanism & Flow Pattern

The mechanism of scavenging will be illustrated and explained by Figure 10. The A-A cut section plane is used to show the mass exchange, between main chamber and pre-chamber volume, in which the uniform length and colour velocity vectors are used to demonstrate the direction of flow. The illustrated results belong to the case OP2, pre-chamber variant V1. The colours illustrate the distribution of EGR. The scaling of EGR is used only up to 0.5 so differences get more distinguishable.

On picture (a) of Figure 10, a few degrees after gas exchange top dead centre one can clearly see that mass is only transferred from pre-chamber volume to the main chamber volume, indicated by the vectors in each hole pointing outwards. In this case (OP2) inlet valves open around 375 °CA. Up to that time, gas with EGR = 1 is leaving the pre-chamber volume. That means residual gas mass is decreasing, but the fraction of residual gas within the pre-chamber stays constant, because gas is only flowing out of

the pre-chamber, without any gas with EGR level lower than 1 entering the pre-chamber. Therefor the level within the pre-chamber volume is not decreasing.

This is also shown by the EGR curves in Figure 7 for OP2, which show that EGR level is left at EGR =1 until inlet valves open. For OP1 it can be observed that the decrease in EGR level happens later that inlet valve opening timing. This is due to the fact, that in contrast to OP2, OP1 represents a throttled operation point. At inlet valve opening timing the inlet ports still feature a lower pressure than the cylinder.
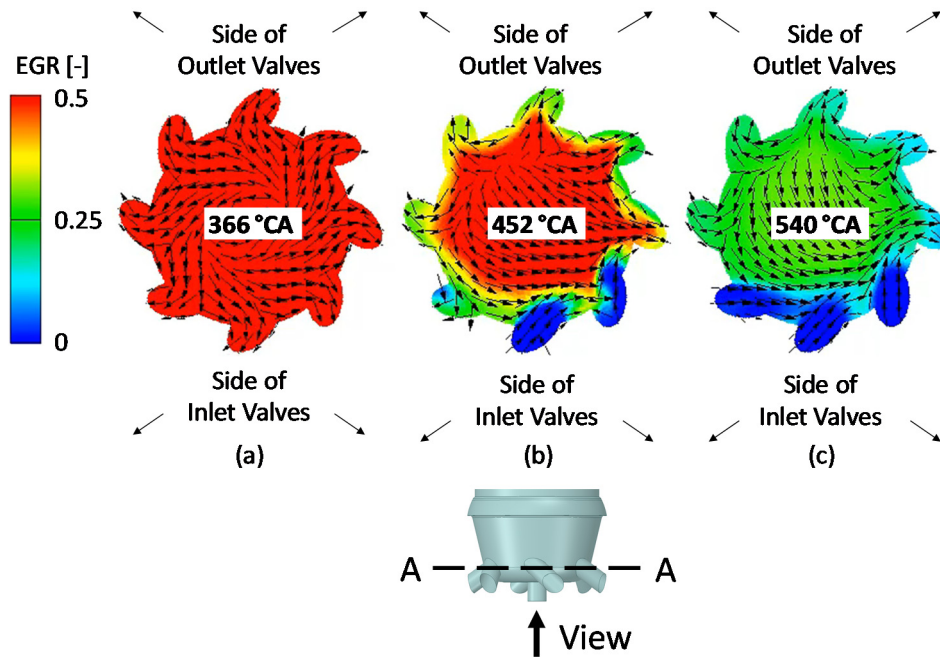
Figure 10: Scavenging mechanism (residual gas mass fraction EGR)

In picture (b) it two of the 8 shown holes implicate a massflow from the main chamber to the pre-chamber, while the rest of the holes show an outward flow. The entering gas seems to have an EGR level as low as around 0 indicating, that the pre-chamber volume is fed with fresh air. This picture represents a flow through the pre-chamber volume, which in consequence decreases the EGR level.

When the flow from the intake ports enter the main chamber a portion of it stagnates at the side of the pre-chamber spark plug cap, which is oriented towards the inlet valves generating a small over-pressure compared to the back side of the cap, which is oriented to the outlet valves. Even slow pressure differences as low as 5 mbar are sufficient to establish the scavenging process. The swirl created by the tangential inclination of the holes has an upward movement within the pre-chamber volume, which is caused by the vertical inclination denoted by the α-angle in Figure 4. This leads to the scavenging of also the upper parts of the pre-chamber volume.

The swirl induces a flow through its core from top down. The described phenomenon & flow pattern is true for both EGR and Φ. This can be seen in Figure 11 showing a typical structure of distribution for Φ for all variants with tangentially oriented radial holes. The distribution for EGR has already been shown in Figure 7.

159
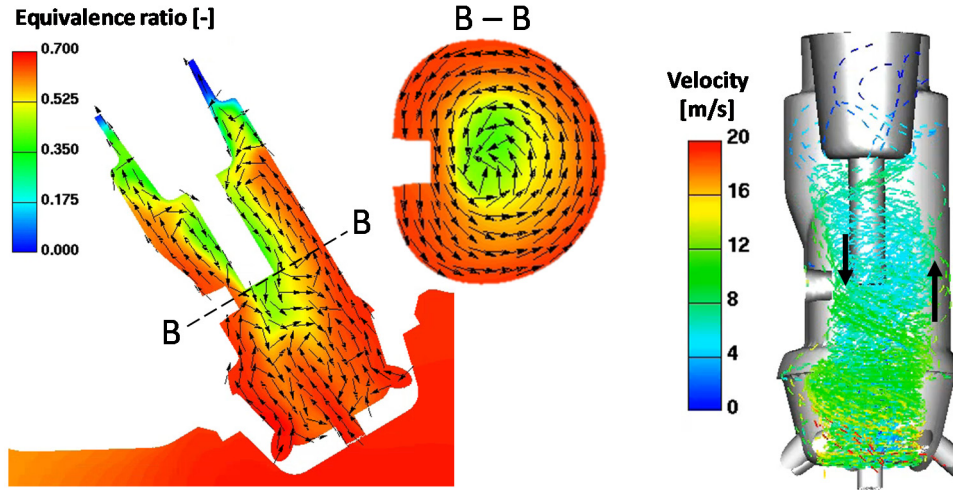
Figure 11: Typical flow pattern including EGR distribution at 25 °CA bITDC at OP1

3.2.4   Correlations

In the following section correlations between the different pre-chamber geometries and the CFD results at 695 °CA will be made, to evaluate the pre-chamber variants with respect to ignition condition. In Figure 12 pre-chamber variants V1, V3 and V12 were chosen, to show the correlations between EGR, tke and some of the geometrical parameters. In these plots a tradeoff between scavenging and tke is depicted.
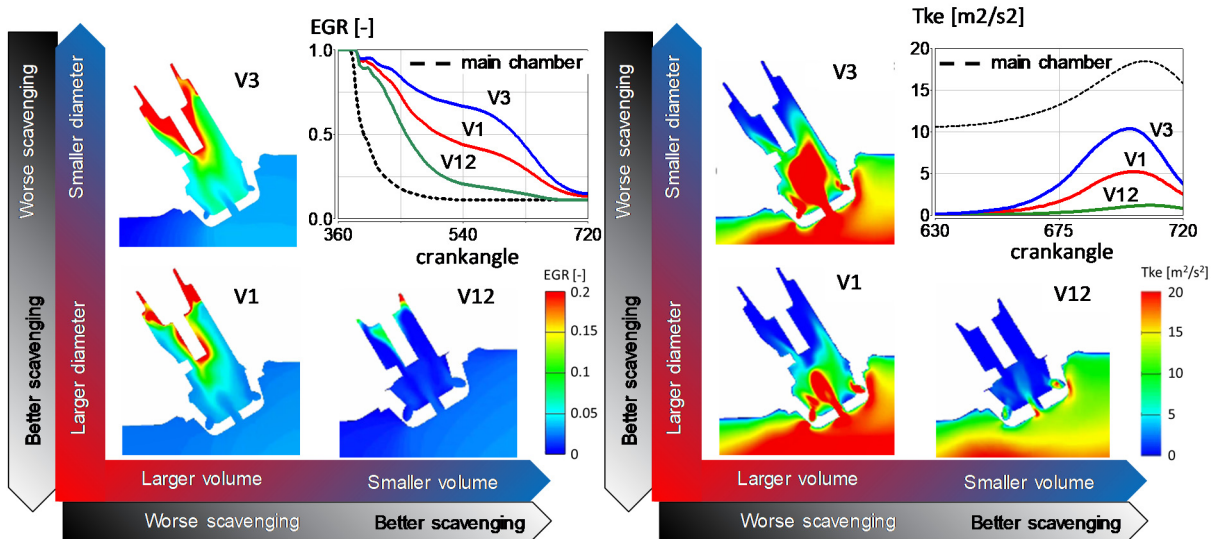
Figure 12: Correlations of geometry, EGR and tke at OP2

One can see that decreasing the volume or increasing the hole diameters have the same effect on EGR and tke. But while decreasing the volume or increasing the hole diameters help increase the scavenging quality, it deteriorates the tke.
The change in hole diameters will change the total flow cross section A. The ratio between A and the pre-chamber volume V is called the A/V ratio, which is widely known to be a value for the characterization of pre-chamber geometries.

Additionally to the above mentioned correlations Figure 13 illustrates lambda (=1/Φ) and the CFD results are also plotted against the geometrical characteristic A/V. The values are representing the conditions at 25 °CA bITDC (695 °CA). Here the circles in

light blue represent the operation point OP1 and the dark blue operation point OP2. The numbers in the circles represent the pre-chamber variant.

It can be seen that in terms of lambda OP1 has a wider range than OP2 and some variants have a very lean mixture condition, for example V12 with around 1.95. This is very critical because at low loads combustion is per se more challenging, but shows at the same time that much can be done by geometrical variation only.

Analysing the variants which had a good scavenging quality, namely V12 and V2, the results indicate, that best scavenging behaviour is not correlating with highest enrichment within pre-chamber.
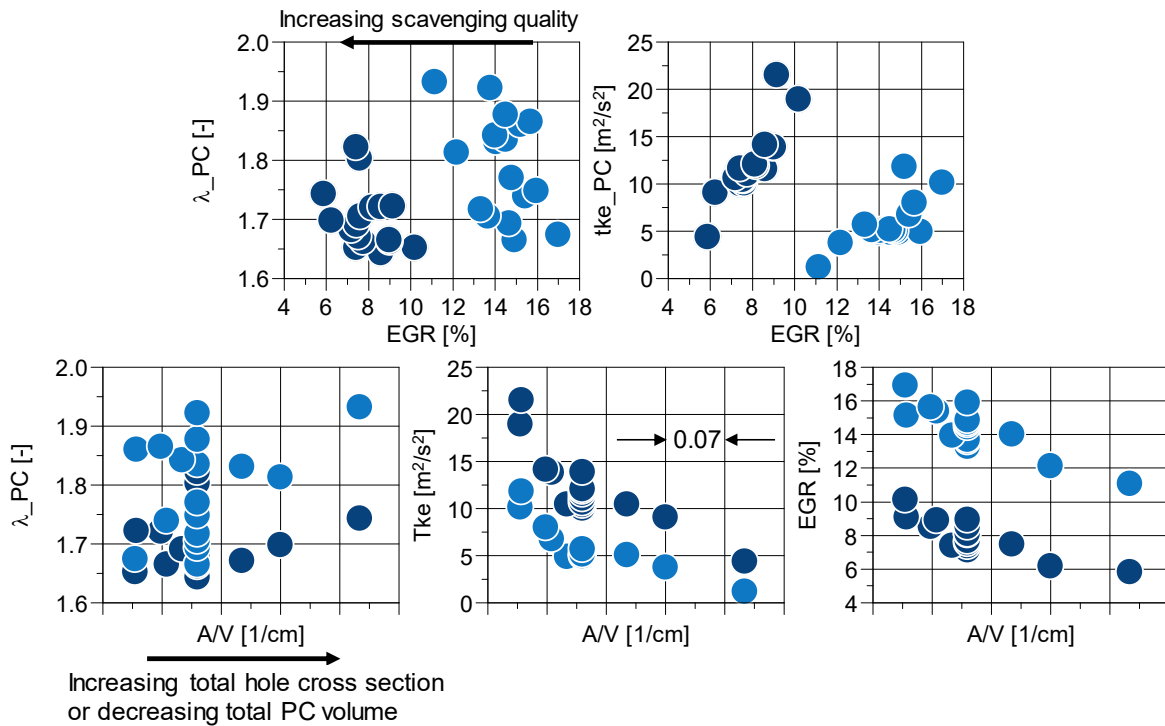
Figure 13: Correlations between geometries and several CFD results

Looking at the plots of A/V ratio, another major deduction of the results is that at the same A/V there is a very broad range of lambda in the pre-chamber achievable. This means, only by changing the orientation and angles of the pre-chamber geometries one can obtain very different results with respect to enrichment of the pre-chamber volume. The aforementioned influence of hole diameters and volume on tke and EGR can be observed in the A/V plots.

This A/V ratio is not only relating the geometrical design of the pre-chamber to EGR, tke, lambda at ignition timing, but it will particularly have an influence on the combustion. While the volume represents the magnitude of mixture energy stored into the pre-chamber and theoretically accessible for combustion, the flow cross section will be key to the magnitude the pressure of the pre-chamber will exceed the pressure in the main-chamber. Low A/V will lead to a higher pressure difference between pre-chamber and main chamber (Δp) and therefor further penetration of the jets into main chamber than a variant with higher A/V ratio. This jets can be either hot gases without a flame transported into main chamber, involving intermediate species (radicals) and products of combustion or flame jets, which involve an active flame within [1],[4].

3.2.5 CFD Ranking

Based on the results shown in Figure 13, a scoring model was used to rank the different pre-chamber variants among each other. This ranking was used to decide, which variants will be used for engine test-bench Different weightings for egr, lambda and tke were used for the scoring. After evaluating scorings for each considered weighting scenario in a crank angle region, which is relevant with respect to ignition timing four pre-chamber variants were chosen as illustrated in Figure 14.
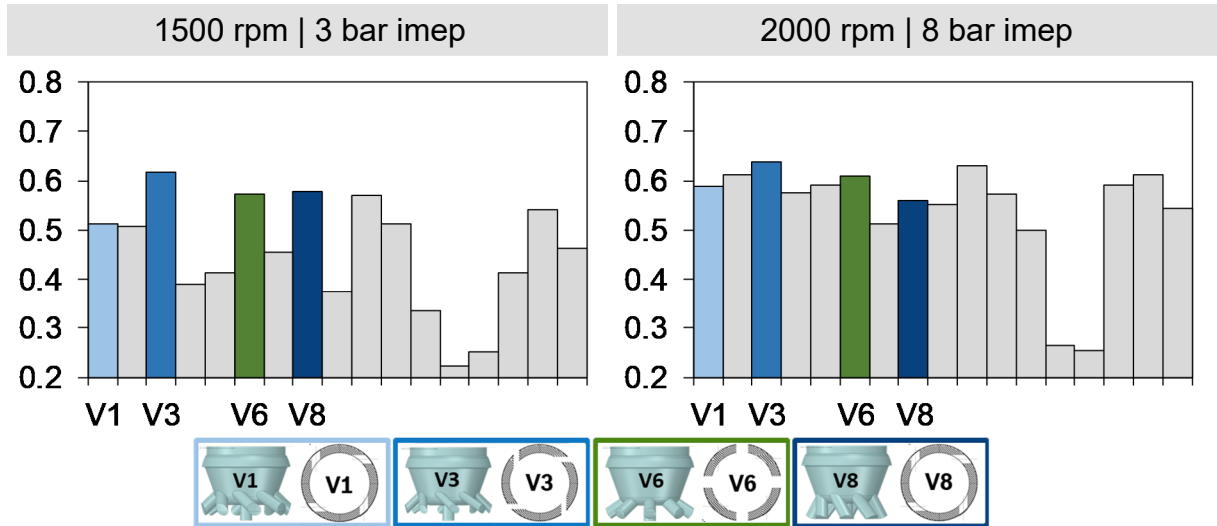
Figure 14: Scoring of all pre-chamber variants

The values on the y-axis represent the score with a minimum of 0 and a maximum of 1 based on the principle of the scoring model. Beneath the scoring diagrams the variants which were chosen for the engine test-bench are shown, which include variation of orientation of the radial holes on the horizontal plane (V6), change of the vertical inclination of the holes (V8) and change in A/V ratio (V3) compared to the reference variant (V1). The choice of V1, V3, V6 and V8 could unfortunately not been made solely based on the CFD results, but also on the availability of samples.

4 Engine Test-Bench

The CFD investigations were able to give an insight into the mixture preparation within the pre-chamber and enables the evaluation of the conditions at ignition timing. The question that arises from those simulations is: Is a ranking based on the CFD results with respect to EGR, tke and lambda within the pre-chamber at ignition timing matching the ranking that results from test-bench measurements? A standard spark plug (SP) was used for the reference measurements, thus all pre-chamber variants are compared to it.

The operation points, which were used for the engine test-bench measurements can be found in Table 2. Compared to the CFD simulations at the test-bench operation point OP1 was adapted slightly. The difference in engine speed and load was expected to be negligible. To understand the basic effects of changing from the standard to pre-chamber spark plug lambda, SOI, FHR50% position and ignition timing were varied for OP1 and OP2 with engine parameters kept constant. The valve timings where chosen based on preliminary investigations for homogenous lean combustion operation.

Table 2: Engine operation points

Operation Points	Engine Speed [rpm]	Imep [bar]	SOI1 [°CA b. ITDC]
OP1	1250	2.7	330
OP2	2000	8	330

4.1   Engine & Test Bench Setup

Investigations were performed on a multi-cylinder engine. The engine is equipped with direct fuel injection in central mounted position, which is preferable to analyze the effect of injection strategies on the pre-chamber ignition operation. To analyze combustion and gas exchange the engine is equipped with high pressure indication in the main chamber and low pressure indication within intake and exhaust ports. A high-energy ignition coil was applied on the engine. A more detailed overview on the engine and test-bench setup can be found in *Table 3.*

Table 3: Engine & test-bench data

Layout	2.0 L, inline four cylinder, turbo charged
Fuel injection	DI, central mount, MHI, solenoid @ 35 MPa
Compression ratio	9.8 (without pre-chamber)
Ignition Energy	~ 140 mJ
Oil & Coolant Temperature	90 °C
Fuel	RON 95

4.2   Results

Measurements were performed keeping all engine parameters constant at each operation point for each spark plug, like it was done in the CFD simulations. For all variants and the conventional spark plug lambda, SOI and FHR50 was varied. Under lean operation conditions in general the combustion is deteriorated, because additional to the residual gas the excess air increases the fraction of inert gas within the total mixture. This has an influence on both, a stable flame kernel development and the combustion speed. To investigate and evaluate whether or not the chosen passive pre-chamber spark plugs can enhance combustion and outperform the conventional spark plug will be part of the following section.

4.2.1 Lambda, SOI and FHR50% Variation

In *Figure 15* measurements at OP1 are illustrated. These measurements represent results at FHR50% = 6 ° position for the lambda and SOI variation. Injection timing for lambda and FHR50% variation was set to SOI = 330 °CA bITDC position
As can be seen, stable engine operation with pre-chamber spark plug variants is only possible within a very narrow lambda range, indicating no advantage over the conventional spark plug. Even though the chosen engine roughness limit for comparing lean limit performance was put to CoV ≤ 3 %, measurements above the CoV limit are also illustrated, when engine operation was possible. With the pre-chamber variants lean limit decreases by Δlambda of 0.3 compared to the SP.

Higher combustion stability of the SP is also indicated by later ignition timing which alludes to a faster combustion (mainly FHR00-10% phase). All spark plugs show comparable fuel consumption at lambda = 1 the isfc (indicated specific fuel consumption).
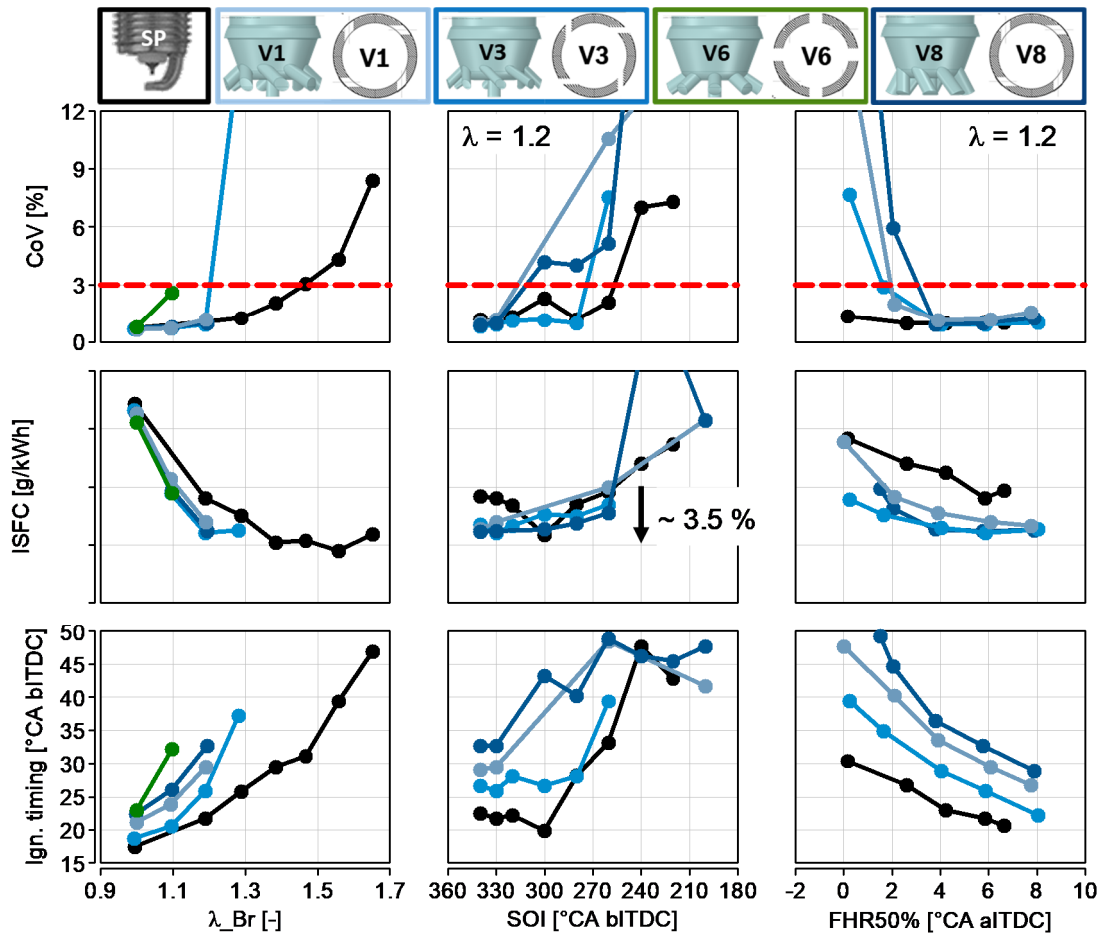
Figure 15: Comparison SP to pre-chamber, Lambda, SOI, FHR50 variation for OP1

However, under lean conditions an isfc advantage of the pre-chamber variants over the SP can be observed. The isfc advantage of the pre-chamber variants over the pre-chamber might indicate a correlation with the aforementioned lower combustion speeds. But this is not consistent, because V1 with slower combustion than V3 has higher isfc, though.

Anyway, the reason for the isfc advantage of the pre-chamber might be related to lower wall heat losses due to lower temperatures as a results of slower combustion especially in the first stage of combustion (FHR00-10%). Longer FHR00-10% durations on the other hand will lead to an increase of efficiency loss due to overall burn duration (dQ/dPhi).

The variant V6 shows the poorest overall performance. This is a very distinctive result, because this variant is amongst the top scoring variants shown in the CFD ranking plots shown in Figure 14. This already shows that the ranking which bases only on the ignition condition within the pre-chamber volume (EGR, tke, lambda) is not always sufficient to predict the performance of a pre-chamber spark plug.

Variations of SOI and FHR50% are illustrated at a lambda = 1.2, at which most of the pre-chamber variants are performing stable combustion.

The SOI variation shows that the pre-chamber variants are generally more sensitive with respect to the timing of the mixture preparation. The choice of SOI = 330 ° CA

bITDC proofs to be within the optimal range for the pre-chamber variants as well as for the conventional spark plug (SP). Comparing the pre-chamber variants among each other it can be stated, that the pre-chamber variant V3 shows both, a good lean limit, high robustness with SOI variation and high combustion speeds.
No significant difference between the spark plugs behavior with respect to optimal combustion phasing could observed.

In Figure 16 results at OP2 are illustrated, with FHR50% = 6 ° and SOI = 330 bITDC. Due to the higher load point all spark plugs show better lean limit performance or respectively higher combustion stability. Similarly as for OP1 the conventional spark plug is superior to the pre-chamber variants tested. The maximum achievable lambda difference between the conventional spark plug and pre-chamber is decreased from Δlambda = 0.3 for OP1 to Δlambda = 0.2 for OP2.
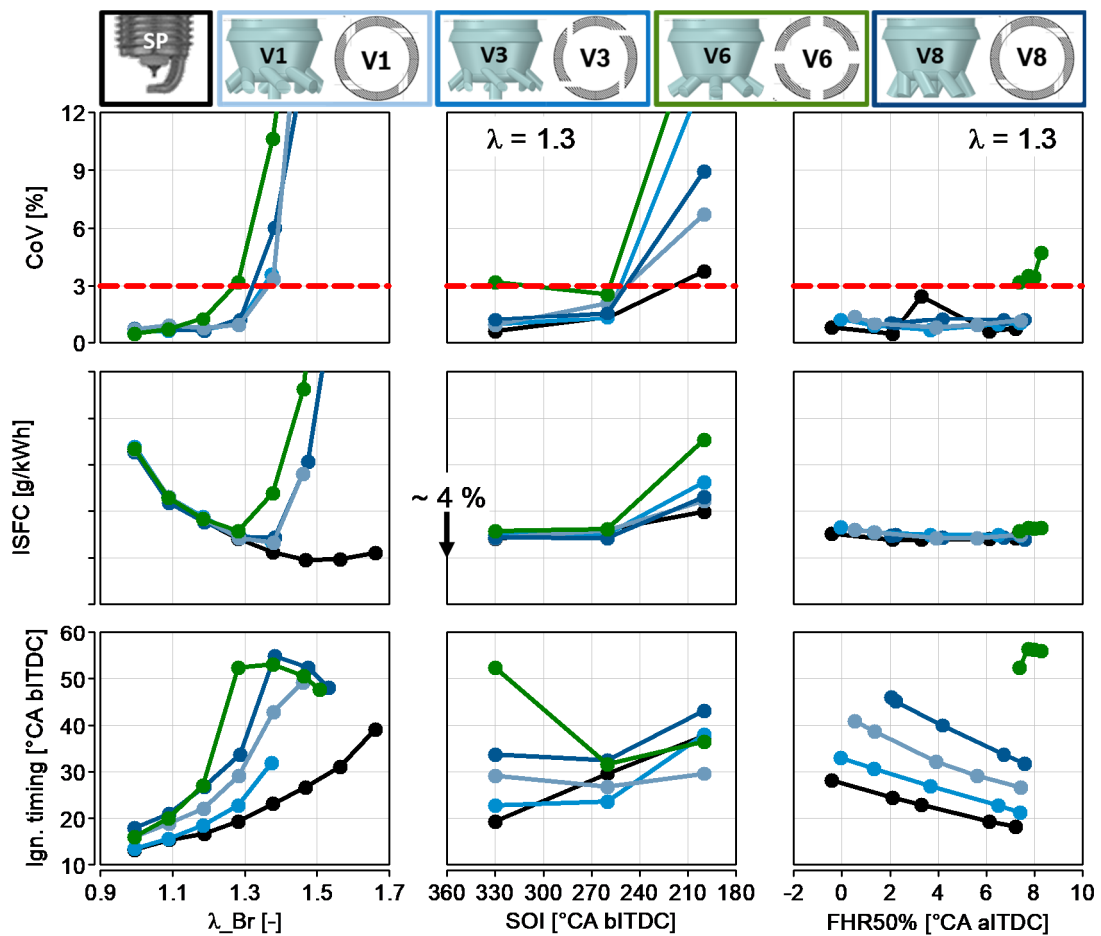
Figure 16: Comparison SP to pre-chamber, Lambda, SOI, FHR50 variation for OP2

The higher loads increase combustion stability within the main chamber in general due a higher volume specific chemically bound energy density of the mixture, higher temperatures and higher charge motion and therefor higher tke and better homogenization of the mixture at ignition relevant timings. This is valid for both, the pre-chamber spark-plug and the conventional spark plug. Therefor this will lead to a shorter overall combustion duration. With around a maximum fraction of 1% of total fuel captured in the pre-chamber at ITDC, the improved condition of the main chamber is therefor, leading to a decrease in FHR00-10 and FHR10-90 for both spark plug systems.

In consequence, this enables the conventional spark plug as well as the pre-chamber spark plugs to ignite at a later timing to achieve the same FHR50% position as for low loads. This, on the other hand, gives more time for the process of filling the pre-chamber with a richer gas mixture. For low loads overall combustion conditions deteriorate, therefor the pre-chamber must ignite earlier, as well as the conventional spark plug. However, if measures cannot be taken the passive pre-chamber will always have a leaner mixture. This leads to even longer combustion duration which leads to even earlier ignition timings, with even higher lambda. This process is amplified towards lower loads resulting in longer combustion durations and combustion instabilities. For example, in the above figure at lambda = 1.3 the ignition timing for variant V1 is at 30 °CA bITDC while ignition timing for SP is around 19 °CA bITDC to achieve the same FHR50%. The CFD for this operation point at 30 °CA bITDC predicts a lambda of around 1.8. Another good example of this phenomenon is the variant V6, which achieves poorest combustion stability. The variant cannot be operated at a combustion phasing earlier than FHR50% = 8 °CA aITDC for lambda = 1.3 at OP2. The other variants show a higher stability towards earlier ignition at OP2 than at OP1 (*Figure 15*). Early SOI timings show the advantage of combustion speed for the SP, while at later SOI V1 and V3 show slightly later ignition timings.

4.2.2   Comparison of Rankings

At this point the engine results are compared to the CFD results with respect to ranking among the pre-chamber variants. In fact, the ranking found at the engine-test bench differs partially significantly from that made based on the CFD results. This comparison is shown in Table 4. The test-bench ranking is based on lean limit level, CoV and combustion speed. The worst performing pre-chamber variant for both, OP1 and OP2 on the engine test-bench was found to be V6, which is, especially at OP2 the second best in the CFD ranking.

Table 4: Comparison of Rankigns

Operation Points	OP1 (1500/3i or 1250/3i)	OP2 (2000/8i)
CFD Ranking	V3, V8, V6, V1	V3, V6, V1, V8
Test-Bench Ranking	V3, V1, V8, V6	V3, V1, V8, V6

Furthermore, V1 shows acceptable matching at high load and rather bad matching at low load.

These results indicate, that differences among the pre-chamber variants with respect to residual gas mass fraction levels based on the CFD results are not having a significant impact on the combustion. This is clearly shown by the fact that variant V3, which has the highest residual gas mass fraction compared to the other three variants, is the best performing pre-chamber spark plug for both operation points.

Based on this comparison it becomes clear only using EGR, tke and lambda values to compare pre-chamber variants among each other is not sufficient. It shows that the quality of the combustion phase cannot be predicted solely be the mixture formation-only simulation.

5   3D-CFD Combustion Simulation

A 3D-CFD simulation with a focus on charge motion and mixture formation has been carried out. Based on the simulation results four samples were manufactured, which

were then tested on the test bench described above. The results is, that the CFD-simulation-based performance ranking of the different spark plugs variants does not coincide with that from the test bench. Thus with a subsequent CFD combustion simulation, the previous ranking is to be verified.

For this purpose, the calculation models of the engine including boundary conditions from chapter 3 are used. In particular constant adiabatic wall temperatures, pressure boundary conditions at the inlet and outlet ports as well as the spray conditions for gasoline injection from chapter 3 were assumed.

For a better comparability with the experimental results, the lambda and the ignition timing (Table 5) for the individual variants are used for the 3D CFD combustion simulation.

Table 5: Lambda and Start of ignition at OP 1 and OP 2

Variant	Variant 1 @OP1	Variant 3 @OP1	Variant 6 @OP1	Variant 8 @OP1
Lambda	1,3	1,3	1,1	1,3
Start of ignition [° CA]	673	680	669	678
Variant	Variant 1 @OP2	Variant 3 @OP2	Variant 6 @OP2	Variant 8 @OP2
Lambda	1,5	1,5	1,3	1,5
Start of ignition [° CA]	680	684	675	671

5.1 Validation with Testing

The combustion simulation starts when the exhaust port is open and stops shortly before the exhaust port opens again after combustion. EZFM 3-Z is used as combustion model and the turbulence model k-ζ-f being an enhancement of the RANS k-ε model, is applied.

The low load point at 1500 rpm and 3 bar indicated mean effective pressure (IMEP) (OP1) is calculated, as well as the load point at 2000 rpm and 8 bar IMEP (OP2).

5.1.1 Validation at OP 1

Figure 17 shows the pressure curve of the individual variants calculated with CFD (solid lines) in comparison to the test bench results (dotted lines). The black and grey colors represent the pressure of variant 1 on the test bench. Here the maximum, the minimum and the average pressure curves are shown. The pressure difference between measured maximum and minimum peak pressure is around 12 bar.
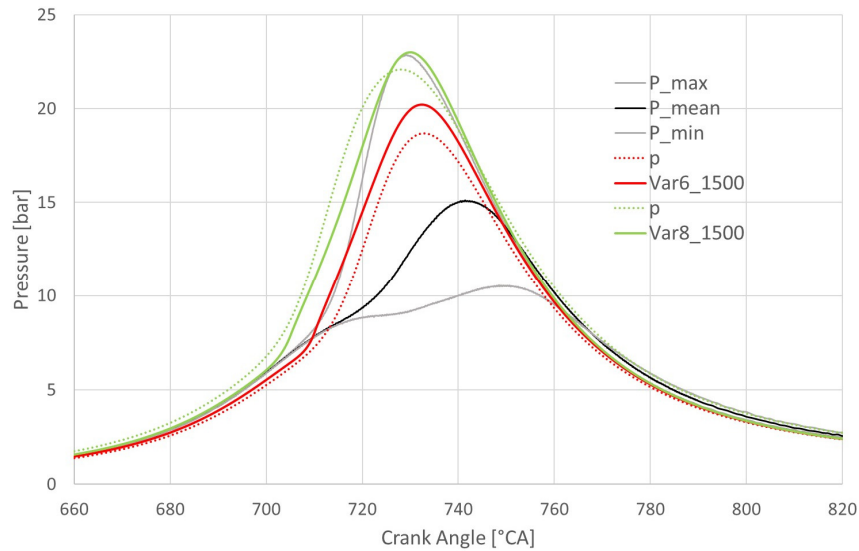
Figure 17: Comparison of CFD Results with OP 1 at test bench

Thereby a good agreement of the averaged pressure curves from simulation and measurement can be observed. The aim of the validation is to show that it is possible to achieve comparable results with the same boundary conditions and results like lambda and ignition time from the test bench. For this purpose, the combustion parameters were modified. The validation at the operating point OP 1 has succeeded very well, since the combustion parameters remained identical in the variants of the same lambda.

5.1.2   Validation at OP 2

Figure 18 shows the validation at the operating point OP 2. Again, the maximum, minimum and average pressure curves of variant 1 is shown. At this Operating point the variance of pressure between maximum and minimum is lower than at OP 1. It is worth noting that all variants match the test bench results very well. Only the variant 3 exhibits a slightly larger deviation. For this deviation an in-depth explanation is given in the section 5.2.2. All variants with the same lambda can be run with the same combustion parameters.
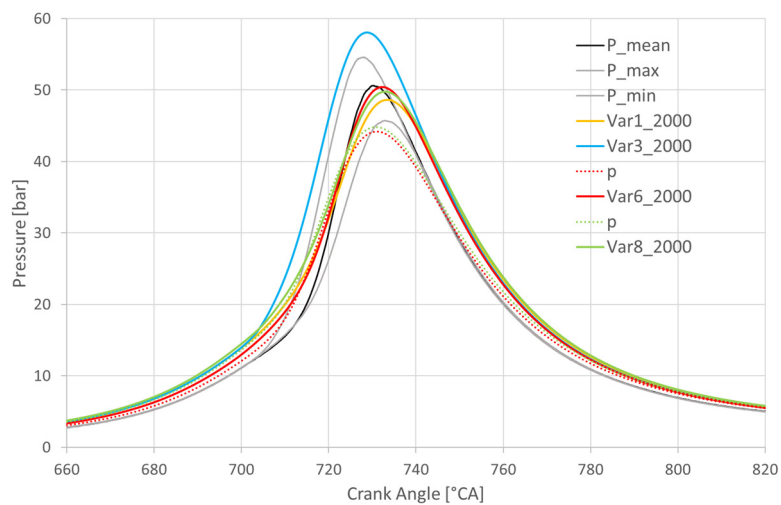
Figure 18: Comparison of CFD results with OP 2 at test bench

5.2   Combustion Simulation results

5.2.1 OP 1
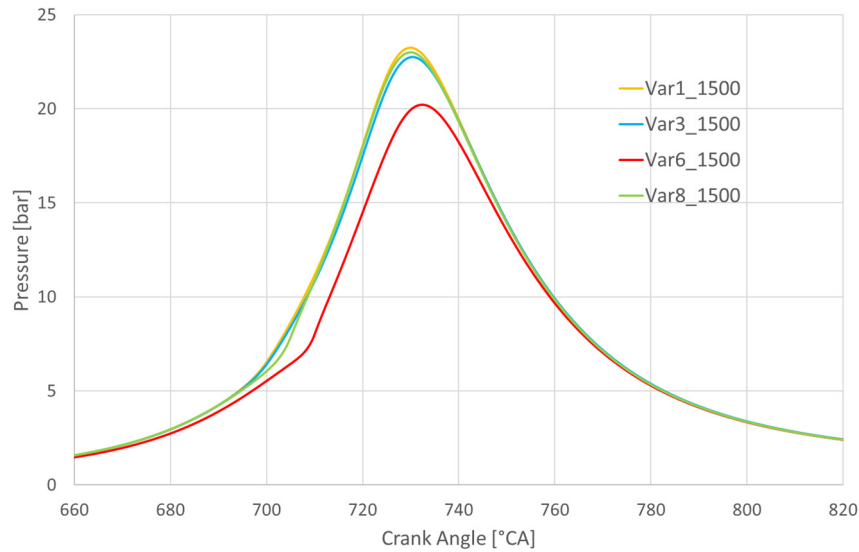
Figure 19: Peak pressure all variants at OP 1

Figure 19 shows the pressure curve of the 4 variants at 1500 rpm at 3 bar IMEP (OP 1). It can be clearly seen that the variant 6 deviates strongly from the other variants. Table 5 shows that it is not possible for the variant 6 to perform at the comparable level with the remaining variants at this operating point with the same lambda, even at much earlier ignition times.

When, as described in chapter 3, the flow in the pre-chamber is analyzed, it can be seen that the flow direction in variant 6 is opposite to the direction of the combustion chamber (Figure 21) at the time of ignition. In variant 1, instead the flow is guided upwards on the inner wall by the tangential bores and, at ignition, the flow direction is pointing from the middle of the pre-chamber towards the combustion chamber (Figure 20).

This is the reason why the combustion predominantly moves into this direction. Figure 20 and Figure 21 show the flame front (Fluctuation Intensity) as it behaves as combustion progresses. The three related images are each taken at a distance of 1 ° CA and start with the left picture shortly after the ignition. In Figure 20 it can be seen over time that the flame front moves within 2 ° KW clearly towards the combustion chamber.
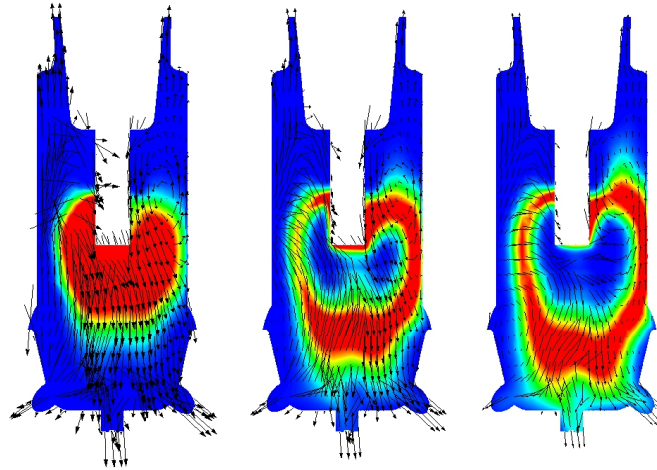
Figure 20: Fluctuation Intensity and velocity vector from Variant 1
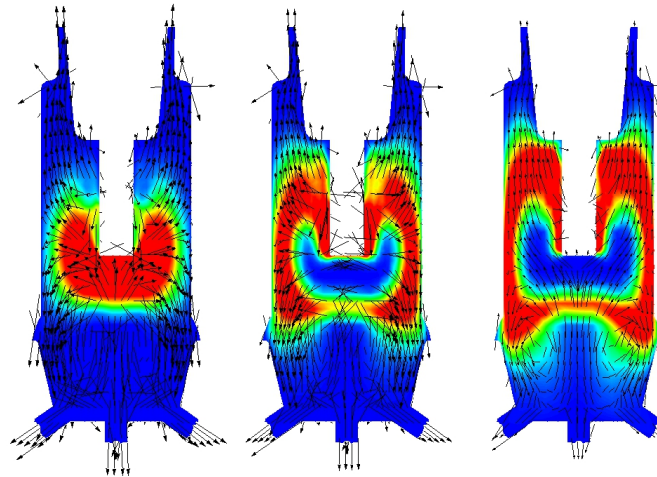
Figure 21: Fluctuation Intensity and velocity vector from Variant 6

In variant 6 (Figure 21) the flame front moves in the opposite direction during the same period (2 ° CA) of time. This flow behavior is graphically underplayed by the velocity vectors. Figure 22 shows the lambda distribution of variants 1 and 6 including the velocity vectors. Please note, that the averaged lambda values of 1.1 and 1.3 are set for the calculation of variant 6 and variant 1 at OP 1, respectively (see Table 5). Consequently, even in variant 1, a significantly higher lambda can be seen in the upper part of the pre-chamber spark plug. But this is not critical for this variant as the combustion moves into the non-lean mixture. Variant 6 shows in Figure 22 a significantly lower peak pressure curve and therefore a much slower combustion even though it has a lower lambda and an earlier ignition timing (see Table 5). It can be seen from the right-hand image of Figure 22 that the combustion moves in the direction of a lean mixture and is therefore also significantly slowed down. Therefore, it is also understandable that this variant cannot perform well with the same lambda at the operating points OP 1 and OP 2 as the other variants.
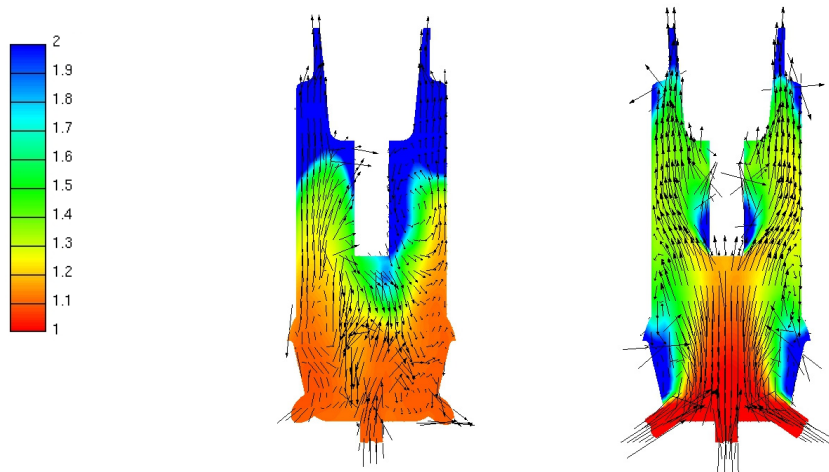
Figure 22: Lambda distribution Variant 1 and Variant 6

5.2.2 OP 2
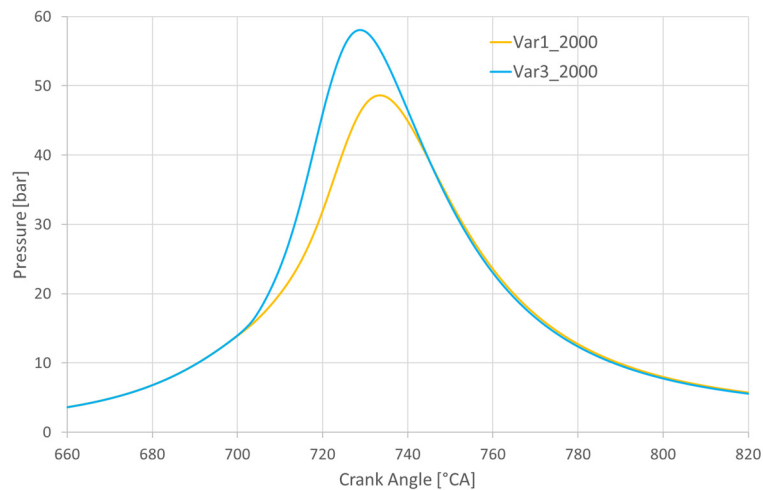
Figure 23: Peak Pressure of Variant 1 and 3 at OP 2

At operating point 2000 rpm and 8 bar IMEP, the variant 3 compared to variant 1 obviously has a much higher peak pressure and an earlier MFB50 (Figure 23). Despite the same lambda and even later ignition (about 5 ° CA) the variant 3 shows the much faster combustion. Compared to the operating point OP 1 (Figure 24) variant 1 seems to burns slightly faster. Therefore, it is quite surprising how strong the difference in the operating point with the higher load between these variants becomes. Both variants have the same geometric design of the pre-chamber spark plug. Both variants have the same number of holes and both have the same structure i.e. 8 tangential and one central hole. The only difference between these two variants is the diameter of the holes and thus the ratio of pre-chamber volume to the sum all holes' cross sections (V/A). By changing this ratio, the pressure in the pre-chamber increases significantly to the pressure values in the main combustion chamber during combustion (Figure 25).

This significant increase of the pre-chamber pressure causes a faster flame propagation in and a deeper flame penetration of the main combustion chamber and thus results in a significantly faster combustion in the main chamber.
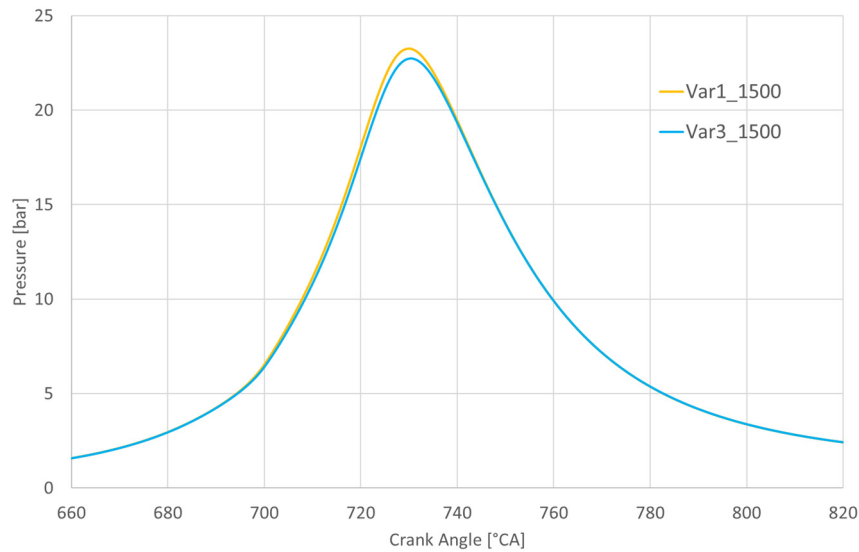
Figure 24: Peak Pressure of Variant 1 and 3 at OP 1

One observes that the penetration length of the torch of the variant 3 is much longer than from Variant 1. At the operating point OP 1, this difference is significantly less which is reflected in the nearly coinciding pressure curve (Figure 24). However, since variant 3 is ignited 7 ° CA later a faster combustion process has to be related with this variant.
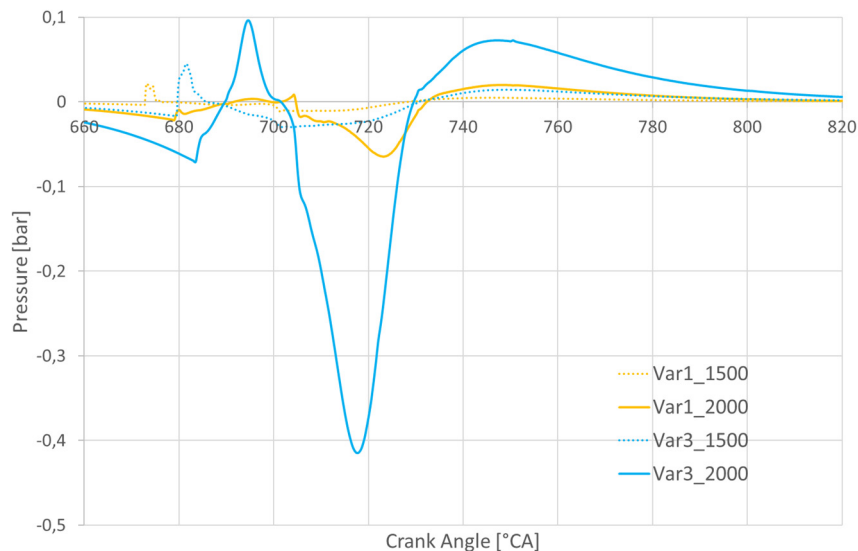
Figure 25: Pressure difference between pre-chamber spark plug and main chamber

5.3   Comparison of all results

For the OP1 the results can be rated by means of Figure 19. Variant 6 is easy to define on last place but all other variants are very close together. Table 5 shows the difference

in Ignition timing and therefor variant 3 is the best because of the latest time. Between variant 8 and 1 the pressure is slightly higher for variant 1, but on the other hand variant 8 will be ignited 5° CA later. So the ranking of OP 1 is listed in Table 6.

At OP 2 (Figure 18) the ranking for variant 3 is because of the very fast combustion and the latest time of ignition easy to define. All other variants are very similar in peak pressure. For variant 6 because of the weakness oi ignite higher lambda it is obviously to rank variant 6 on the last place. The ranking for variant 1 and 8 results from the ignition timing. Table 5 shows that variant 1 can be ignited 9° CA later as variant 8, therefor the ranking is defines as shown in the Table 6.

Table 6: Ranking of the Variants

Operation Points	OP1 (1500/3i)	OP2 (2000/8i)
CFD Ranking	V3, V8, V6, V1	V3, V6, V1, V8
Test-Bench Ranking	V3, V1, V8, V6	V3, V1, V8, V6
CFD Combustion Ranking	V3, V8, V1, V6	V3, V1, V8, V6

6   Summary and Outlook

To evaluate the potential of the passive pre-chamber under homogeneous lean conditions, various pre-chamber spark plug geometries were designed on basis of a reference geometry. These geometries were then implemented into a 3D CFD in-cylinder model. The influence of the geometrical parameters of the pre-chamber spark plug on scavenging, turbulence generation and air-fuel mixture supply in the pre-chamber volume at two operation points were investigated. The chosen operation points contain of a low engine speed low load operation point (OP1) and one operation point at high part-load at mid-range engine speed (OP2).

To compare the pre-chamber variants amongst each other for both operation points EGR, tke and equivalence ratio were integrated and averaged within the pre-chamber volume at 25 °CA before ignition top dead center (bITDC) to represent ignition conditions. Based on these values correlations among EGR, tke and lambda on the hand and the A/V ratios of the pre-chamber geometries to EGR, tke and lambda on the other hand were examined and explained. Hereafter, a ranking based on those CFD results including different weighting scenarios using EGR, tke and equivalence ratio values was derived. Four variants were chosen to be evaluated on the test-bench on a multi-cylinder engine against a conventional spark plug.

For OP1 and OP2 and an engine roughness limit of CoV ≤ 3 % the highest lambda is achieved with the conventional spark plug. However, at the low load operation point (OP1) under lean conditions the passive pre-chamber spark plug variants show a fuel consumption advantage over the conventional spark plug. At isfc optimal engine operation the combustion speeds of the pre-chamber variants are lower than for the conventional spark plug.

On basis of these engine test-bench results a ranking was derived based on the performances of the pre-chamber using engine roughness/stability and maximum achievable lean limit as criteria.

The comparison between the CFD rankings which so far were solely made based on evaluating the condition in the pre-chamber at ignition timing (without combustion) and the engine test-bench ranking of the pre-chamber variants displayed significant discrepancies. To understand this divergence 3D-CFD combustion simulations were conducted additionally to the aforementioned simulations of gas exchange and mixture preparation.

In order to verify the results of the test bench or the differences between the two results, the 3D-CFD combustion simulation was performed. The combustion simulation was validated with the measurement results. The same combustion parameters were used for the different variants with respect to the same operating points as long as they had the same lambda. Variant 6 deviated significantly from the other variants. This difference could also be explained on the basis of the combustion results, furthermore the difference between variants 1 and 3 is clarified with the A/V ratio.

The influence of the ratio of area to volume (A/V) is decisive for the combustion result. As a result of the combustion simulation a new ranking for the pre-chamber variants was made. This new ranking matched better to the ranking from the engine test-bench than the original CFD ranking which was derived from simulations without combustion considered.

Due to the fact that hardware test and investigations are expensive 3D-CFD combustion simulation is an attractive alternative to develop pre-chamber spark plugs.

In fact, this study showed that for CFD support of pre-chamber spark plug design development combustion simulation is necessary.

Literatur

[1] M. Blankmeister, W. Niessner, M. Günther, R. Tröger, C. Grünig, Optimization of Passive Chamber Spark Plugs to Improve Lean Mixture Operation in Gas Engines, 2nd International Conference on Ignition Systems for Gasoline Engines 2014

[2] W. Niessner, A. Schenk, A. Ernst, U. Sander, Zündkerze für eine mit Gas betriebene Brennkraftmaschine, 2009 Patent DE 102010004851 B4

[3] C. Heinz, S. Kammerstätter, T. Sattelmayer, Vorkammerzündkonzepte für stationär betriebene Großgasmotoren, MTZ - Motortechnische Zeitschrift Issue 1/2012

[4] S. Biswas, S. Tanvir, H. Wang, L. Qiao, On ignition mechanisms of premixed CH4/air and H2/air using a hot turbulent jet generated by pre-chamber combustion, Applied Thermal Engineering 106 (2016) 925–937

3.4 Numerical Investigation of Spark Ignition Processes in Natural Gas Engines with the Advanced Spark Ignition Model

Gunesh Tallu, Michael Frambourg, Matthieu Prouvier, Michael Weißner, Axel Winkler

Abstract

Spark ignition in an internal combustion engine is a complex physical phenomenon, which takes place in a very short time of a few milliseconds but influences the whole succeeding combustion process. A detailed understanding of this process can be gained with the help of experiments focused on ignition or its detailed modelling in Three Dimensional Computational Fluid Dynamics (3D CFD) simulations. A novel modelling approach for spark ignition was presented during 3rd International IAV conference "Ignition Systems for Gasoline Engines" in 2016.

In the extension of the previous study, the present publication focusses on the application of the new model for a monovalent CNG engine with induced ignition. This engine is based on the Volkswagen 4-Cylinder 2.0 litre TDI® Diesel engine converted to operate with homogeneously premixed natural gas air mixture ignited with a serial production spark plug. The engine is operated on the engine test bench at different predefined operating points within the EU funded project GasOn (project # 652816, Horizon2020).

Prior to the spark ignition investigation of this engine, different detailed kinetic mechanisms for natural gas combustion are studied. These mechanisms are analysed for their behaviour in ignition delay and laminar flame speed simulations. From this analysis, suitability of each mechanism for a specific application is derived. Based on this study a mechanism for the current application is chosen. This mechanism is then coupled with the advanced spark ignition model to analyse the spark ignition processes in the CNG engine at different operating points varying only in the relative air-fuel ratio. Good agreement is observed between the simulation results and experimental data.

Kurzfassung

Die Zündung in einem Verbrennungsmotor ist ein komplexes physikalisches Phänomen, welches innerhalb weniger Millisekunden erfolgt aber das gesamte sich

anschließende Verbrennungsverhalten beeinflusst. Ein detailliertes Verständnis dieses Prozesses kann mit Hilfe zündungsspezifischer Experimente und/oder detaillierter Modellierung innerhalb dreidimensionaler Strömungssimulationen gewonnen werden. Ein neuentwickelter Modellierungsansatz für den Zündprozess wurde während der 3 Internationalen IAV-Tagung "Zündsysteme für Ottomotoren" in 2016 erstmalig vorgestellt.

Als Erweiterung zu der vorherigen Studie wird in der vorliegenden Veröffentlichung als Anwendungsfall für das neue Zündmodell ein monovalenter CNG-Motor mit Fremdzündung behandelt. Der Motor basiert auf dem 4-Zylinder Volkswagen 2.0 Liter TDI® Dieselmotor, der nach einer Umrüstung mit einer homogenen Erdgas-Luft Mischung betrieben und das Gemisch mit einer Serien-Zündkerze gezündet wird. Im Rahmen des EU-Projektes GasOn (Projekt-Nr.: 652816, Horizon2020) wird der Motor am Motorprüfstand bei unterschiedlichen vordefinierten Betriebspunkten gefahren.

Im Vorfeld der Analyse der Zündung des Motors werden unterschiedliche detaillierte Reaktionsmechanismen für Erdgas betrachtet. Die Mechanismen werden hinsichtlich Zündverzug und laminarer Flammengeschwindigkeit evaluiert. Auf dieser Basis wird ein Mechanismus für die aktuelle Applikation ausgewählt. Dieser Mechanismus wird mit dem neuartigen Zündmodell gekoppelt, um den Zündprozess im Versuchsträger bei unterschiedlichen Betriebspunkten zu untersuchen. Für eine Lambda-Variation wird eine gute Übereinstimmung zwischen Messung und Simulation erreicht.

1 Introduction

1.1 Motivation for Monovalent CNG Engines

Increasing demand for lowering CO_2 emissions has led to the need of improved technologies for the automotive sector. Besides the new electric mobility solutions, which will become more present on the market in the future, the internal combustion engines will remain the most important part of the powertrain for next decades. Compressed Natural Gas (CNG) has two main advantages of high knock resistance and low CO_2 emissions. High knock resistance is not being exploited in the state of the art bivalent CNG engines to the fullest. Designing an engine, mainly for CNG, with higher compression ratio and an improved ignition system will lead to a significant CO_2 reduction of up to 25% compared to a diesel engine. Especially for lean conditions, besides other factors, the ignition is a key challenge to realize a stable and complete combustion. Therefore, there is a need to investigate the ignition process in detail.

1.2 Need of Ignition Modelling

For spark ignited (SI) engines, the capability of emission reduction lies on a number of factors. One of them is the successful ignition of the charge in a wide range of operating conditions. The spark ignition is a complex physical phenomenon which takes place in a very short time (milliseconds), but influences the whole succeeding combustion process. A detailed understanding of this process can be gained with

the help of ignition focused experiments or detailed modelling in Three Dimensional Computational Fluid Dynamics (3D CFD) simulations.

In state of the art 3D CFD combustion simulations, ignition is achieved through the introduction of a substantial amount of energy at the predefined spark plug position at a given point in time (spark ignition timing). It is considered that the ignition is always successful and, after reaching a predefined size, the flame kernel is converted into a fully propagating flame. This approach is simple but not sufficient to correctly reproduce physical effects of the flow field and mixture conditions in the near spark plug area on the inflammation phenomena and subsequent flame propagation process. Hence, detailed 3D CFD modelling based on the physics of the ignition phenomena taking place over the spark duration is required.

Details on the development of the novel modelling approach for spark ignition can be found in [1]. This model is summed up here in Section 2. In the extension of the previous study, the presented model is here applied for the analysis of a spark plug ignited natural gas engine.

2 Advanced Spark Ignition Model

An overview of the spark ignition phenomenon is described in short. The spark ignition phenomenon takes place in three phases: breakdown, arc discharge and glow discharge. These are utilised to characterise any type of coil ignition system. Changes in voltage and current over the spark duration signify these three phases. In the breakdown phase, lasting nanoseconds, large rise in the voltage in very short time is seen. Here, the initial electrical contact between the electrodes takes place. In the arc discharge phase, drop in the current and voltage is observed due to the arcing between the electrodes. Finally, in the glow discharge phase, visual glow is seen with a drop in current, whereas a rise in the voltage is observed. In these three phases, inflammation takes place at different stages. This starts from the plasma formation and its expansion in the breakdown phase. Subsequently, with the exchange of initial radicals of C, H, O and N between the cooling plasma and the surrounding, initial combustion reactions are started. Chemical energy support from these reactions increases gradually, which is termed as flame kernel, and finally it should be sufficient enough to cater to the turbulence in the surrounding. After the spark discharge duration, the flame kernel then converts into a fully propagating turbulent flame. [2]

The advanced spark ignition model numerically describes the above stated spark ignition phenomenon in 3D CFD simulations. The model can be sub-divided into three different parts. They are flame kernel initialisation, flame kernel growth and transfer to turbulent combustion model. In the first sub-model, effects of discharge of breakdown energy, plasma formation and expansion are modelled. Depending upon the breakdown energy from the ignition coil, the relative air-fuel ratio (λ) in the surrounding and the plasma temperature, the initial flame kernel size at the time of spark ignition is determined. This flame kernel is represented with Lagrangian marker particles between the spark plug electrodes. Throughout the application of the model, this approach is utilised to capture the interaction between the flow field in the surrounding and the flame kernel.

In the next part of the model, increased contribution of the flame kernel in the form of chemical energy is considered and the change in the size of the flame kernel over the arc discharge and glow discharge duration is computed. For this purpose, the spark discharge power, the changes in the flame kernel specific heat, the changes in the pressure and the specific heat of the surrounding are accounted for the calculation of the chemical source term in the mass and the energy conservation equations. Closure of these equations is achieved with the help of the flame kernel speed model. This model comprises of laminar flame speed, velocity contribution of the plasma and a correlation between laminar and turbulent flame speed as per Herweg et al. in [3].

Before the initial size of the fully propagating flame is given as an output from the advanced spark ignition model to the level-set G-equation turbulent combustion model, few conditions are checked. The critical flame kernel radius, which caters mainly as the least progress parameter for the flame kernel, is calculated throughout the spark discharge duration. This parameter directly correlates growth of the flame kernel with mixture conditions and turbulence in the surrounding flow field. Another parameter is the flame kernel movement, which considers only the effect of turbulence in the flow field on the flame kernel disposition. Over the spark discharge duration, if the flame kernel movement exceeds a predefined experimental value then the spark ignition model can predict an event of restrike. After successful completion of these two conditions, transfer from the spark ignition model to the turbulent combustion model takes place.

To consider the effects of detailed chemical kinetics on the flame kernel growth, the specific heat capacity of the flame kernel and the laminar flame speed are calculated in advance in form of tables with different detailed chemical kinetic mechanisms at different mixture conditions (varying in λ, pressure, temperature and exhaust gas recirculation ratio (ψ)). These mixture conditions are studied before hand from the 3D CFD engine simulations. Then the pre-calculated tables are coupled with the spark ignition model to read the values of these properties for each cell in the flame kernel as per its conditions. Study and selection of the detailed chemical kinetic mechanism for this engine case is discussed in the next section.

3 Study of Detailed Mechanisms

Study of different detailed mechanisms for their individual behaviour in terms of ignition delay and laminar flame speed are presented in this section. For this purpose, suitable experiments of ignition delay and laminar flame speed are simulated with 0D and 1D chemistry solvers. Rather than selecting a mechanism suitable for the application, mechanisms are at first analysed for their individual advantages and drawbacks.

The CNG utilised for the investigations at the engine test bench is a typical H-Gas, which includes methane up to 90%. Therefore, in all the simulations, CNG is represented by the properties of methane. Three different detailed kinetic mechanisms for methane or natural gas combustion are considered for this study. Table 1 lists these mechanisms with their individual application range of pressure, temperature and equivalence ratio (ϕ). First of them, MFC, is the mechanism developed by Reaction Design (Ansys Inc.) within the Model Fuel Consortium. This

mechanism is mainly developed for combustion of C_1-C_5 hydrocarbons and is validated extensively for its application range. The application range is wider compared to current application, with the widest temperature applicability amongst the three mechanisms. GRI, is a well known mechanism for natural gas combustion, developed by Gas Research Institute of University of California, Berkley. The widest application range amongst the three mechanisms over ϕ is observed for this mechanism. Lastly, a mechanism from chemistry solution experts from Sweden, LOGE AB developed for combustion of C_1-C_5 hydrocarbons is considered in this study. This mechanism can be applied over the widest pressure range.[4], [5], [6]

Table 1: Application range of detailed chemical kinetic mechanisms [4], [5], [6]

Mechanism	Species	Reactions	Application Range		
			Temperature [K]	ϕ [-]	Pressure [bar]
MFC [4]	528	3214	298 - 1800	0.3 - 4.0	0.6 - 60.0
GRI [5]	53	350	1000 - 2500	0.1 - 5.0	0.1 - 20.0
LOGE [6]	362	3449	600 - 1400	0.1 - 3.0	1.0 - 120.0

3.1 Ignition Delay Time

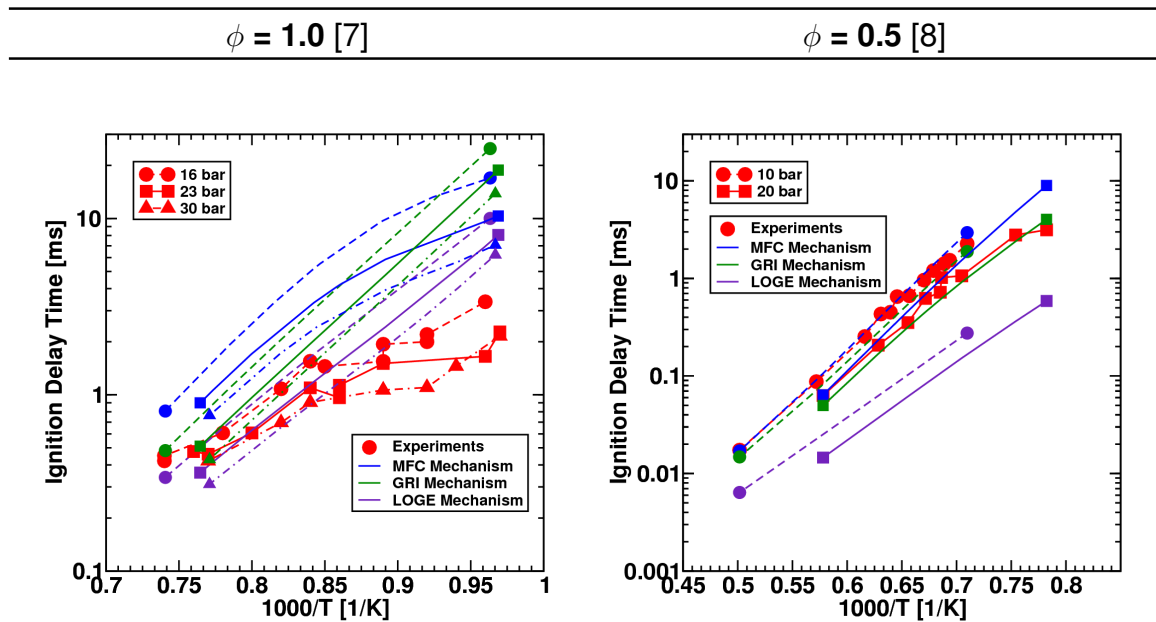*Figure 1: Comparison of detailed chemical kinetic mechanisms for ignition delay time against experiments in [7] (left) and [8] (right)*

First of all, a comparison of the simulation results for ignition delay time with the three mechanisms is presented in Figure 1 in the form of ignition delay diagram. Here, as per the current application, two different experiments for methane by Huang et al. [7]

(Figure 1, left) at stoichiometric conditions and Zhang et al. [8] (Figure 1, right) at $\phi =$ 0.5 are simulated. For both set of results, it can be seen that, as the pressure increases, ignition delay time decreases. With the change in temperature from 1000 K to 2000 K, ignition delay decreases. These fundamental behaviours are reproduced by all the three mechanisms. Further, for the stoichiometric conditions, a typical negative temperature behaviour in the temperature range between 1000 K and 1200 K is observed. With the comparison of simulation results, at three pressure levels, only the MFC mechanism could reproduce this behaviour but with substantial difference against the experimental data. This behaviour at relatively higher temperature needs further experimental investigation. Overall in the higher temperature region, experimental results are reproduced by the simulation with MFC and GRI mechanisms, whereas at relatively lower temperature, simulation results with LOGE mechanism are closer to the experimental data. The results for lean conditions show that, for both pressure levels at higher temperature, simulation results with MFC and GRI mechanisms are in good accordance with the experimental data. For intermediate temperature range, difference between simulation and experiments is least for GRI mechanism.

3.2 Laminar Flame Speed

A comparison between simulation results and experimental data for laminar flame speed is presented in Figure 2. Here, the behaviour of the laminar fame speed against variation in pressure (Figure 2, Left) and variation in ϕ (Figure 2, Right) from Elia et al. in [9] is studied. With increase in pressure, decrease in the laminar flame speed is observed and change in the equivalence ratio away from stoichiometric condition results in decrease in the laminar flame speed. These behaviours are reproduced by all the three mechanisms. Analysing the results for the variation in pressure, it is observed that, over the whole range of pressure variation, simulation results with LOGE and GRI mechanisms are in good accordance with the experimental results. With variation in ϕ, it can be seen that, at and near stoichiometric conditions, the experimental data is reproduced with good accuracy by the simulation results of GRI and MFC mechanisms. However, as the conditions diverge from this equivalence ratio area, simulation results with LOGE mechanism are able to reproduce the experimental data accurately.

Summarizing these results, it can be seen that, each mechanism has its own forte in different areas. MFC mechanism is found suitable for reproduction of ignition delay results at higher temperature range and lean mixtures as well as the NTC behaviour, whereas it can also reproduce the laminar flame speed near stoichiometric mixture composition and at lower pressures. GRI mechanism is suitable at the higher pressure conditions for both ignition delay time and laminar flame speed. LOGE mechanism is rather applicable in intermediate temperature and pressure range for ignition delay time simulations and can be used in rich and lean mixture conditions for laminar flame speed simulations. Therefore, based on these findings, three mechanisms are further evaluated for the suitability of their results in direct coupling with the advanced spark ignition model in 3D CFD simulations and these results are presented in section 4.4.

Temp. = 470 K, ϕ = 1.0 [9]   **Pressure = 1 bar, Temp. = 298 K** [9]
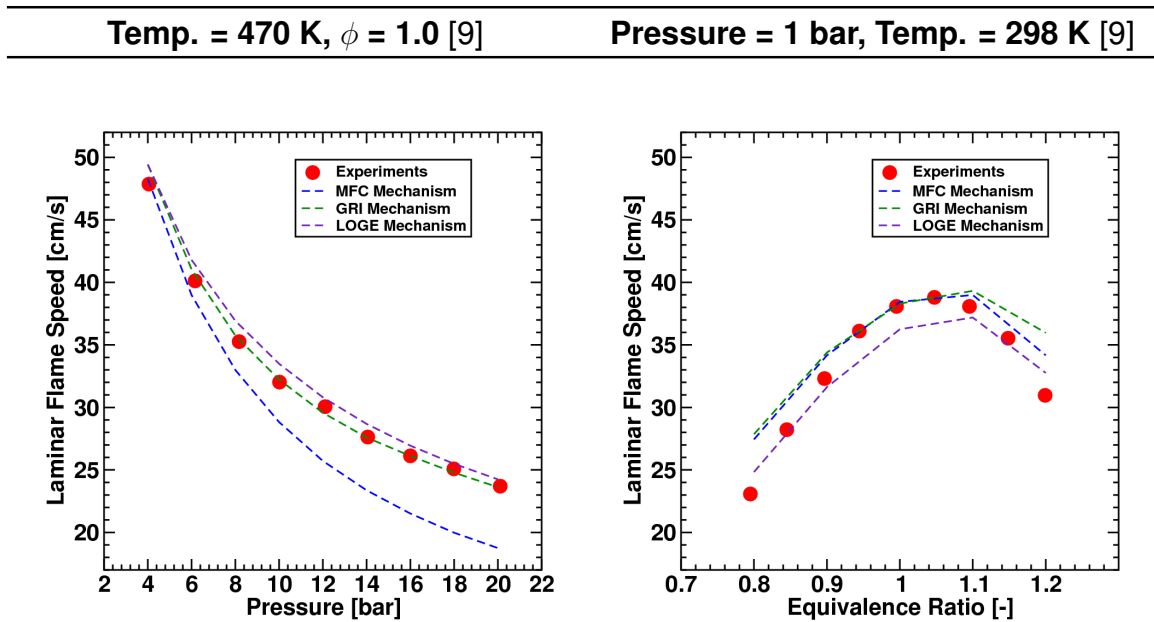
Figure 2: Comparison of detailed chemical kinetic mechanisms for laminar flame speed against experiments in [9] for pressure variation (left) and variation in equivalence ratio (right)

4 Model Application on Engine Case

4.1 Engine Details
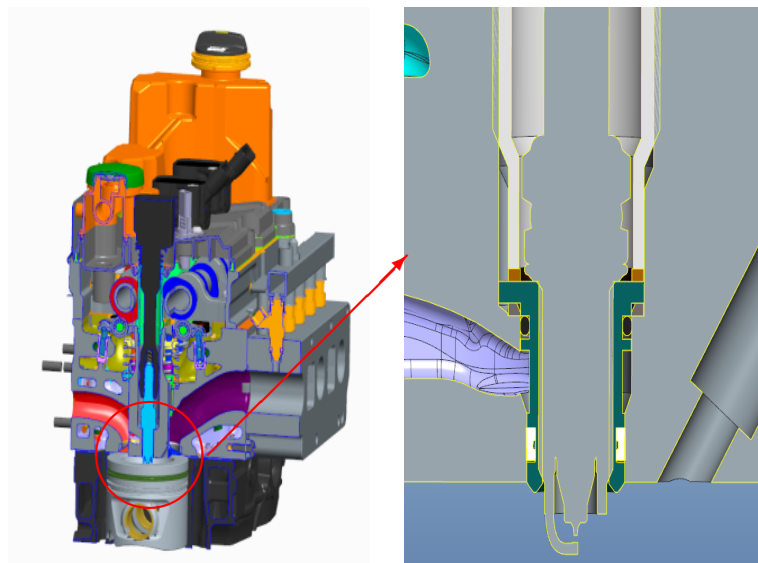
Figure 3: Depiction of the engine with central position of spark plug

As stated in Section 1, a monovalent CNG engine can exploit the property of the high knock resistance of CNG to the fullest. This can be done by an early centre of combustion and/ or with a higher compression ratio. The engine used in this project is

based on the Volkswagen 2.0 litre diesel engine as explained by Neusser et al. in [10], which is very robust and capable of peak cylinder pressures of up to 190bar. Engine bore and stroke are 81.0mm x 95.5mm. The compression ratio has been modified to 14.5 by a new piston bowl. As shown in Figure 3, the spark plug is located centrally in the place of the former diesel injector and supplied with electric energy by a standard ignition coil. The engine is run on premixed homogeneous mixture of air and CNG. For this purpose, a gas mixer from Heinzmann as given in [11] is utilised. The engine manifolds are further modified to adapt to this new type of combustion process. For the purpose of measurement on the engine test bench, pressure sensors from Kistler of Type 6041A are utilised on all the 4 cylinders, whereas the intake manifold of cylinder 1 is equipped with an uncooled pressure sensor from Kistler of type 4007C. The exhaust pressure of cylinder 1 is measured with a cooled pressure sensor from Kistler of type 4011A. A Lambda sensor is mounted behind the turbine. For each operating point, at least 300 fired cycles are utilised for further investigation.

4.2 Details of Operating Points

As stated in Section 1, one of the advantages of such a combustion system is the leaning of the mixture, leading to a reduction in fuel consumption and an increase in the efficiency of the engine. Nevertheless, it is to investigate if there is a limit in leaning the mixture at which the engine still runs stable.

For this purpose, three engine operating points labelled as A, B, and C are defined, in such a way that they represent a variation only in the premixed natural gas air mixture. Description of the relevant parameters for the operating points is listed in Table 2. The centre of combustion is kept constant at $8°$ CA after Top Dead Centre (aTDC) and hence, accordingly with the increase in the value of λ, Spark ignition Timing (ST) is advanced.

Table 2: Details of operating points selected for simulation

| Parameter	Value		
Operating Point	A	B	C
Speed [rpm]	1500		
Load [Nm]	100		
λ [-]	1.0	1.5	1.8
Intake manifold pressure [bar]	0.74	0.95	1.20
Spark ignition timing [$°$ CA bTDC]	17.2	27.2	52.8

4.3 3D CFD Simulation Setup

The setup for 3D CFD simulation of the above-stated operating points of the engine with the help of the software VECTIS from Ricardo Software is described here. For this purpose, representative geometry of a single cylinder with intake and exhaust port

is considered in the simulation domain. Figure 4 shows the discretization of the geometry at TDC. Here it is seen that, the exhaust port (right) and the intake port (left) are discretized with a Cartesian mesh with a cell size of 2 mm, whereas a mesh cell size in the cylinder geometry (centre) of 1 mm is chosen. For the purpose of complete geometrical representation of the spark plug electrodes, the cell size near the spark plug is kept to 0.5 mm. The properties of methane are used for the representation of natural gas in the simulation domain. As discussed above, natural gas and air mixing takes place in the gas mixer at least 0.5 m before the inlet of intake manifold. Therefore, it is assumed that air and natural gas are homogeneously mixed when they enter the intake port. Accordingly, the mass flow rate at each degree crank angle of homogeneous air natural gas mixture at individual λ is utilised as inlet boundary condition on the intake port inlet. This mass flow rate is generated from 1D CFD simulation. On the exhaust port outlet side, averaged measured pressure on engine exhaust port at every $0.5°$ CA for one four stroke cycle is utilised. Starting from the maximum exhaust valve opening at $245°$ CA aTDC ($245°$ CA) till $80°$ CA aTDC ($800°$ CA), the simulation is carried out with moving mesh for piston, intake and exhaust valves. The timestep utilised over the whole simulation is $0.01°$ CA and it is reduced to $0.005°$ CA during the phases of ignition and combustion.
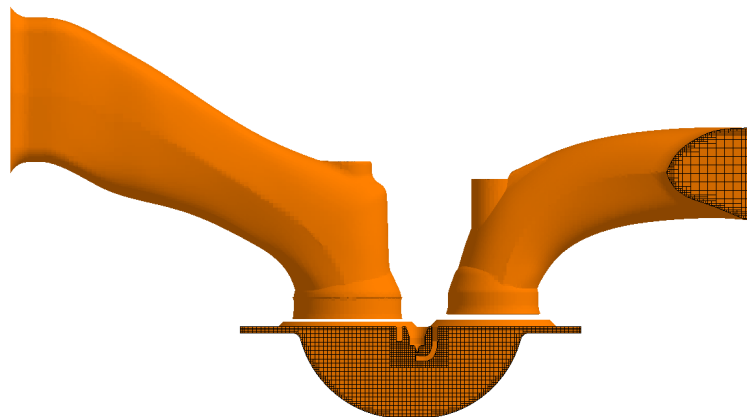
Figure 4: Simulation domain with single cylinder at TDC (centre) including intake port (left) and exhaust port (right)

4.4 Comparison of Mechanisms in 3D CFD Engine Simulation

In addition to the comparison presented in Section 3, the mechanisms are compared in the conjunction to their application with the advanced spark ignition model in the 3D CFD simulation. Aim of this study is also to analyse the effect of different detailed mechanisms on the spark ignition process on the basis of Operating Point (OP) A. For this purpose, as stated in Section 2, Combustion Progress Variable (CPV) and laminar flame speed tables for the three selected mechanisms over the application parameter range are generated. The details of these pre-calculated tables can be found in Table 3. Numbers in the brackets show the interval at which each parameter is incremented over the range of that parameter in the tabulation. The range of each parameter is selected based on the engine simulations till the spark ignition timing, which are presented for OP A hereafter.

Table 3: Range of parameters for pre-calculated CPV and laminar flame speed tables for study of kinetic mechanisms in the engine

Table	Pressure [bar]	Temperature [K]	ϕ [-]	ψ [%]
CPV	1 - 90 (15)	500 - 1500 (100)	0.5 - 1.2 (0.1)	0 - 10 (10)
Laminar Flame Speed	1 - 40 (10)	300 - 800 (100)	0.5 - 1.3 (0.2)	0 - 10 (10)

Before comparing the results obtained with the detailed mechanisms, it is important to analyse the conditions in the combustion chamber till spark ignition timing. Figure 5 shows the mixture conditions and flow field at the spark ignition timing for OP A. A homogeneous distribution of the fuel mass representing the stoichiometric mixture in the combustion chamber is observed. This suggests that the homogeneity of the mixture is held intact till the spark ignition timing. The distribution of Turbuelnt kinetic energy (TKE) is plotted in the top right sub-figure. It is observed that overall turbulence level is low in the combustion chamber. Intermediate turbulence level is observed in the top central part of the combustion chamber besides the spark plug. With the help of velocities plotted on the central plane of the combustion chamber and in the spark plug electrode gap, it can be observed that a typical diesel swirl motion is not present in this case. Rather a flow field colliding at the centre of the combustion chamber from both sides is present.

low   Fuel mass fraction [-]   high   low   TKE [m^2/s^2]   high

Velocity field at central plane   Velocity field at the spark plug

low   In-plane velocity [m/s]   high
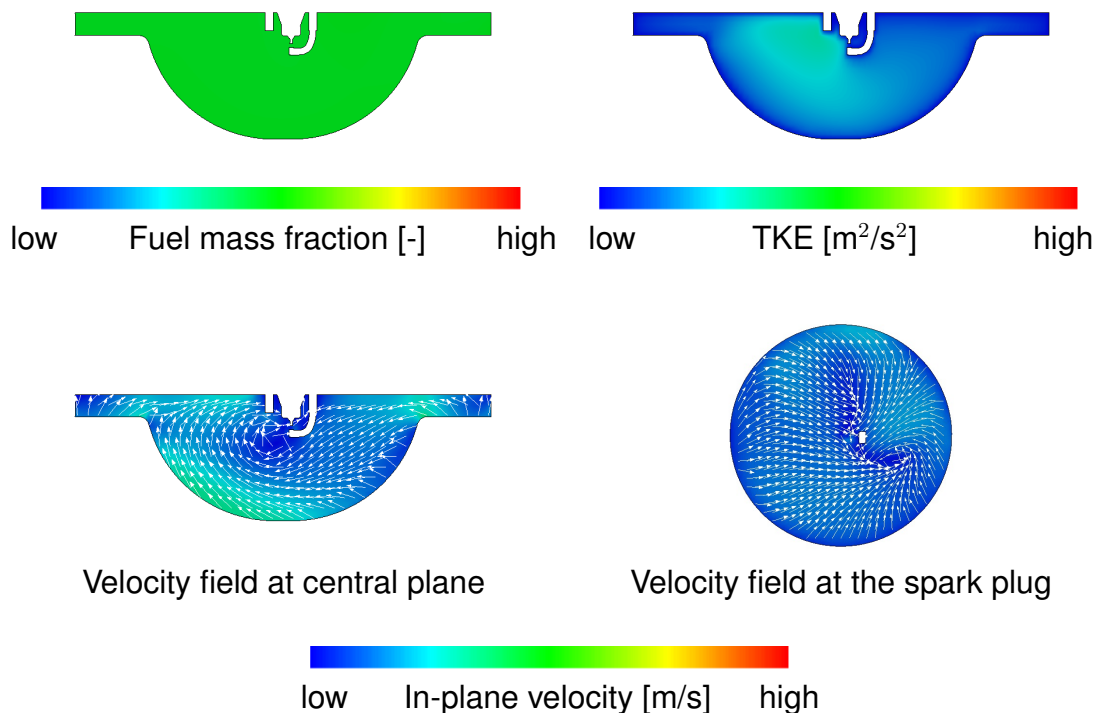
Figure 5: Conditions in the combustion chamber at spark ignition timing for OP A (703° CA)

On the basis of this analysis, a study of the selected detailed chemical mechanisms is carried out. For this purpose, results of the advanced spark ignition model in the form

of the flame kernel radius are compared. Figure 6 presents this comparison for simulations without detailed mechanism (1-step mechanism) and with the three selected mechanisms after Spark ignition Timing (aST) till the end of spark discharge duration of 2 ms which are $18°$ CA for engine speed of 1500 rpm. For individual simulations, results of the flame kernel radius are plotted only till its transition into the flame. Faster growth of the flame kernel is predicted by both MFC and LOGE mechanisms than that of GRI and 1-Step mechanisms. Therefore, for these two cases, the flame kernel reaches the size required for its transition into the flame at least $5°$ CA earlier than that of for GRI and one step mechanisms. These results can be correlated back to the simulation results of the ignition delay and the laminar flame speed for detailed mechanisms from section 3. It can be seen that, these two mechanisms (LOGE and MFC) either over-predict the laminar flame speed or under-predict the ignition delay time for respective conditions in the engine experiments.
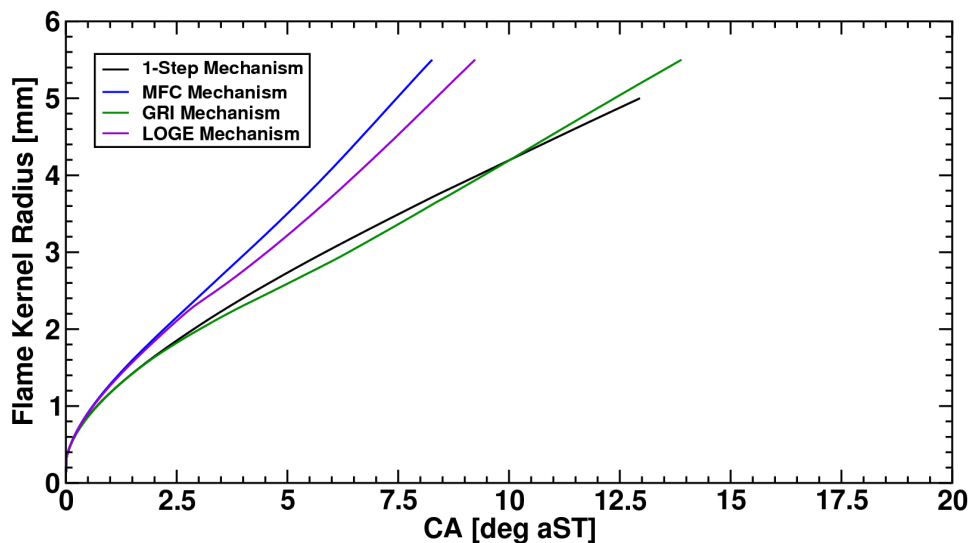
Figure 6: Flame kernel radius over time for OP A for simulations without detailed mechanism and with the three detailed mechanisms

Figure 7 shows the comparison of the simulated pressure curves without detailed chemical kinetic mechanism and with the three studied mechanisms against the experimental data. It can be seen that, all the simulation results (with and without detailed mechanisms) are in very good agreement with the experimental data in the initial phase of the combustion after the spark ignition timing. Later, the simulation results deviate for individual cases of detailed mechanisms. The simulation results with GRI mechanism are in good accordance with the experimental data. The simulation results with the 1-step mechanism (without detailed mechanism) can also reproduce the experimental data with good accuracy. Rather the simulation results with MFC and LOGE mechanism overpredict the maximum cylinder pressure as well as the pressure decrease in the expansion phase. Similar to the results of the flame kernel radius, these results can be deduced again with the results from section 3. Therefore, from this comparison GRI mechanism is utilised for the further analysis.
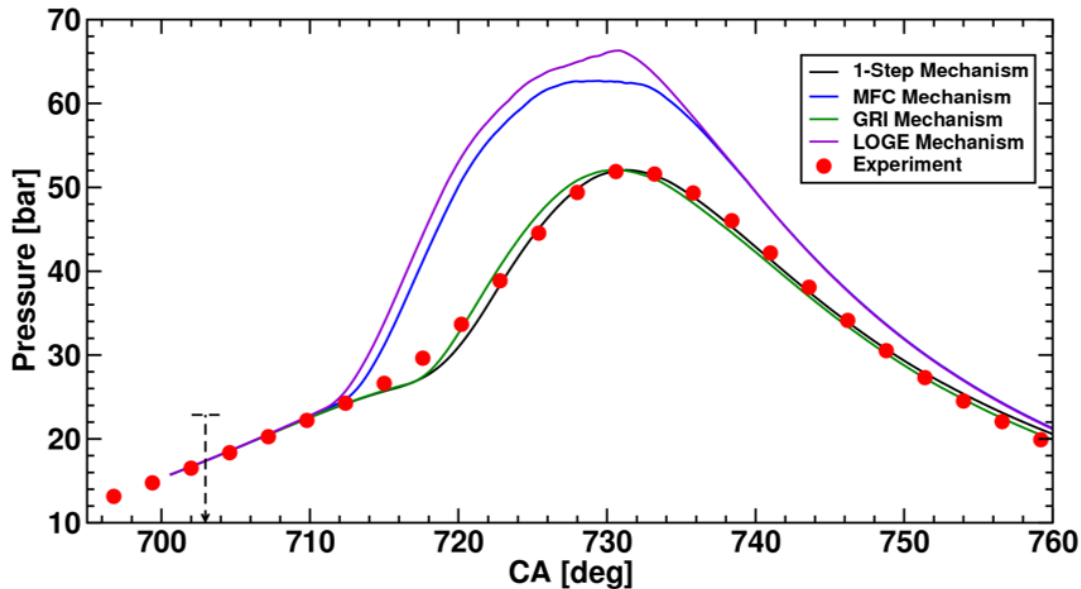
Figure 7: Comparison between simulation results without detailed chemical kinetics, with three detailed kinetic mechanisms and experimental data for cylinder pressure of OP A; Arrow indicates the spark ignition timing for OP A

4.5 Results of 3D CFD Engine Simulation

Results of the 3D CFD engine simulation with the selected detailed kinetic mechanism are presented in this section. To study the behaviour of the advanced spark ignition model for different values of λ over the stable engine operating range, results for operating points A, B and C are compared.

Similar to the previous study, conditions in the combustion chamber at spark ignition timing are analysed for OP B and OP C in Figure 8. With the help of an adjusted scaling of green area representing stoichiometric air fuel mixture, homogeneous fuel distribution of respective values of λ is observed for both operating points. Distribution of TKE and the velocity fields are similar to OP A for both operating points. The differences observed are mainly due to the difference in the spark ignition timing and hence resulting into the different timing of analysis in the compression stroke. Quantitative comparison of different parameters in the vicinity of the spark plug also showed very less changes except the differences pertaining to the changes due to different values of λ. Another effect of the different spark ignition timings and the different intake manifold pressure (as given in Table 2) is the difference in the cylinder pressure at spark ignition timing. This can be seen in Figure 11. At the time of spark ignition for each operating point, depicted with the arrow of individual colour, as the value of λ increases, due to increase in the intake manifold pressure, increase in the cylinder pressure at the individual spark ignition timing is observed. Detailed discussion of results presented in Figure 11 is carried out separately later in this section.

| OP B | OP C | OP B | OP C |

low   Fuel mass fraction [-]   high   low   TKE [m²/s²]   high

Velocity field at central plane   Velocity field at the spark plug

low   In-plane velocity [m/s]   high
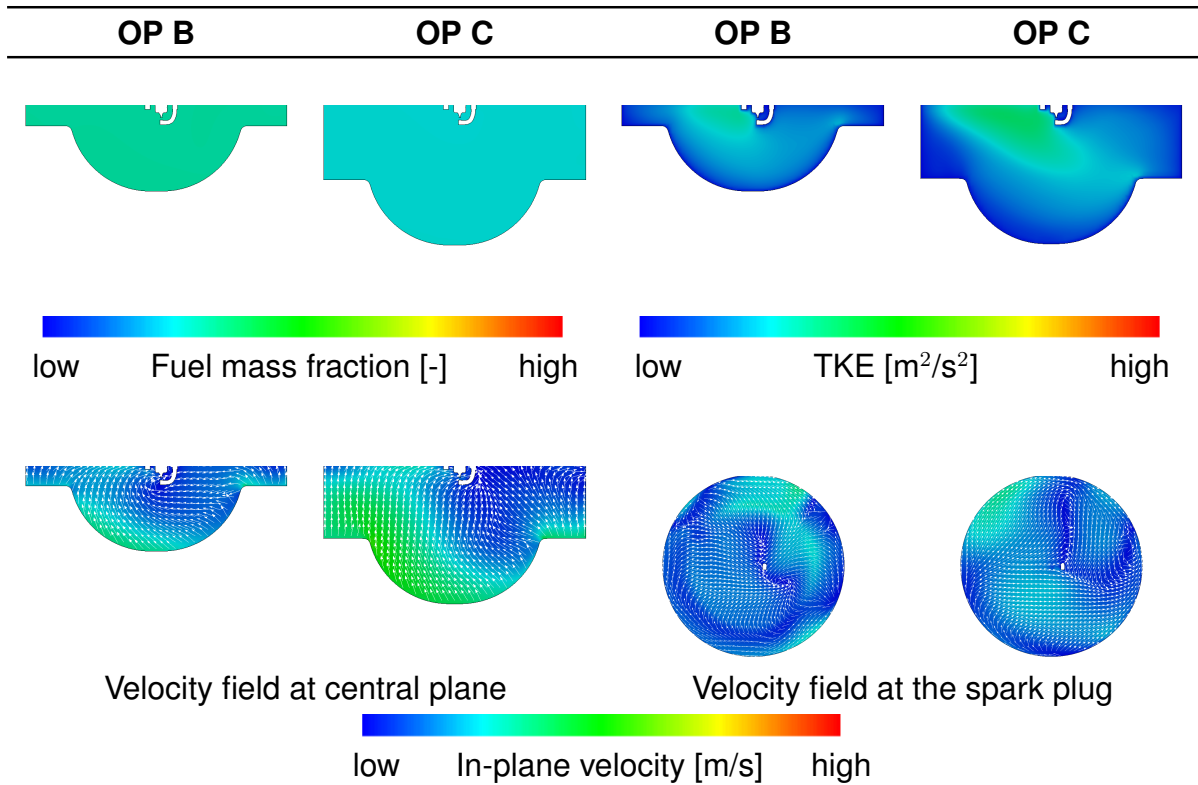
Figure 8: Conditions at spark ignition timing for OP B (692.5° CA left) and OP C (668° CA right)

Initial results of the advanced spark ignition model in the form of the flame kernel development over the spark discharge duration for three operating points are shown in Figure 9. Here, the growth of the flame kernel is plotted only till its transition into a fully propagating flame. It is seen that, as the value of λ increases, the final flame kernel radius before its transition into the flame decreases. This can be correlated with the results of laminar flame speed in Section 3.2, where, deviation from stoichiometric mixture conditions results in a decrease in the laminar flame speed. Analysing these results in detail, it can be seen that, for OP A ($\lambda = 1.0$), the required size of the flame kernel for its transition into fully propagating flame is achieved earlier ($\sim 14°$ CA aST) than other operating points. This transition time is based on the parameters such as, mixture strength, flow field conditions and pressure in the surrounding. As the difference between the transition time for OP A and that for other operating points is large, the dominating factor for the transition time is the mixture condition. Least difference in the transition time for OP B and OP C is observed, as in this comparison, changes in pressure at the spark timing are more effective than that of changes in the mixture condition. This shows that the advanced spark ignition model gives one parameter i.e. flame kernel radius, which relates all the conditions in the surrounding against the progress of the spark ignition process in the engine.

Results of the flame kernel progress are visualised in Figure 10 with the help of representation of the G-Scalar over the spark duration for the three operating points OP A, OP B and OP C. Here, it should be noted that, in case of the advanced spark ignition model, for the purpose of representation, the envelope of scalar G with the value equal to zero is created around the current flame kernel position. This should

Figure 9: Flame kernel radius over time for OP A (λ 1.0), OP B (λ 1.5) and OP C (λ 1.8)

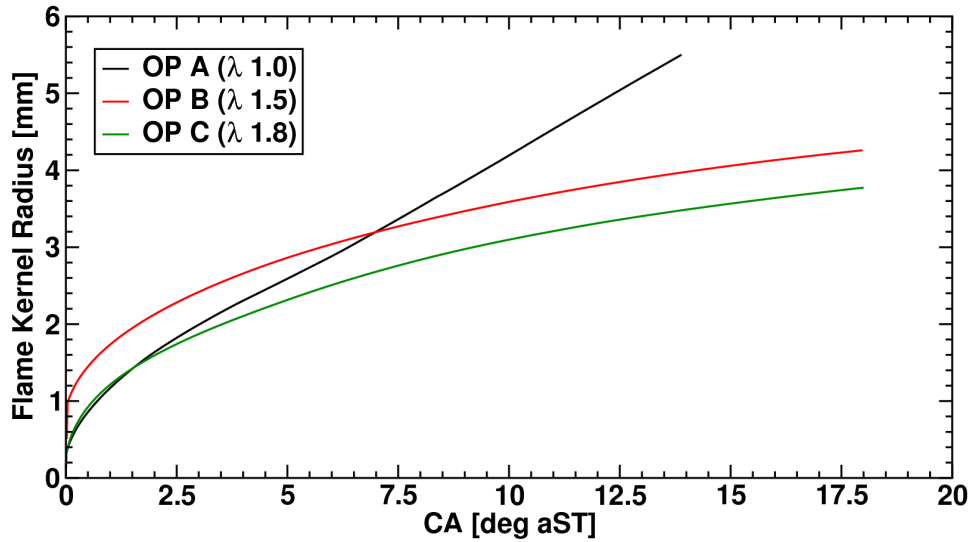not be confused with the approach, where G scalar directly represents the flame surface. For the purpose of frame of reference, locations of the spark plug (in the centre), the intake valves (on the left side of the spark plug) and the exhaust valves (on the right side of the spark plug) are shown in one of the representations. At individual spark timing, comparatively smaller but still differential sizes of flame kernel are found for each operating point. At 4.5° CA aST, for stoichiometric conditions, comparatively larger growth of the flame kernel in this duration is observed. This trend continues till 13° CA aST, which results in the transition of the flame kernel in the fully propagating flame. At this point of time, for other operating points, the flame kernel size is still attaining this minimal flame kernel size for the transition. At the end of the discharge duration, at 18° CA (2.0 ms) aST, OP B and OP C have attained this size, and are on the verge of transition. Here at this point of time, but for OP A, the growth in the already transited flame size is observed. These results can be correlated with the results discussed above and hence, validate each other.

Results in the form of comparison of cylinder pressure between experimental data and simulation results for the considered three operating points are presented in Figure 11. It can be seen that, at the spark ignition timing for all the operating points experimental data and simulation results are in very good agreement. This indicates that the simulation method and the boundary conditions utilised for this engine simulation are appropriate. Furthermore, overall combustion simulation results are in good accordance with experimental data. As discussed before, due to the increased air requirement for the leaning of the mixture, intake manifold pressure is increased for a higher value of λ. Effectively this results in the higher maximum combustion pressure. This trend, as observed in the experimental data, is reproduced by the simulation results. Spark ignition and initial phases of the combustion are reproduced accurately for all the three operating points by this simulation method. Apart from the results of OP C, the maximum pressure and its timing are predicted accurately by the simulation. In the case of OP C, value of maximum pressure is correctly reproduced but an early pressure rise resulting in an offset in the timing of maximum pressure by

OP A	OP B	OP C

At ST

4.5° CA (0.5 ms) aST

14° CA (1.4 ms) aST

18° CA (2.0 ms) aST
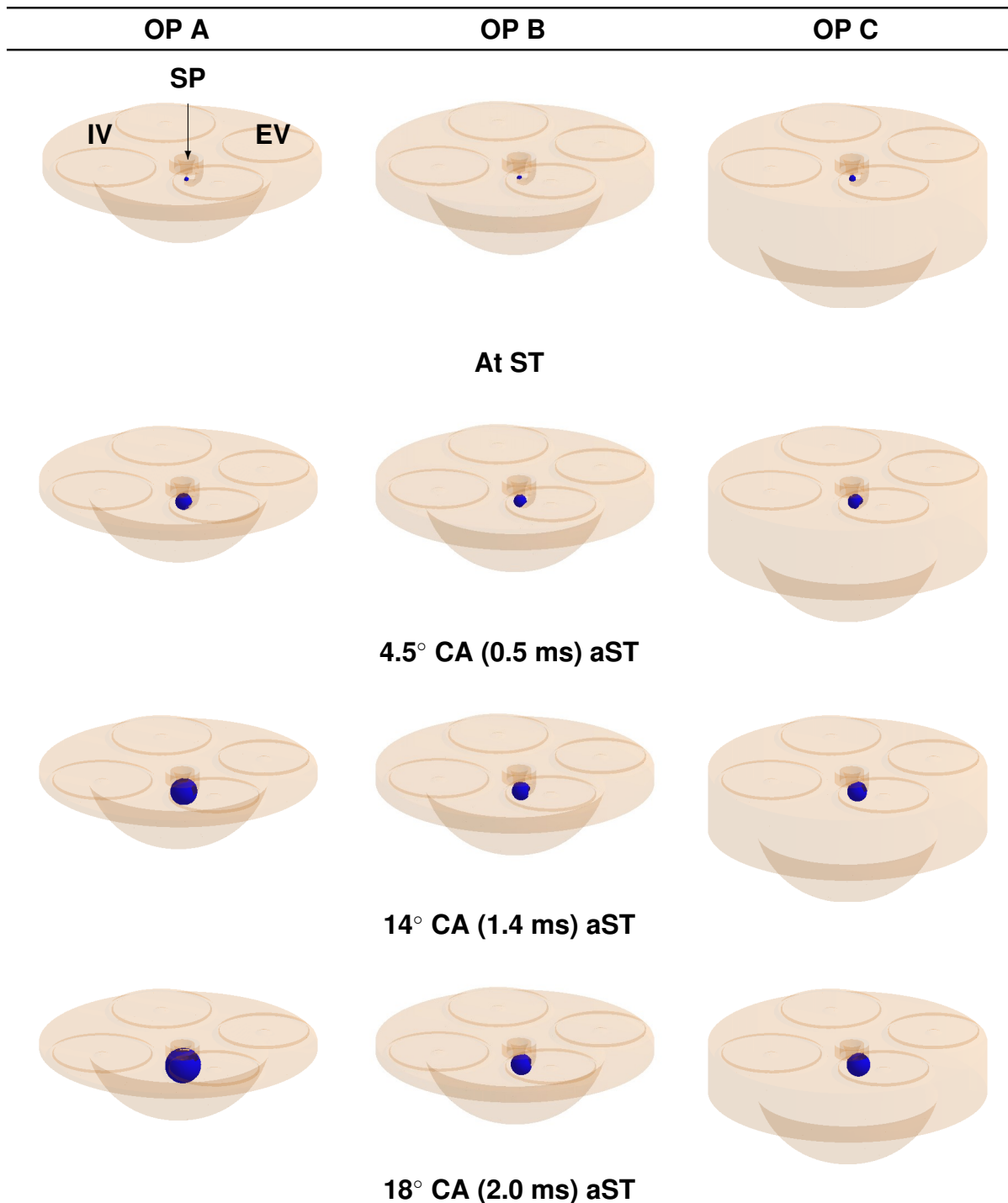
Iso-Surface G=0 representing flame kernel or flame for sub-figure of OP A at 18° CA aST

Figure 10: Flame kernel growth for OP A (λ 1.0), OP B (λ 1.5) and OP C (λ 1.8); IV: Intake Valve, EV: Exhaust Valve, SP: Spark Plug, ST: Spark Ignition Timing

4.8° CA is observed. This can be correlated with the fact that, as shown in Figure 2 (right), at lean conditions, the difference between the simulated and the experimental laminar flame speed is increasing. Similar differences are also seen in the expansion phase, where for OP A the simulation results show a faster drop of pressure compared to the experimental data.
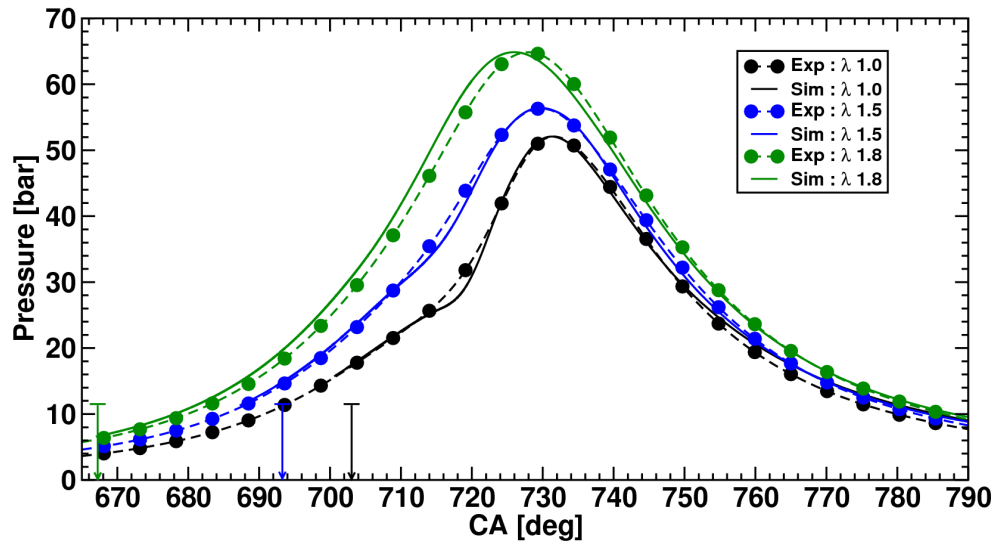
Figure 11: Comparison of cylinder pressure between simulation results and experimental data for OP A (λ 1.0), OP B (λ 1.5) and OP C (λ 1.8) with arrows showing the spark ignition timing for each OP

5 Conclusion

In this paper, the previously presented approach of modelling of the spark ignition is further validated on a natural gas engine. The Volkswagen 2.0 litre serial diesel engine is modified to be operated as a monovalent natural gas engine ignited with a serial spark plug. Engine operating points are chosen in such a way that they represent only a variation in the relative air-fuel ratio at same load and speed. These points are calculated with the help of the advanced spark ignition model in the 3D CFD simulations.

For the purpose of simulation with the advanced ignition model, priorly, a comparative study of 3 available natural gas combustion mechanisms for ignition delay time and laminar flame speed for different experimental conditions is carried out. MFC mechanism is found suitable for the engine operational temperature range, whereas GRI mechanism is seen appropriate at high pressure conditions. LOGE mechanism shows its suitability over the broader equivalence ratio. These three mechanisms are further analysed in the 3D CFD simulation of one engine operating point, OP A. With the help of tabulation approach, these detailed mechanisms are coupled in 3D CFD simulations. Here, comparison of the simulation results against experimental data shows that GRI mechanism can reproduce the results of the experiments to a very good accuracy. Therefore, this mechanism is utilised for further investigation.

Comparison of the simulated pressure curve and the experimental data for the three operating points during the different phases of combustion viz. ignition or early phase, centre of combustion and expansion phase, show very good agreement. As a result of the advanced ignition model in the form of flame kernel radius, an ignition progress parameter is presented. This parameter shows the effects of the conditions near the spark region on the flame progress. For the simulated operating points, changes in the flame kernel radius against the relevant changes in air-fuel ratio and pressure are

observed. In this way, it can be stated that, the advanced spark ignition model is able to reproduce ignition events for this type of engine with good accuracy.

Acknowledgement

References

[1] G. Tallu, L. M. Beck, M. Prouvier, A. Winkler, M. Frambourg, and E. Shapiro. 3D CFD modelling and simulation of spark ignition inclusive turbulence effects and detailed chemical kinetics. *Ignition Systems for Gasoline Engines : 3rd International Conference, Berlin*, Addon:9–25, 2016.

[2] R. Maly and M. Vogel. Initiation and propagation of flame fronts in lean CH4-Air mixtures by the three modes of the ignition spark. *Symposium (International) on Combustion*, 17:821–831, 1979.

[3] R. Herweg and R. Maly. A fundamental model for flame kernel formation in S.I. engines. *SAE Technical Paper 922243*, 1992.

[4] Ansys Inc. *CHEMKIN MFC - Reaction Design*. Ansys Inc., San Diego, 2015.

[5] G. Smith, D. Golden, M. Frenklach, N. Moriarty, B. Eiteneer, M. Goldenberg, C. Bowman, R. Hanson, S. Song, Jr. W. Gardiner, V. Lissianski, and Z. Qin. GRI-MECH 3.0, 2014.

[6] L. Seidel, C. Netzer, M. Hilbig, K. Hoyermann, T. Zeuch, F. Mauss, P. Oßwald, K. Kohse-Höinghaus, and U. Stuckmeier. LOGEfuel Natural Gas Mechanism LOGE AB (Sweden), 2016.

[7] J. Huang, P. G. Hill, W. K. Bushe, and S. R. Munshi. Shock-tube study of methane ignition under engine-relevant conditions: Experiments and modeling. *Combustion and Flame*, 136(1):25–42, 2004.

[8] Y. Zhang, Z. Huang, L. Wei, J. Zhang, and C. Law. Experimental and modeling study on ignition delays of lean mixtures of methane, hydrogen, oxygen, and argon at elevated pressures. *Combustion and Flame*, 159(3):918–931, 2012.

[9] M. Elia, M. Ulinski, and M. Metghalchi. Laminar burning velocity of methane-air-diluent mixtures. *Journal of Engineering for Gas Turbines and Power*, 123(1):190–196, 2000.

[10] H. J. Neußer, J. Kahrstedt, H. Jelden, H. J. Engler, R. Dorenkamp, S. Jauns-Seyfried, and A. Krause. Volkswagen's new modular TDI generation. *33rd International Vienna Motor Symposium*, 2012.

[11] Heinzmann Gruppe. Gasmotorenmanagement : Produktkatalog. Technical report, Heinzmann GmbH & Co. KG, Münster, 2017.

4 Visualization

4.1 Ignition Diagnostics based on Spark-Induced Breakdown Spectroscopy for Gas-Engine Applications

Laura Merotto, Thomas Kammermann, Davide Bleiner, Patrik Soltic

Abstract

Spark ignition engines involve cyclic variation of the combustion process. A better understanding of the underlying mechanisms driving these variations is of major importance for the optimization in terms of emissions and fuel economy. The location and growth rate of the initial flame kernel is one of the factors affecting the magnitude and timing of the peak cylinder pressure. In turns, the rate of development of the initial flame kernel is mainly affected by the local fuel concentration and homogeneity near the spark gap and the local flow conditions, such as turbulent structure and magnitude. Currently, natural gas-dedicated engines with direct injection combustion concepts are being developed to improve the thermal efficiency and take advantage of the lower CO_2 emissions compared to gasoline and diesel. The higher knock resistance of methane allows increasing the compression ratio, but this also makes it a more challenging environment to successfully initiate combustion, especially in lean or stratified combustion or at high EGR conditions. This leads to higher requirements on the ignition system and on the control of the mixture formation process.

A diagnostic tool for providing information on the mixture composition at the spark plug during spark timing is highly valuable for research and development purposes. Spark-Induced Breakdown Spectroscopy (SIBS) is a measurement technique in which the plasma formed by spark generation between two electrodes is used as the excitation source for optical emission spectroscopy. The light emission from the species excited by the plasma is related to the local mixture conditions, and therefore can be used as a diagnostic tool to deliver information on local conditions around the spark plug during the ignition attempt. In SI engines, SIBS can be used in the combustion chamber with minor engine modifications and is therefore a promising alternative to other investigation techniques, as Laser-Induced Breakdown Spectroscopy (LIBS), where a laser has to be coupled to the combustion chamber.

In this work, different quiescent mixture compositions at ambient temperature and elevated pressure conditions were investigated in a constant volume cell. A spectrometer and an intensified camera were used to capture the plasma emission from the electrical discharge in order to develop a SIBS-based measurement technique for ignition events investigation.

The role of methane, air and hydrogen on the electrical discharge characteristics and the plasma emissions were investigated. Moreover, atomic and molecular spectral emissions in different ambient conditions and for different mixtures were analyzed and compared, with the aim to obtain a deeper insight on the SIBS response to the complex

physical and chemical phenomena underlying the ignition event. Results show that the proposed technique is a compact and versatile tool for applications involving atomic and molecular species detection in different ambient conditions.

Kurzfassung

Ottomotoren unterliegen zyklischen Variationen im Verbrennungsprozess. Ein vertieftes Verständnis der zugrunde liegenden Mechanismen, welche diese zyklischen Schwankungen antreiben, ist fundamental in Bezug auf die Optimierung von Emissionen und Kraftstoffverbrauch. Der Ort des Flammenkerns und dessen Wachstumsrate sind wichtige Faktoren, welche die Amplitude und den Zeitpunkt des maximalen Zylinderdrucks beeinflussen. Die Entwicklungsgeschwindigkeit des anfänglichen Flammenkerns wird wiederum hauptsächlich durch die lokale Brennstoffkonzentration und -homogenität in der Nähe der Funkenstrecke und die lokalen Strömungsbedingungen, wie turbulente Struktur und Größe, beeinflusst. Gegenwärtig werden Motoren für magere Gemische und für direkteinspritzende Verbrennungskonzepte entwickelt, um den thermischen Wirkungsgrad zu verbessern und die, im Vergleich zu Benzin und Diesel, geringeren CO_2-Emissionen zu nutzen. Die höhere Klopffestigkeit von Methan erlaubt es, das Kompressionsverhältnis zu erhöhen. Dies führt jedoch auch zu erschwerten Bedingungen um eine Verbrennung erfolgreich einzuleiten, insbesondere im Mager- und Schichtladungsbetrieb sowie bei hohen Abgasrückführraten. All diese Faktoren erhöhen die Anforderungen an das Zündsystem und an die Steuerung des Gemischbildungsprozesses.

Ein Diagnosewerkzeug zum Bereitstellen von Informationen über die Gemischzusammensetzung an der Zündkerze während des Zündzeitpunkts ist sehr wertvoll. Funkeninduzierte Plasmaspektroskopie ist eine Technik, bei der das durch Funkenbildung zwischen zwei Elektroden gebildete Plasma als Anregungsquelle für die optische Emissionsspektroskopie verwendet wird. Die Lichtemission der durch das Plasma angeregten Spezies hängt vom lokalen Gemisch ab und kann daher als ein Diagnosewerkzeug verwendet werden, um während des Zündversuchs Informationen über örtliche Bedingungen um die Zündkerze zu liefern. In Ottomotoren kann diese Methodik mit minimalen Motormodifikationen in der Brennkammer eingesetzt werden und ist daher eine vielversprechende Alternative zu anderen Untersuchungstechniken wie laserinduzierte Plasmaspektroskopie, bei welcher ein Laser in den Brennraum gekoppelt werden muss.

In dieser Arbeit wurden verschiedene ruhende Gemischzusammensetzungen bei Umgebungstemperatur und erhöhten Druckbedingungen in einer Konstantvolumenzelle untersucht. Ein Spektrometer und eine intensivierte Kamera wurden verwendet um die Plasmaemission der elektrischen Entladung zu erfassen, um eine SIBS-basierte Messtechnik für die Untersuchung von Zündereignissen zu entwickeln.

Die Rolle von Methan, Luft und Wasserstoff auf die elektrischen Entladungseigenschaften und die Plasmaemissionen wurden untersucht. Darüber hinaus wurden atomare und molekulare Spektralemissionen unter verschiedenen Umgebungsbedingungen und für verschiedene Gemische analysiert und verglichen, um ein besseres Verständnis der Spektren der komplexen physikalischen und chemischen Phänomene zu erlangen, die dem Zündvorgang zugrunde liegen. Die Ergebnisse zeigen, dass die erarbeitete Methodik ein kompaktes und vielseitiges Werkzeug für Anwendungen ist, bei denen atomare und molekulare Spezies unter verschiedenen Umgebungsbedingungen detektiert werden.

1   Introduction

The combustion process in spark ignition engines involves cyclic variation of combustion, thus resulting in difficult optimization in terms of engine emissions and fuel economy since, for example, fast burning cycles are critical for knock and slow burning cycles deteriorate efficiency. Several investigations have been performed in the last decades with the aim to overcome these difficulties.

Lean-burn spark-ignition (SI) engines have been developed to improve fuel economy and reduce emissions [1–3]. Although lean operation has proven to result in such important advantages [4], mixture air to fuel (A/F) ratio increase results in more prominent cycle-by-cycle variations in flame development, limiting the lean-burn operation range. Therefore, aim of research in this framework is to achieve the understanding needed to ensure an extension of the current limits of A/F ratio for engine operation. In order to do so, the investigation of local mixture conditions around the spark plug is of major importance, since they determine the successfulness of the ignition attempt, and in turn affect the initial flame growth and the establishment of turbulent combustion.

As an alternative to homogeneous mixtures as they are typically achieved with port-fuel injection direct injection enable charge stratification [5,6], i.e. the fuel/air mixture can be fuel-richer around the spark plug. Previous research show [7] that the growth rate and location of the initial flame kernel is one of the major factors affecting the magnitude and timing of the peak cylinder pressure. Several studies [8,9] show that the ignition limits in terms of air to fuel ratio are strongly affected by the presence of turbulence in the flow. In turns, the rate of development of the initial flame kernel is affected by the local fuel concentration near the spark gap [2]. Therefore, a need for better understanding and control of such a concentration arises.

Currently, natural gas-dedicated engines with stoichiometric or lean-burn combustion concepts are being developed to improve the thermal efficiency and take advantage of the lower CO_2 emissions compared to gasoline and diesel. The higher knock resistance of methane allows increasing the compression ratio compared to today's bivalent engines found in the passenger car sector. But this also affects the demands on an ignition system due to higher pressures at spark timing, resulting in an increased demand on the insulation resistance on the coil and spark plug. This makes it a more challenging environment to successfully initiate combustion. Recent developments in gas engines include direct injection strategies. Reynolds et. al. [10] have investigated a direct-injection lean-burn natural gas engine. Their results show that better fuel consumption is obtained at higher air to fuel ratios when a stratified charge is used. In [11] the effect of different injection strategies for methane, hydrogen and hydrogen-enriched methane in a spark ignition engine are investigated. The authors show that direct injection direction and timing affect mainly the early phase of combustion, whereas the later combustion phase is mainly influenced by the global stoichiometry and the fuel composition. It is important to notice that air to fuel ratio measurements are of great importance in such engines, because within charge stratification, fuel concentration is higher close to the spark plug, thus resulting in higher flames temperature and higher NO_x emissions [11]. Other concepts, like systems with actively fueled prechambers, have also gained on attention [12]. In such concepts, where the stoichiometry within the prechamber can differ significantly from the stoichiometry of the main combustion chamber, non-intrusive optical measurement fuel concentration measurement techniques are the only option for stoichiometry diagnostics in the prechamber.

Various approaches have been used by several researchers to measure the air to fuel ratio or fuel concentration in SI engines, including Laser induced breakdown Spectroscopy (LIBS). LIBS is a well established measurement technique in the research community [13,14], and the laser pulse can be successfully used as a diagnostic tool for a variety of applications, including engines. Ferioli and Buckley[15] demonstrated the possibility to obtain quantitative air/fuel equivalence ratios for methane and propane in air. The applicability of LIBS in a single cylinder engine using the ratios of the H_α/O_{777}, the H_α/N_{746} and $H_\alpha/N_{742-746}$ emission lines were tested, showing good results and suggesting this method for in-cylinder, cycle resolved air-fuel ratio measurements [16]. Phuoc and White [17] discussed simultaneous laser ignition and equivalence ratio measurement using laser-induced gas breakdown in methane–air and hydrogen/air mixtures using H_α (656 nm) and the O triplet near 777 nm. Rahman and Kawahara [18] measured the equivalence ratio using LIBS and discussed the accuracy of spatially, temporally, and spectrally resolved measurements. However, it is difficult to apply a LIBS system to equivalence ratio measurements around a spark plug due to the difficulty with laser access in a practical SI engine [19].

Spark-induced breakdown spectroscopy (SIBS), a measurement technique in which the source of excitation is the energy delivered by an electric spark discharge, is a feasible alternative to laser spectroscopy methods in SI engines, and can be used in a combustion chamber with no engine modifications, except an optical access. In this technique, the signal detection and spectroscopy is similar to LIBS; however, spark generation occurs between two electrodes, and the spark itself is used as the light source to obtain information on the mixture concentration through spectral analysis of the light emitted by the excited species. Spark-induced breakdown spectroscopy can be used as a diagnostic tool to characterize the local mixture conditions around the spark plug during the ignition attempt.

From SIBS spectral response, the local fuel-air equivalence ratio of different fuels such as methane [7,20], hydrogen [18], propane and isooctane [21] can be derived or plasma temperatures [22] determined. Ando and Kuwahara [23] and Fansler et al. [21] reported measurements of the equivalence ratio at the spark gap using the ratio of CN (388 nm) and OH (306 nm) emission intensity from the spark. They determined the cycle-resolved local fuel/air ratio in the spark gap, and evaluated the utility of SIBS as an engine diagnostic tool. However, they reported that it is difficult to detect the equivalence ratio under lean mixture conditions due to lack of the linearity of CN/OH emission intensity ratio. In [18], the authors sought to characterize the effects of ambient pressure at ignition timing on spectral line emissions and to improve the accuracy of SIBS measurements by taking into account the pressure dependency of atomic emissions. Spectrally resolved emission spectra of plasma generated by a spark plug were measured through an optical fiber housed in the center electrode of the spark plug. A calibration map representing the correlation of air excess ratio (air/fuel) with both intensity ratio and pressure at ignition timing was created by taking into account the effect of the corresponding pressure at ignition on spectral line intensity. The calibration line and calibration map were subsequently used for quantitative measurements of the local air excess ratio for both port injection and direct injection strategies to investigate the effects of the corresponding pressure at ignition timing on the accuracy of SIBS measurements.

Kawahara [20] also determined the local equivalence ratio of a methane/air mixture in a laminar premixed flame using SIBS with a fiber-coupled intensified charge coupled device (ICCD) spectrometer. The emission intensities of OH, CN, and NH spectra

under several equivalence ratio conditions were measured and discussed as a way to measure the equivalence ratio using the intensity ratios of CN/OH and CN/NH. In this investigation, the intensity ratio of the H_α/O atomic emission lines is used to measure the equivalence ratio of a premixed mixture and compared with the applicability of the intensity ratios of CN/OH and CN/NH. However, their results showed that the H_α/O intensity ratio is more suited for measuring the equivalence ratio than CN/NH under lean mixture condition, thus suggesting that further investigation is needed in order to better understand the ongoing processes and to further improve SIBS technique reliability and versatility.

With this aim, SIBS as a diagnostic tool for methane/air and hydrogen enriched methane mixtures in engine relevant conditions was spatially and temporally investigated at Empa [24]. In this work, the spectral signal dependency on air/fuel equivalence ratio as well as on methane substitution by hydrogen was investigated focusing on spectral emissions of OH, NH and CN. Spatially resolved measurements provided insight in the molecular emissions distributions along the spark gap. Results showed that although a dependence of the intensity ratios of CN_{388}/OH_{306} and CN_{388}/NH_{336} on the fuel-air ratio was found, shot to shot repeatability was high, thus suggesting further investigation on the atomic emission lines in order to further improve the technique.

The present work presents the SIBS-based diagnostic tool developed at Empa for ignition diagnostics for engine applications. The technique shows a high versatility, allowing investigation of different quiescent mixture compositions at ambient temperature and elevated pressure conditions using a small constant volume cell. A spectrometer and an intensified camera are used to capture the plasma emission from the electrical discharge, and spectral emissions are analyzed in order to gather information on the local mixture composition around the spark plug. Spectral emissions in different ambient conditions and for different mixtures are compared and discussed, with the aim to obtain a deeper insight on the SIBS response to the complex physical and chemical phenomena underlying the ignition event. First, different single gases' emissions are discussed; then, the spectral response from two components blends is taken into account, discussing the different results obtained from inert and reactive mixtures. Atomic and molecular emissions are considered and compared.

Results show that the proposed technique is a compact and versatile tool for applications involving atomic and molecular species detection in different ambient conditions. A fiber-optic equipped spark plug is then presented, which is the first step in running engine application of the proposed SIBS-based diagnostics.

2   Methods

2.1.   Experimental setup

The experimental setup used for the present work was developed for spectral and temporally resolved measurements, and is shown in Figure 1. A detailed description of the setup can be found in [24].
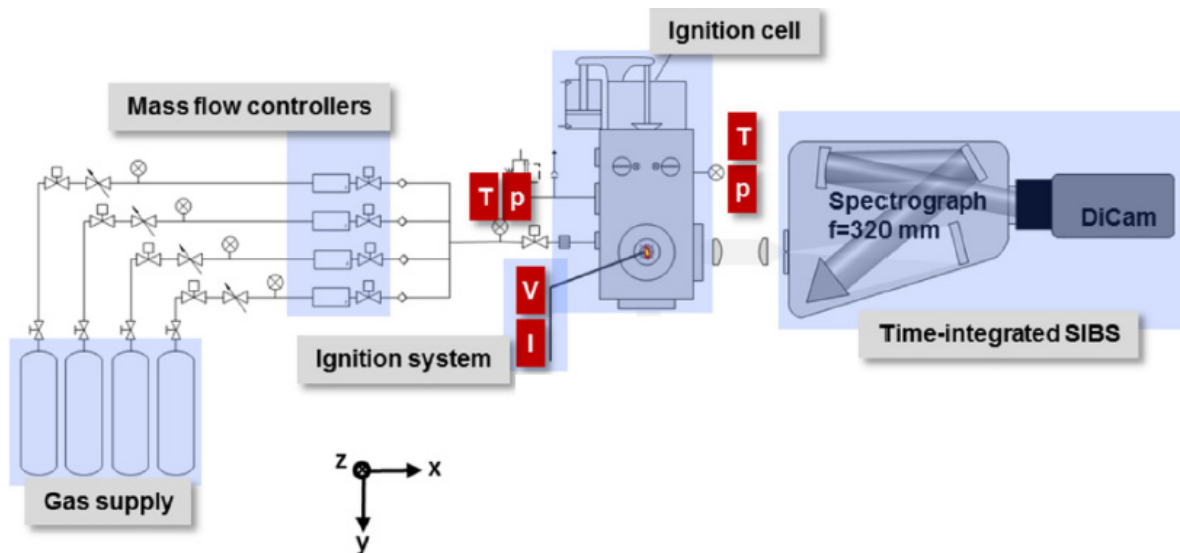
Figure 1: Sketch of the experimental setup for SIBS-based ignition diagnostics.

A small constant volume ignition cell, designed for optical investigation of emissions from sparks in homogeneous quiescent mixtures and coupled with a spectrometer was used. The cell is equipped with pneumatically actuated in- and outlet-valves, an absolute pressure sensor (Keller PAA-33X) for the control of the filling process and with a piezoelectric pressure transducer (Kistler 6052C) to measure the transient in-cell pressure. Gas supply was controlled via mass flow controllers (Bronkhorst).

The ignition system was based on a commercially available ignition coil (BERU), providing 60 mJ of secondary energy with a maximum spark duration of 2.2 ms at 800 V zener load. The coil was mounted on a commercially available M10 thread spark plug (NGK DIMR8A10) with double fine wire electrodes. The electrode gap was 1 mm. Current and voltage signals are captured via a data acquisition card (National Instruments PXI-5105, 60 MHz) or via an oscilloscope with 1 GHz bandwidth (LeCroy Wavesurfer 10).

The light emitted by the spark plasma was collected via a lens system through sapphire windows and transferred to the spectrometer slit. A slit width of 50 µm has been used throughout this study. Wavelength calibration spectra have been captured from a mercury neon lamp. A grating of 150 mm^{-1} was used on the Princeton Instruments spectrograph (Acton IsoPlane SCT 320) with a focal length of 320 mm. An intensified CCD camera (PCO DiCam Pro) with a detector size of 1280×160 pixels was used to collect the spectra, with a resulting spectral resolution of 1.7 nm for the 150mm^{-1} grating.

A custom made trigger box was used to trigger the intensified CCD camera after the breakdown phase, using the secondary current as trigger input. The output signal of the comparator has an intrinsic delay of 50 ns, but allows overcoming the jitter with respect to the ignition timing of the coil ignition system. This ensures that the chosen gate timing with respect to the breakdown (time = 0) remains the same within a measurement series.

2.2.   Electrical discharge structure and triggering strategy

The information that can be obtained analyzing spectral emissions strongly depend on the triggering strategy, i.e. on the time range selected for acquiring the optical measurements. It is well known [8] that the electrical discharge occurring between the spark plug electrodes can be divided into three phases (breakdown, arc and glow discharge), characterized by different time scales.
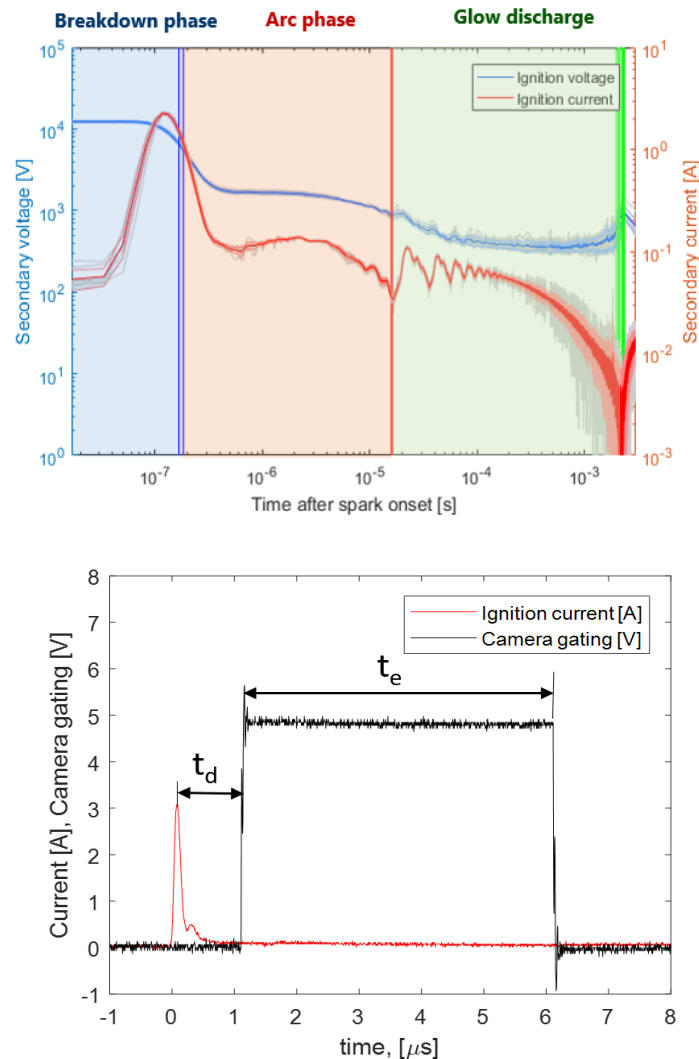
Figure 2: Top: Electrical discharge structure. Depending on the triggering strategy selected, it is possible to focus the measurement in the breakdown phase, in the arc phase or in the glow phase. Bottom: illustration of camera exposure time (t_e) and triggering delay (t_d).

The physical phenomena underlying the electrical discharge structure have a major impact on the spectral emissions features, and therefore on the information obtainable from this kind of analysis. Namely, breakdown occurrence causes the gas molecules in the ignition area to break into atoms and ions. Molecular recombination starts after some hundreds nanoseconds [8] from breakdown, thus leading to significantly different spectral emissions. Consequently, if measurements are triggered closer to the time at which breakdown occurs, atomic lines will appear in the spectral emission, while

molecular emissions will be revealed some microseconds or milliseconds after breakdown.

The general structure of an electrical discharge is sketched in the left part of Figure 2, while the right part shows a typical secondary current signal and the camera gating time. The exposure time (t_e) is the time interval during which a spectral emission is acquired. The time delay (t_d) between the secondary current spike due to breakdown occurrence and the onset of the camera gating is also indicated, and will be referred to as "delay" in the following sections.

Both the exposure time and the delay affect the spectral emissions' features, as discussed in the following section.

3.   Results and discussion

3.1.   Single gases emissions: effect of exposure time and delay

As mentioned in the previous section, different emissions can be measured depending on the gating strategy selected. In order to select a gating strategy for the gases investigated in this work, preliminary tests were performed varying the exposure and the delay with the aim to optimize the signal to noise ratio. Results showed that the better signal to noise ratio is obtained when the spectra acquisition is gated right after the breakdown occurs.

An example of emission spectra is given in Figure 3 for 5 µs exposure time and in Figure 4 for 2 ms exposure time. The spectra recorded using four different pure gases (air, hydrogen, nitrogen and methane) are shown, together with an indication of the main emission lines recognizable.
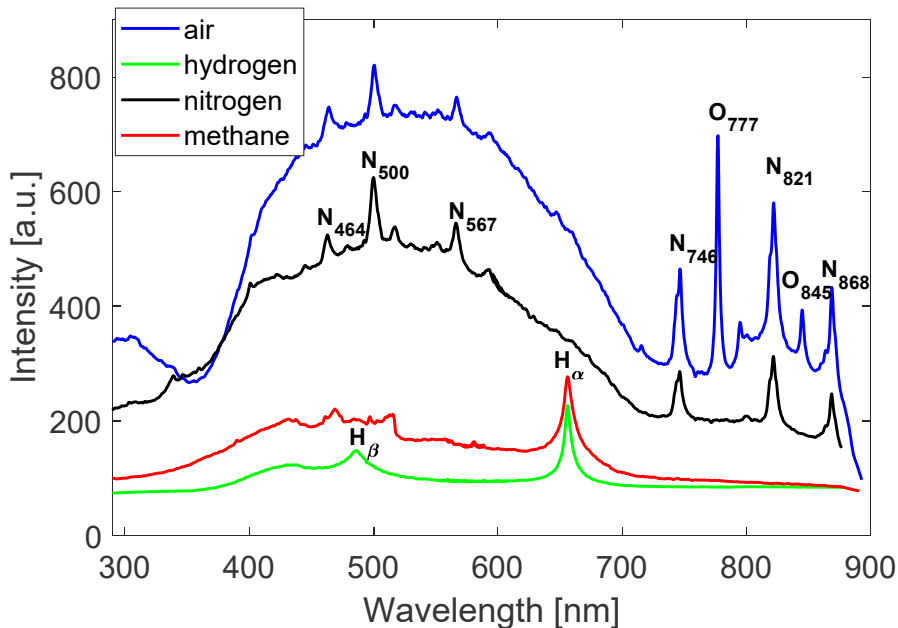
Figure 3: Spectral emissions for pure gases (air, hydrogen, nitrogen and methane) at 10 bar absolute pressure. Exposure time t_e = 5 µs, delay t_d = 0.
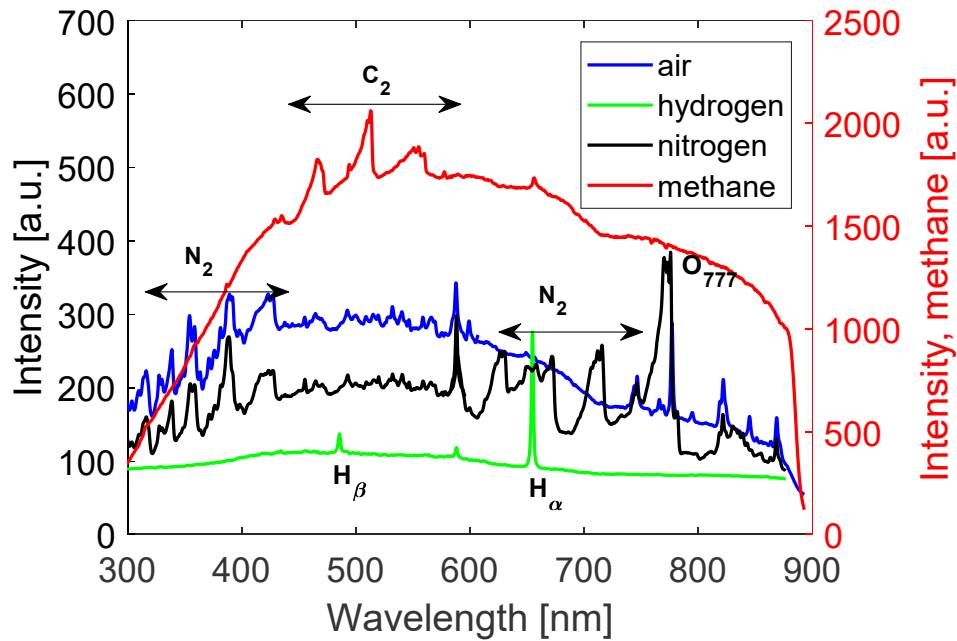
Figure 4: Spectral emissions for pure gases (air, hydrogen, nitrogen and methane) at 10 bar absolute pressure. Exposure time t_e = 2 ms, delay t_d = 0. Due to high continuum emission, methane spectral signature is plotted on a secondary axis (right, red axis).

The exposure time is not the only gating parameter affecting the measurements features: delay also plays a major role, as can be seen from the spectra plotted in Figure 5, in which emissions obtained from pure air at different delays are plotted. Tests were performed at 10 bar ambient pressure, and the exposure time is 100 ns.
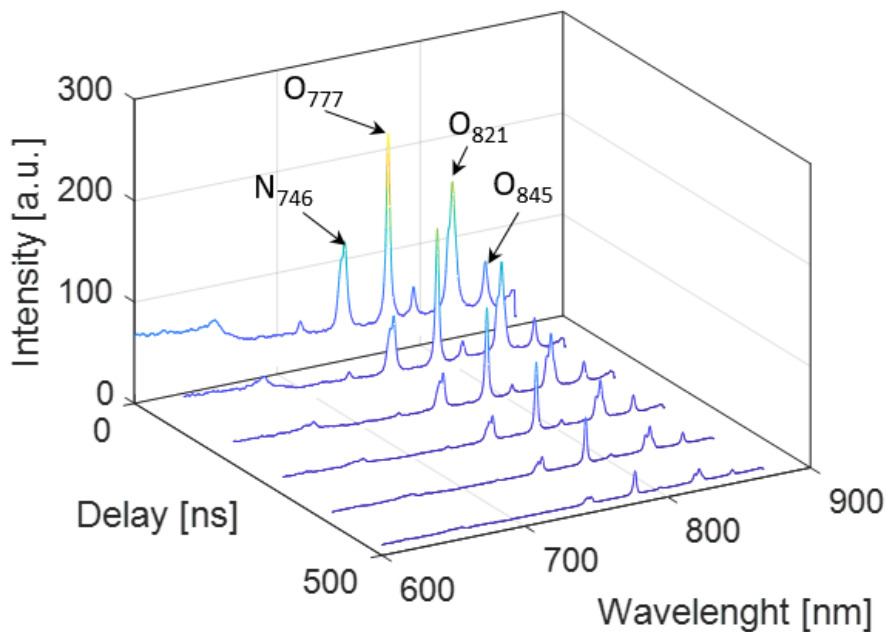
Figure 5: Spectral emissions obtained for air at different delay times. The camera exposure is 100 ns, and absolute pressure is 10 bar.

It can be noticed from Figure 5 that both the continuum emission and the atomic lines measured steadily decrease with time. In particular, the emission intensities from nitrogen at 746 nm and from oxygen at 777 nm decrease towards a minimum value, and they can be clearly recognized up to a delay value of approximately 1 µs, as shown in Figure 6. The atomic peaks ratios follow a different trend (Figure 7), being around 0.5 immediately after breakdown, and approaching a value of approximately 1 as the delay increases towards 1000 ns. It can therefore be concluded that the choice of delay and gating times is of major importance for correlations of peak intensity ratios with other parameters.
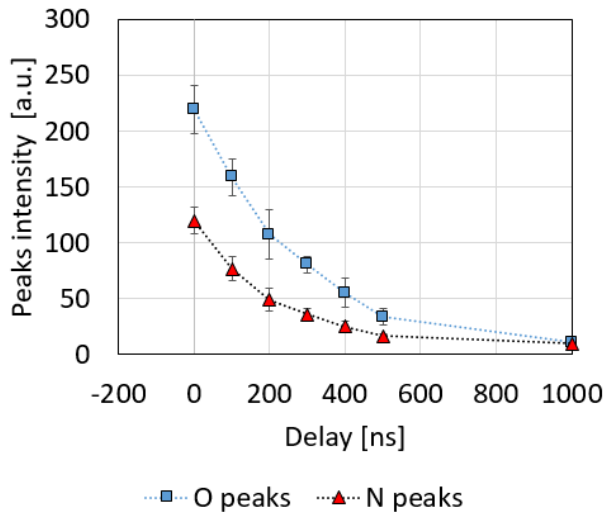

Figure 6: Oxygen (777 nm) and Nitrogen (746 nm) peaks intensity vs. delay time. Pure air, p = 10 bar.
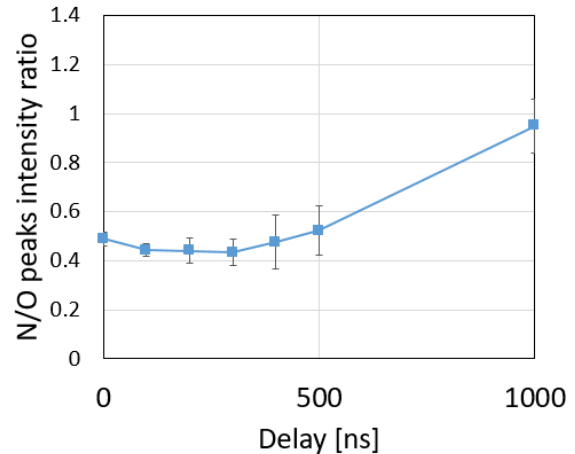
Figure 7: Nitrogen (746 nm) and Oxygen (777 nm) peaks intensity ratio vs. delay time. Pure air, p = 10 bar.

Based on the results reported for air, and based on similar results (not reported here) for other gases or mixtures, it was possible to estimate the time range after breakdown in which the emissions of interest are visible, and thus to select the most appropriate gating strategy for each case, as reported in the following sections.

3.2. Methane/hydrogen mixtures: non-reactive cases

The effect of hydrogen addition to methane was investigated, by measuring the spectral emissions of mixtures having hydrogen volume percentage ranging from 0 to 100%. Tests were performed at 2 bar, with exposure time of 300 µs. The obtained results are shown in Figure 8. The exposure time is long enough for the C_2 Swan bands to clearly appear in the spectra, between 468 and 557 nm. With increasing hydrogen content, these peaks intensity steadily decrease, while the hydrogen Balmer-α line increases. When 100% hydrogen is used, also the Balmer-β line becomes prominent enough to be clearly recognized at 486 nm.
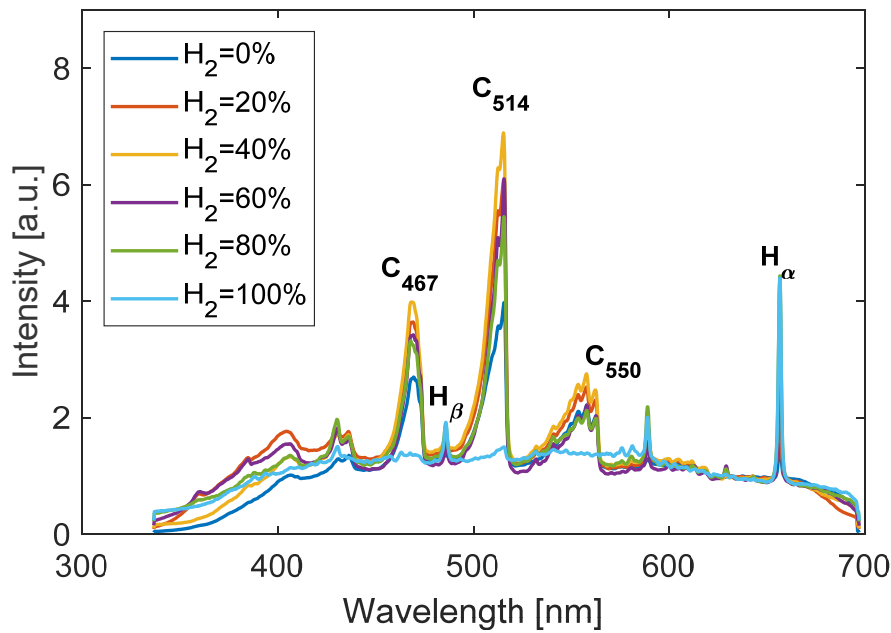
Figure 8: Spectral emissions for methane/hydrogen mixture with different volumetric hydrogen content. Absolute pressure 2 bar, exposure time t_e = 300 µs.

In order to quantify the peaks intensity variation with hydrogen addition, the peaks of hydrogen (H_α) at 656 nm and the peaks of the Swan bands at 514 (C_{514}) and 550 (C_{550}) were considered. The H/C peak intensity ratios vs. hydrogen content are plotted in Figure 9. Considering H_α/C_{514} it can be noticed that the ratio varies only slightly (0.4-0.5) up to a hydrogen content of approximately 60%. With further increase, the H/C increase becomes steeper, changing from 0.8 for 80% H_2 to 4.8 for 100% H_2. A similar behavior is obtained with H_α/C_{550}, with peaks intensity ratio increasing from about 1 to 4.7.
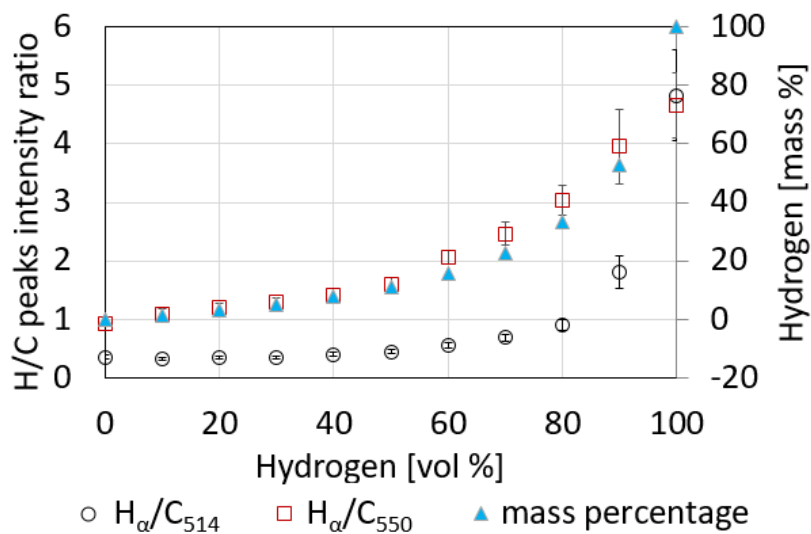
Figure 9: H/C ratio variation vs. hydrogen content in methane, for the mixtures containing different hydrogen percentages. The hydrogen mass percentage corresponding to the volume percentage is also shown (right y-axis).

This trend can be explained taking into account the mass percentage variation with respect to the volume percentage variation. Namely, the H/C intensity ratios follow the same trend as the hydrogen mass percentage (also shown in Figure 9), thus showing that the spectral emissions can be used as a diagnostic tool also in the methane/hydrogen case.

3.3.   Methane/air mixtures: reactive cases

Molecular and atomic emissions for a methane/air mixture at stoichiometric conditions ($\lambda = 1$) were investigated, and the spectral emissions were compared to the spectra obtained for the corresponding pure gases. Tests were performed at 10 bar, the delay with respect to breakdown was set to 0, and the exposure times were 2 ms for molecular emissions measurements and 5 µs for atomic emission measurements. Results are shown in Figure 10 and Figure 11. When the results for the mixture are compared to the results obtained for the single gases at the same conditions, it can be seen that the overall spectral emission change significantly depending on the exposure time.

At long exposure times (2 ms, Figure 10), the spectral signature for methane/air mixture does not show the same features as the corresponding pure gases. In particular, the carbon Swan bands for C_2 which appear in the pure methane spectral emissions disappear with the presence of oxygen and nitrogen.
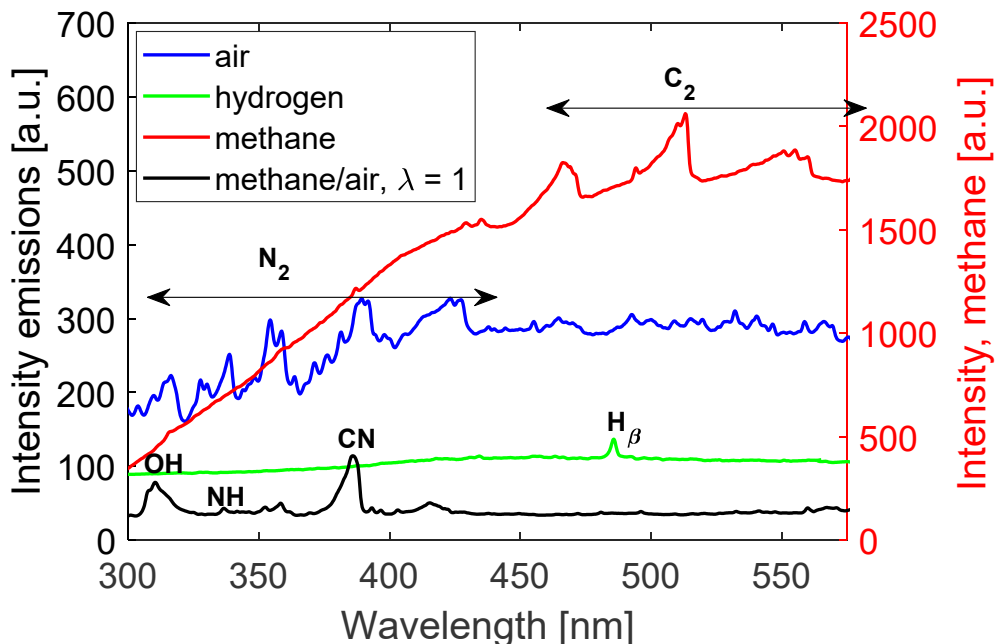
Figure 10: Spectral emissions for pure gases and for methane/air mixture, at 2 ms exposure time, absolute pressure 10 bar.

Shortly after breakdown (exposure 5 µs, Figure 11), the atomic emission of hydrogen at 656 nm, nitrogen at 746 nm and oxygen at 777 nm can be clearly recognized. The same atomic lines are recognizable when the spectral emissions of the corresponding pure gases are examined.
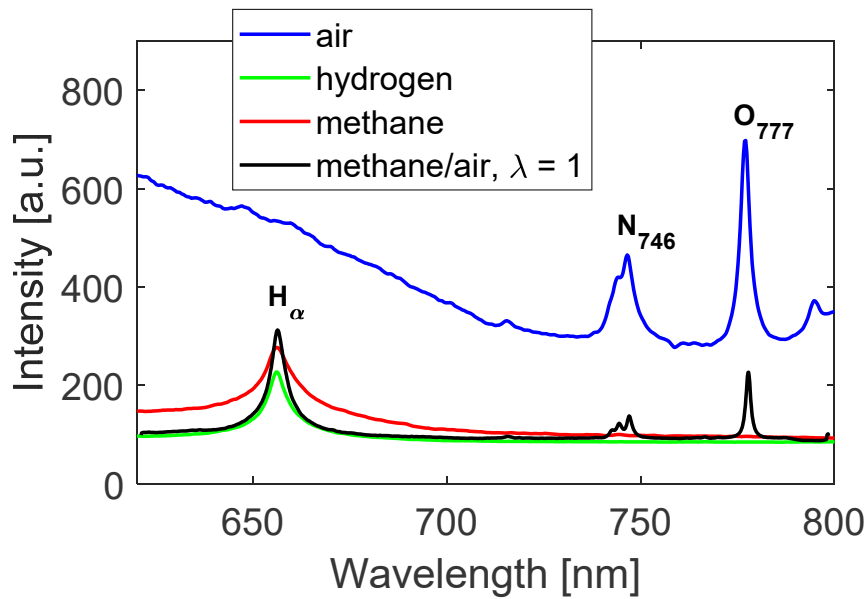
Figure 11: Spectral emissions for pure gases and for methane/air mixture, at exposure time t_e = 5 µs, absolute pressure 10 bar.

The correlation of spectral emissions features to the mixture air to fuel ratio was investigated for methane/air mixtures at different air to fuel ratios. Tests were performed at 10 bar absolute pressure, with 2 ms exposure time.

The molecular emission lines used are CN at 388 nm, OH at 306 nm and NH at 336 nm. Figure 12 shows the obtained spectra for air to fuel ratio (λ) ranging from 0.6 to 1.4. The corresponding molecular ratios (CN/NH and CN/OH) are plotted in Figure 13.
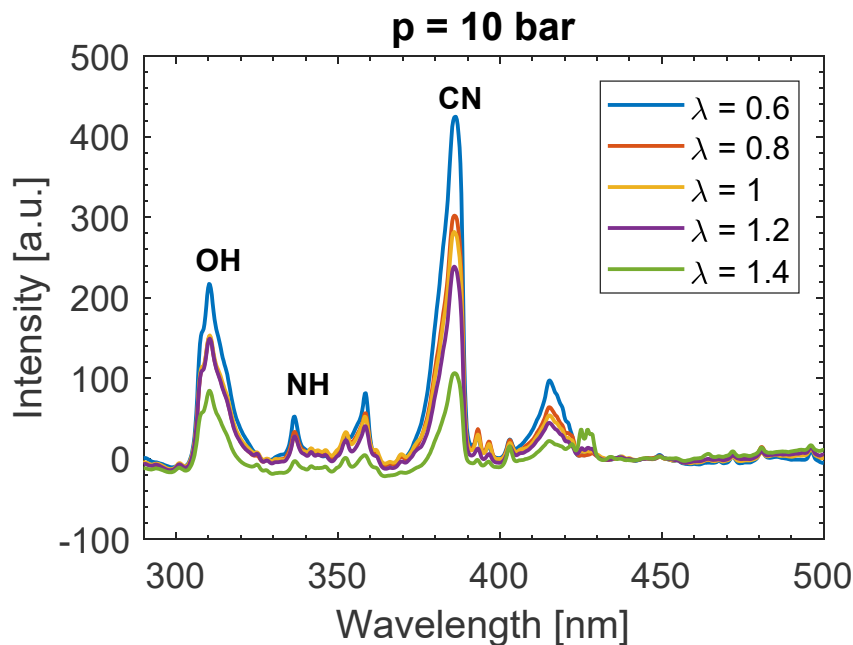
Figure 12: Spectral emissions for methane/air mixture for different air to fuel ratios. Exposure time: 2 ms.

Although a decreasing trend in molecular ratios towards lean mixtures is obtained, the shot to shot variations are high. This can be explained taking into account the long exposure time selected, which results in measurements' high sensitivity to phenomena such as re-strikes, re-attachments, plasma channel deflections.
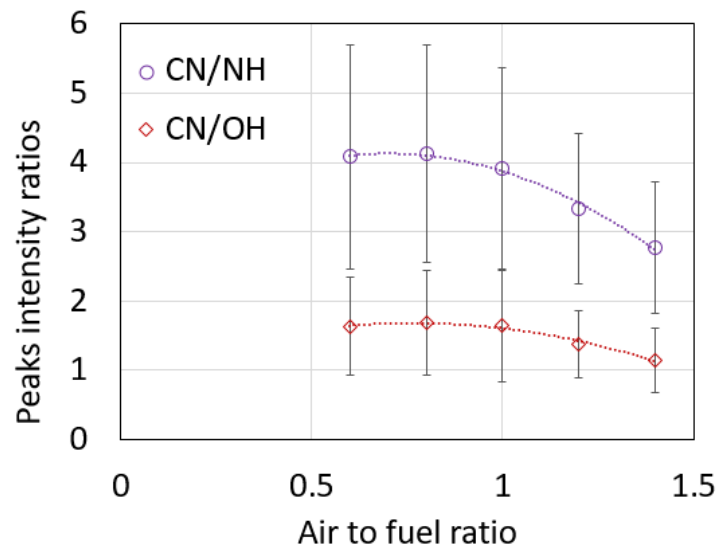
Figure 13: CN/NH and CN/OH intensity ratios at different air to fuel values.

In order to improve the standard deviation on the results, a similar investigation was performed taking into account atomic emissions. In this case, an exposure time of 5µs was used and the emission lines for H_α (656 nm), N (746 nm) and O (777 nm) were taken into account.

The emission spectra obtained, and the calculated trends for H/O and H/N ratios are shown in Figure 14 and Figure 15, respectively.
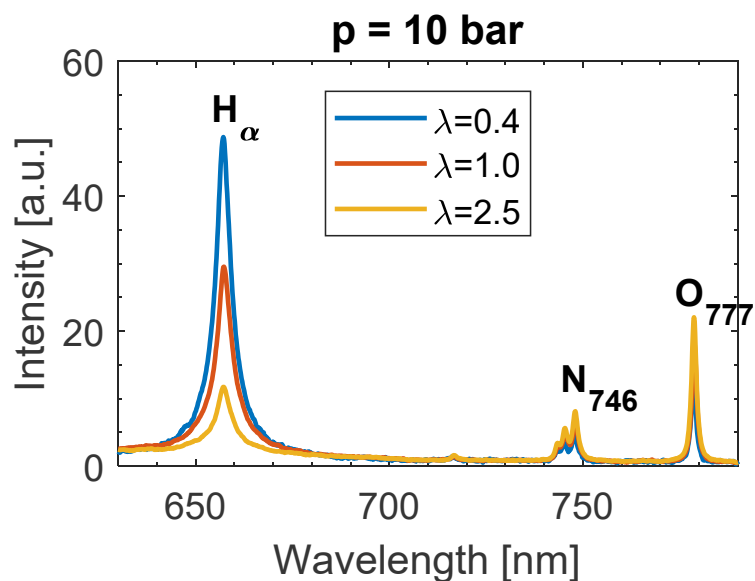
*Figure 14: Spectral emissions for methane/air mixture for different air to fuel ratios.
Exposure time: 5 µs.*
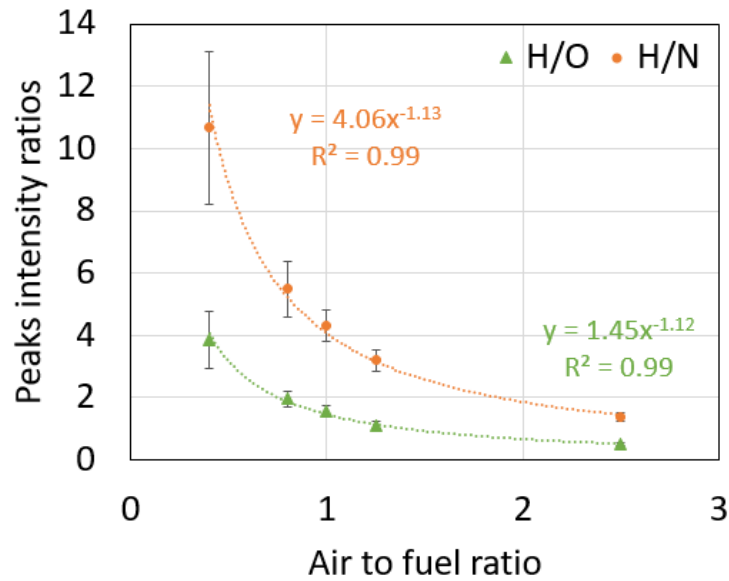
Figure 15: H/O and H/N intensity ratios at different air to fuel values.

In this case, a clearer trend is obtained, which allows correlating the air to fuel ratio with the peaks intensity ratios, and thus obtaining information on the local mixture concentration. The best signal to noise ratio is obtained for H/O ratio.

4.   Conclusions and future work

A SIBS-based diagnostic technique for local air to fuel ratio investigation was successfully developed for ignition characterization in a small constant volume cell.
Results are presented in this paper for different quiescent mixture compositions at ambient temperature and elevated pressure conditions. The role of methane, air and hydrogen on the electrical discharge characteristics and the plasma emissions are discussed. Moreover, spectral emissions in different ambient conditions and for different mixtures were compared and discussed, with the aim to obtain a deeper insight on the SIBS response to the complex physical and chemical phenomena underlying the ignition event. Emissions from single gases (pure air, methane, hydrogen and nitrogen) were measured at different exposure times, showing that atomic emission lines from oxygen, nitrogen and hydrogen can be recognized at shorter gating, while molecular emissions (C_2 and N_2) can be identified for longer exposure time. The role of delay time was also discussed, showing that atomic peaks in air at 10 bar can be recognized up to approximately 1 µs from breakdown. Peak intensity ratios of di-atomic carbon with the hydrogen Balmer-α was measured in methane-hydrogen mixtures with hydrogen volumetric content ranging from 0 to 100%, showing a matching trend with the hydrogen mass fraction in the mixture. Finally, reactive methane/air mixtures were investigated both in terms of molecular and atomic emissions vs. air to fuel ratio. Results show that a lower shot to shot variation and a clearer trend with mixture composition is found when atomic lines are used, with best signal to noise ratios for H/O ratios.

The results reported in this paper show that the proposed technique is a compact and versatile tool for applications involving atomic and molecular species detection in different ambient conditions.

In order to apply the SIBS-based diagnostic tool to running engines, further development is needed. For this purpose, a modified spark plug with fiber optics was designed and implemented with the aim to transfer the SIBS diagnostic technique from the constant volume cell to engine test rigs. Work is ongoing to test the feasibility of the fiber-optics equipped spark plug for SIBS diagnostics in the setup described in this paper, and subsequently in running engines.

Acknowledgements

References

[1]   U. Spicher, T. Heidenreich, Stratified-charge combustion in direct injection gasoline engines, in: Adv. Direct Inject. Combust. Engine Technol. Dev., Elsevier, 2010: pp. 20–44. doi:10.1533/9781845697327.20.

[2]   Aleiferis PG, Taylor AMKP, Ishii K, Urata Y, The nature of early flame development in a lean-burn stratified-charge spark-ignition engine, Combust. Flame. 136 (2004) 283–302. doi:10.1016/j.combustflame.2003.08.011.

[3]   Y. Takagi, A new era in spark-ignition engines featuring high-pressure direct injection, Symp. Int. Combust. 27 (1998) 2055–2068. doi:10.1016/S0082-0784(98)80052-0.

[4]   P. Danaiah, R. Kumar P, V. Kumar D., Lean Combustion Technology for Internal Combustion Engines: a Review, Sci. Technol. 2 (2012) 47–50. doi:10.5923/j.scit.20120201.09.

[5]   J.H. Weaving, Stratified Charge Engines, in: J.H. Weaving (Ed.), Intern. Combust. Eng. Sci. Technol., Springer Netherlands, Dordrecht, 1990: pp. 137–171. doi:10.1007/978-94-009-0749-2_5.

[6]   T.D. Fansler, D.L. Reuss, V. Sick, R.N. Dahms, Invited Review: Combustion instability in spray-guided stratified-charge engines: A review, Int. J. Engine Res. 16 (2015) 260–305. doi:10.1177/1468087414565675.

[7]   R.M. Merer, J.S. Wallace, Spark spectroscopy for spark ignition engine diagnostics, SAE Tech. Pap. (1995). doi:10.4271/950164.

[8]   R. Maly, Spark ignition: its physics and effect on the internal combustion engine, in: Fuel Econ., Springer, 1984: pp. 91–148.

[9]   D.R. Ballal, A.H. Lefebvre, The influence of flow parameters on minimum ignition energy and quenching distance, Symp. Int. Combust. 15 (1975) 1473–1481. doi:10.1016/S0082-0784(75)80405-X.

[10] C.C.O.B. Reynolds, R.L. Evans, Improving emissions and performance characteristics of lean burn natural gas engines through partial stratification, Int. J. Engine Res. 5 (2004) 105–114. doi:10.1243/146808704772914282.

[11] H. Biffiger, P. Soltic, Effects of split port/direct injection of methane and hydrogen in a spark ignition engine, Int. J. Hydrog. Energy. 40 (2015) 1994–2003. doi:10.1016/j.ijhydene.2014.11.122.

[12] P. Soltic, T. Hilfiker, S. Hänggi, R. Hutter, M. Weissner, Ignition- and combustion concepts for lean operated passenger car natural gas engines, in: Sustain. Altern., FKFS, Stuttgart, 2017.

[13] W. Lee, J. Wu, Y. Lee, J. Sneddon, Recent Applications of Laser-Induced Breakdown Spectrometry: A Review of Material Approaches, Appl. Spectrosc. Rev. 39 (2004) 27–97. doi:10.1081/ASR-120028868.

[14] L. Merotto, M. Sirignano, M. Commodo, A. D'Anna, R. Dondè, S. De Iuliis, Experimental Characterization and Modeling for Equivalence Ratio Sensing in Non-premixed Flames Using Chemiluminescence and Laser-Induced Breakdown Spectroscopy Techniques, Energy Fuels. 31 (2017) 3227–3233. doi:10.1021/acs.energyfuels.6b03094.

[15] F. Ferioli, S.G. Buckley, Measurements of hydrocarbons using laser-induced breakdown spectroscopy, Combust. Flame. 144 (2006) 435–447. doi:10.1016/j.combustflame.2005.08.005.

[16] S. Joshi, D.B. Olsen, C. Dumitrescu, P.V. Puzinauskas, A.P. Yalin, Laser-induced breakdown spectroscopy for in-cylinder equivalence ratio measurements in laser-ignited natural gas engines, Appl. Spectrosc. 63 (2009) 549–554.

[17] T.X. Phuoc, F.P. White, Laser-induced spark for measurements of the fuel-to-air ratio of a combustible mixture, Fuel. 81 (2002) 1761–1765. doi:10.1016/S0016-2361(02)00105-9.

[18] K.M. Abdul Rahman, N. Kawahara, D. Matsunaga, E. Tomita, Y. Takagi, Y. Mihara, Local fuel concentration measurement through spark-induced breakdown spectroscopy in a direct-injection hydrogen spark-ignition engine, Int. J. Hydrog. Energy. 41 (2016) 14283–14292. doi:10.1016/j.ijhydene.2016.05.280.

[19] M.H. Morsy, Review and recent developments of laser ignition for internal combustion engines applications, Renew. Sustain. Energy Rev. 16 (2012) 4849–4875. doi:10.1016/j.rser.2012.04.038.

[20] N. Kawahara, E. Tomita, S. Takemoto, Y. Ikeda, Fuel concentration measurement of premixed mixture using spark-induced breakdown spectroscopy, Spectrochim. Acta Part B At. Spectrosc. 64 (2009) 1085–1092. doi:10.1016/j.sab.2009.07.016.

[21] T.D. Fansler, B. Stojkovic, M.C. Drake, M.E. Rosalik, Local fuel concentration measurements in internal combustion engines using spark-emission spectroscopy, Appl. Phys. B Lasers Opt. 75 (2002) 577–590. doi:10.1007/s00340-002-0954-0.

[22] N. Kawahara, S. Hashimoto, E. Tomita, Spark discharge ignition process in a spark-ignition engine using a time series of spectra measurements, Proc. Combust. Inst. 36 (2017) 3451–3458. doi:10.1016/j.proci.2016.08.029.

[23] K. Kuwahara, H. Ando, Diagnostics of in-cylinder flow, mixing and combustion in gasoline engines, Meas. Sci. Technol. 11 (2000) R95–R111. doi:10.1088/0957-0233/11/6/202.

[24] T. Kammermann, W. Kreutner, M. Trottmann, L. Merotto, P. Soltic, D. Bleiner, Spark-induced breakdown spectroscopy of methane/air and hydrogen-enriched methane/air mixtures at engine relevant conditions, Spectrochim. Acta Part B At. Spectrosc. 148 (2018) 152–164. doi:10.1016/j.sab.2018.06.013.

4.2 Spatio-temporally Resolved Emission Spectroscopy of Inductive Spark Ignition in Atmospheric Air Condition

Wooyeong Kim, Choongsik Bae, Tobias Michler, Olaf Toedter, Thomas Koch

Abstract

Current transistorized coil ignition (TCI) system consists of ignition coil and spark plug, whose electrical properties, structure and gas composition determine entire discharge processes and therefore the early stage of combustion. In this work, a new measurement and diagnostic technique were developed and tested to investigate the early phases of spark ignition process. The spark discharge of commercial TCI system was analyzed by using spatio-temporally resolved optical emission spectroscopy to find out the Interrelation of the characteristic evolution of discharge with the formation of reactive species inside the activated volume.

The emission spectra of inductive spark discharge in atmospheric air were measured at the range of wavelength from 300 to 800 nm, while the secondary voltage and current of spark ignition system were acquired simultaneously. An optical probe with linearly arranged glass fiber bundle was used to achieve spatial distribution of emission intensity vertically along the electrode gap of spark plug. At the same time, the time series of emission spectra were illustrated by using the precise gate shift operation of intensified CCD camera mounted on the spectrograph.

The emission of electronically excited species such as molecular nitrogen, atomic oxygen and electrode material were effectively measured with the spectral resolution of 0.2 nm. During the abrupt increase of current in breakdown phase, only molecular nitrogen emission was exclusively detected. It was followed by the atomic oxygen and electrode material, which are closely related to the flame initiation and electrode wear respectively. The activated volume of spark discharge near cathode showed higher emission intensity for all the aforementioned species in comparison with the region near anode. The electronic, vibrational and rotational temperatures of the discharge were calculated by using additional spectra measurement at selective wavelength range with spectral resolution of 0.1 nm. Alongside the calorimetric measurement, the temperature profile over position and time allowed the quantitative evaluation of energy-transfer efficiency of spark discharge into the gas mixture.

1   Introduction

Spark ignition is a way of initiating the combustion process of fuel-air mixture by generating electrical discharge in the combustion chamber of internal combustion engine. Current spark-ignition (SI) engines for passenger cars are equipped with transistorized coil ignition (TCI) systems, which comprise of an ignition coil and a spark plug for each cylinder. The ignition coil has primary and secondary coils, which provide high-voltage electric potential between the middle and ground electrodes of spark plug. The spark ignition is apparently the most important process of SI engine operation, since the thermodynamic condition of mixture at ignition timing directly affects the fuel consumption and the pollutant emission of the engine [1].

The conventional TCI system, however, acts as a technology which limits further efficiency improvement, because the advanced combustion process results in unfavorable thermodynamic condition for igniting the fuel-air mixture. Therefore, various types of alternative ignition systems have been developed and tested while aiming at extending ignitibility limit and/or reducing the burn delay. The application of non-thermal plasma has been recognized as the most promising solution in the recent decades. Nevertheless, the traditional combination of ignition coil and spark plug still remains as the only available mass-production ignition system due to its high cost-effectiveness and reliability at most of engine operation points.

Spark discharge is a phenomenon with dynamic nature, thus it accompanies sudden changes in its physical property and close-to-zero repeatability in real experiment condition. The term "spark discharge" may have to be recognized as a collective term describing a phenomenon, in which a plasma channel is generated with bright and sudden "flash" between two electrodes. In addition, the spark discharge process of automotive spark ignition system does not follow the well-known voltage-current profile of gas discharges [2], since in the case of coil ignition the charge carriers cannot be steadily provided with increasing discharge current as assumed in the gas discharge physics.

This work aimed to characterize the spark discharge process for automotive application by developing a package of diagnostic technique and analysis tool on the basis of established theory and experimental approaches in the gas discharge physics. Based on this experimental data, the sequence of reactive species formation and variation of discharge temperature were investigated and illustrated in the form of both spatially and temporally resolved information. There exist a great number of related previous studies and methodologies to be reviewed, but this literature work is instead to be properly covered in the authors' publication [3]. The essential backgrounds for the experimental approaches and data analysis are included in corresponding sections.

2   Experimental setup

2.1   Spark ignition system and electrical measurement

The spark discharge was generated between the central and ground electrodes of a commercial spark plug in atmospheric-pressure air. A commercial spark plug was mounted in a tinplate chamber, which ensures electromagnetic shielding from the surroundings. The chamber and the entire measurement devices were placed in an air-conditioned laboratory facility. A commercial ignition coil was used to provide ignition voltage to the spark plug electrodes. The discharge voltage was measured by a high-voltage probe (Tektronix P6015A), and the current was measured by a current monitor

(Pearson Electronics 2877). The measured voltage and current were acquired by a four-channel oscilloscope (LeCroy WaveRunner 6030A with bandwidth of 350 MHz) with triggered data-logging function (Figure 1).

2.2   Spectroscopic measurement

The light emission of spark discharge was transmitted through a fiber-optic cable, in which seven glass fibers are linearly arranged at both ends (Figure 2). The glass fibers have core diameter of 100 μm and numerical apparatus of 0.22. One end of the cable was located in front of the spark plug electrodes, while the 3-dimentional positioning of the cable end was adjusted by using precise optomechanical devices (Figure 3). The other end of the cable was adapted to the entrance slit of a spectrograph, so that the light was transmitted while the spatial distribution of emission can be maintained. The spectrograph (Acton Research Corporation SP-2556 with focal length of 500 mm) was equipped with three different gratings, among them the gratings with density of 1200 and 600 grooves/mm were used in the experiment. An intensified charge-coupled device (ICCD) camera (Princeton Instrument PI-MAX with full-size resolution of 1024x256 pixels) was mounted to the spectrograph to record the spectra. The gain, gate timing and gate width were programmed by the Programmable Timing Generator (PTG) module of the spectrograph. The PTG ensures a precise gate control in sub-nanosecond range.

2.3   Calibration for spectroscopic measurement

Precise calibration is necessary to minimize errors, which may arise from every part of the whole optical system. A calibration lamp using low-pressure discharge of gaseous mercury and argon (LOT-Oriel LSP035) was used for the wavelength calibration of spectrograph system and calculation of spectral resolution. The intensive atomic emission lines of mercury and argon lie from 200 to 450 nm and 700 to 800 nm respectively, thus these could cover the wavelength ranges of interest.

Besides, the luminous intensity of the ray arriving the spectrograph may be locally reduced due to the inconsistent transmittance of the optical components, especially the fiber optics in this setup. To compensate this, the transmittance of the system was also calculated by measuring the continuous emission spectra of a tungsten calibration lamp (Osram WI 17/G). Here, the absolute transmittance was not able to obtain, but the spatial distribution of relative transmittance was calculated and used in the post-processing of spectra.
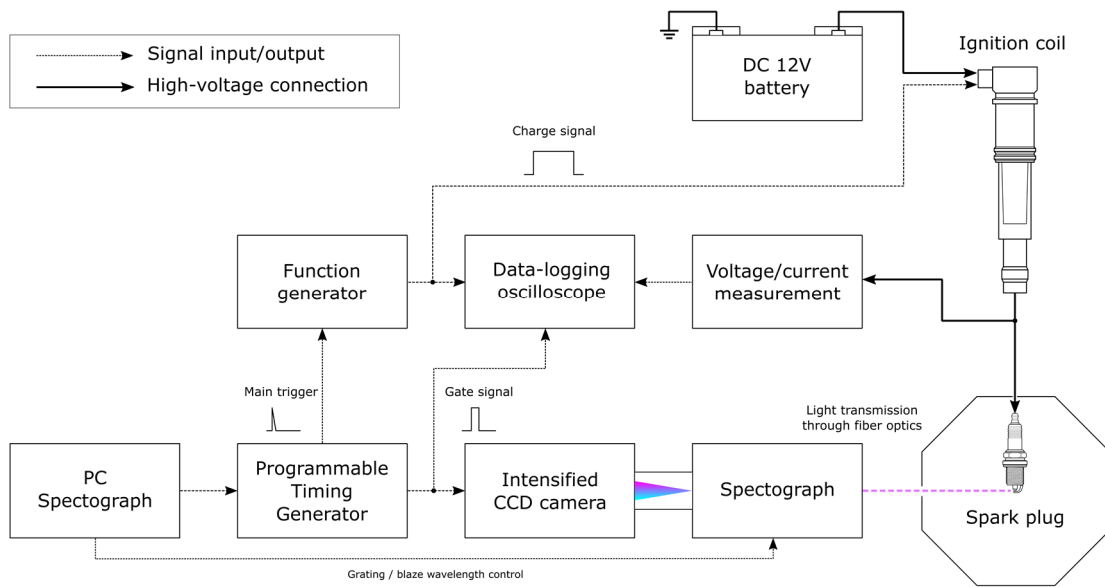
Figure 1: Schematic diagram of the experimental setup.
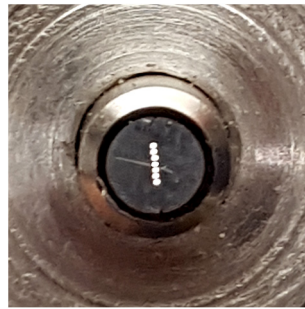
Figure 2: Linear bundle end of the fiber-optic cable.
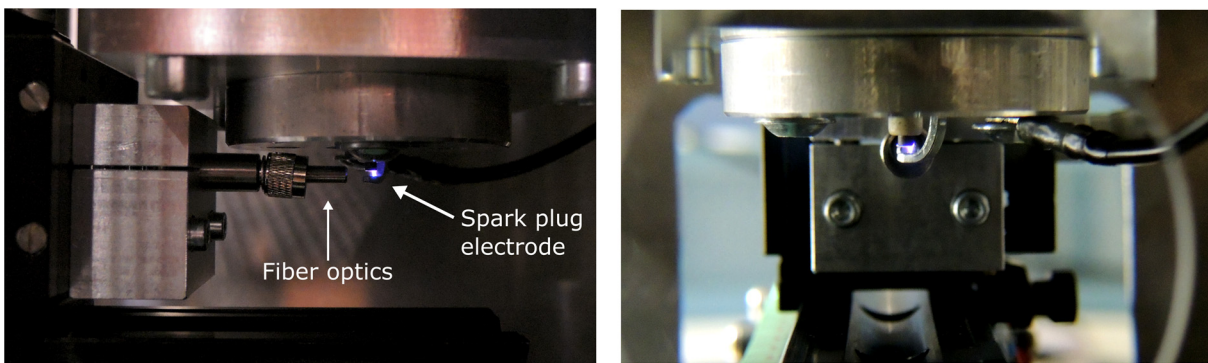
Figure 3: Configuration of spark plug and fiber optics with optomechanical components.

2.4   Signal synchronization

The test campaign was designed to be driven by automated macro process of spectrograph control system. Figure 4 schematically shows how trigger signals of the measurement system were synchronized. A measurements begins with giving start trigger

from the control PC of spectrograph to PTG. The PTG then generates a trigger to the function generator to charge the ignition coil. At the same time, another identical trigger is generated from the PTG to the oscilloscope to acquire voltage and current data from each measuring devices (probes). The PTG is also controlled by the spectrograph PC, in which the gate delay and gate width of intensified CCD camera can be controlled. The macro process is so programmed that the gate delay increases by gate width after each measurement. The gate signal for each measurement is also acquired by the oscilloscope simultaneously.

The gate timing sweep scheme is illustrated in Figure 5 with secondary voltage and current profile. The initial gate width was set to 10 µs to secure both temporal resolution and sufficient signal-to-noise ratio. After 400 µs from the breakdown (start of discharge), the gate width had to become longer up to 100 µs, since the luminous emission of the glow discharge phase was much weaker than the breakdown and arc phase. This does not actually deteriorate the temporal resolution, because obviously a rapid change in physical properties in this phase is unlikely to occur. For each time step, the measurement was repeated for ten times.

In summary, three sets of electrical data – secondary voltage, secondary current, and ICCD gate time – and one spectrum are achieved after each measurement. This synchronization scheme facilitates creating a time series of spatially-resolved spectra by arranging the spectra by each gate timing in the post-processing.
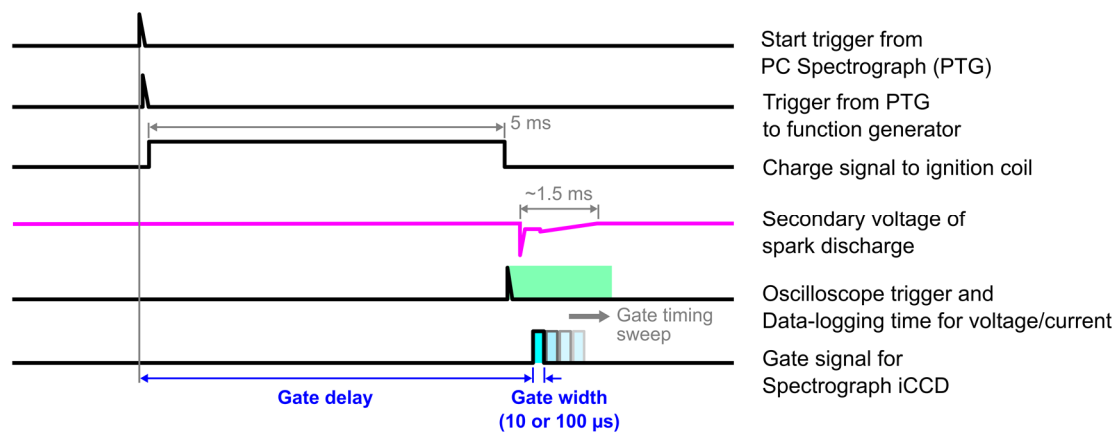
Figure 4: Synchronization of main trigger with charge signal, oscilloscope trigger and gate time for spectrum measurement (PTG: Programmable Timing Generator).
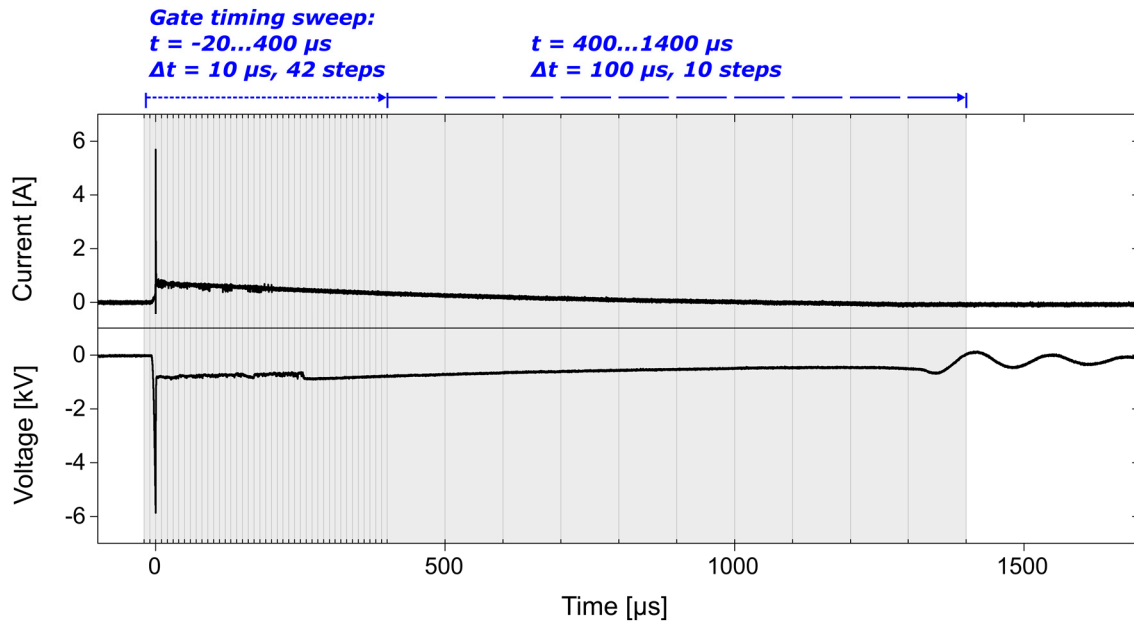
Figure 5: Gate timing sweep scheme with two different gate width.

3   Results and discussion

3.1   Time series of emission spectra

Figure 6 shows the time series of measured emission spectra of spark discharge in two wavelength ranges. In this measurement, the central wavelength was varied from 300 to 780 nm with 40 nm step by using the grating with 600 grooves/mm. In combination with the entrance slit width of 100 μm, the spectral resolution (FWHM, full width at half maximum) of measured spectra was calculated to be 0.2 nm.

Here, the spatially-distributed emission intensities were added together and mean values of ten repetition were calculated. To highlight the temporal variation in emission lines, the spectra with time step of 10 μs were merged to show the spectra variation consistently with fixed time step of 100 μs. In Figure 6, only the first spectra at t=0 in each diagram were measured with time step of 10 μs. Each spectrum was normalized with its gate delay to fairly compare the emission intensity.

In the whole wavelength range, the emission intensity was dramatically reduced just after the breakdown – around 90% on peak-value basis. Most of the emission peaks were easily recognizable on the basis of previous studies on atmospheric-condition air discharge [4, 5] and spectroscopic data [6, 7]. In the breakdown phase, nitrogen molecule (N_2) emitted intense light – the second positive system (C-B) between 300 and 400 nm and the first positive system (B-X) between 600 and 800 nm – with its distinct rotational-vibrational structure. As breakdown ended, the well-known atomic emission of oxygen (O 1) in 777 nm sharply increased. As the oxygen emission decreased gradually, relatively intense and sharp emission lines were detected for around 200 μs. These peaks between 340 and 360 nm are the atomic emission lines of nickel (Ni 1), which is the one of the major elements of electrodes. This time scale approximately corresponds to the conventional definition of arc discharge phase. After then, roughly in the transition towards glow discharge, the molecular ion of nitrogen (N_2^+) emission – the first negative system in 391 nm – became as intensive as the N_2 emission. After

214

400 µs, no sudden change in spectrum took place, and the intensity decreased globally until the end of discharge.
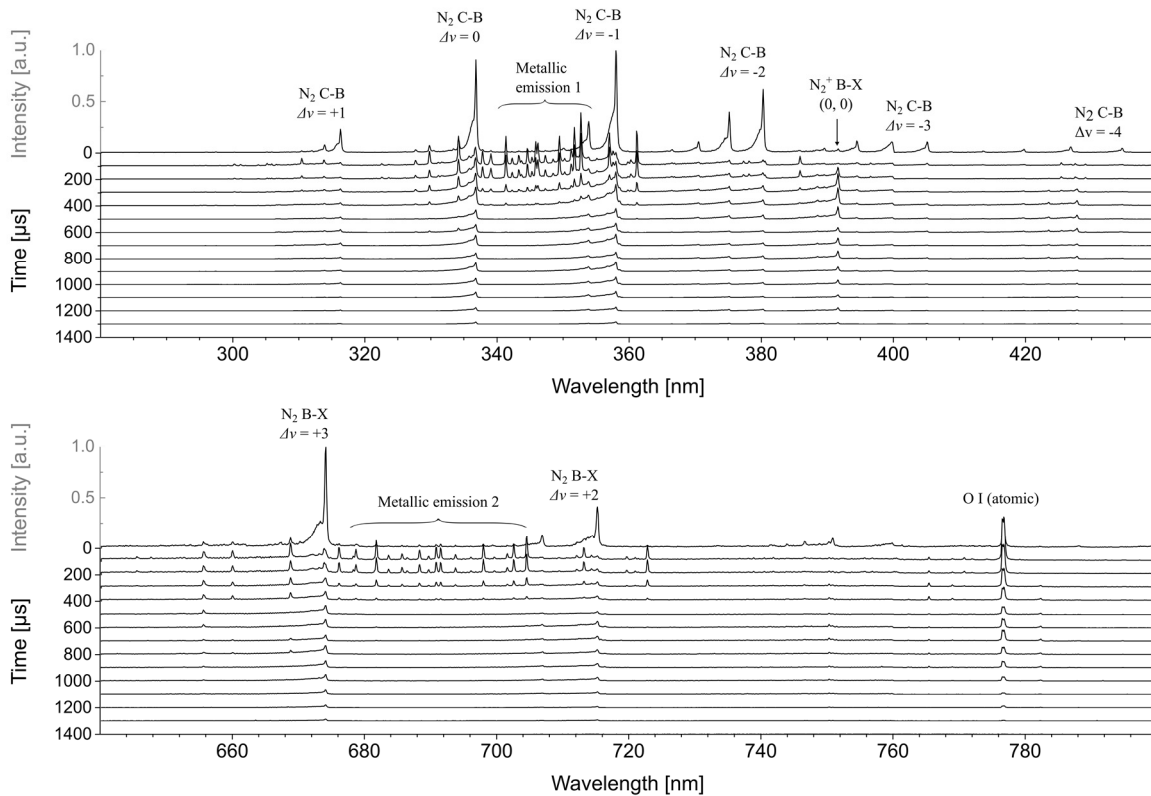
Figure 6: Time series of emission spectra of spark discharge.

3.2   Spatio-temporal distribution of reactive species formation

The measured spectra were post-processed to track the formation of reactive species within the spark discharge. Four emission peaks were selected:
- N_2 C-B (0, 0) emission at 337.0 nm,
- Ni I atomic emission at 341.4 nm,
- N_2^+ B-X (0, 0) emission at 391.2 nm, and
- O I atomic emission at 777.1 nm.

Figure 7 shows the distribution of peak intensities in color on time and position axes. Each diagram in this figure – and some of the following figures – contains seven strips of data, which represent the light emission transmitted via seven glass fibers. The "position" denoted here represents the vertical position from the ground electrode (anode), thereby the upper most strip corresponds to the closest position to the central electrode (cathode). Each data point is an averaged value of ten repetitions.

In all the four diagrams, the upper half of the region generally shows higher emission intensities than the lower half. This indicates that the formation of these species occurs more actively near the cathode than the anode. As watching the variation on the time axis, the time, in which each species formation is most active, lies side by side for the four species. Since the emission intensity represent the concentration of excited species, this result clearly identifies the dynamics of the early spark discharge process by establishing the sequence of reactive species formation.
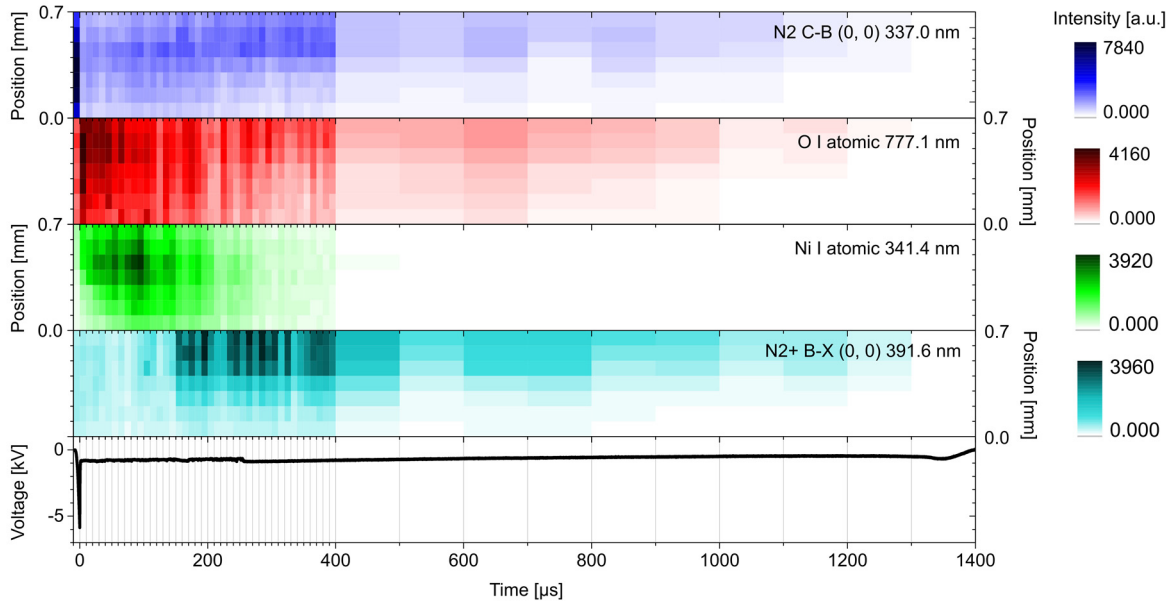
Figure 7: Spatio-temporal distribution of peak intensities of reactive species along with the secondary voltage. The y-axis of each diagram represents the spatial position from ground electrode of spark plug.

3.3   Temperature calculation process

The emission spectra, especially those of diatomic molecules like N_2 or OH, have been widely used to calculate the temperature of gas discharges [8-10] and also of hydrocarbon flames [11]. Since the electron and heavier neutral molecules are often not equally excited, the temperature of gas discharge cannot be defined simply as that of the gases in ambient condition. Commonly used terms are the electronic (T_{el}), vibrational (T_{vib}) and rotational temperature (T_{rot}) to describe electron and gas temperatures, which are not equal in most of plasma under non-equilibrium condition [12-13].

For the temperature calculation, higher spectral resolution is beneficial since the rotational structure of a diatomic molecule can be obtained. In this set of experiment, the grating with 1200 grooves/mm was selected, and the FWHM was calculated to be 0.1 nm. Two central wavelength of 355 and 385 nm were chosen: In 355 nm, N_2 C-B (0, 1) can be measured with sufficient signal-to-noise ratio, in 385 nm, both N_2 C-B and N_2^+ B-X (0, 0) can be measured.

An open-source spectrum simulation program [14] was integrated in an iteration routine. This in-house program runs the spectra simulation program with a matrix of temperatures (T_{rot}, T_{vib}, T_{el}) and generates simulated spectra. For each measured spectrum, the sum of square error was calculated to find the best fit with the least error among the matrix of simulated spectra.

3.4   Spatio-temporal variation of discharge temperature

In the analysis of following temperature estimation, a wider time step was used in order to increase signal-to-noise ratio for the calculation with less error. The data of breakdown phase was unchanged with its own 10 µs time step, but for arc and glow phase the previous time steps were merged to 100 and 200 µs respectively.

3.4.1 Rotational and vibrational temperatures – from N_2 emission at 355 nm

The rotational (T_{rot}) and vibrational temperatures (T_{vib})of discharge were obtained by comparing measured spectra with simulated spectra at wavelength between 345 and 365 nm. In this range, N_2 C-B emission is found with two distinct peaks – vibrational band (0,1) at 357.6 nm and (1,2) at 353.6 nm [15]. Figure 8 shows samples of best-fit results from breakdown and glow discharge phases. These temperatures are also illustrated in spatio-temporally resolved style in Figure 9. The T_{rot} in breakdown phase reached only 500 K, while the temperature increased immidiately from the next time step. In glow discharge phase between 600 and 1000 µs, the T_{rot} increased up to 3300 K, and the discharge cooled down slowly with time so that the T_{rot} was still about 2200 K at the very end of the discharge. The T_{vib} in breakdown phase was by far higher than T_{rot} by reaching 5000 K. In glow phase T_{vib} showed similar tendency as for T_{rot}. The temperatures obtained here in arc discharge phase between 100 and 400 K seems controversial, since the T_{vib} was calculated to be by far lower than T_{rot} [13]. The validity of this part of result will be discussed in the last section.
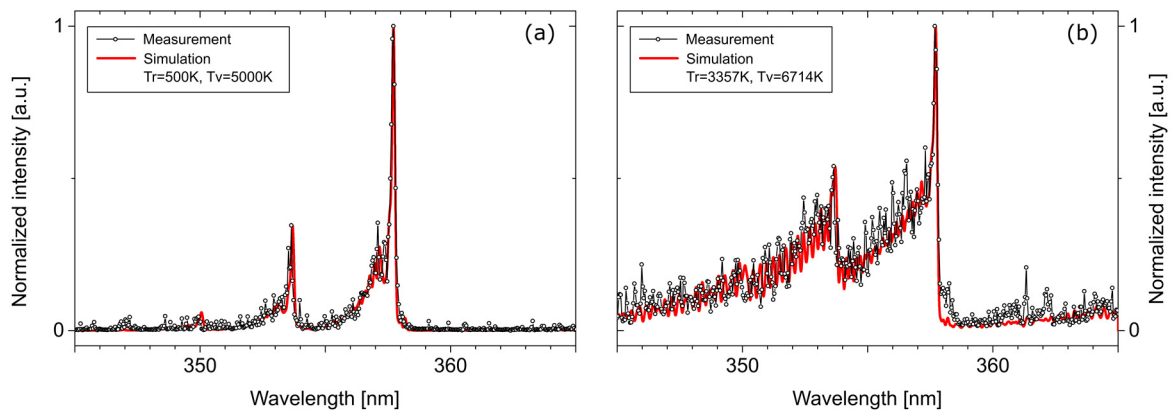
Figure 8: Best-fit results for (a) breakdown and (b) glow discharge phase for wavelength between 345 and 365 nm.
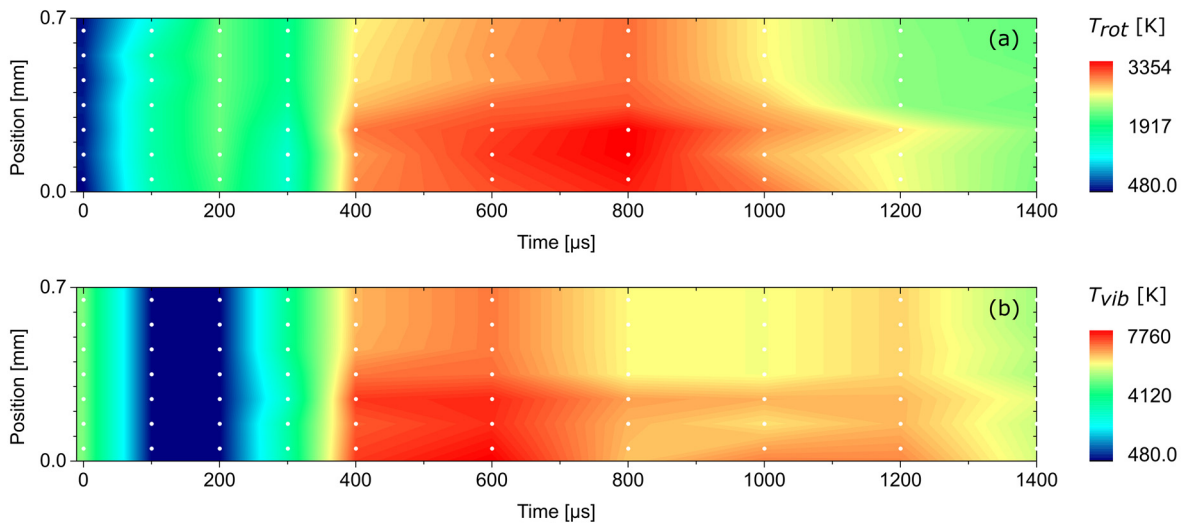
Figure 9: spatio-temporal variation of (a) rotational and (b) vibrational temperature of spark discharge.

3.4.2 Electronic temperature – from N_2 and N_2^+ emission at 385 nm

The electronic temperature (T_{el}) was obtained by comparing spectra at wavelength between 375 and 395 nm. Here, N_2 C-B emission with (0,2) band at 380.4 nm and the band head of N_2^+ B-X emission (0,0) at 391.2 nm are located. Figure 10 shows the best-fit results for breakdown and glow phase. Here, one can clearly notice the difference in the shape of spectra for two examples. The difference results from the relative intensity of N_2^+ at 391.2 nm over N_2 at 380.4 nm. The N_2^+ emission was almost neglibable in breakdown phase, and as a result an extremely high T_{el} up to about 18000 K was obtained. After then, as also well illustrated in Figure 6, the N_2^+ emission increases rapidly and disappears rather slowely until the end: Oppositely, the T_e was reduced and maintained its level at around 10000 K (Figure 11).
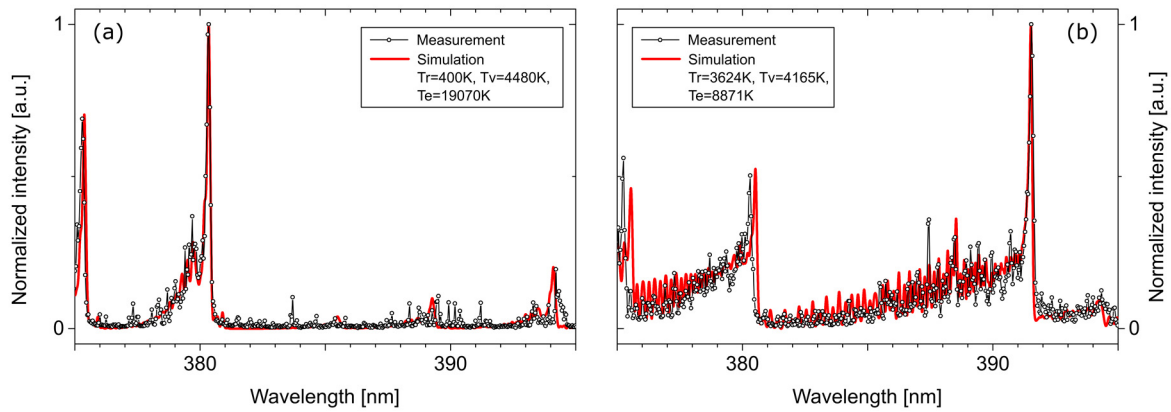
Figure 10: Best-fit results for (a) breakdown and (b) glow discharge phase for wavelength between 375 and 395 nm.
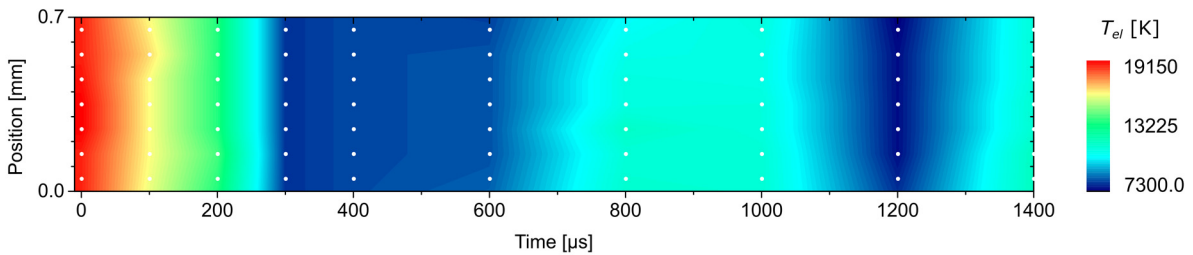
Figure 11: Spatio-temporal variation of electron temperature in spark discharge.

3.4.3 Summary with error analysis

Figure 12 illustrates the sum of square error for each best-fit results for two wavelength ranges. The darker the color of surface is, the higher the error is, i.e. the more the measured and simulated spectra deviate. Thus, it clearly indicates that the reliability of results for T_{rot} and T_{vib} is insufficient especially in the arc discharge phase between 0 and 300 µs. This verifies what caused the conflicting results discussed with Figure 9. Two reasons possibly account for this result: First, there exist numorous and intense atomic emission of nickel during arc phase, which overlap in large part with the existing N_2 emission. Second, even though there exist some measured spectra with relatively less intense Ni peaks, the N_2 emission does not show its distinct rovibrational structure. This may results either from a severely non-equilibrium state of discharge or an error induced from limited spectral resolution.

For T_e calculation, the sum of square error was globally higher than previous case, but this resulted from a wider "oscillation" of rotational structure and wavelength offset of measured spectra, as typically shown in Figure 10 between 375 and 380 nm. Looking into best-fit results individually, this can be improved by investing more computing effort with shorter and more temperature steps.

In summary, Figure 13 illustrates the spatially-averaged temporal development of T_{rot}, T_{vib}, and T_{el} of the spark discharge. The data points resulting in high sum of error are partly masked to avoid any misleading information.
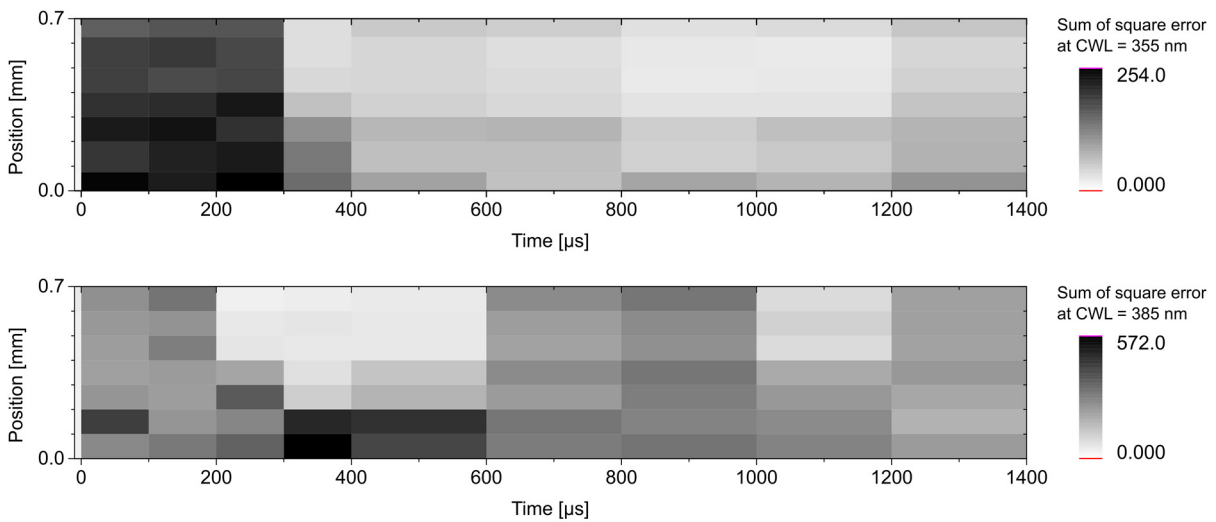
Figure 12: Sum of square error calculated from the best-fit results.
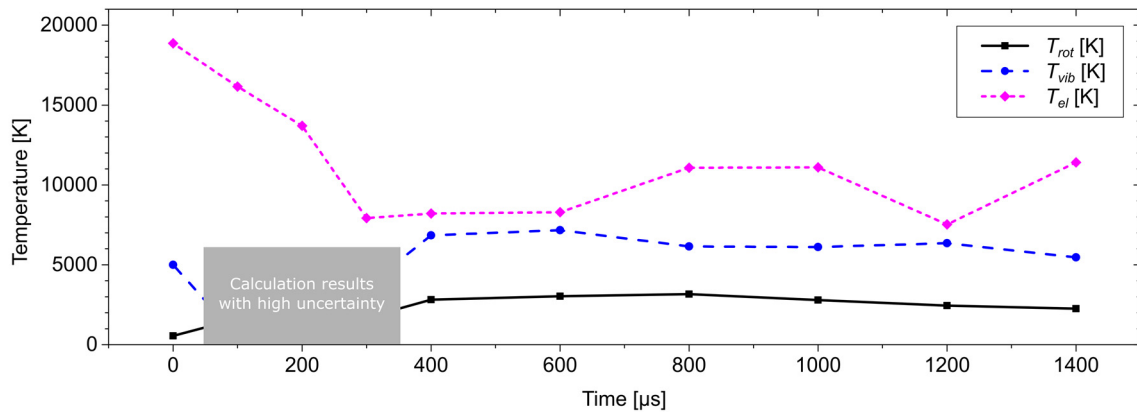
Figure 13: Temporal variation of rotational, vibrational, and electronic temperature of spark discharge.

4 Conclusions

The spark discharge of conventional automotive spark ignition system was investigated by measuring the time series of spatially-resolved emission spectra in atmospheric-pressure air condition. The experimental approach developed in this work was capable of resolving the electrode gap of spark plug in seven individual strips. The synchronization of electrical and spectroscopic measurement enabled to reconstruct the measured data into time series of information.

The major findings and remarks in this work are the following:

- The time series of peak intensity from selected reactive species showed a distinct sequence in order of N_2–O–Ni–N_2^+.
- The emission intensity was higher in the cathode-near region than in the anode-near region for the entire wavelength range.
- The breakdown phase showed the most intensive emission, which mainly consists of the emission from N_2 C-B transition and B-X transition. The rotational temperature (T_{rot}) of breakdown discharge was calculated to be 500 K, vibrational temperature (T_{vib}) was about 5000 K. Electronic temperature(T_{el}) reached 20000 K and was the highest during the entire spark discharge process.
- The arc discharge phase was characterized by strong atomic emission of oxygen at 777 nm followed by increase in metallic emission, in this work from nickel. The nickel atomic emission was also more intensitve in cathode-near region. These emission clearly verifies the electrode wear process of spark plug.
- In the glow discharge phase the metallic emission disappears and only weak N_2 and N_2^+ B-X emission remain. The emission intensity ratio of N_2^+ to N_2 increased within the transition into glow discharge, and this had a correlation with the increase in T_{rot} up to 3000 K and decrease in T_{el} down to 10000 K. The T_{rot} was not relaxed to ambient temperature and remained to 2200K even the discharge process ended.

Acknowledgment

References

[1]   Heywood, J. B. (1988). *Internal Combustion Engine Fundamentals*. McGrow-Hill.

[2]   Bazelyan, E. M., & Raizer, Y. P. (1997). *Spark discharge*. CRC Press.

[3]   Kim, W., Toedter, O., Koch, T., Bae, C. (2018). *Spatio-temporally resolved spectroscopic diagnostics and electrical analysis of automotive spark ignition system*. Manuscript submitted for publication.

[4]   Laux, C. O., Spence, T. G., Kruger, C. H., & Zare, R. N. (2003). Optical diagnostics of atmospheric pressure air plasmas. *Plasma Sources Science and Technology*, *12*(2), 125.

[5]   Šimek, M. (2014). Optical diagnostics of streamer discharges in atmospheric gases. *Journal of Physics D: Applied Physics*, *47*(46), 463001.

[6]   Sansonetti, J. E., & Martin, W. C. (2005). Handbook of basic atomic spectroscopic data. *Journal of Physical and Chemical Reference Data*, *34*(4), 1559-2259.

[7]   Pearse, R. W. B., & Gaydon, A. G. (1976). *Identification of molecular spectra*. Chapman and Hall.

[8]   Moon, S. Y., & Choe, W. (2003). A comparative study of rotational temperatures using diatomic OH, O2 and N2+ molecular spectra emitted from atmospheric plasmas. *Spectrochimica Acta Part B: Atomic Spectroscopy*, *58*(2), 249-257.

[9]   Nassar, H., Pellerin, S., Musiol, K., Martinie, O., Pellerin, N., & Cormier, J. M. (2004). N2+/N2 ratio and temperature measurements based on the first negative N2+ and second positive N2 overlapped molecular emission spectra. *Journal of Physics D: Applied Physics*, *37*(14), 1904.

[10]   Ono, R., Nifuku, M., Fujiwara, S., Horiguchi, S., & Oda, T. (2005). Gas temperature of capacitance spark discharge in air. *Journal of applied physics*, *97*(12), 123307.

[11]   Brockhinke, A., Krüger, J., Heusing, M., & Letzgus, M. (2012). Measurement and simulation of rotationally-resolved chemiluminescence spectra in flames. *Applied Physics B*, *107*(3), 539-549.

[12]   Lochte-Holtegreven, W. (1968). *Plasma-diagnostics*. North-Holland Publication.

[13]   Britun, N., Gaillard, M., Ricard, A., Kim, Y. M., Kim, K. S., & Han, J. G. (2007). Determination of the vibrational, rotational and electron temperatures in N2 and Ar–N2 rf discharge. *Journal of Physics D: Applied Physics*, *40*(4), 1022.

[14]   da Silva, M. L. (2007). An adaptive line-by-line—statistical model for fast and accurate spectral simulations in low-pressure plasmas. *Journal of Quantitative Spectroscopy and Radiative Transfer*, *108*(1), 106-125.

[15]   Gilmore, F. R., Laher, R. R., & Espy, P. J. (1992). Franck–Condon factors, r-centroids, electronic transition moments, and Einstein coefficients for many nitrogen and oxygen band systems. *Journal of physical and chemical reference data*, *21*(5), 1005-1107.

4.3 Influence of the Electrical Parameters of the Ignition System on the Phases of Spark Ignition

Tobias Michler, Wooyeong Kim, Olaf Toedter, Thomas Koch, Choongsik Bae

Abstract

With a focus on the spectra of N2 at 377nm, N_2^+ at 391nm, N at 500nm and O at 777nm, this paper investigates the influence of additional capacities on the spectrum of spark ignition. For this, an ignition spark with different additional capacities in front of the spark plug was scanned in time. With an increase in capacity, the intensity and duration of an arc discharge, supplied by this capacity, increases strongly. This results in an increase in emissions of nickel in the gas. An increase in the second positive system of nitrogen at 391nm can be observed when the capacity increases. Compared to this the first negative system decreases with increasing capacity. Only during the glow discharge, a strong emission near the cathode was observed. Atomic nitrogen was only observed in the breakdown and capacitive arc modes. With an increase in capacitors the oxygen was reduced.

Kurzfassung

Untersucht wurde der Einfluss der Kapazität auf das Spektrum der Funkenzündung. Im Mittelpunkt der Untersuchung standen die Spektren von N_2 bei 337nm, N_2^+ bei 391nm, N bei 500nm und O bei 777nm. Dabei wurde ein Zündfunken mit verschiedenen, unmittelbar vor der Zündkerze, montierten Kapazitäten zeitlich abgetastet. Dabei konnte vor allem eine starke Erhöhung der kapazitiv gespeisten Bogenentladung beobachtet werden. Diese resultiert in eine Erhöhung der Nickelemission im Gas. Die 2. pos. Gruppe von Stickstoff bei 337nm weist in dem kapazitiven Bogen eine höhere Intensität auf sobald die Kapazität wächst. Zusätzlich zeigt das Spektrum der 1. neg. Gruppe von Stickstoff bei 391nm erst zum Einsetzen der Glimmentladung eine hohe Leuchterscheinung welche sich auf die Kathode beschränkt. Des Weiteren konnte atomarer Stickstoff nur im Bereich des Durchbruchs und der kapazitiven Bogenentladung gefunden werden. Bei atomarem Sauerstoff konnte eine Reduktion der Emission beobachtet werden.

1 Introduction

The efficiency of SI-engines can be improved significantly by using leaner mixtures [1]. Leaner mixtures cause a reduction of flame velocity and, therefore, a lower heat release at the same input of energy. In order to diminish this effect, prechamber spark plugs could be an opportunity. These spark plugs penetrate the combustion chamber with coils of burning gas. The result is a large area of affected unburned gas which leads to an increase in heat release and an improved combustion.

The problem inherent to the prechamber spark plug is that purging and the involved tail gas reduce the ignition probability related to the air-fuel ratio at the spark plug. To

support the pre chamber spark plug technology, more investigations of the spark plug ignition process and the entire ignition system are required.

The ignition spark will be investigated by examining the characteristics of the spectral and electrical properties. The schematic electrical setup of an ignition system is shown in Figure 1. A Variation of the capacitor (C_{Add}) directly in front of the suppression resistor (R_{SP}) shows the influence of parasitic or applied passive electrical components on the spark and, hence on the ignition behavior. Due to the positioning of the added capacitor, right in front of the suppression resistor, the capacity acts like C_{SP1}.
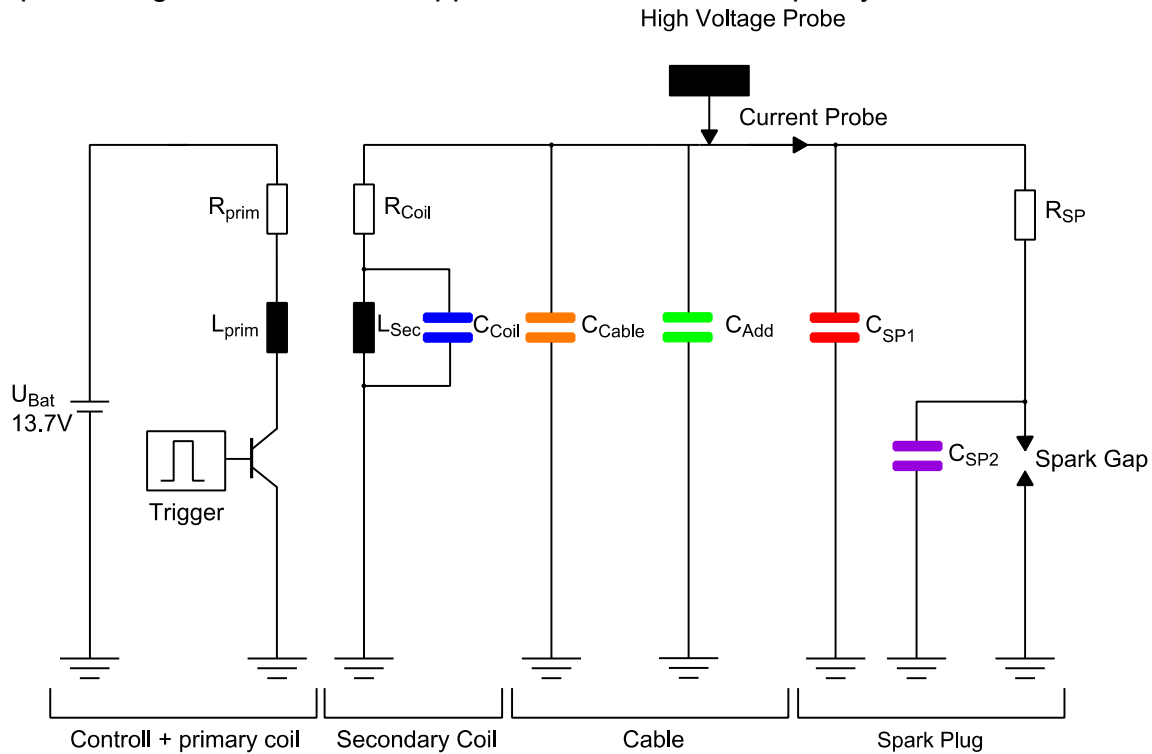
Figure 1: Schematic setup of an ignition system (derived from [2])

The ignition spark can be divided into the three discharge mechanisms breakdown, arc mode and glow mode [3]. These three phases source their energy from different parts of the ignition system. The different types of energy sources result in different types of discharge characteristics, here described as capacitive discharge and inductive discharge. Table 1 gives a rough overview of the distribution of the energy sources which supply the discharges.

Table 1: Overview of the type of discharges in a spark plug

Capacitive discharge		Inductive discharge
Breakdown	Arc discharge	Glow discharge

The difference in the mechanism is based mainly on the physical processes for emitting electrons. Ahead of the breakdown an initial electron forms an avalanche whose number of charge carrier increases further. This context is explained by Equation (1) [4].

$$\gamma * (e^{a * d_{electrodes}} - 1) \geq 1 \qquad (1)$$

with:

- γ: retroactivity coefficient
- a: ionization number
- $d_{electrodes}$: gap between electrodes

As soon as the critical number of electrons of about 10^6 to 10^8 is exceeded, the discharge mechanism changes from the avalanche to the streamer mechanism [5] [6]. Due to this change a streamer head is formed by electrons which possess a much higher mobility than the ions. Behind the streamer head, one finds the so-called streamer tail. At the boundary surface between these regimes recombination processes can lead to strong emitted rays. These rays can ionize the gas around the streamer head. This leads to a faster movement of the head, as compared to pure collision ionization. Due to by this faster movement, the breakdown happens one power of ten faster. The voltage directly ahead of the breakdown is at its maximum and can be score numbers of about 40kV. After formation of this first discharge channel the gap voltage decreases as described by Toepler´s law [7]. The number of charge carriers passing the channel increases, which results in a higher conductivity in the gap.

The arc discharge is driven by the so-called thermionic field emission of electrons. This is a mixture of thermionic emission, where the electrons are emitted by the high temperature of the cathode, and field emission. Field emission provides electrons by tunneling through the cathode surface. In case of thermionic emission, the work function of the electrons is reduced by the so called Schottky effect [8]. This facilitates the electrons to tunnel through the material of the electrode surface. In most cases the necessary current density cannot be applied. The materials hit by a high current density channel were evaporated by the cathode from a narrow area at the front of the cathode [9]. This area has a range of about one mean free path. The electric field that increases by this accumulation of material allows tunnel processes through the cathode surface material. Electrode materials with a high melting point can evaporate only in a very small area of the cathode referred to as cathode spot. Another characteristic of the arc discharge are the very low values of voltage of only some umpteen of volts.

The glow mode is dominated by collision processes in the gas. It is relatively independent of the collision processes at the cathode. Electrons will be generated mainly by inelastic particle collisions in the gas. The field accelerates the electrons in the gas. If the kinetic energy is high enough, the electrons are able to ionize the atoms and molecules in the gas. Because of the ionization more electrons are released, which sustain the current flow. A high voltage of a few hundreds of volts makes the difference between the glow discharge and the arc mode.

2 Experimental Setup

2.1 Data Acquisition

The oscilloscope LeCroy Waverunner 6030 with a rise time of 4.67ns was used to determine the electrical indicators of current and voltage. A Tektronix P6015A positioned immediately in front of the terminal nut was used to quantify the high voltage of the secondary path. To gauge the current, a current probe Pearson Current Monitor Model 2877 with a rise time of 2ns and a critical frequency of 200MHz was used. Data recording was done at a sampling rate of 10MS/s. Calculation of the electrical energy was carried out using the following formula (2):

$$E_{elec} = \int_{o}^{t_{Spark}} (u(t) - R_{SP} * i(t)) * i(t) dt \qquad (2)$$

with:
- E_{elec}: Electrical energy [J]
- t_{Spark}: Spark duration [s]
- $u(t)$: Voltage [V]
- $i(t)$: Current [A]
- R_{SP}: Suppression resistor [Ω]

For spectroscopy a Princeton Instruments Aceton SP-2500 with a PI-MAX 2 ICCD camera was used. A 600g/mm grating and a slit width of 20µm were used. Data acquisition was done using the program Winspec. With the aid of the spectrograph software, the camera and the ignition coil were triggered. The measurement procedure is described in the literature [10].
A Matlab based script allowed alignment of the data from the oscilloscope and the spectrograph. Assessment of the electrical and spectral data for each spark within the recorded timing window, based on the common trigger signal, was achieved using the same script.

2.2 Setup

Figure 2 shows the schematic setup for spectroscopic and electrical data acquisition. The spark plug and the ignition coil are arranged in a metal housing to protect the measurement devices from EMC. A spark plug with an electrode of nickel and a gap of 0.9mm was used. The resistance of the spark plug (R_{SP}) was 6.5kΩ. The coil used had ignition energy of 90mJ and an initial current of approx. 150mA.

2.1.1 Electrical Setup

From the PC controlling the spectrograph a trigger signal was sent to a function generator. Without sigificant delay, the latter transmitted another trigger signal to the ignition coil and the oscilloscope. The signal served as a trigger signal for the record and as the dwell time signal for the ignition coil. A 13,7V car battery was used as a DC power supply. From the ignition coil a high voltage ignition cable leads directly to the high-voltage probe. To this cable, the additional capacitors (C_{Add}) were attached. The probe the Pearson current monitor for determining the secondary current was placed

right behind the probe. Another ignition cable without resistance closes the high voltage circuit to the spark plug.

2.1.2 Spectroscopic Setup

The Programmable Timing Generator (PTG) was triggered by the PC of the spectro-graph. The signal from the PTG was transferred to the CCD camera with a well-defined delay. This timing delay was not constant and changed its time lag. The delay was put together by the gate duration and the number of iterations passed through. For this reason the first 40μs had a gate window of 2μs. From 40 to 400μs the window was 10μs, and after that, the time window was 1000μs. An exact description of the meas-urement method is given in [10]. Using the software Winspec the gate and the gain for the explorative area of wavelengths were defined. Transferred by an UV-objective the light of the ignition spark was guided to the 20μm slit of the spectrograph. The following wavelengths were used for evaluation: N_2 (337nm SPS), N_2^+ (391nm FNS) [11], Ni (341nm), N (500nm) and O (777nm) [12].
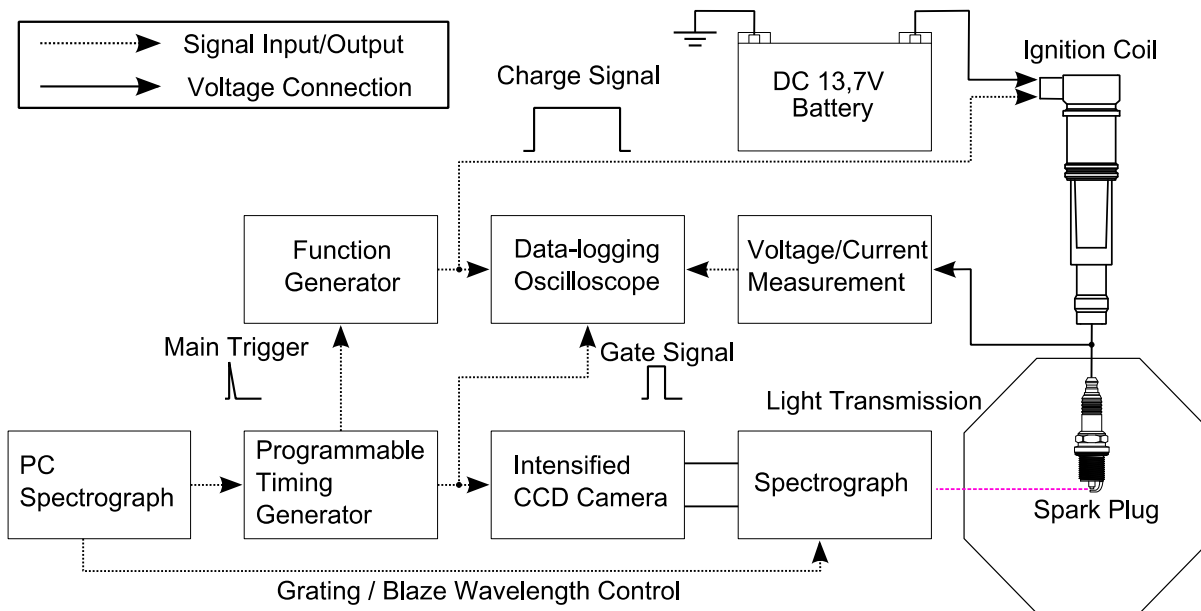
Figure 2: Schematic measurement setup [9]

3 Results

The results of spark emission spectroscopy and if the evacuation carried out after-wards are shown in Figure 3. On the left axis the distance from cathode to anode (in mm) is plotted. The right axis shows the cumulated electrical energy of arc and glow discharge. The measured intensities of the species named in Chapter 2.1.2 are col-ored. On the axis of abscissae, the spark duration is plotted. The breakdown was de-fined by an instant of zero. In the red box, the area discribed in the following section is emphasized (lower picture).
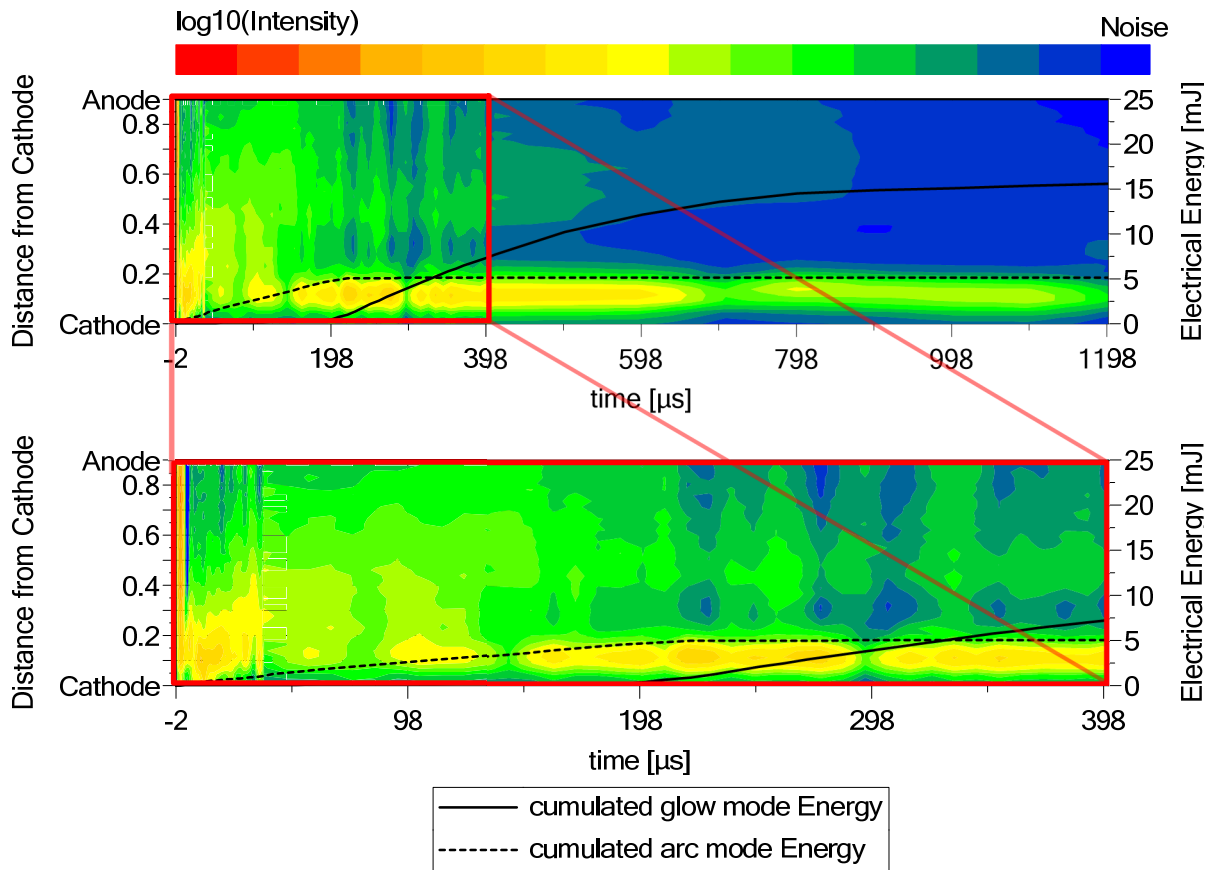
Figure 3: Intensity of N_2 at 337nm and electrical energy of arc and glow modes at 1 atm during a spark with a duration of 1200µs. Above: Entire spark. Below: First 400 µs of the spark.

The wavelengths of N_2 and N_2^+ were chosen because of the possibility to calculate the temperature with this two species. Also they were a good indicator for the energy trans-ferred to the gas. Atomic nitrogen was chosen to get an indicator of the ability to dis-sociate the gas. To estimate the effects of the wear and to differentiate the arc and the glow mode the nickel line was observed. At last the atomic oxygen line was observed to get an indicator for the inflammability.
In this work the dimension "Counts" will stand for the dimension of the measured in-tensity.

3.1   Ni at 341nm

The emission of nickel through the emission line at 341,48nm for different capacitors C_{Add} is shown in Figure 4. An important indication of arc discharge action is the enhanced emission of electrode materials as markers of the thermionic emission. During the breakdown only a small amount of nickel is traceable. During the variation of capacitors the radiation intensity is constantly lower than 2000 counts while the breakdown continues. Whenever the capacity mainly supplies arc discharge, the intensity increases rapidly more than tenfold. This effect grows with rising capacity. For the time the discharge is fed by the capacitors very high intensities of the cathode material nickel are measured. In fact there were some thousand counts of the radiation. With an increase in the capacitors the duration of the arc discharge and the duration of the height of the intensity remain at a very high level. When the current decreases, the emission gets weaker too. Nickel can be found primarily near to the cathode. By rising the capacity the radiation penetrates slightly deeper into the gap of the ignition spark. As soon as the discharge source changes to the inductance supply the qualities fall to approx. 4000-8000 counts. An independence of the penetration length in addiction to the capacity can be observed. With the commencement of the glow mode, the intensity decreases to values below 2000 counts. The emission can be proven only in the immediate vicinity of about 150µm around the cathode.
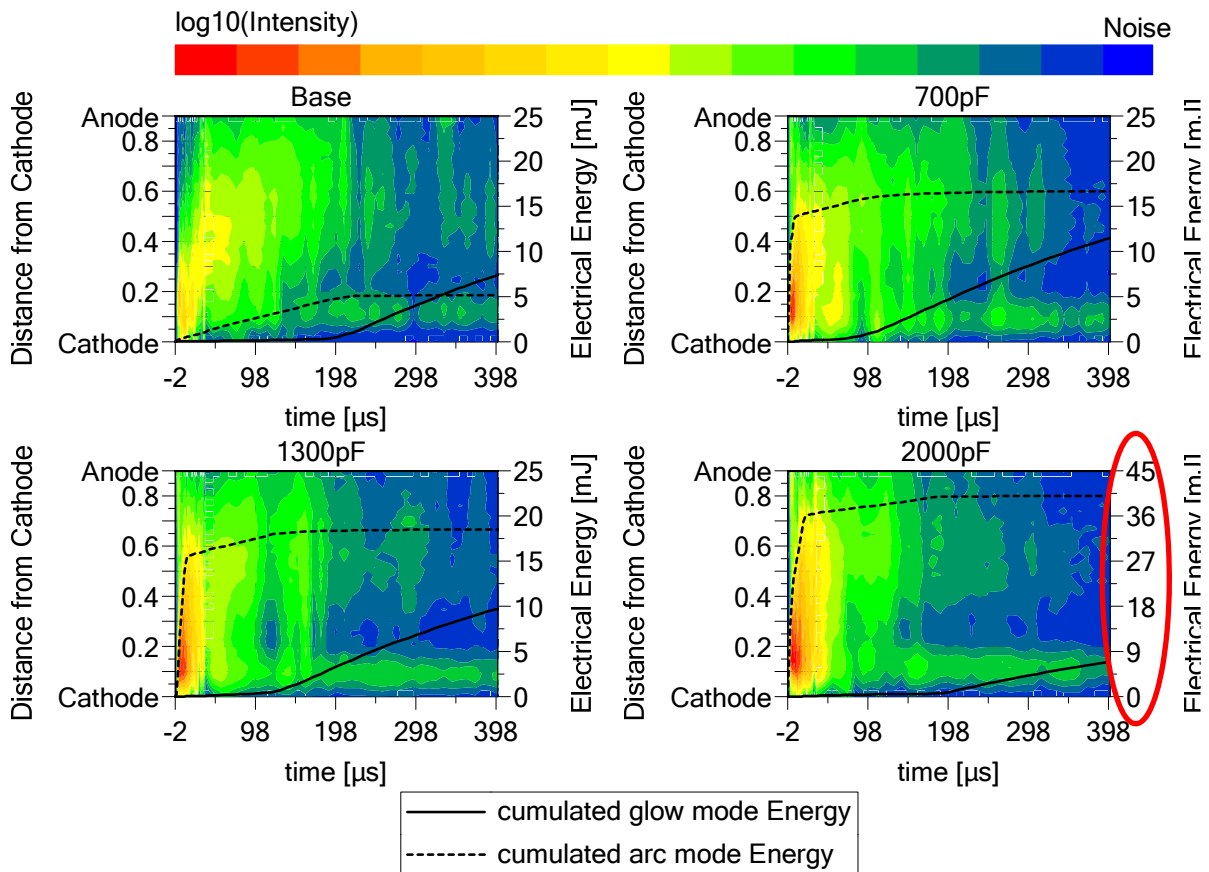
Figure 4: Variation in capacity from 0 to 2000pF for the emission of Ni at 341nm during the first 400µs.

3.2 N_2 at 337nm (Second Positive System)

A variation in capacitors leads directly to a higher intensity during the breakdown. The intensity increases from about 24000 to over 52000 (from 0pF to 2000pF). Figure 5 shows the increase in the duration of intensity (from about 2 to 40µs) and the intensity itself by accretive capacity during capacitive arc discharge. The intensity increases by about the multiplier of 2.7 when using an additional capacity of 2000pF. A nonlinear, slightly declining trend in the increase can be observed. While the capacitive discharge is active, the emission stays as a function of the capacitor increase. With increasing capacitor, the intensity that penetrates the gap, in direction of the anode, slightly increases. Subsequent to the arc discharge elicited by the capacitive discharge, an arc with energy supply from the inductance occurs. The duration of this phase reduces the increasing capacity from about 200-400µs to 50-100µs. During the period of the inductively supplied arc discharge the stimulation of N_2 is less intensive and percolates nearly the whole space in the gap. As soon as the glow discharge occurs an intensive luminous negative glow at a distance from 0 to 200µm from the cathode can be observed. Only in this range, an increased intensity can be found. In the remaining gap, one finds only a small fraction of the ray.
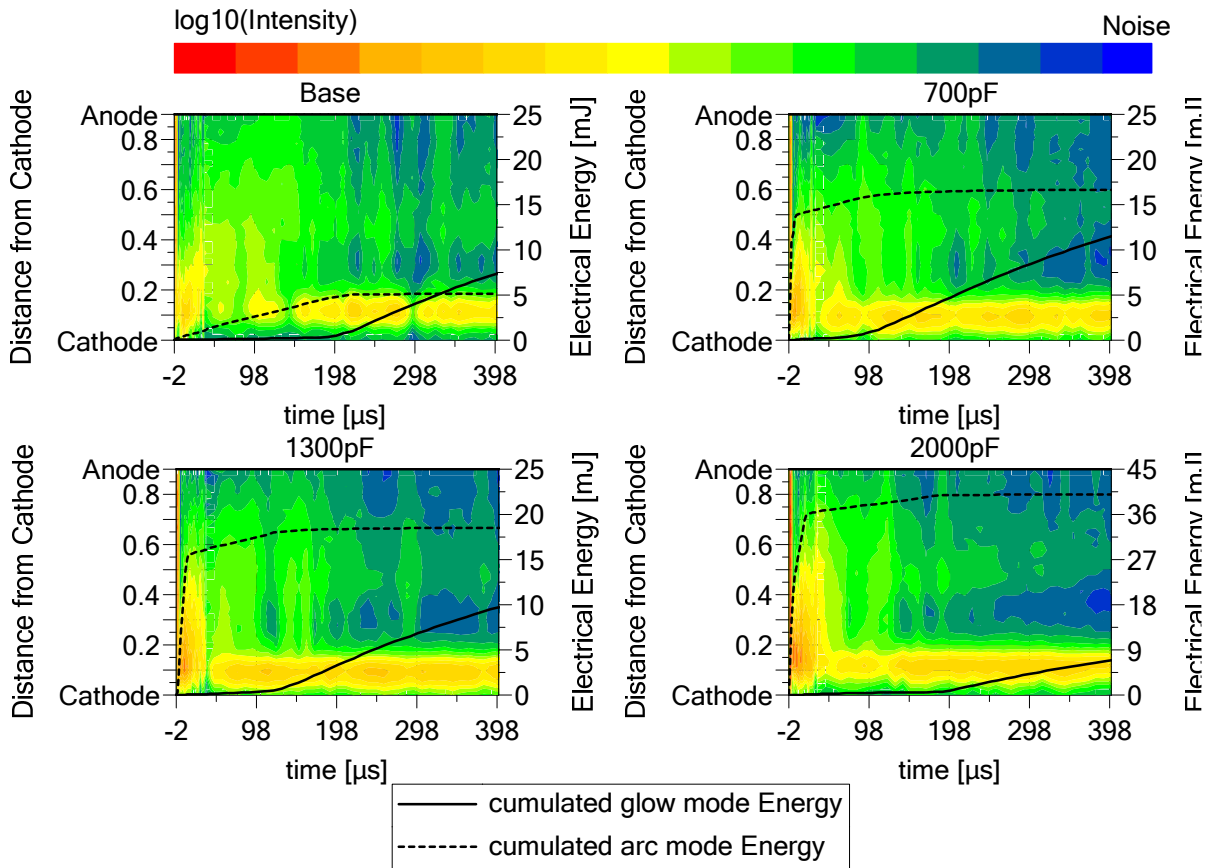
Figure 5: Variation in capacity from 0 to 2000pF for the emission of N_2 at 337nm during the first 400µs.

3.3 N_2^+ at 391nm (First Negative System)

In Figure 6 the emission of nitrogen at 391nm is shown. During the whole time, the emission is restricted to the area of the cathode. During the breakdown, only a slight increase in emission can be observed. The intensity increases from about 1000 to 3000 counts with increasing capacitor. Over the course of the arc discharge supplied by the capacity the radiation intensity of nitrogen along the spark gap is very low. Only near by the cathode, a minor light emission can be perceived. The intensity in this area roughly reaches 2000 counts. For all capacitors the intensities are gaining the same values. For the inductively supplied arc mode, the same observations can be made. Analogous to the capacitive discharge, the intensity of radiation nearby the cathode is slightly exceeded. Also in this area, the intensity does not exceed the 2000 count level. The remaining area does not show any strong radiation. If transitions between arc and glow discharge occur, a strong increase in intensity can be observed. Immediately 5000-8000 counts can be detected. These values are measured up to a distance of about 200µm from the cathode. Beyond this section only a weak radiation is recorded.
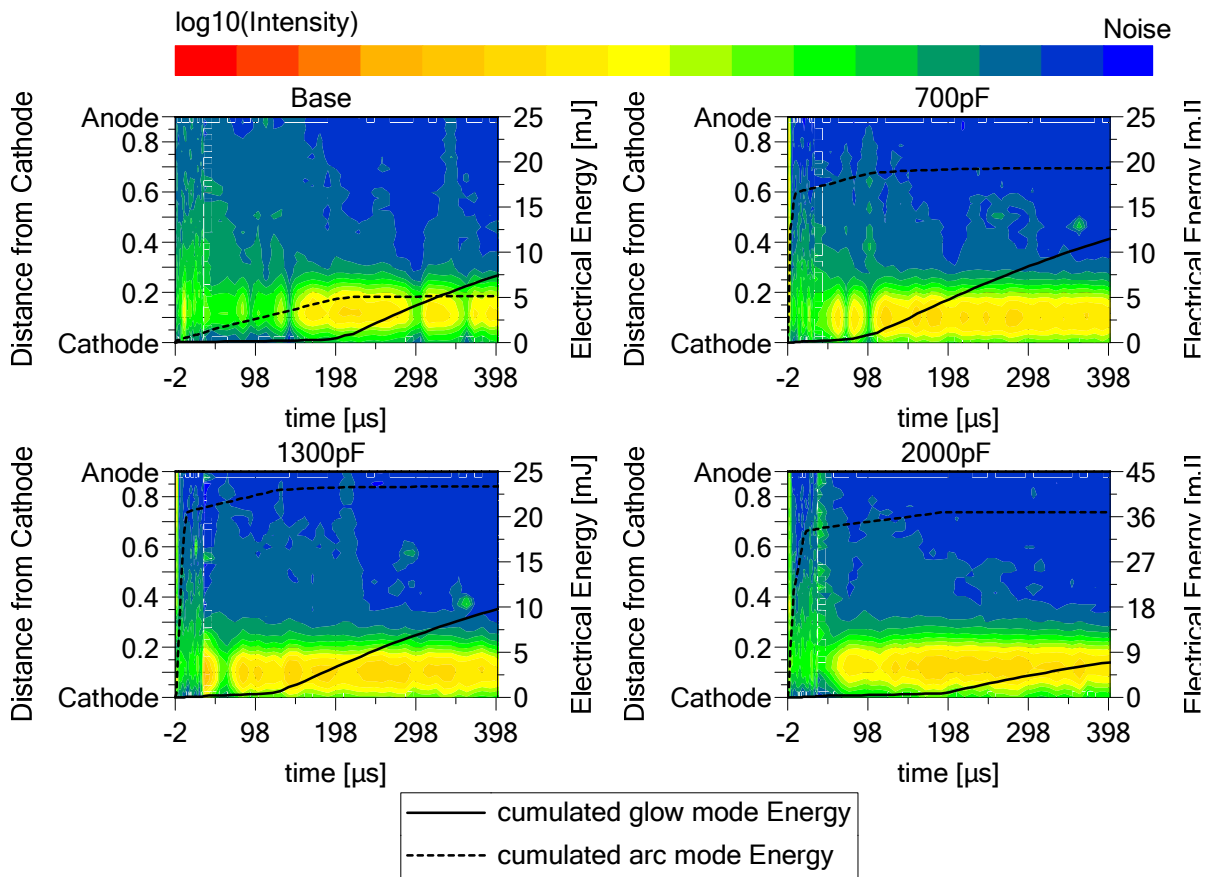
Figure 6: Variation in capacity from 0 to 2000pF for the emission of N_2 at 391nm during the first 400µs.

3.4   N at 500nm

The radiation intensity of atomic nitrogen can be found at a wavelength of 500nm. This trend is shown in Figure 7. During the breakdown the signal without an additional capacitor cannot be differentiated compared to the background noise. In the case of an added capacity of 2000pF the emission is above 8000 counts. Hence a high increase with respect to the signal without capacitor can be reached. With the start of the capacitive discharge, in the arc mode, an abrupt increase in intensity can be observed. By raising the capacity, the maximum value raises too. The penetration length of the radiation, however, is only little influenced. As long as the discharge is fed by the capacitors, the intensity is at a very high level. If the energy input occurs through the inductance the emission suddenly vanishes. No changes in this behavior can be observed whenever the transition between arc and glow discharge appears. Only a very facile radiation around the cathode is perceived. This radiation occupies a space of about 200µm up to the cathode. Beyond this region, no radiation can be found.
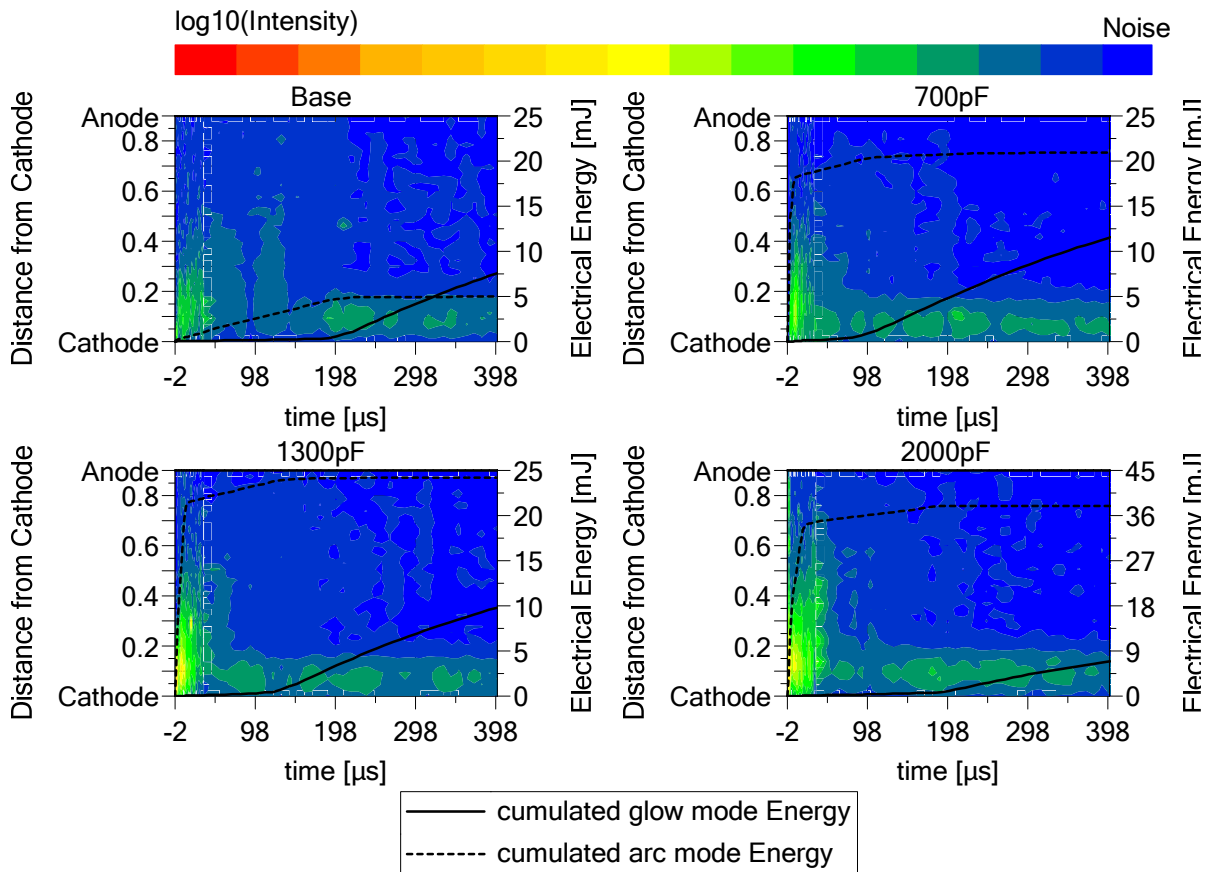
Figure 7: Variation in capacity from 0 to 2000pF for the emission of N at 500nm during the first 400µs.

3.5   O at 777nm

Figure 8 shows the emission of triplet oxygen at a wavelength of 777nm. In the break-down, a strong increase in intensity from 10000 to approx. 55000 counts is detected. This increase behaves nearly linear. From cathode to anode the radiation rises. The radiant intensity drops only shortly after the breakdown. The reduction in intensity with increasing capacity is an interesting and unexpected behavior. During the period of the capacitive duration of the arc discharge, the values of the radiation can be measured in a relatively low range of 1000 to 3000 counts. A decrease in the current results in a slightly grow of intensity. Also the extension in direction to the anode is slightly affected. A reduction of the current lowers the penetration lengths marginally. A strong increase in radiation can be found as soon as the energy source switches from the capacitors to the inductance. The maximum values are observed once there is no additional capacitor. These values can exceed 8000 counts. The penetration length remains nearly the same and is independent of the capacity. As an example, a penetration of the radiation at about 600µm from the cathode was measurable. When the transition from arc to glow discharge arises, the radiation gradually vanishes out of the space between the electrodes. Only around the cathode, up to a distance of 200µm, the radiant intensity remains like the previous similar level.
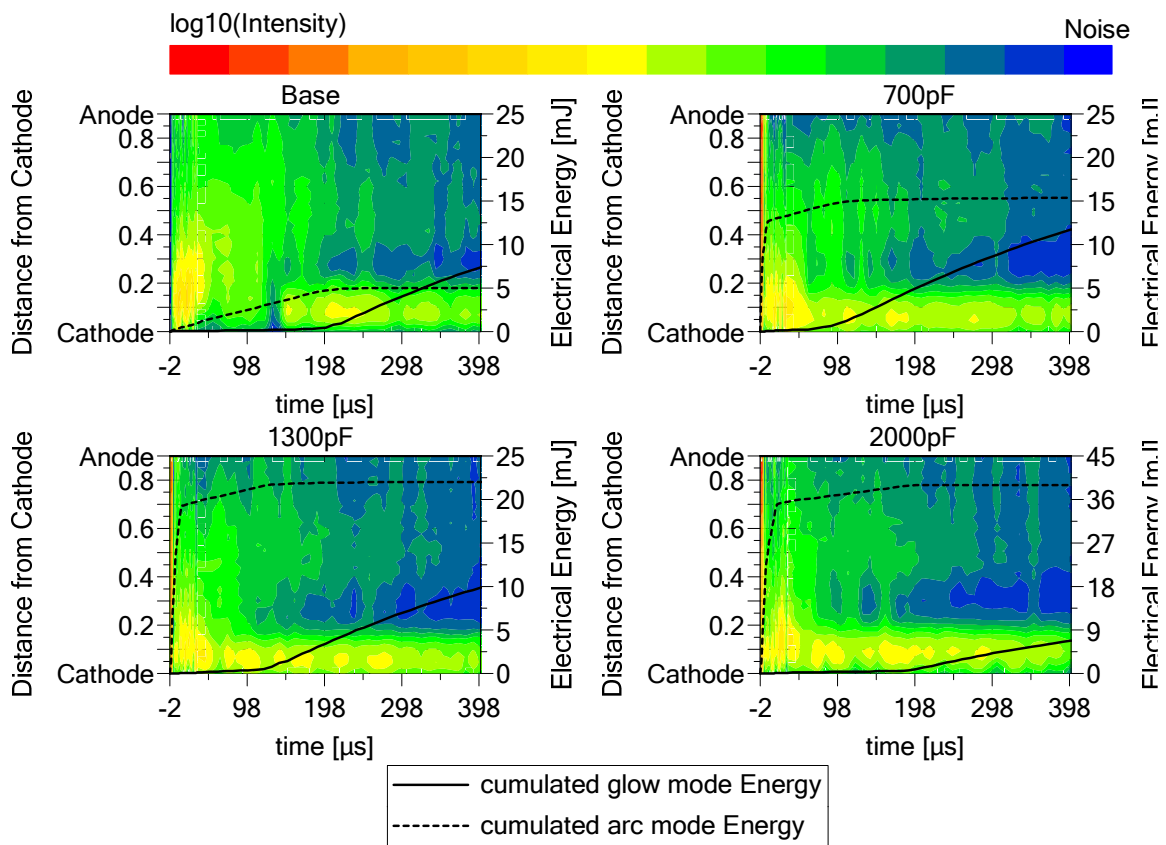
Figure 8: Variation in capacity from 0 to 2000pF for the emission of O at 777nm during the first 400µs.

4 Discussion

In this chapter the trends from chapter 3 were discussed and described with help of the plasma physical effects.

4.1   Ni at 341nm

The maximum voltage before the breakdown, on average amounts about 5kV. Compared to this, the static ignition voltage according to Paschen, amounts to 3.8kV for the given system. Thereof, a shock factor of 1.32 can be calculated. These high overvoltages in combination with the rough surface of the cathodes lead to the breakdown mechanism of streamer [13]. In consideration of the fact that this mechanism expires mostly in the gas, then interacting with the cathode, the nickel emission in the gas is very low.
Following the breakdown, the arc discharge, which gets its energy from the capacitors, occurs. Caused by the high sublimation temperatures of 3003K [14] for nickel and the low current of about 600mA, the maximum diameter of the cathode spots is 10 to 30µm [15] [2]. With the diameter as a measure for the plasma channel of the arc discharge, current densities between $8.5*10^4$ und $7.6*10^5$ A/cm² can be estimated. As described in [16], these densities lie between the transition from thermal and thermionic-field arc. An increased intensity and penetration length is caused directly by the higher density of electrode material in the gas.
After the period of capacitive discharge, the inductive time of the arc mode follows. As soon as the capacity is fully discharged, the current rapidly decreases to a lower level. A small step at the end of the capacitive discharge of about 150mA, without an additional capacity, to 100mA at 2000pF characterizes the end of the capacitive arc. Caused by the reduced current, the intensity and the duration of the inductive arc mode decrease. Up to current of approx. 100mA, a very stable arc can be observed. Certainly up to a current of 20mA, some rare transitions between arc and glow discharge are noticeable.
As the glow discharge sets in, the emission of nickel nearly disappears. Only close to the cathode is a small intensity of the cathode material measureable. This is caused by the low interaction of the glow discharge with the cathode. Mainly some atoms are released from the cathode by the effect of sputtering [17].

4.2   N2 at 337nm

The capacity only affects the intensity of the breakdown. With its increase the maximum intensity grows from 24000 to 52000 counts. Furthermore, the intensity grows with the distance to the cathode. This leads to the conclusion, that, due to inreased and faster energy storage, more electrons are available to excite the gas. The breakdown should be caused by a streamer. In the streamer head, considerable ionization and excitation occur. The streamer head is normally near to the anode. This could explain the growing intensity with increasing distance to the cathode.
During arc discharge from the capacitive source, the intensity and the penetration lengths have a high status. With decreasing current, both values are decreasing, too. Especially near to the cathode, the intensity is very high. This is caused by the electrons, which have a very high energy level after exiting the cathode surface. Because of this, the electrons are available for exciting the nitrogen at a very early stage. The

space between the electrodes is mostly occupied by the positive column of arc discharge. The emission of radiation in the positive column is decreases from the cathode in direction to the anode. Probably the electrons lose their energy during their travel though the positive column on account of, collision processes. This leads to a decrease in excited states in the case of constant gas density. With the higher duration of action and the slight increase in current, the penetration length increases too. It should be noted, that the excitation cross section of the second positive system (SPS) significantly increases with a rise in electron temperature [18]. Due to this, more molecules can be excited by electron collisions.

During the inductive arc mode a homogenous trend in radiation is measurable. Like in the case of the capacitive arc, the positive column occupies nearly the whole space between the two electrodes. The high energy of the electrons, when leaving the cathode surface leads to a high intensity directly in the vicinity of the cathode. With the increased capacity, the intensity at the cathode increases, too. An earlier transition from arc phase to glow discharge can be identified as the reason for this transition.

As the glow discharge sets in, the intensity nearby the cathode rises strongly. As long as a transition between the two modes is active, a high intensity at the cathode as well as an increased radiation of the positive column can be observed. When the glow discharge dominates, the intensity above a distance of 200µm from the cathode decreases permanently. Because of the pressure (1 bar) and the electrode gap of 0.9mm, no positive column can be observed [19]. This area is referred to as Faraday dark space. Electrons could not accumulate the necessary energy to excite the molecules. This is caused by the high pressure and the small field which are leading to more collisions in the gas. The emission maximum is in a small distance from the cathode. At departure of the cathode the electrons have a very small energy of about 1eV [19]. With this energy, no atoms or molecules can be excited. With rising distance from the cathode, the electron temperature is increasing. This results in a higher excitation of the N_2 molecules.

4.3 N_2^+ at 391nm

The nitrogen radiation band of 391nm is a simply ionized nitrogen molecule. It has a very high ionization energy level of 15.58eV [20]. Like the SPS of nitrogen the FNS behaves similarly during the breakdown. With an increased capacity, the intensity grows. The maximum intensity is near to the anode. This can be explained analogously to the SPS. Caused by a higher energy storage, more electrons, from the capacitive storage are available in the breakdown. This leads to a higher excitation in the gas.

Only in direct proximity to the cathode, does a capacitive arc show an increased radiation of N_2^+. With 150-200µm, the penetration length is in a well-known-range. As the cathode surface is withdrawn, the energy of the electrons is the highest. According to this ionization of nitrogen near the cathode can be provided by the high electron temperature. With increasing distance from the cathode the energy of the electrons decreases by collisions in the gas. Therefore the discharge has not enough energy anymore to ionize the nitrogen.

The inductive arc behaves identically to the capacitive one and will therefore not be explained in this chapter.

Whenever the transition to the glow mode occurs, the first negative system (FNS) of nitrogen can be observed with a high intensive glow near the cathode. Caused by the high velocities of the electrons in this area, the degree of ionization and miscellaneous

excitation occurs [21]. In the remaining area between the electrodes, radiation is prevented in the Faraday dark space. The electrons have lost their whole energy in this zone almost completely and, hence, have to be accelerated again to effect further excitation.

4.4   N at 500nm

During breakdown, the intensity of atomic nitrogen strongly increases with the capacity. With increasing distance to the cathode, this intensity decays very fast. This behavior could be explained by a loss in electron temperature from cathode to anode. This causes a reduction in the dissociation probability of atomic nitrogen. Unfortunately, this explanation could not be confirmed during the preparation of this paper.

During arc discharge caused by the capacitor, a moderate intensity of radiation can be observed. With an increase in capacity and due to this, a capacitive arc with a longer duration and higher current, the atomic nitrogen density in the gas increases, too [22]. During this kind of arc, and, hence, with that a rapidly decreasing current, the emission of N at 500nm decreases, too. Regarding the mechanism of the arc discharge, when charge carriers mainly are triggered by the thermionic-field emission from the cathode, the change in penetration length can be explained as follows. With an increasing distance from the cathode, the thermal energy of the electrons is declining. This is caused by the process of inelastic collisions in the gas. After a certain distance, the electrons do not have enough energy anymore. The electrons are no longer available for dissociating the dinitrogen.

As inductive arc discharge sets in, the emission decreases rapidly. As long as this arc is active, nearly no emission can be measured. Probably, this effect depends on the reduced electron temperature and, hence, the lower chance of dissociating the molecule.

After transition to the glow discharge, the emission rises slightly in the zone of negative glow. This is assumed to be caused by the collection of ions and electrons with a higher energy level [19]. This glow is very low compared to the glow in case of capacitive arcs. The remaining spark gap is fully filled by the Faraday dark space with its very low electron energy.

4.5   O at 777nm

The transition from ^5P to $^5S^0$ of OI (dissociated and excited directly from electron collisions [23]) revealed at a wavelength of 777nm. The dissociation and ionization of OI by electron collisions follows the following equation (3) [24]:

$$e^- + O_2 \rightarrow O^- + O \qquad\qquad (3)$$

During breakdown, the intensity grows from the cathode to the anode. This indicates the formation of a streamer head. In this head, the ionization potential caused by electrode collisions and photoemission seems to dissociate and excite the oxygen.

During the capacitive arc discharge not much of the ionized oxygen at 777 nm can be measured. With an increase in capacity, the maximum intensity and the penetration length decrease. Unfortunately, the reason for this behavior could not be identified yet. A possible cause for this phenomenon could be a reduced excitation cross section. In

[25] and [26], the excitation cross section of the triplet oxygen at 777nm has its maximum at 16eV. Beyond this, this value rapidly decreases. For example, at an electron temperature of 26eV, the excitation cross section is halved compared to the maximum value. As an alternative, another energy level, e.g., the higher excitation level at 844 could be excited. Unfortunately, no alternative energy level was found. A potential reason for this is that the energy level is outside of the measurement range of the spectrograph.

A different trend is shown by the inductive arc discharge. Without an additional capacitor, a higher intensity and the penetration length, especially at the start of the discharge, can be observed. A final reason for this phenomenon could not be found. At this point, the same presumptions as for the capacitive arc, with the reduced excitation cross section, can be made. Only the higher radiation at the beginning of the discharge can be explained by the higher current of inductive compared to the capacitive arc. In direction to the anode, the intensity is constantly reducing. This is likely to be caused by the higher electron energy at this stage of the discharge.

As the glow discharge sets in, the emission can be located near to the cathode, where the negative glow takes place. The high densities of ions and electrons in this area result in a high radiation density of the species. The remaining dark area between the cathodes is the Faraday dark space where no emission can be found. In this area, the energy of ions and electrons is not high enough to dissociate, and with this reaction, to ionize the dioxygen to atomic oxygen.

5 Conclusion

An increase in capacity leads to very different results regarding the emission of the species N_2, N_2^+, N, Ni, and O from an ignition spark. Table 2 gives an overview of the effects, from a variation in C_{Add} to the emissions of the species, with the nomenclature: ++ strong increase, -- strong reduction, and 0 no effect to the considered parameters. In principle, a growth in the radiation intensity of N_2, atomic nitrogen and especially nickel with an increase in the capacitor can be observed. All species, except for nickel, were increased in intensity by the capacity during breakdown. Particularly for the nickel emissions, the enhanced mechanism of arc discharge can be determined. Only a minor to no influence of the capacity on the remaining phases, the inductive arc, and the glow discharge was observed. This decrease is caused by the lesser disposal of energy from the inductive source. The first negative system of nitrogen at 391nm is largely unaffected by the capacity. During both arc discharges, the radiation of this system is only at a low level. The radiation increases as glow discharge starts. Only in the negative glow nearby the cathode, radiation is measurable. Considering the atomic oxygen triplet state at 777nm, the behavior of the radiation is different. With increasing capacity, the intensity, penetration length and duration of the radiation decrease. A final statement to concerning thesis phenomena could not be made so far. A possible reason for these effects could be the change in the excitation cross section of this species.

Table 2: Impact of additional capacitors on the different phases of ignition sparks. (++) strong increase, (+) increase, (0) no influence, (-) decrease, (--) strong decrease.

Discharge Mode / Species	Characteristic Value	N_2	N_2^+	N	Ni	O
Wavelengths [nm]		337	391	500	341	777
Breakdown	Intensity	++	+	+	0	+
	Penetration Length	0	0	0	0	0
	Duration	0	0	0	0	0
Capacitive Arc	Intensity	+	0	++	++	--
	Penetration Length	+	0	0	+	--
	Duration	++	0	++	++	--
Inductive Arc	Intensity	-	0	0	-	-
	Penetration Length	0	0	0	0	--
	Duration	-	-	0	-	-
Glow Discharge	Intensity	0	0	0	0	0
	Penetration Length	0	0	0	0	0
	Duration	-	-	0	-	-

Literature

[1]   J. Heywood, *Internal Combustion Engine Fundamentals,* New York: McGraw-Hill Inc., 1988.

[2]   J. Rager, *Funkenerosion an Zündkerzenelektroden,* Saarbrücken, 2006.

[3]   R. R. Maly und M. Vogel, „Initiation and Propagation of Flame Fronts in Lean CH4-air Mixtures by the three modes of the ignition spark," in *Symposium (International) on Combustion*, 1979.

[4]   H. Reather, *Electron Avalanches and Breakdown in Gases,* London: Butterworths, 1964.

[5]   L. Loeb, *Basic Prozess of Gasous Electronics,* Berkley: University of California Press, 1960.

[6]   J. Meek and J. Craggs, *Electrical Breakdown of Gases,* New York: John Wiley & Sons, 1978.

[7]   M. Toepler, "Über Funkenspannungen," *Annalen der Physik,* vol. 324, pp. 191-209, 1906.

[8]   W. Schottky, "Über spontane Stromschwankungen in verschiedenen Elektrizitätsleitern," *Annalen der Physik,* vol. 362, pp. 541-567, 1918.

[9]   W. Ramberg, "Über den Mechanismus des elektrischen Lichtbogens," *Annalen der Physik,* vol. 12, pp. 319-352, 1932.

[10]   W. Kim, T. Michler, O. Toedter, T. Koch and C. Bae, "Time resolved emission spectroscopy for spark investigation," *International Conference on Ignition Systems for Gasoline Engines,* 6-7 12 2018.

[11]   F. R. Gilmore, R. R. Laher and P. J. Espy, "Franck-Condon Factors, r Centroids, Electronic Transition Moments, and Einstein Coefficients for Manx

Nitrogen and Oxygen Band Systems," *Journal of Physical and Chemical Reference Data,* vol. 21, pp. 1005-1107, 1992.

[12]   A. Kramida and Y. Ralchenko, "NIST Atomic Spectra Database, NIST Standard Reference Database 78," 1999. [Online]. Available: https://www.nist.gov/pml/atomic-spectra-database. [Accessed 05 06 2018].

[13]   A. Küchler, Hochspannungstechnik, 3. ed., Schweinfurt: Springer, 2009, p. 178.

[14]   Y. Zhang, J. R. G. Evans and S. Yang, "Corrected Values for Boiling Points and Enthalpies of Vaporization of Elements in Handbooks," *J. Chem. Eng. Data,* vol. 56(2), pp. 328-337, 11 01 2011.

[15]   B. Jüttner, "Cathode spots of electric arcs," *J. Phys.D: Appl. Phys.,* no. 34, pp. R103-R123, 21 08 2001.

[16]   A. Bauer, „Der Einfluss des individuellen Ionenfeldes auf die Thermo-Feldemission," *Beitr. Plasmaphys. (Beiträge aus der Plasmaphysik),* Bd. 6, Nr. 4, pp. 281-298, 24 03 1966.

[17]   J. Coburn und E. Kay, „Positive-ion bombardment of substrates of rf diode glow discharge sputtering," *J. Appl. Phys.,* Bd. 43, p. 4965–4971, 1972.

[18]   H. H. Brömer und F. Spieweck, „Emission und Schwingungsverteilung der 1. neg. Gruppe und der 2. pos. Gruppe in einem," *Zeitschrift für Physik,* Bd. 184, Nr. 5, pp. 481-491, 1965.

[19]   A. Fridman and L. A. Kennedy, Plasma Physics and Engineering, 2 ed., CRC Press, 2011.

[20]   „National Insitute of Standards and Technology," [Online]. Available: https://webbook.nist.gov/cgi/cbook.cgi?Formula=N2&NoIon=on&Units=SI&cTG =on&cIE=on. [Zugriff am 19 09 2018].

[21]   M. Lieberman und A. Lichtenberg, „Qualitative characteristics of glow discharges," in *Principles of Plasma Discharges and Material Processing*, New York, Wiley, 2005, p. 537.

[22]   E. Honanton, J. M. Palomares, M. Stein, X. Guo, R. Engeln, H. Nirsch und F. E. Kruis, „The transition from spark to arc discharge and its implications with respect to nanoparticle production," *J. Nanopart. Res.,* Nr. 15, 28 05 2013.

[23]   J. Jašík, P. Macko, V. Martišovitš, P. Lukáč und P. Veis, „Time Resolved Actinometric Study of Pulsed RF Oxygen Discharge," *Czechoslovak Journal of Physics,* Bd. 54, Nr. 6, pp. 661-676, 2004.

[24]   A. Kulikovsky, „Production of chemically acitve species in the air by a single positive streamer in a nonuniform field," *IEEE Transactions on Plasma Science,* Bd. 25, Nr. 3, pp. 439-446, 06 1997.

[25]   P. Julienne and J. Davis, "Cascade and radiation trapping effects on atmospheric atomic oxygen emission excited by electron impact," *J. Geophys. Res.,* vol. 81, no. 7, pp. 1397-1403, 01 03 1976.

[26]   Y. Itikawa und A. Ichimura, „Cross Sections for Collisions of Electrons and Photons with Atomic Oxygen," *J. Phys. and Chem. Ref. Data,* Bd. 19, Nr. 3, pp. 637-651, 3 05 1990.

5 Combustion/Pre-ignition

5.1. Microwave Enhanced Combustion on a Constant Volume Combustion Chamber for Lean Combustion and EGR Dilution

Terry Alger, Barrett Mangold, Yilun Luo, Jess Gingrich, Sterling Kinkler

Abstract

The effect of microwave enhancement on combustion was investigated using a spherical, constant-volume combustion chamber. Microwave energy at 2.45 GHz was coupled into the spherical chamber using a quarter-wavelength dipole antenna. Standing waves of high-strength electrical fields were created to enhance the flames ignited by a spark plug. Pressure traces of combustion with and without microwaves were recorded to compare the combustion improvements. Microwave power levels and discharge durations were also varied to understand their impact on the level of improvement. Results indicated that the microwave system can effectively accelerate combustion and improve cycle stability for dilute combustion, including lean burn at about 0.8 equivalence ratio and stoichiometric operation with 20% exhaust gas recirculation (EGR) dilution.

1 Introduction

In the last decade, stringent emission mandates and a high demand for fuel economy have continuously driven the development of new engine technologies towards cleaner and more efficient combustion applications. Engine efficiency continues to improve with dilution, lean or EGR, through cooler combustion, reduced throttling and improved thermodynamic working fluid properties [1]. The efficiency improvements gradually deteriorate at higher dilution levels due to a reduction in the combustion efficiency and the protracted burn durations in the engine [2]. Excessive combustion durations impose a hard limit to the amount of dilution that can be tolerated due to combustion instability [3].

To overcome these negative effects on engine efficiency, new technologies have been developped to extend the dilution limit. New port and combustion chamber designs have improved charge preparation and turbulence levels, which lead to a faster flame development [4]. However, increasing the turbulence level can have a negative impact on volummetric efficiency and does not couple well with other efficiency improvememnt technologies like Miller cycle operation [5]. Advanced ignition systems, such as micro-pilot [6], multiple spark plugs [7], pre-chamber [8], corona ignition [9] and high energy ignition [10][11] can improve the ignition performance and reduce burn duration by igniting in multiple locations or for longer durations, but at an increased hardware cost and higher in-use costs associated with durability and energy consumption. In addition, while ignition systems have a positive impact on the initial flame kernel propagation rates, they have no influence during the fully turbulent portion of the combustion event.

Microwave enhanced combustion was conceived as a possible solution to the limitations associated with high levels of EGR dilution for positively ignited engines. MEC improves the reaction kinetics alone through the potential to deliver energy directly to the flame front in the form of electromagnetic excitation of reaction species above and beyond what can be accomplished thermally [12]. Becuase it is a field, the MEC solution also has the potential to improve combustion throughtout the entire combustion period, and not only during the inital kernel formation period.

In this study, we developpd a microwave system to conduct MEC experiments on a laminar burning velocity (LBV) vessel. A microwave antenna was designed to effectively couple microwave energy inside the LBV vessel and generate high-intensity standing waves of electromagnetic fields for MEC. Microwave frequency, pulse duration and duty cycle were evaluated and optimized for the MEC performance. Experimental results indicated that the MEC system can effectively accelerate combustion and reduce cyclic varibility for lean and EGR diluted combusion.

2   Experimental Setup

2.1   Microwave Antenna

For the LBV vessel, the inner diameter is very close to the free-space wavelength of the microwave energy produced by the microwave generator at 2.45 GHz. Therefore, to efficiently couple microwaves into the vessel cavity, it is optimal to establish the internal microwave standing waves following electric and magnetic field strength contours for the spherical cavity mode, TM101 [13], as illustrated in Figure 1.

Horizontal Cross-Section (ref.)   Vertical Cross-Section (ref.)

Magnetic Field − − − − − − −   Electric Field ⎯⎯⎯⎯⎯
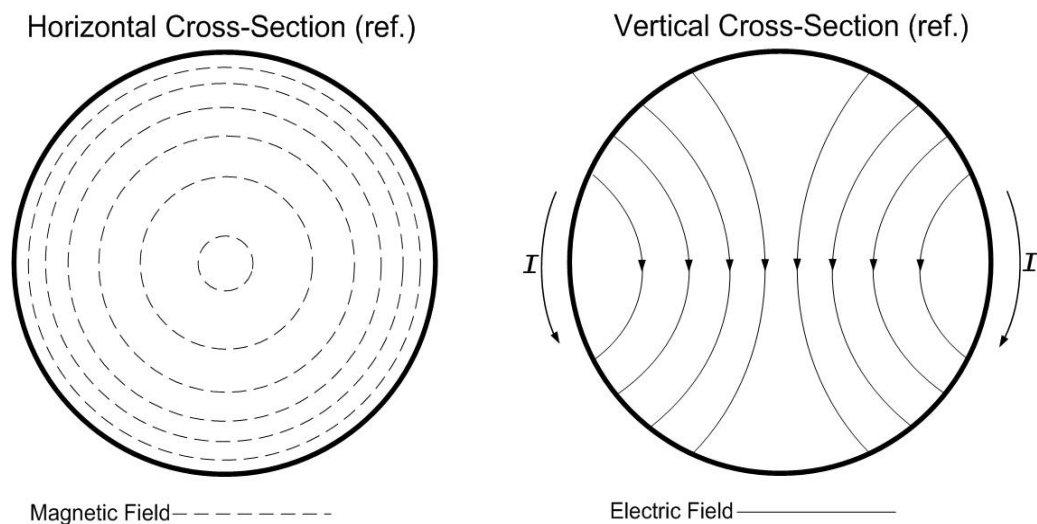
Figure 1: Cross-Section of Spherical Cavity Mode, TM101

MW energy can be coupled into a chamber by many methods. To work in conjunction with the transmission line and the chamber characteristics, a electrical-field coupler type microwave antenna was recommended to generate the TM101 mode fields [14]. Therefore, a micorwave antenna was developped in the form of quarter-wave ground-plane dipole as illustrated in Figure 2. The antenna was integrated within a coaxial feed-through to receive microwave power from the amplifier, and ultimately installed in

the MEC/LBV test setup. This development facilitated experimental MEC testing with both magnetic and electric field combustion chamber internal coupling methods.
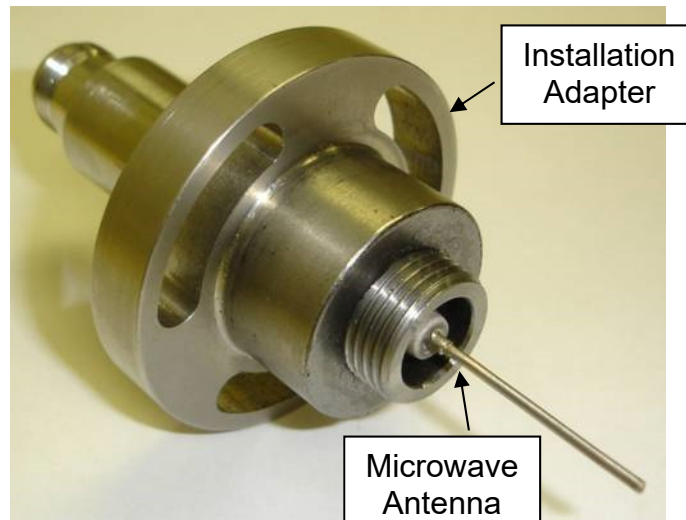
Figure 2: Microwave Quarter-wave Dipole Antenna Installed in the LBV Vessel Adaptor

2.2   Microwave System

The microwave system was integrated with the LBV vessel. A microwave power signal was synthesized by a microwave generator to the desired peak power and pulse duty cycle with a maximum of 2 kW and 100%, respectively. Its forward and reflected power were measured by a directional coupler and power meters. Finally, the microwave signal was transmitted through a coaxial feed-through and coupled into the LBV vessel via a microwave antenna. A circulator was implemented next to the antenna to absorb the reflected energy for power overload protection. Microwave instrumentation components and signals were included as well as interfaces with data acquisition. The system structure of MEC combustion test MW delivery and instrumentation are shown in Figure 3.
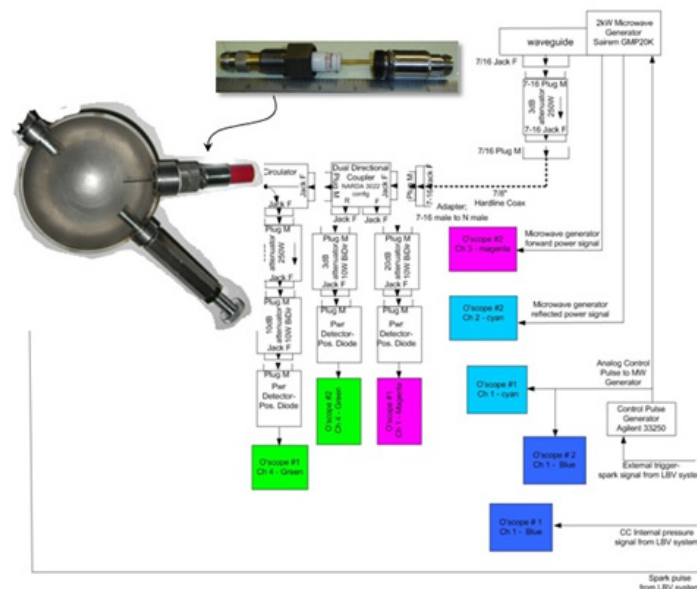
Figure 3: MEC system for Combustion Tests

An LBV internal pressure signal was routed to the MEC instrumentation setup to include measurements of the chamber internal pressure with the other MEC test signal traces and data files. Finally, the spherical LBV combustion chamber and the spark ignition circuit and spark plug are schematically included in the diagram. The physical integrated MEC MW delivery and instrumentation system and the LBV combustion chamber system is shown in Figure 4.
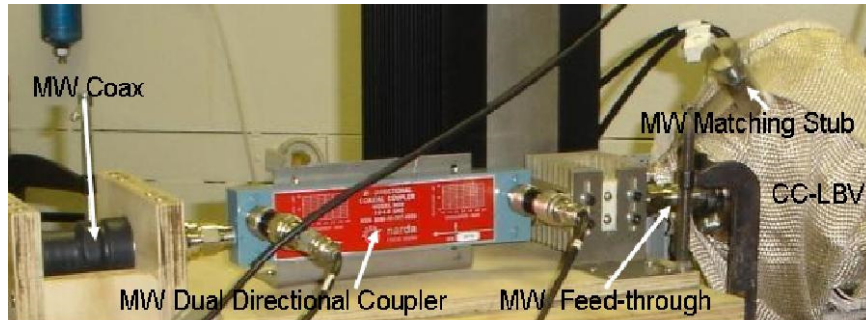
Figure 4: Integrated MEC /LBV Components during Preparation for Combustion Testing

3 Results and Discussions

MEC testing on the LBV vessel investigated the potential for enhanced combustion using standing waves of electromagnetic (MW) fields. The MEC testing was conducted at varying levels of dilution and with variations of MW coupling and configuration. MEC/LBV testing continued to be conducted in an "interleaved" test technique (MW-No MW) in order to limit potential influences on test results by un-related or relatively long-term drift in test conditions.

During the test interval, interactive test/modify/test experiments were conducted to optimize the MEC performance. Testing began with the more familiar MW magnetic loop-in-the-LBV configuration and then migrated to testing with the MW antenna configuration. Different microwave pulse widths and discharge timings were evaluated. By the end of the test interval, refinements in configuration and technique produced significantly accelerated combustion events with MW power applied. These tests were conducted using the e-field coupler microwave antenna configuration and at dilute A/F conditions.

3.1 MEC performance on Lean Combusiton

In this test, MEC was evaluated at a constant lean A/F ratio, 0.8, diluted by dry lab-grade air. The microwave power levels in the LBV vessel were from 0.7 kW to 1.6 kW. Room temperature iso-octane fuel was used and, the normal combustion time interval (time between ignition and maximum internal pressure) was 160 ms. Continuous microwave power was applied for a period of 160 milliseconds, starting one millisecond prior to ignition. Increasing levels of continuous microwave power were applied within the LBV during the MEC tests. Several series of multiple interleaved MW-No MW tests were performed at each MW power level to acquire relevant combustion data.

5.1. Microwave Enhanced Combustion on a Constant Volume Combustion Chamber for Lean Combustion and EGR Dilution

For these tests, it was found that microwave power levels above a threshold of 1kW consistently yielded larger than 10% reduction in the time required to reach peak pressure and also significantly improved combustion data variability, compared to combustion tests without microwave. Figure 5 illustraed results from a series of interleaved (MW-No MW) combustion tests using 1.6 kW of continuous MW power. Tests using pulsed microwave around 50% duty cycle resulted in 80%-90% of the pressure rise acceleration achieved with continuous microwave (Figure 6).
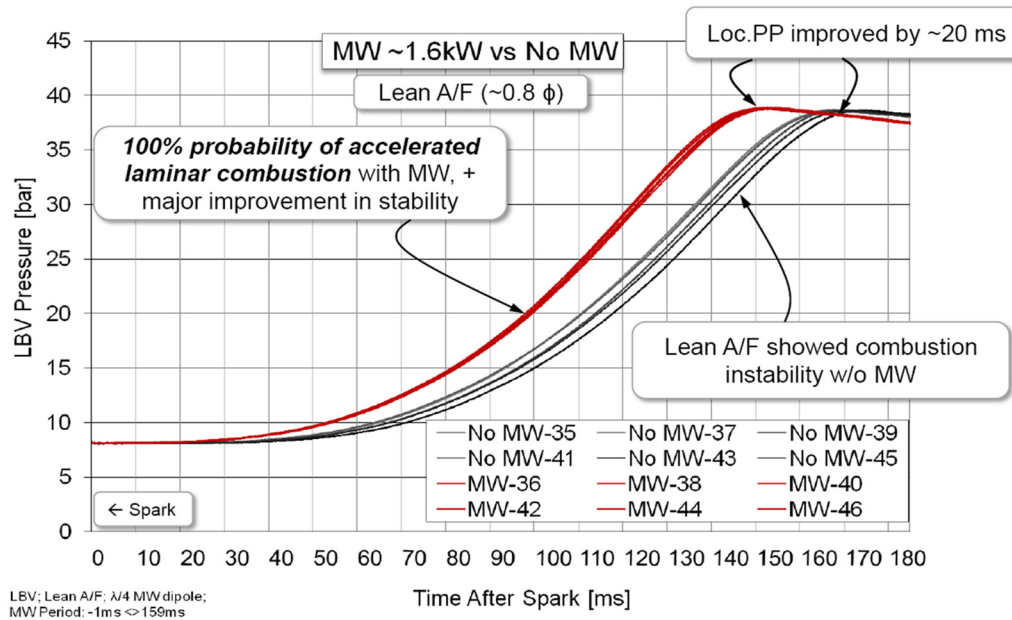

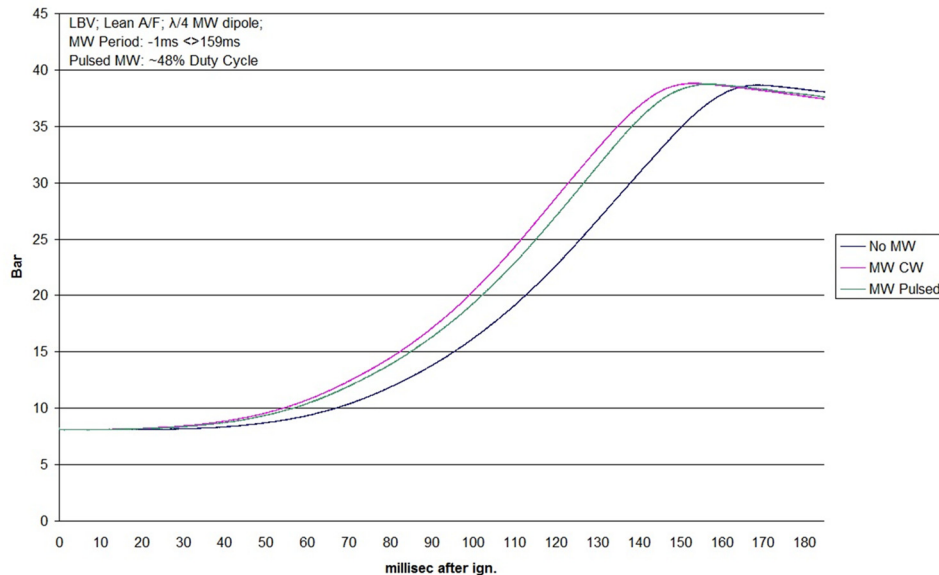Figure 5. MEC Lean Combustion Results by Continuous Microwave at 1.6kW

Figure 6. MEC Lean Combustion Results by Continuous and Pulsed Microwave at 1.4kW

Relatively high, time-varying reflected microwave energy was observed to be associated with the microwave combustion acceleration process (Figure 7), and the indicated

acceleration process appeared to be continuous under steady and pulsed microwave conditions. Microwave instrumentation signals showed continuous growth of the indicated (by the reflected power signal) acceleration process during intervals between MW pulses when the MW power was off. When MEC tests with microwave power applied but without ignition were conducted, combustion did not occur.
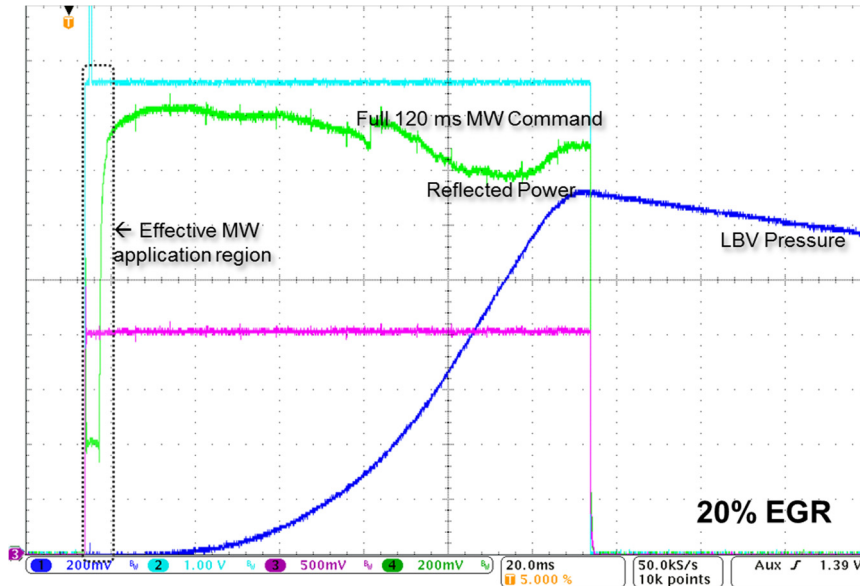
Figure 7. Example MEC MW Instrumentation Signal Traces - Accelerated Combustion Test

3.2 MEC performance on EGR Combusiton

The MEC performance was evaluated in the LBV at stoichiometric A/F ratios and 20% EGR dilution. For these tests, EGR was simulated through additional N_2 dilution. The normal combustion time interval (time between ignition and maximum internal pressure) was 120 ms. The MEC/LBV physical setup was the same as used in the lean MEC experiment to facilitate direct result comparisons. The MW power start timing was swept between -1ms and +4ms relative to ignition, in 1 ms steps. Continuous microwave power levels of about 1.3 kW were applied for durations of 120 ms for tests with microwave. All MEC testing was conducted using the previously described interleaved (MW- no MW) procedures to limit potential influences on test results by un-related or relatively long-term drifts in test conditions. Emissions were continuously sampled and evaluated to assure maintenance of the target conditions. Comparative analysis was conducted on emissions collected during special sequences of consecutive MW combustion tests and consecutive No MW tests.

MEC testing with under stoichiometric A/F ratios with 20% EGR dilution yielded essentially the same MEC combustion acceleration results. Microwave accelerated time to peak pressure by 10% for the stoich EGR case (Figure 8). The cycle stability was improved as well. Also, as found in the lean MEC testing, relatively high and time-varying reflected microwave energy was observed to be associated with the microwave combustion acceleration process, and the indicated acceleration process appeared to be continuous under steady and pulsed microwave conditions.
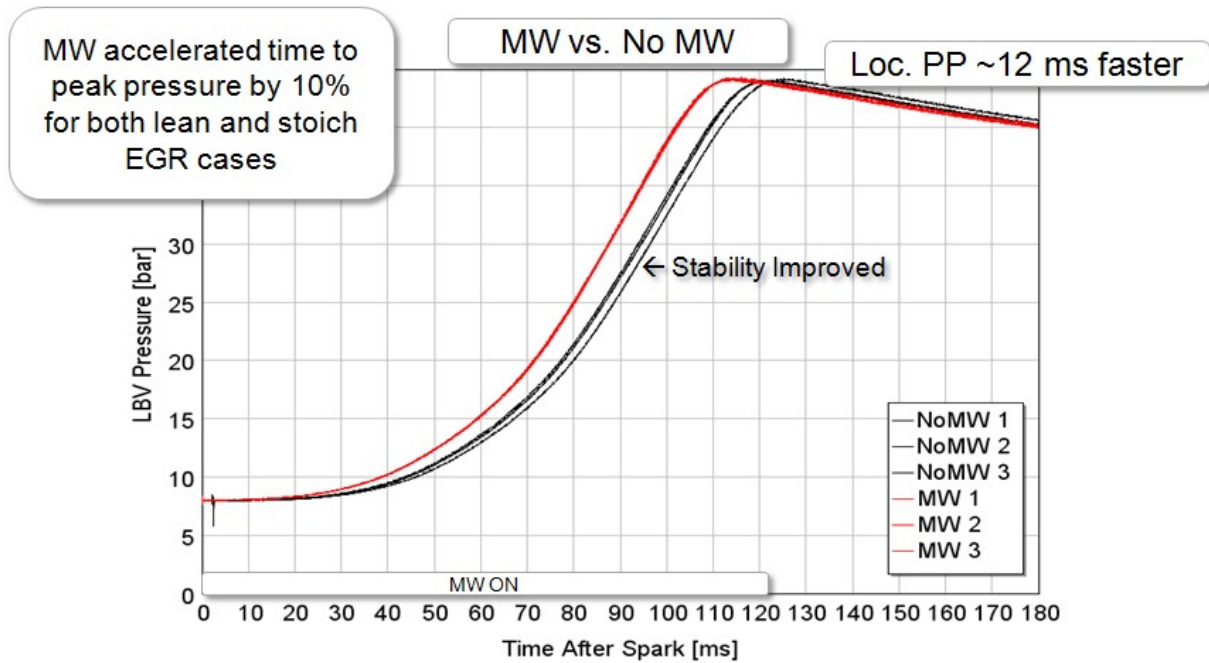
Figure 8. MW Can Accelerate Stoichiometric EGR Combustion

4   Conclusion

In summary, the MEC system established a high intensity field inside a conducting vessel and enhanced the combustion rates for a LBV vessel. Experimental results indicated that at a power level higher than 1 kW, the MEC using a electrical field coupler antenna can effectively improve flame development and cycle stability for dilute combustion – either at lean conditions (0.8 equivalence ratio) or stoichiometric operation with 20% EGR. This proved that fundamental resonance of MW radiation could positively impact dilute combustion on time-scales appropriate for internal combustion engines.

Literature

[1]   Fischer, M., Kreutziger, P., Sun, Y., and Kotrba, A., "Clean EGR for Gasoline Engines – Innovative Approach to Efficiency Improvement and Emissions Reduction Simultaneously," SAE Technical Paper 2017-01-0683, 2017, https://doi.org/10.4271/2017-01-0683.

[2]   Alger, T., Gingrich, J., Mangold, B., and Roberts, C., "A Continuous Discharge Ignition System for EGR Limit Extension in SI Engines," SAE Int. J. Engines 4(1):677-692, 2011, https://doi.org/10.4271/2011-01-0661.

[3]   Chen, W., Madison, D., Dice, P., Naber, J. et al., "Impact of Ignition Energy Phasing and Spark Gap on Combustion in a Homogenous Direct Injection Gasoline SI Engine Near the EGR Limit," SAE Technical Paper 2013-01-1630, 2013, https://doi.org/10.4271/2013-01-1630.

[4]   Yoshihara, Y., Nakata, K., Takahashi, D., Omura, T. et al., "Development of High Tumble Intake-Port for High Thermal Efficiency Engines," SAE Technical Paper 2016-01-0692, 2016, https://doi.org/10.4271/2016-01-0692.

[5]   Zhao, Jinxing. (2017). Research and application of over-expansion cycle (Atkinson and Miller) engines – A review. Applied Energy. 185. 10.1016/j.apenergy.2016.10.063.

[6]   Azimov, U., Tomita, E., and Kawahara, N., "Ignition, Combustion and Exhaust Emission Characteristics of Micro-pilot Ignited Dual-fuel Engine Operated under PREMIER Combustion Mode," SAE Technical Paper 2011-01-1764, 2011, https://doi.org/10.4271/2011-01-1764.

[7]   Nandakumar Kartha, B., Vijaykumar, S., and Reddemreddy, P., "Thermodynamic Split of Losses Analysis of a Single Cylinder Gasoline Engine with Multiple Spark Plug - Ignition Coil Configurations," SAE Technical Paper 2016-32-0008, 2016, https://doi.org/10.4271/2016-32-0008.

[8]   Yamanaka, K., Shiraga, Y., and Nakai, S., "Development of Pre-chamber Spark-plug for Gas Engine," SAE Technical Paper 2011-01-1870, 2011, https://doi.org/10.4271/2011-01-1870.

[9]   Cimarello, A., Grimaldi, C., Mariani, F., Battistoni, M. et al., "Analysis of RF Corona Ignition in Lean Operating Conditions Using an Optical Access Engine," SAE Technical Paper 2017-01-0673, 2017, https://doi.org/10.4271/2017-01-0673.

[10]   Ogata, K., "A High Energy Ignition System for EGR Combustion Engine," SAE Technical Paper 2017-01-0675, 2017, https://doi.org/10.4271/2017-01-0675.

[11]   Yu, S., Xie, K., Yu, X., Wang, M. et al., "High Energy Ignition Strategies for Diluted Mixtures via a Three-Pole Igniter," SAE Technical Paper 2016-01-2175, 2016, https://doi.org/10.4271/2016-01-2175.

[12]   Groff, Edward G, Krage, Mark K, General Motors Laboratories, Microwave Effects on Premixed Flames, Combustion and Flame 56: 293-306, 1984

[13]   Constantine Balanis, "Advanced Engineering Electromagnetics," 2nd ed., pp. 549-566, 2012

[14]   Constantine Balanis, "Antenna Theory Analysis and Design," 3rd ed., pp.151-165, 2005.

5.2 Lean Limit Expansion up to Lambda 2 by Multi-Point Microwave Discharge Igniter

Atsushi Nishiyama, Yuji Ikeda, Takeshi Serizawa

Abstract

The main challenge to run the engine at ultra-lean or high EGR conditions depends on robust ignition of the mixture i.e. generation of a repeatable and robust ignition kernel to subsequently ignite the fuel-air mixture. We had developed microwave enhanced ignition system in which regular spark is augmented by microwaves which generates a bigger size plasma where. large pool of active radicals effectively increased the initial flame speed, engine efficiency, extended the lean limit and resultant decrease in COV of IMEP.

Recently, we developed another plasma-based ignition device named Microwave Discharge Igniter (MDI) which works on the principle of microwave resonation within a cavity. MDI is a compact ϕ 4.5 mm plug with a quarter coaxial cavity resonator built into its structures. It receives the microwave (MW) pulse signal at 2.45 GHz from a semiconductor-based MW generator which can be controlled to produce very precise pulse characteristics such as pulse width, pulse number and pulse frequency, with time resolution down to 0.1 µs. The MDI has been shown to have very good combustion performance, including dilution and lean limit extensions.

An igniter for gasoline engine also needs to be robust. Hence, the MDI was put under stress and endurance tests. The tests were carried out inside a constant volume chamber at non-reactive condition up to 0.5 MPa. The MDI was controlled to discharge continuously for more than 20 million times, 124-hour straight, mimicking the standard lifetime of 20,000 km highway driving.

The compact size of the igniter means that multi-point ignition inside the combustion chamber is possible. In this study, a 3-point MDI plug with M12 size was developed and tested inside a practical commercially available multi-cylinder engine to evaluate the performance of multi-point ignition. The lean limit was compared with a standard spark ignition system at 1460 rpm engine speed and 20 Nm engine torque condition. As expected, 2-point ignition performed better than single-point, reaching the air-fuel ratio of 31 (approximately Lambda, $\lambda = 2.1$) in cylinders #1 and #3. However, the variance in IMEP of cylinder #2 was higher than that of cylinder #1 and #3 at the same air-fuel ratio for both spark ignition and multi-point MDI. This is caused by cylinder difference of combustion due to the mounting platform constraint imposed on the intake manifolds. Even though the engine used for this study was not optimally designed for higher lean limits at the chosen conditions of this study, the multi-point MDI demonstrated a better load and emission performance tests maintaining exhaust gas temperatures below 300°C and achieving single digit ppm of NO compound emission.

1   Introduction

In an effort to meet demanding regulatory standards prescribed for automobiles, significant research activities have focused on reduction of emissions whiles maximizing efficiency with further downsizing of engines [1]. However, limitation on energy supply and durability concerns restrict conventional ignition systems from operating steadily at ultra-lean burn and high tumble flow/ exhaust gas recirculation (EGR) conditions [2]. Moreover, the maximum achievable EGR is constrained by misfiring and low efficiency due to the retardation effect of diluent on flame kernel growth [3]. Thus, high EGR implies high threshold energy values for successful ignition [4]. This challenge is much more pronounced for alternative fuels. Plasma-assisted ignition and combustion has been shown to extend the limits of lean burn and blowout, as well as reducing emissions and is thus, a viable alternative to conventional spark plug systems [5]-[12].

We have designed, developed and tested an ignition device termed as the Microwave Discharge Igniter (MDI), which works on the principle of microwave (MW) resonation within a quarter coaxial cavity and is capable of breakdown under high pressure conditions [5],[13]-[15]. The MDI is simple, compact in size and is resonated by a 2.45 GHz semiconductor MW oscillator which is finely tuned and controlled. Numerous oscillation patterns are achieved by varying the pulse widths, pulse periods, pulse delay, duty cycle, power per pulse as well as the number of pulses per burst, with tens of nanosecond timescale resolutions. Thus, the MDI is capable of preferential radical production: generating active radicals (O and OH for instance) that are necessary for enhancing low temperature plasma chemistry which not only enhances the plasma after breakdown, but also sustains the discharge for improved combustion performance [16]-[18]. In other words, the MW oscillation pattern affects the induced plasma characteristics, such as the ability to generate non-equilibrium, non-thermal plasmas which accelerates the growth of flame kernel and thereby reducing misfiring at ultra-lean conditions [19]-[22].

Our previous studies conducted in constant volume combustion chambers with optical diagnostics showed that the single point MDI outperforms the conventional spark plug ignition system [14],[23]. Multi-point ignition has been shown to maximize ignition volume, enhance flame development and growth, which in turn increases lean burn limits and dilution rates [24]-[26]. In this study, we demonstrate the capability of an M12, 3-point MDI (each port has a ϕ 4.5 mm plug) to extend the lean burn limit up to Lambda, λ of 2.1, whiles exhibiting comparatively better emission performance. The compactness of this MDI makes it a flexible device amenable to various designs and configurations of combustion chambers with different engine heads. The multi-point MDI was applied to a multi-cylinder commercially available engine and its ignition performance evaluated and compared to a conventional spark plug ignition system at an engine speed of 1460 rpm and a torque of 20 Nm.

2   Experimental Setup

2.1   Microwave Oscillation and Control

The MW oscillation is performed by a semiconductor device which permits varying degrees of oscillation patterns. As shown in figure 1, oscillation patterns with equal pulse
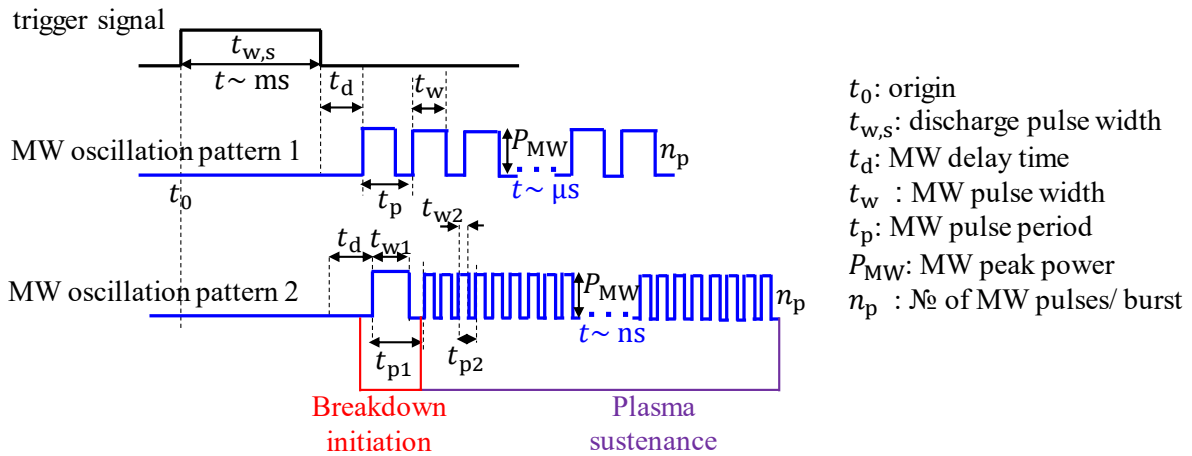
Figure 1: Pictorial representation of MW oscillation pattern and its trigger signal

widths t_w, and equal pulse periods t_p, are possible and labelled as pattern 1. In addition pattern 2 which has different timescales for set 1 (t_{w1}, t_{p1}) and set 2 (t_{w2}, t_{p2}), is attainable and is the most applied pulse train for our MW-enhanced plasma-assisted combustion [13]-[15],[23]. The MW oscillation pattern permits the spatial and temporal control of both the growth and lifetime of the induced plasma which in effect influences the production of active radicals for combustion. The timescales for these oscillation patterns are available from microseconds to nanoseconds levels per pulse at MW output power P_{MW}, of tens of watts to kW level per pulse, achieving several hundreds of millijoules per pulse. The number of pulses per burst n_p, could be varied up to 2400.

The equivalent electric circuit for a single cavity as well as pictures of the 3-point MDI used in this study are shown respectively in figure 2 (a) and figure 2 (b) [15]. Figure 2 (b) also shows the MW-enhanced plasma during the MDI discharge.
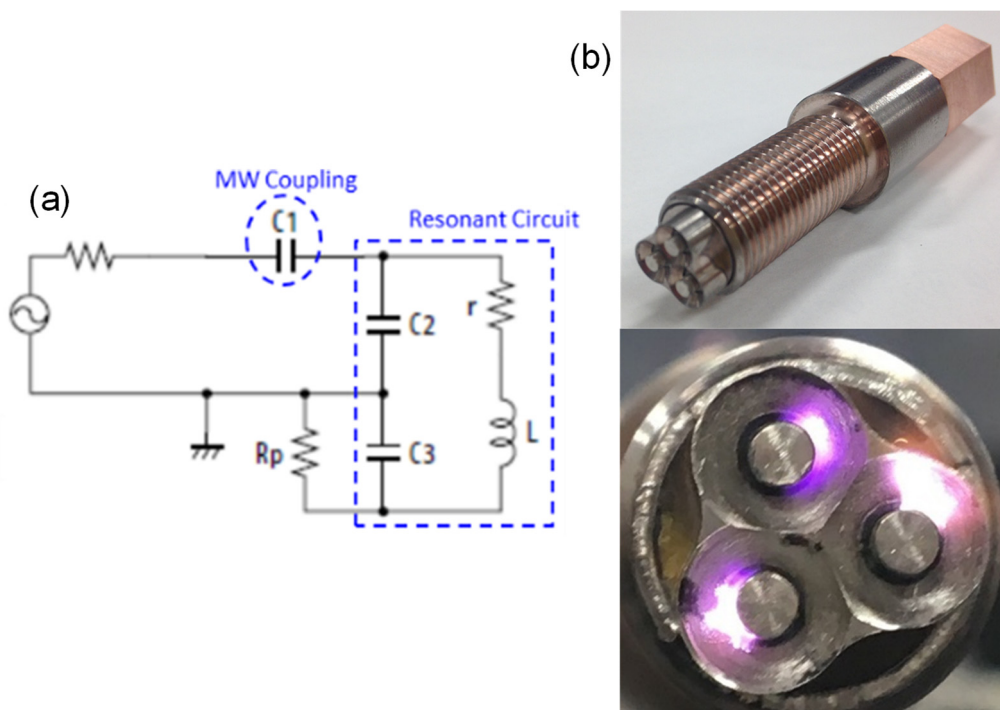
Figure 2: Equivalent electric circuit of a single cavity (a) and pictures of the M12, 3-point MDI used in the experiment (b)
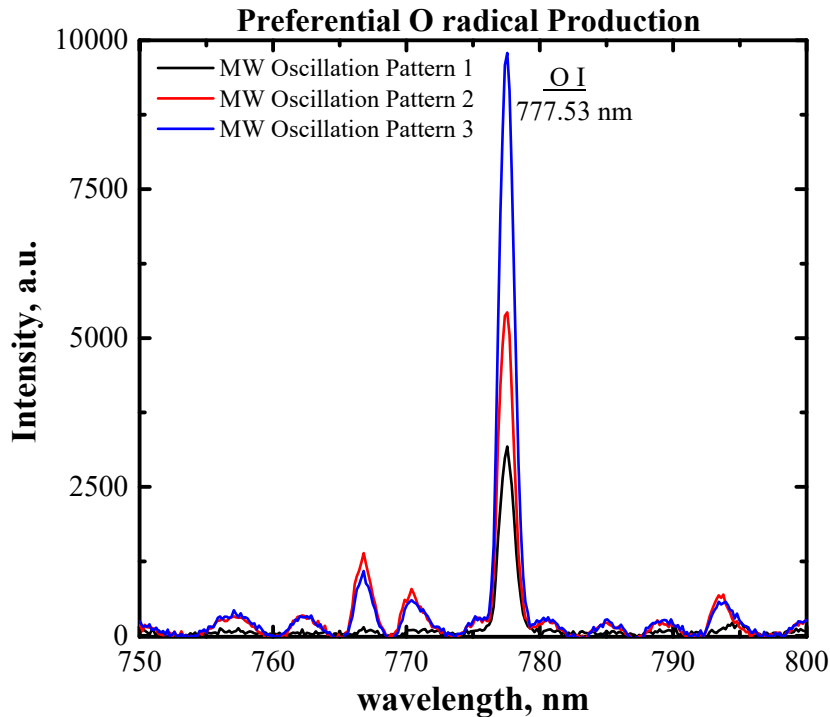
Figure 3: The effect of MW oscillation pattern on O radical production

Each of the ports within the 3-point MDI are separately controlled by three similar MW oscillators. Thus, the MDI could be operated as a single to a 3-port discharge device. This further enhances the capacity to preferentially generate radicals such as oxidizers in high concentration levels for efficient combustion. In past studies, we have shown how these patterns of oscillation can influence the generation of preferred radicals. For instance, figure 3 shows the O radical spectral intensity variations obtained as a result of different MW oscillation patterns. Table 1 describes the parametric values of the oscillation patterns used in figure 3. E_{MW} is the MW input energy per total period.

More so, shown in figure 4 [23] is the effect of oscillation pattern per pulse on plasma characteristics. Longer t_w are required to initiate breakdown and thus it is shown in the figure that, the first pulse spectra have a lot of atomic lines coming from the erosion of electrode and antenna material. Subsequent pulses are short pulsed and thus minimize erosion whiles generating molecular spectra. Figure 5 shows the effect of oscillation pattern on O radical production using the Taguchi Method [13]. O radical is an intermediate species during flame development and growth, and thus knowing the oscillation patterns that influence its production is important. It is observed in the figure that, the parameters that had a positive effect (high signal-to-noise ratio) on O radical production were the number of pulses per burst n_{p2}, and pulse period t_{p2}, for set 2 pulses. These are shaded green in figure 5.

Table 1: MW oscillation used for O radical generation shown in figure 3

Pattern №	MW Oscillation Pattern			
	t_{p2}, ms	t_{w2}, ms	n_{p2}	E_{MW}, mJ
1	2	0.1	1400	232
2	2	0.3	700	344
3	2	0.2	1400	456
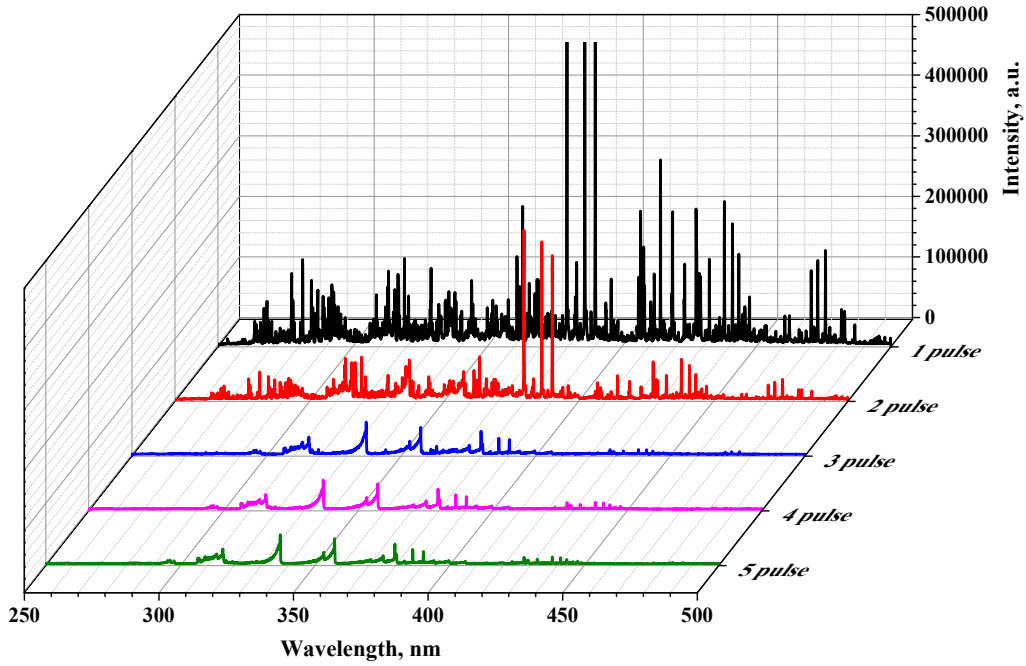
Figure 4: The effect of MW oscillation pattern variation per pulse on plasma characteristics
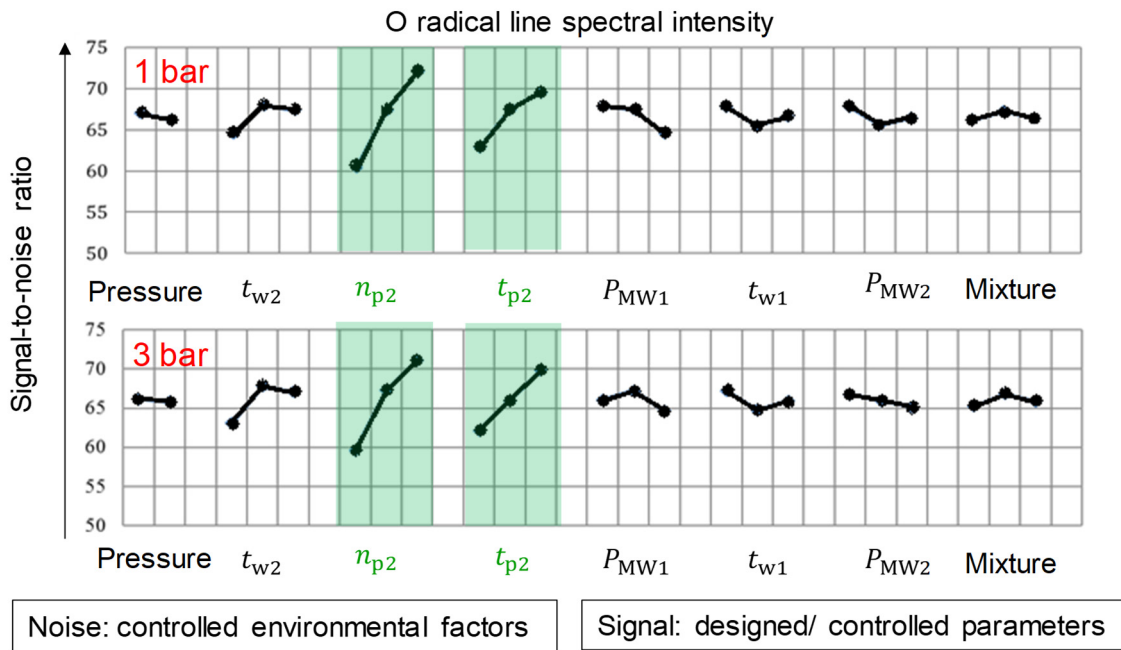
Figure 5: The effect of MW oscillation pattern on O radical production using Taguchi method

2.2   Constant Volume Combustion Chamber

In previous studies [13],[15], stress and endurance tests of the single MDI were performed in a constant volume combustion chamber. The single MDI device was test-ran continuously for 10 hours at wide-open-throttle load condition and then also continuously for 100 hours at IMEP of 550 kPa part load condition. Both test-runs were conducted at engine speeds of 3000 rpm. Under these test conditions, the MDI was

Table 2: Experiment conditions of the stress test in the constant volume chamber

Parameter	Condition
№ of discharges	Over 20 million times
Frequency of discharge	50Hz (equivalent to ignition interval of 6000rpm)
Gas	N2 (non-reactive, no oxidation)
Pressure	0.5 MPa
Flow rate	< 1000 mL/min (for gas exchange)

robust, flexible and also outperformed the conventional spark ignition system. The constant volume chamber used for previous as well as for this study, is a pent-roof type with a capacity of 185 cc and is supplied with propane-air mixture from a pre-mixing tank. The temperature of both the chamber and its contents were set at 298 K during the test-runs. The MDI is installed in the center of the pent-roof and the chamber is equipped with a piezo-electric transducer (Kistler 6052 C) for pressure measurements.

The stress tests were performed in a non-reactive medium with pressure of 0.5 Mpa. The MDI discharge was carried out continuously for 124 hours, over 20 million discharge times replicating an equivalence of the standard lifetime of 20,000 km high-way driving. The experimental conditions at which the stress tests were performed are as shown in table 2. These tests led to the erosion of electrode material as well deposition of substances on the MDI outer parts. The erosion and deposition have the potential to restructure the MDI's geometry and thus affects its resonance performance. Pictures of the MDI before, during and after the stress tests are shown in figure 6 [15].
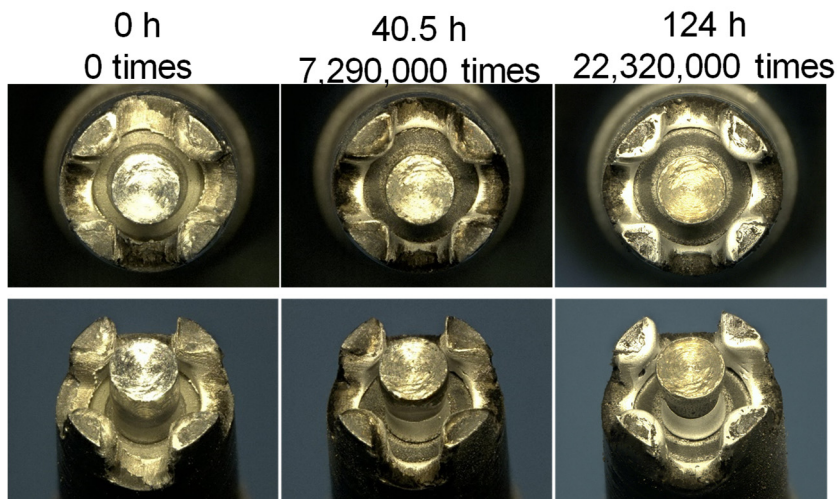
Figure 6: Pictures of the single MDI prototype before and after stress tests in a constant volume chamber (top: front view, bottom: tilted angle view)

The semiconductor MW oscillator was capable of self-correction and re-adjusting to a new resonant frequency to ensure successful ignition and preventing misfiring. The self-adjusted resonant frequencies were measured by an RF vector network analyzer and are shown in figure 7. This implies that not only is the MDI able to withstand tens of millions of discharge times, but also the MW oscillator induces the waves at frequencies that ensure efficient coupling with the plasma allowing high combustion efficiency.
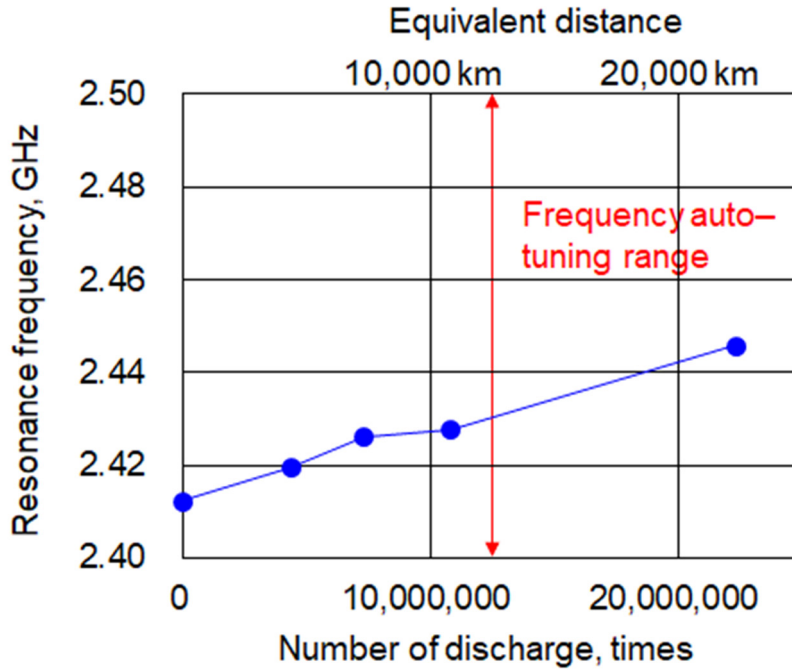
Figure 7: Auto frequency adjustment during the stress test in a constant volume chamber

2.3   Multi-cylinder Production Engine

The specification of the multi-cylinder engine used in this study is given in table 3. The engine is a three-cylinder Daihatsu KF-VE5 naturally aspirated engine with a port-fuel-injection system for the intake. The dimensions of the engine are a bore and a stroke of 63 mm and 70.4 mm respectively, with a total displacement of 658 cc. The engine was not optimally designed for higher lean limits and dilution rates. Hence, all tests performed were conducted at an engine speed of 1460 rpm and a torque of 20 Nm. Data recording was done by a standard data logging system provided by Daihatsu.

Previous results [15] demonstrate that the multi-point MDI outperformed the spark ignition system in all the three cylinders of the production engine. Furthermore, the 2-point experimented MDI exhibited better performance when compared with the single-point experimented MDI, attaining the air-fuel ratio (AFR) of 31.

Table 3: Specifications and operating conditions of the multi-cylinder engine

Parameter	Specification
№ of cylinders	3
Engine model	KF-VE5
Displacement	658 cc
Compression ratio	12.2
Bore x Stroke, mm	63 x 70.4
Fuel injection	PFI
Engine speed	1460 rpm
Torque	20 Nm
EGR rate	0
Excess air ratio	>2.1
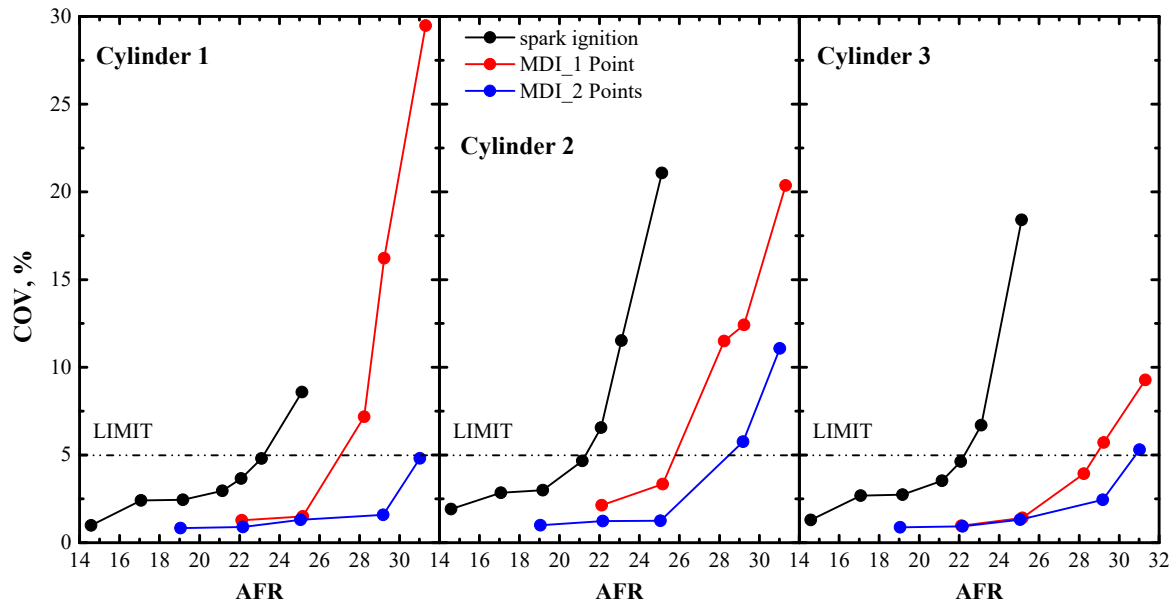
Figure 8: Performance comparison of spark plug and 1/ 2-point MDI in multi-cylinder engine

Even though the engine was not optimally designed for higher lean limits at the experimented low speed and low torque conditions, multi-point MDI demonstrated a better performance when compared with conventional spark ignition systems. The coefficient of variation (COV) for cylinder 2 was the largest under all cases and conditions of study. This is caused by cylinder difference of combustion due to the mounting platform constraint imposed on the intake manifolds. Figure 8 shows the performance comparisons of the ignition systems studied [15].

3   Results and Discussion

3.1   Load Performance Test of Lean Burn

Figure 9 show the variations of the IMEP with CA during the flame development time, that is, between discharge initiation and 10% of cumulative net heat release. The IMEP variations shown are for a 300-cycle test-runs each, for selected AFRs up to the limiting conditions respectively for the spark, 1- and 2-point MDI ignition systems. The lean limit expansion performance is shown only for cylinder 1 of the multi-cylinder engine. We observe that at leaner conditions, long initial combustion period generates low IMEP cycle. The conventional spark ignition system is unstable at AFR of 25; whiles the 1-point MDI becomes unstable beyond AFR of 25. The 2-point MDI performed comparatively better at AFR of 31, emphasizing the significance of the multi-point MDI for enhancing the efficiency of combustion with microwaves.

3.2   Emission Performance Test of Lean Burn

Figures 10 – 12 show the exhaust gas temperatures (before catalyst), the total hydrocarbon (THC) and NO emissions respectively for all the ignition systems studied. Here also, the graphs shown are the performance of cylinder 1 of the multi-cylinder engine. In the case of the exhaust gas temperature, the MDI outperformed the standard spark ignition system, exhausting at relatively low temperatures at comparatively high AFR
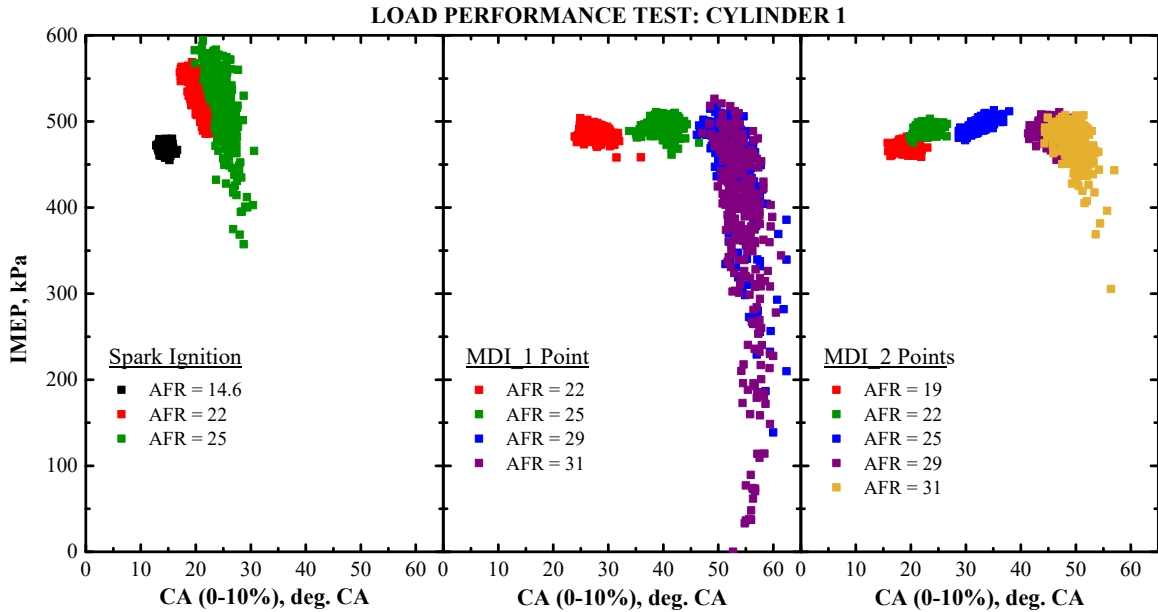
Figure 9: IMEP variation as a function of CA during flame development time for the ignition systems studied

values. Specifically, the multi-point MDI was able to maintain exhaust gas temperatures below 300°C at an AFR value of 31. Moreover, the THC emission of 2-point MDI was the minimum at lean burn conditions. The NO emissions were the highest for 2-point MDI within AFR values of 20 – 25. The multi-point MDI emits single digit ppm of NO compounds at the AFR values of 30 and 31. This makes the MW-assisted combustion a robust and an efficient system compared to combustion via conventional spark ignition. Thus, the multi-point MDI is capable of generating non-equilibrium plasma with active radicals that enhances the combustion process.
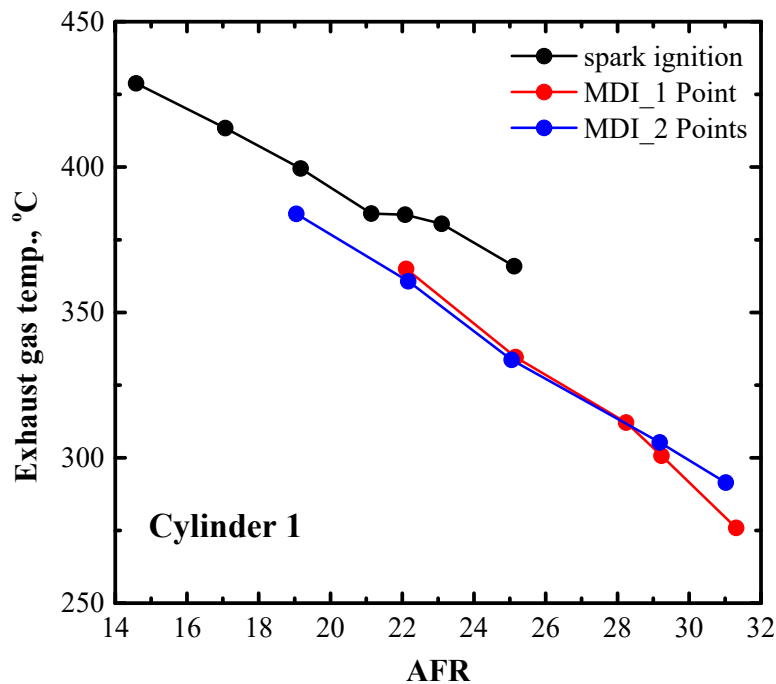
Figure 10: Exhaust gas temperature as a function of AFR for the ignition systems studied
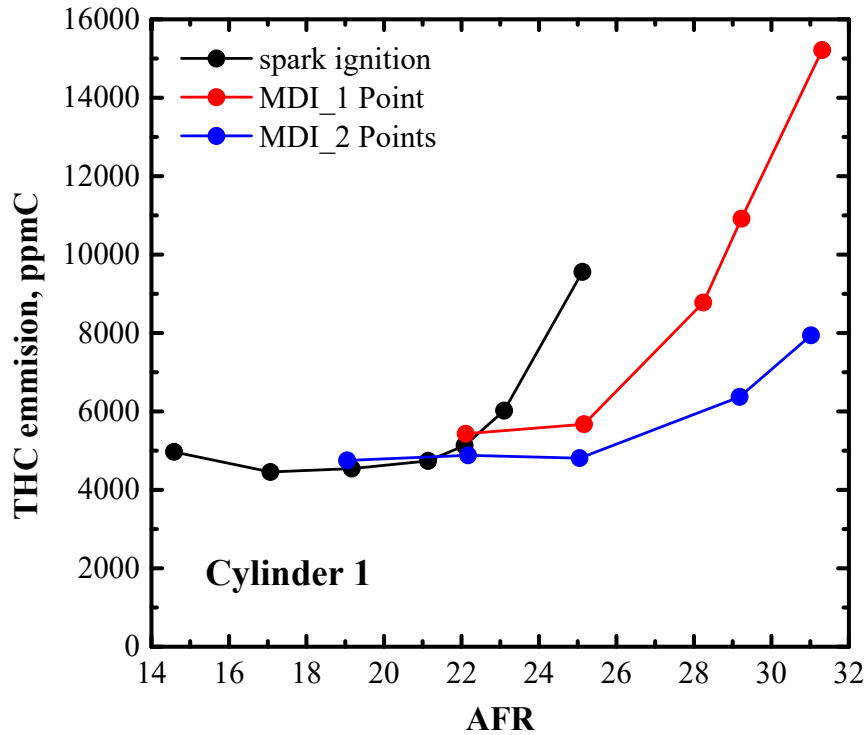
Figure 11: Total hydrocarbon emission as a function of AFR for the ignition systems studied
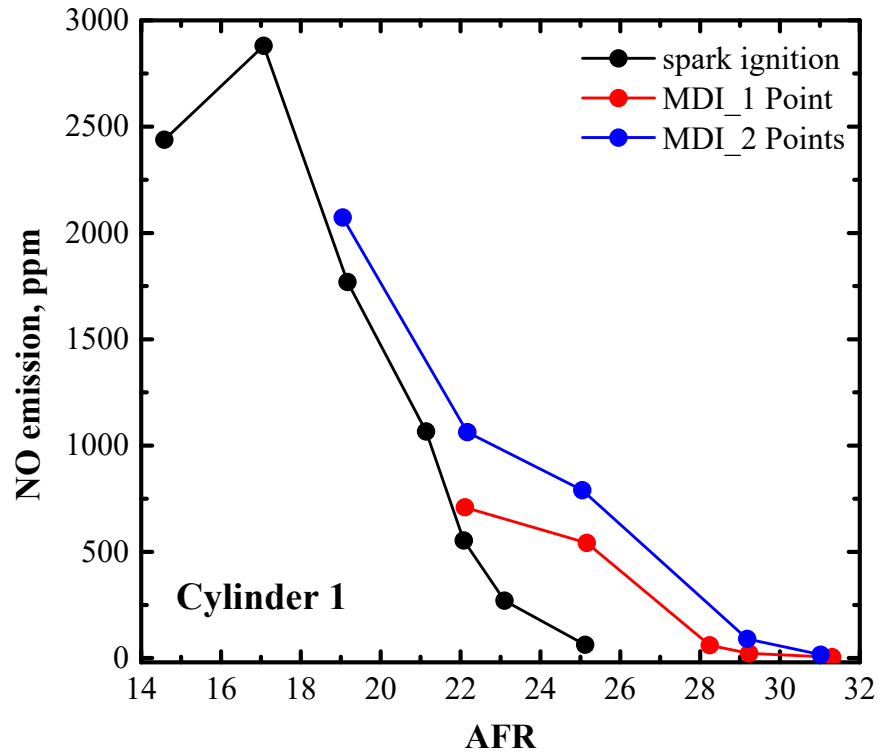
Figure 12: Nitrogen oxide emission as a function of AFR for the ignition systems studied

4   Conclusion

In this study, the essence of MW oscillation pattern for enhancing combustion efficiency was emphasized by comparing the performance of a multi-point MDI to that of a conventional spark ignition system. First, we observed that despite the erosion and deposition effect on cavity structure, the semiconductor MW oscillator is capable of auto-adjusting mechanism, attaining new resonant frequencies for improving combustion efficiency. Thus, the multi-point MDI generated selective active radicals that enhances low temperature plasma chemistry.

Second, considering the test-runs performed on the commercially available multi-cylinder engine (by Daihatsu Motors), the multi-point MDI exhibited a better COV of IMEP performance compared to the conventional spark ignition system. The multi-point MDI extended the lean limit expansion to an AFR of 31 (i.e. λ of 2.1) showing a comparatively better performance than that of the 1-point MDI and spark ignition. Thus, MW coupling for increased combustion efficiency is demonstrably possible with the multi-point MDI device in practical automobile engines.

Third, at higher lean burn limits, the multi-point MDI maintained exhaust gas temperatures below 300°C, and achieved lower THC and NO emissions. Thus, the multi-point MDI would be able to realize the stringent emission regulatory standards for automobiles whiles enhancing the combustion efficiency of the engines.
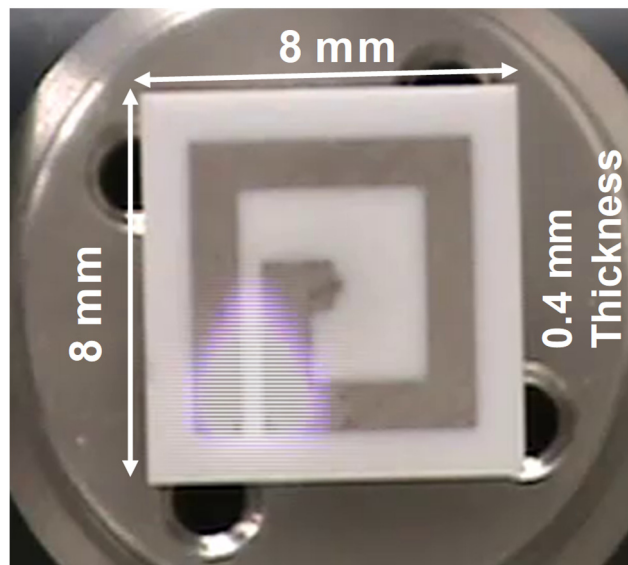
Figure 13: Miniaturized flat-panel plasma igniter with MW-sustained discharge

5   Future Work: A Novel Plasma Igniter [27]

We have developed, tested and currently improving on the design of a miniaturized novel igniter termed as the Flat-Panel Plasma Igniter (FPI). The FPI is an 8 mm × 8 mm × 0.4 mm ceramic panel with conductive inlay for microwave resonation. The image of the FPI with MW-sustained discharge are as shown in figure 13. We have in a previous study examined the performance of the FPI in a constant volume chamber with propane-air mixture where successful ignition was achieved at an equivalence

ratio of 0.6. The FPI's size is a characteristic advantage for various geometries of combustion chambers. We hope that this device would revolutionize the automobile industry and the drive to achieve reduced emissions with highly efficient combustion engines.

References

[1]   Johnson, T. and Joshi, A., "Review of Vehicle Engine Efficiency and Emissions," *SAE Technical Paper* 2017-01-0907, 2017, https://doi.org/10.4271/2017-01-0907.

[2]   Hakariya, M., Toda, T., and Sakai, M., "The New Toyota Inline 4-Cylinder 2.5L Gasoline Engine," *SAE Technical Paper* 2017-01-1021, 2017, https://doi.org/10.4271/2017-01-1021.

[3]   Yao, M., Zhang, Q., Liu, H., Zheng, Z. et al., "Diesel Engine Combustion Control: Medium or Heavy EGR?," *SAE Technical Paper* 2010-01-1125, 2010, https://doi.org/10.4271/2010-01-1125.

[4]   Tromans, P. S., and Furzeland R. M., "An analysis of Lewis number and flow effects on the ignition of premixed gases," *Symposium (International) on Combustion*. Vol. 21. No. 1, 1988, pp 1891-1897, https://doi.org/10.1016/S0082-0784(88)80425-9.

[5]   Ikeda, Y., Padala, S., Makita, M., and Nishiyama, A., "Development of Innovative Microwave Plasma Ignition System with Compact Microwave Discharge Igniter," *SAE Technical Paper* 2015-24-2434, 2015, https://doi.org/10.4271/2015-24-2434.

[6]   Wolk, B., DeFilippo, A., Chen, J.Y., Dibble, R., Nishiyama, A., and Ikeda, Y. "Enhancement of flame development by microwave-assisted spark ignition in constant volume combustion chamber," *Combustion and Flame*, Vol. 160, 2013, pp. 1225-1234, https://doi.org/10.1016/j.combustflame.2013.02.004.

[7]   Ma, J.X., Alexander, D.R., and Poulain, D.E. "Laser spark ignition and combustion characteristics of methane-air mixtures," *Combustion and Flame*, Vol. 112, 1998, pp 492-506, https://doi.org/10.1016/S0010-2180(97)00138-7.

[8]   Shiraishi, T., Urushihara, T., and Gundersen, M.A., "A trial of ignition innovation of gasoline engine by nanosecond pulsed low temperature plasma ignition," *J. Phys. D: Appl. Phys.*, Vol. 42, No. 13, 2009, 135208, https://doi.org/10.1088/0022-3727/42/13/135208.

[9]   Kim, H. H., Takashima, K., Katsura, and S., Mizuno, A., "Low-temperature NOx reduction processes using combined systems of pulsed corona discharge and catalysts," *J. Phys. D: Appl. Phys.,* Vol. 34, 2001, pp 604–613, https://doi.org/10.1088/0022-3727/34/4/322.

[10]   Khacef, A., Cormier, J.M., and Pouvesle, J.M., "NOx remediation in oxygen-rich exhaust gas using atmospheric pressure non-thermal plasma generated by a pulsed nanosecond dielectric barrier discharge," *J. Phys. D: Appl. Phys.,* Vol. 35, No. 13, 2002, pp 1491-1498, https://doi.org/10.1088/0022-3727/35/13/307.

[11]   Czemichowski, A. "Gliding arc. Applications to engineering and environment control," *Pure & Appl. Chem.*, Vol. 66, No. 6, 1994, pp 1301-1310.

[12] Shiraishi, T., "Possibility of the new Ignition System using the low Temperature Plasma having dual Functions of strengthening Ignition for SI Combustion and promoting and controlling Autoignition of HCCI Combustion" *1st IAV International Conference on Advance Ignition Systems for Gasoline Engines*, Expert Verlag, Berlin, 2012, pp 82-94.

[13] Le, M., Padala, S., Nishiyama, A., and Ikeda, Y., "Control of Microwave Plasma for Ignition Enhancement Using Microwave Discharge Igniter," *SAE Technical Paper* 2017-24-0156, 2017, https://doi.org/10.4271/2017-24-0156.

[14] Padala, S., Nagaraja, S., Ikeda, Y., and Le, M., "Extension of Dilution Limit in Propane-Air Mixtures Using Microwave Discharge Igniter," *SAE Technical Paper* 2017-24-0148, 2017, https://doi.org/10.4271/2017-24-0148.

[15] Le, M., Nishiyama, A., Serizawa, T., and Ikeda, Y., "Applications of a multi-point Microwave Discharge Igniter in a multi-cylinder gasoline engine," *Proceedings of the Combustion Institute*, 2018, https://doi.org/10.1016/j.proci.2018.06.033.

[16] Moisan, M., and Zakrzewski, Z." "Plasma sources based on the propagation of electromagnetic surface waves," *J. Phys. D: Appl. Phys.,* Vol. 24, No. 7, 1991, pp. 1025-1048, https://doi.org/10.1088/0022-3727/24/7/001.

[17] Gerstein, M., and Choudhury, P.R., "Use of silane-methane mixtures for scramjet ignition," *Journal of Propulsion and Power*, Vol. 1, No. 5, 1985, pp. 399-402.

[18] Wang, F., Liu, J.B., Sinibaldi, J., Brophy, C., Kuthi, A., Jiang, C., Ronney, P., and Gundersen, M.A. "Transient plasma ignition of quiescent and flowing air/fuel mixtures," *IEEE Transactions on Plasma Science*, Vol. 33, No. 2, 2005, pp. 844-849, https://doi.org/10.1109/TPS.2005.845251.

[19] Potts, H., and Hugill, J., "Studies of high-pressure, partially ionized plasma generated by 2.45 GHz microwaves," *Plasma Sources Sci. Technol.*, Vol. 9, No. 1, 2000, pp. 18-24, https://doi.org/10.1088/0963-0252/9/1/304.

[20] Ogura, K., Yamada, H., Sato, Y., and Okamoto, Y., Excitation temperature in high-power nitrogen microwave-induced plasma at atmospheric pressure," *Applied Spectroscopy*, Vol. 51, No. 10, 1997, pp. 1496-1499, https://doi.org/10.1366/0003702971938984.

[21] Laroussi, M., and Roth, J.R., "Numerical calculation of the reflection, absorption, and transmission of microwaves by a nonuniform plasma slab," *IEEE Transactions on Plasma Science*, Vol. 21, No. 4, 1993, pp. 366-372, https://doi.org/10.1109/27.234562.

[22] Ju, Y., Guo, H., Maruta, K., and Liu, F., "On the extinction limit and flammability limit of non-adiabatic stretched methane-air premixed flames," *Journal of Fluid Mechanics*, Vol. 342 1997, pp. 315-334, https://doi.org/10.1017/S0022112097005636.

[23] Shcherbanev, S., De Martino, A., Khomenko, A., Starikovskaia, S. et al., "Emission Spectroscopy Study of the Microwave Discharge Igniter," *SAE Technical Paper* 2017-24-0153, 2017, https://doi.org/10.4271/2017-24-0153.

[24] Zheng, M., Yu, S., and Tjong, J., "High energy multipole distribution spark ignition system," *3rd IAV International Conference on Advance Ignition Systems for Gasoline Engines*, Springer International Publishing, Switzerland, 2017, pp 109-130.

[25] Morsy, M. H., and Chung, S. H., "Laser-induced multi-point ignition with a single-shot laser using two conical cavities for hydrogen/air mixture," *Exp. Therm. Fluid. Sci.*, Vol. 27, No. 4, 2003, pp. 491-497, http://dx.doi.org/10.1016%2FS0894-1777(02)00252-2.

[26] Ronney, P. D., "Laser versus conventional ignition of flames," Opt. Eng., Vol. 33, No. 2, 1994, https://doi.org/10.1117/12.152237.

[27] Padala, S., Le, M., Nishiyama, A., and Ikeda, Y., "Ignition of Propane-Air Mixtures by Miniaturized Resonating Microwave Flat-Panel Plasma Igniter," SAE Technical Paper 2017-24-0150, 2017, https://doi.org/10.4271/2017-24-0150.

6 Pre-chamber Ignition 1

6.1 Development of a Pre-chamber for Spark Ignition Engines in Vehicle Applications

Christoph Müller, Bastian Morcinkowski, Christof Schernus,
Knut Habermann, Tolga Uhlmann

Abstract

Future gasoline engines in hybrid powertrains for passenger cars and light commercial vehicles will also continue to require further reductions in fuel consumption and emissions. A major step towards increasing efficiency is represented by lean operation. Here, pre-chamber jet ignition systems, which are already being used successfully in large gas engines, offer the potential of realizing lean burn coupled with lowest nitrogen oxide emissions.

As part of the EU funded EAGLE project, FEV together with the Institute for Internal Combustion Engines at the RWTH Aachen University and other partners, have developed a pre-chamber for an efficient ignition jet process. Based on the objective to present a high efficiency and low emission lean burn engine for use in electrified powertrains, the pre-chamber and the associated cylinder head environment have been developed, calculated, designed and tested on the single cylinder engine test bench. The tools used for the CAE-based design are derived from the standards, but were adapted and extended to the development of the pre-chamber.

The resulting lean engine burn process, with its drastically improved lean burn capability and with low raw emissions, offers excellent conditions for further improving the efficiency of electrified powertrains.

Kurzfassung

Auch bei zukünftigen Ottomotoren in hybridisierten Antrieben für PKW und leichte Nutzfahrzeuge wird die weitere Verbrauchs- und Emissionsabsenkung gefordert. Einen großen Schritt zur Wirkungsgradsteigerung repräsentiert der Magerbetrieb. Hier bieten Zündstrahlverfahren, wie sie bereits erfolgreich bei großen Gasmotoren eingesetzt werden, das Potenzial, Magerverbrennung gepaart mit niedrigsten Stickoxidemissionen zu realisieren.

FEV hat gemeinsam mit dem Lehrstuhl für Verbrennungskraftmaschinen an der RWTH Aachen und weiteren Partnern im Rahmen des von der EU Co-finanzierten EAGLE-Projekts eine Vorkammer für ein effizientes Zündstrahlverfahren entwickelt. Ausgehend von der Zielsetzung, einen Mager-Ottomotor mit hohem Wirkungsgrad und niedrigen Emissionen zur Anwendung in elektrifizierten Antriebsträngen darzustellen, wurden die Vorkammer und die zugehörige Zylinderkopfumgebung entwickelt, berechnet, konstruiert und am Einzylindermotor-Prüfstand untersucht. Die dabei benutzen Werkzeuge zur CAE-basierten Auslegung entstammen den Standards, wurden jedoch zur Entwicklung der Vorkammer angepasst und erweitert.

Das resultierende ottomotorische Magerbrennverfahren bietet durch seine drastisch verbesserte Magerlauffähigkeit, verbunden mit niedrigen Roh-Emissionen, eine hervorragende Voraussetzungen für die weitere Wirkungsgradverbesserung von elektrifizierten Antriebsträngen.

1   Introduction

Further fuel consumption and emission reduction of combustion engines for passenger cars and light duty vehicles will be required in future. This holds true even in highly electrified powertrains, even though the requirements may significantly differ from to-day´s conventional applications, see Figure 1. In hybridized powertrains, which e.g. incorporate internal combustion engines as range extenders (REX) in serial or dual-mode configuration, the peak propulsion power demand is generated by the e-ma-chine(s), while the combustion engine provides the base load. In this case, the required engine map is narrowed, while simultaneously other requirements such as e.g. high efficiency are enforced, depending on the specific application.
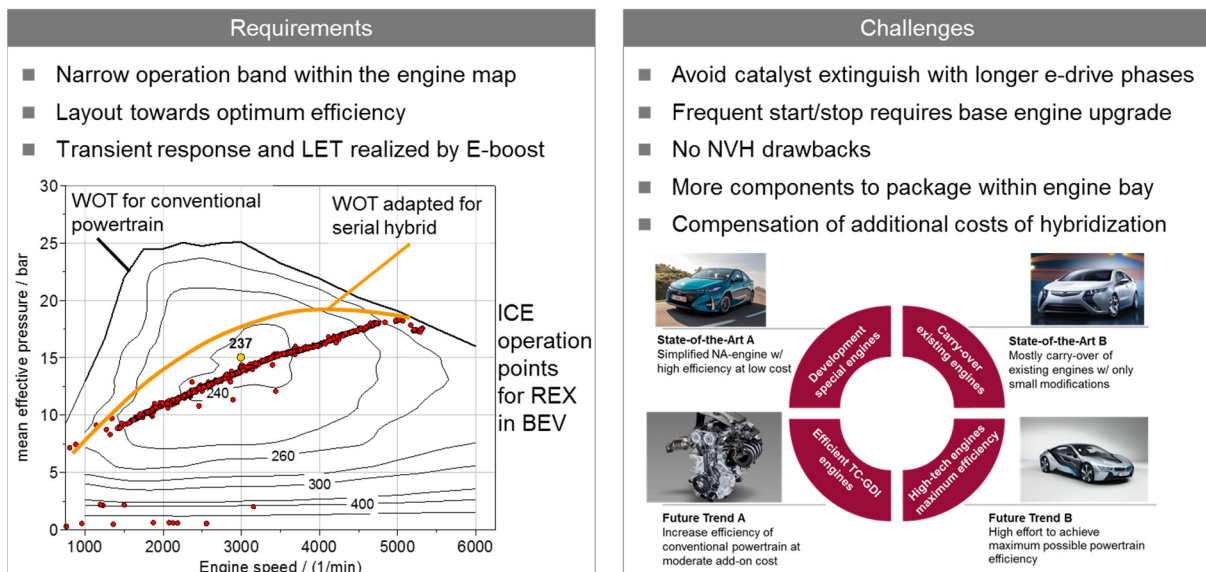
Figure 1: Requirements and challenges for combustion engines in hybrid powertrains

In a previous project, FEV and TMG have jointly developed a spark-ignition (SI) engine for the future with the aim of high thermal efficiency and low emission [1]. In order to accomplish the high efficiency target, a homogeneous lean burn combustion process has been selected as the technology enabler. As shown, the lean burn limit can be shifted to a relative air fuel ratio of up to 1.9 with still reasonable cyclic variation levels with a significant effort in specific development for lean operation and with the applica-tion of a high energy ignition system.

However, to shift the limit further or apply homogeneous lean burn operation in an engine with a smaller bore, the capability of a conventional spark ignition is limited. To enable ultra-lean homogeneous operation with relative air fuel ratios above 2, an igni-tion system is required, which not only reduces cyclic variations, resulting from the burn delay, but also reduces the burn duration and thus improves the combustion stability.

As flame quenching can be one reason for a slow and unstable combustion, a space ignition system may help to enhance the lean burn capability. With point ignition, as realized by a conventional spark plug, the energy transfer is locally restricted and can only be increased by flow. Furthermore, the flame travel is long. With space ignition, the ignition system itself ignites a larger share of the combustible volume. The energy transfer is higher and the flame travel is reduced.
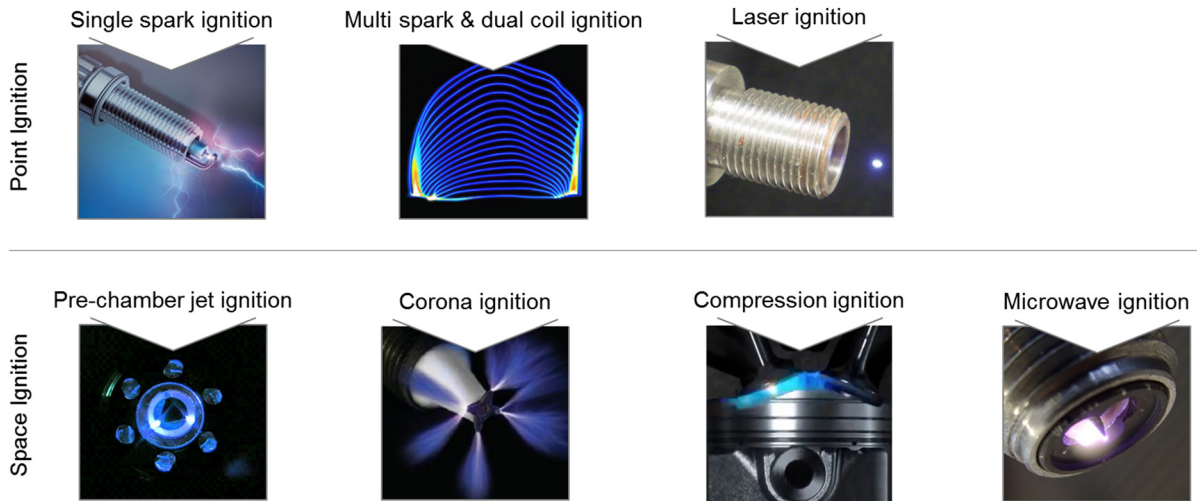
Figure 2: Multiple options to ignite large volumes (pictures by Beru, Federal Mogul, Delphi, Photonics)

As figure 2 indicates, there are various ignition systems for both categories, point and space ignition. Considering the previously discussed challenges of ultra-lean homogenous operation, in particular the pre-chamber ignition offers some important advantages. It supplies a large quantity of turbulent hot gas to the main combustion chamber to ignite the highly diluted mixture. Hence, it is one of the space-igniting techniques [2, 3, 4].

According to the classification shown in figure 3, the mixture in the pre-chamber, which is ignited by a spark, can be realized in two different ways: Whereas in so called passive pre-chambers, the air-fuel-mixture around the spark plug is mainly created during the compression stroke by the charge entering from main combustion chamber, active pre-chambers do have an additional external fuel feeding.

For ultra-lean conditions, the active pre-chamber operation is favored for external fuel enrichment allowing a stoichiometric or slightly rich mixture in the pre-chamber, without compromising the homogeneous lean mixture formation in the main combustion chamber. The dosing can be done either by a check valve, commonly used in commercial gas engines, or by a separate injector. Active pre-chambers can be supplied with either liquid or gaseous fuels.
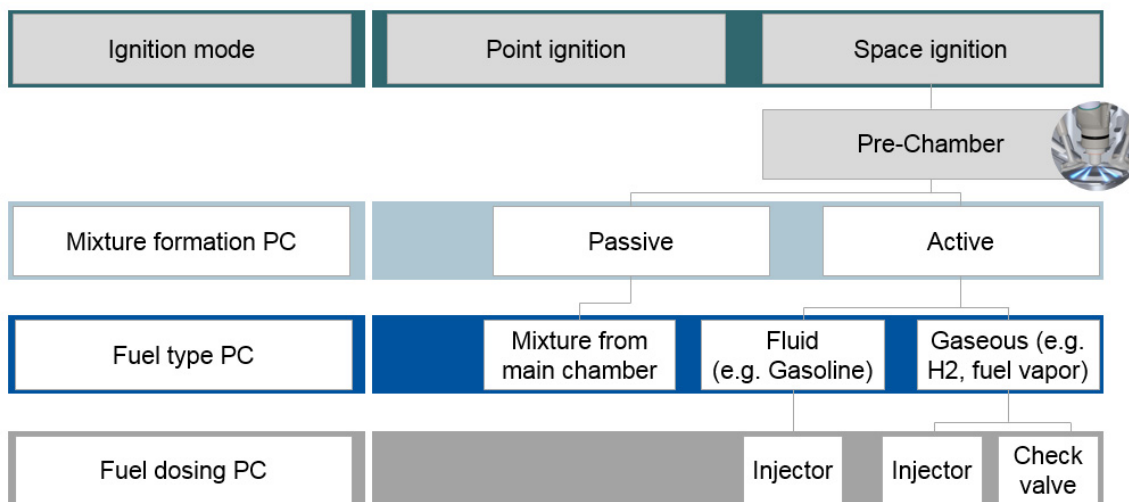
Figure 3: Classification of different pre-chamber configurations

Compressed Natural Gas (CNG) as a gaseous fuel is already being successfully used for both, passenger car gas engines as well as commercial gas engines. In comparison to liquid fuels, gaseous fuels have some advantages with regard to mixture formation. For the fuel supply to an active pre-chamber there are examples using fuel vapor [5], a pre-mixed fuel / air mixture [2, 4], methane [2] or hydrogen [6]. Bearing in mind that the powertrain should be installed in a vehicle, reasonable applications for passenger cars might differ from the ones for commercial engine applications. Fuel vapor could be generated onboard by a vaporizer or taken from canister purge. Hydrogen could be generated by fuel reforming, and CNG could be considered for BI-fuel or CNG operated engines.

However, considering the fuel supply infrastructure for passenger cars, liquid injection into the pre-chamber remains a very attractive option, although there are challenges for the mixture formation and risks with regard to particulate emissions to be considered.

2   Boundary Conditions

For the application in a hybrid powertrain, driving cycle simulations have indicated that BFSC at high load is most relevant for CO2-Emissions. Therefore, emphasis for the layout of the engine is placed on these operation points, while keeping in mind that also low load and idle operation conditions are to be considered.

In order to achieve low engine raw emissions as well as high efficiency, ultra-lean operation with a relative air-fuel-ratio of 2 and above is aimed for the entire engine operation map. As this should be achieved with a homogeneous mixture in the combustion chamber, enriching strategies in the pre-chamber by the spray target of the main chamber injector were not taken into account.

An active pre-chamber was chosen to be integrated in the all new cylinder head to achieve the above mentioned project targets. The active pre-chamber is supplied with either gasoline fuel or gaseous fuels. In any case, a separate injector is provided in the pre-chamber for this purpose. This allows a precise fuel metering as well as flexible adjustment of the injection timing.

All experimental investigations were carried out with a single cylinder engine (SCE) at the Institute for Combustion Engines (VKA) of the RWTH Aachen University. The main engine specifications are listed in table 1.

The cylinder head design allows realization of geometric compression ratios between 11 and 16.

Table 1: Single cylinder engine specification

Bore	75 mm
Stroke	90.5 mm
Stroke / Bore Ratio	1.206
Displacement	399 cm³
Peak pressure capability	170 bar
Geometrical Compression Ratio	11-16
Injection System	DI, 350 bar, lateral injector
Fuel	RON 98
Active pre-chamber enrichment with	Gasoline or gaseous fuel (CNG, H2)

The long stroke of 90.5 mm and the arrangement of the valves, combined with the intake port and the combustion chamber shape, generate a charge motion level, which is comparable to state-of-the-art turbo-charged engines.

For an optimum central position of the ignition system in the combustion chamber, a lateral DI injector position was chosen. To allow a fair comparison between the pre-chamber and the conventional ignition system, the engine can either be operated with a conventional ignition system or with the pre-chamber ignition system. The pre-chamber assembly in the new cylinder head is displayed in Figure 4.
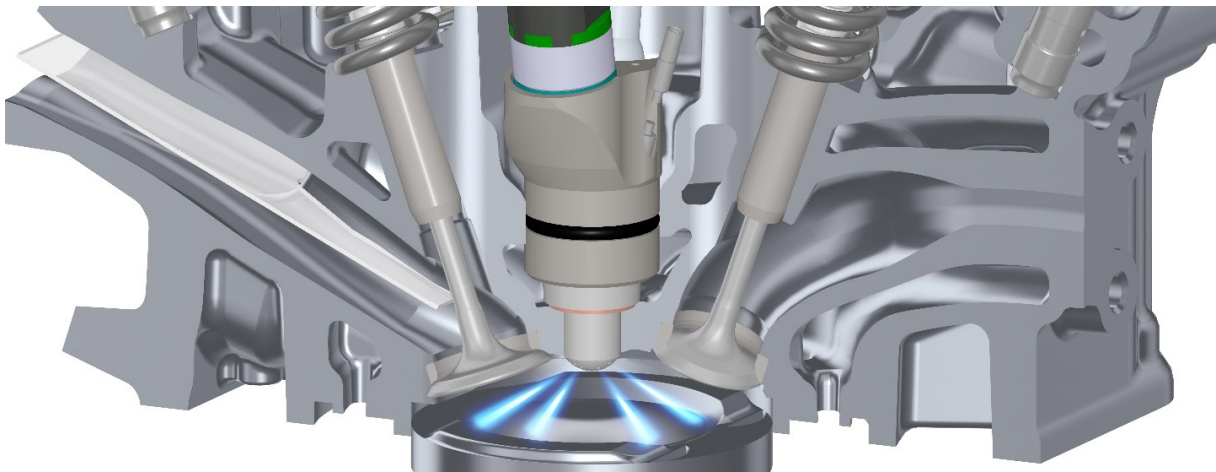
Figure 4: SCE cylinder head with pre-chamber

3   Layout Process

The pre-chamber design was performed with the help of various simulation tools, see figure 5. At first, 3D CFD simulations of the flow and mixture formation were carried out in order to obtain an initial estimate of the turbulence and mixing levels in the pre-chamber. These data serve as input for 0D simulations of the pre-chamber. Based on these simulations, basic parameters like hole size diameters, number of holes, chamber volume etc. can be pre-determined. Purposeful parameter sets are then selected

and refined with CFD simulations including combustion modelling. The results are finally validated in the single cylinder engine test program.
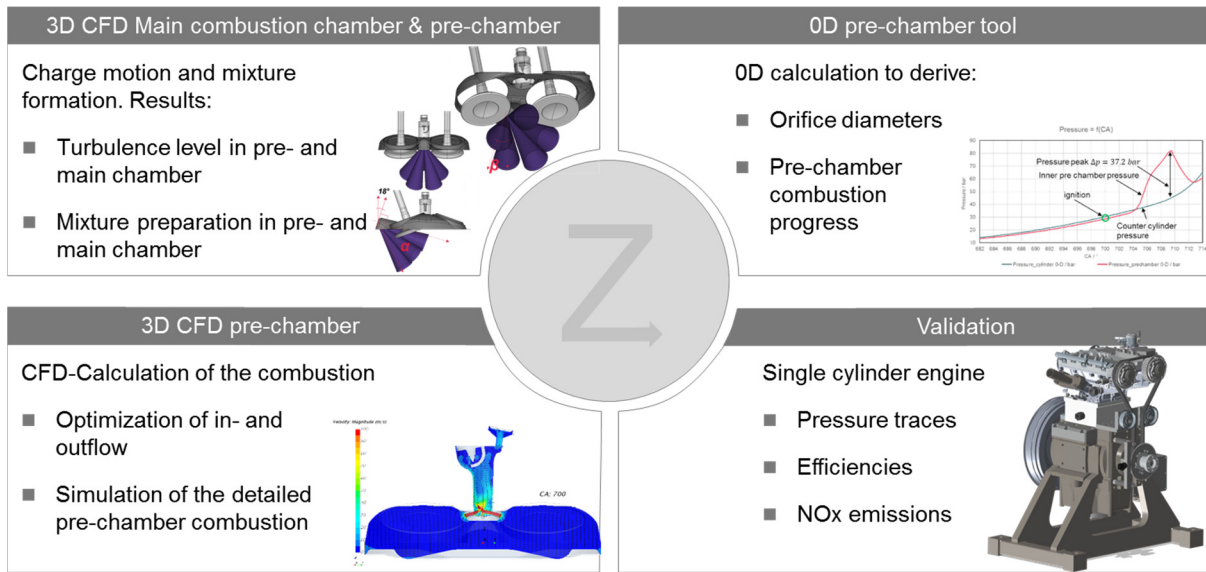
Figure 5: Development of the pre-chamber using 0D and 3D simulation tools

The design optimum found for the location of the 4-hole pre-chamber has an offset in lateral direction and height, see Figure 6. This supports the rotation of the gas flows entering the pre-chamber and allows them to move along the longitudinal axis without significant dissipation losses. Compared to a conventional pre-chamber design, the turbulence level can be more than doubled by this which significantly improves the mixture formation in the pre-chamber. This results in a much faster combustion and finally in a larger penetrating power of the hot gas jets entering the main combustion chamber.
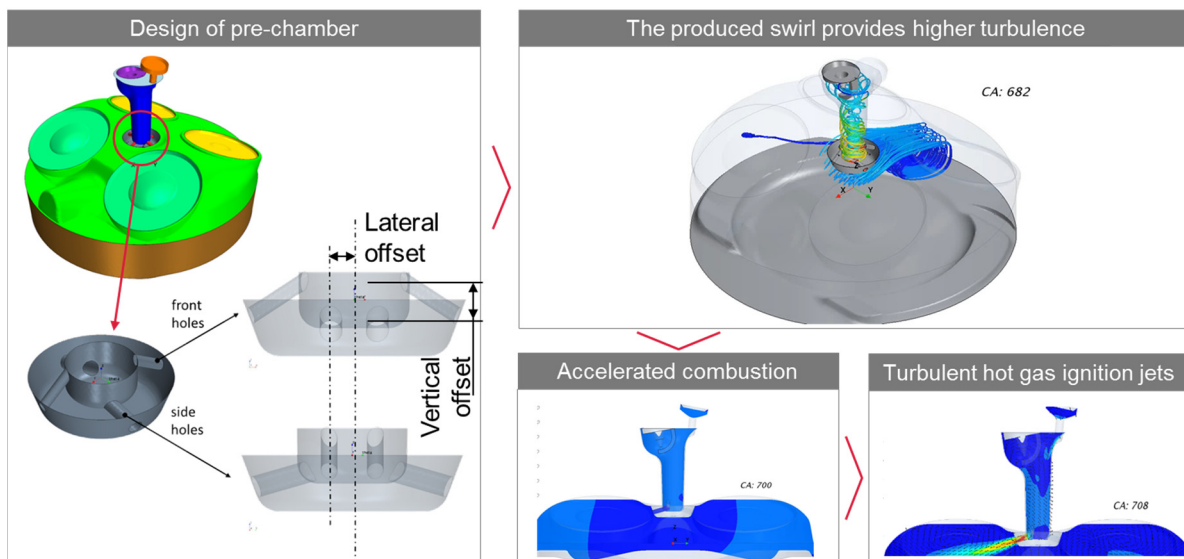
Figure 6: Optimized pre-chamber design

For the ultimate validation of the layout process described above, 3 pre-chamber designs were selected for manufacturing, see Figure 7. These pre-chambers have a different arrangement of the jet holes, but the same pre-chamber inner volume (~ 3 % of

compression volume). Also, the overall jet hole cross section was kept constant for all variants. This means the ratio of the spray hole areas and the pre-chamber volume (A/V) remains constant (~0.03 cm^{-1}).
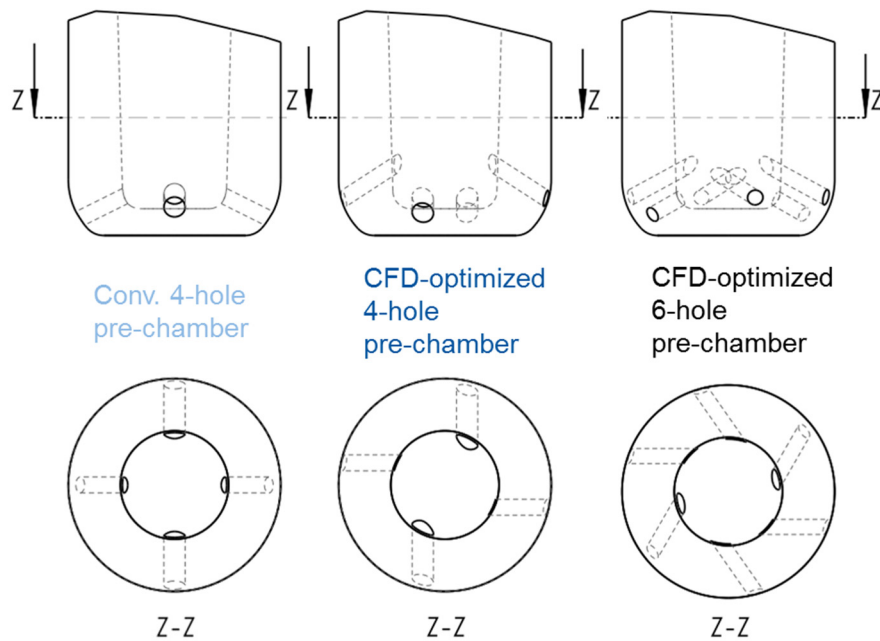
Figure 7: Tested pre-chamber jet hole designs

While the conventional pre-chamber layout only has 4 holes oriented perpendicular to outer round surface, the CFD optimized 4-hole pre-chamber has the same holes with a small side and a significant height offset to introduce a swirl in the pre-chamber. A similar approach was used for the CFD optimized 6-hole pre-chamber. For both 4-hole and the 6-hole pre-chambers, the orientation of the holes has been designed in such a way that the swirl is supporting the turbulent kinetic energy level at the spark plug during the charging phase of the pre-chamber, while during the discharging phase, the turbulent jets have a long free travel to ignite the mixture in the main combustion chamber as homogeneously as possible.
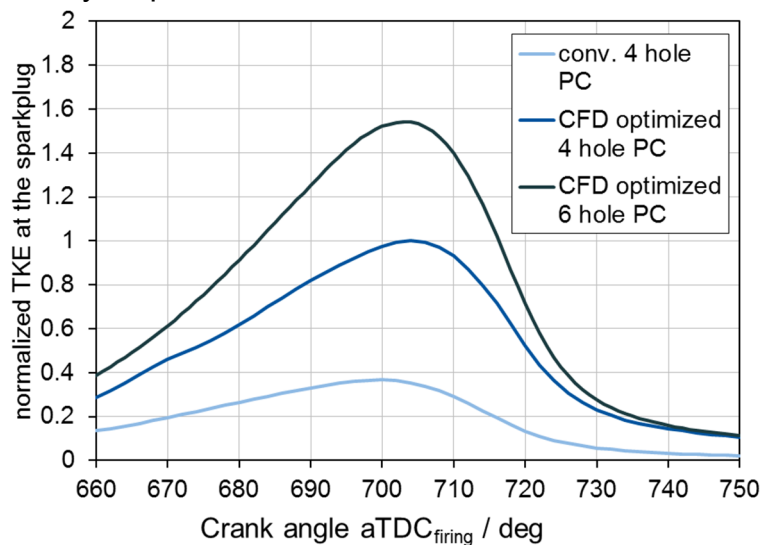
Figure 8: Normalized turbulent kinetic energy at the spark plug in the 3 selected pre-chambers

The turbulent kinetic energy in the pre-chamber at the spark plug is the smallest for the conventional pre-chamber, see Figure 8. The CFD-optimized 6-hole pre-chamber generates a peak turbulent kinetic energy level which is roughly 50% higher than the maximal value of the CFD-optimized 4-hole pre-chamber. It can be expected that this version should the most support the mixture formation in the pre-chamber and reduce the burn duration. This should maximize the potential for lean burn operation. However, the very turbulent charge motion complicates the inflammation in the pre-chamber and thus places higher demands on the ignition system.

4   Engine Test Results

The following results have been obtained on a single cylinder engine test bench. The operation points investigated are highlighted in green in Figure 9. The following analysis will focus on 3 operation points, which are most relevant for operation in hybrid powertrain applications:

- 2000 1/min, 12bar (IMEP)
- 2000 1/min, 15 bar (IMEP)
- 4000 1/min, 16 bar (IMEP)
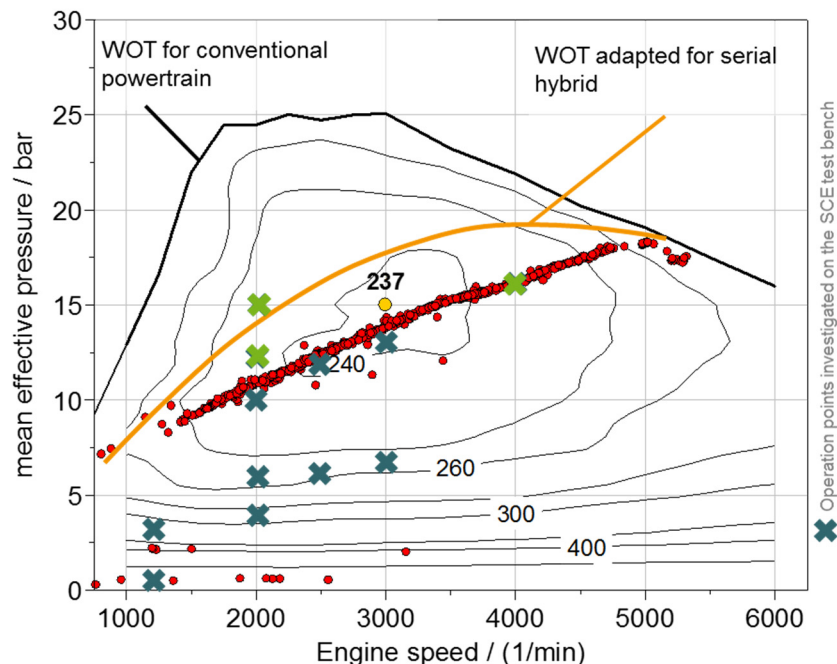
Figure 9: Operation points of pre-chamber ignition system on SCE test bench

For all results shown, the engine operated under similar boundary conditions. An MFB50% sweep has shown that the commonly used MFB50% timing at 7-8° CA aTDC is also the optimum for engine efficiency at ultra-lean operating conditions with the presented pre-chambers. Therefore, the spark advance was set to 7-8° CA aTDC for MFB50%, if there was no knocking limitation which required retarded ignition timing. The valve timing of the conventional valve lift profiles was set to a small valve overlap. All results with pre-chamber operation were realized with a geometric compression ratio of 13.0. For conventional spark plug operation, the compression ratio was slightly

higher. The relative air fuel ratio was determined via exhaust gas measurement according to Spindt [7, 8]. It represents the global value as it considers main combustion chamber and pre-chamber fuel. For the determination of the engine efficiency results, also both fuel fractions were taken into account.

4.1   Comparison of different pre-chambers

With a small amount of gas injected into the pre-chamber, the lean burn capability of the engine can already be improved. Figure 10 compares the CFD-optimized 4-hole pre-chamber with a high turbulence level due to swirl introduced with a conventional four hole pre-chamber. At 2000 1/min, 15 bar (IMEP) the burn delay of the non-optimized pre-chamber is following the same trend as the spark ignited engine. As a result the lean burn limit can be shifted from a relative air-fuel-ratio of 1.6 to 1.8 only.
Dosing the same small amount of CNG into the optimized pre-chamber with 4 jet holes, while keeping all other boundaries constant, the lean burn limit can be extended to 2.2. Although the hydrocarbon emissions are increasing towards ultra-lean conditions, it is possible to still achieve the same level of hydrocarbon emissions with the pre-chamber at these ultra-lean conditions as with the spark ignited operation at stoichiometric conditions.
With all pre-chamber variants, the burn duration (5%-90%) can be reduced by about 5 ° crank angle in stoichiometric conditions. In lean condition, these advantages improve further. When spark plug operated, the burn duration increases with increasing mixture dilution, in the case of pre-chamber operation, an almost constant burn duration over the entire air-fuel-ratio range is maintained.

Figure 10: Emissions, efficiency, burn delay and duration for different configurations at 2000 1/min, 15 bar (IMEP)

Increasing the fuel amount injected into the pre-chamber from 0.05 kg/h (~0.83 mg/cycle) up to 0.15 kg/h (~2.5 mg/cycle), the lean burn limit can be shifted even further with the same CFD-optimized 4-hole pre-chamber. While the burn delay is significantly reduced, the burn duration is the same up to relative air-fuel-ratio 1.8 and only slightly reduced above it. However, still a remarkable lean global relative air-fuel-ratio of 2.7 can be achieved.
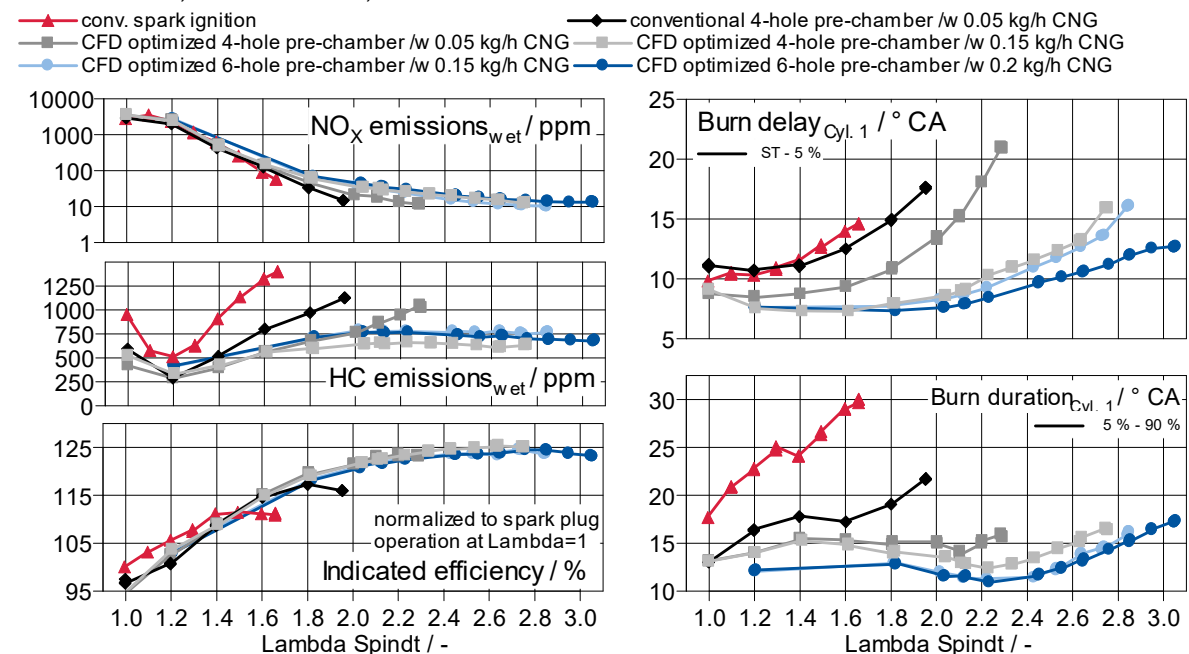
Increasing the fuel injection quantities into the CFD-optimized 4-hole pre-chamber to a mass flow of 0.2 kg/h (~3.3 mg/cycle), is not giving any benefit with regard to lean burn capability or stability, compared to operation with 0.15 kg/h CNG mass flow.

Further lean burn potential can be exploited with the CFD-optimized 6-hole pre-chamber. With the higher turbulent kinetic energy level at the spark plug (see figure 8), a better tolerance at high CNG mass flow is achieved. While the 6-hole pre-chamber achieves similar burn delay and lean burn capability as the 4-hole pre-chamber with a CNG mass flow of 0.15 kg/h, it provides a slightly reduced burn duration due to the increased ignited volume of the 6-hole pre-chamber, compared to 4-hole pre-chamber. The burn duration is almost the same, even if the pre-chamber is supplied with 0.2 kg/h. However, at higher relative air-fuel-ratios, the burn delay is reduced.

Considering high efficiency and low engine out emissions as a target for such an engine application, the recommended operating range should be set between relative air-fuel-ratios of 2.3 and 2.8. Within this range, the hydrocarbon (HC) emissions as well as the nitrogen oxide (NOx) emissions are on a constant low level. Whereas the HC-Emissions with 750 ppm are clearly below the HC emission of the spark plug operated engine at stoichiometric conditions, the NOx emissions are in a range of only 25 – 10 ppm.

The engine was knock limited with spark plug and pre-chamber ignition system at stoichiometric conditions, but also in lean conditions up to Lambda 2.2. Thus, the efficiency is drastically increased towards lean conditions. However, also beyond Lambda 2.2, the overall efficiency still raises slightly so that the sweet point is reached at a relative air fuel ratio of 2.5 for the 4-hole pre-chamber and at a relative air fuel ratio of 2.7 for the 6-hole pre-chamber. As the efficiency drop would be rather small, if the engine is not operated exactly at the sweet spot, the named range for operation seems to be reasonable.

Figure 11 shows ignition and burn stability for the variations discussed. The CFD-optimized 4-hole pre-chamber offers a good stability with comparable low CNG mass flow of 0.05 kg/h, until reaching a relative air-fuel-ratio of 2. With the 6-hole pre-chamber, at 0.2 kg/h CNG mass flow the standard deviation for MFB05, MFB50 and MFB90 can be kept on a very low level even for a relative air-fuel-ratio of 3. With regard to ignition and combustion stability, the pre-chamber ignition system provides a wide operating range.

Lambda-Sweep
IMEP = 15 bar; n = 2000 1/min; CR13.0
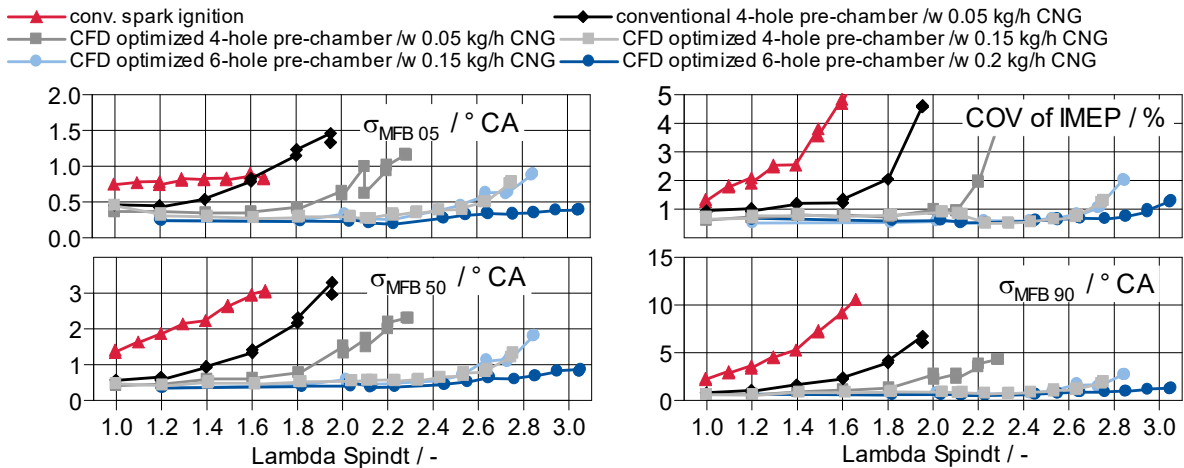
Figure 11: Ignition and burn stability for different configurations at 2000 1/min, 15 bar (IMEP))

To also cover higher power demands, the ultra-lean combustion should be capable of higher engine speeds and loads. Therefore, the operation point n = 4000 1/min and IMEP = 16 bar was investigated. Usually, combustion of highly diluted mixture becomes more critical at higher speeds, as the spark advance demand increases with the engine speed.

As shown in figure 12, the lean burn capability can be increased significantly by the application of a pre-chamber ignition system. In comparison to the conventional spark plug operated engine, the lean burn limit can be shifted from a relative air fuel ratio of 1.6 to 2.3 or 2.4 with a CNG mass flow of 0.2 kg/h (~1.67 mg/cycle). Following the same trend as for the 2000 1/min / IMEP = 15 bar operation point, the burn duration is shortest for the 6-hole pre-chamber. But also with the 4-hole versions, the burn duration can significantly be reduced, compared to the spark plug mode. The burn delay is, like for lower speeds, mainly defined by the amount of fuel with is injected into the pre-chamber.

Between a relative air-fuel-ratio of 2.0 and 2.4, an almost constant engine efficiency and constant HC emission concentration can be realized. Also the NOx emissions are on a low level between 60 and 25 ppm. Of course, higher relative air-fuel-ratios yield in a higher (emission) mass flow.

Lambda-Sweep
IMEP = 16 bar; n = 4000 1/min; CR13.0
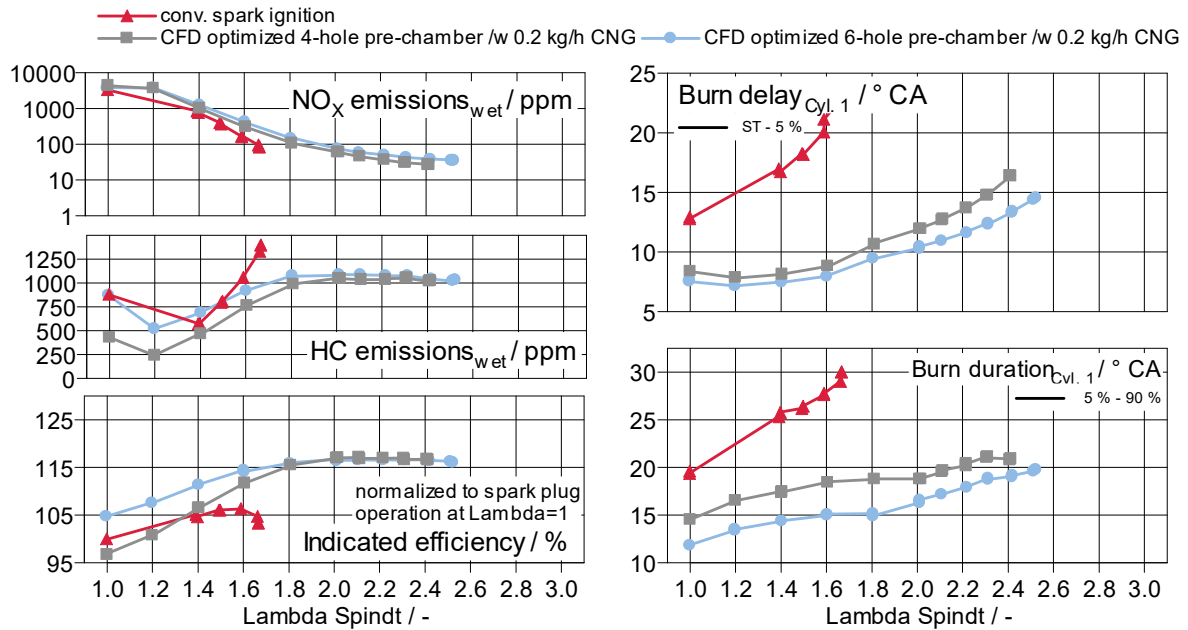
Figure 12: Emissions, efficiency, burn delay and duration for different configurations at 4000 1/min, 16 bar (IMEP)

4.2   The influence of different pre-chamber fuels

The results discussed so far have been created with CNG fuel supply for the pre-chamber ignition system. However, CNG might not always be the first choice for the pre-chamber fuel supply, as it requires a second fuel tank and a specific gas injection system in the vehicle.

From a fuel supply infrastructural point of view, direct injection of gasoline into the pre-chamber is the most obvious solution. This however involves some challenges, too: The spray target, the linked mixture formation as well as the dosing of the very small amount of liquid fuel into the pre-chamber provide very unusual boundary conditions for the layout of a direct fuel injection system.

To round off the picture, the injection of hydrogen has also been investigated. The results are shown in comparison to CNG and liquid gasoline injection in figure 13.

Compared to CNG, hydrogen and gasoline have a shorter burn duration in the pre-chamber. Thus, a higher pressure difference between pre-chamber and main combustion chamber is created. While the burn delay in lean operation conditions is noticeably affected by this fact, the burn duration shows no clear trend. The displayed differences are in the range of measurement and operation accuracy.

Overall, the lean burn capability is best, when gasoline is supplied to the pre-chamber system, although a long burn duration results at a relative air-fuel-ratio of 2.6. A stoichiometric operation of this pre-chamber is not possible with 0.075 kg/h gasoline fuel mass flow. For these operation points, even a passive operation of the pre-chamber is an alternative, as the pre-chamber fuel is not really required for the ignition and consequentially reduces engine efficiency.

Lambda-Sweep
IMEP = 12 bar; n = 2000; 1/min CR13.0; CFD optimized 4-hole pre-chamber
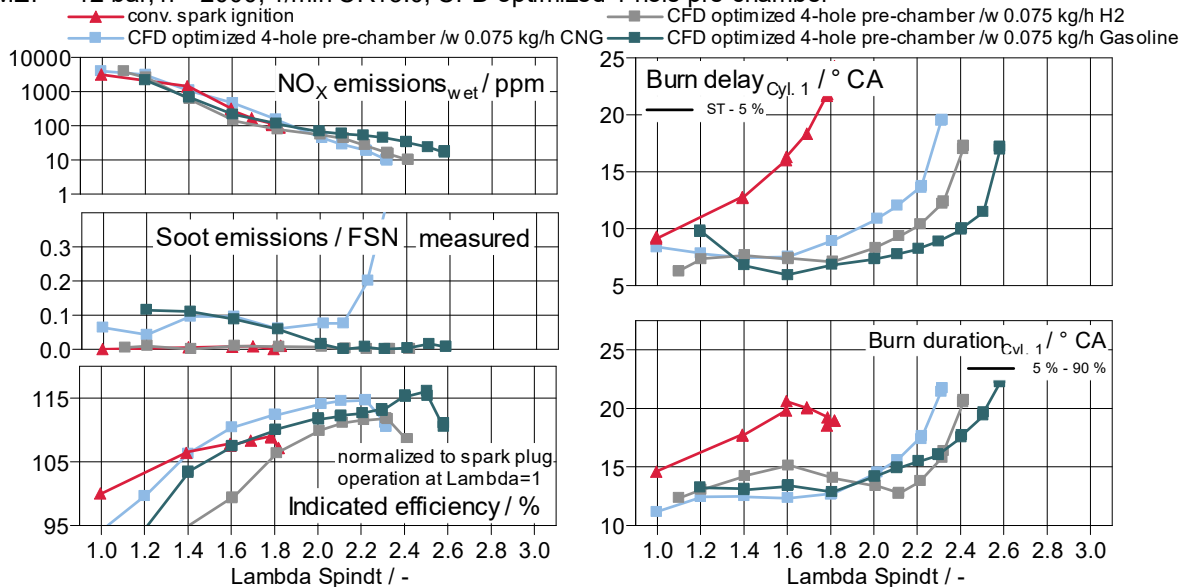
Figure 13: Emissions, efficiency, burn delay and duration for different pre-chamber fuels at 2000 1/min, 12 bar (IMEP)

Although the operation with hydrogen indicates similar advantages with regard to burn delay and burn duration, the overall efficiency is significantly lower. This is related to the higher calorific value of hydrogen. As most of the pre-chamber fuel energy is used for ignition of the mixture in the main chamber, and only a small share is contributing to the work performed onto the piston, the engine has a higher efficiency, when the same burn delay and burn duration are achieved at the same relative air fuel ratio with less energy consumed in the pre-chamber.

Nevertheless, the use of hydrogen has strong advantages with regard to particulate emissions. While CNG and gasoline fuel supply to the pre-chamber result in local areas with rich air fuel ratios, where some particulate emissions are being created, hydrogen supplied pre-chamber operation creates very low particulate emissions over the entire relative air-fuel-ratio range.

With gasoline fueling into the pre-chamber, the particulate emissions are significantly reduced for highly diluted mixtures, indicating that higher pressure and the highly diluted mixture are supporting mixture formation in the pre-chamber in leaner conditions.

5   Conclusion

Based on the objective of demonstrating a high efficiency and low emission ultra-lean burn engine for use in electrified powertrains, a suitable pre-chamber space ignition system with the associated cylinder head environment have been developed and investigated experimentally on a single cylinder engine test bench. Standard CAE-tools, which were used for the development, were adapted and expanded with regard to the specific requirements of the pre-chamber configuration.

It could be shown that smart use of CFD-tools allowed pre-optimization towards a high maturity level. It turned out that the jet hole configuration is of crucial significance. With the optimized configuration, a large air/fuel-ratio window of stable combustion can be realized, providing excellent pre-conditions for calibration. The fuel introduced into the

pre-chamber (CNG, gasoline or hydrogen) has only a relative small influence on the overall operating behavior.

6   Outlook

The resulting engine lean burn process, with its drastically improved lean burn capability and low raw emissions, provides excellent preconditions for further improving the efficiency of electrified powertrains. **Next steps should focus on:**

- Further insight into the extreme lean combustion process
- Assessment of the emission behavior towards adapted requirements for the exhaust aftertreatment system
- Further definition of an ultra-lean combustion system for automotive application

Acknowledgement

References

[1]   P. Luszcz, K. Takeuchi, P. Pfeilmaier, M. Gerhardt, P. Adomeit, A. Brunn, C. Kupiek, B. Franzke: "Homogeneous Lean Burn Engine Combustion System Development Concept Study"; 18th Stuttgart International Symposium, 13-14th March 2018

[2]   R. Böwing: "Der Einfluß von Zündung und Zylinderinnenströmung auf die Verbrennung in Ottomotoren mit hoher Ladungsverdünnung, Dissertation RWTH Aachen 2000

[3]   M. Bunce, H. Blaxill: "Sub-200 g/kWh BSFC on a Light Duty Gasoline Engine", SAE Technical Paper 2016-01-0709, 2016, doi:10.4271/2016-01-0709

[4]   M. Sens, E. Binder, P.-B. Reinicke, M. Rieß, T. Stappenbeck, M. Woebke: „Die Vorkammerzündung und vielversprechende Komplementär-Technologien" – 27. Aachener Kolloquium 2018

[5]   M. Schumacher, M. Wensing: "A Gasoline Fuelled Pre-Chamber Ignition System for homogenous Lean Combustion Processes", SAE Technical Paper 2016-01-2176, 2016, doi:10.4271/2016-01-2176

[6]   G. Lumsden, H.C. Watson : "Optimum Control of an S.I. Engine with a $\lambda=5$ Capability", SAE Technical Paper 950689, 1995, doi:10.4271/950689

[7]   R. Spindt, "Air-Fuel Ratios from Exhaust Gas Analysis," SAE Technical Paper 650507, 1965, https://doi.org/10.4271/650507

[8]   D. Bresenham, J. Reisel, and K. Neusen, "Spindt Air-Fuel Ratio Method Generalization for Oxygenated Fuels," SAE Technical Paper 982054, 1998, https://doi.org/10.4271/982054

6.2 Study of Gasoline Pre-chamber combustion at Lean Operation

Noritaka Kimura, Hiroki Kobayashi, Naohiro Ishikawa

Abstract

Regulations and other demands to enhance automobile fuel economy are growing increasingly strict to reduce CO_2 as a measure to address the issues of global warming. The goal of this study was to enhance the fuel economy in high-load operation of a gasoline engine for hybrid vehicles, which is a useful means of addressing this issue. Technology for achieving lean combustion in high-load operation was studied to realize higher brake thermal efficiency by increasing the ratio of specific heat compared to theoretical air-fuel ratio (stoichiometric) EGR combustion. Issues for applying lean combustion to high-load operation include 1) the increased oxygen molarity results in increased knocking tendency compared to stoichiometric EGR combustion, and 2) increased leanness results in greater combustion variation due to the ignition delay period and the delayed second half of the combustion period. In order to solve these issues at lean operation, several combustion methods are examined on test bench. In this test study, Pre-chamber stratified combustion has an advantage of lean operation performance. Ignitability and high-speed combustion period of pre-chamber combustion was secured by setting the ignition areas inside the pre-chamber to the rich side relative to the total air-fuel ratio (A/F). NOx emissions are an issue for stratified combustion, but NOx emissions can be reduced by setting the pre-chamber A/F to approximately 23 and by making the pre-chamber volume sufficiently small compared to the main combustion chamber volume. Tests were performed using a single-cylinder engine to determine the pre-chamber volume and the diameter and number of jet nozzles. The pre-chamber volume and the diameter and number of jet nozzles were set under the restriction of $dP/d\theta$, which is the index of combustion noise, as the target value or less. This specification realized minimum advance for the best torque (MBT) operation with an A/F of 35 at 2000 rpm, IMEP 810 kPa. The heat release characteristics of pre-chamber combustion shows that unlike the typical combustion pattern using strong flow, the heat release characteristics have two peaks. The first peak is the flame state wherein the jet flame has spread throughout the entire combustion chamber. This shows that the amount of heat released inside the pre-chamber enabled the flame jets from the jet nozzles to spread within the main combustion chamber. The second peak is the state wherein the unburned gas around the spread jet flames is all burning instantaneously. This combustion state results in rapid and stable combustion during the second half of combustion. This combustion characteristic realized MBT lean combustion in high-load operation. The balance between the compression ratio and the surface volume ratio (S/V) was reviewed to counter the drop in efficiency due to the increased S/V as a result of adding a pre-chamber, and this enabled MBT operation at 2000 rpm, IMEP 870 kPa, A/F 35 with an IMEP variation rate of 1.2 %, a main combustion period of 18 deg, and NOx of 30 ppm. Together with the effects of heat insulation coating inside the pre-chamber, this enhanced the brake thermal efficiency by +2 point compared to stoichiometric EGR combustion.

1   Introduction

Action to reduce emissions of CO_2, thought to be a cause of climate change, has been advancing in recent years. While the electrification of vehicles is advancing, hybrid vehicles, using a combination of internal combustion engine and electric motors, are expected to be the mainstream for the time being. For the internal combustion engine of a hybrid vehicle to make the most of an operating condition of good thermal efficiency, ongoing effort is necessary to broaden that range and further raise thermal efficiency within it.

2   Target of This Research

In raising efficiency at the most efficient point for a hybrid vehicle engine, Tagishi et al. [1] have raised brake thermal efficiency to the equivalent of 45% in a Miller Cycle gasoline engine using cooled EGR combustion at the theoretical air-fuel ratio (stoichiometric) and stroke/bore ratio (S/B) of 1.5, with late inlet valve close timing (IVC). The specifications of this engine are shown in Table 1 as ENG_A. Working towards 50% brake thermal efficiency as the next step, the targets are set to raise thermal efficiency three points, through waste heat recovery and heat loss reduction technology, and achieving the remaining two points by increasing the ratio of specific heat. This research studied the lean combustion as a means of raising theoretical thermal efficiency compared to stoichiometric EGR, through improved ratio of specific heat. For target air-fuel ratio (A/F), Fig. 1 shows the resulting change in brake thermal efficiency calculated for EGR combustion and lean operating conditions, using a 1D simulation of a case with minimum advance for best torque (MBT) and main combustion period (MFB 10-90%) fixed at 25 deg. It was stipulated that at least A/F 28 was necessary to attain the 2 points of thermal efficiency.
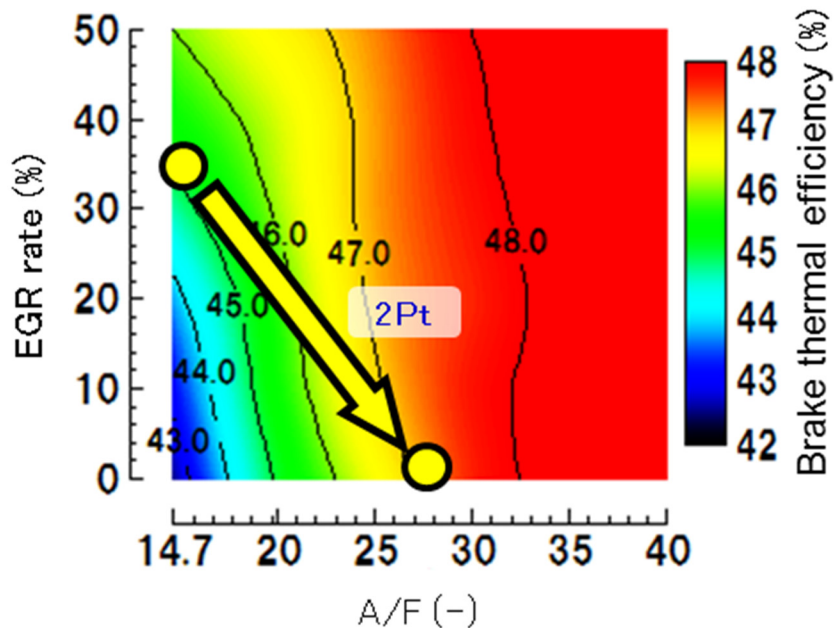
Figure 1: Brake thermal efficiency on EGR combustion and lean combustion using 1-D simulation

The test engine under assessment was the ENG_B single cylinder engine shown in Table 1. This engine was intended to replace future hybrid engines, and had S/B of 1.5, based on the research results from Tagishi et al.

Table 1: Test engine specifications of pre-chamber combustion

	ENG_A	ENG_B
Bore (mm)	81	73
Stroke (mm)	121.6	109.5
Stroke Bore ratio	1.5	
Displacement (cm^3)	627	458
Compression ratio	17	
Effective compression ratio	12.5	
Intake port	Tumble port	Filling port
Tumble ratio	1.8	0.4
Main fuel supply	DI	PI / DI
Ignition energy (mJ)	450	60
Air supply	Super charged	

3   Issue of Lean Combustion under High Load

3.1   Knocking Performance

The ignition timing at knocking event was retarded at the same dilution rate by changing the dilution gas from EGR to air. Figure 2 shows the MFB 50% crank angle against dilution rate by EGR and air at 2,000 rpm and IMEP of 810 kPa. With dilution with air at the same 35% as EGR dilution, the knocking ignition timing was retarded by at least 12 deg from MBT. Therefore, the thermal efficiency declined, despite of the increased ratio of specific heat due to air dilution. That appears to be due to promotion of the oxidation reaction due to elevation of the oxygen mole fraction, caused by replacement of EGR by air as the dilution gas [2]. To raise thermal efficiency in lean combustion under high load, it is necessary to achieve reduction of knocking tendency on a par with EGR combustion.
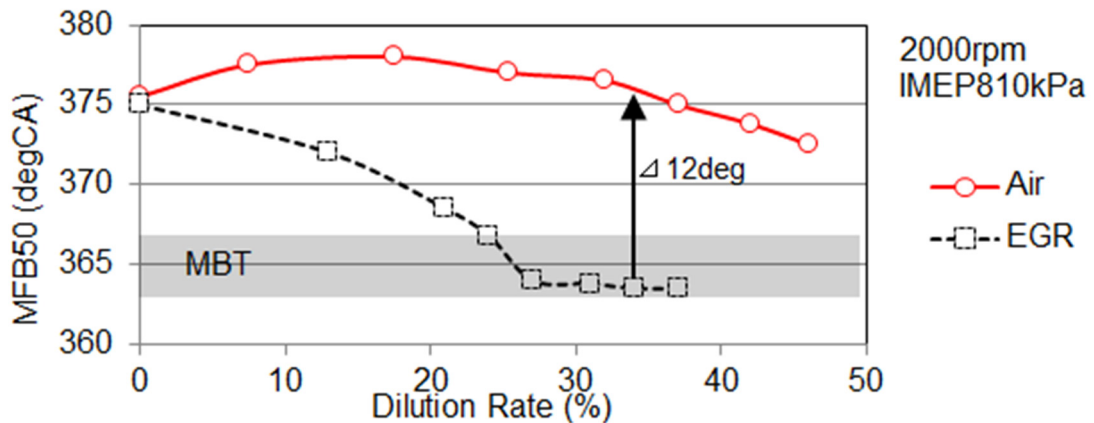
Figure 2: Effect of dilution rate to MFB 50% characteristics

3.2   Lean Limit Performance

Figure 3 shows the lean limit characteristics and combustion period at IMEP 600 kPa, which allows MBT operation. Operation at above A/F 30 is not possible under the combination of in-cylinder flow and high energy ignition that attained EGR 35%. That appears to be the case because of greater combustion variation due to the ignition delay period (IG-MFB2%), and the delayed second half of the combustion period (MFB50-90%). Ignition delay and second half combustion period should be shortened in order to extend the lean limit A/F.
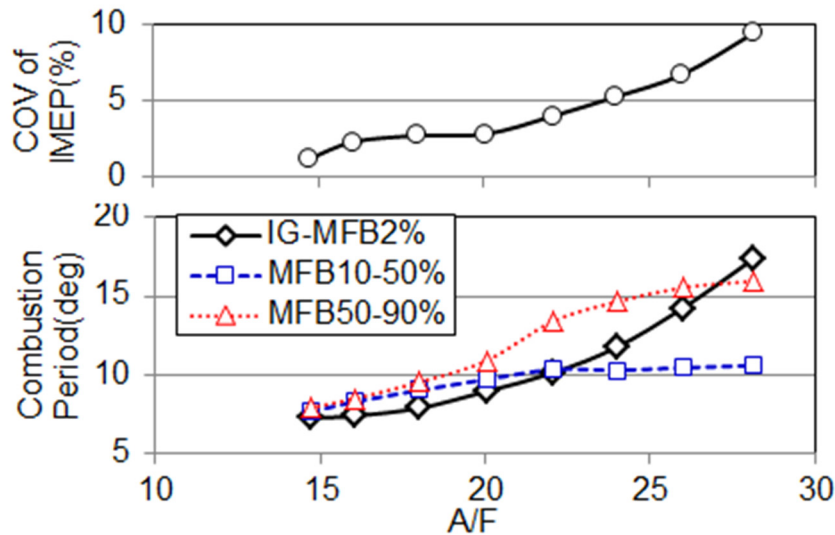
Figure 3: Combustion characteristics

4   Combustion Concept

4.1   Pre-Chamber Combustion Concept

Pre-chamber combustion, which is one of the stratified charge combustion, was researched as a solution for the above issue. Figure 4 shows the engine configuration for pre-chamber combustion. A pre-chamber is provided in the center of the combustion chamber and equipped with a spark plug, and with dedicated direct injection (DI), in order to set A/F in the pre-chamber richer than main combustion chamber A/F. Furthermore, a port injector (PI) supplies a lean fuel-air mixture. In the second half of the compression stroke, part of the lean fuel-air mixture in the main combustion chamber side flows into the pre-chamber, so that the A/F at ignition is determined by the mixture of that flow with the fuel-air mixture generated in the pre-chamber by injection within it. Figure 5 shows the combustion mode, as calculated by CFD. Ignition causes combustion inside the pre-chamber, and pressure inside the pre-chamber rises (Fig. 5①). The pressure differential between the pre-chamber and the main combustion chamber causes jet flame to spread into the main combustion chamber (Fig. 5②) and burn the lean fuel-air mixture in the main combustion chamber (Fig. 5③).
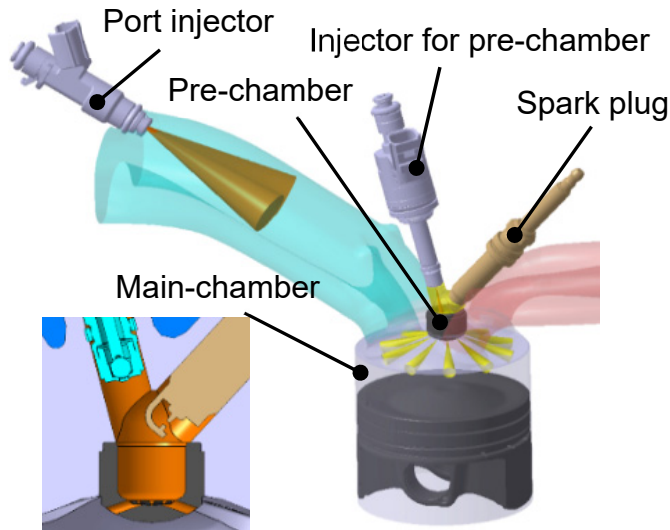
Figure 4: Engine configuration of pre-chamber combustion
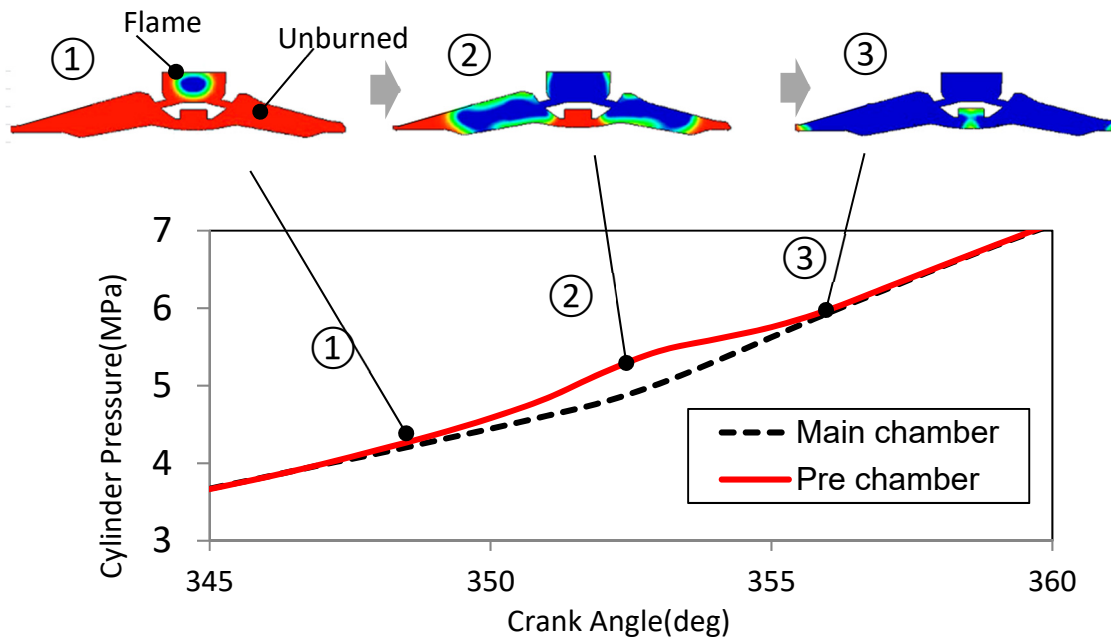
Figure 5: Pre-chamber combustion process at 2000rpm IMEP810kPa

4.2   Stratified Combustion Issues and Responses

NOx emission, an issue of stratified combustion, was approached as described below. Figure 6 shows the trend of NOx emission against A/F. This indicates that the highest value of NOx occurs close to A/F 17, and that almost no emission generate at A/F 27 or above. In stratified combustion using DI in a conventional SI engine, the setting is close to the stoichiometric level [3], out of consideration of factors such as cycle variation of A/F around the spark plug, so highly localized NOx emission from that area has been an issue. For pre-chamber combustion, the NOx target is set at 50 ppm or less

on the assumption of the use of an after treatment system for lean combustion [4] under efficiency point load. The A/F target is set in the pre-chamber close to 23, and set in the main combustion chamber at 36 or more. The reduction in NOx emission achieved was examined by keeping the pre-chamber volume 5-10% relative to the main combustion chamber. Figure 7 shows the calculated values of NOx emission for each pre-chamber volume against pre-chamber internal A/F. It was considered possible to reduce NOx emission to 50 ppm or less by using an appropriate pre-chamber volume and setting 23 as the pre-chamber internal A/F.
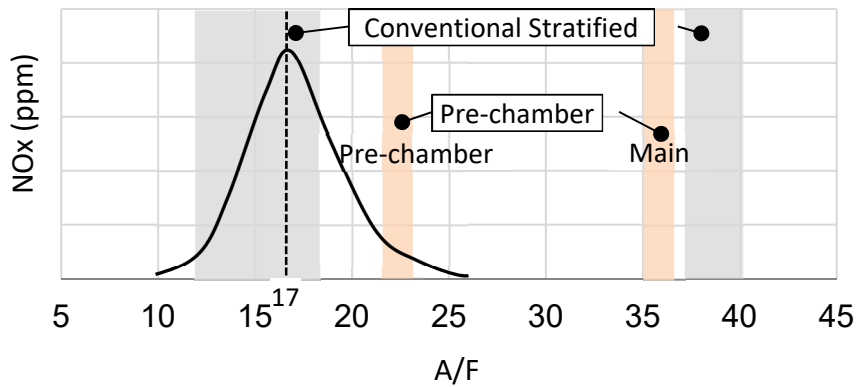
Figure 6: Stratified concept of Pre-chamber combustion
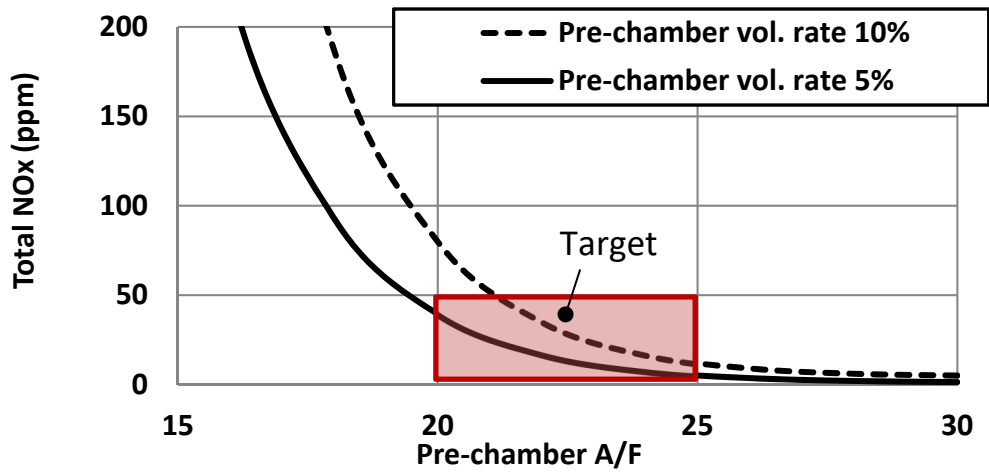
Figure 7: Relation of pre-chamber A/F, Vol and NOx

4.3   Setting Pre-chamber Specifications

The pre-chamber specifications have a major impact on main-chamber combustion. Figure 8 shows the main design parameters for the pre-chamber. The sensitivity of pre-chamber volume, number of pre-chamber nozzles, nozzle diameter, and nozzle cross-sectional area calculated from nozzle diameter and number of nozzles were confirmed. The direction of the jet was set to a direction that avoids heat losses to the combustion chamber wall and piston surface.
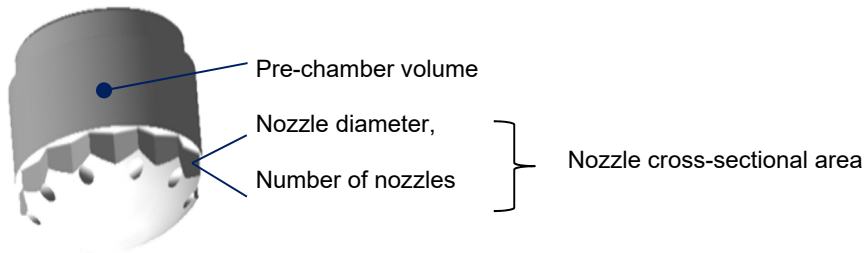
Figure 8: Design parameters of pre-chamber

Figure 9 shows NOx emission against pre-chamber volume, dP/dθ, which is an index of combustion noise, and the characteristics of main combustion period and thermal efficiency, under operating conditions of 2,000 rpm engine speed and IMEP 810 kPa, and A/F 35. A maximum was set for dP/dθ, which is an indicator of combustion noise, from the characteristic of shorter combustion period in the pre-chamber. The smaller the pre-chamber volume, the more the NOx emission and dP/dθ can be reduced, but there is a tendency for the combustion period of MFB 10-90% to increase. Results found no loss of thermal efficiency with pre-chamber volume up to 2.0 cm^3, but reduced thermal efficiency with further volume reduction. That appears to be the case because as pre-chamber volume is reduced, the proportion of rich fuel-air mixture is also reduced, which reduces NOx. At the same time, the amount of thermal energy provided from the pre-chamber to the main chamber is reduced because there is less mixture in the pre-chamber, which appears to reduce dP/dθ and increase combustion period. The change in thermal efficiency appears to be a reduction because, under A/F 35 operating conditions, the thermal energy supplied from the pre-chamber to the main chamber cannot maintain combustion stability. From the above performance results, the pre-chamber volume was set at 2.0 cm^3, which minimizes NOx emission and dP/dθ without reducing thermal efficiency.
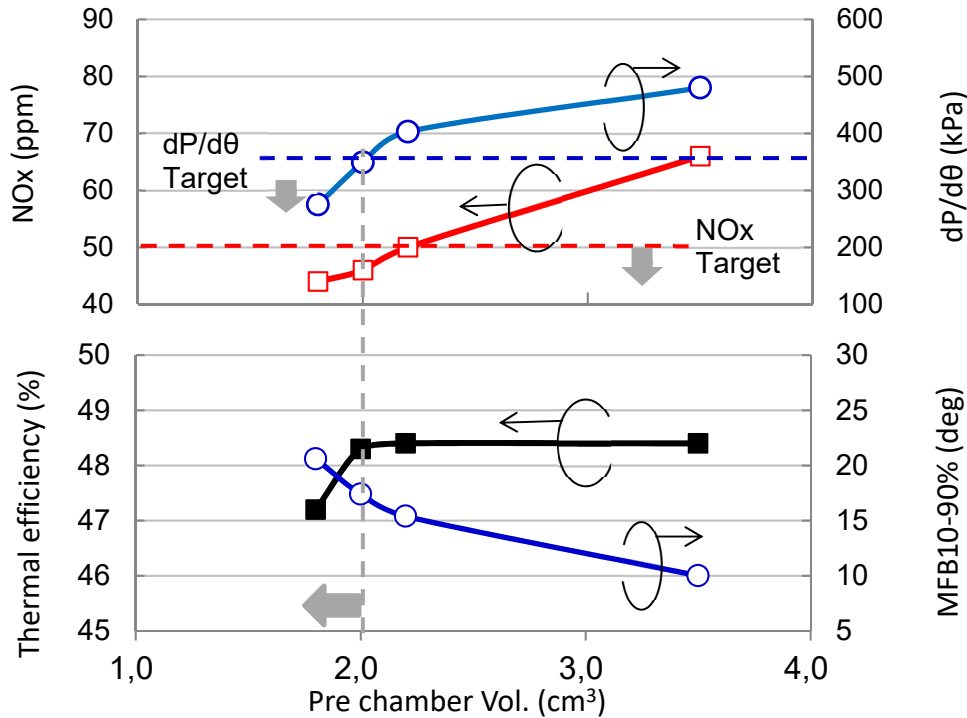
Figure 9: Comparison of pre-chamber volume on NOx and thermal efficiency

Figure 10 shows performance characteristics with variation of total cross-sectional area of pre-chamber nozzles with pre-chamber volume of 2.0 cm^3 and under operating conditions of 2,000 rpm engine speed, IMEP 810 kPa, and A/F 35. The smaller the total cross-sectional area of pre-chamber nozzles, the more NOx emission can be reduced, but dP/dθ rises. The combustion period of MFB 10-90% reduces as total cross-sectional area of pre-chamber nozzles is reduced, but thermal efficiency peaks when total cross-sectional area of pre-chamber nozzles is 20 mm^2, declining when the area is smaller or larger. That means that the smaller the total cross-sectional area of pre-chamber nozzles, the higher the pressure increase in the pre-chamber, and the higher the thermal energy supplied to the main chamber, so that combustion stability can be obtained. Therefore, it becomes possible to retard the MBT ignition timing while obtaining equal combustion stability, so that peak in-cylinder temperature is lower and NOx emission can be reduced. It appears that the change in thermal efficiency is a reduction because when total cross-sectional area of pre-chamber nozzles is above 20 mm^2, the rise in pre-chamber pressure is lower, so less thermal energy is supplied from the pre-chamber to the main chamber. Therefore, it becomes impossible to maintain combustion stability under A/F 35 operating conditions, and thermal efficiency declines. If the total cross-sectional area of pre-chamber nozzles is reduced, on the other hand, pressure in the pre-chamber rises, and thermal energy supplied to the main chamber is increased, but there is increased heat loss in the pre-chamber itself, and thermal efficiency declines. Here, we set optimal total cross section area was set as 20 mm^2, at which dP/dθ is at or below the target value and thermal efficiency is maximized. The specific design values were set at 10 pre-chamber nozzles and Φ1.6 mm as the pre-chamber nozzle diameter.
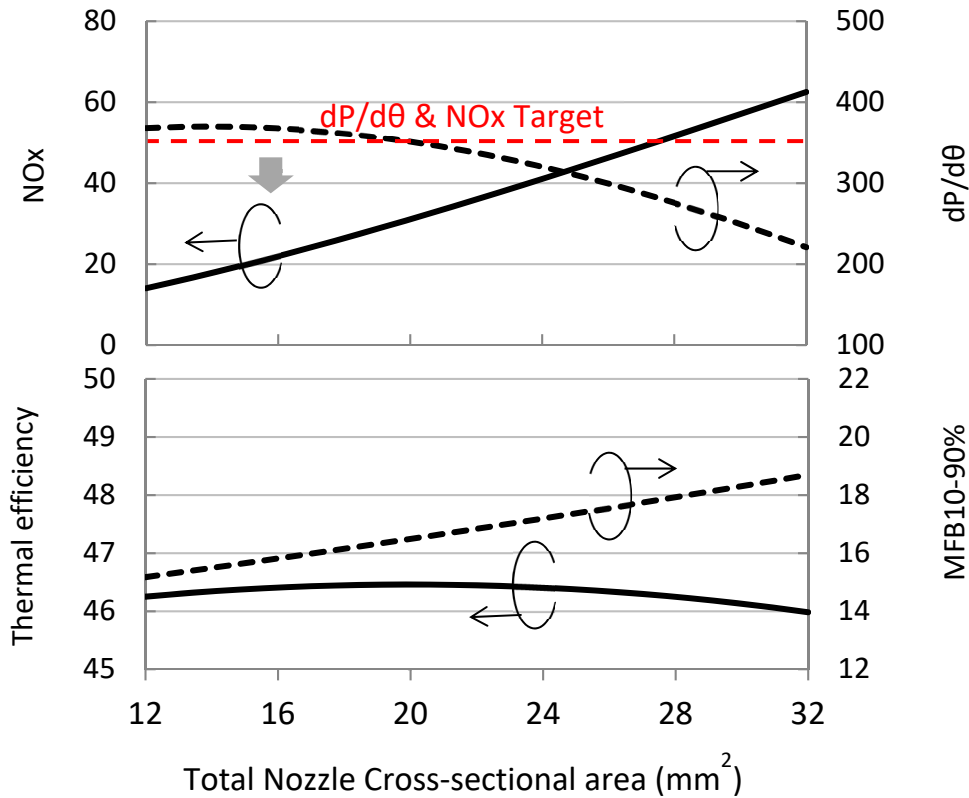
Figure 10: Comparison of total nozzle cross-sectional area on NOx and thermal efficiency

Figure 11 shows performance after optimized setting of the pre-chamber. It presents various performance results against A/F under high load operating conditions of 2,000 rpm engine speed and IMEP 810 kPa. Combustion stability was attained at COV of IMEP3% or less up to A/F 38. It was also confirmed that under conditions of A/F 30 or higher, the MFB 50% crank angle, which indicates knocking level, achieved MBT operation, producing a major reduction in knocking compared to homogeneous lean operation.
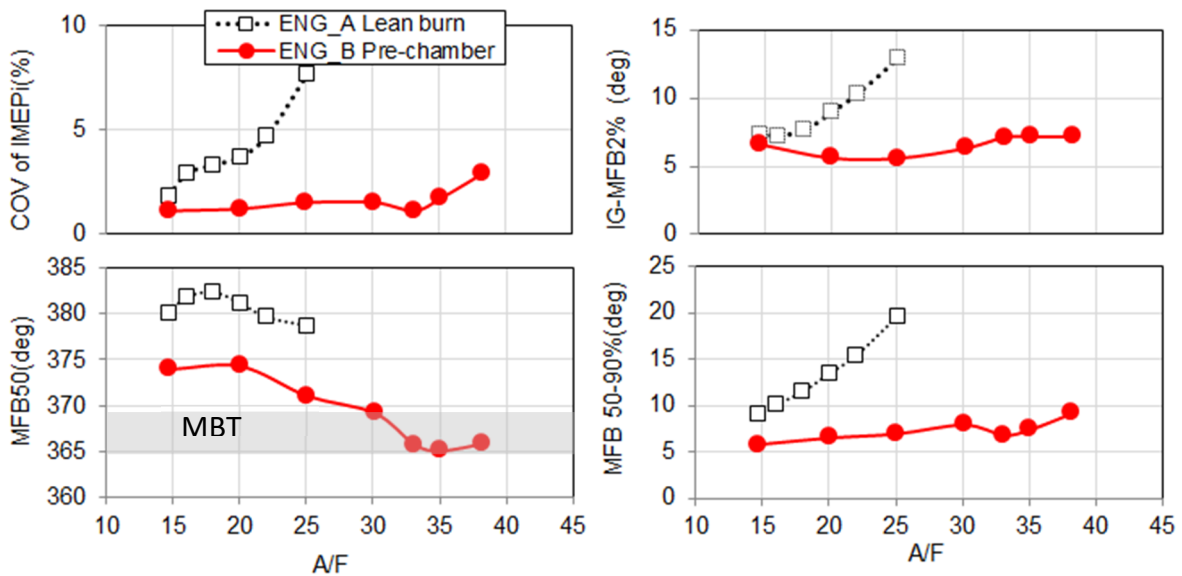
Figure 11: Lean characteristics of pre-chamber combustion

Figure 12 shows the mass fraction of burned fuel (MFB) at EGR35% for ENG_A with A/F 35 combustion by pre-chamber combustion at ENG_B, and the non-dimensional value ndQ/dθ of dQ/dθ at the gross calorific value. Pre-chamber combustions, and particularly second-half combustion after MFB 50, are rapid, and reference to ndQ/dθ shows a combustion mode with two peaks. Combustion visualization was used in order to directly observe this phenomenon. Figure 12 also shows a bottom-view flame visualization image. The state of combustion at the first peak in Fig. 12① is the time at which the jet flame from the nozzle has just spread into the combustion chamber. It can be seen that the jet flame decelerates at that time, and then volumetric ignition in the surrounding area causes the heat release in Fig. 12②. The characteristics of each combustion phase are as follows:

① The heat generation of the gas in the pre-chamber is thought to cause the jet flame to propagate into the main chamber, and flame is able to spread throughout the combustion chamber, even if the fuel-air mixture in the main combustion chamber is lean. This accelerates the initial combustion.

② The quantities of heat held by each of the multiple propagated jet flames causes instantaneous combustion of unburned areas around each jet flame, accelerating second-half combustion and reducing combustion variation.

To summarize, setting the pre-chamber A/F to around 23 shortens the ignition delay in lean pre-chamber combustion, and heat release inside the pre-chamber causes the jet flames from the nozzles to propagate into the main combustion chamber. After that, the lean fuel-air mixture around each jet flame burns instantaneously, making second-half combustion faster. This produces a stable combustion.
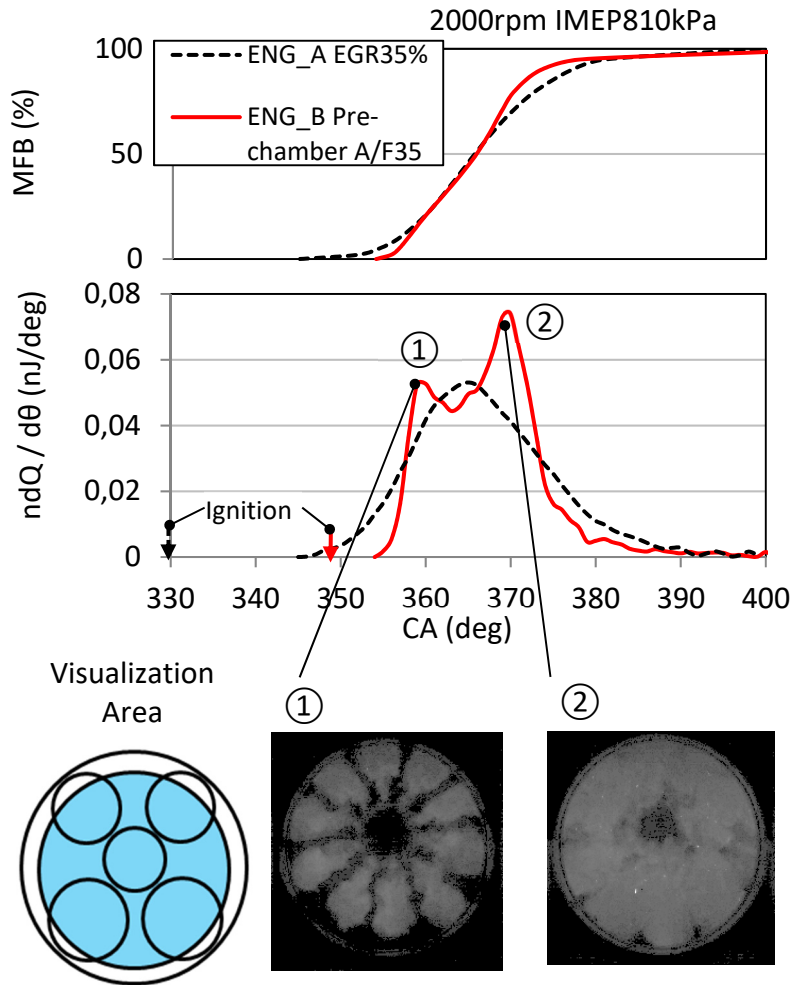
Figure 12: Combustion characteristics and flame visualization of Pre-chamber combustion

4.4   Technologies to Reduce Heat Losses in the Pre-chamber

The surface area to volume ratio (S/V) has a major influence on combustion within the pre-chamber, and the pre-chamber is thought to increase heat losses to the walls, so the reduction of heat losses within the pre-chamber was addressed. In order to reduce heat losses, a coating of insulative material was applied on the inner walls of the pre-chamber, covering the area indicated in red in Figure 13. The proportion of surface area covered was 37%. An insulative material with thermal conductivity of less than 1 W/mK was applied with a thickness of 500um. Thermal conductivity of base pre-chamber material is less 26 W/mK. Figure 14 shows performance results under operating conditions of 2,000 rpm engine speed, IMEP 810 kPa, and A/F 35. The results indicated a reduction of 0.8 points in heat loss, and an improvement of 0.5 points in thermal efficiency.

Coating area
Thermal Conductivity < 1 W/mK
Thickness 500um

Base material
Thermal Conductivity 26 W/mK
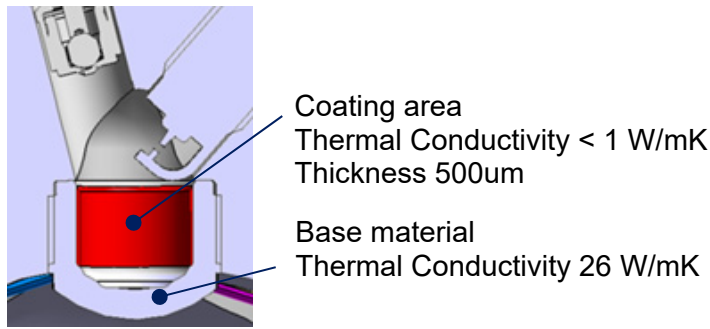
Figure 13: Thermal insulation coating area of pre-chamber
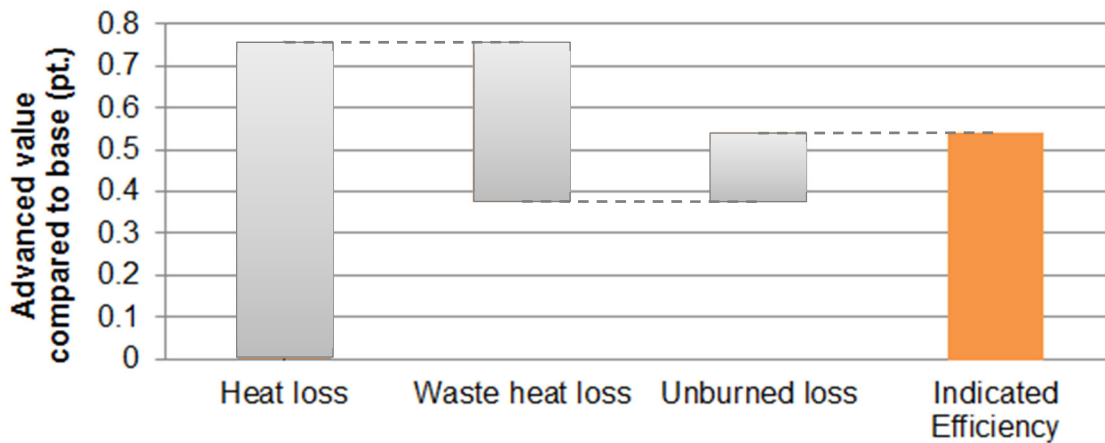
Figure 14: Effects of insulation coating on pre-chamber

4.5   Combustion Chamber S/V Setting

In a pre-chamber combustion engine, the combustion chamber S/V is much higher than in a regular gasoline engine. For a given pre-chamber volume, this impact increases with compression ratio. Therefore, the relationship between compression ratio and combustion chamber S/V was studied. Figure 15 shows the thermal efficiency sensitivity map obtained from comparative tests of compression ratio and S/V. As Step 1 in the diagram, it was confirmed the performance of reducing combustion chamber S/V by lowering the compression ratio, in order to check the influence of combustion chamber S/V. Results obtained indicated that, while lowering compression ratio reduced theoretical thermal efficiency, thermal efficiency was actually improved because of large effects in reducing heat losses and unburned fuel losses. As Step 2 in the diagram, it was shown that thermal efficiency improving by optimizing the shape of the combustion chamber and further reducing combustion chamber S/V. Based on the above results, the compression ratio setting for the pre-chamber combustion engine was reviewed, including the shape of the combustion chamber, and set 16 as the compression ratio.
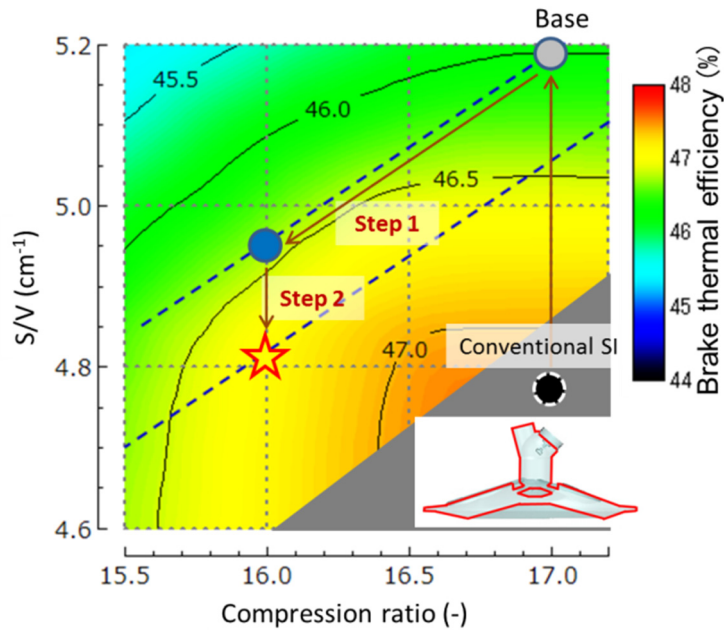
Figure 15: Effects of S/V and compression ratio on brake thermal efficiency of pre-chamber combustion engine

4.6   In-cylinder Flow Setting

The in-cylinder flow setting for the ENG_A which achieved 45% brake thermal efficiency was a high tumble port setting, intended to raise the flame propagation speed. However, in pre-chamber combustion, the combustion mode changes, so it appeared that the required in-cylinder flow setting would also change. Figure 16 shows the results of a comparison of performance between two port specifications with different tumble ratios. The tumble ratio of port A is 0.4, and that of port B is 1.8, and the results are for operating conditions of 2,000 rpm engine speed and IMEP 510 kPa. Results of the performance comparison indicate that the difference in tumble ratio causes no change in combustion period, and that combustion stability was reduced with the port B specification, which has a higher tumble ratio. The reason why there was no change in combustion period appeared to be that, in pre-chamber combustion, the presence of the spark plug in the pre-chamber means that enhanced flow does not promote initial flame kernel growth as it normally does in an spark-ignition engine. Figure 17 shows the results of subsequent analysis of in-cylinder flow by CFD, to analyze the loss of combustion stability. It shows the in-cylinder flow speed distribution at a crank angle of 80 deg before top dead center (BTDC) in the compression stroke, after fuel injection in the pre-chamber and velocity of the gas flow through the nozzle of pre-chamber. It can be seen that there is almost no gas exchange between the main chamber and the pre-chamber at port A, but there is remaining tumble flow at port B, causing gas exchange between the main chamber and the pre-chamber. Fuel which was injected in the compression stroke through a dedicated DI injector within the pre-chamber, in order to retain it within the pre-chamber, flows into the main chamber due to this residual tumble flow, so that the amount of fuel in the pre-chamber at the start of combustion changes for each cycle. As a result, it appears that the thermal energy supplied from the pre-chamber to the main chamber also varies for each cycle, as does combustion in the main chamber, reducing combustion stability. From the above, Port A with the

lower tumble ratio was selected for the Pre-chamber combustion in-cylinder flow specifications.
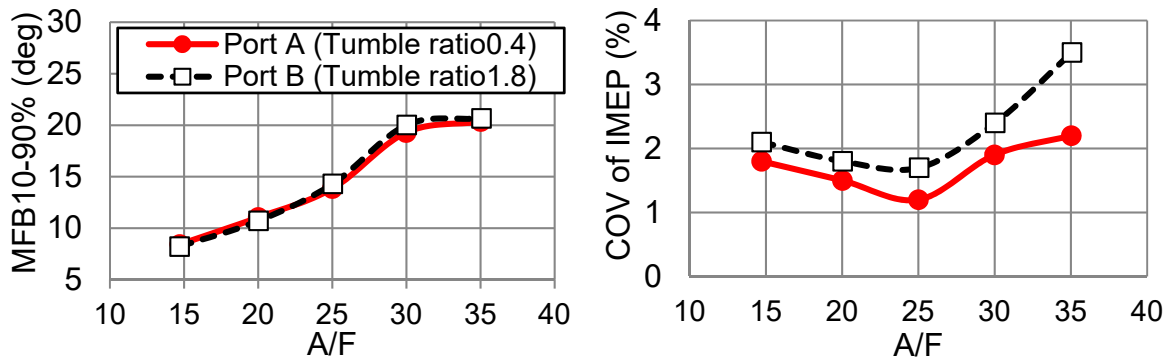
Figure 16: Performance result of Intake ports with different tumble ratios

Port A   Port B
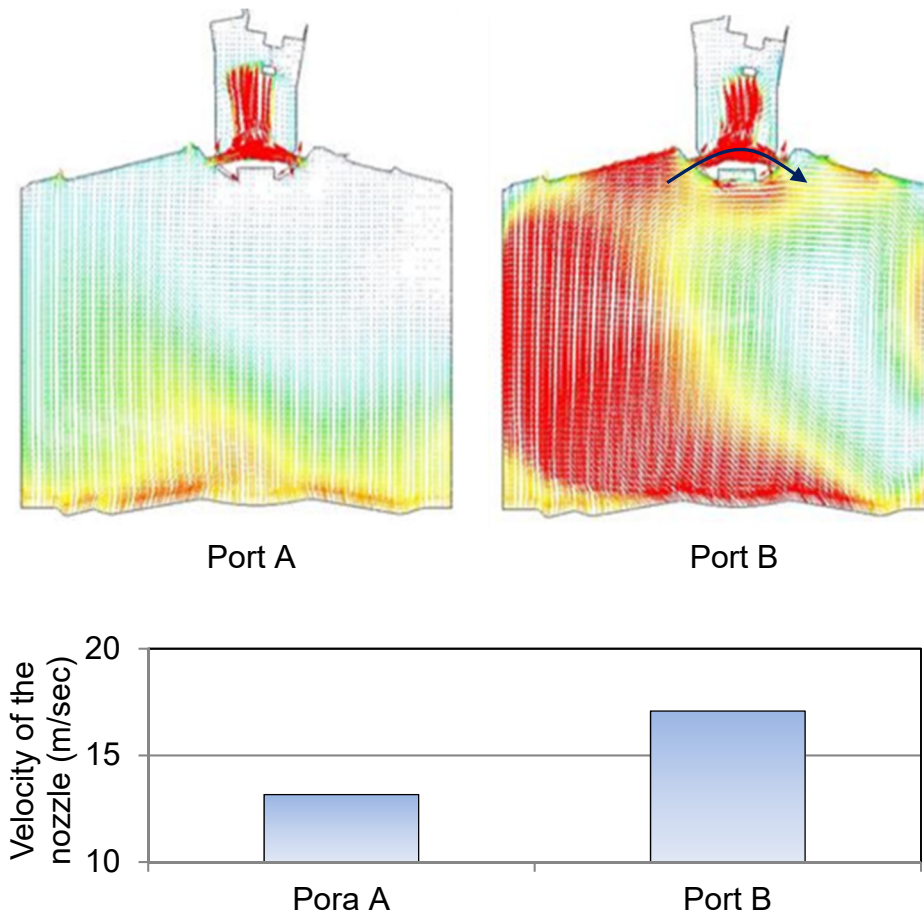
Figure 17: In-cylinder flow by CFD at crank angle 80 degBTDC

5   Results

Confirmation of the final value was attained in a single-cylinder engine which applies to all the pre-chamber combustion engine technologies described above. Table 2 shows the final engine specifications. The calculation of brake thermal efficiency used mechanical friction equivalent to an in-line four-cylinder engine the same as that used in the research which attained 45% brake thermal efficiency, and supercharger losses estimated by 1D simulation.

Table 2: Final test engine specifications

Number of cylinders	1
Displacement volume (cm^3)	458
Bore (mm)	73
Stroke (mm)	109.5
Stroke Bore ratio	1.5
Compression ratio	16
Effective compression ratio	12.5
Pre-chamber volume (cm3)	2
Nozzle diameter (mm)	1.6
Number of nozzles	10
Pre-chamber specification	Thermal insulation coating
Intake port	Filling port
Tumble ratio	0.8
Air supply	Super charged
Fuel supply (main / pre)	PI / DI
Ignition energy (mJ)	60

Figure 18 shows performance results against A/F under high load operating conditions of 2,000 rpm engine speed and IMEP of 870 kPa. Figure 19 shows a breakdown of the brake thermal efficiency improvement compared to ENG_A at EGR35%. Combustion stability attained COV of IMEP3% or less up to A/F 40, and MBT operation was achieved at A/F 35, attaining a 2-point improvement compared to 45% brake thermal efficiency. At the same time, NOx emission of 30 ppm was attained under the A/F 35 conditions at which the brake thermal efficiency improvement was attained.
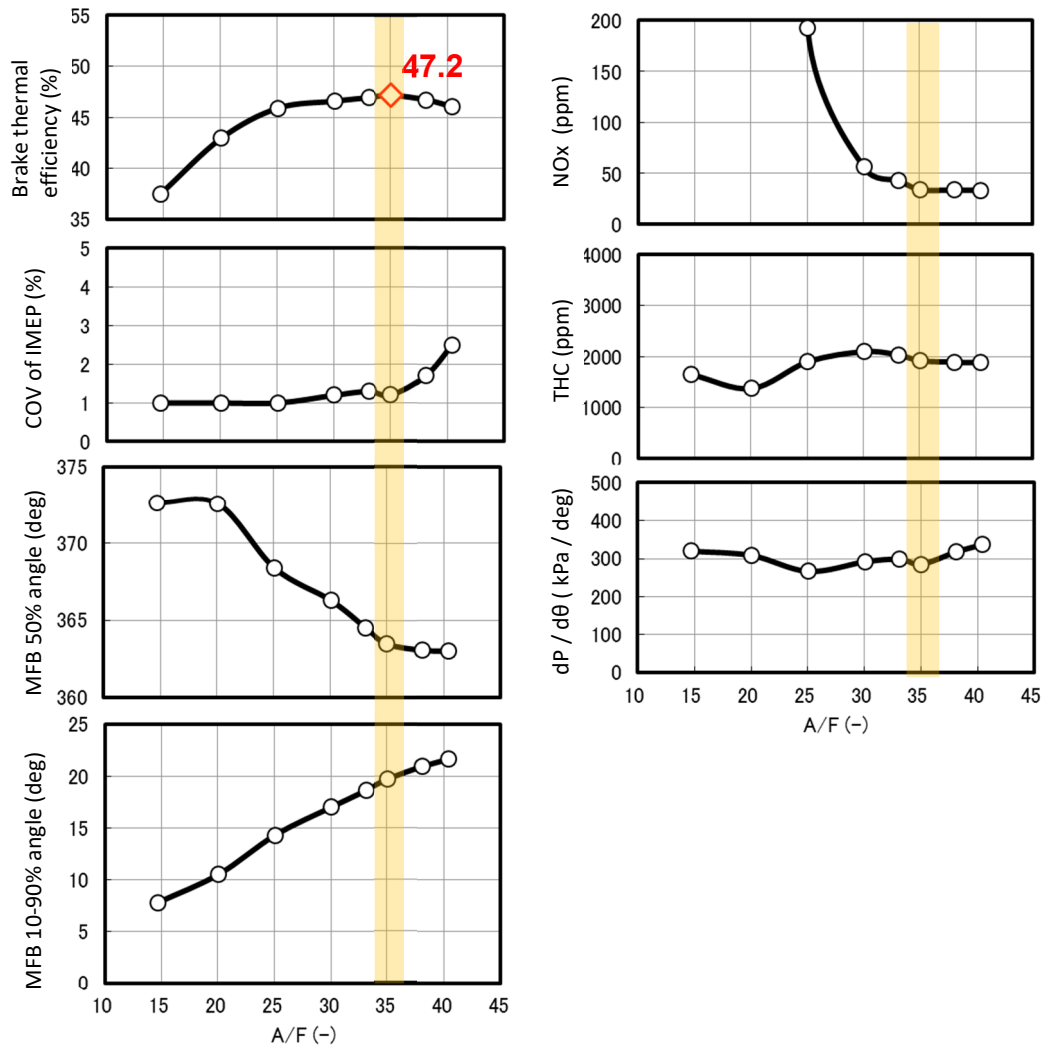
Figure 18: Lean characteristics of high load by test engine specifications
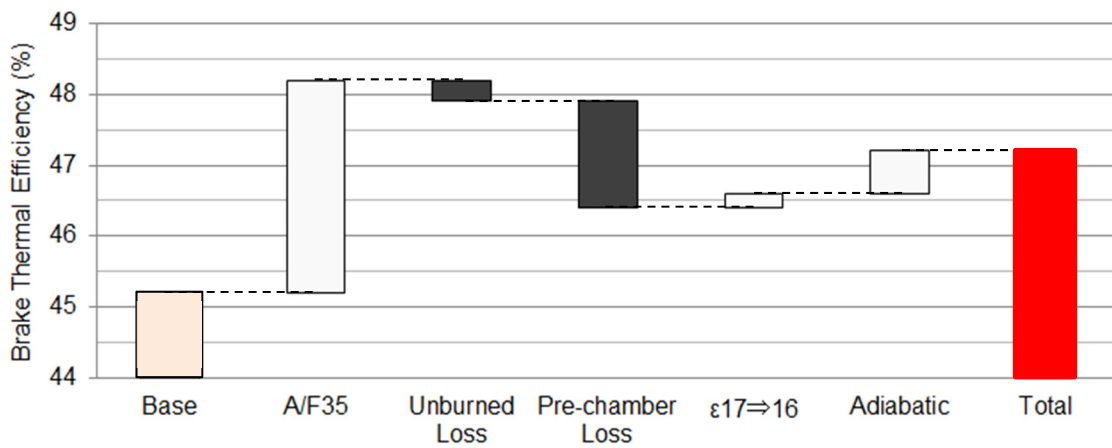
Figure 19: The influence of pre-chamber combustion at engine speed 2,000 rpm IMEP 870 kPa

6   Summary

The research of lean combustion using pre-chamber combustion obtained the following results:

(1) Brake thermal efficiency attained +2 points in comparison to ENG_A, which attained 45% brake thermal efficiency under stoichiometric EGR conditions. NOx under these conditions was below the target value.

(2) In a single-cylinder engine with a mechanical compression ratio of 16, optimization of pre-chamber design and reduction of various losses associated with the addition of a pre-chamber enable stable MBT operation at A/F 35, with 2,000 rpm engine speed and IMEP 870 kPa.

This research was validated on a single-cylinder engine. Hereafter, toward practical applications in a multi-cylinder engine for automobiles applying these achievements, two outstanding topics for future study are development of a supercharger system able to combine partial load with power point operation, and development of catalyst adapted to lean burn combustion.

Literature

[1]   Tagishi, R., Ikeya, K., Takazawa, M., Yamada, K.: In Pursuit of Thermal Efficiency in Gasoline Engines, Proceedings of the Society Of Automotive Engineers Of Japan, No.121-14, (2014)

[2]   Nakata, K., Nogawa, S., Takahashi, D., Yoshihara, Y., Kumagai, A., Suzuki, T.: Engine Technologies for Achieving 45% Thermal Efficiency of S.I. Engine, SAE Technical Paper 2015-01-1896, doi:10. 4271/2015-01-1896, (201)

[3]   Abe, S., Ishikawa, N., Tekeda, N., Akimoto, S., Matsuura, H.: Optimization of Combustion Chamber for Direct Injection Gasoline Engine Employing Center Injection System, Society of Automotive Engineers of Japan, No. 2004-08-0448

[4]   Takeori, H., Wada, K., Matsuo, Y., Morita, T., Konomoto, T., Murata, Y., Kimura, M., Miyauchi, A.: Study of an Aftertreatment System for HLSI Lean-burn Engine, SAE Technical Paper 2018-01-0945, doi:10.4271/2018-01-0945, (2018)

6.3 Pre-chamber Ignition System for Homogeneous Lean Combustion Processes with Active Fuelling by Volatile Fuel Components

Moritz Schumacher, Tim Russwurm, Michael Wensing

Abstract

The combustion of homogeneous lean or diluted mixtures would significantly increase the efficiency of SI engines, but common spark ignitions systems are incapable to ignite these mixtures.

Pre-chamber ignition systems burn a small portion of the charge in a separated chamber, which is connected to the main chamber by multiple small orifices. The combustion in the pre-chamber generates hot gases, which penetrate the main chamber, increase the turbulence and ignite the mixture on multiple sites. This leads to an increased turbulent flame speed and an extended lean and dilution limit, if the mixture in the pre-chamber is kept stoichiometric.

Pre-chamber ignition systems have been investigated since the 1970s for passenger cars and are today commonly used in large gas engines. The adaption of the pre-chamber fuelling system to passenger car engines is not trivial, due to the problematic mixture preparation in the pre-chamber. Injection of a gaseous fuel in the pre-chamber would require a second fuel system with high pressure storage tank. Liquid gasoline direct injection in the pre-chamber is difficult due to the small space available for mixture preparation and the high surface to volume ratio, resulting in insufficient evaporation especially during cold start conditions.

To overcome this problem, we developed a pre-chamber ignition system with active fuelling by volatile fuel components, which facilitates the integration in passenger cars. The system uses a mixture of air saturated with gasoline vapour for the pre-chamber fuelling. This gaseous mixture is typically found in the fuel tank above the liquid level and hence available in passenger cars.

Former publications by the authors already proved the ability to enrich the pre-chamber and stabilize the combustion at homogeneous lean operation. Recent work focused on the optimization of the pre-chamber fuelling system and the pre-chamber geometry. To simulate the fuel tank atmosphere under different environment settings, a system was built, which saturates air with volatile gasoline components. This mixture gets compressed and dosed to the pre-chamber by a solenoid valve. Multiple prototypes of the pre-chamber with different volumes and geometry were investigated in a full engine at characteristic operating points regarding thermal efficiency, combustion process and emissions. These prototypes incorporate a spark plug, fuelling valve, thermocouple and pressure transducer. The results show the ability to ignite homogeneous lean mixtures with $\lambda \approx 2.0$. Optimum operation was achieved with $\lambda = 1.85$ at 4.5 bar IMEP and 1500 rpm. This operating point showed an efficiency gain of 15 % compared to stoichiometric spark plug operation and NO_x emissions below 20 ppm.

The technology enables the usage of actively fuelled pre-chambers in passenger cars. The volatile fuel components for the pre-chamber fuelling are available in the fuel tanks atmosphere and thus allow a single fuel solution with inexpensive components.

Kurzfassung

Homogen magere oder durch Restgas verdünnte Zylinderladungen können die Effizienz von Otto-Motoren signifikant erhöhen. Jedoch sind gewöhnliche Zündsysteme nicht in der Lage, homogen magere Gemische zu entflammen.

Vorkammer-Zündsysteme entflammen eine geringe Ladungsmenge in einer separaten Kammer, die durch mehrere kleine Bohrungen mit dem Hauptbrennraum verbunden ist. Die Verbrennung in der Vorkammer generiert heiße Gase, die in den Brennraum eindringen und dort die Turbolenz erhöhen und die Ladung an mehreren Stellen gleichzeitig entzünden. Damit wird die turbulente Flammengeschwindigkeit erhöht und die Magergrenze erweitert, wenn das Gemisch in der Vorkammer stöchiometrisch bzw. zündfähig bleibt.

Vorkammer-Zündsysteme wurden bereits seit den 1970er Jahren für PKW untersucht und werden heute gewöhnlich in großen Gasmotoren eingesetzt. Die Adaption des Vorkammer-Kraftstoffsystems auf einen PKW ist auf Grund der problematischen Gemischaufbereitung in der Vorkammer komplex. Das Einblasen von gasförmigem Kraftstoff würde ein zweites Kraftstoffsystem mit einem Hochdruck-Gastank benötigen. Flüssige Kraftstoffe direkt in die Vorkammer einzuspritzen ist kritisch, da nur wenig Platz zur Gemischaufbereitung vorhanden ist und durch das hohe Oberflächen- zu Volumen Verhältnis besonders im Kaltstart schlechte Verdampfungsbedingungen vorliegen.

Um dieses Problem zu lösen haben wir ein Vorkammer-Zündsystem mit aktiver Spülung durch leichtsiedende Komponenten des Otto-Kraftstoffes entwickelt, welches die Fahrzeugintegration vereinfacht. Dieses System verwendet ein Gemisch aus Luft und Kraftstoffdämpfen zur Kraftstoffanreicherung der Vorkammer. Dieses Gemisch kann typischerweise in Kraftstofftanks oberhalb des Flüssigkeitsspiegels gefunden werden und ist somit in PKW verfügbar.

Frühere Publikationen der Autoren haben bereits gezeigt, dass die Anreicherung der Vorkammer so erfolgen kann und eine Stabilisierung der Verbrennung bei mageren Betriebspunkten möglich ist. Diese Arbeit konzentriert sich auf die Optimierung des Vorkammer-Kraftstoffsystems und die Verbesserung der Geometrie der Vorkammer. Um die Tankatmosphäre bei verschiedenen Umgebungsbedingungen zu simulieren, wurde ein System zur Anreicherung von Luft mit Kraftstoffdämpfen aufgebaut. Dieses Gemisch wird verdichtet und über ein Magnetventil getaktet der Vorkammer zugeführt. Mehrere Prototypen der Vorkammer mit unterschiedlichen Volumen und Geometrien wurden im Vollmotor bei charakteristischen Betriebspunkten hinsichtlich der thermischen Effizienz, des Verbrennungsprozesses und der Emissionen untersucht. Diese Prototypen enthalten eine Zündkerze, ein Spülungsventil, ein Thermoelement und einen Drucksensor. Die Ergebnisse zeigen die Fähigkeit des Systems Gemische bis $\lambda \approx 2{,}0$ zu entflammen, wobei ein optimaler Betrieb bei $\lambda = 1{,}85$, 4,5 bar IMEP und 1500 1/min erzielt wurde. An diesem Betriebspunkt konnte die Effizienz um 15 % gesteigert werden bei NO_x-Rohemissionen unter 20 ppm.

Diese Technologie ermöglicht den Einsatz einer aktiv gespülten Vorkammer in PKW. Die leichtsiedenden Kraftstoffanteile für die Vorkammer sind in der Tankatmosphäre vorhanden und erlauben eine Ein-Kraftstoff-Lösung mit günstigen Komponenten.

1   Introduction

Facing stricter emission limits and imminent bans on diesel vehicles entering city centres, the gasoline engine remains an important bridging technology to a fully electric mobility sector. In principle, gasoline engines offer much better raw emission characteristics in real operation than diesel engines. However, the efficiency of diesel engines is not achieved with conventional stoichiometric, homogeneously operated gasoline engines. The thermal efficiency of gasoline engines can be increased significantly above current levels through high compression ratios and the combustion of lean mixtures or mixtures diluted with exhaust gas. The compression ratio has a direct effect on the efficiency of the gasoline process, while the charge dilution has an indirect effect via a higher isentropic exponent of the diluted and therefore colder charge. Further advantages result from reduced wall heat losses due to lower combustion temperatures and reduced charge exchange losses due to dethrottling.

With conventional ignition systems, however, the poor flammability of highly diluted air-fuel mixtures and the increased tendency to knock at high compression ratios represent a hurdle. The direct injection with stratified charge enables the thermodynamic benefits of lean mixtures but it leads to high NO_x emissions and is only possible in a limited operating range due to cyclic fluctuations in the mixture formation.

To meet the high requirements for ignition systems in modern engines many concepts have already been discussed in the technical literature. The aim is usually to extend the electrical discharge in time and space to increase the probability of stable flame core formation. A distinction must be made between direct current systems and alternating current systems. In the former case, several conventional ignition coils can be connected in parallel and operated alternately or simultaneously, thus producing a strong spark with virtually no time limit [1, 2]. In spatial terms however, the spark remains limited to the gap between the electrodes. In contrast, a corona ignition using high-voltage alternating current with frequencies in the MHz range can achieve a wide spatial expansion of the discharge. The entire combustion chamber is used as a counter electrode and a strong inhomogeneous electric field is generated which locally exceeds the ionization threshold, resulting in a corona discharge [10]. In contrast, laser ignition works without electrical discharge, whereby a pulsed laser beam is focused in the combustion chamber to locally ionize the mixture. The resulting plasma strongly absorbs the laser radiation, resulting in a rapid increase in temperature and pressure, which ignites the charge [3].

These systems have in common, that the ignition energy is taken from the vehicle's electrical system, limiting the possible ignition energy to a few 100 mJ per event. Furthermore, the systems mentioned are limited to ignition alone; an additional function, such as increasing the charge motion, is not possible.

Pre-chamber ignition systems burn a small portion of the charge in a separate chamber, which is connected to the main chamber by multiple transfer ports. The hot gases generated by the pre-chamber combustion penetrate the main chamber, increase the charge motion and ignite the mixture on multiple sites. The energy for ignition is drawn from a chemical reaction, whereby the possible ignition energy of electrical systems is far exceeded. The ignition via a spark plug in the pre-chamber is possible if the mixture in the pre-chamber is kept near stoichiometric. With lean or diluted mixture in the main chamber a separate fuelling system for the pre-chamber is necessary.

Such systems have been developed since the 1970s and are today commonly used in large natural gas engines. The early investigations until 1975 where summarised by Roessler and Muraszew [4]. Dale and Oppenheim [5] later reviewed advanced ignition

systems in 1981 and categorised the pre-chamber systems based on the pre-chamber size and the specific size of the transfer ports. Toulson, Schock and Attard wrote a more recent review on pre-chamber ignition systems in 2010 [6].

The pre-chamber ignition systems can be categorised based on the pre-chamber volume and the specific size of the transfer ports. Gussak et al. showed in their work, that a pre-chamber volume of 2…3 % of the combustion chamber volume and a transfer port cross-section area of 0.03… 0.04 cm²/cm³ (referenced to the pre-chamber volume) lead to the most favourable results [7, 8].

Gussak et al. used a fuelled pre-chamber, which was designed in such a way that the burning gases from the pre-chamber are strongly cooled in the transfer channels, whereby the combustion of the gases stops. According to Gussak's explanation, the resulting gas jets contain partially burnt, active radicals that ignite the mixture in the cylinder at many points simultaneously. In further research on this topic, Yamaguchi et al. were able to identify four possible ignition processes. These range, depending on the specific cross-sectional area of the transfer channels, from a pure chemical chain reaction via a combined active radical and thermal reaction to a pure flame propagation through the transfer channels [9]. The work of Gussak and Yamaguchi shows the most important design parameters of a pre-chamber ignition system:

- A large volume of the pre-chamber provides more energy for ignition and charge motion generation in the combustion chamber but requires more fuel and increases wall heat losses.
- The geometry of the transition channels and the wall temperature of the pre-chamber influence the chemical reactivity and temperature of the escaping gas jets and thus the ignition process in the combustion chamber.

An essential requirement of pre-chamber ignition systems is that the mixture inside the pre-chamber must be ignitable. In the case of a lean mixture in the combustion chamber, the pre-chamber must therefore be enriched with fuel. The fuel used to enrich the pre-chamber is another important design parameter. The smaller the pre-chamber, the more difficult it is to meter the required quantity of fuel. Due to the small dimensions and charge motion in the pre-chamber, mixture formation with liquid fuels is very demanding and gaseous fuels are preferred [10–12].

The use of gaseous fuels instead of liquid fuels additionally facilitates the metering of the fuel quantity and mixture formation in the pre-chamber, because the volumes are considerably larger due to the lower density. Pre-chamber ignition systems that are purged or fuelled with gaseous fuels have been intensively investigated over the past 20 years. Very high lean running limits of $\lambda > 2$ could be achieved with hydrogen as pre-chamber fuel by Watson et al. [13, 14]. Their so-called "Hydrogen Assisted Jet Ignition" (HAJI) was further developed by Watson, Boretti and Toulson and also investigated with propane and methane as pre-chamber fuel [15, 16]. The system uses a gasoline direct injector for the pre-chamber, other concepts use gas valves in combination with a check valve, such as the APIR system by Couet et al. [10]. Similar systems using methane for pre-chamber flushing have been investigated by Geiger et al. [17] and Getzlaff et al. [11].

The "Turbulent Jet Ignition" (TJI) by Attard et al. from Mahle Powertrain LLC [18] marks the state of the art in the field of combustion processes with pre-chamber ignition for passenger cars. Their concept uses a gasoline direct injector positioned directly in the pre-chamber. First experiments were carried out with gaseous fuels for pre-chamber

enrichment, followed by measurements with vaporized gasoline [19] and direct injection of liquid gasoline into the pre-chamber with the aid of a modified injector [12]. With vaporized gasoline as fuel for the pre-chamber, an indicated efficiency of 41.9 % with NO_x emissions below 10 ppm could be achieved at medium engine load [19]. This system was further developed at Mahler Powertrain LLC by Bunce and Blaxill et al., whereby detailed combustion analyses, investigations in optically accessible engines [20, 21], as well as RANS-based simulations were carried out [22]. With Mahle's TJI system a very high lean operating limit of $\lambda > 2$ and very fast combustion speeds could be achieved. However, recurring problems occurred due to deposits in the direct injector of the pre-chamber. This injector was operated with low fuel pressure and extremely small injection holes to dose the required low mass flows. This operation is expected to cause considerable coking problems and the self-cleaning of the injector tip observed with conventional direct injectors does not seem to work [21]. Furthermore, due to the positioning of the direct injector in the pre-chamber, the system requires a lot of installation space which is not available in modern gasoline engine cylinder heads without massive design changes.

Pre-chamber ignition systems are currently used in large gas engines, whereby the described advantages can be fully exploited [23, 24]. On a passenger car scale, equally high lean limits with associated increased efficiency at lowest NO_x emissions are achieved [19]. The use in passenger car engines has so far failed due to the availability of a gaseous fuel for enriching the mixture in the pre-chamber.

The core idea of the concept in this work is therefore to generate the required mixture of gaseous fuel and air for the pre-chamber in the vehicle. The gas atmosphere in the fuel tank above the liquid level is used for this purpose. This gasoline-vapour-air-mixture mainly contains volatile fuel components such as butane and pentane with a concentration of approx. 60 wt. % at room temperature. The use of this gases eliminates the need for additional fuel for the pre-chamber and the tank ventilation system common in passenger cars already provides some of the required components.

The authors showed in pervious publications that the volatile components of common gasoline fuels can be used to enrich the pre-chamber sufficiently for stable combustion processes up to $\lambda = 1.6$. This work shows results of an advanced fuelling system and pre-chamber, as wells as the influence of different vapour conditions and different geometrical characteristics on the combustion process.

2   Methodology

2.1   Test engine setup

As test engine a common 1.8 L four-cylinder DI-engine with turbocharger and variable intake and exhaust valve phasing was used. The engine was operated with 100 bar injection pressure and 95°C ± 1°C coolant temperature. The oil temperature is limited to 95°C ± 2°C by the internal oil-water heat exchanger of the engine. To reduce the samples of prototypes only one cylinder is fired while the other three are closed by a sealing plate in the intake. The main geometrical characteristics of the engine are shown in Table 1.

The operation point is kept steady over all measurements to 1500 rpm and 4.5 bar indicated mean effective pressure IMAP. This point was identified as a medium load point with high relevance to WLTP fuel consumption earlier [25].

The engine is equipped with a low-pressure sensor in the intake and tempered high pressure sensors Kistler 6041B in the cylinders. Both the pressure in the pre-chamber

and in the cylinder were measured with a resolution of 0.36°CA and averaged over 100 cycles. All energetic calculations include the fuel mass flow of the combustion chamber and the pre-chamber, whereby both are measured by coriolis mass flow meters.

Table 1: geometrical characteristics of the test engine

Displacement volume per cylinder	450 ccm
Stroke	84.1 mm
Bore	82.5 mm
Rod length	148 mm
Compression ratio	9.6
Valves per cylinder	4
Intake valve diameter	33.9 mm
Exhaust valve diameter	28.0 mm
Injector position	side

2.2   Pre-chamber fuelling system

The focus of this work is the analysis of the behaviour of a pre-chamber ignition system with active fuelling by volatile fuel components. As already mentioned, these volatile fuel components are available in the gas atmosphere in typical gasoline tanks. The concentration of the volatile fuel or HC components in the tank atmosphere depends on the vapour pressure of the gasoline and the pressure and the temperature inside the tank. The amount of fuel injected into the pre-chamber must be metered so that a stochiometric mixture is reached inside the pre-chamber at spark timing. In case of a lean mixture in the main chamber an under-stochiometric air-gasoline-vapour mixture must be injected in the pre-chamber. The gasoline-vapour-air-mixture in the fuel tank is very fuel-rich and therefore suitable to enrich the mixture in the pre-chamber. As the gasoline-vapour or HC-concentration in this mixture depends on the surrounding conditions, the injected mass into the pre-chamber must be corrected to the HC-concentration. It is also possible to control the HC-concentration of the injected mixture by additional devices to increase the scavenging volume and the oxygen content in the pre-chamber.

To investigate the influence of these parameters, different fuel vapour concentrations and fuel mass flows into the pre-chamber were investigated. These measurements require a flexible fuel system in both volume and HC-concentration. At 20°C the fuel vapour in the fuel tank contains around 60 wt. % HC, mainly propane and butane. A typical detailed composition of the fuel vapour is shown in [26].
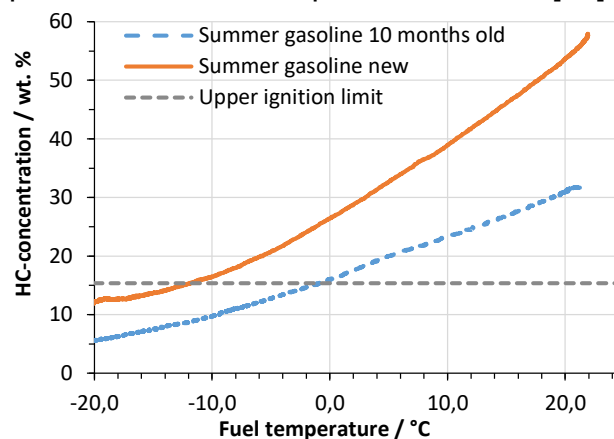
Figure 1: HC-concentration in the vapour versus fuel temperature

The main idea behind the fuelling system used for this study is the dependence of vapour pressure on temperature. Figure 1 shows the HC-concentration in the air-gasoline-vapour-mixture versus the gasoline temperature. Thus, different HC-concentrations can be achieved through variant fuel temperatures. Additionally, different environmental conditions like engine start in the winter can be simulated.
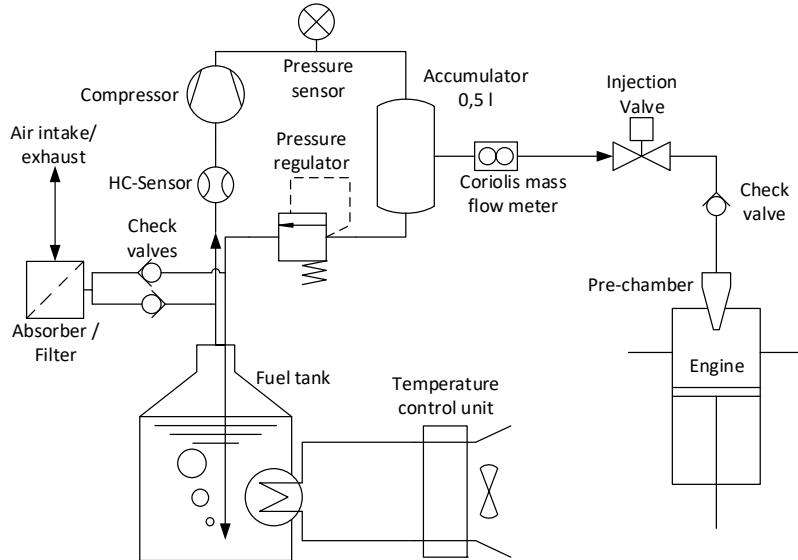
Figure 2: flow chart of the pre-chamber fuelling system

Figure 2 shows the flow chart of the fuelling system. The system contains a 20-litre fuel canister with integrated coolant pipes to temper the gasoline according to the desired HC-concentration in the area above the fuel level. To keep enough area for gasoline vapour, the canister is filled with no more than 10 litre gasoline. The connected external cooling device can be set between -20°C and +60°C. At the top of the fuel tank, a fuel resistant vacuum pump sucks off the gasoline-vapour-air-mixture. The sensor for the HC-concentration is positioned directly before the pump. After the compressor the pressure is measured, followed by a small pressure accumulator tank. This accumulator is needed to dampen pressure pulsations from the pump. Additionally, the line to the engine is positioned in the middle of the tank.

Thus, condensed gasoline components drop of and are feed back to the fuel tank. Condensation occurs if the partial pressure of one component exceeds its vapour pressure for the actual temperature. Condensation can be prevented by increasing the temperature or reducing the absolute or partial pressure of the relevant component.

At the bottom of the accumulator tank a second connection leads back to the bottom of the fuel tank after passing the pressure controller. The compressor's discharge flow exceeds the necessary value for fuelling the pre-chamber, so there is always a certain amount of gasoline-vapour-air-mixture that circulates back into the tank. In that way, the fuel pressure can be kept constant for different consumptions of the pre-chamber. A check valve between the pressure controller and the fuel tank supplies fresh air to the system when mixture is delivered to the pre-chamber. As the air intake line ends at the bottom of the fuel tank, there is always a circulation of gas through the liquid gasoline leading to a constant HC-concentration in the gasoline-vapour-air-mixture.

2.3   Pre-Chamber system

The entire pre-chamber setup contains the pre-chamber fuelling system, the solenoid valve and the pre-chamber. In the pre-chamber body a check valve is included to seal

the injection line against combustion pressure. This enables a very compact design of the pre-chamber and its injection line, so the entire system fits into a common cylinder head by replacing the spark plug. The pre-chamber itself is made from a high-strength copper alloy, that was already used earlier as pre-chamber material [25]. Figure 3 shows the measurement setup.
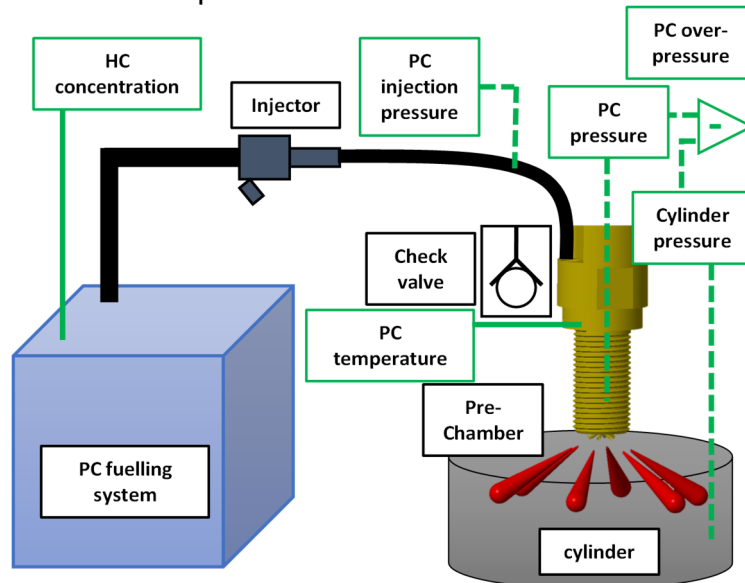
Figure 3: Pre-chamber system

To investigate the pre-chamber pressure, a Kistler 6113B pressure measuring spark plug was installed. The pressure in the pre-chamber injection line between injector and check valve is also measured. To characterize the performance of the pre-chamber, the signal pre-chamber overpressure was created artificially by subtracting the cylinder pressure value from the pre-chamber pressure value. Thus, the pre-chamber ignition can be evaluated online during the measurements regarding timing and intensity. Apart from the pressure measurements, the setup also records the temperature of the pre-chamber body with a thermocouple and the HC-concentration as shown in 2.2.

2.4   Pre-chamber geometry

In this work, four different pre-chambers were analysed. Thereby the following three parameters were varied:
- Pre-chamber volume
- Diameter of the transfer holes
- Length of the transfer holes

All pre-chambers have six orifices for the connection between pre-chamber and cylinder. Table 2 summarizes the main geometrical properties of the used pre-chambers.

Table 2: Pre-chamber geometry

Pre-chamber	Volume / cm³	Hole diameter / mm	Hole length / mm
VK 1	1.34	0.9	1.9
VK 1-1	1.34	1.0	1.9
VK 3	1.70	1.0	1.9
VK 4	1.70	1.0	4.5

The pre-chamber volume corresponds to 2.5 % or 3.25 % of the compression volume, the transfer port cross-section/volume ratio has been constant to $\approx$ 0.028 cm^2/cm^3 for VK 1, VK 3 and VK 4 whereas VK 1-1 has a larger ratio of 0.035 cm^2/cm^3.

3   Results

3.1   Pre-Chamber geometry

The various pre-chamber geometries were tested at a variation of lambda. Figure 4 shows the combustion duration from 5 % to 90 % mass fraction burned (MFB in crank angle, the 50 % MFB (center of combustion and the combustion stability (covariance of IMEP for the three tested geometries. The start of combustion in the main chamber was defined as timing with the highest pressure rise rate of the pre-chamber overpressure. Mathematically, this is the inflection point of the rising edge in the pre-chamber overpressure signal.

All pre-chambers were fuelled with a gasoline-vapour-air-mixture that contains an HC-concentration of around 45 % in the pre-chamber fuelling system. The pre-chamber fuelling mass was optimized in a previous step.

It is visible, that the geometry has a major impact on the performance of the pre-chamber ignition system. In general, the small orifice diameter of 0.9 mm shows the least promising behaviour. It shows the longest combustion duration and the latest centre of combustion. This was controlled to 8°CA after TDC if possible, VK 1 was set to 20°CA due to poor general running stability and long burning durations.

The longer orifices of VK 4 do not lead to a better stability of the combustion. On the contrary, the combustion duration with VK 4 was increased compared to VK 3 with the shorter holes. In the rich section, both the long holes and the smaller diameter show stability problems, running the engine at stochiometric mixture was not possible.

Both VK 3 and VK 1-1 show a good overall performance. The lean limit for VK 1-1 can be set to $\lambda \approx$ 1.85 with a COV of less than 4 %. The smaller pre-chamber volume shows a slightly shorter combustion duration at lean mixtures whereas the lager pre-chamber can reach a very good stability and short burning durations around λ = 1. The indicated efficiency raises along with higher fuel-air-ratio as long as the combustion stability remains under 5 % COV. VK 1 and VK 4 show lower efficiency due to later centre of combustion. At λ 1,85 VK 1-1 reaches an indicated efficiency of 37 %.

In order to achieve low NO$_x$ raw emissions, a high fuel-air ratio is required. Figure 5 shows the NO$_x$ raw emissions logarithmically plotted over lambda during operation with VK 1-1. This clearly indicates that a NO$_x$ concentration of less than 20 ppm can only be achieved with λ > 1.8. At this operating point, the load on the exhaust aftertreatment system can be significantly reduced.

To get a closer impression on the pre-chamber behaviour, the pressure curves can be analysed. As an example, the values for cylinder pressure and pre-chamber pressure for VK 3 at λ = 1.65 are shown in Figure 6. Additional to these two measured values, the pre-chamber overpressure is drawn in Figure 6. It is defined as the difference between pre-chamber and cylinder pressure. This value can be used to compare different pre-chamber geometries at a predefined operating point – while for each pre-chamber design the timing showing the optimum efficiency is applied.

The pre-chamber overpressure at λ = 1.65 for the four different geometries is shown in Figure 7. In this comparison VK 4 shows the earliest ignition timing, but the ignition delay between pre-chamber and main cylinder is so long, that the MFB 50 % point cannot be earlier than 11° after TDC. With both VK 1-1 and VK 3 the desired MFB

50 % of 8° after TDC is possible. The pre-chamber VK 1 ignites very slowly but develops the highest peak pressure of around 15 bar. Nevertheless, VK 1 shows the poorest running stability due to longest burning duration and the late pressure peak.
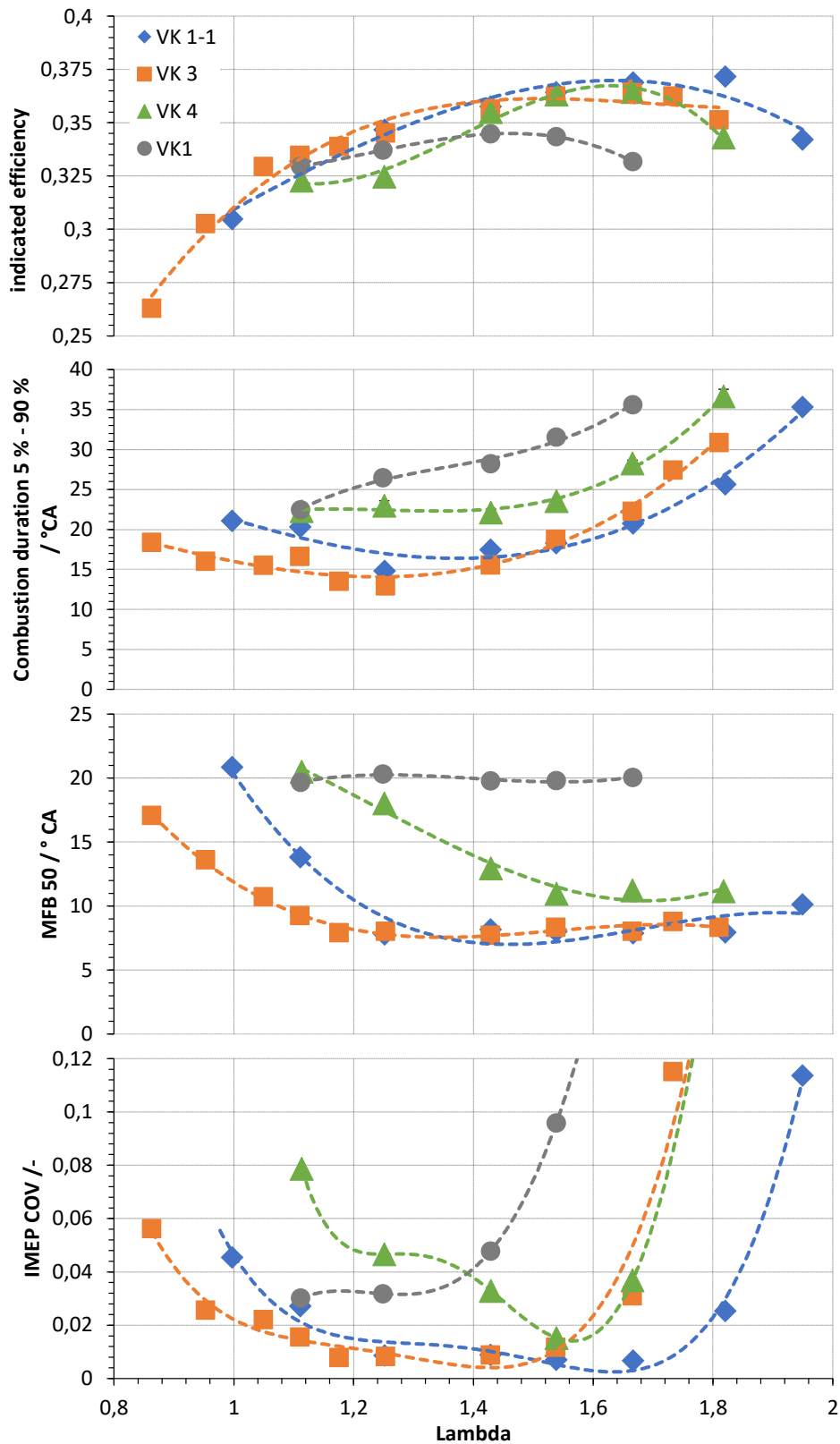
Figure 4: Variation of lambda with four different pre-chamber geometries at 4.5 bar IMEP and 1500 rpm
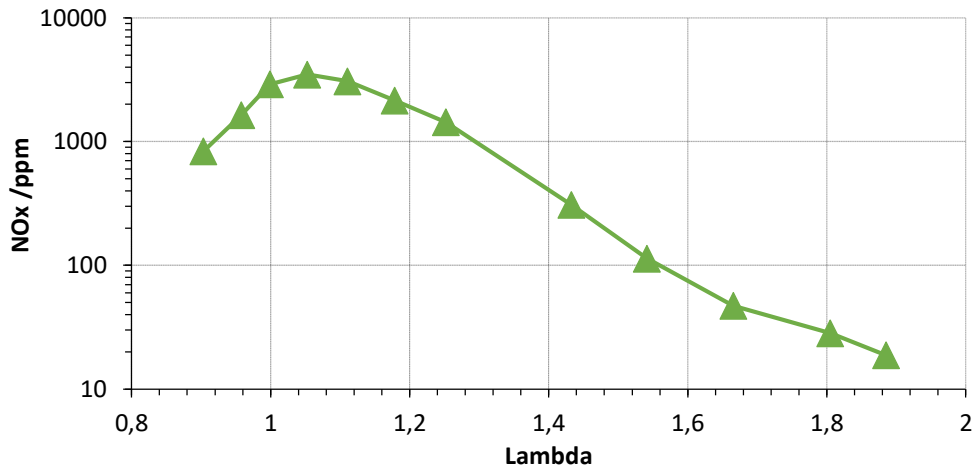
Figure 5: NO$_x$ raw emissions for VK 1-1 at 4.5 bar IMEP and 1500 rpm
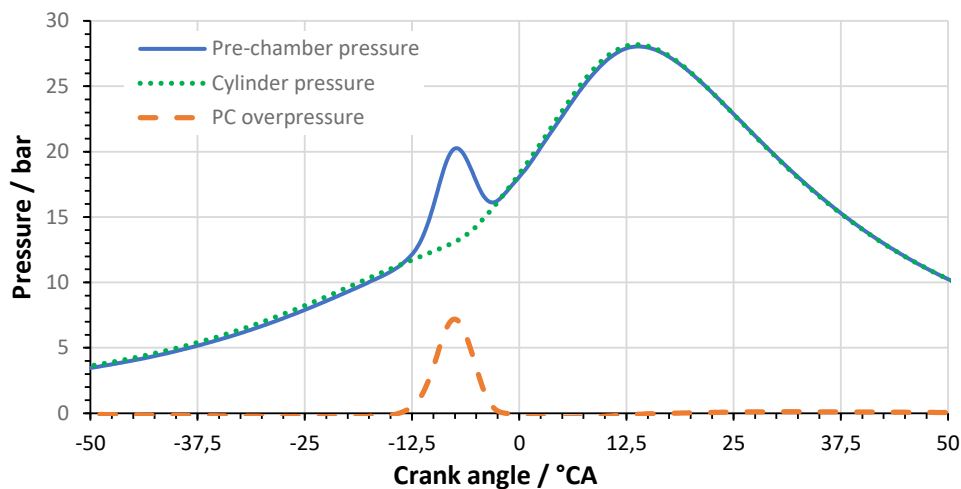
Figure 6: Pressure in pre-chamber and cylinder with PC overpressure for VK 3 at λ = 1.65, 4.5 bar IMEP and 1500rpm

In Figure 7 a clear insight into the physical conditions of the pre-chamber can be gained. The observation of VK 4 shows that the longer connection orifices between pre-chamber and cylinder directly generate a higher ignition delay between the pre-chamber and main combustion chamber. The desired centre of combustion at 8° cannot be achieved, although a sufficient overpressure can be generated in the pre-chamber at an early timing. This indicates that the combustion reaction is more delayed by the higher heat dissipation in the longer boreholes, so that there is a longer time until combustion starts in the main combustion chamber.

The comparison between VK 1 and VK 1-1 clearly shows the influence of the borehole diameter. VK 1 delivers a significantly slower reaction in the main cylinder and thus also a lower combustion stability, although the highest overpressure is generated in the pre-chamber. It was also not possible to achieve the desired combustion centre with this geometry. The combustion in the pre-chamber could not be started at a sufficiently early point in time. The comparison with VK 3 indicates that the worsening is related to the absolute bore diameter of 0.9 mm, not to the ratio of the bore cross-section to the pre-chamber volume. The smaller diameter leads both to a poorer mixture preparation in the pre-chamber and to a long ignition delay from the pre-chamber into the main combustion chamber.
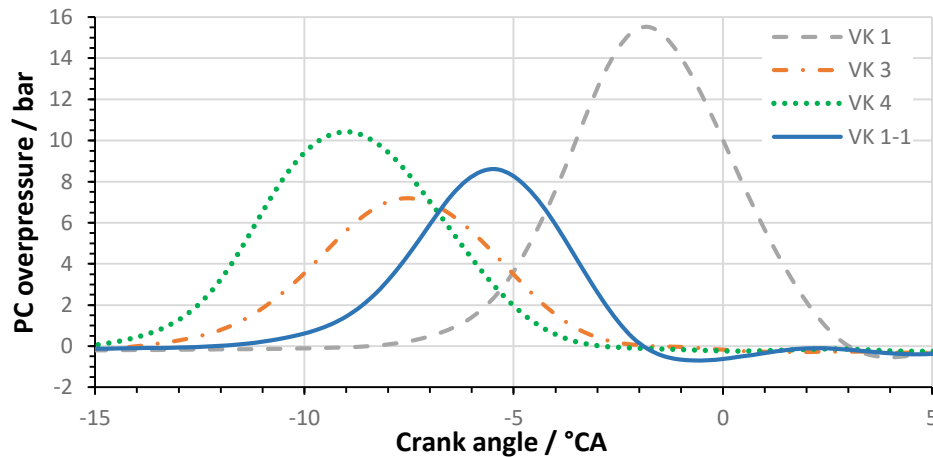
Figure 7: Pre-chamber overpressure at λ = 1.65, 4.5 bar IMPEP and 1500 rpm

3.2   Pre-Chamber fuel mass flow

One focus of this work was evaluating the pre-chamber performance at different fuelling conditions. To investigate this, both operation point and pre-chamber geometry was kept constant. The fuel-air-ratio was set to λ = 1.65 and all investigations were made with geometry VK 3, which showed a good performance in this operation point previously. Figure 8 shows a variation of the fuel mass flow to the pre-chamber at different HC-concentrations in the vapour. The different HC-concentrations in the vapour were achieved by alternating the temperature of the fuel in the pre-chamber fuelling system, as described earlier.

The first diagram shows that the system can supply the pre-chamber with the desired HC-concentration during the entire measurement. The temperature was set to -4°C for 28 %, 7.5°C for 45 % and 20°C for 63 % HC in the vapour. On the horizontal axis the fuel mass flow into the pre-chamber is plotted. This is calculated from the mass flow into the pre-chamber that is measured via a coriolis flow sensor and the HC-concentration of the gasoline-vapour-air-mixture. The second plot shows the opening time of the used solenoid injector to dose the flow. The timing for this injector fixed for all operating points to start of injection at 270 °CA before TDC. The running stability is again shown in the covariance of the IMEP. With the medium HC-concentration a wide band of fuel mass flows lead to a stable combustion. Only the smallest amount of fuel (≈ 19 g/h shows a slight increase of incomplete combustion.

The scavenging with the leaner mixture with 28 % HC shows some issues in the low mass flow region. However, when 40 g/h is reached, all HC-concentrations can provide a suitable amount of fuel-air-mixture in the pre-chamber.

Very rich mixtures beyond 60 g/h can only be reached with the rich vapour with the used injector. An injector with higher flow rate would be necessary to reach higher mass flow rates. A good firing condition with all HC-concentrations is reached with a supply of 40 g/h in this operating point. The used pre-chamber injector shows a suitable flow rate for medium HC-concentrations. The optimal injector size depends on the HC-concentration that is used in the system.
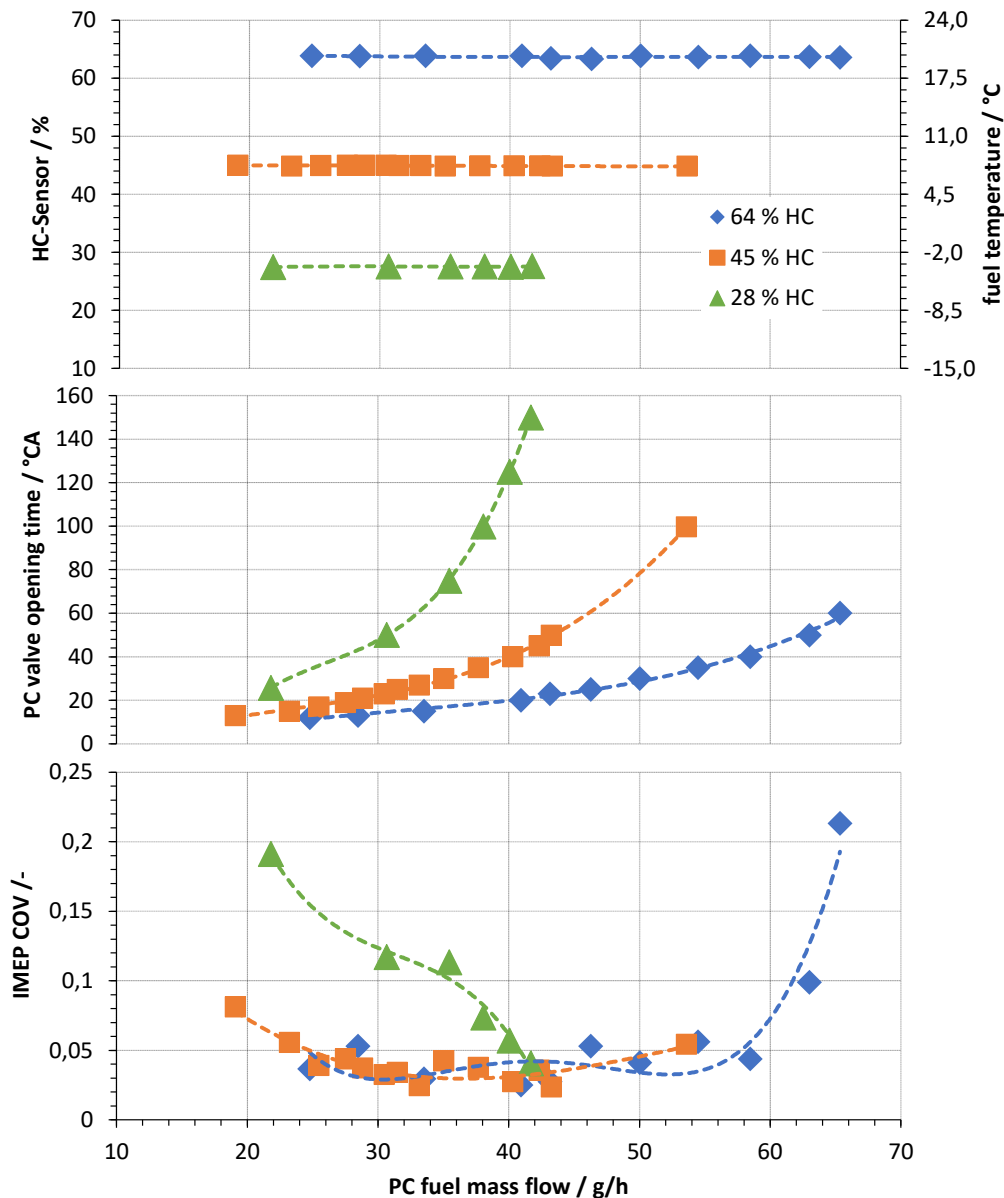
Figure 8: Variation of PC fuel mass flow for different HC-concentrations with VK 3 at
λ = 1.65, 4.5 bar IMEP and 1500 rpm

The combustion timing shows also an interesting behaviour in this variation. In Figure 9 it is shown, that the desired centre of combustion is closely reached by all measurement points.

However, there is a significant difference between the measured HC-concentrations. Just as Figure 8 already indicates, the low HC-concentration shows longer combustion durations at low fuel mass flows. Combustion stability is insufficient even if the combustion duration can be compensated with an earlier ignition timing (the centre is close to 8°CA before TDC). From Figure 8 it is known, that the high HC-concentration shows problems at very high mass flow rates, due to over rich pre-chamber. The IMEP COV is above 10 %. This is not visible in the timing diagrams. When the pre-chamber ignites, the burning duration is on level with the other values. Nevertheless, it is not visible, that more than one out of ten cycles do not lead to any combustion at all. The only hint is the larger variance of the 50 % MFB point.
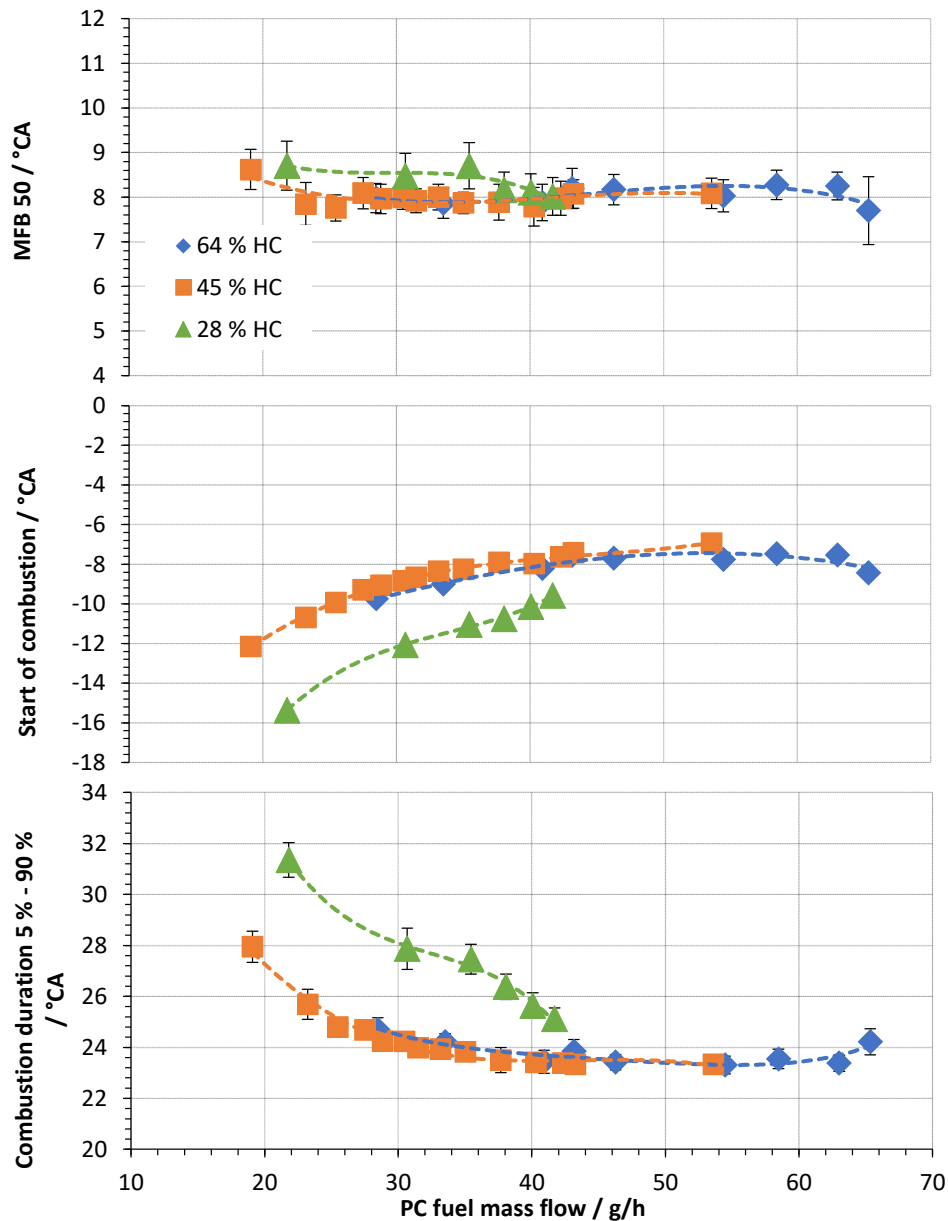
*Figure 9: Combustion timing values for the variation of PC fuel mass flow for different
HC-concentrations with VK 3 at λ = 1.65, 4.5 bar IMEP and 1500 rpm*

In the design of the active scavenged pre-chamber ignition system, the supply of air-gasoline-vapour-mixture into the pre-chamber is one major objective of development. As explained earlier, this system uses the combination of a solenoid fuel injector and a check valve to dose the gasoline-vapour-air-mixture into the pre-chamber. Figure 10 shows the pressure in the injection line of the pre-chamber between injector and check valve together with the triggering signal of the injector. The injector is triggered at 270°CA before TDC and opens for 20°CA, 30°CA and 60°CA, respectively.

The graphs in Figure 10 show that the setup is working well in all conditions. Opening of the injector leads to a quick raise in the pressure, dependant on the opening duration. This pressure peak relaxes into the pre-chamber until the compression pressure is higher than the line pressure due to the piston movement. Only a very small amount of air-gasoline-vapour-mixture is pushed back into the line until the check valve closes. This is visible in the small pressure raise between 120°CA and 60°CA before TDC. Generally, the pressure signal shows a small spread with, so the pre-chamber did not suffer from unstable fuelling conditions.
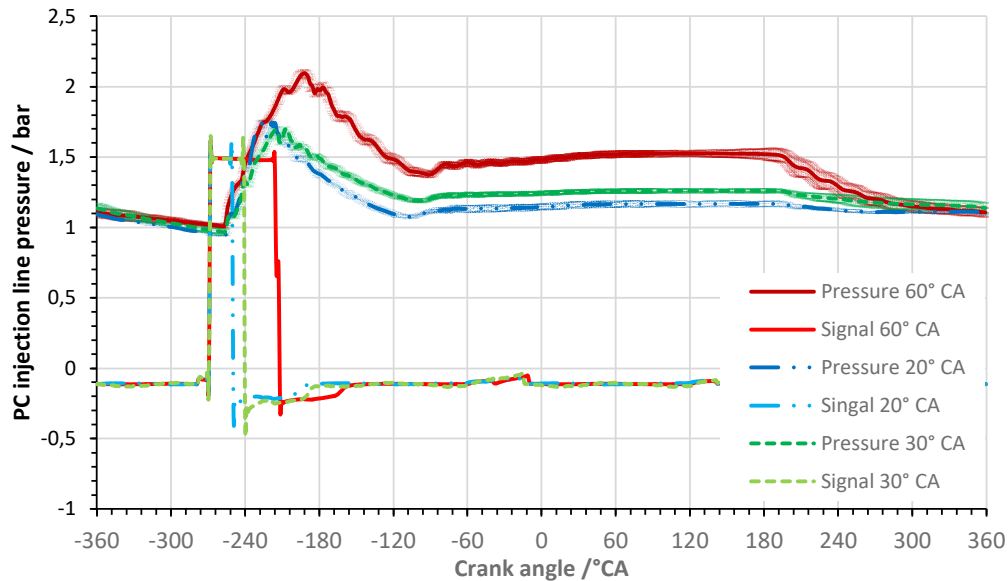
Figure 10: Pressure in the PC fuel line between solenoid injector and check valve for long, medium and short injector duty cycle

3.3   Active Pre-Chamber scavenging with air

One problem of passive pre-chamber systems without active scavenging is the tolerable EGR-rate. Inside the pre-chamber a higher concentration of exhaust gasses can be found due to the scavenging conditions. This problem can also be found at high EGR-rates when the pre-chamber is scavenged with a rich mixture of air and fuel vapour. To overcome this problem, an additional solenoid valve was installed to the pre-chamber fuelling line to inject air additionally to the air-gasoline-vapour-mixture. Thus, the amount of oxygen inside the pre-chamber can be increased, what results in better combustion stability. For air and the air-gasoline-vapour-mixture two different valves are used, so the scavenging with air can be done in the exhaust stroke. An example is shown in Figure 11.
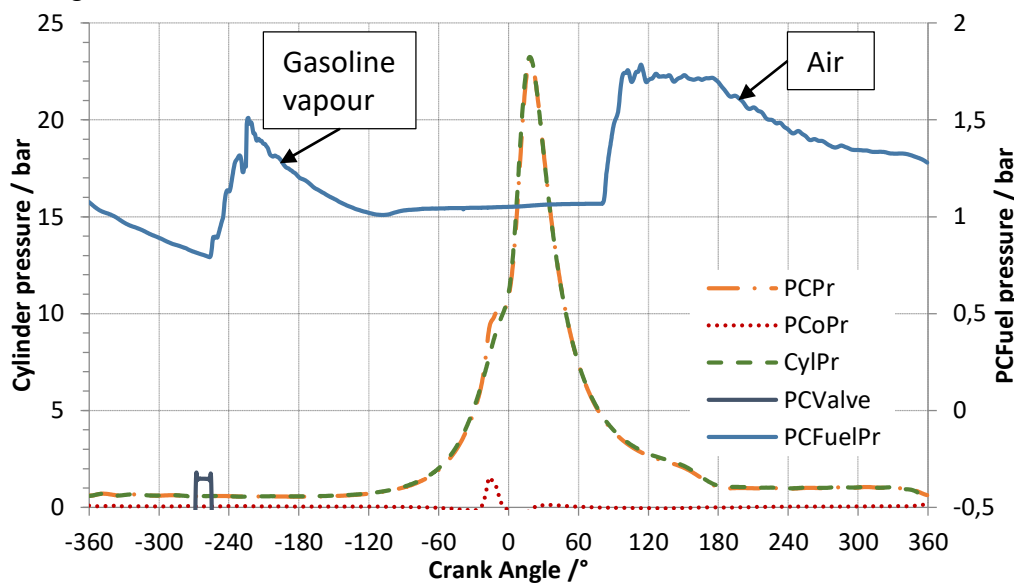
Figure 11: Pre-chamber (PC) at high EGR-rate with additional air scavenging. PCPr: PC pressure; PCoPr: PC overpressure; CylPr: cylinder pressure, PCValve: PC fuel valve duty cycle; PCFuelPr: pressure in PC injection line

For one cycle, the pressure values in the main cylinder, in the pre-chamber and in the pre-chamber fuelling line are plotted. In the pressure of the pre-chamber injection, two pressure peaks are visible. The first one during the intake stroke provides the rich air-gasoline-vapour-mixture, the second one in the exhaust stroke scavenges parts of the burned gases out of the pre-chamber and increases the oxygen concentration in the pre-chamber.
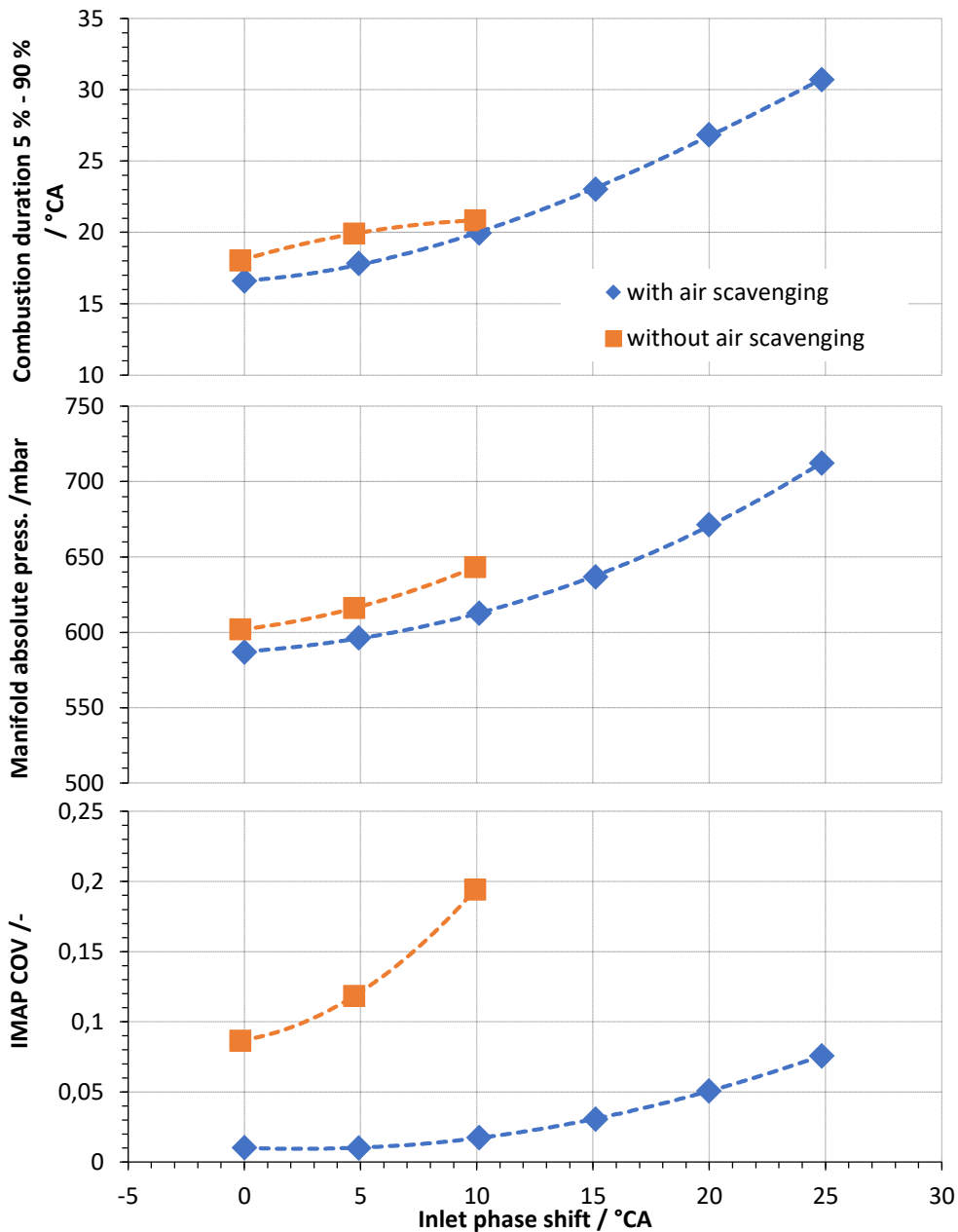
Figure 12: Combustion duration, manifold absolute pressure and combustion stability for the variation of intake phase timing at λ = 1.0, 4.5 bar IMEP and 1500 rpm

In this measurements, only internal EGR trough shift of the intake valve timing was investigated. By moving the inlet phase towards early valve timing, parts of the burned gases are flushed backwards into the manifold and cause the dilution of the cylinder charge. The variation of the intake phase shift is shown in Figure 12 for VK 3 with and without additional scavenging with air. In both measurements the pre-chamber was

supplied with air-gasoline-vapour-mixture at 270°CA before TDC as shown in   Figure 11. The operation point was again at 4.5 bar IMEP and 1500 rpm. As the dilution is done by burned gas, the fuel-air ratio is stochiometric. The highest EGR-rate was approx. 20 % according to a 1D-simulation.

It is visible in the lowest diagram in Figure 12, that the pre-chamber has a lower combustion stability at $\lambda = 1$ than in the lean operation points. Over all measured points, the usage of the additional air can significantly increase the combustion stability. The manifold absolute pressure shows the increasing dilution. However, the system suffers from higher combustion durations at high EGR-rates. Further investigations are needed to find better operation parameters for shorter combustion durations at high EGR-rates. Here both the amount and timing of the air scavenging must be optimized together with the amount of gasoline-vapour-air-mixture and the timing of the two solenoid injectors.

4   Conclusions

This paper describes an actively scavenged pre-chamber system as a possibility of high-energy ignition for the homogeneous lean or diluted operation of a passenger car gasoline engine. A gasoline-vapour-air-mixture, as present in car fuel tanks above the liquid phase, is used to supply the pre-chamber. The HC-concentration of this mixture is detected by an HC-sensor and the mixture is actively fed to the pre-chamber via a timing valve controlled by time and quantity. The pre-chamber is designed in such a way that it can replace the spark plug in a current engine without requiring additional installation space. Various pre-chamber geometries and operating states were investigated. It was shown that the best results were achieved with a pre-chamber volume of approx. 2.5 % of the compression volume and a diameter of the transfer orifices of 1.0 mm. This enabled stable operation at $\lambda = 1.85$ with a combustion stability of below 3 % COV. Smaller bores and long bores show a higher ignition delay between the pre-chamber and the main combustion chamber. The investigation of various gasoline-vapour-air-mixture has shown that stable operation with a wide range of HC-concentrations is possible if the flushing parameters are adjusted accordingly. Operation with high residual gas contents can also be enabled with the active pre-chamber if it is actively purged with fresh air after each cycle. The potential of the actively fuelled pre-chamber ignition with a fuel vapour-air mixture from the tank could be demonstrated. For stable operation, however, it is necessary to understand the geometry and operating parameters, as these have a major influence on the performance of the system.

Literature

[1] N. Iida, Research and Development of Super-Lean Burn for High Efficiency SI Engine: Challenge for Innovative Combustion Technology to achieve 50% thermal efficiency, Okayama, Japan, 2017.

[2] J. Hahn, M. Schenk, F.X. Schauer, C. Sauer, G. Weber, C. Schwarz, From glow tube to corona – challenges to the ignition systems of future SI engines, in: J. Liebl, C. Beidl (Eds.), Internationaler Motorenkongress 2017, Springer Fachmedien Wiesbaden, Wiesbaden, 2017, pp. 123–145.

[3] S. Lorenz, Impulskettenzündung mit passiv gütegeschalteten Laserzündkerzen unter motorischen Bedingungen. Dissertation.

[4] W.U. Roessler, A. Muraszew, Evaluation of Prechamber Spark Ignition Engine Concepts: EPA-650/2-75-023, 1975.

[5] J.D. Dale, A.K. Oppenheim, Enhanced Ignition for I. C. Engines with Premixed Gases, in: SAE International Congress and Exposition, SAE International, Warrendale, PA, United States, 1981.

[6] E. Toulson, H.J. Schock, W.P. Attard, A Review of Pre-Chamber Initiated Jet Ignition Combustion Systems: SAE Paper 2010-01-2263, SAE International, Warrendale, PA, 2010.

[7] L.A. Gussak, V.P. Karpov, Y.V. Tikhonov, The Application of Lag-Process in Prechamber Engines: SAE Paper 790692, in: Passenger Car Meeting & Exposition, SAE International, Warrendale, PA, United States, 1979.

[8] L.A. Gussak, M.C. Turkish, D.C. Siegla, High Chemical Activity of Incomplete Combustion Products and a Method of Prechamber Torch Ignition for Avalanche Activation of Combustion in Internal Combustion Engines: SAE Paper 750890, in: SAE Automobile Engineering and Manufacturing Meeting, SAE International, Warrendale, PA, United States, 1975.

[9] S. Yamaguchi, N. Ohiwa, T. Hasegawa, Ignition and burning process in a divided chamber bomb, Combustion and Flame 59 (1985) 177–187.

[10] S. Couet, P. Higelin, B. Moreau, APIR: A New Firing Concept for the Internal Combustion Engines - sensitivity to knock and in-cylinder aerodynamics: SAE Paper 2001-01-1954, in: International Spring Fuels & Lubricants Meeting, SAE International, Warrendale, PA, United States, 2001.

[11] J. Getzlaff, J. Pape, C. Gruenig, D. Kuhnert, R. Latsch, Investigations on Pre-Chamber Spark Plug with Pilot Injection: SAE Paper 2007-01-0479, in: SAE World Congress & Exhibition, SAE International, Warrendale, PA, United States, 2007.

[12] W.P. Attard, H. Blaxill, A Single Fuel Pre-Chamber Jet Ignition Powertrain Achieving High Load, High Efficiency and Near Zero NOx Emissions: SAE Paper 2011-01-2023, SAE International, Warrendale, PA, 2011.

[13] E. Toulson, H.C. Watson, W.P. Attard, The Effects of Hot and Cool EGR with Hydrogen Assisted Jet Ignition: SAE Paper 2007-01-3627, in: Asia Pacific Automotive Engineering Conference, SAE International, Warrendale, PA, United States, 2007.

[14] H.C. Watson, Lawrence J., "A High Efficiency Low Emission Biofuel Heat Engine, Solar '97, Australian and New Zealand Solar Energy Society, Ed. Canberra, A.C.T. 1997.

[15] E. Toulson, H.C. Watson, W.P. Attard, Gas Assisted Jet Ignition of Ultra-Lean LPG in a Spark Ignition Engine: SAE Paper 2009-01-0506, in: SAE World Congress & Exhibition, SAE International, Warrendale, PA, United States, 2009.

[16] A.A. Boretti, H.C. Watson, The lean burn direct injection jet ignition gas engine, International Journal of Hydrogen Energy 34 (2009) 7835–7841.

[17] J. Geiger, S. Pischinger, R. Böwing, H.-J. Koß, J. Thiemann, Ignition Systems for Highly Diluted Mixtures in SI-Engines: SAE Paper 1999-01-0799, in: International Congress & Exposition, SAE International, Warrendale, PA, United States, 1999.

[18] W.P. Attard, P. Parsons, A Normally Aspirated Spark Initiated Combustion System Capable of High Load, High Efficiency and Near Zero NOx Emissions in a Modern Vehicle Powertrain: SAE Paper 2010-01-2196, SAE International, Warrendale, PA, 2010.

[19] W.P. Attard, H. Blaxill, A Gasoline Fueled Pre-Chamber Jet Ignition Combustion System at Unthrottled Conditions: SAE Paper 2012-01-0386, SAE International, Warrendale, PA, 2012.

[20] M. Bunce, H. Blaxill, Sub-200 g/kWh BSFC on a Light Duty Gasoline Engine: SAE Paper 2016-01-0709, in: SAE 2016 World Congress and Exhibition, SAE International, Warrendale, PA, United States, 2016.

[21] M. Bunce, H. Blaxill, Methodology for Combustion Analysis of a Spark Ignition Engine Incorporating a Pre-Chamber Combustor: SAE Paper 2014-01-2603, SAE International, Warrendale, PA, 2014.

[22] P. Chinnathambi, M. Bunce, L. Cruff, RANS Based Multidimensional Modeling of an Ultra-Lean Burn Pre-Chamber Combustion System with Auxiliary Liquid Gasoline Injection: SAE Paper 2015-01-0386, in: SAE 2015 World Congress & Exhibition, SAE International, Warrendale, PA, United States, 2015.

[23] A. Shah, Improving the Efficiency of Gas Engines using Pre-chamber Ignition: Doctoral Thesis (2015).

[24] A. Shah, P. Tunestal, B. Johansson, Effect of Pre-Chamber Volume and Nozzle Diameter on Pre-Chamber Ignition in Heavy Duty Natural Gas Engines: SAE Paper 2015-01-0867, in: SAE 2015 World Congress & Exhibition, SAE International, Warrendale, PA, United States, 2015.

[25] M. Schumacher, M. Wensing, A Gasoline Fuelled Pre-Chamber Ignition System for Homogeneous Lean Combustion Processes, in: SAE 2016 International Powertrains, Fuels & Lubricants Meeting, SAE International, Warrendale, PA, United States, 2016.

[26] K. Na, Y.P. Kim, I. Moon, K.-C. Moon, Chemical composition of major VOC emission sources in the Seoul atmosphere, Chemosphere 55 (2004) 585–594.

7 Alternative Ignition Systems

7.1 Transient Plasma Ignition (TPI) for Automotive Applications

Sayan Biswas, Isaac Ekoto, Riccardo Scarcelli

Abstract

Transient plasma ignition (TPI) – where high-energy, non-equilibrium plasma ignites flammable mixtures – has been found to promote faster flame propagation rates through a combination of larger volume ignition kernels and the generation of active radicals that enhance flame speeds. For the present study, ignition and early flame propagation characteristics of TPI were investigated within a custom-built optically accessible spark calorimeter for near-atmospheric stoichiometric mixtures of propane and air. Transient plasma was generated using an available high-voltage (~ 25 kV peak), short duration (~12 nanosecond) pulse generator. Two electrode configurations were investigated: (1) a wide-gap pin-to-pin and (2) a groundless partial dielectric barrier discharge (DBD) igniter with a flush mounted and exposed anode tip. Each electrode was expected to promote faster initial burn rates through some combination of reduced heat transfer losses, formation of radical species favorable for ignition, and distributed ignition sites within the combustion chamber. Important post-discharge products were bulk-sampled from non-flammable fuel/air mixtures and speciated via gas chromatography. The impact of the post-discharge products on the flame speeds and auto-ignition delay times were evaluated using the 0-D combustion commercial solver CHEMKIN PRO. High-speed schlieren imaging was used to characterize discharge streamer phenomena and flame propagation rates. Flame propagation measurements were benchmarked against a similar operating point that used a high-energy inductor coil spark plug (93 mJ).

For transient plasma discharges in air, the pin-to-pin electrodes generated strong twin streamers that bridged the electrode gap. Complementary discharge modeling indicates elevated electron densities and atomic oxygen concentrations, especially around the anode tip. Conversely, air discharge imaging of excited state atomic oxygen for the groundless partial DBD igniter indicates strong negative corona streamers that propagate up along the insulator surface toward the expose anode. Corresponding post-discharge sampling and speciation via gas chromatography reveals substantial dissociation of parent fuel molecules into smaller hydrocarbon constituents. Complementary CHEMKIN PRO modeling indicates these species will increase laminar flame by up to 20%. Finally, it was found that both the pin-to-pin and groundless partial DBD igniters increased flame propagation rates by a factor of 2 relative to the inductor coil spark igniter due to a combination of reduced electrode heat losses, larger ignition volumes, and the formation of radicals that increase initial flames speeds.

1.   Introduction

The aggressive move of modern spark-ignited (SI) gasoline engines towards challenging dilute and boosted combustion regimes necessitate new and robust ignition devices. Heavy charge dilution by exhaust gas recirculation (EGR) or air can improve fuel efficiency and lower engine-out pollutant emissions [1]. Benefits include (1) reduced throttling losses, (2) lower heat transfer losses and (3) low nitrogen oxide (NOx) and particulate (PM) emissions [2]. However, reduced flame propagation speeds at relative comparable stoichiometric conditions result in combustion stability issues.

Transient Plasma Ignition (TPI) is a promising advanced ignition technology that utilizes short pulse (~10s of nanoseconds), high-voltage (15 kV+) electrical discharges to generate highly energized low-temperature plasma (LTP). Conventional inductor coil spark plugs utilize point-based thermal plasmas that have electron energies in equilibrium with the bulk-gas energy but have fallen out of favor due to poor tolerance to dilution by air or exhaust-gas recirculation [3]. Conversely, LTP ignition has gained increased attention as a way to promote the formation of radical species favorable for combustion. Broadly speaking, plasma-assisted ignition systems sorted by increasing reduced electric field strength (i.e., electric field strength, E, normalized by the gas number density, N) include: microwaves [4, 5], radio-frequency resonant discharges [6, 7], and transient plasma discharges [8, 9].

The major benefit of transient plasma over other LTP technologies is the higher E/N that leads to increased ionization and dissociation rates due to limited collisional electron energy transfer effects [10]. Fast voltage rise-times can result in E/N values greater than 100 Townsend with electron energies above 10 electron volts, while the short pulse widths enable modest discharge energies (10s of mJ) [11, 12]. Transient plasma discharges have been used to extend dilution tolerance limits through the formation of active radicals that shorten ignition delays [13] and rapid volumetric heating via electron energy transfer processes [14-16]. Ignition has been observed to start from the electrode tips, with inhomogeneous propagation into the bulk gas [17, 18].

Previous studies have shown that TPI generates radicals and other electronically excited species over a relatively large volume [13-18]. However, fundamental TPI mechanisms – particularly at engine relevant conditions – remain poorly understood. In the present study, ignition and early flame propagation characteristics were investigated within a custom-built optically accessible spark calorimeter undergoing TPI. An available high-voltage (25 kV peak), short duration (~12 nanoseconds) pulse generator was used to generate transient plasma. Two different electrode configurations were tests: (1) an opposed pin-to-pin electrode and (2) a groundless partial dielectric barrier discharge (DBD) electrode. For the pin-to-pin configuration, faster initial burn rates are expected through the formation of distributed ignition sites and strong field concentrations at both the anode and cathode tips. Transition to breakdown is avoided through a combination of short pulse widths and large inter-electrode distances (5.2 mm). For the groundless partial DBD electrode, the anode is surrounded by approximately 1.5 mm of a dielectric alumina ceramic in the shape of a cone frustum, with the anode surface exposed and flush mounted with the ceramic tip. Ignition is expected to happen at the exposed anode, with significant enhancement of the flame speeds resulting from negative corona surface discharges that surround the

insulator. Flame propagation measurements were benchmarked against those from a similar operating point that used a high-energy inductor coil spark plug as the ignition source.

2.   Experimental Approach

2.1. Ignition Testing Vessel

All experiments were performed in the stainless steel 316 custom-built, optically accessible, spark calorimeter illustrated in Figure 1 (a). The experimental apparatus has been discussed in detail by Wolk and Ekoto [19], with a brief summary presented here. The calorimeter has an internal volume of 29 cm^3. To visualize the TPI event, 3 optical UV grade quartz (Corning 7980) windows were installed in the calorimeter body. A 20 mm diameter front viewing window enabled direct imaging and fluorescence signal collection from the laser measurement. Two orthogonally installed side windows with 16 mm diameter clear apertures of 12.7 mm allowed for a pulsed light for schlieren imaging of the streamer volume and ignition kernel to pass through the chamber. The initial calorimeter temperature, $T_{initial}$, was heated to 70°°C using resistive heat tape connected to temperature controllers with the temperature monitored using embedded K-type thermocouples. The calorimeter was filled to the desired pressure (1.3 bar absolute) using fuel and desiccated air. Key specifications and operating conditions of the calorimeter are reported in Table 1.

Table 1: Calorimeter specifications and operating conditions.

Internal volume (cm^3)	29
Distance between electrodes (mm)	5.2 mm
Initial temperature (°C)	70
Initial pressure – speciation (bar)	1.1 – 6.1
Initial pressure – ignition (bar)	1.3
Voltage (kV)	10.3 – 25.0
Gas density (kg/m^3)	1.1 - 6.2
Oxidizer composition (% volume)	20.95% O_2, 78.08% N_2, 0.93% Ar, 0.04% CO_2
Fuel	C_3H_8
Purge and fill cycle time (s)	120

To generate the transient plasma discharges within the calorimeter, a Transient Plasma Systems Inc. SSPG-101-HF high-voltage (25 kV peak) pulse generator with a ~12-ns full width at half max (FWHM) pulse width and 5 ns rise time was used. A low-impedance inline attenuator probe was used to monitor pulse voltage and current for each discharge event. Two distinct types of electrodes were tested. For the opposed electrode configuration, the relative position of the anode and cathode is schematically shown in Figure 1 (b). The high-voltage anode was built by modifying an NGK DP7EA-9 size M12 non-resistor spark plug. The plug J-hook and top 1 cm of the outer body ground were removed, with the anode tip machined to a rounded point (~125 µm radius of curvature) to maximize local electric field strengths, while maintaining relatively repeatable discharge characteristics. The anode was centrally positioned at the top of the calorimeter. A 3.18 mm diameter stainless steel rod was used as the cathode. The cathode tip was a cone frustum with a 0.65 mm diameter top surface. The cathode was installed from the calorimeter base and secured in place by a Swagelok fitting. A

constant inter-electrode distance of 5.2 mm was maintained throughout for the present study.

(a)

(b)

(c)
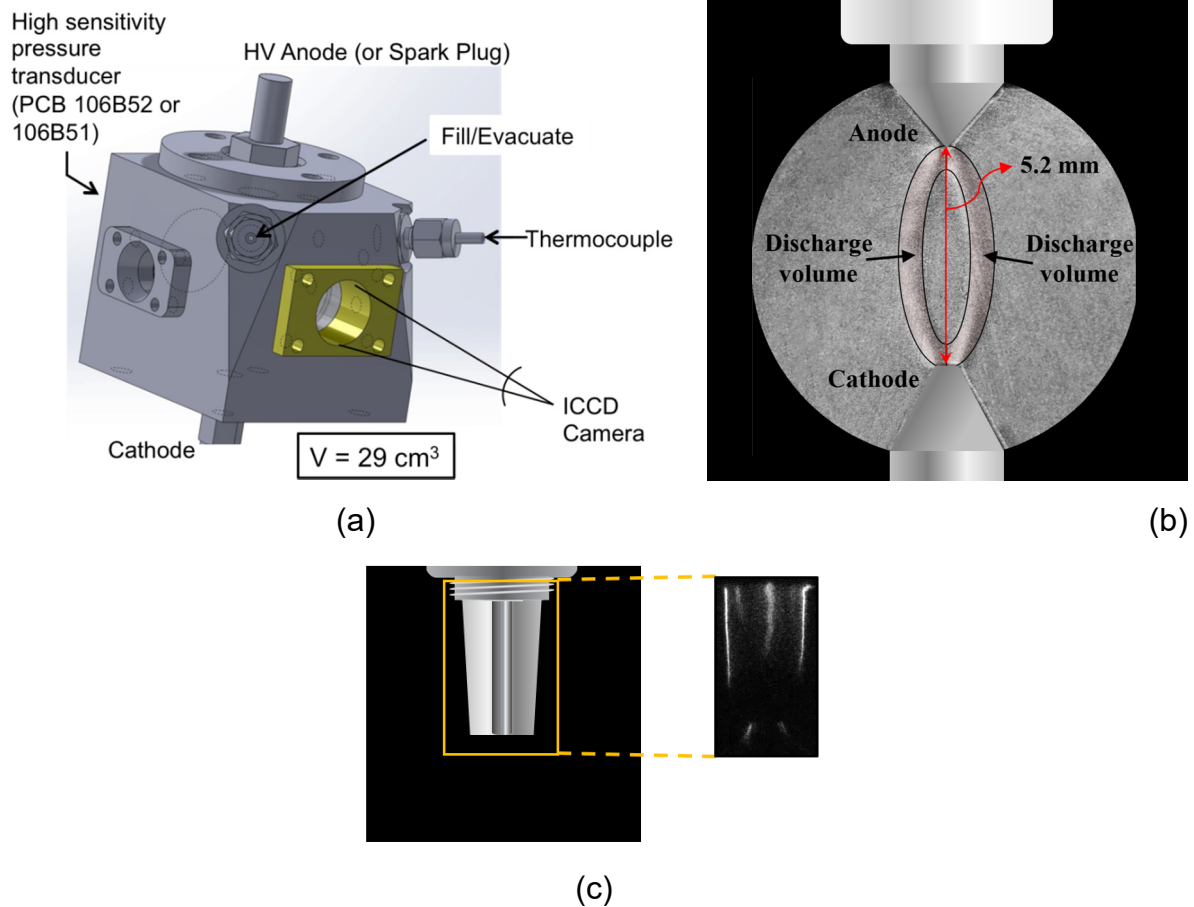
Figure 1: (a) 3D model of the optically accessible spark calorimeter. Electrode configuration and LTP discharge for (b) schematic of the pin-to-pin electrode with a complementary schlieren image of the discharge streamers, (c) schematic of the groundless partial DBD electrode and a complementary image of discharge excited state atomic oxygen.

A schematic of the groundless DBD electrode configuration is shown in Figure 1 (c). The electrode is a modified M12 Brisk silver center electrode non-resistor spark plug (MR12S) that has the J-hook removed and insulator tip exposed, with the anode ground flush to the surface of the ceramic.

Measured profiles of voltage, current, and integrated power for a 19.2 kV peak voltage discharge are presented in Figure 2. Only a fraction of the pulse energy was deposited into the gas as LTP, with the remainder reflected back and forth between the anode and the pulse generator. Voltage and current oscillations were damped by some combination of cable resistance and radiative emission, with little LTP energy addition after the first reflection as evidenced by the nearly invariant integrated power values after each reflection.
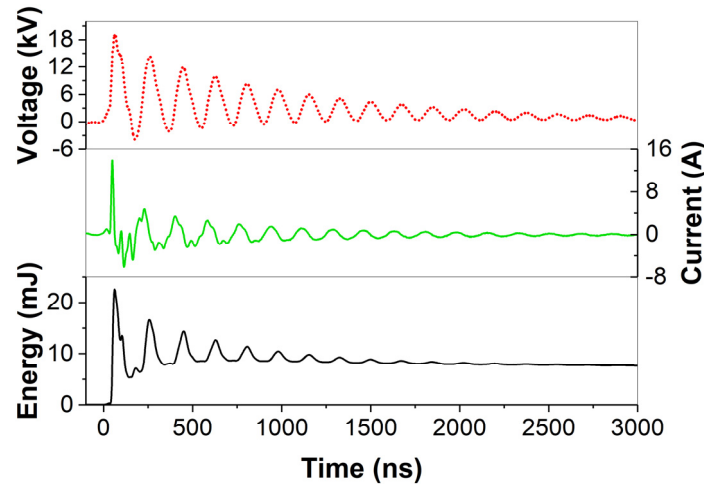
Figure 2: Instantaneous voltage, current, and integrated power in 20.95% O_2 at 70°C.

2.2. Experimental Conditions

Voltage and initial pressure conditions for the sampling and discharge imaging experiments are summarized for both electrode configurations in Table 2 and are plotted on the breakdown transition diagram in Figure 3.

Table 2: Experimental conditions.

		Initial pressure (bar)	
#	Voltage (kV)	Pin-to-pin	Partial DBD
1	10.3	1.2	–
2	14.4	1.5	1.5
3	14.4	2.1	–
4	19.2	2.1	3.0
5	22.5	–	4.5
6	25.0	–	6.1

For the pin-to-pin configuration, peak voltages were varied between 10.3 and 19.2 kV, while initial pressures were varied between 1.2 and 2.1 bar. For the groundless partial DBD electrode, a broader range of initial pressures (1.5 – 6.1 bar) and discharge voltages (14.4 – 25.0) was examined due to the lower propensity of the electrode to transition to breakdown. Experimental conditions were selected to investigate: (1) initial pressure variations with a fixed peak voltage, (2) variations in discharge voltage for a fixed pressure, and (3) discharge characteristics near the breakdown limit.

Also overlaid on the breakdown transition diagram for the pin-to-pin electrode (Figure 3a) is a plot of calculated breakdown voltage in air obtained from an empirical correlation developed by Pashley et al. [20]. For the current setup, the correlation underestimates breakdown voltages for initial pressures below 2.5 bar, possibly due to the truncated pulse that inhibits the time available for transition to breakdown. Conversely, the correlation overestimates breakdown voltages for higher initial pressures, likely due to the increased propensity for breakdown to occur during one of the reflected pulses described above rather than during the initial pulse. Nonetheless, there was good agreement between the correlation and measured breakdown.
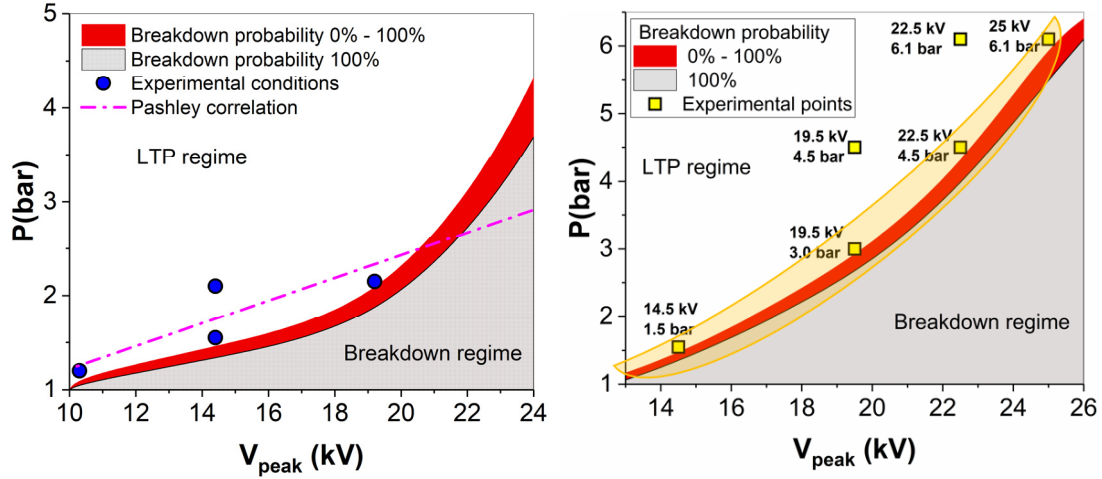
Figure 3: Experimental conditions for TPI.

2.3. Pressure-Rise Calorimetry

To estimate the globally averaged discharge temperature within the plasma streamer channels, pressure-rise calorimetry was performed in conjunction with schlieren imaging. The bulk-averaged thermal energy deposited into the calorimeter gas mixture, $E_{thermal}$ due to discharge is expressed as,

$$E_{thermal} = \int \Delta u d\mathbb{V} = \int \rho c_v \Delta T d\mathbb{V} = \frac{c_v}{R} \mathbb{V} \Delta P = \frac{\mathbb{V}\Delta P}{\gamma - 1} \tag{1}$$

where the variable u is the internal energy, $\mathbb{V}$ is the calorimeter volume, ρ is the gas density, c_v is the specific heat for air at constant volume, R is the gas constant, ΔT is the change in streamer gas temperature, ΔP is the change in calorimeter pressure, and γ is the air specific heat ratio. For each experimental condition, ΔP was calculated as the ensemble average of the peak pressure rise from 50 discharges. Due to the small ΔP encountered in the experiments, a constant γ (= 1.4) based on the initial gas temperature was assumed. To ensure that residual discharge products did not persist between runs and possibly influence the subsequent discharge, chamber contents after each run were cycle-purged twice using fill and vacuum solenoid valves connected to the gas supply and an available vacuum turbo-pump. Chamber fill pressure was accurately controlled using a Proportion-Air QPV pressure control valve. Differential chamber pressures were measured using a PCB 106B51 high-sensitivity pressure transducer (145 μV/Pa). The transducer was secured to the calorimeter using an acetal mounting adapter for electrical isolation with the signal amplified by a Kistler 5134B coupler. All data were recorded using a LeCroy HDO 6054 500 MHz high-definition oscilloscope. Recorded pressures were filtered by a 1 kHz low-pass filter during post-processing to remove noise from the discharge event.

2.4. Schlieren Imaging

Schlieren imaging was performed for each discharge using a pulsed green LED and a PI-MAX 4 camera operated at 10 μs exposure time; a schematic of the setup is shown

in Figure 4 (a). The camera was phase-locked with the discharge timing to record one image 1 µs after every discharge event. Schlieren images were post-processed to remove noise and increase contrast.

(a)

(b)
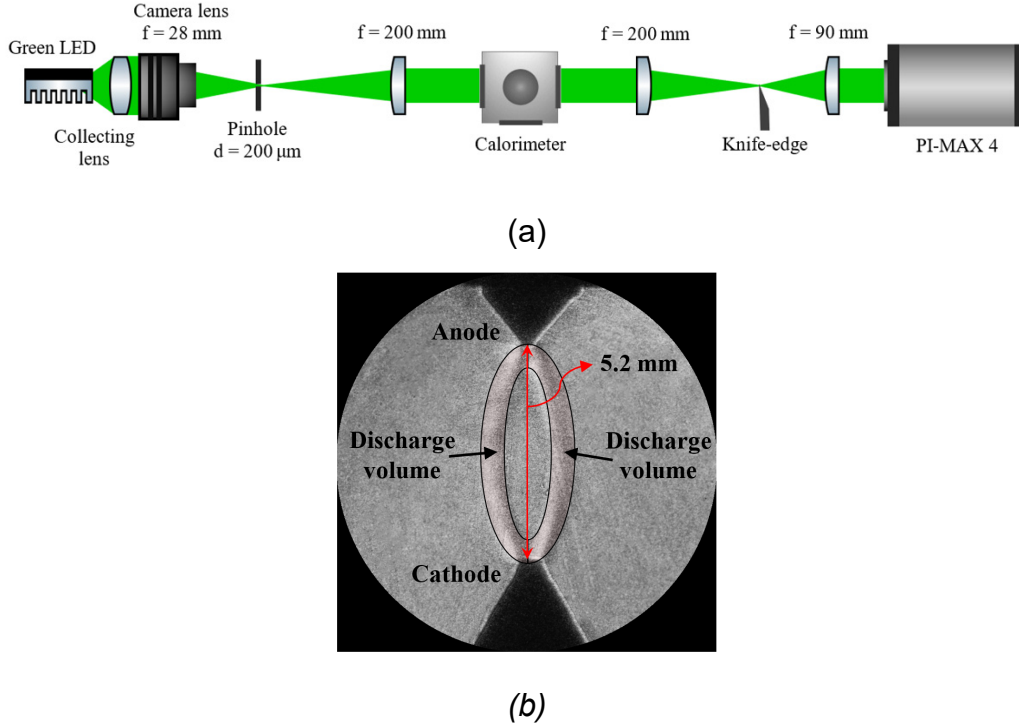
Figure 4: (a) Schematic of schlieren imaging to visualize the streamer discharges. (b) Identification of major schlieren image features for the pin-to-pin discharge.

For the pin-to-pin electrode, 2 dominant streamer channels were always observed in the schlieren images that connected the anode to the cathode, as illustrated in Figure 4 (b). The total streamer volume, $\mathcal{V}$, was estimated under the assumption that each branch was axisymmetric. Streamer channel edge detection in the schlieren image was determined by employing the Marr-Hildreth edge detection routine [21]. The spatially averaged translational temperature within the plasma streamer channel, T_{plasma}, was then calculated using $E_{thermal}$ and $\mathcal{V}$ as follows:

$$T_{plasma} = T_{initial} + \Delta T = T_{initial} + \frac{E_{thermal}}{\rho c_p \mathcal{V}} \tag{2}$$

Values for T_{plasma} estimated from Equations (1) and (2) are plotted in Figure 4 (c).

2.5.   Post-discharge gas sampling and speciation

Post-discharge products from propane/air mixtures were acquired using a solenoid sampling valve that was connected the ignition test vessel to an evacuated and heated 0.5-liter sampling bottle. The equivalence ratio was maintained below the flammability limit to gain insight into the type and quantity of species generated from the transient plasma discharge. Sampling bottle hydrocarbon constituents were analyzed using an SRI Instruments Multi-Gas Analyzer gas chromatograph (GC) that contained a slow eluting 2-meter Restek Hayesep-N column, with hydrocarbon detection by a flame

ionization detector (FID). The column also contained a methanizer that enabled concurrent CO and CO_2 Measurements.

3.   Numerical Model

3.1   Plasma discharge model

Only a general overview of the numerical modeling method is provided here; a more detailed description can be found in [22, 23]. Two-dimensional axisymmetric numerical simulations were performed using VizGlow – a general purpose self-consistent, multi-species, multi-temperature, non-equilibrium plasma solver that can be specialized to model high-pressure corona, glow or streamers discharge of interest [24]. Governing differential equations that account for the production, destruction, and transport of multiple charged and neutral species and the electron energy distribution are solved in conjunction with the Poisson's equation for the self-consistent electrostatic field. Photoionization, which is an important source of background electrons, is also accounted for.

Electrode surfaces are treated as equipotential surfaces for the electrostatic potential solution and as solid surfaces with wall boundary processes for the species density and temperature equations. A numerical grid consisting of a mixed triangle and quadrilateral cells is used for the simulations, with refined triangle cells used at the electrode surfaces to properly account for the electrode geometry so that the static electric field is properly predicted. The discharge voltage profile is matched to experimentally measured traces, with the minimum 2×10^{-13} s time step set such that the dynamics of the transient voltage discharge are well captured. A total of 150 ns simulation time includes the entire first pulse oscillation from the experiments when most electrical energy is deposited into the gas.

The air plasma chemical kinetic mechanism consists of 18 species: e, O_2, O_2^*, $O_2(a1)$, $O_2(b1)$, O_2^+, O_2^-, O, O^-, O_4^+, O_2+N_2, N_2, $N_2(a1)$, $N_2(A)$, $N_2(B)$, $N_2(C)$, N_2^+, and N_4^+. The initial electron number, e, density is set at 10^3 cm^{-3}, which is also the default ground level for all considered species other than O_2 and N_2. Reaction rate pathways from the streamer plasma mechanisms were obtained from literature [25, 26], while electron impact reactions of O_2 and N_2 were generated offline using the Boltzmann solver BOLSIG+ [27] and cross-sectional data for N_2 and O_2 [25]. Energy lost to different rotational, vibrational, and electronic excitations combined into a single electron energy loss pathway.

3.2   0D CHEMKIN PRO flame speed and auto-ignition delay modeling

Discharge product concentrations from the sampling and gas chromatography results were used as input boundary conditions to model flame speeds and auto-ignition delays via CHEMKIN-PRO for stoichiometric mixtures. Based on complementary discharge imaging of excited state atomic oxygen, it was assumed that all discharge products constrained and homogeneously distributed within the 1 mm volume surrounding the electrode surface, with measured concentrations from the GC sampling results accordingly adjusted based on the ratio of the chamber volume to the assumed discharge volume.

4.   Results and Discussions

Results are divided into three subsections. The first two sections respectively describe transient plasma discharge characteristics for the pin-to-pin and groundless DBD electrode configurations for nonflammable fuel/air discharges. The third subsection discusses TPI characteristics for stoichiometric mixtures of propane and desiccated air.

4.1   Discharge Characteristics: Pin-to-pin Electrode Configuration

As mentioned in the Experimental Approach, the pin-to-pin electrode configuration was selected for examination because it produces strong local field concentrations at both the anode and cathode tips. As a result, radical generation favorable for ignition promotion along with increased temperature from the relaxation of vibrationally and electronically excited species are both expected to be high in these regions.

The schlieren image in Figure 5 was acquired shortly after a 19.2 kV discharge into a 2.0 bar ambient of air. The discharge led to the formation of twin streamers that joined at the anode and cathode but separated near the midpoint of the electrode gap. Note that the orientation of streamers changes randomly. The image in Figure 5 was the image from a set of 50 images that had the streamer channels were most closely oriented orthogonal to the camera and thus best illustrates the streamer features. Complementary numerical simulations likewise predict the appearance of twin streamers, with maximum concentrations of atomic oxygen and electron density predicted to occur near the anode. The location of maximum atomic oxygen generation is strongly dependent on the local electric field which in turn is a function of the electrode geometry. Table 3 compares the temperature and atomic oxygen number density from experiment and numerical simulations.
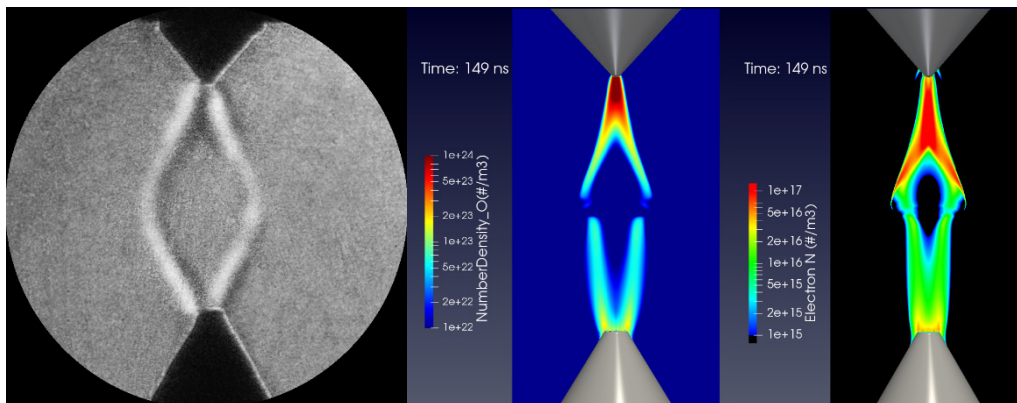

Figure 5: Post-discharge schlieren image from a 19.2 kV transient plasma discharge in 2.0 bar of air along with complementary VizGlow simulation predictions of atomic oxygen and electron density distributions.

Table 3: Comparison of discharge characteristics in terms of LTP temperature and atomic oxygen number density from experiments and numerical simulation.

Experimental condition	Simulations		Experiments	
	O (#/m^3)	T (K)	O (#/m^3)	T (K)
14kV - 1.5bar	0.9E^{+24}	770	1.3E^{+24}	779
19kV - 2.0bar	1.8E^{+24}	938	2.1E^{+24}	1094

Similar images were acquired at different initial pressure and peak discharge voltage combinations (not shown). In all instances, the peak streamer separation distance slightly biased toward the lower cathode. Moreover, as the discharge voltage increased, the separation distance between each streamer likewise increased.

In Figure 6, discharge energy (measured by an in-line voltage and current probe) as a function of peak discharge voltage is plotted along with the corresponding energy deposited into the gas (measured from the pressure-rise calorimetry). The plot also includes an estimate of the bulk-averaged streamer temperature acquired from the combined calorimetry and schlieren measurements described earlier. As expected, the total discharge energy is proportional to the peak discharge voltage. However, the fraction of energy deposited into the gas increases with higher discharge energies, which results in a non-linear increase in streamer temperature. Note for the peak discharge voltage of 19.2 kV; the average streamer temperature was measured for three different initial pressures (2.0, 2.5, and 3.0 bar). As can be seen in Figure 6, streamer temperatures were virtually identical due to the fact that streamer volume was inversely proportional to initial pressure.
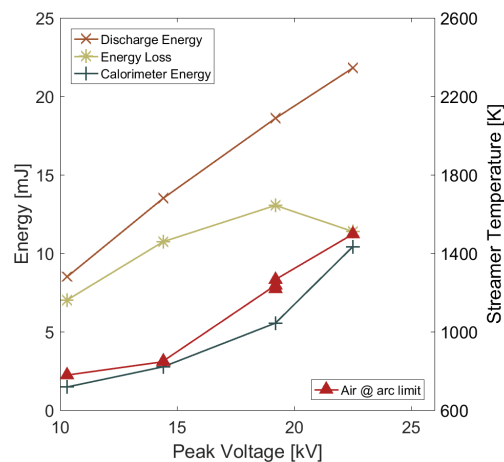
Figure 6: Measured discharge, energy deposition into the gas, energy lost from the system, and the estimated mean streamer temperature.

Since translational temperature is perhaps the most important parameter for ignition, there is a clear advantage to higher discharge voltages. However, for small gaps or low ambient densities the discharge transitions to breakdown.

Finally, note that sampling of non-flammable discharge products was performed for the pin-to-pin configuration, but no measurable concentrations of discharge products were obtained regardless of the condition. Despite the elevated electric fields within the

vicinity of the anode, the small volumes around the electrode tips led to the negligible generation of active radicals on a global scale.

4.2   Discharge Characteristics: Groundless partial DBD Electrode Configuration

The groundless partial DBD electrode was selected because it was assumed to be more resistant to breakdown transition. In addition, a larger discharge volume is preferential for lean/dilute charge mixtures where ignition is more challenging. LTP discharge characteristics from the groundless partial DBD electrode are shown in Figure 7 for discharges with peak voltages near the breakdown limit for the respective initial pressure. Discharge characteristics shows that the streamers start from the remaining portion of the spark plug ground and vertically extend toward the anode. The streamer length and luminescence increased with increased discharge voltage and initial pressure. However, the location of the streamers in successive discharge is stochastic. The expectation is that each streamer acts as both a local ignition site and enhances initial flame burn rates due to the favorable radical formation. Tests of these hypotheses will be described in the following section.
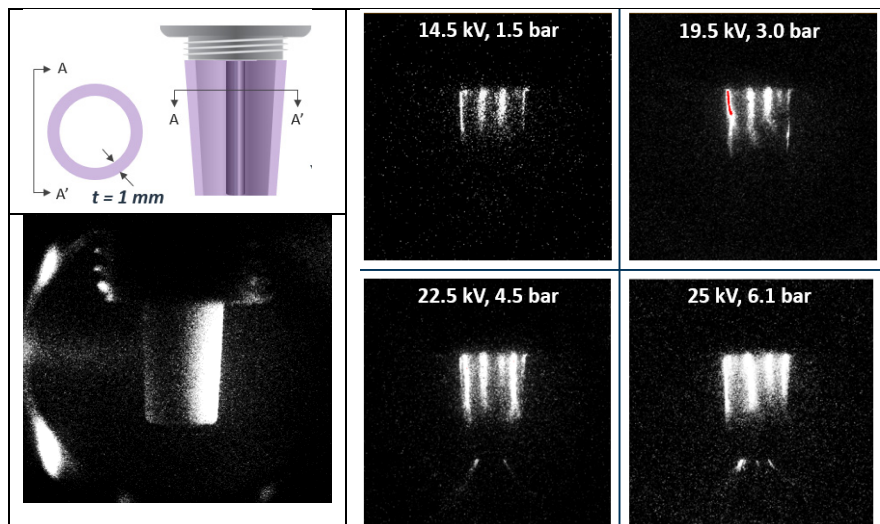
Figure 7: Schematic of the groundless partial DBD electrode including the assumed discharge active area, and qualitative images of O*.

For post-discharge product sampling, discharges were performed in propane/air mixtures. The 2% propane concentration was below the lean flammability limit. To generate statistically meaningful post-discharge products, 10 discharges, 10 milliseconds apart was repeated 60 times.

Figure 8 plots the speciated post-discharge products formed from the LTP discharges, where the initial pressure was adjusted so that breakdown was avoided for the respective discharge voltage. Several hydrocarbon products with carbon numbers less than 3 were formed, which include: methane, CO, acetylene, ethylene, propylene, cyclopropane, acetone. Methane, acetylene, CO, and cyclopropane concentrations, in

particular, were found to increase substantially with higher peak voltages, while remaining species concentrations were relatively stable.
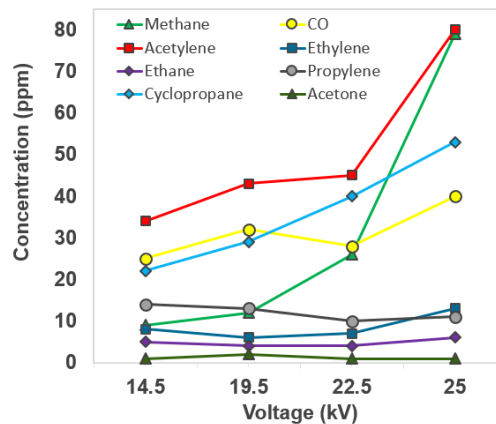
Figure 8: GC measurement of post LTP discharge species formed by groundless DBD electrode discharges.

The effect of initial pressure for a fixed discharge voltage and discharge voltage for a fixed initial pressure on post-discharge product formation is shown in Figure 9. For the ambient pressure variation, most species concentrations were unchanged except for CO and acetylene, which decreased substantially when the initial pressure was increased. When peak voltage was changed for a fixed initial pressure, all discharge products increased; with increases for acetone, cyclopropane, methane, and CO being the most pronounced.

(a)   (b)
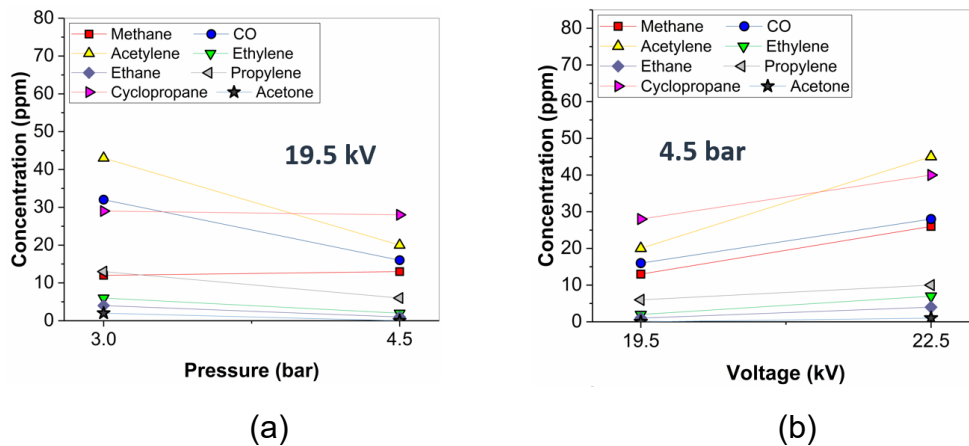
Figure 9: The effect of (a) pressure, (b) voltage on post-discharge product formation.

To explore the effect of post-discharge products on charge reactivity, CHEMKIN PRO simulations were performed. Discharge product concentrations from the condition with 19.2 kV peak voltage and 2.0 bar initial pressure were used, with the balance of fuel set to be the parent propane mixture. Table 4 shows the volume percentage of LTP products and additional propane/air concentration.

Table 4: Volume percentage of mixture components used in the CHEMKIN PRO model.

% by Vol.	LTP products + propane/air	Propane/air
O_2	20.2	20.2
N_2	75.8	75.8
Propane	2.5	4
Methane	0.26	
CO	0.22	
Acetylene	0.51	
Ethylene	0.1	
Propylene	0.12	
Cyclopropane	0.26	
Acetone	0.03	

In Figure 10, flame speed and ignition delay predictions from the CHEMKIN modeling are compared with an equivalent equivalence ratio of propane/air mixture. Figure 10 (a) shows that with increased pressure, ignition delays decreased in the presence of post-discharge products by up to 20%, which suggests that the mixture becomes more reactive. Conversely, Figure 10 (b) shows that flame speeds increased in the presence of discharge products by up to 20%, which suggests faster initial ignition kernel growth rates can be expected.

(a)   (b)
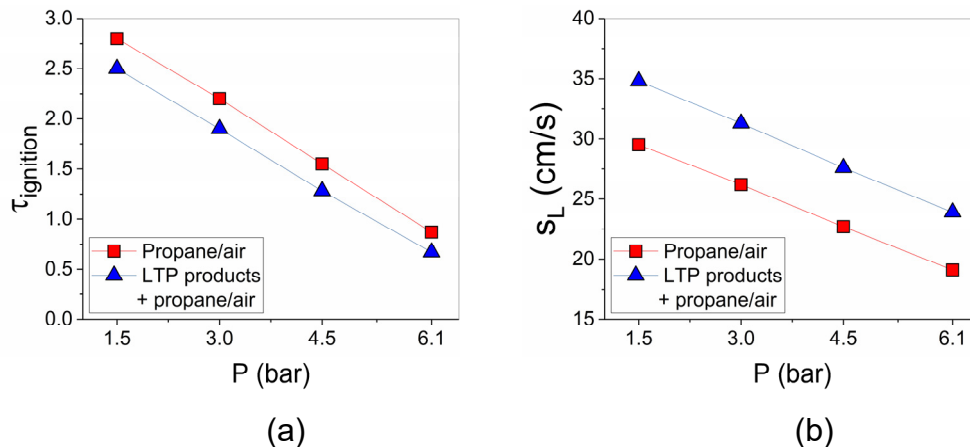
Figure 10: The effect of post-discharge products on (a) ignition delay, (b) laminar flame speed.

4.3 Transient Plasma Ignition Flame Propagation Characteristics

Schlieren image sequences of ignition kernel development and subsequent flame propagation at discrete times after the discharge are plotted in Figure 11 for the pin-to-pin and groundless partial DBD electrodes, along with a comparison to ignition form a high-energy (93 mJ) inductor coil spark plug igniter. The fuel was propane, while the oxidizer was desiccated air. Concentrations were fixed at stoichiometric conditions (6.45% propane in air). The initial pressure was 1.3 bar absolute. Pulse bursts of 5 and 10 pulses were examined for TPI (ignition was not achieved for a 5 pulse burst for either TPI igniter at the conditions examined). In all cases, the dwell between successive pulses was 100 µs. Peak voltage and pulse number are tabulated at the end of the respective sequence. Note that for the groundless partial DBD electrode,

two sets of images were acquired: (1) electrode tip in view to examine ignition processes along the insulator, and (2) electrode tip at the upper edge of the image to examine flame propagation processes in detail.

The ignition location of TPI is key information that helps combustion system developers design optimal electrodes. For the pin-to-pin configuration, ignition was achieved for a peak pulse voltage of 15 kV and pulse burst of 10. Ignition initiated at both the cathode and anode, and quickly bridged the gap following one of the two discharge streamers. For the groundless DBD electrode, the peak voltage needed to be increased to 24 kV for ignition to occur. Ignition started at the exposed anode tip, with a hemispherical laminar flame front developing shortly thereafter. Initially, this flame front propagated outward from the tip, but quickly moved up along the DBD surface.

For both TPI electrodes, the resultant flames kernels consumed the field of view within 3.0 milliseconds after the start of the discharge, whereas the flame from the inductor coil igniter had consumed only half of this area by the same time. From the image sequences, the flame front location was estimated as a function of time after the discharge and plotted in Figure 12. These profiles again illustrate that TPI flame propagation rates were roughly double compared to the discharge from the inductor coil spark plug, with very little difference observed for the pin-to-pin and groundless partial DBD ignition.

Figure 11: Sequence of images showing ignition kernel development in TPI compared to inductive spark for different voltage and pulse repetition rate.
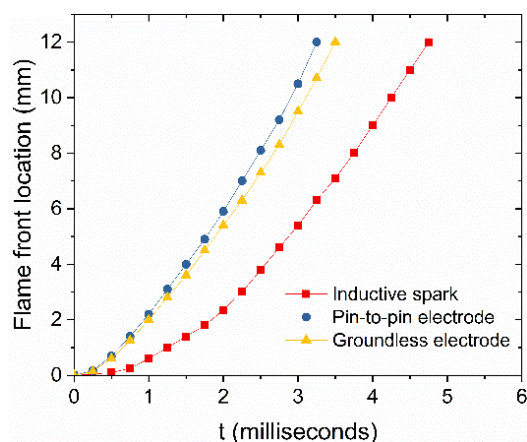
Figure 12: Time history of flame front displacement in TPI and spark ignition.

Note that the while both TPI systems performed similarly, the groundless partial DBD igniter was much more resistant to electrical breakdown. Figure 11 illustrates sequences characterized by breakdown or arcing events. In each instance, highly luminous discharges are visible within the within the first millisecond after the first discharge. The breakdown voltages were only 3 kV higher for the pin-to-pin electrode, whereas they were 5 kV higher for the groundless partial DBD electrode. Accordingly, the DBD electrode is slightly more forgiving, although it comes at the cost of higher energy draw.

5.   Conclusions

The present paper discusses the characteristics of nanosecond transient plasma and TPI in an optically accessible, spark calorimeter at gasoline engine relevant densities. Major findings are as follows:

- o   Discharge characteristics from pin-to-pin show that the existence of twin streamers that bridge the electrode gap. Complementary plasma modeling simulations illustrate that peak atomic oxygen number and electron densities occur near the anode. Post-discharge streamer temperatures increase with higher discharge voltages, likely due to higher energization of vibrational and electronic states that subsequently relax and form heat.

- o   For groundless partial DBD electrode, multiple negative corona streamers initiate from the remaining ground thread and extend towards the anode. Bulk-sampling with speciation via GC indicates extensive dissociation of the parent fuel molecule into smaller hydrocarbon components. Complementary flame speed modeling that uses these concentrations as an initial condition indicate increased flame speeds of up to 20%. Accordingly, these post-discharge products may play a vital role in flame kernel development rates.

- o   For both TPI electrodes, a 10-pulse burst (at 10 kHz) was required to achieve sustainable ignition kernel development, with fewer pulses leading to the gradual extinction of the developed kernel. These results suggest the energy within the kernel must be systematically replenished in order to sustain ignition in the earliest phases.

- o   The pin-to-pin TPI electrode initiates ignition at both the anode and cathode, with the initial flame kernel quickly propagating up along one or both of the discharge streamers that result from the discharge. The groundless partial DBD

electrode initiated ignition at the electrode tip, with combustion propagating outward into the bulk gas and quickly up along the insulator surface.

- o Relative to a conventional inductor coil ignition system (93 mJ), both TPI igniters roughly doubled the flame propagation rates.
- o Larger discharge voltages were needed to initiate TPI with the groundless partial DBD electrode relative to the pin-to-pin configuration (24 vs. 15 kV). However, the groundless partial DBD electrode was much less prone to arc due to the design that shielded the anode from the propagating negative corona streamers. Thus, despite the higher energy draw, the groundless DBD electrode likely is a more robust design.

Future work will explore the possible extension of these TPI electrodes to lean and dilute conditions. Moreover, the ability of these electrodes to promote ignition at pressures and temperatures relevant to those within a realistic engine chamber will be investigated. These results will be complemented by detailed plasma dynamics and computational fluid dynamic simulations that attempt to capture all relevant processes.

Acknowledgments

References

1.   Dunn-Rankin, D., "*Lean combustion : technology and control*. 2008, Amsterdam; Boston: Academic Press. xi, 261 p., 8 p. of plates.
2.   Rapp, V., N. Killingsworth, P. Therkelsen, and R. Evans, "*Lean-Burn Internal Combustion Engines,*" 2016: p. 111-146.
3.   Dale, J.D., M.D. Checkel, and P.R. Smy, "*Application of high energy ignition systems to engines,*" Progress in Energy and Combustion Science, 1997. 23(5-6): p. 379-398.
4.   Nishiyama, A. and Y. Ikeda, "*Improvement of Lean Limit and Fuel Consumption Using Microwave Plasma Ignition Technology,*" SAE International Technical Paper, 2012. 2012-01-1139.
5.   Michael, J.B., T.L. Chng, and R.B. Miles, "*Sustained propagation of ultra-lean methane/air flames with pulsed microwave energy deposition,*" Combustion and Flame, 2013. 160(4): p. 796-807.

6.   Leonov, S.B. and D.A. Yarantsev, "*Plasma-induced ignition and plasma-assisted combustion in high-speed flow,*" Plasma Sources Science and Technology, 2007. 16(1): p. 132-138.

7.   Chintala, N., A.N. Bao, G.F. Lou, and I.V. Adamovich, "*Measurements of combustion efficiency in nonequilibrium RF plasma-ignited flows,*" Combustion and Flame, 2006. 144(4): p. 744-756.

8.   Bozhenkov, S.A., S.M. Starikovskaia, and A.Y. Starikovskii, "*Nanosecond gas discharge ignition of H 2 − and CH 4 − containing mixtures,*" Combustion and Flame, 2003. 133(1): p. 133-146.

9.   Kosarev, I.N., N.L. Aleksandrov, S.V. Kindysheva, S.M. Starikovskaia, and A.Y. Starikovskii, "*Kinetic mechanism of plasma-assisted ignition of hydrocarbons,*" Journal of Physics D: Applied Physics, 2008. 41(3).

10.   Starikovskiy, A. and N.L. Aleksandrov, "*Plasma-assisted ignition and combustion,*" Progress in Energy and Combustion Science, 2013. 39(1): p. 61-110.

11.   Sjöberg, M., W. Zeng, D. Singleton, J.M. Sanders, and M.A. Gundersen, "*Combined Effects of Multi-Pulse Transient Plasma Ignition and Intake Heating on Lean Limits of Well-Mixed E85 DISI Engine Operation,*" SAE International Journal of Engines, 2014. 7(4): p. 1781-801.

12.   Sevik, J., T. Wallner, M. Pamminger, R. Scarcelli, D. Singleton, and J. Sanders, "*Extending Lean and Exhaust Gas Recirculation-Dilute Operating Limits of a Modern Gasoline Direct-Injection Engine Using a Low-Energy Transient Plasma Ignition System,*" Journal of Engineering for Gas Turbines and Power, 2016. 138(11): p. 1-9.

13.   Sun, W., M. Uddi, S.H. Won, T. Ombrello, C. Carter, and Y. Ju, "*Kinetic effects of non-equilibrium plasma-assisted methane oxidation on diffusion flame extinction limits,*" Combustion and Flame, 2012. 159(1): p. 221-230.

14.   Wolk, B., A. DeFilippo, J.Y. Chen, R. Dibble, A. Nishiyama, and Y. Ikeda, "*Enhancement of flame development by microwave-assisted spark ignition in constant volume combustion chamber,*" Combustion and Flame, 2013. 160(7): p. 1225-1235.

15.   Mintusov, E., A. Serdyuchenko, I. Choi, W.R. Lempert, and I.V. Adamovich, "*Mechanism of plasma assisted oxidation and ignition of ethylene–air flows by a repetitively pulsed nanosecond discharge,*" Proceedings of the Combustion Institute, 2009. 32(2): p. 3181-3188.

16.   Kosarev, I.N., N.L. Aleksandrov, S.V. Kindysheva, S.M. Starikovskaia, and A.Y. Starikovskii, "*Kinetics of ignition of saturated hydrocarbons by nonequilibrium plasma: CH_4-containing mixtures,*" Combustion and Flame, 2008. 154(3).

17.   Cathey, C., J. Cain, H. Wang, and M.A. Gundersen, "*OH production by transient plasma and mechanism of flame ignition and propagation in quiescent methane-air mixtures,*" Combustion and Flame, 2008. 154(4).

18.   Singleton, D., S.J. Pendleton, and M.A. Gundersen, "*The role of non-thermal transient plasma for enhanced flame ignition in C2H4-air,*" Journal of Physics D: Applied Physics 2011. 44(2): p. 022001-22002.

19.   Wolk, B. and I. Ekoto, "*Calorimetry and Imaging of Plasma Produced by a Pulsed Nanosecond Discharge Igniter in EGR Gases at Engine-Relevant Densities,*" SAE International Journal of Engines, 2017. 10(3).

20.   Pashley, N., R. Stone, and G. Roberts, "*Ignition System Measurement Techniques and Correlations for Breakdown and Arc Voltages and Currents,*" SAE Technical Paper 2000-01-0245, 2000.

21. Marr, D. and E. Hildreth, "*Theory of Edge Detection,*" Proceedings of the Royal Society of London. Series B, Biological Sciences, 1980. 207(1167): p. 187-217.
22. Scarcelli, R., A. Zhang, and T. Wallner, "*Multi-dimensional modeling of non-equilibrium plasma for automotive applications,*" SAE Technical Paper 2018-01-0198, 2018.
23. Zhang, A., R. Scarcelli, T. Wallner, D. Breden, A. Karpatne, L.L. Raja, I. Ekoto, and B. Wolk, "*Numerical investigation of nanosecond pulsed discharge in air at above-atmospheric pressures,*" Journal of Physics D: Applied Physics, 2018. 51(34).
24. VizGlow. *http://esgeetech.com/*.
25. Kossyi, I.A., A.Y. Kostinsky, A.A. Matveyev, and V.P. Silakov, "*Kinetic scheme of the non-equilibrium discharge in nitrogen-oxygen mixtures,*" Plasma Sources Science and Technology, 1992. 1(3): p. 207-220.
26. Pancheshnyi, S., M. Nudnova, and A.Y. Starikovskii, "*Development of a cathode-directed streamer discharge in air at different pressures: Experiment and comparison with direct numerical simulation,*" Physical Review. E, Statistical, Nonlinear, And Soft Matter Physics, 2005. 71(1).
27. Hagelaar, G.J.M. and L.C. Pitchford, "*Solving the boltzmann equation to obtain electron transport coefficients and rate coefficients for fluid models,*" Plasma Sources Science and Technology, 2005. 14(4): p. 722-733.

7.2 Numerical Simulation of a Nano-pulsed High-voltage Discharge and Impact on Low-temperature Plasma Ignition Processes for Automotive Applications

Riccardo Scarcelli, Sayan Biswas, Isaac Ekoto, Douglas Breden, Anand Karpatne, Laxminarayan Raja

Abstract

Spark-ignition (SI) processes are facing some challenges with the SI engine research continuing to move towards extremely dilute operation. Typical response from the automotive OEMs is to increase the spark energy to hundreds of mJs. However, this approach reduces the spark-plug lifetime due to erosion. In recent years, several low-temperature plasma (LTP) technologies (e.g. microwave, nanosecond pulsed discharge, Corona discharge) have been proposed for automotive applications as a substitute for the conventional SI process, yet no LTP ignition models are available for commercial computational fluid dynamics (CFD) codes for the evaluation and optimization of these advanced ignition systems.

This paper summarizes recent efforts to model LTP generated by a nano-pulsed high-voltage discharge in a multi-dimensional fashion. Streamer discharges between two pin electrodes are modeled through 2-D computations using the non-equilibrium plasma commercial solver VizGlow. The impact of key parameters such as peak voltage and gas density on the characteristics of the streamers is evaluated. The experimental dataset is used to validate the numerical predictions in terms of thermal and chemical properties of the generated plasma at the end of the discharge. Then, the impact of the post-discharge characteristics on the LTP ignition process is evaluated in combustion simulations performed using the CFD code CONVERGE.

Introduction

In the last decade, the performance of automotive spark-ignition (SI) engines has been continuously improved by means of the aggressive enhancement of several specific engine parameters, including intake pressure, in-cylinder turbulence, compression ratio, and exhaust gas recirculation (EGR), leading to the demonstration of 40-45% brake thermal efficiency for gasoline SI engines [1],[2]. However, current ignition strategies for high-efficiency engines still rely mostly on the conventional spark-plug technology. Elevated spark energy values (hundreds of mJs) can improve combustion stability at more dilute operating conditions, but also accelerate electrode erosion rates that ultimately shorten spark-plug lifetimes.

In the last few years, low-temperature plasma (LTP) devices have shown the potential to enhance ignition and eliminate many of the issues related to spark-delivered thermal plasma such as heat losses, erosion, and material ablation [3]. SI engine testing using a nano-pulsed high-voltage discharge has demonstrated that it is possible to extend the EGR dilution tolerance with respect to conventional spark-plugs [4]. However, the

LTP characteristics and the ignition mechanism from LTP in an engine are poorly understood, creating a major barrier for development, optimization, and practical application to internal combustion engines (ICEs).

What stands out in the engine CFD community is that there are no models available to simulate LTP ignition, and this negatively affect the research on such non-conventional technique applied to ICEs. Also, most of the plasma assisted ignition (PAI) research community focuses on below-atmosphere or atmospheric plasmas [5], with 0-D global reactor studies of the plasma-combustion chemistry enhancements [6]. However, at engine-like conditions, LTP becomes highly non-uniform in space, and the plasma characteristics can vary significantly in the gap region between the electrodes.

This paper aims at modeling the non-equilibrium plasma generated by a pulsed nano-second discharge in a high-fidelity, multi-dimensional fashion and providing quantification of the chemical and thermal properties of the plasma. Simulations are validated through experimental data obtained from calorimetry combined with advanced diagnostics. The impact of plasma properties on ignition processes at low temperature is the evaluated through CFD combustion calculations that use detailed kinetics.

1   Numerical Model

1.1   Simulation Approach

In this paper, both non-equilibrium plasma 2-D simulations and CFD combustion 3-D simulations are performed. Figure 1 shows the computational domain simulated with VizGlow and CONVERGE, used for non-equilibrium plasma 2-D simulations and CFD combustion 3-D simulations respectively. The test case geometry of interest consists of a pin-to-pin electrode configuration installed in an optically accessible calorimeter.
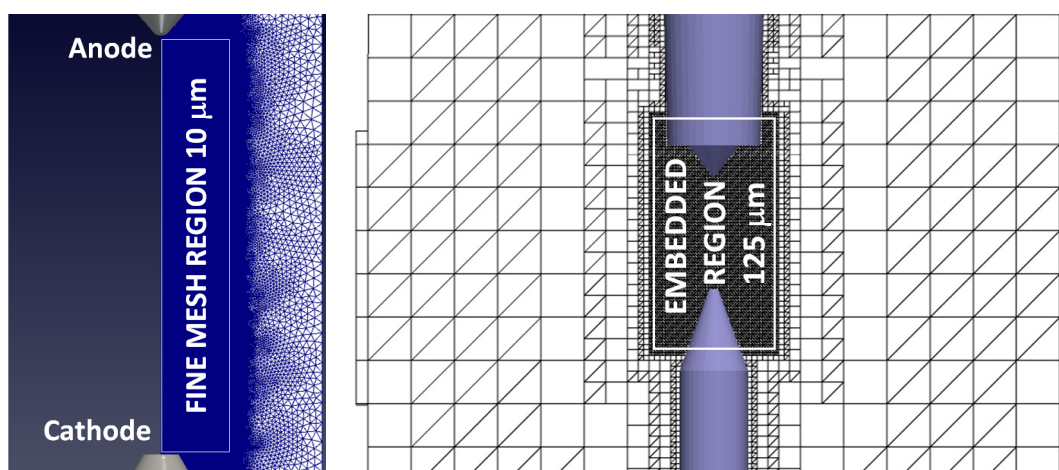
Figure 1: Computational domain in VizGlow (left) and CONVERGE (right)

Non-equilibrium plasma calculations are performed with VizGlow in the fluid region between the two electrodes, which corresponds only to a small portion of the entire calorimeter domain. The boundary conditions imposed in VizGlow consist of an axis-symmetric solution with respect to the axis between the two electrodes and open symmetry for the remaining fluid boundaries of the 2-D domain. The anode and cathode are defined as solid walls, with the electrical pulse (voltage) applied to the anode and

a fixed electrostatic potential condition used for the cathode. The inter-gap region (5.2 mm in length) is meshed with fine (10 μm) quadrilaterals. The mesh size quickly increases outside of the fine region, as indicated in Figure 1, through the adoption of triangle cells at increasing length. The total mesh count is 80,000.

CFD combustion calculations are performed with CONVERGE and simulate the entire calorimeter geometry. All the boundaries of the simulation domain are set to solid walls. A slice of the 3-D domain is shown in Figure 1 and emphasizes the use of embedding (fixed mesh refinement) to increase the mesh resolution (down to 125 μm) in the inter-gap region without significantly affecting the total cell count. Initial cell count is 200,000, but additional computational cells are introduced outside of the embedded region by means of the adaptive mesh refinement (AMR) algorithm implemented in CONVERGE, which is used to resolve velocity and temperature gradients across the flame. Maximum cell count of the CFD simulations is 300,000 as an effect of AMR.

To summarize the simulation approach followed in this study, 2-D non-equilibrium plasma simulations are performed first with VizGlow and leverage experimental data (voltage profile as boundary condition applied to the anode) to model the streamer discharge phase. 3-D CFD combustion simulations are performed next with CONVERGE and leverage the output from VizGlow to initialize the ignition calculations in the entire calorimeter domain.

1.2 Non-equilibrium plasma calculations

VizGlow is a general purpose self-consistent, multi-species, multi-temperature non-equilibrium plasma solver [7] that can be specialized to describe high-pressure corona, glow, or streamers discharge of interest. A number of governing equations are solved in conjunction with the Poisson's equation for the self-consistent electrostatic field in the plasma. These differential equations account for the production/destruction and transport of multiple charged and neutral species and the electron and bulk gas energy distribution. The photoionization mechanism is an important source of background electrons for the streamer propagation in air mixtures, and is also accounted for in the model. Species continuity equations are formulated as the following:

$$\frac{\partial n_k}{\partial t} + \vec{\nabla} \cdot \vec{\Gamma}_k = \dot{G}_k \qquad (1)$$

where k is the species index. All the involved species are solved except for one neutral species, which is the dominant background species. The gas chemistry source term $\dot{G}_k$ is calculated using a finite-rate chemistry mechanism. The number density of the dominant background is calculated based on ideal gas law at specified total gas pressure and gas temperature, by subtracting all other species handled by this species continuity equation. A plasma chemical kinetic mechanism for air is used in this study. The mechanism consists of a total of 18 species: E, O_2, O_2^*, O_2a1, O_2b1, O_2+, O_2-, O, O-, O_4+, O_2+N_2, N_2, N_2a1, N_2A, N_2B, N_2C, N_2+, N_4+. Here, E is electrons, O_2^* is the excited Herzberg state, O_2a1 is the singlet delta, and O_2b1 is a singlet sigma excited states of molecular oxygen, N_2a1, N_2A, N_2B, and N_2C are electronically states of molecular nitrogen, species symbols with "+" indicate positive ions, and "-" indicate negative ions. We also note cluster ions O_4+, O_2+N_2, and N_4+ that are stable forms. The species number flux term $\vec{\Gamma}_k$ is obtained using the drift-diffusion approximation, which

is accurate at pressures of 100 mTorr and higher and at room temperature when the mean free path of the species (on order of μm) are much smaller than the characteristics length scales of the geometry (on order of mm). Electron energy transport is accounted for by solving the electron temperature using the electron energy conservation equation:

$$\frac{\partial e_e}{\partial t} + \vec{\nabla} \cdot \left((e_e + p_e)\overrightarrow{u_e} - \kappa_e \vec{\nabla} T_e \right) = e\vec{\Gamma}_e \cdot \vec{\nabla}\phi - e\sum_i \Delta E_i^e r_i - \frac{3}{2} k_B n_e \frac{2m_e}{m_b}(T_e - T_g)\bar{v}_e \tag{2}$$

The right-hand side of the electron energy equation incorporates three source terms: Joule heating, inelastic collisional heating, and elastic collisional heating, respectively. The bulk temperature is obtained by solving the energy conservation equation:

$$\frac{\partial e_h}{\partial t} + \vec{\nabla} \cdot \left(-\kappa_h \vec{\nabla} T_h \right) = \sum_k eZ_k \vec{\Gamma}_k \cdot \vec{\nabla}\phi + \frac{3}{2} k_B n_e \frac{2m_e}{m_b}(T_e - T_h)\bar{v}_e - e\sum_i \Delta E_i^h r_i \tag{3}$$

The simulations performed in this study leverage the assumption that the bulk fluid motion is omitted, due to the small temporal scale of the discharge. Therefore, local mean velocity $\vec{u}_h$ is equal to zero and does not appear in Equation 3, while pressure is fixed. Additional details of the non-equilibrium plasma simulation methodology used in this study, including the full description of the plasma mechanism, can be found in literature [8].

1.3   CFD combustion calculations

The CFD ignition and combustion numerical simulations are performed with CONVERGE, release 2.3.17, a general-purpose computational fluid dynamics code that calculates incompressible or compressible, chemically-reacting fluid flows in complex three-dimensional geometries. CONVERGE's automated mesh generation based on modified cut-cell Cartesian method [9] helps to simplify the modeling process. Simple orthogonal Eulerian grids with embedded mesh refinements and AMR are used in this study. Continuity, momentum, and energy equations are solved and turbulence is modeled by the RNG k-ε RANS model. A well-stirred reactor combustion model (SAGE solver) with multi-zone approach and a 110 species iso-octane mechanism developed for low-pressure applications [10] are used in this study to simulate combustion. Modeling of heat transfer between fluid and solid is usually achieved by activating CHT modeling in CONVERGE. However, due to the short deposition (≈ 100 ns) and the low-temperature nature of the plasma, CHT calculations are not performed in this study and the electrode surfaces in CONVERGE are treated as boundaries with an imposed fixed temperature.

Simulation of ignition relies on mixed thermal energy and species deposition at the end of the plasma discharge. In the proposed numerical setup, there is no need to switch from ignition to combustion modeling. The mixed energy/species deposition has the effect of elevating the internal energy and increasing the concentration of reactants. Combustion is simulated through detailed chemistry with reaction rates defined in Arrhenius-form and therefore is automatically triggered by the increase of thermal and chemical energy imposed at each pulse. Up to 5 pulses are simulated in a mixture of air and iso-octane, in quiescent conditions, at an equivalence ratio of 1.0, with a pulse repetition rate of 10 kHz, equivalent to a dwell time of 100 μs.

There are two main assumptions made by the authors in this study: first, the results of the nano-pulsed discharge in a stoichiometric mixture of air and fuel (input to CONVERGE) are considered to be equivalent to the ones obtained in air only (output from VizGlow). This assumption is justified by the small concentration of the fuel with respect to air in a stoichiometric mixture. Secondly, in a train of pulses, the assumption is made that the results of the nanosecond pulsed discharge do not change from pulse to pulse. This assumption will have to be analyzed more in depth and verified, as it is known that the discharge regime could transition from glow into spark with the increase of number of pulses. However, the goal of this study is to demonstrate that LTP ignition can be practically simulated using conventional CFD engine tools, and the authors defer the development of an accurate LTP ignition model for multi-pulse applications to a later time.

2 Results

VizGlow simulations describe the streamer discharge between two pin electrodes when a high-voltage nanosecond pulse is delivered at the anode. Depending on the operating condition, the experimental voltage profiles feature a steep rise around t = 40-60 ns, peak at about t = 70-90 ns, and drop to zero after t = 150 ns. Figure 2 shows the evolution of the discharge on a temporal scale for a peak voltage value of 14 kV and an initial pressure of 1.5 bar (here referred as to case 1). Initial temperature in simulations, as well as in all experiments, is 70°C (343 K).
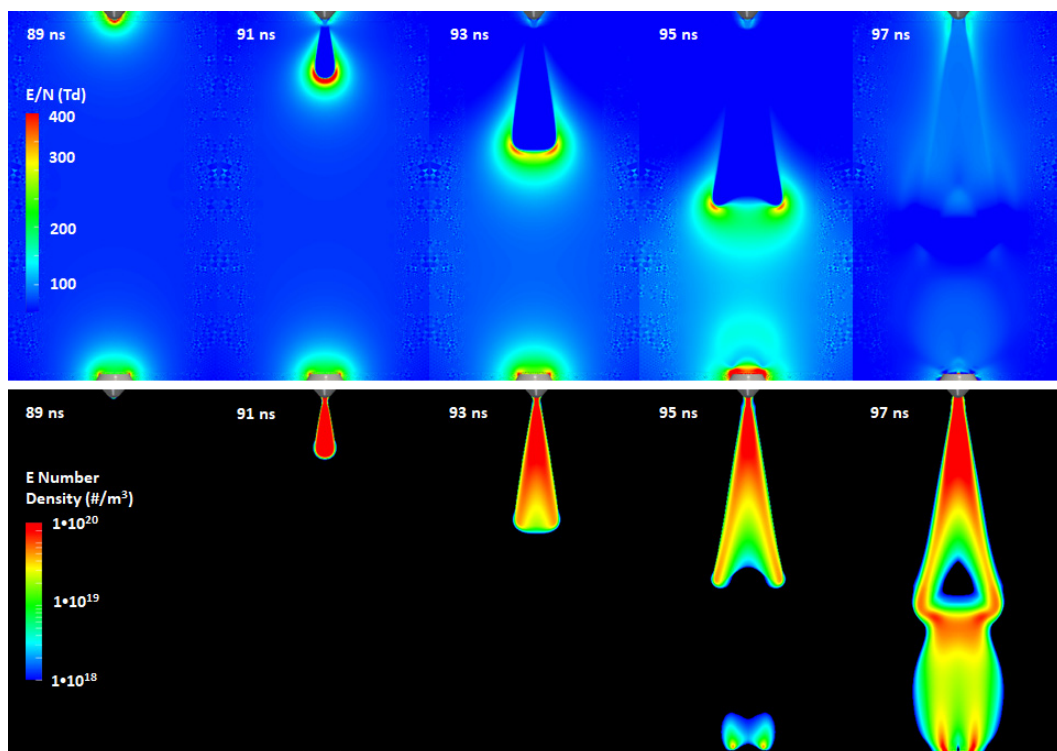
Figure 2: Streamer induction and propagation for case 1 (14 kV, 1.5 bar)

Positive and negative streamers are induced at the tip of both electrodes when the reduced electric field E/N, with N being the number density, becomes greater than the

breakdown field value. After induction, streamers quickly propagate towards the opposite electrode, and eventually bridge the gap in a very short (about 5 ns) time. Once the streamers bridge the gap, the plasma can remain in a glow (streamer) regime or transition to a spark regime depending on the characteristics of the inter-gap region, in particular the reduced electric field value. The operating condition shown in Figure 2 ultimately results in a glow discharge. When the voltage drops, the electrical current between the electrodes decreases and the spark is avoided.

Figure 3 shows the streamer formation and propagation at higher pressure and higher peak voltage values than case 1 (19 kV and 2.0 bar, here referred as to case 2). The timescales for case 2 are comparable with the ones for case 1, the slightly faster streamer induction being due to the shape of the voltage pulse for 19kV, which features a steeper increase than for 14 kV, resulting in the streamer induction occurring approximately 20 ns earlier. Both the reduced electric field and the electron number density distributions are similar to the ones for case 1, with the exception that case 2 shows an increased streamer branching due to the increased pressure in the gap. The streamers bridge the gap again in a very short timeframe, which is comparable with the one shown in case 1. Case 2 also does not transition into a spark and results into a true LTP condition.
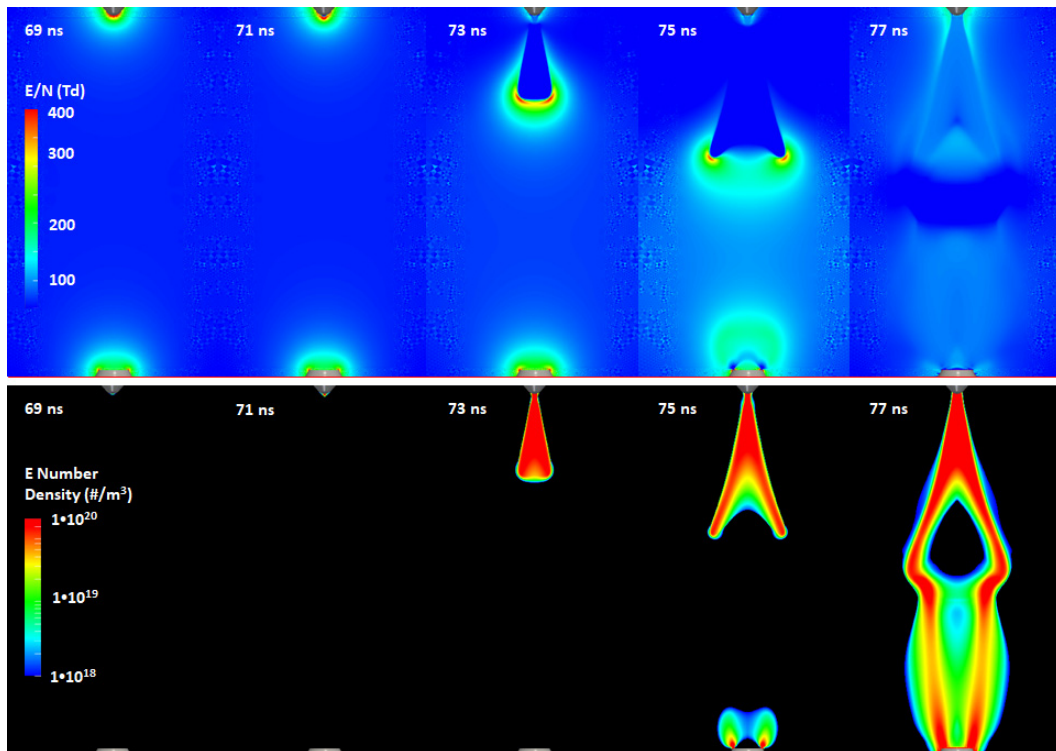
Figure 3: Streamer induction and propagation for case 2 (19 kV, 2.0 bar)

Figure 4 shows the characteristics of the non-equilibrium plasma for case 1 and case 2 at the end of the discharge (t = 150 ns), meaning after the voltage applied to the anode has dropped to zero. The chemical component of the plasma is represented by atomic oxygen O, while the thermal component is represented by temperature.
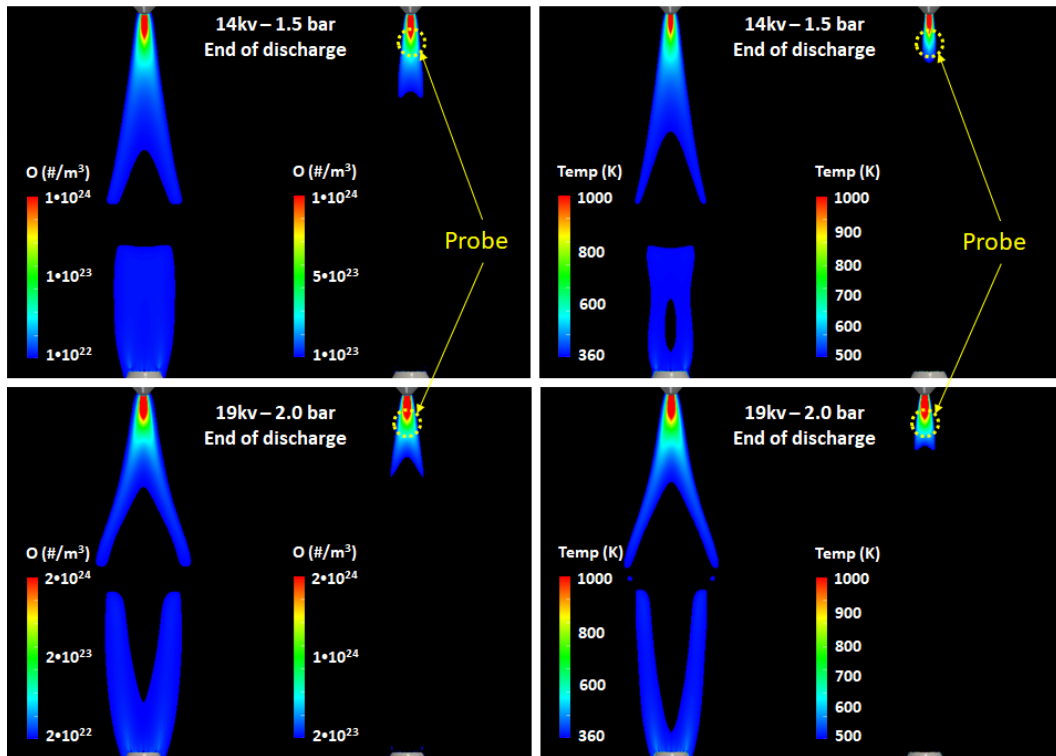
Figure 4: O (left) and Temperature (right) distributions for case 1 (top) and case 2 (bottom). Both are shown using two different scales to emphasize local distributions

It can be seen that, while the generation of atomic oxygen and the increase of temperature involve the entire region between the electrodes, the most relevant O generation and temperature increase are both observed in the close proximity of the anode only. This is due to the specific electrode geometry, which features a rounded tip shape with enhanced local electric field at the anode and a flat top surface, with consequent lower field enhancement, at the cathode. For the same reason, positive streamers (i.e. streamers directed to the cathode) are induced and start propagating earlier than negative streamers, as can be seen in both Figure 2 and Figure 3.

It is known that the location of the largest generation of active radicals and excited molecules is crucial to characterize, since the LTP ignition mechanism will be triggered first in that portion of the domain [11]. In Figure 4 it can be seen that such location is well defined by a conical frustum which has a length of approximately 1/8 of the total gap size. Figure 4 also shows the location of the experimental probe used for the quantitative O-TALIF measurements. Table 1 shows a comparison between simulation and experiments in terms of atomic oxygen produced in the proximity of the anode and temperature in the gap. Table 1 shows that the non-equilibrium plasma simulations closely match experimental data.

Table 1: Comparison of plasma properties between modeling and experiments

Test condition	Simulation		Experiment	
	O (1/cm^3)	T (K)	O (1/cm^3)	T (K)
14.4 kV, 1.5 bar	0.9 x 10^{18}	770	1.3 x 10^{18}	779
19.2 kV, 2.0 bar	1.8 x 10^{18}	938	2.1 x 10^{18}	1094

Once the characteristics of the plasma calculated using simulations are validated against experimental data on quantitative basis, the impact of plasma properties on LTP ignition mechanism can be properly evaluated. Figure 5 shows how the thermal and non-thermal components of the plasma are taken into account. Both energy (which translates into temperature increase) and O species are deposited in a region that has the same size of the region shown in Figure 4 and that represents the part of the domain with the most significant increase of temperature and O concentration.
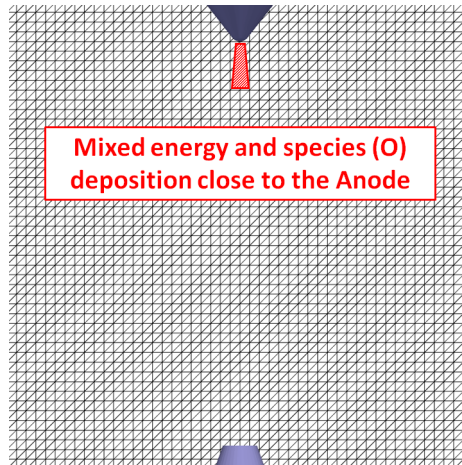
Figure 5: Approach chosen to initialize ignition calculations in CONVERGE.

The LTP discharge is simulated in a multi-pulse fashion. For both the two operating conditions evaluated in this paper, a number of subsequent pulses is simulated at a fixed pulse repetition rate, i.e. one pulse every 100 μs. The impact of the number of pulses on the modeled LTP ignition process is shown in Figure 6 and Figure 7.
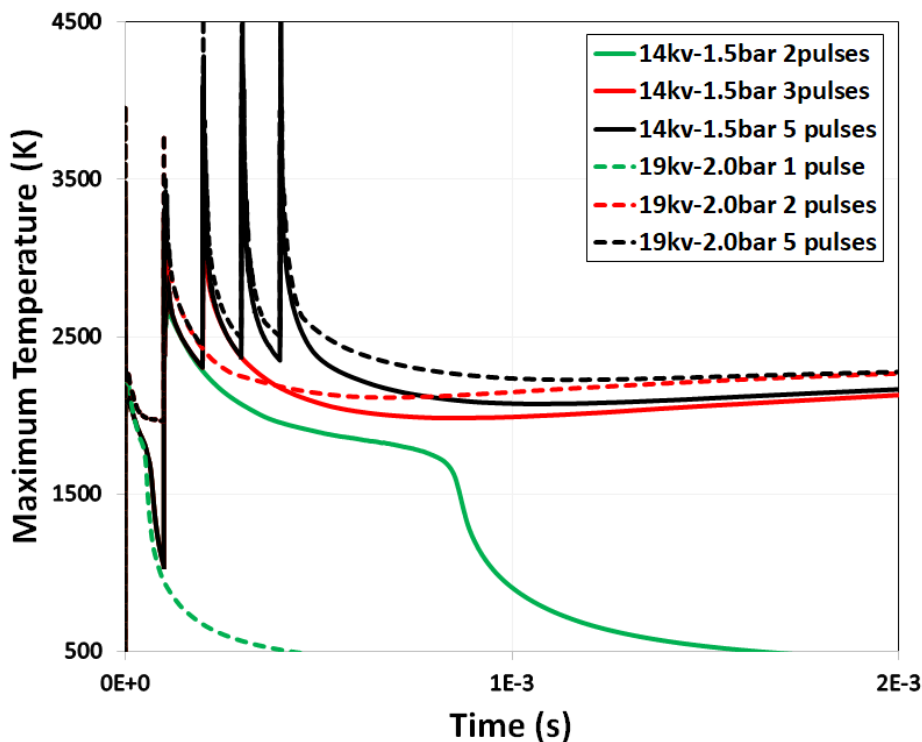
Figure 6: Impact of number of pulses on maximum CFD temperature
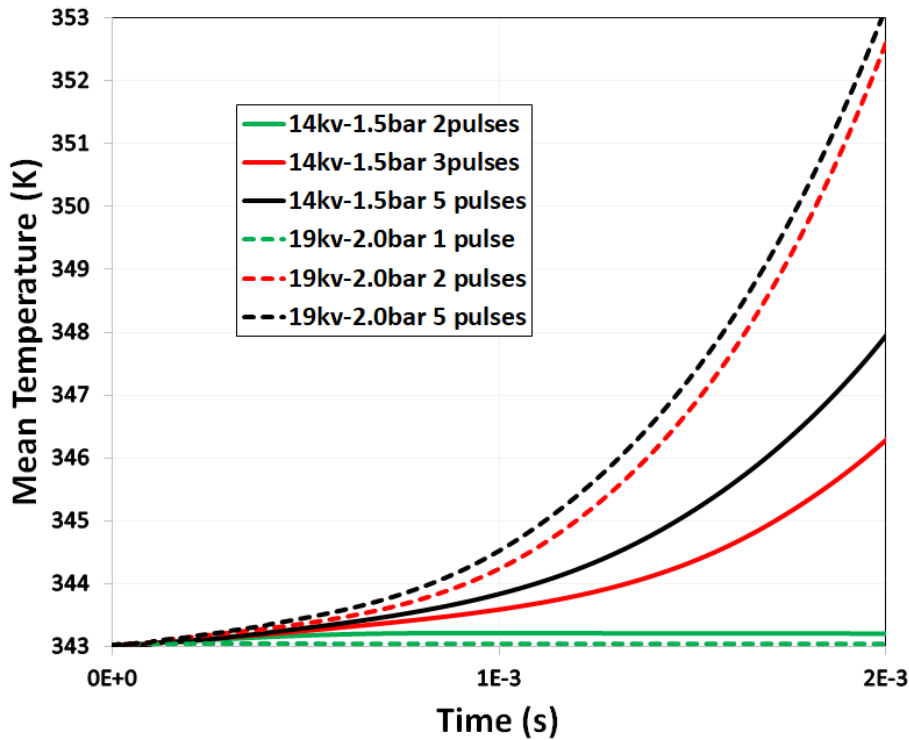
Figure 7: Impact of number of pulses on mean CFD temperature

Not shown in this paper, although a combined energy/species deposition is simulated, chemistry is activated by the low-temperature chemical component. Depositing a thermal energy that increases the local temperature to 800-1000 K alone is not capable of triggering the chemical reactions in a way that leads to self-sustained kinetics.

There is a clear effect of the number of pulses on mixture ignitability that can be observed looking at both the maximum (Figure 6) and mean (Figure 7) temperature values calculated in the full calorimeter CFD combustion cases. Case 1 (14 kV, 1.5 bar) requires at least 3 pulses to ignite, while case 2 (19 kV, 2.0 bar) requires at least 2 pulses. Also adding more pulses beyond a minimum required number does not seem to be decisive. In particular, case 2 features faster combustion than case 1. For case 2, applying 2 or 5 pulses does not make a significant difference.

This can also be observed in Figure 8 that shows the distribution of OH mass fraction for case 2, when 1 pulse, 2 pulses, or 5 pulses are applied to the electrodes. The amount of radicals generated with only 1 pulse is not sufficient to trigger chemical reaction in a self-sustained fashion. Adding one pulse will turn the discharge into a successful ignition process. From 3 pulses on, only limited benefits can be observed in the flame kernel growth. Nevertheless, it is worth pointing out that the specific operating condition is stoichiometric and is also evaluated at quiescent conditions. Under lean or dilute cases, and in presence of a non-quiescent flow conditions, a larger number of pulses could be required due to the low flame laminar speed and continuous displacement of the radicals that are deposited during the nano-pulsed discharge as an effect of the flow.
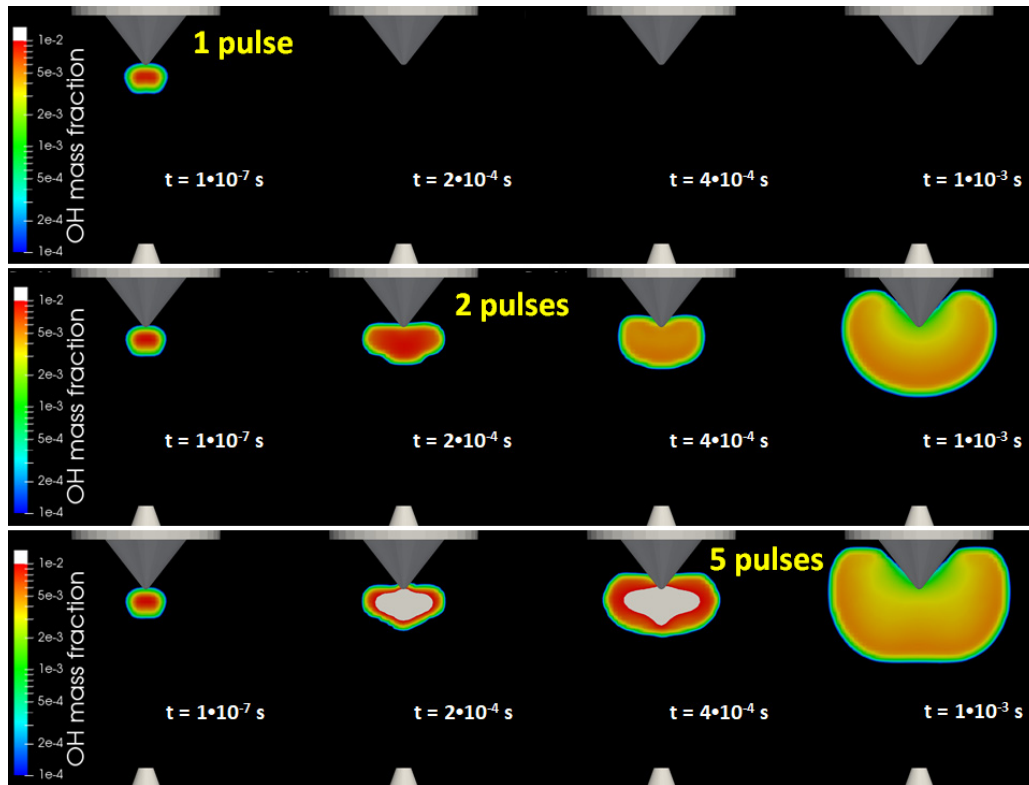
Figure 8: OH distribution for case 2 (19 kV, 2.0 bar) for 1, 2, and 5 pulses

3   Conclusions

This paper leveraged multi-dimensional simulations to investigate the characteristics of non-equilibrium plasma generated by nanosecond pulsed high-voltage discharge in a pin-to-pin electrode configuration. The goal of this study was to evaluate the post-discharge thermal and chemical plasma properties and their impact on LTP ignition processes. Main conclusions can be listed as follows:

- Non-equilibrium plasma simulations correctly predicted the evolution of the streamer discharge in the gap between the electrodes, and the resulting discharge output for a single-pulse discharge, that was experimentally observed to be in the glow regime.

- Simulation results closely matched two key quantities, namely atomic oxygen and temperature, measured in optically accessible calorimetry for a single-pulse discharge. In particular, simulations well matched the quantity of ground state atomic oxygen measured in experiments via O-TALIF at the same location.

- The impact of both types of deposition, i.e. thermal and non-thermal, was evaluated using CFD in a multi-pulse fashion. Results, not shown in this paper, highlighted that at such deposition values, the chemical component is the most important one.

- CFD combustion simulations showed the impact of the number of pulses on the LTP ignition mechanism. A minimum number of pulses was identified to trigger ignition successfully for each case. Non-stoichiometric mixture and the presence of non-quiescent flow will likely alter the number of pulses required for successful LTP ignition.

Acknowledgments

Literature

[1] Takahashi, D., Nakata, K., Yoshihara, Y., Ohta, Y. et al., "Combustion Development to Achieve Engine Thermal Efficiency of 40% for Hybrid Vehicles," SAE Technical Paper 2015-01-1254, 2015.

[2] Ikeya, K., Takazawa, M., Yamada, T., Park, S. et al., "Thermal Efficiency Enhancement of a Gasoline Engine," SAE Int. J. Engines 8(4):1579-1586, 2015.

[3] Briggs, T., Alger, T., and Mangold, B., "Advanced Ignition Systems Evaluations for High-Dilution SI Engines," SAE Int. J. Engines 7(4):1802-1807, 2014.

[4] Sevik, J., Wallner, T., Pamminger, M., Scarcelli, R., et al., "Extending Lean and Exhaust Gas Recirculation-Dilute Operating Limits of a Modern Gasoline Direct-Injection Engine Using a Low-Energy Transient Plasma Ignition System," J. Eng. Gas Turbines Power 138(11):112807, 2016.

[5] Starikovskaia, S.M., "Plasma-assisted ignition and combustion: nanosecond discharges and development of kinetic mechanisms," J. Phys. Appl. Phys. 47(35):353001, 2014.

[6] Aleksandrov, N. L., Kindysheva, S. V., Kosarev, I. N., Starikovskaia, S. et al., "Mechanism of ignition by non-equilibrium plasma", Proc. Combust. Inst. 32 205–12, 2009.

[7] VizGlow User Manual v2.2, Esgee Technologies Inc., Austin, Texas, USA,, http://esgeetech.com/

[8] Anqi Zhang et al 2018 J. Phys. D: Appl. Phys. 51 345201.

[9] Richards, K.J., Senecal, P.K., Pomraning, E., CONVERGECFD 2.3.0 Theory Manual, Convergent Science Inc., Madison, WI, 2016.

[10] Givler, S.D., Raju, M., Pomraning, E., Senecal, P.K., Salman, N., Reese II, R.A., "Gasoline Combustion Modeling of Direct and Port-Fuel Injected Engines, using a Reduced Chemical Mechanism", SAE Technical Paper 2013-01-1098, 2013.

[11] Dan Singleton et al 2011 J. Phys. D: Appl. Phys. 44 022001.

7.3 New Developments and Optimization of The Advanced Corona Ignition System (ACIS)

John Burrows, Kristapher Mixell

Abstract

This paper describes the application of modelling and experimental methods to the development of igniters for a corona ignition system. Steps are described to address the problems typically encountered when designing such an igniter, including electrical, thermal, and durability concerns. Solutions are presented for "streamer" designs in which corona propagates freely in space through the combustion chamber, leading to excellent ignition. In addition, novel solutions are presented for "barrier discharge ignition" (BDI) igniters which allow many of the drawbacks formerly encountered with this igniter type to be avoided.

1 State of the Art

Corona ignition systems have been tested since the 1960s in a wide variety of designs, but can be divided into four broad groups, here assigned the following descriptive names:

1. Arc design: a high frequency electric field causes an arc-like plasma to be formed between two electrodes, either in free air or over a surface or a combination of both. Arc formation is encouraged and arc current is limited by the driving circuit.
2. Steamer design: a high frequency electric field, locally much higher than the global value, causes streamers of branching corona discharge spreading out directly from the electrode into the surrounding air towards the grounded metal engine. System geometry is chose to minimize or avoid arc formation.
3. Barrier Discharge (BDI) design: an insulator completely surrounds the high voltage electrode and prevents the possibility of arc formation. High frequency electric field penetrates this insulator and causes corona discharge in the air around the plug.
4. Pulse design: application of a pulse of high voltage causes a plasma between the high voltage electrode and either the structure of the engine or a second electrode designed for this purpose. Duration of the pulse is controlled such that the time available is too short for arc formation.

1.1   Arc Design Igniters

Arc igniters may be represented by the design shown in Figure 1 [1]. In this case the central electrode is energised with a high voltage of moderate frequency (kilohertz to megahertz), and this ionises the air between the electrodes, here over the surface of the insulator to create a Projected Surface Discharge (PSD) design.
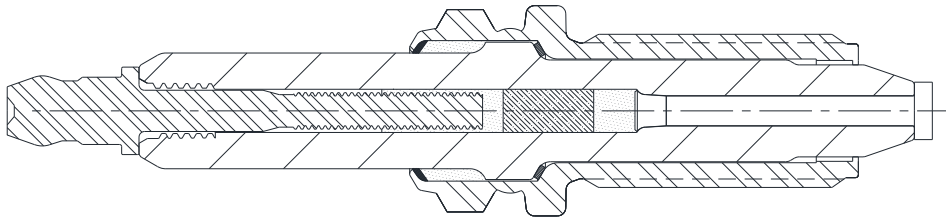
Figure 1: Exemplary design of an arc igniter.
Reference [1]

This type of system is also applicable to conventional sparkplug design and may be used to generate an ignition event of arbitrary duration or power. This has the following desirable features for ignition:
- Duration and current of the event are arbitrary, set by the drive circuit.
- The high frequency along with optional formation over an insulator surface, as in the case of the example in the figure, allows a wider spacing between electrodes and hence an ignition source of larger spatial extent than would be possible with conventional inductive or CDI ignition.
- Damage to the electrodes may be controlled by modulating the voltage and current applied.
- Installation requirements are trivial as the corona is only formed at locations within the control of the plug designer and hence within a well-defined envelope.

However, the following limitations are observed:
- Only one path is energised at a time, as the low-conductivity arc shunts all available energy in a single channel. A single arc path may tend to persist across many cycles of the drive voltage; although it may form new arc paths periodically, only one is energised at a time. Hence spatial extent of the ignition source is limited.
- Flame propagation may be limited by proximity to the insulator surface in some designs.
- Wear of the electrodes may be reduced but cannot be eliminated because significant current still flows between electrode surfaces.
- Many designs have thermal difficulties at high load due to the large exposed central electrode area, coupled with the long projection of the insulator required to achieve the correct spark position.
- Surface discharge designs provide the largest possible ignition source but may suffer from cold fouling problems due to carbon shunting. Addition of an air gap mitigates this problem but leads to a large rise in required voltage.

1.2   Streamer Design Igniters

This type of igniter, shown in Figure 2 [2], has a high frequency (megahertz to tens of megahertz), high voltage electrode configured to give a local electric field which is higher than the global field.
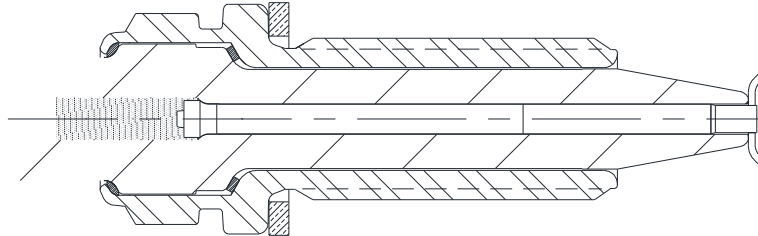
Figure 2: Exemplary design of a streamer igniter
Reference [2].

High field close to this electrode causes ionization of the local air and this ionization spreads out in a branching pattern away from the electrode. This has the following beneficial results:
- Large spatial extent of the branching corona.
- Persistence of the streamers: in contrast to the arc design where only one path exists at a time, multiple steamers may simultaneously form and be maintained and even grow throughout the ignition event.
- This gives multiple ignition sources far from combustion chamber surfaces.
- Current from the electrodes is small unless an arc is formed. Electrode life is not impacted by electrical erosion.
- Energy transfer from corona to gas is very good, leading to improved overall system efficiency.

Amongst the drawbacks are:
- A locally high electric field is required, which is often achieved by using sharp electrode tips. These are difficult to cool adequately and may be subject to corrosion in operation.
- If the corona streamer reaches a grounded engine component, an arc will form which reduces ignition quality and can lead to electrode damage over time. Adequate space is needed around the igniter and this can limit compression ratio.
- Following from the point above, if the electrode is close to a grounded surface (for example the piston at TDC) then the peak local field is comparable to the average field and a corona streamer will never form, or will break down immediately into an arc.
- Careful control of the applied energy is required in order to avoid arcing and the associated drop in ignitability. This requires additional content in the control electronics and additional calibration effort.

1.3 Barrier Discharge Ignition (BDI)

Barrier discharge igniters, such as represented in Figure 3, exist in several different formats. They typically use a high voltage electrode driven with a high frequency (megahertz to tens of megahertz).
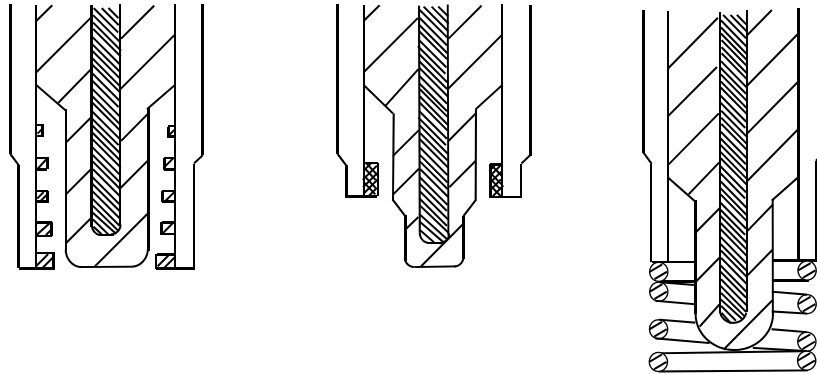
Figure 3: Exemplary designs of a Barrier Discharge Igniter (BDI).
From Left to right, Figures 3.1, 3.2 and 3.3
References [3] and [4].

Figure 3.1 [3] shows a design where the high voltage electrode is surrounded by a largely cylindrical insulator, with a cylindrical ground element spaced from this. An annular corona discharge is formed due to the high electric field formed between the insulator surface and the ground. Features on the ground, insulator or (with less effect) the central electrode may be added to reduce the voltage required to achieve corona discharge. This scheme has the following beneficial behaviours:

- Arc formation is impossible; calibration effort and control system complexity may therefore be reduced.
- The central electrode is not exposed and hence not subject to corrosion by combustion gas, nor to electrical erosion.
- The central electrode is completely covered and the ground "electrode" is, by virtue of the construction, at a low temperature. This avoids any high-load thermal problems which may affect other designs.
- Energy transfer from corona to gas is good, although this may be partially offset by proximity to the insulator and ground.
- The corona may form simultaneously wherever the electric field is high and may be maintained for the duration of the corona event, giving an increased probability of ignition.
- The location of corona formation is controlled by the plug design and known in advance. Extra space around the igniter for corona formation is not required.

Naturally, these benefits must be considered in light of some disadvantages:

- To achieve sufficient electric field, this type of design requires a higher drive voltage than those discussed above. This means that the system has a higher energy requirement which impacts the entire power supply chain.
- Large exposed insulator cross section can lead to high forces on the insulator from motion of combustion gasses. Mechanical design requires care.
- The ignition location is not optimal:

- o In the plug of Figure 3.1, corona formation takes place in the plug counterbore region which is retracted from the main combustion chamber. The early flame must propagate out of this region before the main charge can be burned.
- o Figure 3.2 [3] shows a scheme designed to reduce this limitation, where the extent of the ground electrode is limited and the corona location is projected as far as possible towards the chamber. Some additional benefit is achieved by the shape of the insulator near the tip. The situation is improved but ignition is still between electrodes and with limited projection from the metal walls of the plug.
- o Figure 3.3 [4] shows another scheme to overcome these limits. In this case the ground electrode, which may have various forms, is projected into the combustion chamber. Again, there is some limited improvement but this time at the expense of thermal performance: an electrode which is slight enough to present no impediment to the flame will also be very difficult to keep cool, especially at high load.

Note that an alternative scheme is similar to Figure 3.1 but has the insulator covering the ground electrode and the air gap immediately adjacent to the central electrode [4]. This scheme is less common as it is prone to arcing from the central electrode to other grounded engine parts, reducing its effectiveness.

1.4   Pulse Design Igniters

These designs, such as represented in Figure 4 [5], generally have (but are not required to have) open electrodes exposed to the combustion chamber. To create ignition a pulse at very high voltage is applied to an electrode which ionizes the gas in the combustion chamber, either between a single electrode and the walls of the combustion chamber, or between relatively widely-spaced electrodes. The length of the pulse must be extremely short, in the order of tens of nanoseconds, and is controlled to avoid arc formation.
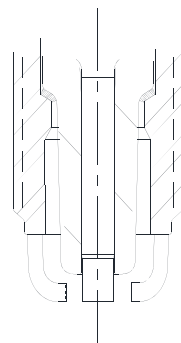
Figure 4: Exemplary Pulse Design Igniter.
Reference [5].

This system is beneficial because:
- Ignition over a large volume is possible, leading to the possibility of near-optimal combustion.

- Calibration effort is reduced due to the inherent resistance to arc formation.
- Avoidance of arc also allows the system to have minimal electrical erosion of the electrodes.
- Energy transfer to the gas is good, leading to the possibility of a highly efficient system.

However, there are some obstacles to adoption:
- To deliver large ignition volumes, a very high voltage pulse is required. With more conventional voltages (20-30kV), the size of the ignition source is greatly restricted (for example, 1.5mm gap between electrodes).
- Delivery of the extremely short pulse required can be very difficult and systems capable of this are technically immature. There may be difficulties in packaging and durability of the system.

2 Optimisation of Streamer Plug Designs

Previous designs favoured by Federal-Mogul have mostly been of the "streamer" type. These plugs have the multiple benefits of excellent ignition performance, relative ease of driving circuit design, and similarity in construction to conventional sparkplugs. This latter advantage is especially important if a product is to successfully transition from the test environment and into the mass market. The advantages to be gained by using spatially extended corona igniters are well known [6, 7, 8], and methods of implementing such systems have been previously developed [9]. Critical to the success of any such system is the ability to manage the ever-increasing thermal loads presented by modern engine developments, and to manage high electrical stresses in order to meet the desire for smaller plug envelopes in future engines.

2.1 Thermal Optimisation

Consider for this discussion the designs of long reach m12 with a flat external gasket seat, as this plug represents the current design most widely adopted in the automotive marketplace. The considerations presented here are applicable to plugs of every different thread size.

Initial designs were coloured heavily by the electrical requirements of the system; specifically the requirement for high dielectric strength and low capacitance of the high-voltage components which translates directly into a higher system efficiency. These designs had the following common features:
- The smallest possible central electrode diameter, allowing the insulator to be thicker and so increasing dielectric strength and reducing capacitance.
- The largest possible insulator diameter, for similar reasons.
- Omitting the lower internal seat of the insulator, which again allows a thicker insulator to be used in the critical region inside the thread body. This may be achieved by:

- o   Seating the insulator in the larger body of the shell, instead of inside the thread body.
- o   Alternatively, by using an interference fit between shell and insulator [17].

In addition, alternative insulator materials may be used. Conventional sparkplugs use alumina due to its well-known thermal, electrical and mechanical properties, coupled with its wide application and manufacturability. But other materials are possible in an effort to reduce capacitance, most notably boron nitride, which allows a considerable reduction in capacitance of the plug.
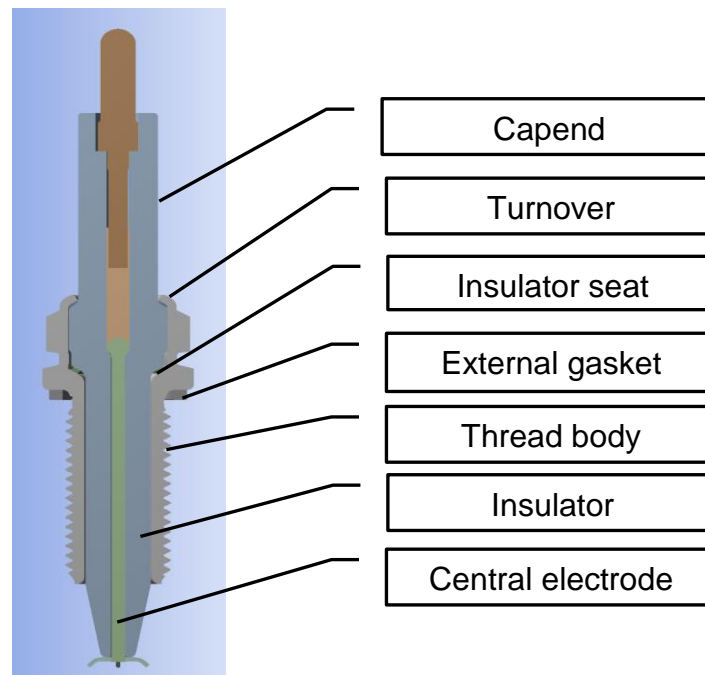
Figure 5: Early Igniter Design
Optimised for Electrical Performance

Figure 5 shows an igniter with these features. This design has a small-diameter central electrode (typically 1-1.5mm diameter) surrounded by alumina insulator (typically 8mm diameter), this electrode extending at this small diameter through the complete threaded portion of the plug. Owing to the small diameter, the electrode is of a single material, usually a nickel-based alloy. Addition of a thermally conductive core, usually a copper alloy, is possible but would result in only a small thermal benefit due to the very limited cross section which can be included. The insulator is seated inside the shell at the location of the larger diameter portion, in order to maintain maximum possible thickness. Portions of the design in the capend region are close to conventional sparkplug practice.

For illustration purposes, a heat load typical of a mass production engine of current design is applied, with a fixed metal temperature and a heat load representing around 100 kW/l, or IMEP of 20-25 bar, for example. This heat load does not represent a specific engine design, but can be used to compare between plugs in a qualitative manner; it has been previously demonstrated that this type of analysis closely follows the changes observed in testing of physical parts. Figure 6 shows the temperature field predicted for a typical conventional sparkplug with this heat load applied.

Here the ground electrode, which has a copper core to assist in thermal control, reaches the highest temperature at around 820°C. The insulator reaches around 810°C and the central electrode, again cooled with a copper core, does not exceed 780°C. As a target for design, an insulator temperature in the range 750-850°C is desirable; this range is cool enough to avoid the possibility of preignition due to hot-spots on the surface, while hot enough to allow burn-off of combustion deposits. The metal electrodes may be safely operated close to 950°C but it is advisable for good durability to keep the electrode temperatures low and certainly under 900°C.
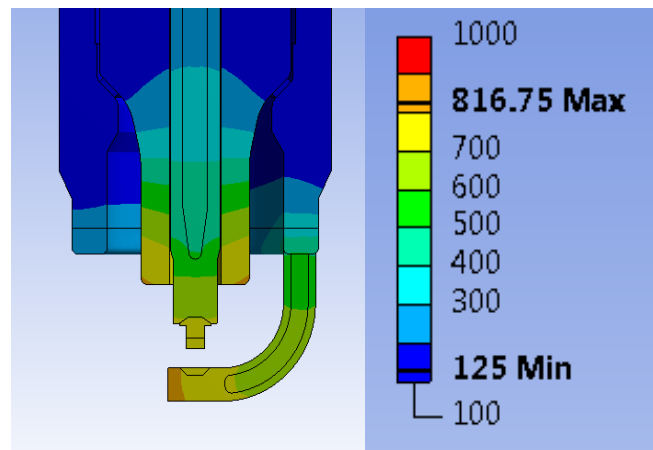
Figure 6: Example Spark Plug Thermal Field [°C]
Representative FEA load applied

Compare these results with the temperature field in Figure 7, representing the igniter design of Figure 5, having the same corenose length as the conventional sparkplug shown above. Temperatures throughout the firing end assembly are far too hot for safe operation: all components are well over 1000°C. Note that, in this analysis, the very high temperatures lead to a disproportionate cooling effect from radiation; at more realistic temperatures the difference between this and cooler designs would be even greater.
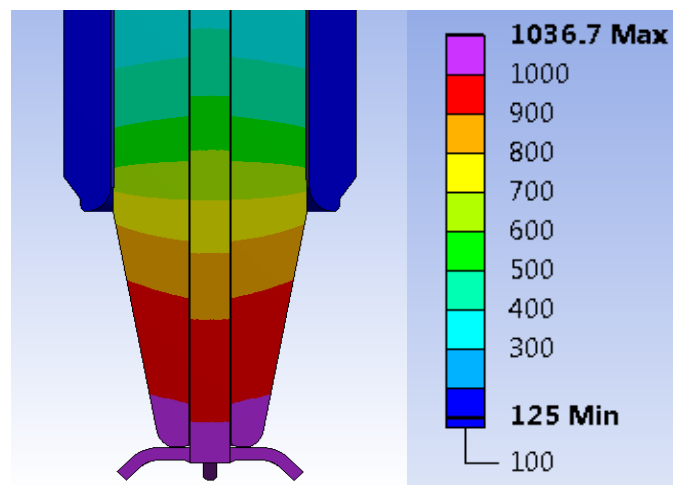
Figure 7: Early Igniter Design: Thermal Behaviour
Temperature [°C]

Although designs of this type were able to operate successfully in an engine, the specific output was limited to around 10-12bar IMEP due to the high operating temperatures at higher load. Steps were taken to cool the plug, for example by filling the gap between insulator and shell with a thermally conductive ceramic-based adhesive [10], but durability of such solutions was marginal.

An obvious first optimisation step is to include a copper core to cool the central electrode and hence star tip and insulator [11]. Due to the very limited amount of copper which can be added to a small diameter electrode, the electrode cross section is increased, even if this has some detrimental effect on parasitic capacitance and dielectric strength. Figure 8 shows how the temperature is affected with the same example FEA loading.
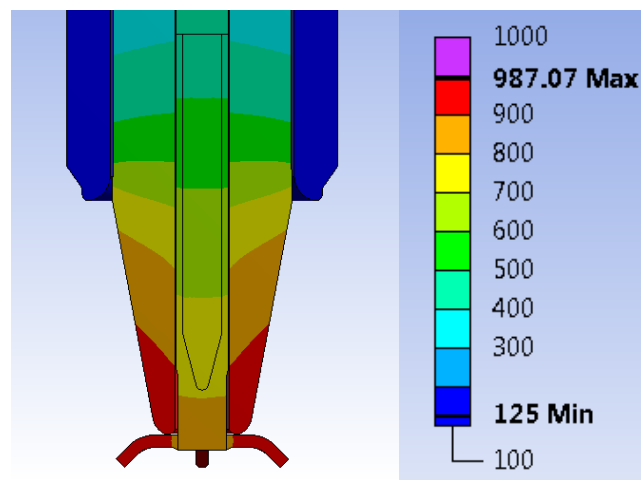
Figure 8: Modified Central Electrode [°C]
Copper-cored nickel alloy (lower portion) and solid copper (upper portion)

In this case it is clear that a very useful reduction in temperatures has resulted: the insulator peak is under 990°C while the star and central electrode fall to 965 and 890°C respectively. This is up to 100°C lower than the previous design and is a big contribution to a design suitable for higher output engines.

It is apparent from Figures 7 and 8 that there is a large temperature differential between the insulator and the shell in the portion of the plug close to the combustion chamber. The high temperature in the insulator in this region hampers design efforts to reduce corenose and electrode temperatures. A number of schemes can be devised to reduce this temperature difference, for example as shown in Figure 9.

In the upper image of Figure 9, the insulator is inserted from the top; an assembly method known as "forward assembly". The insulator diameter is reduced towards the combustion chamber end in order to provide a seat for the insulator to contact the shell. This provides good thermal contact and leads to a great reduction in insulator temperature in this region. A ceramic insert is placed between the shell and the insulator from below, bonded with a ceramic adhesive or by other suitable method [12]. This insert allows the insulator diameter to be effectively increased in this region and still allows assembly of the plug while helping to control parasitic capacitance. These modifications reduces the insulator to 920°C while the star and central electrode fall to 915°C and 785°C respectively.

348
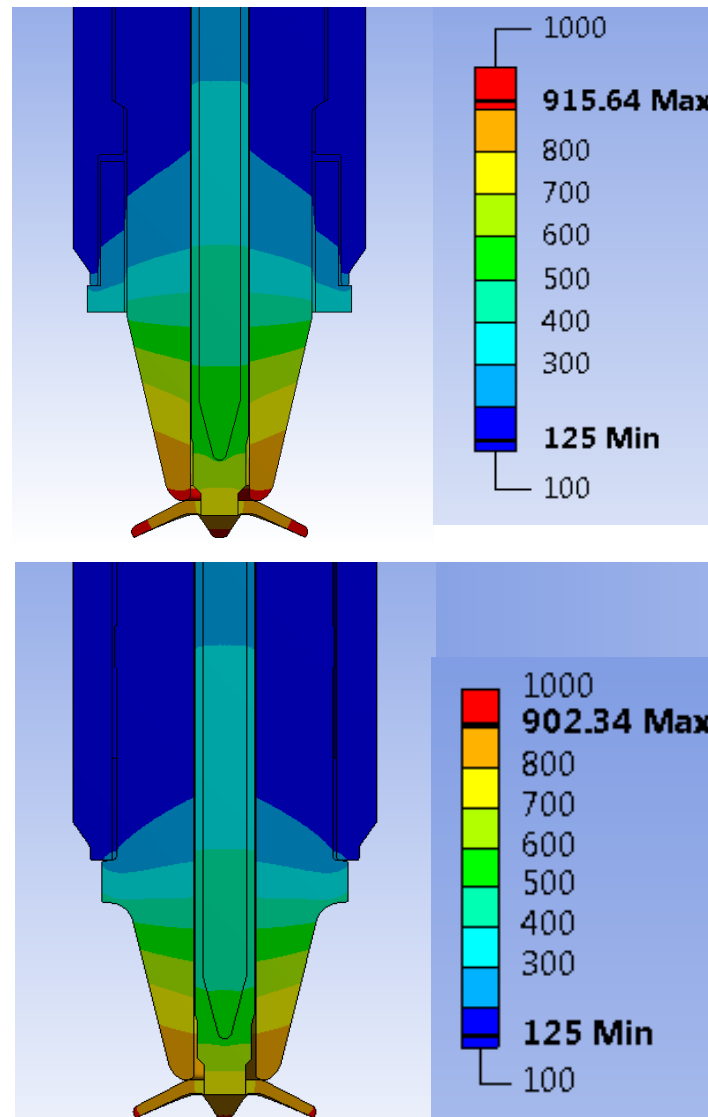
Figure 9: Modified Lower Insulator/Shell Connection [°C]
Upper Image: Forward Assembled with Insert
Lower Image: Reverse Assembled with Braze

Now the lower image of Figure 9 shows a different construction method known as "reverse assembly". In this case the insulator largest diameter is the flange at the base of the corenose which is coplanar with the end of the shell. Here the insulator is inserted into the shell from below and retained in the region just above the flange, typically by an intermediate part such as by brazing the ceramic to the shell [13]. There is no retention of the insulator at the capend which allows for reduced stresses and a simplified assembly. The excellent heat transfer from insulator to shell at the brazed joint, coupled with the fact that there is no reduction in insulator outside diameter at the joint, make this an attractive option. Temperatures in this design fall to 900°C for the insulator, and 900°C and 770°C for the star tip and central electrode respectively.

There are two final contributors to the high temperatures observed in streamer-type corona igniters: the high temperature rise across the thin star tips and the high insulator projection required in early designs.

Modifications to the star tips can give a useful temperature reduction, mostly leading to improved durability rather than safer high-load operation. Most notably changes to the diameter of the central electrode as it connects to the star, profile and material of the base star shape, the addition of thermally conductive star tips where the temperature is highest, and especially use of precious metal tips which have the twin benefits of high thermal conductivity and high resistance to corrosion/erosion, as is well known from conventional sparkplug design.

However, a more powerful solution for reduced temperature may be borrowed directly from conventional sparkplug design: shorter corenose length. Original designs such as that in Figure 5 were not optimal in respect of corona formation location, having a tendency to form corona over the surface of the insulator to the shell. To avoid this undesirable situation, the corenose was made longer than was thermally optimum. Careful development of the electrical design has reduced the need for this longer corenose and allowed this parameter freedom to be reduced, subject to analysis of corona formation in the combustion chamber, as previously described [9] elsewhere.
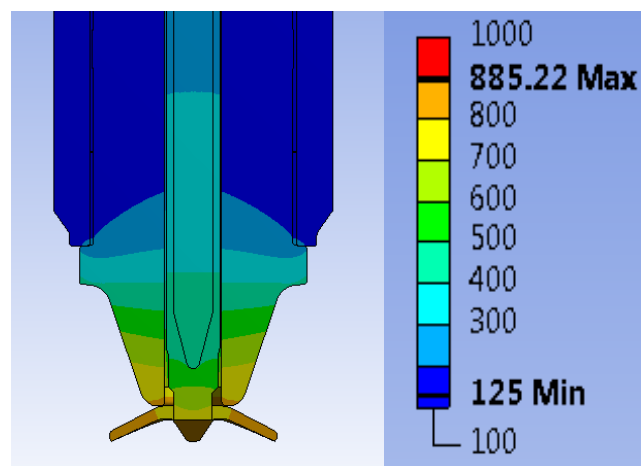
Figure 10: Reduced Corenose Length [°C]

Figure 10 shows the temperatures which may be achieved with this modification. Insulator temperature falls to 815°C with star tip and central electrode predicted at 885°C and 735°C respectively. All temperatures are in the optimal range. Plugs of this design have been shown to run safely at full power in an engine of 30 bar IMEP or more. Figure 11 summarises the optimisations and the results achieved. As mentioned above, design changes can bring all temperatures into the optimal range, but further modifications to star material and geometry can give an additional fall in star tip temperature if this is required to meet durability targets in a particular application.

Table 1: Cumulative Results of Thermal Optimisation

Plug Configuration				Predicted Temperatures [°C]		
Figure	Copper core central electrode	Reverse assembled	Shorter corenose	Insulator	Central Electrode	Star tip
6	Spark plug with copper core electrodes			809	778	817 (GE)
7	No	No	No	1036	1026	1037
8	Yes	No	No	987	890	964
9 upper	Yes	Insert	No	916	786	913
9 lower	Yes	Braze	No	900	770	902
10	Yes	Braze	Yes	813	735	885
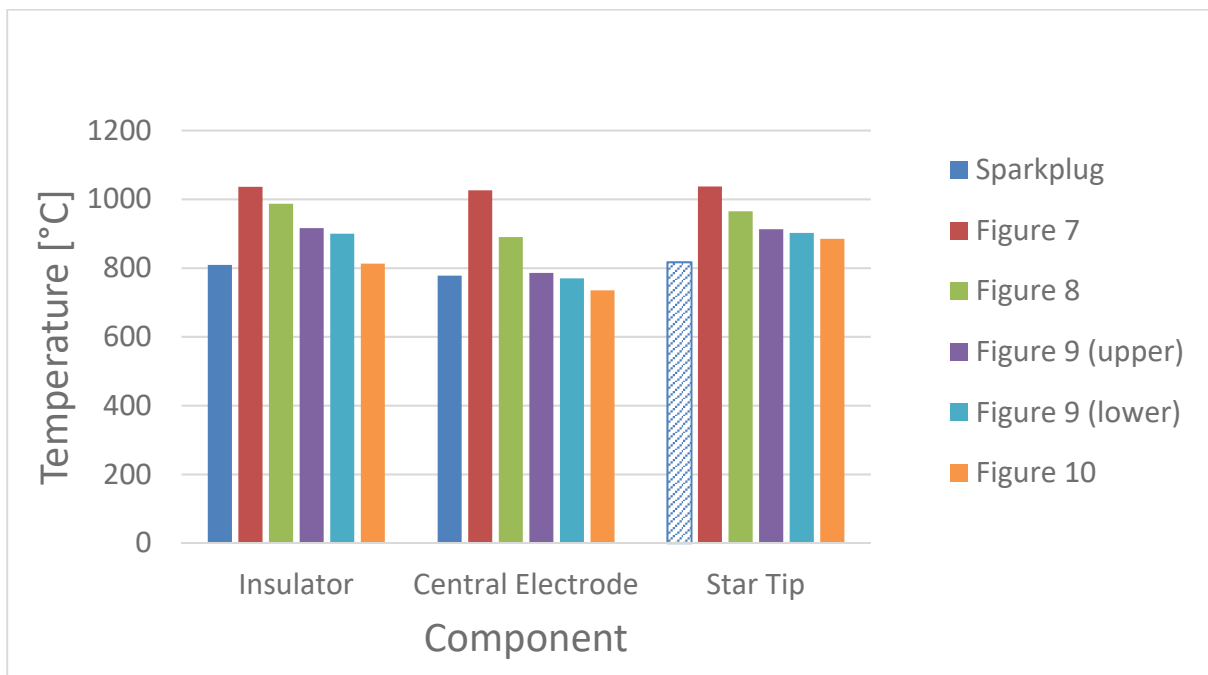
Figure 11: Cumulative Results of Thermal Optimisation
Graphical representation of data in Table 1
Note: sparkplug has ground electrode, not star tip

2.2   Electrical Optimisation

For a streamer igniter design, there are only a few requirements which must be met electrically:

1. For best ignition performance, the ignition location (here, the star tips) should be placed to allow the largest possible corona, depending on the combustion chamber geometry.
2. To ensure that corona is formed in the correct location, the electric field must be maximised in the air at this location i.e. at the igniter star tip in this case. To avoid wasting energy in corona produced at other locations which will not provide an ignition source, the electric field must be significantly higher at the star tip than in air surrounding any other location of the igniter.
3. To reduce the opportunity for corona formation over the insulator surface and subsequent arc formation, the gradient of the field over this surface should be managed.
4. To avoid failure of the igniter, the electric field in the insulator should be low enough that there is no danger of dielectric failure in service, taking into account the thermal and electrical loads encountered.
5. The above requirements should be met while capacitance to ground is minimised.

Each of these requirements is considered in turn below.

2.2.1 Location of Corona Formation

Methods to place the corona source correctly have been previously described [9] and can be summarised by saying that the corona should be located equidistant from all grounded surfaces at time of ignition. This will not be discussed further here.

2.2.2 Electric Field in Air

In order to satisfy the requirement for high local electric field, it is possible to create designs where a high voltage is applied in a small air gap in the igniter, usually in conjunction with a BDI or partially BDI-like design [14]. Corona can form in this small gap and then expand out towards the main combustion charge, either due to continued electrical energy addition, by in-cylinder gas motion, or by the onset of combustion. However, the approach taken here is to use one or more sharp tips to give a high field concentration, directly exposed to the combustion gas. The relationships controlling this high field are well known [15], in general requiring the sharpest possible electrode tip to give the best possible performance.

Figure 12 shows the total electric field at the tip of a streamer igniter design. This FEA result depends on the analysis method used and care must be taken in setting up the problem [16]. In this work a quasi-static analysis is used, with the electrode energised with 1V and the mesh size is fixed in all relevant areas of the model. This makes the results directly comparable between models and between different areas in the same model, and allows results to be directly scaled to give values for any applied voltage. In this case, the peak electric field is 3330 V/m with per volt applied. As the model is quasi-static and therefore linear, this may be restated as a geometrical parameter of the design by normalising for applied voltage, giving a "field concentration factor" of

3330 m^{-1} for this location in this design i.e. for every volt applied, the field here will increase by 3330 V/m.
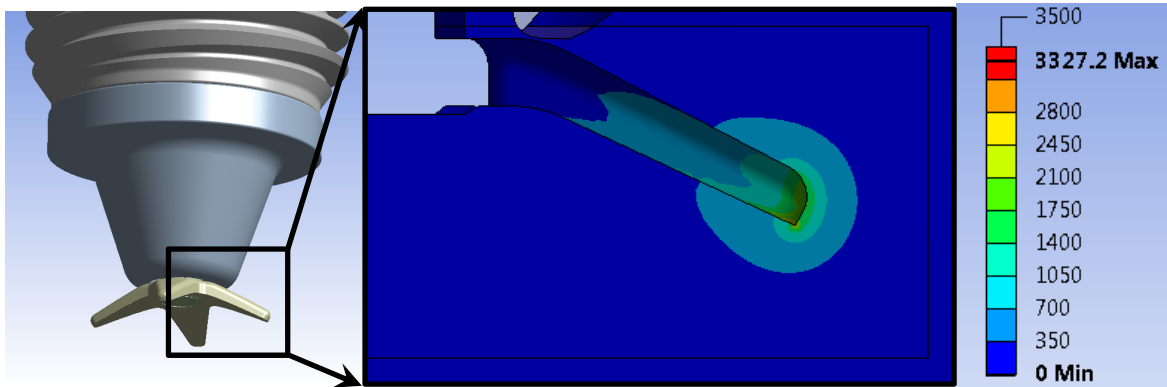
Figure 12: Electric Field Strength at Star Tip [V/m]
1V applied, fixed mesh size

Now in order to avoid having parasitic corona throughout the igniter, we must ensure that corona forms preferentially at the desired location. Corona can only form in ionisable materials which, in the case of corona igniters, means the air gaps in and around the igniter structure. Analysis of these air gaps shows where design changes can help reduce this parasitic corona and improve system efficiency. Figure 13 shows a section through the body of the igniter in cutaway view, cutting through the central electrode, insulator and shell. This igniter shows the features previously described for thermal control, with additional optimisation for brazed assembly: the cavity in this figure is used to help manufacturability of the product and guarantee a hermetic seal in the final assembly.
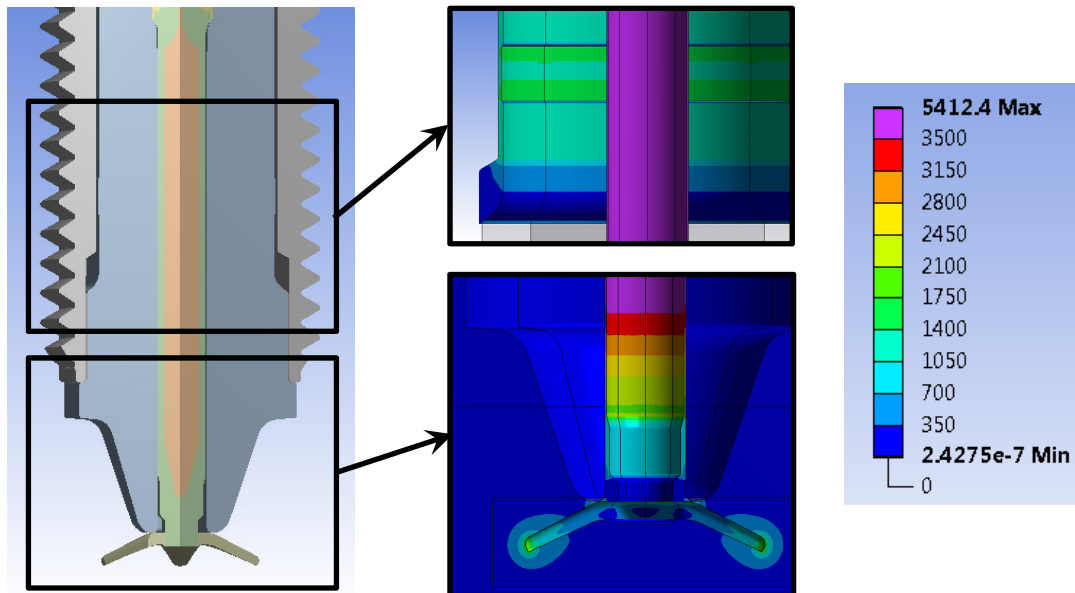
Figure 13: Electric Field Strength in Air Gaps in and around Igniter [V/m]
1V applied, fixed mesh size

Now considering Figure 13, it is desirable that the electric fields calculated in these air gaps are significantly lower than at the star tip as shown in Figure 12. Here we see two areas inside the igniter which need some modification:

- Between the central electrode and the bore of the insulator is a high electric field: up to 5400V/m giving a field concentration factor of 5400 m^{-1}. This is far higher than the field at the star tip (3330 m^{-1}) and is indicative of parasitic corona formation in this area during operation. As corona formation here will be adjacent to the central electrode which is exposed at the star tip, there is no associated danger of arc formation over the insulator surface, but this does represent a significant source of inefficiency as this corona will not contribute to ignition.

- Around the outside of the insulator, the field concentration factor is in the region of 1400 m^{-1} which is much lower than at the star tip and so is unlikely to cause serious problems. However, higher corona energy could still lead to parasitic corona formation in this area, so steps to reduce this would be beneficial.

There are a number of actions which could reduce this undesirably high electric field:

1. The gap could be completely closed by design [17].
    a. By co-moulding of the parts
    b. By interference fit
    c. By bonding the parts together e.g. by chemical bonding
2. The gap could be filled with a non-ionisable material [10].
    a. By an insulator such as epoxy or ceramic adhesive
    b. By a conductive material such as solder, braze or an organic or inorganic filler loaded with conductive material, for example carbon.
3. The surfaces could be coated in a conductive material such that each side of the gap is electrically connected, preventing the formation of a potential difference and hence an electric field [18].
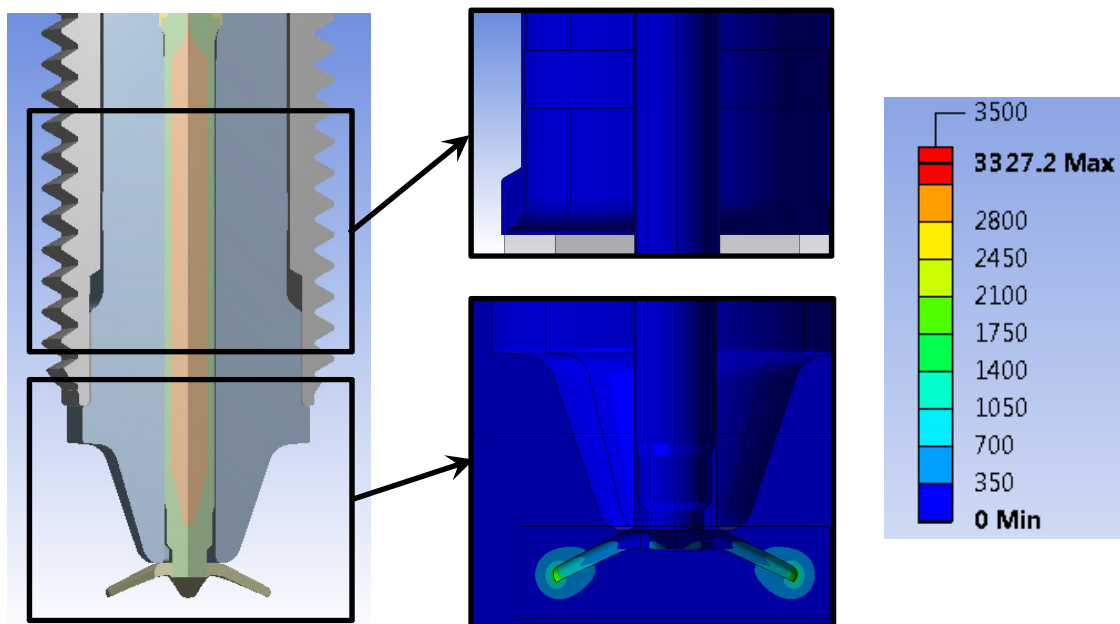
Figure 14: Electric Field Strength with Conductive Coating on Insulator [V/m]
1V applied, fixed mesh size

After considerable FEA and experimental work, it was determined that the most successful solution is to coat the insulator surface with a conductive material. This solution has excellent durability, has almost no effect on the construction process and has no impact on the thermal and mechanical performance after assembly, problems which affect many of the other solutions. The type of coating used in each area does not need to be the same and depends on local conditions [18]: for example the high temperature close to the combustion chamber may require a metal-based coating, while the upper areas of the capend can be treated with a simpler and cheaper carbon-based alternative.

Figure 14 shows the electric field throughout the igniter with the addition of these coatings. Clearly observed is the complete removal of the possible locations for parasitic corona formation within the structure of the igniter. This technique may be applied throughout the igniter assembly: not just in the "spark plug" component, but also in the coil and any connection between the two.

2.2.3 Corona Propagation over Insulator Surface

It is possible for corona to break down into an arc between the high voltage electrode and the grounded engine structure, which leads to all the energy being shunted into a single path, causing a large drop in corona volume and commensurate fall in ignitability performance. This is especially likely over the surface of the insulator where the field required for propagation is lower [19] and may be further reduced by combustion deposits or fuel wetting on the insulator. Ideally this would be achieved by making the field concentration factor very low in all locations except at the star tip. Figure 14 showed how it was possible to reduce electric field in the air gaps inside the igniter to almost zero. However, this method clearly cannot be applied to the corenose of the insulator where a high electrical insulation between central electrode and ground is required. Figure 15 shows the electric field specifically at the root of the corenose, at its interface with the shell, showing (at top) a field concentration factor of around 1530 m^{-1} in the case where the part is perfectly manufactured, rising to 2440 m^{-1} when there is a gap of just 25μm between the flange and the end of the shell (at bottom);

1538V/m
With no gap

2437V/m
With 25μm gap
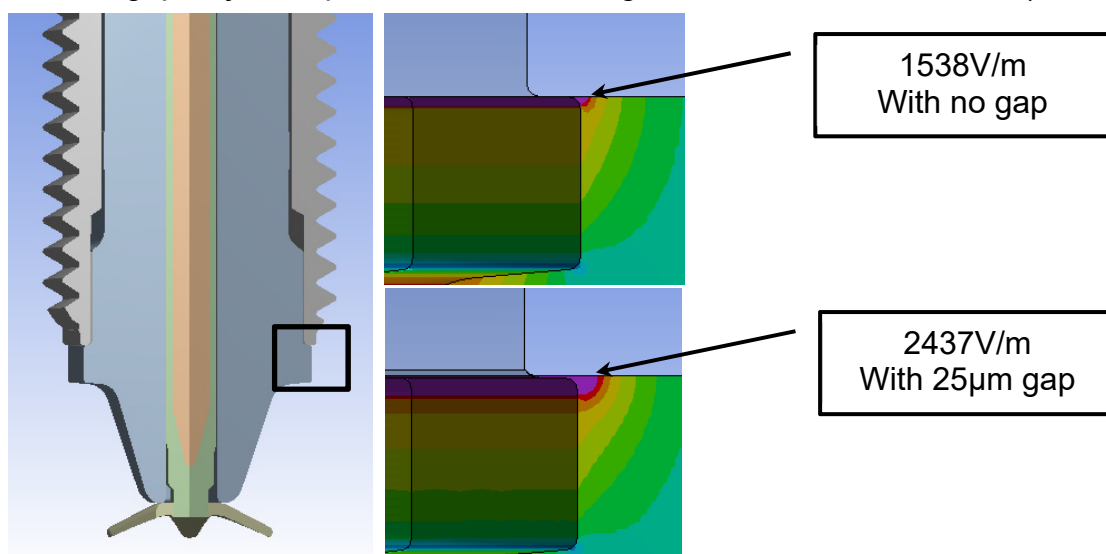
Figure 15: Electric Field at Insulator Corenose Root [V/m]
1V applied, fixed mesh size
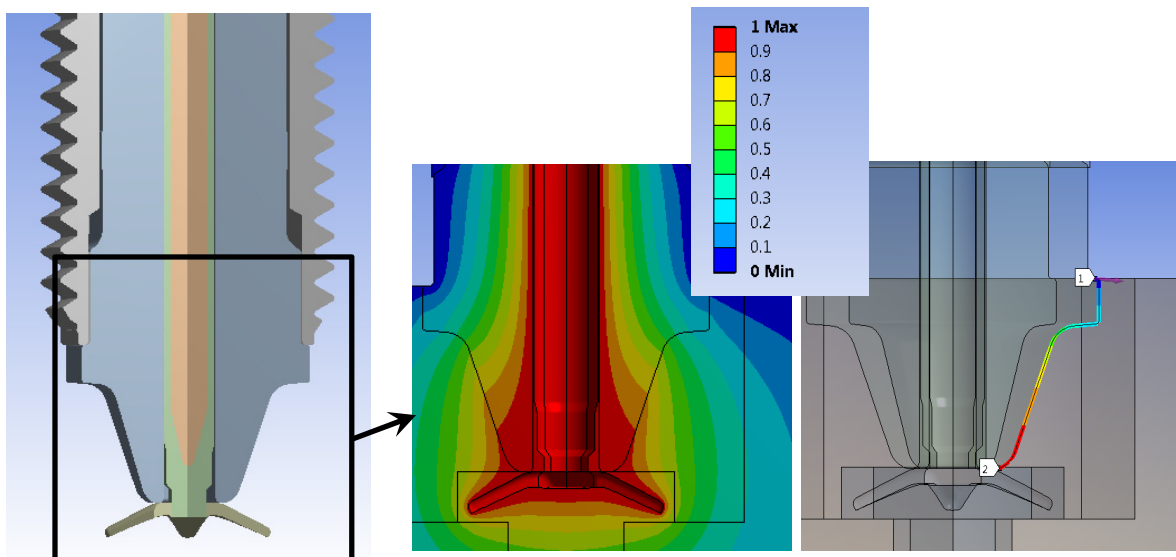
Figure 16: Voltage at Insulator Corenose Region [V]
1V applied, fixed mesh size

compare these values to 3330 m^{-1} at the star tip and it is clear that some corona formation might be expected here at higher voltages in real igniters.

Corona formation in the air around the igniter is driven by the total electric field, as discussed above. However, once this corona has formed, its propagation over the insulator surfaces is controlled by electric field in the direction of the surface, which requires a special method of analysis. Figure 16 shows a detail view of the corenose region of a corona igniter previously discussed in Figure 14. In this figure the possible path for arc formation over the insulator is identified (between "1" and "2" in the right image) and the voltage along this path plotted. If the electric field is evaluated in the direction of this surface, it is possible to evaluate the propagation of corona [9].

Consider the situation at the interface between shell and insulator at location "1" when a positive voltage is applied at the central electrode. Once a high electric field has ionised the surrounding air, the positive ions are immediately attracted to the grounded shell, leaving a cloud with negative charge. This cloud is attracted to the positive central electrode but cannot move directly due to the interposed insulator; it therefore propagates over the surface of the insulator so long as it is moving in the direction of increasing voltage, that is: positive electric field. If the corona can propagate all the way to the central electrode, an undesirable arc will form. To avoid this, the shape of the insulator is carefully designed to ensure that the gradient of electric field measured in the direction of the surface, is not conducive to this arc formation [9]. Of course, this does not prevent arc formation in the free air of the combustion chamber; this must be addressed, as in section 2.2.1, by proper placement and geometry of the igniter.

In Figure 17 we see an evaluation of the electric field over the surface of the insulator between "1" and "2" as defined above, starting from the shell and finishing at the central electrode. This figure shows how the negatively charged corona formed as described above is unable to propagate over the surface of the insulator due to the reversal of electric field created by the flange at Y=0.1mm. The flange has a number of beneficial effects:

- It increases the distance over the corenose, reducing the chance of arc formation and fouling. In this design, around 1.5mm is added to the distance over the surface.
- It creates a field reversal as shown in Figure 17 which prevents propagation of corona over the surface and prevents arc formation. The flange need not cover the end of the shell; the angle and length of the sides of the flange is important but the extent need only be small. Here it is less than 0.4mm and covers less than half of the shell firing face, but performance is excellent.
- There is a secondary reduction in field at Y=1.5mm which is often enough to arrest corona propagation (depending on applied voltage), giving increased arc protection.
- It provides a mechanical limit for the insulator during "reverse assembly" which sets the geometry of the firing end accurately.

These benefits allow a shorter corenose to be used which allows greater freedom in locating the corona inception point, increased ability to maintain compression ratio by keeping the igniter away from the piston, and allows operation at a higher specific load than would otherwise be possible due to improved thermal management.
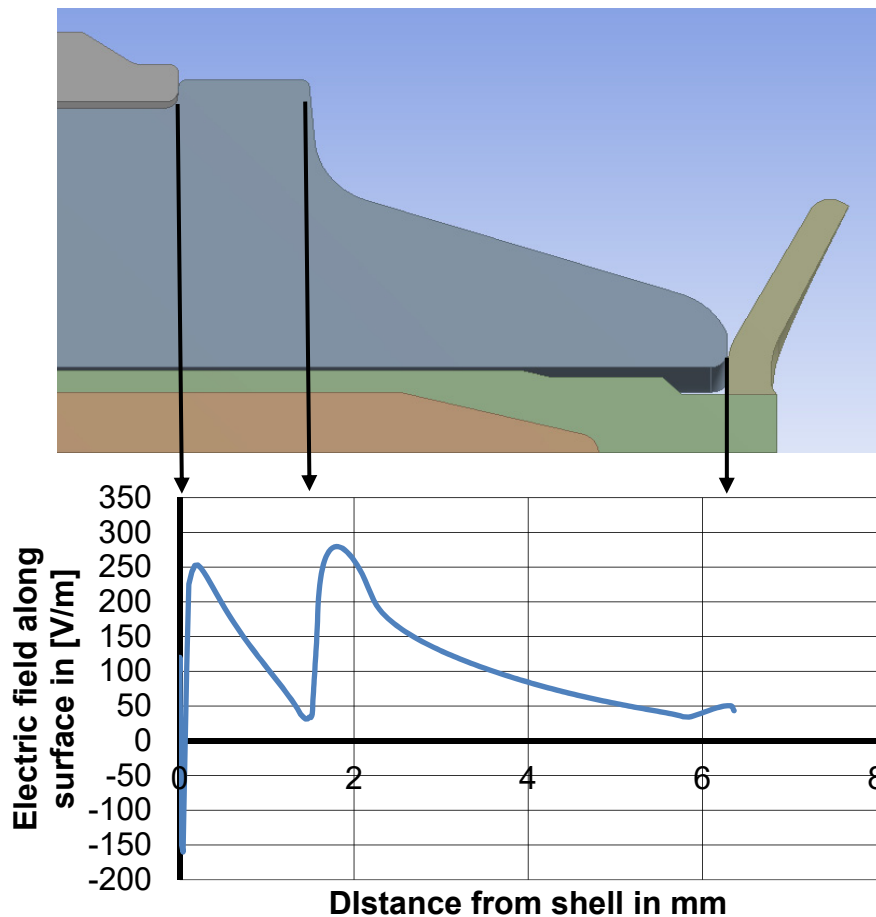
Figure 17: Electric Field over Insulator Corenose Surface [V/m]
1V applied, fixed mesh size

357

2.2.4 Electrical Safety of Insulator

Development of an insulator design for a corona igniter is based heavily on extensive experience when using similar materials in sparkplug applications. The dielectric strength of alumina insulators depends on a number of factors:

- Composition and structure of the insulator material.
- The average electric field; that is, the voltage across the material divided by the thickness of the material.
- The presence of any local stress-raisers which lead to locally high electric fields in or adjacent to the insulator.
- Material thickness; since ceramic materials always contain defects in their structure and failure may be described statistically based on the number and distribution of such failures in the sample. The result is that the strength per mm decreases as thickness increases, even if the actual strength is still increasing.
- High temperature reduces ceramic strength as it approaches the softening temperature of the glass phase in the alumina. Careful composition of the material reduces this but it cannot be eliminated.

For a typical sparkplug geometry, these factors result in a dielectric breakdown strength of around 16kV/mm for a standard production alumina ceramic under operational conditions. Using this as a limit for corona igniter design has proved reasonable in testing performed internally, since the frequency and pattern of application of the high voltage has not been shown to alter this result significantly.
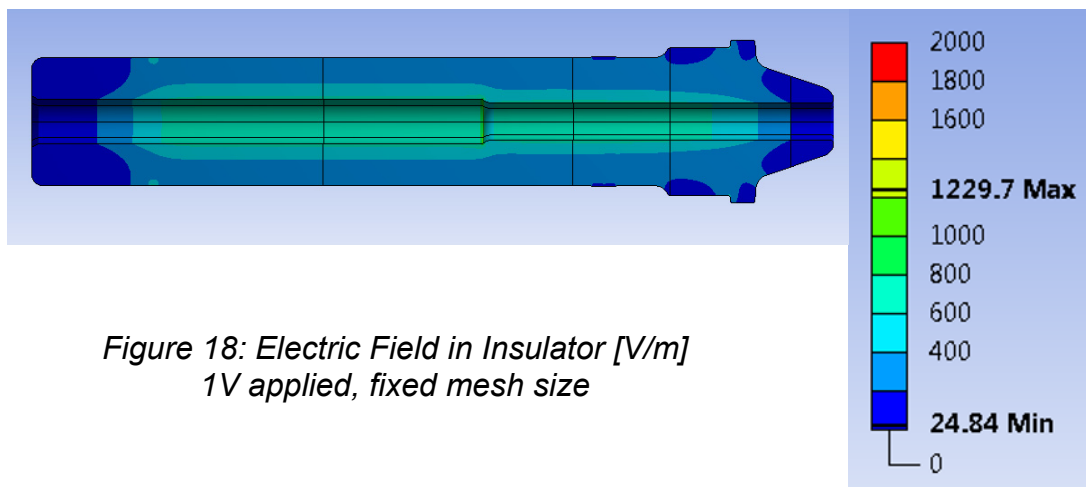
Figure 18: Electric Field in Insulator [V/m]
1V applied, fixed mesh size

Figure 18 shows how electric field in the insulator varies with 1V applied. The average field in the insulator is 386V/m meaning the bulk breakdown strength would be around 84kVpp. Local peak values close to the insulator bore are 480V/m, which is not high enough to significantly reduce this estimate. A local maximum of 1230V/m occurs at the central electrode head and this reduces the estimate slightly to around 75kVpp. No insulator failures have been noted in this region with igniters of this design, indicating that the analysis is valid and allowing the calculation of a worst-case safety margin of around 15-25% over lifetime and operating range, based on known existing engine operating maps

2.2.5 Control of Parasitic Capacitance

Many of the steps taken above, while necessary, lead to a higher parasitic capacitance and a reduction in electrical performance of the system. The initial design of Figure 7 had a firing-end capacitance of around 7pF when manufactured in boron nitride. However, this material had mechanical difficulties as well as an ability to absorb moisture, making it unsuitable for use where the target engine must perform cold starting. In conjunction with improved manufacturability, this led the adoption of alumina as the material of choice; this change caused the capacitance to increase to around 17pF.

Features which increased capacitance during the design optimisation include:
- Use of alumina ceramic.
- Adoption of a thicker copper-cored central electrode.
- Use of a lower internal seat in the shell.
- Conductive coatings for control of parasitic corona formation.

But these increases were offset by additional design changes:
- Larger shell bore allowing larger insulator diameter.
- Subsequent removal of the internal shell seat with the adoption of "reverse assembly" construction.
- Reducing the length of the capend portion to cut down the amount of high-permittivity alumina in the design.

Cumulatively these changes result in an increase from 17pF to 19pF total capacitance of the firing end. Now the total capacitance connected to the high voltage tip is the parameter which controls the system behaviour. This total capacitance includes not only the firing end but also the output side of the coil and any connection between the two. In designs suitable for installation in automotive engines, the total parasitic capacitance is in the region of 35pF from all sources. In this context, an increase of around 2pF represents only 6% which is an acceptable increase in view of the improved mechanical and thermal robustness which can be achieved.

3 Igniter Downsizing

As previously mentioned, there is a desire in the marketplace for plugs of ever-smaller dimensions in order to facilitate the implementation of direct injection strategies, more complex valvetrains, and to help facilitate the cooling required for increasd specific output. While the designs above may easily be expanded to make larger plugs with 14mm or 18mm thread bodies, reducing the size presents different challenges:
- Thermal management becomes difficult as the projection into the chamber must be maintained for good ignition, making the corenose long and thin. In conjunction with the limited diameter central electrode this can make the plugs run hotter than optimal.
- Smaller insulator diameter leads to reduced dielectric strength and increased loss due to parasitic capacitance.
- The connection between the firing end and the rest of the igniter assembly becomes difficult as there is a very high electric field across the upper end of the insulator which increases as diameter decreases.
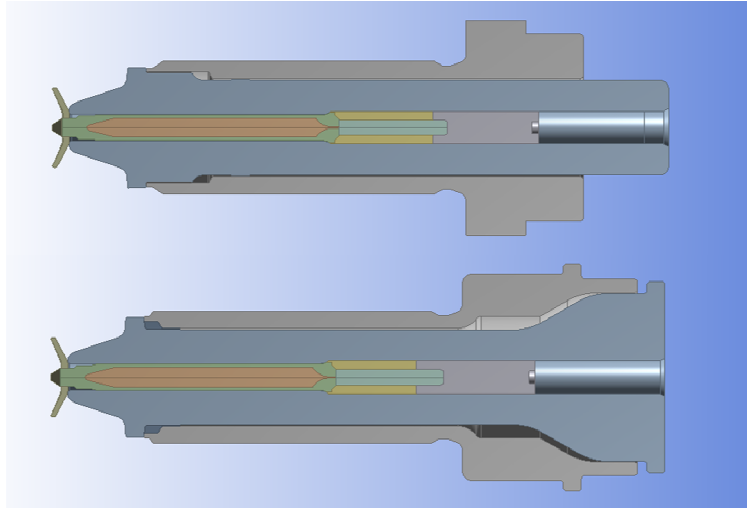
Figure 19: m12 "Barbell" Design for Size Reduction

Consider a possible solution to some of these problems, implemented in a 12mm thread body, and shown in Figure 19. The upper image shows the optimised "reverse assembly" part as previously discussed (previously in Figure 10), while the lower image shows an example of the "barbell" design developed specifically for small diameter variants [20]. This has the following features:

- Insulator corenose shape is identical giving similar performance, including ignitability.
- Insulator diameter is slightly reduced under the corenose flange leading to a possible increase in capacitance. This is offset by the larger diameter insulator at the "capend" region.
- Assembly is still similar to "reverse assembly" in that the insulator is held in a single region close to the firing end of the shell, affixed as before by a hermetic seal such as solder, brazing or similar.
- The shell is formed around the insulator by a specially-developed process, designed to install the insulator into the shell without mechanical stress.
- The "capend" of the insulator has a large diameter, both to reduce parasitic capacitance and to increase the electrical strength of this connection.
- In this case, the central electrode is unchanged between designs, giving near-identical thermal performance.

This design allows the possibility of reduced diameter, either with the same central electrode for similar thermal performance, or with a specially-developed smaller diameter central electrode to give improved electrical performance. Figure 20 shows an example of such a design, both the computer model and the physical parts, with Table 2 showing the performance which can be achieved, taking the optimised plug of Figure 10 as a baseline.
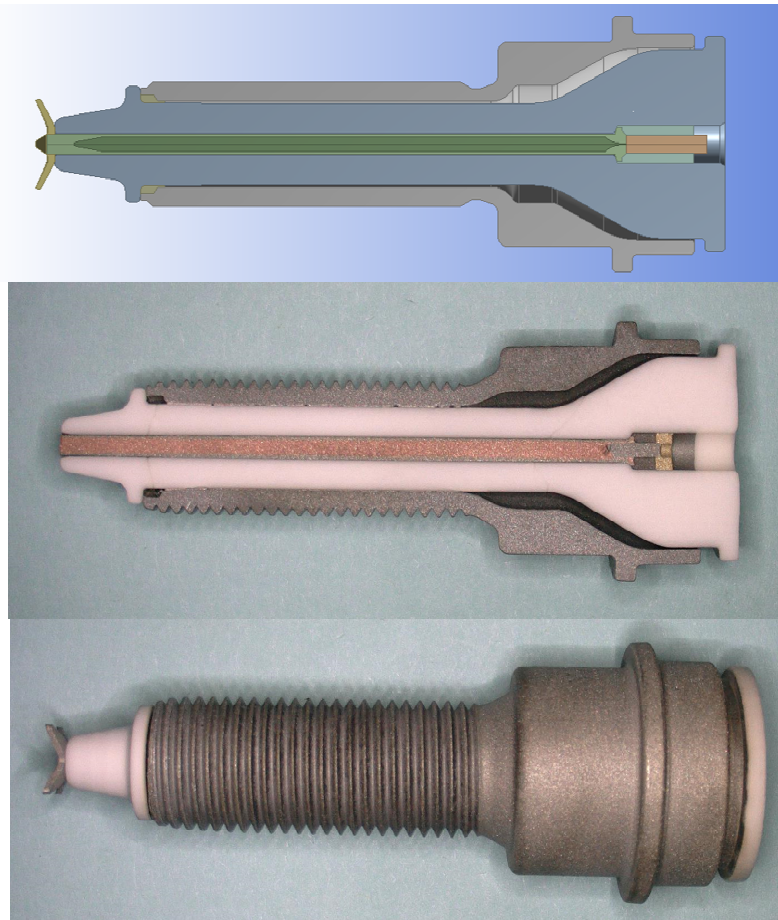
Figure 20: m10 "Barbell" Design for Size Reduction

Table 2: Thermal and Electrical Performance of Downsized Igniter

Design	Star temperature	Insulator temperature	Demand voltage	Dielectric strength (insulator)	Dielectric strength (connection)	Parasitic capacitance
m12 reverse assembly	100%	100%	100%	100%	100%	100%
m12 barbell	100%	100%	100%	100%	394%	110%
m10 barbell (cool)	+11°C ≈102%	+51°C ≈107%	100%	83%	394%	133%
m10 barbell (hot)	+26°C ≈104%	-1°C ≈100%	100%	100%	394%	96%

Notes:

- The "cool" m10 barbell has similar central electrode to optimised m12 design. This controls the central electrode and star temperature at the expense of dielectric strength and capacitance. The thinner insulator corenose section leads to higher local temperature. This may be addressed in electrode design.

- The "hot" m10 barbell is as shown in Figure 20. A small diameter electrode improves electrical parameters, while a specially-developed copper core process offsets the temperature increase. Insulator temperature is additionally controlled by details of the electrode design.

Analytical and experimental work has shown that corona igniter plugs having a 10mm thread body may be manufactured and operated with only a very small penalty in performance. Specially-developed components and assembly methods allow the designer to overcome the potential shortcomings of small diameter igniters in order to achieve electrical behaviour equal or superior to larger diameter plugs, and control the thermal changes to give equivalent temperatures in most locations and only a very modest rise in electrode tip temperature. This work shows the feasibility of downsizing the igniter into a 10mm package.

4   Alternative Solution: BDI

Previous work above has concentrated on the streamer design igniter as this offers excellent ignitability with good system efficiency. As described in section 1 above, BDI plugs offer reduced calibration complexity, elimination of electrode wear, improved thermal management and a relaxed requirement for space envelope in the combustion chamber. This must be offset against a reduction in ignitability (compared to streamer plugs) and a higher power requirement. So the BDI designs discussed above have some potential benefits, provided the efficiency and ignitability is sufficient for engine operation.

The strategy employed to address these problems is three-fold:
1. Expose the insulator corenose as much as possible to the combustion chamber gas to place the insulator surface at a good location for combustion initiation.
2. Deliberately introduce a region of high electric field outside the insulator in order to allow corona inception at an acceptable applied voltage level.
3. Manage the electric field on the insulator surface to ensure that this corona can propagate over the insulator and into the combustion chamber to give best ignitability.

4.1   Electrical Design Process

4.1.1 Expose Corenose to Combustion Gas

Section 1 shows BDI igniters of typical design which have an insulator surrounded by an annular gap and then a grounded surface, allowing the formation of corona in the annular gap. The corona pattern typically generated fills the annular gap with corona but there is little or no projection into the cylinder. Designs have been proposed [3, 4] to improve this but with limited application. Now a design of Figure 21 might provide enhanced ignitability if the surface of the insulator could be covered in corona.
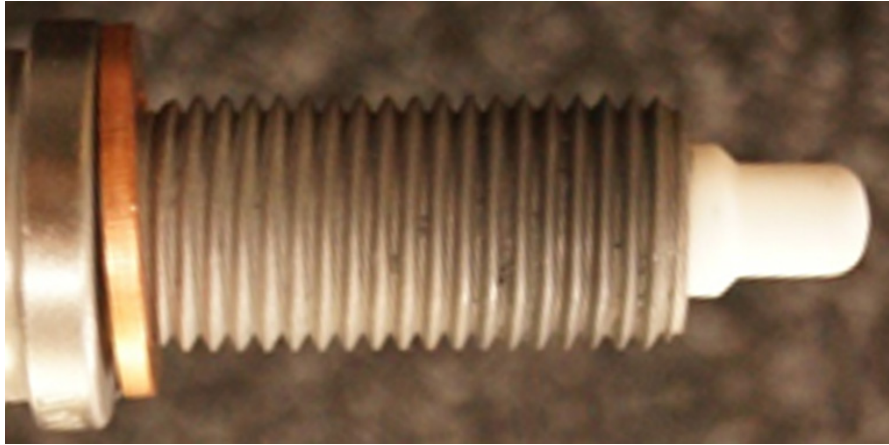
Figure 21: BDI Igniter with Exposed Insulator
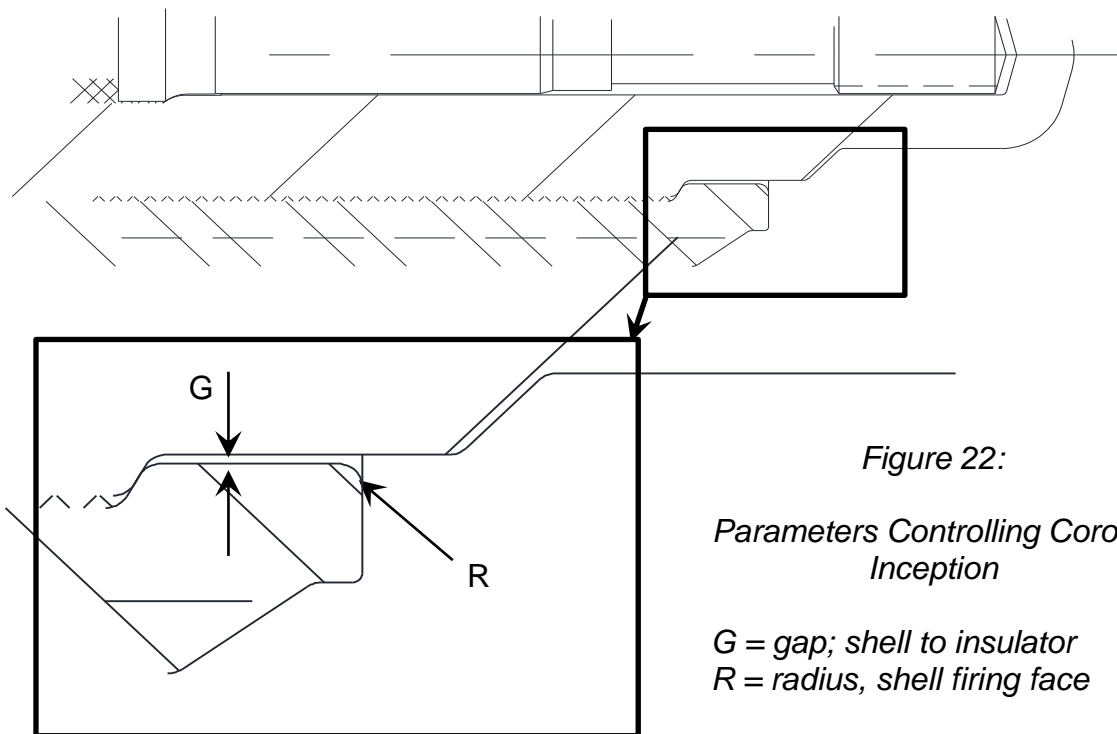
Figure 22:

Parameters Controlling Corona Inception

G = gap; shell to insulator
R = radius, shell firing face

4.1.2 Corona Inception Voltage Control

Steps were taken while designing the streamer plug to prevent the formation of corona except at the tip: reduction of gaps, use of conductive materials, adding features to create a field-reversal to arrest corona propagation. Now the knowledge of those steps allows us to design a BDI plug where corona is deliberately encouraged to occur at a known location and at a known applied voltage. Consider a region around the insulator, where it emerged from the firing face of the shell, as shown in Figure 22. A small gap at G is deliberately created between insulator and shell, and is left open to the combustion chamber at R [21]. The voltage which must be applied in order to create corona may be completely controlled by the geometry in this region; inner and outer diameters of the insulator, the size of the gap G and the radius R of the fillet at the end of the shell. These parameters may be solved analytically or by FEA in order to achieve

corona formation in the desired voltage range, while keeping within the tolerances possible for mass production.

4.1.3 Propagation of Corona over Insulator Surface

Methods for analysis of this propagation have been previously described [9] and applied is Section 2.2.3 above. However, the previous target was to prevent the formation of an arc discharge by preventing or interrupting propagation; here the aim is to promote this propagation. In order to achieve this goal we must ensure that the electric field over the surface of the insulator has the same direction at all locations and is of sufficient magnitude to encourage this propagation. Practically, it may be recognised that this means we will observe a steadily rising voltage over the insulator from root to tip. Figure 23 shows the analysis for the plug of Figure 21 and the result of physical testing. It can be seen that the voltage does not rise from tip to root (with the voltage very close the shell omitted due to high local electric field) as there is a reversal at the arrowed section, and the photograph shows that the corona does not propagate beyond this point. Note that the horizontal graph axis is distance over the surface and therefore is longer than the actual projection of the plug into the chamber.

Addition of sufficient corona energy will eventually allow corona to reach the tip due to the effect of the presence of conductive corona on the surface which changes the shape of the electric field. However, it would be desirable to change the shape of the insulator to remove this restriction and allow improved propagation even at lower energy.
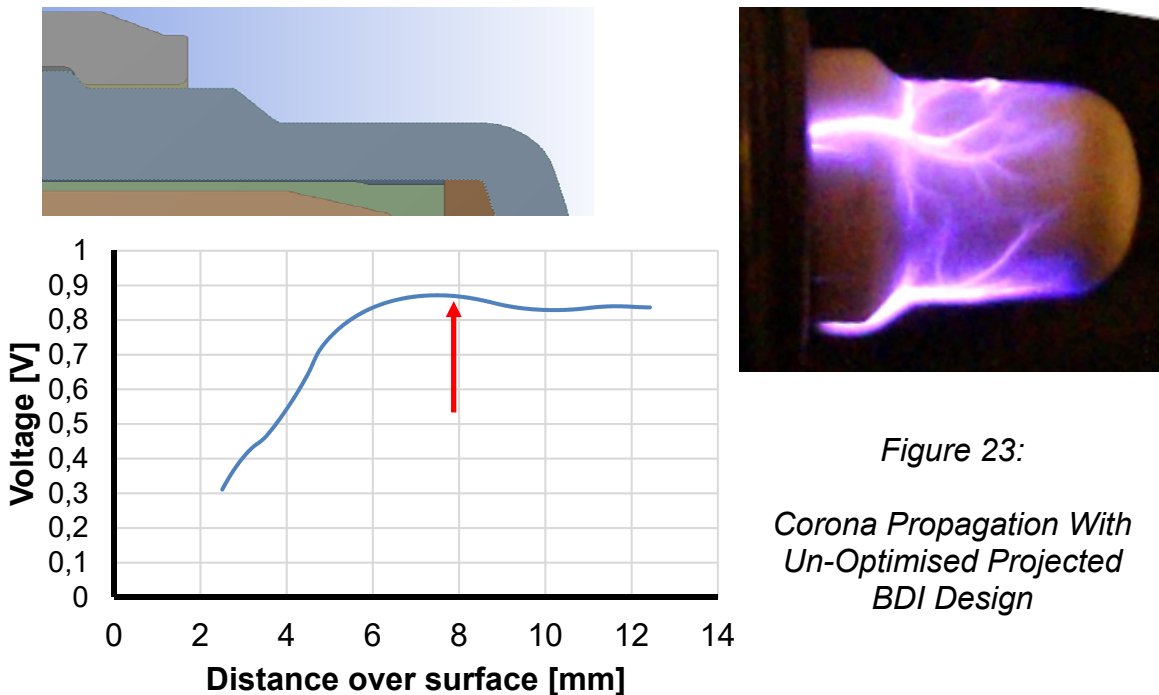
Figure 23:

Corona Propagation With Un-Optimised Projected BDI Design

It has been found that an expression may be derived which predicts if the corona will propagate to the tip of the igniter, based on the length and diameter of the insulator and central electrode, and on the parameters "G" and "R" from Figure 22 above. In addition, in cases where corona will not propagate to the tip, the distance of

propagation may be predicted based on a separate expression [22]. This gives two possible solutions for this problem:

1. Plugs with a low aspect ratio of the insulator, that is corenose length divided by corenose root diameter, are more likely to have good propagation. This allows for the solution where a "skirt" is added to extend the shell into the combustion chamber. This allows the effective corenose length, and hence aspect ratio, to be reduced and allow corona propagation to the tip without changing the location of the ignition. The length of skirt required may be calculated using the equations in reference [22].

2. In the case where this is not practical, it is possible to modify the insulator thickness, starting at a location defined by a predictive expression [22], so that the insulator becomes thinner towards the tip. This modifies the shape of the electric field in the desired manner.

Of course, one or both of these methods may be applied to the same design, since each requires different compromises: the first solution reduces the area of corona available to igniter the mixture, and may have high temperatures in the skirt of the shell; the second solution results in a reduction of insulator thickness at the tip and corresponding fall in dielectric strength in this area. Figure 24 shows examples of each of these solutions, side by side with the original un-optimised design for reference. Notice that the central image shows an igniter or BDI design but "reverse assembly" construction. This change is not material to the design of the plug for corona propagation, provided that the correct diameters are used in the evaluation.
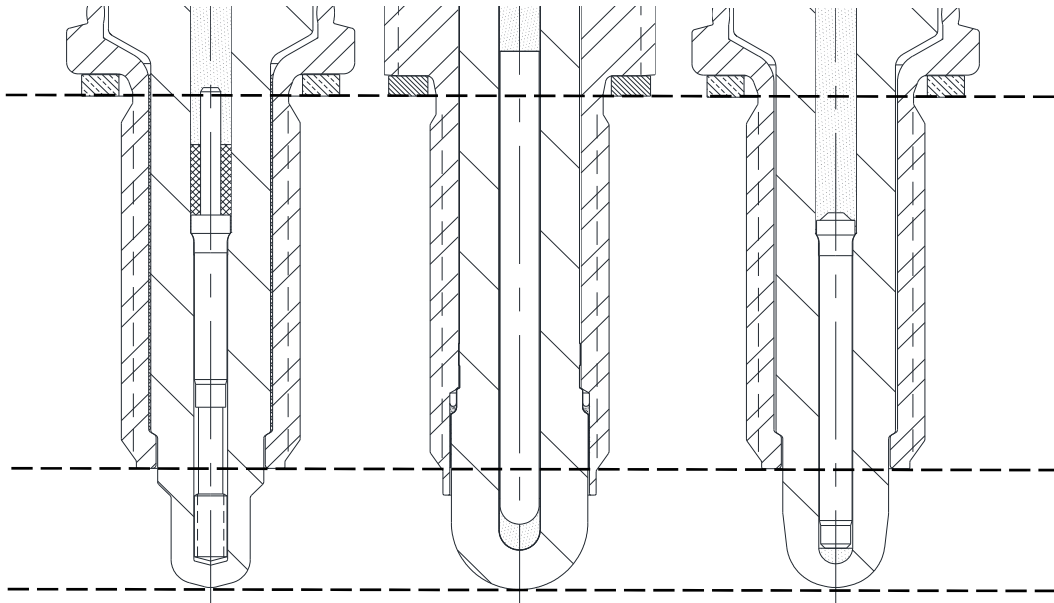
Figure 24: Optimised Projected BDI Designs

Left: un-optimised
Centre: with shell skirt
Right: with reduce insulator thickness

The solution of adding a skirt to the plug shell is trivial and is common practice in sparkplug design. The development here is the ability to know the length required and

the application of this technology to the corona igniter, not for thermal or vibration control (as in conventional sparkplugs) but in order to modify the electric field. Most interesting is the solution with a reduction in insulator thickness towards the tip, and the results of such an optimisation is shown in Figure 25. With the same applied voltage it is possible to form more corona and for the corona to propagate further into the combustion chamber. This design would be expected to provide a superior ignition source when compared to earlier designs.
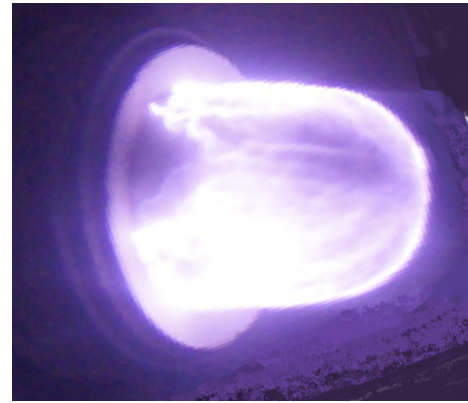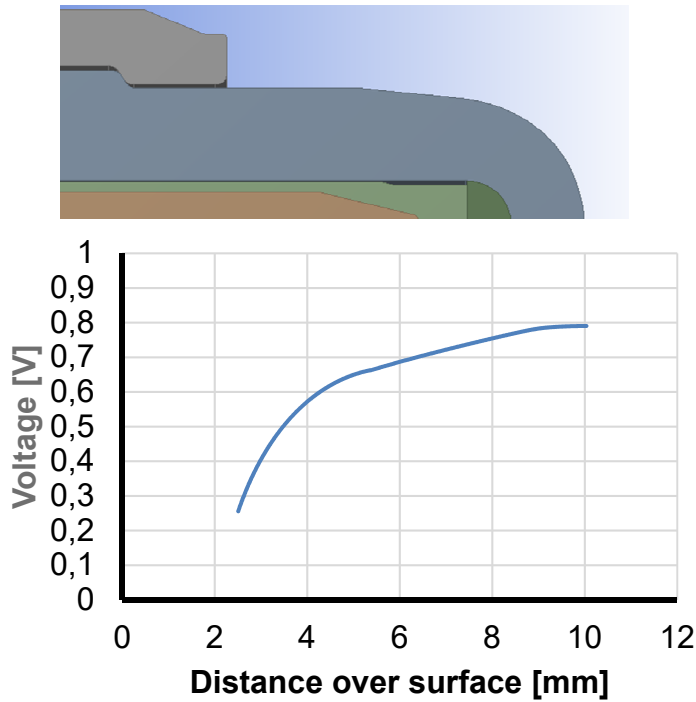
Figure 25:

Corona Propagation With Optimised Projected BDI Design
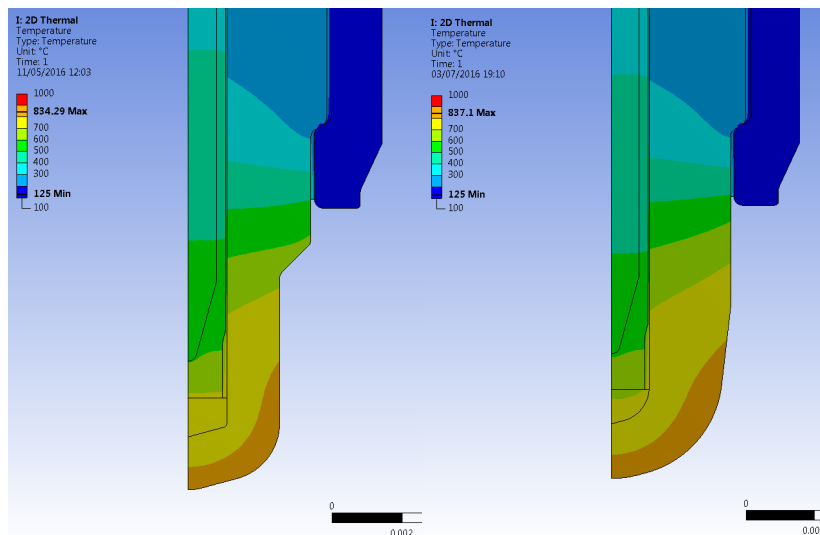
Figure 26: Thermal Performance of BDI Igniters Temperature [°C]

4.2 Thermal Verification

Applying the same thermal loads as those used in Section 2.1 above, we may evaluate the thermal performance of these BDI designs. Previous streamer designs had a maximum temperature on the star tip of around 890°C and an insulator temperature around 815°C, and around 900°C for both in the longer corenose length version. The thermal analysis of Figure 26 shows that the maximum temperature of the BDI plug is around 840°C, well within the safe range for operation despite this igniter having the longer corenose length. This longer length is desirable because the corona will not propagate away from the igniter and through the combustion chamber; increased projection allows the best possible ignition source in this case as there are no concerns about arcing to the piston crown.

4.3 Combustion Results

Igniters of streamer and optimised BDI design were tested in a suitable target engine, against conventional sparkplugs. The engine specifications are typical of a mass-market production engine for automotive use: in-line 4-cylinder, 2 litre displacement, direct injected, turbocharged and with variable valve timing. The engine was operated at a range of speed and load points. For corona igniters, both streamer and BDI, the duration and applied voltage was also varied. In this work the voltage indicated is applied to the drive circuit, not to the igniter directly, and is a proxy for power delivered.

Results from a typical part-load condition, 2000rpm and 9 bar BMEP, are shown in Figure 27 below. It can be seen here that all the optimised BDI igniters perform better than the sparkplugs, showing some additional improvement with increasing voltage. There is a minor sensitivity to corona duration over the limited range tested here. Streamer igniters perform better again than the BDI plugs, showing a strong sensitivity to applied voltage and lesser, but significant, sensitivity to duration.

Results from a typical wide open throttle condition, 4000rpm and WOT, are shown in Figure 28 below. Some relevant points from this graph are:

- Early prototype BDI parts were voltage-limited. Dashed lines in BDI data represent expected performance.
- Both streamer and BDI plugs may be expected perform better than spark plugs if the applied voltage is sufficiently high.
- Best absolute performance is achieved with streamer plugs. However, the falling performance with increasing voltage observed in the streamer plug at 60V applied and 500us corona duration is due to the onset or arc formation at this condition; ignition timing of around 3°BTDC means that the piston is very close to the igniter. Increasing voltage recovers this performance due to operation of the "IOS" system [23]. At shorter corona duration there is insufficient time for arc formation and performance is optimal, shown in the data from streamer plugs operated with 200us corona duration. This is an indication of the performance sensitivity of the streamer plugs at certain operating points and the requirement for careful calibration and suitable measures in place to mitigate these effects.

- Operation of the BDI plugs is not affected by arc formation. This leads to a simpler calibration task and more predictable characteristics in operation.
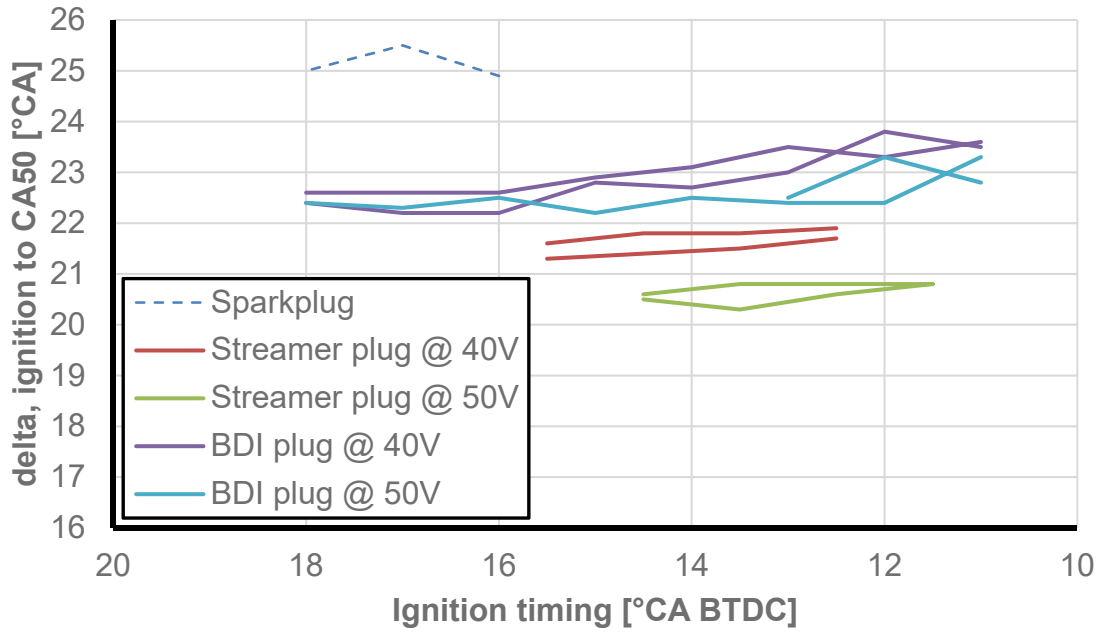
Figure 27: Ignition Performance of all Ignition Sources
2000rpm, 9bar BMEP
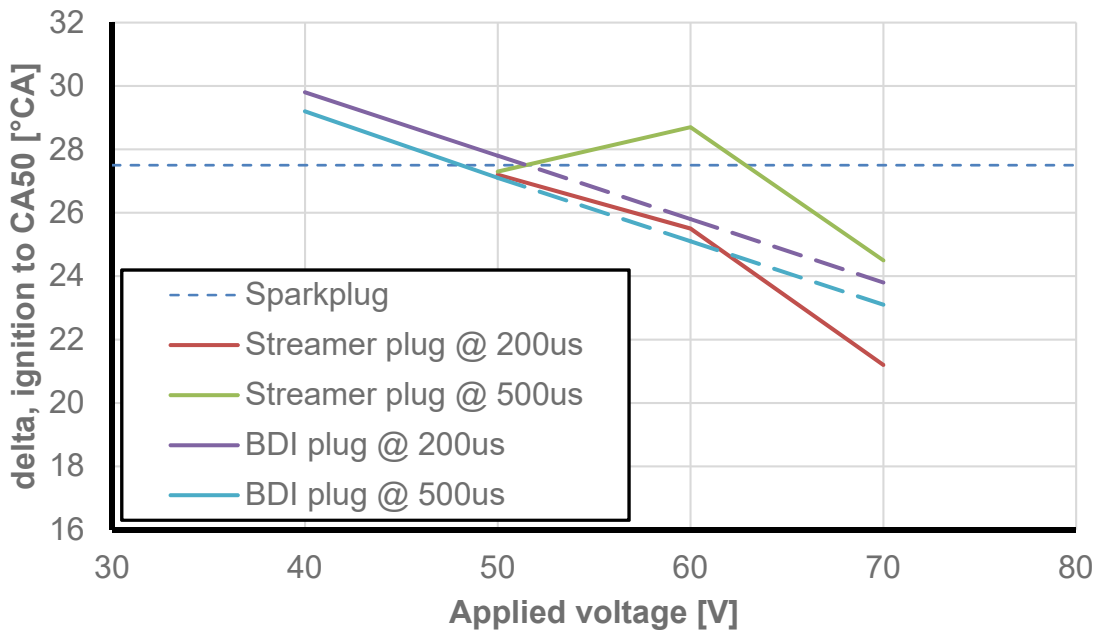
Figure 28: Ignition Performance of all Ignition Sources
4000rpm, WOT

5   Summary and Conclusions

It has been shown how corona igniters of a "streamer" design offer the best available ignition source from a system of this type, and how the firing end of these igniters may be thermally optimised to allow their reliable use in engines with IMEP up to 30 bar and beyond. This has been achieved at the expense of a very minor decrease in system efficiency, in the order of 6%, which is easily offset by material and design changes elsewhere in the system.

It has further been shown that it is possible to reduce the physical size envelope, from the existing 12mm thread in use today, down to a 10mm thread package with minimal impact on electrical performance and a very modest 4% increase in maximum electrode temperature.

An alternative solution is presented which has the potential to provide the following benefits:
- To extend igniter endurance by removing the exposed electrodes.
- To allow operation in engines of still higher specific output by improved thermal performance.
- To remove dependence on the combustion chamber geometry and hence allow easier adoption and potentially higher compression ratio.
- To reduce the calibration effort by removing the possibility of arc formation.
- To reduce cost and complexity of the required electronic system.

The ultimate ignition performance of these optimised igniters is not quite as good as the streamer-type igniter, but this is offset by reduced cost and increased robustness; not only in thermal, mechanical and electrical considerations, but also against sensitivity to calibration and operating conditions. These plug designs may additionally have the described features applied to downsize to 10mm thread body, as described above for the streamer plug. For these reasons this type of design can make an attractive solution in real applications.

References

[1]   Tinwell, P., Burrows, J.A.; *Surface Discharge Spark Plug for I.C. Engines*; UK Patent Application GB2361264 (2001)

[2]   Lykowski et al.; *Igniter*; United States Design Patent US D670246 (2012)

[3]   Okabe et al.; *Barrier Discharge Ignition Apparatus for Internal Combustion Engine*; United States Patent Application Publication US2014/0144402 (2014)

[4]   Kang, M.; *Large Discharge-Volume, Silent Discharge Plug*; United Stated Patent US5469003 (1995)

[5]   Singleton et al.; *Demonstration of Improved Dilution Tolerance Using a Production-Intent Compact Nanosecond Pulse Ignition System*; 3rd International Conference "Ignition Systems for Gasoline Engines" 52-68 (2016)

[6] Schenk et al.; *Challenges to the Ignition System of Future Gasoline Engines – An Application Oriented Systems Comparison*; 3rd International Conference "Ignition Systems for Gasoline Engines" 3-25 (2016)

[7] Idicheria, C.A. and Najt, P.M.; *Potential of Advanced Corona Ignition System (ACIS) for Future Engine Applications*; 3rd International Conference "Ignition Systems for Gasoline Engines" 267-292 (2016)

[8] Ronney et al.; *Transient Plasma Ignition of Quiescent and Flowing Fuel Mixtures*; IEEE Transactions on Plasma Science, Vol. 33, 844 – 849 (2005)

[9] Burrows, J.A. and Mixell, K.I.; *Analytical and Experimental Optimization of the Advanced Corona Ignition System*; 3rd International Conference "Ignition Systems for Gasoline Engines" 315-331 (2016)

[10] Burrows, J.A., Lykowski, J.D. and Hampton, K.; *Corona Igniter with Improved Corona Control*; United States Patent Application Publication US2012/0210968 (2012)

[11] Burrows et al.; *Corona Igniter Including Temperature Control Features*; United States Patent US9010294 (2015)

[12] Durham et al.; *Corona Ignition with Hermetic Combustion Seal*; United States Patent US9787064 (2017)

[13] Burrows et al.; *Corona Ignition Device with Improved Electrical Performance*; United States Patent US9088136 (2015)

[14] Visser et al.; *Ignition System*; United States Patent Application Publication US2009/0188458 (2009)

[15] Javadi, H., Farzaneh, M. and Peyda, A.; *Determination of Electric Field at Inception Based upon Current-Voltage Characteristics of AC Corona in Rod-Plane Gaps*; Iranian Journal of Electrical & Electronic Engineering, Vol. 6, No. 2, June 2010

[16] Krähenbühl et al.; *Numerical treatment of rounded and sharp corners in the modelling of 2D electrostatic fields*; Journal of Microwaves, Optoelectronics and Electromagnetic Applications, Vol 10, No. 1, June 2011

[17] Achstaetter et al.; *HF Ignition Device*; United States Patent Application Publication US2011/0146640 (2011)

[18] Burrows et al.; *Corona Igniter having Improved Gap Control*; United States Patent US8839753 (2014)

[19] Allen, N. and Mikropoulos, P.; *On Streamer Propagation Along Insulating Surfaces*; UMIST, UK; CIGRE, 38-98, (WG04/07) 11 IWD, 1999, pp. 1-5 (1999)

[20] Lykowski, J.D. and Phillips, P.W.; *Igniter Assembly, Insulator Thereof and Methods of Construction Thereof*; United Stated Patent Application US20180291863 (2018)

[21] Burrows et al.; *Corona Igniter having Controlled Location of Corona Formation*; United States Patent US8844490 (2014)

[22] Burrows, J.A., Lykowski, J.D. and Chan, F.X.; *Optimized Barrier Discharge Device for Corona Ignition*; United States Provisional Application No. 62/748,021 (2018)

[23] Burrows J.A.; *System and Method for Controlling Arc Formation in a Corona Discharge Ignition* System; United States Patent US8760067 (2014)

7.4 High Frequency Plasma Enhancement of a Conventional Spark Ignition System to Extend the Operating Range of a Modern Mass-Production Engine

Kevin Stark, Sven Gröger, Marcel van Delden, Gordon Notzon, Wolfgang Eifler, Thomas Musch, Peter Awakowicz

Abstract

Achieving future emission and fuel efficiency standards represents an increasingly challenging aspect in developing modern powertrains. Numerous alternative ignition systems have previously been proposed to replace or enhance the conventional transistor spark ignition concept. Up to now, the robust and simple design of the conventional system, few components and high maximum energy input into combustion chamber continue to justify its use. Rosenberger Hochfrequenztechnik GmbH & Co. KG is working with Ruhr University Bochum on extending this proven ignition concept. To this end, the conventional spark ignition system has been retained and expanded only with a path for coupling a high-power, high frequency (HF) signal. When a spark is conventionally generated, a low impedance conductive channel is formed between the spark plug's electrodes. Since the power input of a conventional ignition coil is limited, the HF signal energy is additionally introduced into this channel thereby creating a controllable and adjustable HF plasma discharge between the electrodes with a much larger plasma volume compared to the original spark. As both the duration and power of the HF plasma discharge can be arbitrarily set, the prerequisite energy for mixture ignition can also be provided beyond previous operating ranges. Experiments on a highly developed mass-production engine (2017 EA 211 Evo model, Volkswagen AG) showed that engine operation could be ensured in various, ignition-critical operating points. A significant fuel consumption advantage was exemplary found in terms of idling. At 1000 min^{-1}, an indicated mean pressure (p_{mi}) of 1 bar, and a corresponding standard deviation less than 0.1 bar, 14 g/kWh could be saved by the extended use of internal exhaust gas recirculation. In addition to engine results, the detailed design of the ignition system and measurement technology required for system analysis are also presented.

Kurzfassung

Das Erreichen künftiger Abgas- und Verbrauchsrichtlinien stellt bei der Entwicklung moderner Antriebsstränge eine zunehmend große Herausforderung dar. In der Vergangenheit wurde eine Vielzahl alternativer Zündsysteme vorgestellt, welche die konventionelle Transistor-Funkenzündung ersetzen oder erweitern sollten. Der robuste und einfache Aufbau, die geringe Anzahl an Bauteilen und der hohe maximale Energieeintrag in den Brennraum rechtfertigen dessen Einsatz jedoch bis heute. Die Firma

Rosenberger Hochfrequenztechnik GmbH & Co. KG arbeitet zusammen mit der Ruhr-Universität Bochum an einer Erweiterung dieses bewährten Zündkonzepts. Das konventionelle Funkenzündsystem wird hierfür beibehalten und lediglich um einen Pfad zur Einkopplung eines hochenergetischen, hochfrequenten (HF) Signals erweitert. Während des konventionell erzeugten Funkens entsteht zwischen den Elektroden der Zündkerze ein leitfähiger Kanal mit niedriger Impedanz. Da die Leistung der konventionellen Zündspule begrenzt ist, wird zusätzlich in diesen Kanal die Energie des HF-Signals eingebracht. Dadurch entsteht eine steuerbare HF-Plasmaentladung zwischen den Elektroden mit einem deutlich größeren Plasmavolumen verglichen mit dem Funken. Sowohl die Dauer als auch die Leistung der HF-Plasmaentladung können beliebig eingestellt werden. Dadurch kann auch außerhalb der bisherigen Betriebsbereichen die für die Entflammung des Gemischs notwendige Energie bereitgestellt werden. Versuche an einem hochentwickelten Großserien-Motor (2017 EA 211 Evo model, Volkswagen AG) zeigten, dass so der Motorlauf in verschiedenen, zündkritischen Betriebspunkten sichergestellt werden konnte. Im Bereich des Leerlaufs konnte beispielsweise ein signifikanter Verbrauchsvorteil festgestellt werden. Bei einer Drehzahl von 1000 min^{-1}, einem indizierten Mitteldruck (p_{mi}) von 1 bar und einer zugehörigen Standardabweichung kleiner als 0.1 bar konnten 14 g/kWh durch den erweiterten Einsatz von interner Abgasrückführung eingespart werden. Neben den motorischen Ergebnissen wird der detaillierte Aufbau des Zündsystems sowie die für eine Analyse des Systems notwendige Messtechnik vorgestellt.

# 1	Introduction

Exploiting the remaining optimization potential of current gasoline engines represents an increasingly major challenge for the industry. One such potential involves improving the combustion process. Studying the cylinder pressure curve of several combustion cycles over time shows that no combustion equals previous ones. While these cycle-to-cycle variations mainly influence driving comfort, they also impact the raw emissions of an internal combustion engine. Furthermore, increasing deviation could lead to an increase in fuel consumption, since a percentage of the optimal centre of heat release is deviated. A prerequisite for the development of modern internal combustion engines is therefore to optimally minimize these cycle fluctuations. Yet simultaneously, the aim is to continuously improve the combustion process's thermodynamic efficiency. Approaches such as the Miller combustion process, the use of high residual gas rates, as well as lean concepts serve to complicate flame propagation and consequently produce irregularity of combustion cycles [1].
The ignition of the mixture forms the basis of gasoline engine combustion. After local inflammation in the area of the spark plug, the flame front spreads independently through the combustion chamber. Modern ignition systems, which work according to the principle of transistor coil ignition, ensure safe ignition across wide operating ranges. Hence due to its relative simplicity, this ignition concept can be found in most automobiles since its invention. However, the constantly more stringent legislation governing consumption and exhaust gas is pushing this concept to its limits. In the following section, the basic structure of a conventional ignition system is described in order to comprehend those limits [2].

1.1   Fundamentals of ignition technology

The conventional transistor ignition system essentially comprises a spark plug, ignition coil, ignition output stage, as well as connection and suppression parts. Former multi-cylinder engines are operated by one ignition coil and an ignition voltage distributor, which connects the ignition coil to the respective spark plug. Modern gasoline engines are equipped with a single-spark ignition coil and an integrated output stage. Each spark plug mounted in the cylinder head is directly connected with this single-spark ignition coil. A minimal connection length between the ignition coil and the spark plug reduces electromagnetic radiation.

Single-spark ignition coils with integrated output stage fundamentally comprise two transformer-coupled coils. If the output stage is switched on by the engine control unit, current flows through the primary coil. The interruption of the primary current leads to the collapse of the magnetic field. Due to this rapid magnetic field change and high winding number of the secondary coil (ratio of about 1: 100 [3]), a high voltage of several 10 kV is induced. The energy stored in the ignition coil can be influenced by varying the timespan between switching on and interrupting the primary current.

Due to the direct contact of the secondary coil and the centre electrode of the spark plug, the parasitic capacitance of the spark plug is charged first. If the breakdown voltage is reached, the parasitic capacitance discharges in a spark plasma between the electrodes of the spark plug. In this phase, the spark plasma is a thin plasma channel with high electron density and high gas temperature that connect the electrodes. A plasma consists (amongst others) of electrons, ions and neutral gas particles. Due to the free charged particles (electrons and ions), the plasma channel is electrically conductive. In the second phase, the residual energy stored in the ignition coil discharges in the plasma channel, resulting in more diffused plasma with lower electron density. The burning voltage in this phase is a few hundred volts, depending on electrode gaps and turbulence in the combustion chamber.

At the ignition timing, (switching off the ignition coil) an ignitable air-fuel mixture must be located at the spark plug electrodes. For stoichiometric and homogeneous fuel-air mixtures ($\lambda = 1$) this condition is fulfilled. Resting, homogeneous and stoichiometric air-fuel mixtures need minimum ignition energy for combustion. To save natural resources, engine operating points that deviate from the stoichiometrically homogeneous mode are increasingly interesting. The energy requirement increases for the ignition of lean air-fuel mixtures ($\lambda > 1$) or with the higher addition of exhaust gas. Investigations in [4] clearly show that high flow velocity, high turbulence intensity, and non-stoichiometric engine operation ($\lambda \neq 1$) lead to increased minimum ignition energy.

Therefore, the development of alternative ignition systems helps to expand the operating range of gasoline engines and can increase their efficiency. In the past, the economic benefit often did not justify the technical effort. The mass production of alternative ignition systems in the automotive sector has so far been limited by the high additional costs compared to conventional robust ignition technology [4].

1.2   High frequency plasma enhanced spark ignition

Spark ignition, based on a single spark ignition coil and spark plug, is proven, robust and inexpensive ignition technology for the automotive sector. A certain operating win-

dow is specified by the use of conventional ignition systems. If environmental regulations or modified fuels force the expansion of this operating window, conventional spark ignition can be enhanced with high frequency (HF) plasma.

As previously mentioned, the spark forms a conductive plasma channel between the spark plug's electrodes. If an HF alternating voltage is simultaneously applied to the centre electrode of the spark plug, an HF alternating current can flow and subsequently an HF plasma discharge is formed between the electrodes. As a first big advantage, the HF plasma discharge is adjustable in duration and power. Typical burning durations are in the range of milliseconds with an active plasma power up to 150 W. The frequency of the applied HF voltage operates in the megahertz range, and generates a diffuse and large-volume plasma compared to conventional spark discharge (see Figure 5). An adjustment of the combustion chamber or spark plug is not required for the operation of the spark ignition system enhanced by HF plasma. In order to avoid power losses, the spark plug itself must be free of any internal resistance.

HF plasma enhanced spark ignition offers the advantage that the gasoline engine can still be operated with conventional spark ignition in its previous operating window. In addition, HF plasma can be added to extend the conventional operating window adjusted to the individual ignition situation, depending on exhaust recirculation, stoichiometry and others. The HF enhancement can therefore be switched on depending on the operating status, and can also be adjusted in terms of burning duration and power.

2   System Realization

2.1   Ignition System

To ensure efficient and cost-effective implementation, the new ignition system is based on a sophisticated combination of conventional components and new HF power components, as shown in Figure 1. On the one hand, the utilized conventional ignition coil (VW part number 05E 905 110) generates a high voltage pulse up to 45 kV. This is connected to the centre electrode of the conventional, resistor-free spark plug and generates the initial spark. On the other hand, an HF power amplifier generates a high frequency alternating signal. This is also connected to the centre electrode of the spark plug via a coupling network, and provides the energy for the HF plasma discharge.
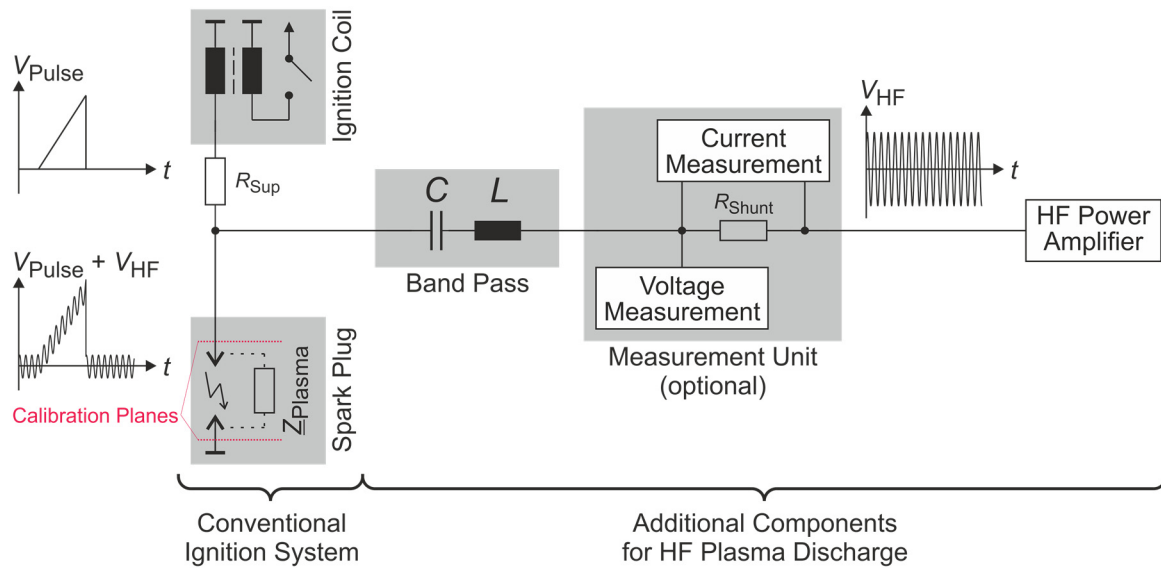
Figure 1: Block diagram of the new ignition system including optional electrical measurement unit.

The amplifier depicted in Figure 2 accords to the Class E principle and is based on a prototype in [5]. It is operated at a frequency of f_0 = 10 MHz and generates an active RMS power of 500 W at a load impedance of 50 Ω. The electrical impedance of the conductive HF plasma discharge $\underline{Z}_{Plasma}$ varies over a wide range due to various conditions at the ignition timing in the combustion chamber. Examples include pressure, turbulence, temperature, and composition of the air-fuel mixture. Therefore, a matching network is integrated into the amplifier. This is optimized to provide a constant high output power over the wide range of load impedances typical for the new ignition system. Thus, for a resistance (real part of the impedance) in the range of 120 Ω < R_{Plasma} < 500 Ω, the output power only varies by about 20%. Furthermore, the power can be adjusted via the supply voltage.
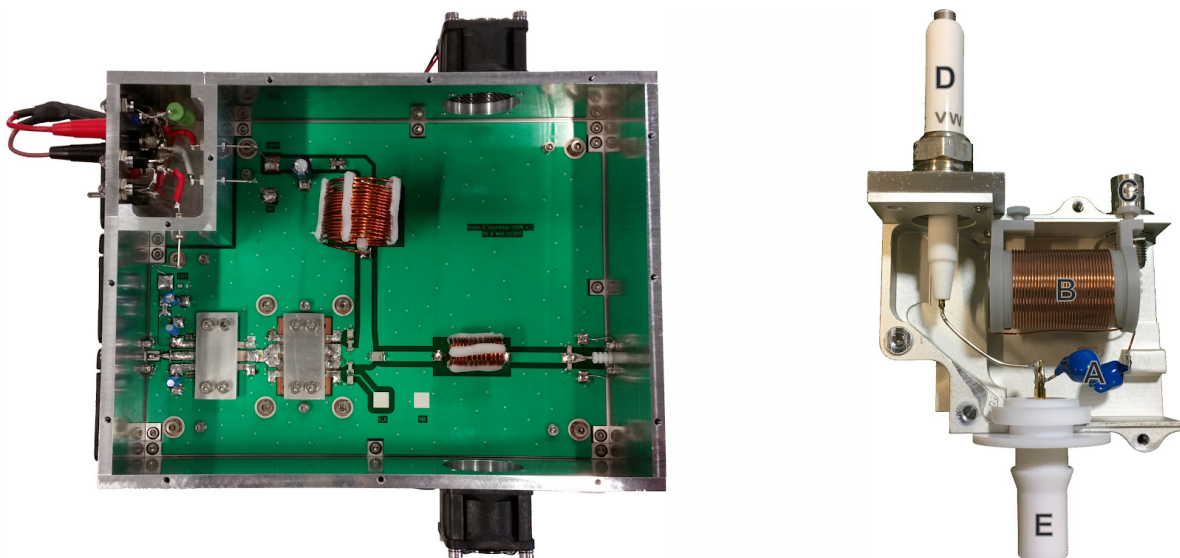
Figure 2: Photograph of the amplifier (left) and combiner box (right) with high voltage capacitors (A), air coil (B), MHV plug (C), auxiliary spark plug (D) and plug for internal resistance-free spark plug (E). Property of Rosenberger Hochfrequenztechnik GmbH & Co. KG.

375

The coupling network is used to decouple the high voltage pulse from the amplifier, and to couple the high frequency signal to the centre electrode. It therefore comprises an LC resonant circuit, which represents a band pass filter with the resonance frequency f_0 = 10 MHz. A cascade of two high voltage capacitors is used to block the high voltage pulse of the ignition coil, which are connected to the end of the spark plug's centre electrode. The capacitance C, and thus the load of the ignition coil, should be respectively low. Otherwise, the peak voltage of the high voltage pulse will decrease. The inductance L is connected to the capacitance on one side and to the MHV plug on the other. The latter is used to connect the optional measurement unit and the HF power amplifier. The inductance L should be respectively low as well to minimize power losses and critical thermal stress of the ignition system. The inductance is therefore realized as an air coil, because it does not exhibit any hysteresis losses. Concerning ideal components, the resonance frequency is

$$ f_0 = \frac{1}{2\pi\sqrt{LC}} . \tag{1}$$

A trade-off between the inductance L and the capacitance C must therefore be made. Due to the comparatively low impedance of the HF plasma discharge, conventional spark plugs without internal resistor must be used. Otherwise, the power losses in the internal resistor would be significant and even higher than the power provided to the HF plasma discharge. Furthermore, the electrodes of spark plugs for modern gasoline engines often consist of platinum, iridium or a combination of both (e.g. NGK 05E905602). These precious metals are particularly suitable, as they exhibit good erosion resistance.

In order to integrate the suppression resistor R_{Sup}, which is required for the high voltage pulse, a conventional spark plug with internal resistance (auxiliary spark plug) is utilized for this prototype. Therefore, the bow-shaped ground electrode is removed and the tip of the centre electrode is connected to the end of the centre electrode of the resistor-free spark plug. The end of the auxiliary spark plug acts directly as a plug for the conventional ignition coil.

In order to ensure high electrical strength of the system, the following components are sealed: Coupling network together with MHV plug to connect the measurement unit / amplifier, auxiliary spark plug, and a plug for the resistor-free spark plug. This design, which is integrated in an aluminum housing optimized for installation space, is referred as "combiner box" in the following sections. The unsealed setup is shown in Figure 2. According to [6], a single amplifier is sufficient for operation on a multi-cylinder engine. Each individual cylinder requires only a dedicated combiner box equipped with an ignition coil. Thus, the additional hardware effort and consequently additional costs of the new ignition system are low compared to conventional ignition systems. The resulting entire ignition system for the four-cylinder series engine used is depicted in Figure 3.
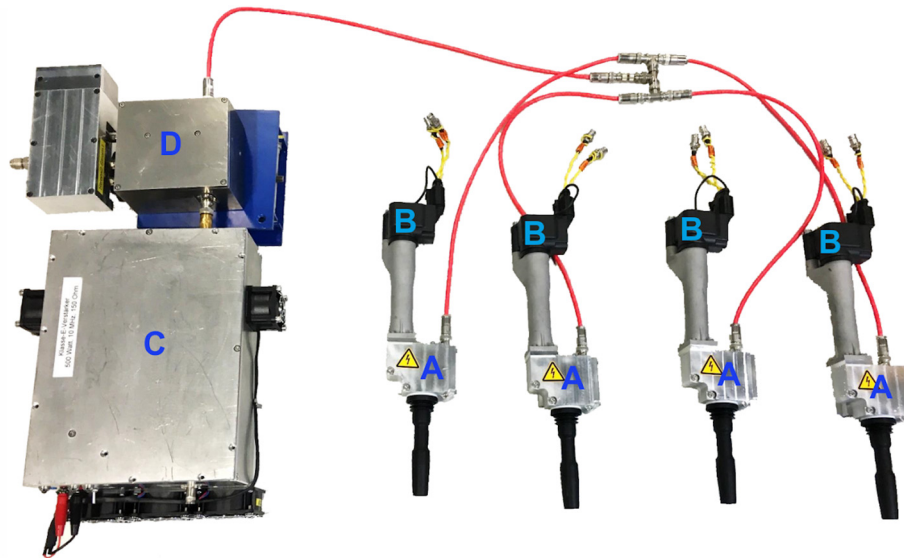
Figure 3: Photograph of the entire ignition system for a four-cylinder engine with four combiner boxes (A) and ignition coils (B), high frequency power amplifier (C), as well as electrical measurement unit (D). Property of Rosenberger Hochfrequenztechnik GmbH & Co. KG.

2.2   Electrical Measurement System

A measuring technique was developed to determine complex plasma impedance $\underline{Z}_{Plasma}$ and active plasma power P_{Plasma} over time. Based on measurement results, the output impedance of the HF power amplifier is matched to the complex plasma impedance $\underline{Z}_{Plasma}$ to maximize power transfer. Furthermore, active plasma power P_{Plasma} can be monitored and regulated.

For this purpose, a developed measurement unit is integrated between the band pass filter and the HF amplifier using MHV connectors, in order to minimize requirements for electric strength, see Figure 1. Two measuring points are located inside the measurement unit. The voltage measurement is realized using a capacitive voltage divider. The current measurement outputs a voltage proportional to the current through the shunt-resistor R_{Shunt}. Hence, two linearly independent measurements are available, which allow for system calibration. According to [7], a system error correction can be performed using a four-port to two-port reduction, and three easy-to-implement calibration standards Open, Short, and Match (OSM). The HF plasma discharge is heated between the spark plug's electrodes. In order to determine the electrical plasma parameters as accurately as possible, the calibration planes were chosen appropriately as illustrated in Figure 1. Accordingly, the calibration standards are placed between the electrodes. Regarding the Open calibration standard, no changes have been made to the spark plug. The Short calibration standard consists of a brass element to short the spark plug's electrodes. As the Match calibration standard, a 150 Ω HF resistor is used, which is in the range of the active plasma resistance R_{Plasma}. The resistor is placed between the electrodes by means of a low-capacitance and low-inductance clamping fixture. This eliminates the need for a soldering process, which would damage the electrodes.

Since the individual system components are built up reproducibly, the calibration procedure needs to be performed only once and can then be transferred to other ignition systems.

By using OSM calibration, the complex plasma impedance

$$\underline{Z}_{\text{Plasma}} = R_{\text{Plasma}} + jX_{\text{Plasma}} , \tag{2}$$

consisting of resistance R_{Plasma} and reactance X_{Plasma}, is determined. Additionally, during the calibration process a voltage measurement at the Match calibration standard is performed once using a voltage probe. Thus, the complex plasma power

$$\underline{S}_{\text{Plasma}} = P_{\text{Plasma}} + jQ_{\text{Plasma}} = \underline{V}_{\text{Plasma}} \cdot \underline{I}^*_{\text{Plasma}} , \tag{3}$$

consisting of active power P_{Plasma} and reactive power Q_{Plasma}, is also determined. The complex voltage $\underline{V}_{\text{Plasma}}$ and the complex current $\underline{I}_{\text{Plasma}}$ are therefore also given by Ohm's law.

Using a Tektronix MSO4034 Digital Storage Oscilloscope (DSO), the output signals of the measurement unit and voltage probe are digitized with 250 MSa/s. The calibration process and evaluation of the measurements are performed automatically inside a developed software environment.

Generally speaking, a plasma is represented by a nonlinear, time-variant impedance. Therefore, the measured signals contain frequency components in multiples of the excitation frequency $f_0 = 10$ MHz. The high sampling frequency ensures that the sampling theorem is fulfilled. A second-order Goertzel algorithm is used to ensure fast and efficient signal evaluation at excitation frequency f_0, performed in steps of 10 µs to achieve a 10 µs time resolution of electrical plasma parameters. The resulting 10 µs window length leads to a sufficiently high frequency resolution of 100 kHz.

For the following investigations, the spark plug was mounted into a pressure vessel with optical windows. The measurements were performed inside synthetic air (21% O_2, 79% N_2) with 5 bar pressure, without air flow, and without turbulence. Figure 4 illustrates the measurement results of the electrical plasma parameters over time.

The falling edge of the ignition coil control signal is used here to trigger the DSO ($t = 0$ s). The HF source is turned on 200 µs before spark ignition, and is turned off 1 ms after spark ignition. Both limits can be set variably. Outside the chosen limits, the measurement results are noisy due to the absence of signal energy. In the 200 µs range before spark ignition ($t < 0$ s) there is no active plasma power P_{Plasma}, because no conductive channel between the electrodes exists ($R_{\text{Plasma}} >>$). Furthermore, the measured RMS open-circuit voltage between the electrodes is $|\underline{V}_{\text{Plasma}}| \approx 540$ V. Right after spark ignition ($t > 0$ s), the active resistance decreases to $R_{\text{Plasma}} \approx 120 \ldots 160$ Ω, the RMS voltage decreases to $|\underline{V}_{\text{Plasma}}| \approx 110$ V, the RMS current increases to $|\underline{I}_{\text{Plasma}}| \approx 750$ mA, and the RMS active power increases to $P_{\text{Plasma}} \approx 70 \ldots 80$ W.

In order to correlate the electrical measurements with optical investigations, time-synchronous measurements were performed. A very fast four-fold camera system (HFSC pro, produced by PCO) was used, comprising four single ICCD (intensified charge-coupled device) cameras with common optical input via beam-splitter optics. The four cameras can be controlled independently of each other. To observe the HF plasma discharge with burning duration of 1 ms time-resolved, the exposure time of each camera was selected to $t_{\text{exp}} = 250$ µs. Camera 1 is triggered when the ignition coil is switched off ($t = 0$ s, see Figure 4). Camera 2 is triggered after the end of the exposure time of camera 1, and cameras 3 and 4 according to cameras 2 and 3 respectively. This results in a sequence of four consecutive images with total exposure time of 1 ms. The image intensifiers of individual cameras were selected so that the intensity of the

four images is comparable. Figure 5 shows the time sequence of pure spark discharge (images A, B, C, D) and HF plasma enhanced spark discharge (images E, F, G, H). The spark discharge in Figure 5 A displays an intensively glowing spark channel between the spark plug's electrodes. The following pictures B, C and D depict the burnout of the spark with lower intensity. Figure 5 E shows the initial spark and HF plasma discharge. Due to the immediate takeover of the HF plasma discharge, a clear distinction between spark and HF plasma discharge cannot be established in this image. The comparison of Figures B, C, D with F, G, H clarifies that the HF plasma has a much larger volume and higher intensity. Both attributes have positive effects on ignition.
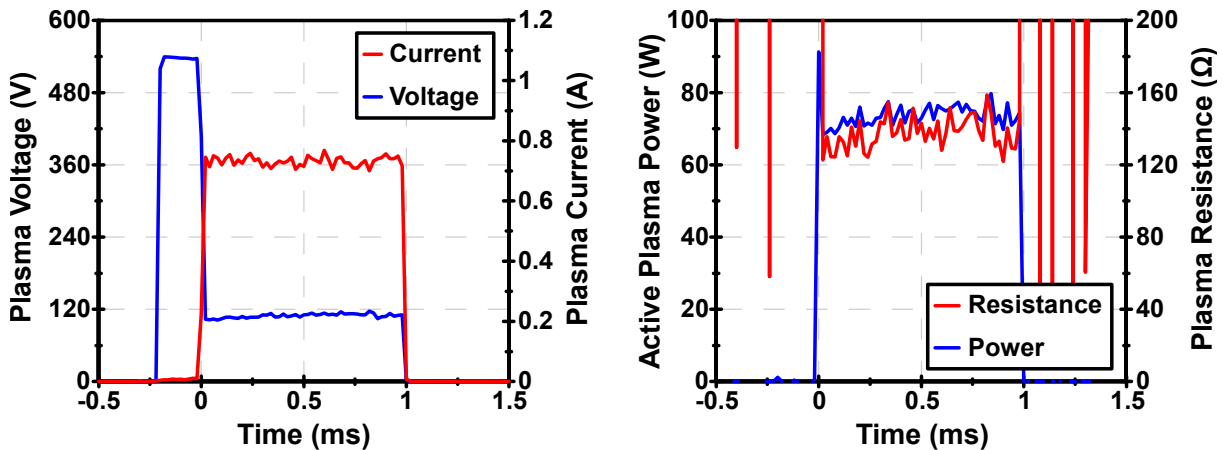

Figure 4: Time-resolved measurement of current and voltage (left) as well as active plasma power and active resistance (right) of HF plasma at 5 bar air in a pressure vessel.
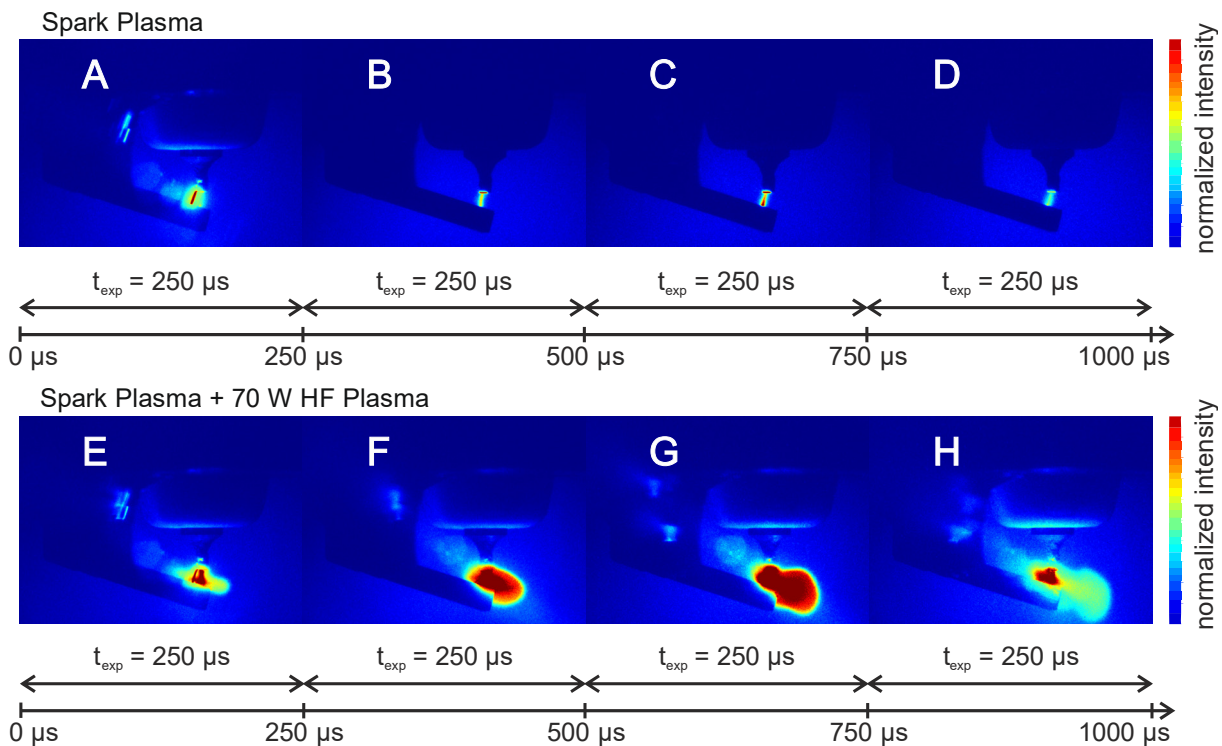

Figure 5: Time-resolved photography of spark plasma (top) and HF support plasma discharge (bottom) in a pressure vessel at 5 bar pressure in synthetic air.

3   Experimental Setup

A modern four-cylinder engine (2017 EA 211 Evo model, Volkswagen AG) was used to measure the following results. The high development level of the TSI engine provides a good basis for a valid and future-orientated estimate of the ignition system's potential. The gasoline engine is equipped with a Generation 4.0 direct injection system and an exhaust gas turbocharger with variable turbine geometry. A stroke/bore ratio of 1.15 results from 85.9 mm stroke and 74.5 mm bore diameter. The compression ratio is 12.5:1. Depending on the operating point, two cylinders can be deactivated by disabling the valve train. The Miller cycle (early closing of inlet valves) can be used by varying the timing of the inlet camshaft by up to 70° CA. The adjustment range of the exhaust camshaft (40° CA) allows variation of the internal recirculated exhaust gas rate, and reduction of the charge exchange losses. The combustion chamber masking, its geometric design, and high tumble concept of the inlet port increase the charge motion in the low RPM range. The nominal power of 96 kW is reached at 1.3 bar boost pressure. Further integrated technologies have a subordinate role in the operating range of an ignition system, and can be found in [8].

Due to its high development level, the test engine exhibits safe ignition conditions in conjunction with the series ignition system across almost all operating ranges. Delayed combustion and misfires can occur due to the exhaustion of secondary measures that increase efficiency. Such secondary measures can include dilution of the charge with high residual gas rates, as well as a considerable increase in air/fuel ratio.

The engine was operated on an engine dynamometer for the tests, which ensured safe operation in ignition-critical areas in addition to ideal monitoring options. The engine's RPM could be kept constant through the bivalent operation of the dynamometer brake (electric motor), even in the case of misfiring. The combustion process could be continuously analyzed during operation by using high and low pressure indication. The intake and exhaust gas systems were comparable to the installation in series vehicles. All tests were conducted with conditioned ambient air and powertrain at operating temperature to improve comparability.

4   Measurement Results and Discussion

The following measurements show a comparison between conventional ignition and ignition enhanced by HF plasma discharge. For the reference measurement, the ignition system presented in section 2.1 was operated without any additional energy from the high frequency amplifier. Comparative measurements have proven that this setup is representative for the series ignition system, since the influence of the band pass on the high voltage pulse is negligible.This setup allows the HF plasma discharge to be switched on and off during operation. The direct influence of additional ignition energy can be rated at constant operating points.

The tests show that the strongest influence of HF plasma discharge typically occurs in the range of critical ignition conditions. Figure 6 illustrates the curve of specific fuel consumption as a function of the camshaft timing "Intake open". An earlier opening of inlet valves increases the area of valve overlap, and thus increases the percentage of residual gas during charge exchange. The higher residual gas ratio increases inhomogeneity in the combustion chamber, and raises the mixture's heat capacity. In order to reduce the charge movement, the speed was set to $n = 1000$ min^{-1} and the load close to idling ($p_{mi} = 1$ bar). Up to a camshaft timing of -5° CA TDC, there is no difference in

fuel consumption between the two systems. At a camshaft timing of -10° CA TDC, operation with conventional ignition was not possible due to delayed combustion and misfiring. In the further course, a significant consumption advantage (14 g/kWh) is evident by the use of the ignition system enhanced by HF plasma discharge. Due to the controllability of the additional energy input, an operating map-dependent precontrol is therefore reasonable. At critical operating points, corresponding additional power can be provided, while the mixture is ignited conventionally by coil discharge in the rest of the operating map.
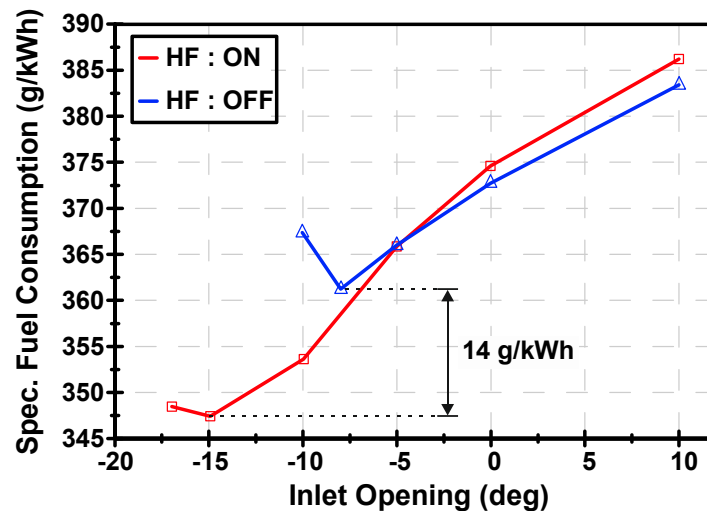
Figure 6: Inlet opening-resolved measurement of specific fuel consumption with (red) and without (blue) HF plasma enhancement at n = 1000 min^{-1}, p_{mi} = 1 bar.

An increase in the standard deviation of the indicated mean pressure of all cylinders above 0.1 was assumed as the test's termination condition as illustrated in Figure 7. In the non-ignition critical range (Inlet Opening > -5° CA TDC) there is no difference between the two systems with regard to the engine's smooth operation. Opening the inlet valves -8° CA TDC already leads to a significant increase in the standard deviation with conventional ignition. Switching on the HF plasma discharge eases this operating point, and achieves acceptable running smoothness up to a camshaft timing of -15° CA TDC.

Increased ignition energy due to using HF plasma discharge has a further effect on ignition delay time. Even where the conventional ignition system ensures inflammation, a reduction in ignition delay time is achieved. This effect increases with higher residual gas ratio, as shown in Figure 7.
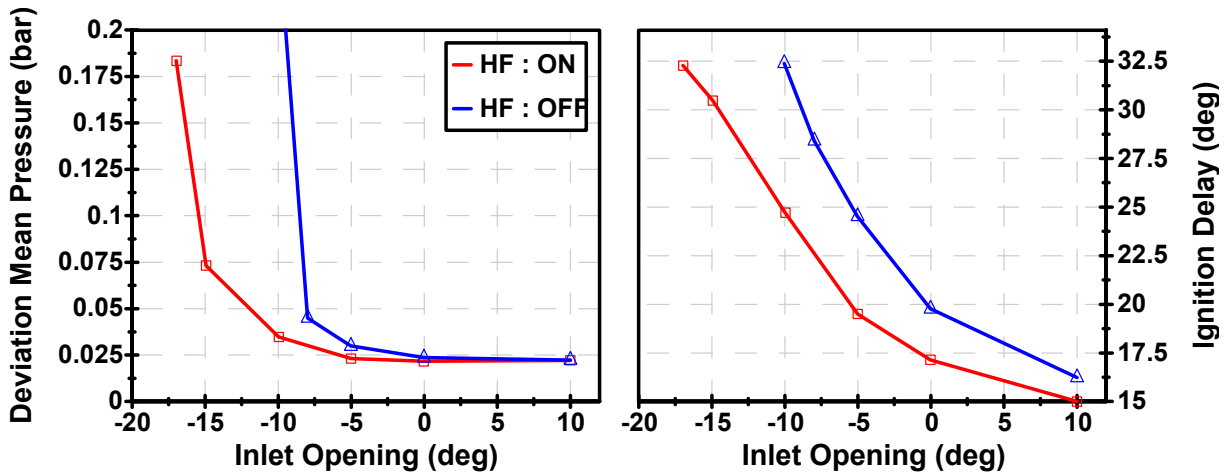
Figure 7: Inlet opening-resolved measurement of the deviation of indicated mean pressure (left) or ignition delay (right) with (red) and without (blue) HF plasma enhancement at n = 1000 min^{-1}, p$_{mi}$ = 1 bar.

As described above, charge motion, residual gas rate and inhomogeneity of the mixture significantly influence inflammation capability. In order to reduce influencing factors, a measurement with higher charge motion and better homogeneity is presented below. For this, n = 2000 min^{-1} at an indicated mean pressure p_{mi} = 2 bar was selected. At this operating point, the critical ignition conditions were created by leaning the mixture, since the residual gas rate cannot be exactly quantified by varying the inlet camshaft timing. Figure 8 illustrates the mean value of the standard deviation of the indicated mean pressure of all cylinders as a function of the variation of air/fuel ratio. Even with reduced influencing factors, a clear advantage compared to conventional spark ignition can be noticed. Reduced ignition delay time can also be observed in Figure 8 (analogous to Figure 7).
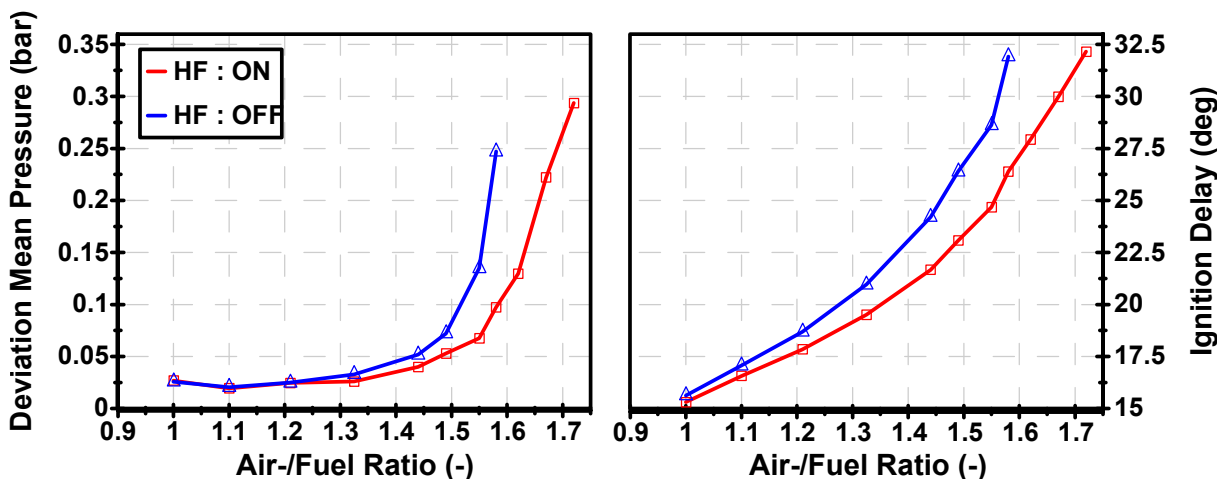
Figure 8: Air-/fuel ratio-resolved measurement of the deviation of indicated mean pressure (left) or ignition delay (right) with (red) and without (blue) HF plasma enhancement at n = 2000 min^{-1}, p$_{mi}$ = 2 bar.

The presented results show that the additional energy enhanced through HF plasma discharge stabilizes the combustion in critical ignition areas. It should be noted that all

presented experiments were performed with electrode geometry, spark position and combustion chamber design optimized for the operation of conventional spark ignition and not for HF plasma operation. It is well-known that electrode geometry in particular strongly influences the stability of plasma. Figure 9 shows the power of the HF plasma discharge supplied to the combustion chamber during the experiment. Optimization of the electrode geometry and the resulting stabilization of plasma channel reduces the deviation of this additional energy input, which leads to a further increase in the mentioned advantages of HF plasma ignition.
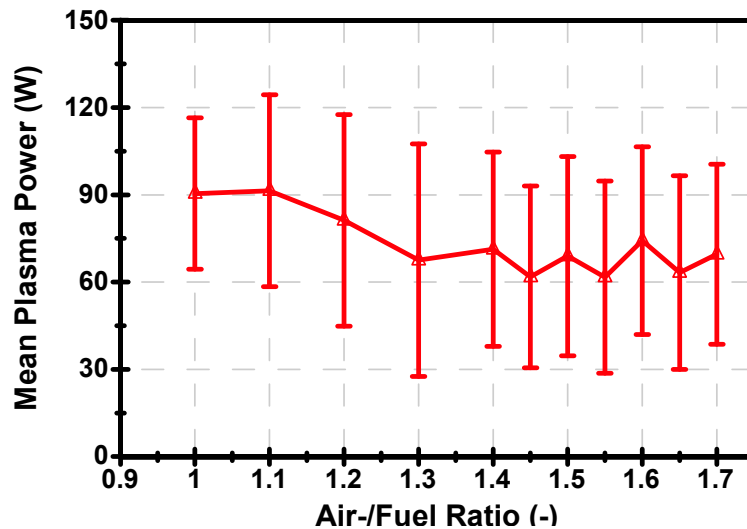
Figure 9: Mean value and measured value interval over 30 readings of time-averaged plasma power P_{Plasma} with 1 ms plasma duration at $n = 2000$ min^{-1}, $p_{mi} = 2$ bar and variation of air-/fuel ratio

5   Summary

This article presented the enhancement of a conventional transistor spark ignition system with a high frequency plasma discharge. The simple integration, option of variable control of additional energy input, as well as large number of series components used serve to reinforce the multitude of application possibilities of the system. The tests proved that the operating range of a modern series engine could be extended. It was shown that significant consumption advantages could be achieved through secondary measures in critical ignition areas. At 1000 min^{-1}, a load close to idle, and a standard deviation of the indicated mean pressure less than 0.1 bar, the specific fuel consumption could be reduced by 14 g/kWh. The volume of HF plasma is clearly larger and the ignition delay is reduced compared to conventional sparks, while the burning duration is not significantly decreased.

The aim, to use as many series components as possible to demonstrate a significant influence of ignition enhancement by using HF plasma discharge, has been successfully fulfilled. Nevertheless, minor adjustments to electrode geometry and materials are advisable in order to exploit the system's full potential. The system concept allows an operating map-dependent precontrol. For particularly difficult ignition conditions an additional real-time control of the supplied HF plasma energy is conceivable.

References

[1]   Internal Combustion Engine Fundamentals, John B. Heywood, 1988, ISBN 0-07-100499-8

[2]   Handbuch Verbrennungsmotoren, van Basshuysen, Richard, Schäfer, Fred, 2015, ISBN 978-3-658-04678-1

[3]   Bosch Grundlagen Fahrzeug- und Motorentechnik, Konrad Reif, 2011, ISBN 978-3-8348-8320-9

[4]   Grundlagen und Technologien des Ottomotors, Helmut Eichlseder, Manfred Klüting, Walter F. Piock, 2008, ISBN 978-3-3211-25774-6

[5]   G. Notzon, T. Busch, M. van Delden, and T. Musch: „A 500 W High Efficiency Class-E Power Amplifier for Heating a Variable Plasma Load at 10 MHz", 10th German Microwave Conference, Bochum, DE, Mar. 2016, pp. 429 – 432

[6]   G. Armbrecht, P. Awakowicz, A. Bergner, M. Fuchs, S. Gröger, T. Musch, G. Notzon, M. van Delden, and M. Wollitzer: „Ignition Device and Method for Igniting an Air/Fuel Mixture", WO002017207098A1, May 30, 2017.

[7]   Schiek, B. Grundlagen der Hochfrequenz-Messtechnik, 1999, ISBN 3-540-64930-1

[8]   Der neue 1,5-l-Vierzylinder-TSI-Motor von Volkswagen, Demmelbauer-Ebner, Persigehl, Görke, Werstat, MTZ, 02 2017

8 Pre-chamber Ignition 2

8.1 Characterization of the Ignition and Early Flame Propagation of Pre-Chamber Ignition System in a High Pressure Combustion Cell

Marcus Wöbke, Paul-Benjamin Reinicke, Michael Rieß,
Lorenz von Römer, Marc Sens

Abstract

The Pre-Chamber spark plug, already in its most simple configuration, allows a cycle fuel consumption reduction of 2-3% (WLTC) by enabling a significant compression ratio increase due to its huge knock mitigation effect. This benefit can be strongly extended in the homogeneous lean burn operation mode with very low nitrogen oxide emissions by a novel approach of injecting a well prepared fuel-air-mixture inside the Pre-Chamber. An increase of the engine compression ratio allows further the development of a new combustion process referred as the Pre-Chamber supported self-ignition process, which enable an increased thermodynamic efficiency at part load operating points of a gasoline engine.
The development of a suitable Pre-Chamber ignition system requires the technical understanding of the Pre-Chamber geometry parameters on the combustion process. The impact of the overflow channel design on the flame propagation and ignition of the fuel-air mixture inside the main chamber must be understood in greater detail. This in turn requires a high-fidelity combustion model which is capable of predicting the impact of the overflow channel geometry on e.g. flame extinction, radical recombination on the walls of the Pre-Chamber orifice and finally the behavior of main chamber inflammation regardless of the Pre-Chamber ignition regime.

Focus of this work is to discuss the impact of the Pre-Chamber geometry onto the inflammation and early flame propagation inside the main combustion chamber by means of experiments in an optical high pressure vessel under simplified boundary conditions. As a basis, the simultaneous high speed measurement of Schlieren and OH* chemiluminescence serve as a fundamental means to analyze ignition performance and early flame propagation in order to develop and validate an accurate combustion model.

Initially, the general impact of the chamber pressure will be discussed emphasizing specifically on the differences between certain Pre-Chamber layouts and the conventional ignition system onto flame speed and ignition probability. Furthermore, variations of e.g. the number of overflow holes, the orifice diameter and the volume of the Pre-Chamber aids to identify the most relevant parameters responsible for flame extinction and combustion performance inside the main chamber.

1   Introduction

1.1   Motivation

Latest and future legislations for automotive emission of pollutants and CO_2 are forcing the industry to develop highly efficient powertrain concepts. As a result, the electrification of powertrains has become a main industry trend and a very promising approach for drastically reducing the local emissions. However, today´s most likely scenario for future powertrains still incorporates the internal combustion engine with varying vigorousness, admittedly not as mere propulsion system (ICE only), but with a major share in combination with light (xHEV) or rather powerful (PHEV) electrification (see Figure 1.1). Consequently, the optimization of the ICE in both terms, efficiency and pollutant emissions is crucial for competing against powertrains with locally zero emissions.
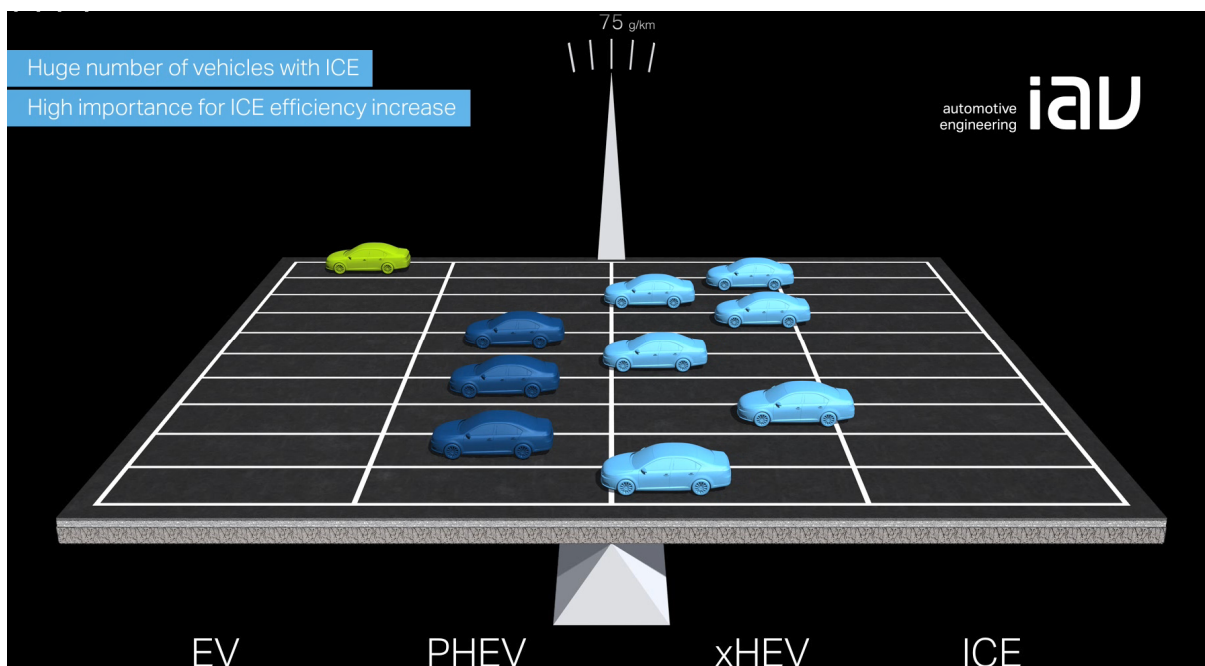
Figure 1.1: IAV's powertrain-share fleet scale with one exemplary prediction of the powertrain mix in 2025 - 2030

During the last 20 years, the ICE passed through a comprehensive development with already considerable improvement of fuel efficiency. Further optimizations become more and more complex and expensive. Several technologies are known with theoretical high potential for reduction of process related efficiency losses such as early intake valve closure (EIVC) strategies or high mixture dilution. However, they come along with system specific drawbacks that limit the full fuel saving potential. For example, a severe mixture dilution with EGR has a positive impact on reducing the throttle losses in part load and knock sensitivity in high load. However, the engine suffers from a deterioration of mixture inflammability and burn rate caused by the increase of inert gas content.

An advanced ignition system as the Pre-Chamber Spark Plug (PCSP) was shown to be a beneficial complementary technology or even act as an enabler for such high potential ICE technologies [1, 24]. Compared to conventional spark plugs the ignition energy of the PCSP increases by more than two orders of magnitude. Furthermore,

the multiple ignition sources, represented by the flame / hot gas jets from the Pre-Chamber lead to a significantly higher mixture coverage approaching a spatial ignition. To summarize, previous publications indicate a great fuel saving potential [1, 24] which makes the PCSP component a very interesting technology – also and specifically because it is relatively easy to integrate into an engine in terms of packaging / costs and supports various combustion systems in its performance.

However, the layout of the Pre-Chamber itself needs to be accurately matched to the needs of the specific engine and its combustion system. Thus, it is of major importance to understand in detail the influence of the numerous Pre-Chamber design parameters (volume, A/V, hole size, surface, material, etc.) onto the inflammation within the Pre-Chamber and subsequently inside the main combustion chamber also under varying boundary conditions, e.g. from engine cold start up to full load operation. These differing boundary conditions demand a compromise layout of the Pre-Chamber, which in turn shall clearly be the optimum one.

A major requirement for approaching the optimal design and an efficient combustion development work, specifically for PCSP based systems with the numerous influencing parameters, is the application of high-fidelity models that enable predictive simulation of the combustion process.

This paper sets out to describe the work performed within an all-embracing PCSP engine development activity, aiming specifically at in-depth explanation of results from combustion bomb experiments. Clearly, these results are used not only to build a thorough understanding of the combustion process, but also to setup and calibrate an accurate combustion model. The latter will be realized in 3D CFD using CONVERGE software including an advanced chemistry solver to describe in detail Pre-Chamber phenomena, such as flame quenching inside the Pre-Chamber bores because of radical recombination on the channel walls, heat withdrawal and reaction-kinetic behavior (see Figure 1.2). The part explaining the virtual development of this overarching scientific work describing Pre-Chamber combustion will be reported in future publications.
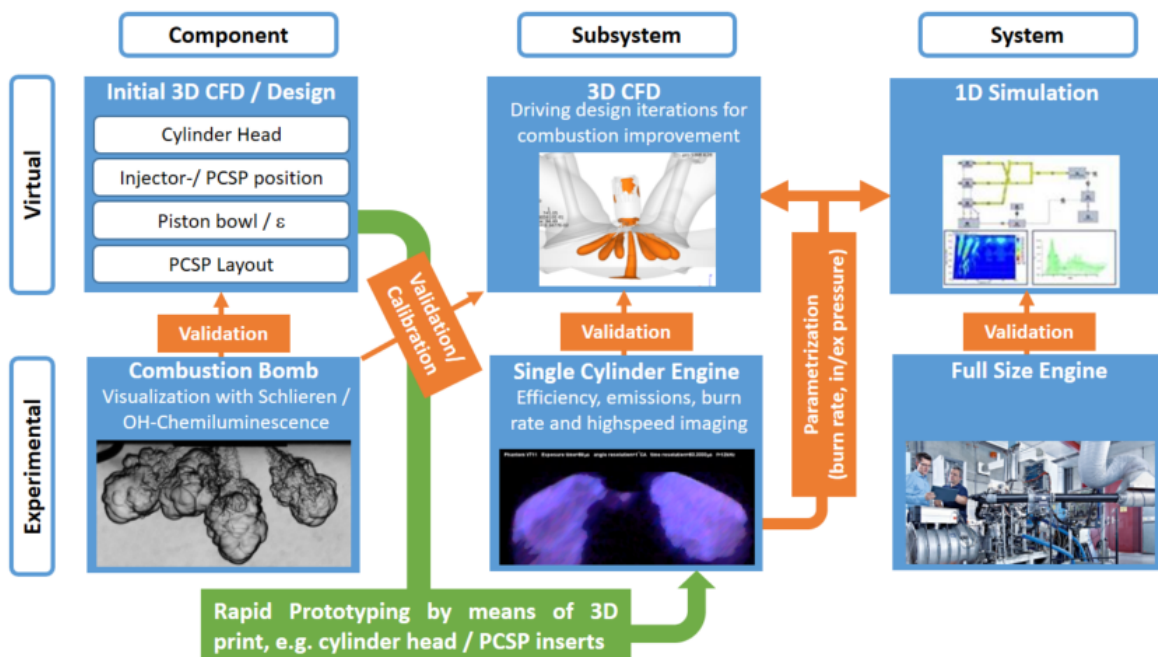
Figure 1.2: Process for Assessment and Development of a PCSP combustion system [24]

1.2   Previous Findings with passive PCSP

Previous investigations of the PCSP on a single cylinder research engine with different complementary technologies, as external cooled EGR and early intake valve closure, show a significant impact of the Pre-Chamber layout to the mixture inflammation and burn rate in the main combustion chamber – especially under critical engine operation conditions [1, 24].

The PCSP ignition system revealed a distinct potential for knock mitigation and thus enabled an increase of compression ratio by 2 to 2.5 units at constant combustion phasing. In-cylinder high speed imaging confirmed the theory of a spatial ignition approach with multiple inflammation zones. In combination with the high ignition energy the PCSP ignition lead to a marked reduction of the pre-reaction time for self-ignition inside the unburnt gas mixture due to shortened ignition delay and combustion duration. Figure 1.3 shows the comparison of combustion parameters for a conventional spark plug and a PCSP system at 2000rpm / 16bar BMEP (knock limited operating point) for two different geometric compression ratios.
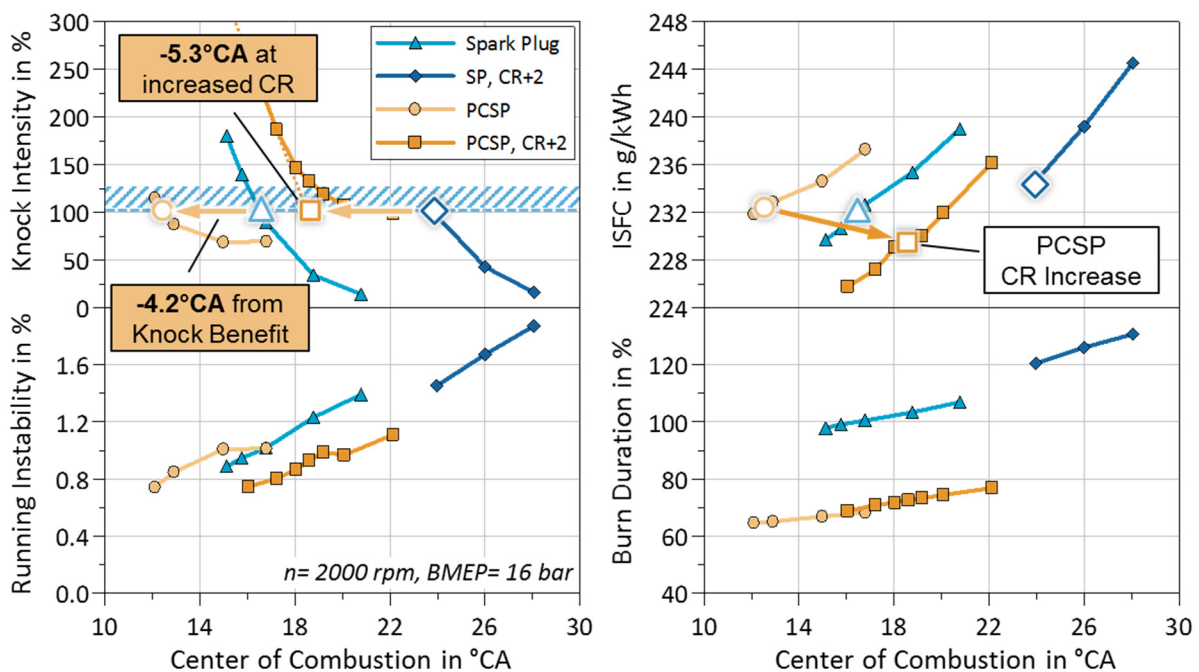
Figure 1.3: Knock mitigation potential of a PCSP compared to a conventional spark plug system for two different compression ratios (10 and 12) [1]

Beside the spacious mixture coverage, the penetrating gas jets of the PCSP generate a high level of turbulence in the main combustion chamber. Both have been found to be very beneficial for the complementary technologies external cooled EGR and EIVC operation – compensating the negative effects by high inert gas fraction and reduced charge air motion, respectively. The grade of improvement possible by the Pre-Chamber ignition system is strongly depended on many different parameters of the PCSP (geometry, material, system integration, etc.). The single cylinder engine investigations in [1] and [24] revealed a mutual interference of these geometrical parameters (e.g. A/V, bore layout, volume, spark location, etc.) on combustion performance on the one hand. On the other hand, certain operating conditions require for example an opposing design of the Pre-Chamber so that the final PCSP layout can only be a compromise.

Especially for engine cold start and high load operation, the requirements for the Pre-Chamber layout seem to be quite conflicting.

Figure 1.4 illustrates the emitted visible light (luminescence) from the in-cylinder combustion (visible optical spectrum) for different PSCP designs, utilizing a high speed camera. The upper row shows the initial phase of combustion with a layout "A" – optimized for high knock mitigation and reduction of fuel consumption in part load – at CA50 of 8°CA (left) and retarded ignition timing (right). Whilst at MBT (Maximum Brake Torque) timing all flame jets, central and lateral, are observed well-distributed inside the main chamber, for late combustion phasing no flames at all are visible. This means, with this PCSP configuration a catalyst heating operation is not possible. The bottom row shows the same comparison with a modified PCSP layout "B" – based on layout "A" with increased central bore diameter.
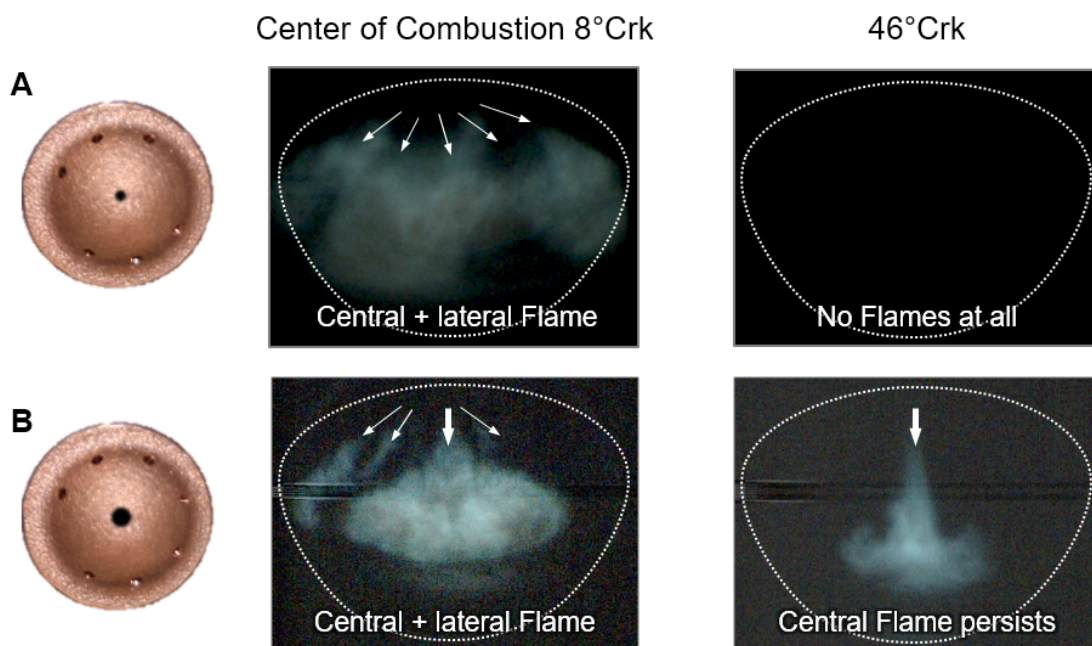
Figure 1.4: High speed camera images from single-cylinder engine: visible light spectrum luminescence of combustion at 1250rpm / 2bar BMEP, two Pre-Chamber variants at base and very late center of combustion [24]

At MBT timing there is a very strong flame jet from the central bore compared to the lateral ones. When retarding the combustion to a CA50 of 46°CA with correspondingly decreasing pressure and temperature, the lateral jets disappear while the jet out of the big central bore still sustains.

Figure 1.5 classifies the two PCSP designs "A" and "B" in a scattering band of various Pre-Chamber layouts in terms of their specific catalyst heating capability. The defined "geometric ratio" represents a multivariate parameter space (containing i.a. A/V, number of bores, bore layout, bore diameter, etc.). It indicates contrary trends for improving the catalyst heating operation and decreasing the knock mitigation potential for example.

The single cylinder engine experiments in [24] identified a further key challenge at the optimization of the Pre-Chamber design. The PCSP comes along with two system specific additional types of wall heat losses, which directly affects the indicated efficiency. One type of heat transfer results mainly from the additional surface of the Pre-Chamber contributing to the total combustion chamber surface. Here, relevant optimization levers are Pre-Chamber material and system integration inside the cylinder head. The

second type of specific wall heat losses is caused by the flame jets of the PCSP. The locally induced turbulence along the jets lead to a significant increase of heat transfer to the main chamber walls – especially at high load. Besides an adjusted flame jet targeting, an optimization of the Pre-Chamber bore geometric parameters could help to avoid direct wall contact and to decrease turbulence close to the walls. For this, a detailed understanding of the impacts of the different parameters to the jet formation and penetration is of particular importance.
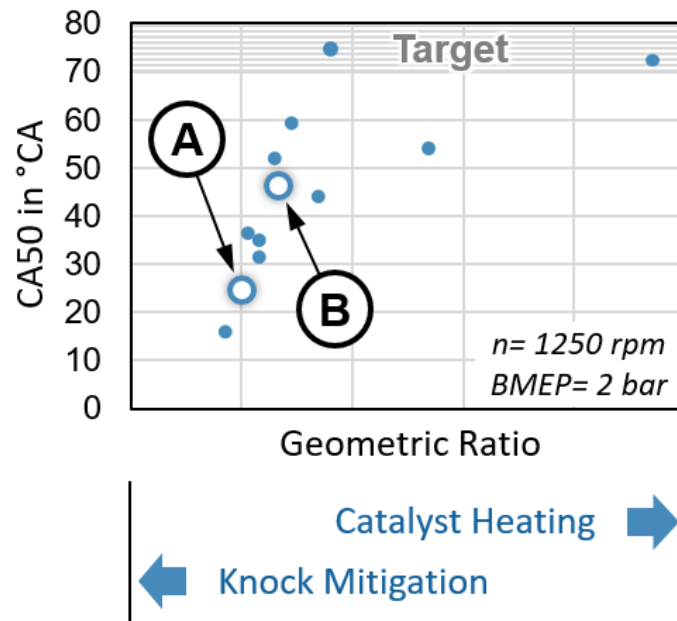
Figure 1.5: Latest possible CA50 across the Pre-Chamber specific geometric ratio for different PCSP layouts at 1250rpm / 2bar BMEP [24]

In the light of the main conclusion of the above described single cylinder engine experiments, some basic thermodynamic considerations shall be stated on a high level in order to better understand the design and result trade-off between low engine load in cold conditions (e.g. catalyst heating) and performance at high load / high temperature (e.g. knocking combustion at boosted operation).

Concerning the conditions inside the combustion chamber, engine cold start clearly poses the most severe challenge for robust inflammation of the main combustion chamber with the Pre-Chamber ignition system. As can be seen in Figure 1.4, it is preferable to enter the regime of flame jet ignition, which means that the flame initiated within the Pre-chamber does not extinguish when passing through the Pre-Chamber orifice. While reasoning as to why this regime is preferable e.g. for engine cold start, the underlying phenomena decisive for either flame or hot gas jet regime shall be discussed first.

Ultimately, the heat loss from the flame to the surrounding walls is the major driver for the flame to extinguish. Referring to what is known as quenching distance, which describes the minimum distance that a flame can propagate through, this parameter is – among others – crucial also for the layout of the Pre-Chamber. Once the flame approaches the orifice, an increasing heat flux to the walls prevents all reactions with high activation energy from being self-sustainable due to an insufficient temperature level. Due to the latter, specifically chain-branching reactions come to a halt so that only

radical recombination reactions are able to take place. Finally, this might lead to ceasing reactions and thus flame quenching [27].

Literature tells that quenching distance is in first order dependent on laminar flame thickness [25, 26, 27] and shows a proportional correlation.

Figure 1.6 in turn shows the dependency of laminar flame thickness on pressure and unburned temperature for a stoichiometric methane/air mixture.
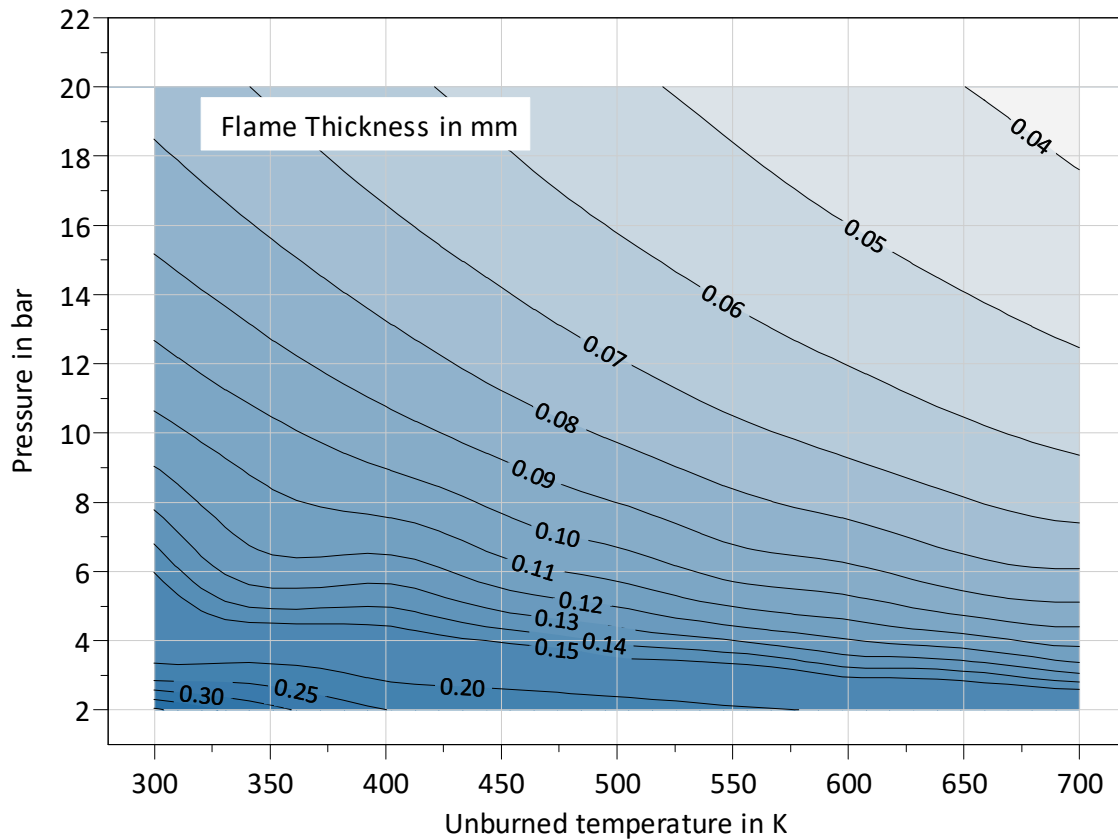
Figure 1.6: Laminar flame thickness dependent on pressure and unburned temperature, calculated at lambda = 1 / EGR = 0% with GRI3.0

It is obvious from the diagram that a decreasing temperature and pressure in the chamber results in a higher flame thickness. Consequently the orifice needs to be bigger to ensure a flame passing through the channel. This behavior is also consistent with observations of Biswas et.al. [25], who could show in combustion bomb experiments that the ignition mechanism shifts from jet ignition regime to flame ignition at increasing pressures.

As for the hot jet ignition regime, the jet consists only of combustion products as the flame has ceased to exist while travelling through the chamber orifice.

Still, a jet of hot gas entering the main combustion chamber is capable to ignite the main chamber mixture even though the number of active radicals it contains is clearly reduced compared to the flame jet regime. Consequently, dominating parameters for the inflammation of the main chamber mixture by hot gas jets is the temperature and mixture of the bulk gas and temperature and the integral turbulence length scale of the hot gas jet. Dependent on the pressure ratio of pre-/and main chamber, the outflow velocity and thus the turbulence level of the hot gas jet is a crucial parameter. In case the turbulence level of the hot gas jet increases so much that the vortexes get as small as the reaction zone thickness, the convective and highly turbulent eddies might cut-

off potential reaction partners from the reaction zone before a self-sustainable chemical reaction is achieved. Increased mixing of cold and unburned mixture with hot reactive gas might lead to local, and in extremum to global quenching of the flame [26], which ultimately results in misfire.

The above described previous findings arise a couple of further questions to the complex interactions of the various Pre-Chamber parameters and their impacts onto the combustion process in the main chamber, that need to be understood in detail for an optimal matching of the PCSP design:

- Impact of total orifice cross section area at constant A/V on combustion performance
- Impact of bore diameter to flame jet structure and penetration as well as turbulent fine structure
- Impact of spark location and bore layout (A/V, bore diameter) to pressure increase inside PCSP
- Impact of spark location and bore layout (A/V, bore diameter) to inflammation delay and flame propagation inside main chamber
- Impact of pressure at ignition to jet penetration
- Impact of A/V or bore diameter to flame extinction
- Impact of ignition regime on inflammation and burn duration in main chamber
- Existence of operating point specific advantages for either flame or hot gas ignition

The present paper tries to examine and answer these questions in the following chapters.

2   High Pressure Combustion Cell

The experimental setup is illustrated in Figure 2.1. The cylindrical steel high pressure combustion cell has a main chamber volume of 2.2 dm^3 and is equipped with 4 circular (diameter 50 mm) quartz windows arranged perpendicular to the spark plug longitudinal axis. A fifth window with a circular quartz window (diameter 100 mm) is located on the opposite side of the spark plug. The modular IAV Pre-Chamber ignition system design known from [1] was used to investigate a broad range of different Pre-Chamber configurations: e.g. volume, spark plug location and the layout of the overflow channels. This modular ignition system insert also enables the use of a conventional M12 spark plug for comparative measurements of the early flame propagation under dormant flow conditions. The ratio of the Pre-Chamber volume to the main chamber volume is around 0.07% and thus much smaller than in a typical engine application (around 2-3%).

The air/fuel mixture inside the combustion cell was heated up to 398 K by eight built-in heating cartridges with a system power of 2800 W integrated in the main chamber walls. To ensure a homogeneous temperature and small natural convection effects of the mixture, four thermocouples (type K) were positioned at the top and on the bottom of the main chamber inside the combustion cell.

The fuel (CH_4 of 99.5% pureness) and the synthetic air (20.5 Vol-% O_2 / 79.5 Vol-% N_2) are injected into the main chamber using the partial pressure method. To ensure a homogeneous mixture in the main chamber and the Pre-Chamber, the gases were injected by two nozzles, one pointing directly at the overflow channels and the other having a swirl element to improve the mixture preparation and homogenization. In preliminary investigations the resting time after the gas being injected was varied between 30 seconds and 10 minutes to study the impact on the combustion process. It was found that a resting time of 2 minutes is enough to gain a homogeneous mixture in the area of optical access. The observed spherical flame propagation induced by a conventional spark plug under different ignition pressure conditions confirms this hypothesis. After each test the combustion cell was drained by a vacuum pump and vented by compressed air to ensure the complete discharge of residual combustion products. The mechanical durability of the combustion vessel limits the maximum peak pressure to 100 bar. This allows a maximum ignition pressure of 18 bar. The mixture inside the Pre-Chamber was ignited by a series production M10 spark plug. The ignition coil was a Delphi Ion sense coil with an ignition energy of 95 mJ and a break down voltage of approx. 23 kV. The spark location and the Pre-Chamber volume was varied by adapter sleeves between the spark plug and Pre-Chamber body. The transient pressure traces were recorded by Kistler 6041B water cooled pressure transducer inside the main chamber and an AVL GH12d pressure transducer inside the Pre-Chamber combined with two Kistler 5018A charge amplifiers. A piezo-resistive Kistler 4045A50 pressure transducer with a Kistler 4603 piezo-resistive amplifier provides the absolute pressure for the piezo electric pressure sensors prior to ignition and is used for the filling of the combustion bomb based on the partial pressure method.
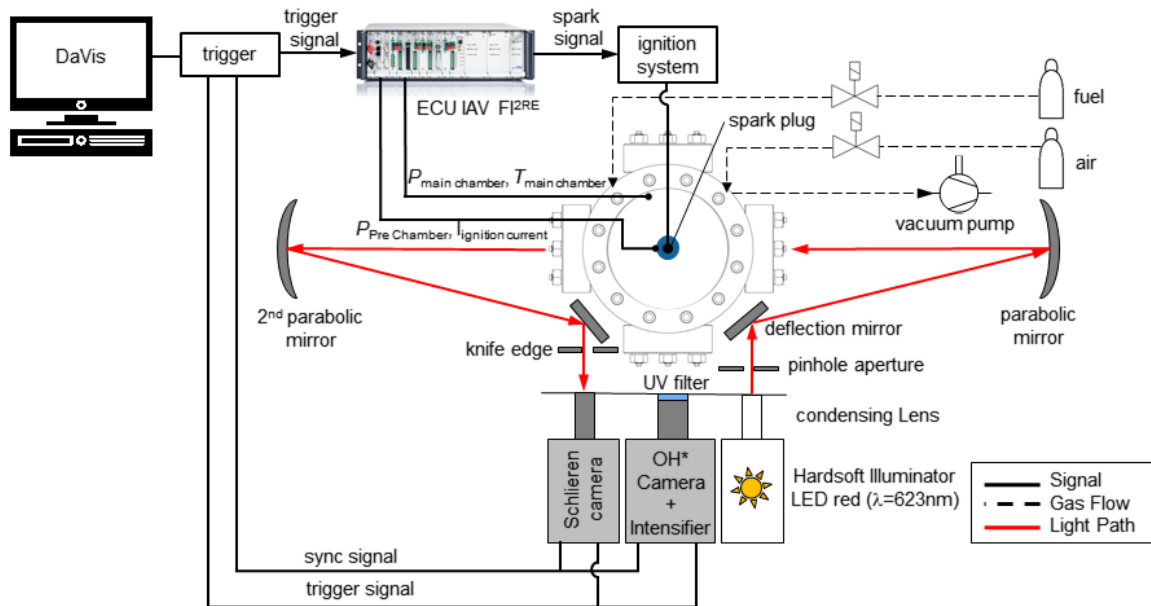
Figure 2.1: Schematic of experimental setup for ignition of premixed methane/air mixture with Pre-Chamber spark plug and conventional spark plug ignition system

2.1   High speed Schlieren and OH* chemiluminescence imaging

The LaVision imaging processing software DaVis with a high-speed controller synchronized and used for triggering the high-speed cameras, the image intensifier and the flexible IAV FI^{2RE} engine control unit. The ECU is equipped with an additional measurement data acquisition card that records the transient pressure traces, the ignition current, the camera triggers and the signals of the thermocouple with a frequency of 2 kHz to cover the complete combustion process. The simultaneously Schlieren and OH* chemiluminescence imaging is performed with a frame rate of 20000 fps.

The high-speed Schlieren technique visualizes the evolution of hot jets and flame jets inside the main chamber. A modified z-type Schlieren setup with two parabolic mirrors and two smaller plane deflection mirrors are utilized to reduce the angle of rotation for the light beam and thus reduce the aberrations errors caused by the parabolic mirrors. A high power LED light source (Hardsoft Illuminator) generates visible red light in wavelength range of 610-660 nm with a luminous flux of 2100 lm to reduce cross-talk effects to the OH* chemiluminescence wavelength range. A Vision Research Phantom v1610 high-speed camera with a resolution of 896x800 pixels and an exposure time of 0.7 µs was used for the Schlieren image capturing. The spatial resolution is 16.0 pixels/mm. [22]

The determination of the heat release and the location of the flame front is possible by imaging of excited species such as OH* or CH* radicals. In this paper the OH* chemiluminescence imaging is used, due to its sharp band passed emittance near 307 nm and the clear separation from the broadband CO_2 signal. Under high pressure conditions the self-absorption characteristic of the OH (ground state) molecules, in the line of sight between the emitter and the detection optics, leads to a reduction in the light intensity of the OH* (exited) radical signal and requires the use of an image intensifier. The OH* intensity is interpreted as a marker for reaction and can be utilized as a useful diagnostic tool to indicate the location of the flame front and its propagation. Lauer &

Sattelmeyer [5] show that the integral chemiluminescence intensities can be correlated to the integral heat release, because the OH* creation is proportional to the CO_2 production inside the flame. [2, 3, 4]

A Vision Research Phantom v1610 along with a video-scope gated intensifier (LaVision high-speed IRO, cathode type: S20 P46) and a 105 mm UV lens were used to detect the exited OH* radicals. A narrow band pass UV-Filter (ASAHI Spectra ZBPA310) around 309±10 nm is used to separate the OH* signal. The image intensifier is synchronized with the high-speed cameras at an image frame rate of 20 kHz. The intensifier gate width is 10 µs and a lens aperture f5.6 was used for each experiment. To achieve the optimal intensity resolution the intensifier gain was adjusted at each shot. The comparability of each experiment with different intensifier gain settings is achieved by an image intensity normalization during the image post processing. The calibrated image intensifier sensitivity function is used for this purpose. The high speed camera operates with a resolution of 896x800 pixels corresponding to a spatial resolution of 10.7 pixels/mm.

2.2   Thermodynamic Post Processing

The first law of thermodynamics is applied to the transient pressure traces to calculate the heat release with a simplified approach in a constant volume vessel. It is assumed that the ratio of specific heats κ is constant. It is estimated as κ= 1.24 for an equivalence ratio of ϕ= 1 at the half temperature between the unburnt mixture temperature and the adiabatic flame temperature. The specific heat of the involved species is calculated by means of NIST (NASA) polynomials. The thermodynamic properties of the mixture are calculated under the assumption of perfect gas mixtures. The simplified heat release is estimated based on the approach of Hohenberg for internal combustion engines, known from [6]. The advantage of this procedure is the easy numeric calculation. Furthermore, the assumption includes an ideal gas and no wall heat losses. The discretized numerical solution for the heat release based on the energy conservation equation is [7]:

$$\left(\frac{dQ_H}{dt}\right)_i = \frac{1}{\kappa-1}\left\{\kappa \cdot p_i \cdot \left(\frac{dV}{dt}\right)_i + V_i \cdot \frac{p_{i+1}-p_{i-1}}{2\Delta t}\right\} \tag{1}$$

The term of a change in volume is set to zero in the investigated case of a constant volume combustion chamber. The integrated heat release is used to define and calculate burn durations and ignition delay times to characterize the velocity for different stages of the complete combustion process. The burnt mass fraction can be correlated to an ideally spherical expanding flame by the following equation:

$$\frac{V_{burnt}}{V_{total}} = \frac{\text{MFB}}{0.75\cdot\text{MFB}+0.25} \tag{2}$$

The total chamber volume is 2186 cm^3 and for simplification it is assumed, that the trace of the normalized integrated heat release corresponds to the mass fraction burned profile. Figure 2.3 illustrates the correlation between the burnt to total volume ratio as a function of the burnt mass fraction. In comparison, the cylinder displacement

volume of typical gasoline engines on the market today usually is less than 500 cm^3 (which corresponds to 22.8% of the combustion bomb volume), while the combustion is already finished long before the piston has displaced this maximum volume. Aiming to understand the behavior of the PCSP combustion in a typical gasoline engine, obviously the focus of the analysis of the bomb combustion needs to be put onto the very early phase of flame progress.

The plot on the right in Figure 2.3 shows typical profiles for the integrated heat release (right axis) and the burnt volume ratio (left axis) for the standard spark plug ignition system and Pre-Chamber spark plug (PCSP). Again, for a proper comparison of the impact of the pre-chamber geometry on the combustion process inside the large combustion bomb in relation to a typical internal combustion engine with a cylinder volume of ~500 cm^3, it is necessary to analyze only the early points of heat release before 10% energy conversion. This heat release conversion time leads already to a slightly higher burnt volume than 500 cm^3 and will be defined as the late phase of combustion in regard to a typical engine combustion chamber. As can be seen from the Figure 2.3, the PCSP shortens the duration between ignition and the 20% energy conversion approximately by 35% compared to a conventional spark plug. The characterization of the early flame development phase will be based on the 2% and 5% energy conversion points. It could be shown, that the slope of the integrated heat release profile is sufficient to detect the 2% energy conversion point without any large numerical errors. On the other hand, a detection of 1% energy conversion timings gave instable and inaccurate results due to a too small gradient and will not be used in this work.
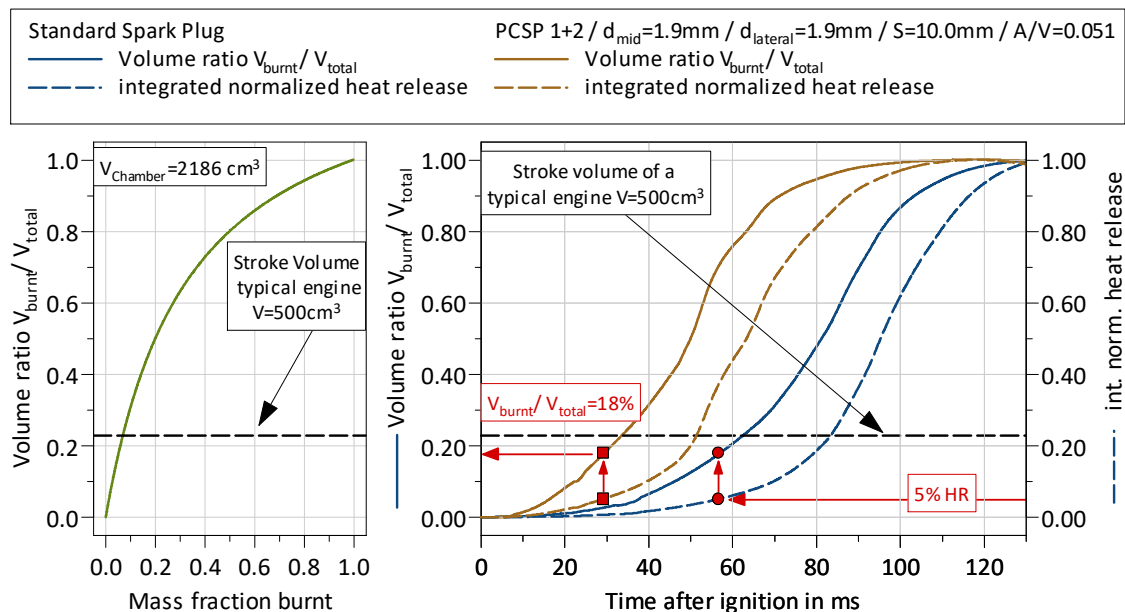

Figure 2.3: Comparison of heat release and burnt volume based on a spherical flame expansion

2.3   Image Post Processing

The Schlieren and OH* chemiluminescence images were acquired from two different perpendicular aspects with unequal spatial resolutions. One pair of lateral windows was used for Schlieren imaging and another perpendicular window provided the optical access for the OH* chemiluminescence image recordings. The comparability of the two imaging strategies necessitates several image post-processing strategies. Calibration measurements performed prior to the image recordings at the location of the spark plug perpendicular to the camera axis. Based on the calibration results the image aberration error is corrected as well the spatial resolution is determined. The following image processing is performed with MATLAB. First the OH* chemiluminescence image is scaled and offset corrected to the Schlieren image to enable a geometric comparison. In a second step an averaged background picture (10 images before the spark event are averaged) prior to ignition was subtracted from all images. The OH* chemiluminescence pictures were recorded with different intensifier gain settings to achieve a high signal-to-noise ratio. These pictures need to be corrected by normalizing it intensity to the minimum of the used intensifier gain during the complete campaign. The calibrated sensitivity function of the image intensifier is used for this purpose. The results enable a comparison of the OH* radical light intensity for different Pre-Chamber layouts and thus would allow a conclusion about the intensity of the early phase of combustion as well as on the ignition mechanism: flame jet or hot turbulent jet inside the main chamber.

2.3.1 Morphological Image Analysis

A morphological analysis of the Schlieren und OH* chemiluminescence images is the prerequisite for generating quantitative results of flame propagation and penetration depth of the turbulent jets.

The morphological reconstruction of the flame front and the burned area of luminous flames is widely discussed in the literature, e.g. [8-21].

There are several evaluated approaches available to detect the flame front, respectively the burned area, depending on the imaging type methodology selected. [11-13] use a combination of Otsu's binarization method and a user calibrated threshold to divide the picture into a burned and unburned area. The major drawback of this approach is that two calibration constants have to be estimated by the user. In addition, this method was developed to binarize images of a full spectrum luminous flame. The Otsu's threshold algorithm, a histogram-based approach, divides the pixels into two classes, so that the intra-class variance is minimized and the inter-class variance is maximized. The resulting threshold is used to binarize the image. This methodology needs images with a high contrast and a big signal-to-noise ratio. For this purpose the background-corrected images are filtered with a two-dimensional Gaussian kernel with a standard deviation of $\sigma = 2.5$ to reduce the fixed pattern and shot noise of the camera and the image intensifier. In a next step, the Otsu's binarization method with three threshold levels is applied. It was found that the use of two different thresholds improves the accuracy during the early flame evolution for the turbulent jets in contrast to the use of a single threshold value with OH* chemiluminescence signals. The upper two threshold levels can be considered as the burned gas area. The remaining noise and false pixel matches are removed by 7x7 pixels median filter. The count of burnt

pixels is the basis for the flame area and flame speed calculation. The Gaussian Filtering method was compared with a median filtering (filter size 7x7 pixels) prior to the Otsu binarization (see Figure 2.2 and 2.3). It was found that the latter method leads to monotonic increasing flame areas with reduced signal noise, when the burnt pixels from the previous time step remains unchanged in the current time step. The method using the Gaussian filtering causes unphysical normalized flame areas much smaller than unity in some cases, due to a high signal-to-noise ratio in the images. For these reasons the adapted Otsu binarization method with a median filtering will be used within this work (see Figure 2.2 and 2.3).
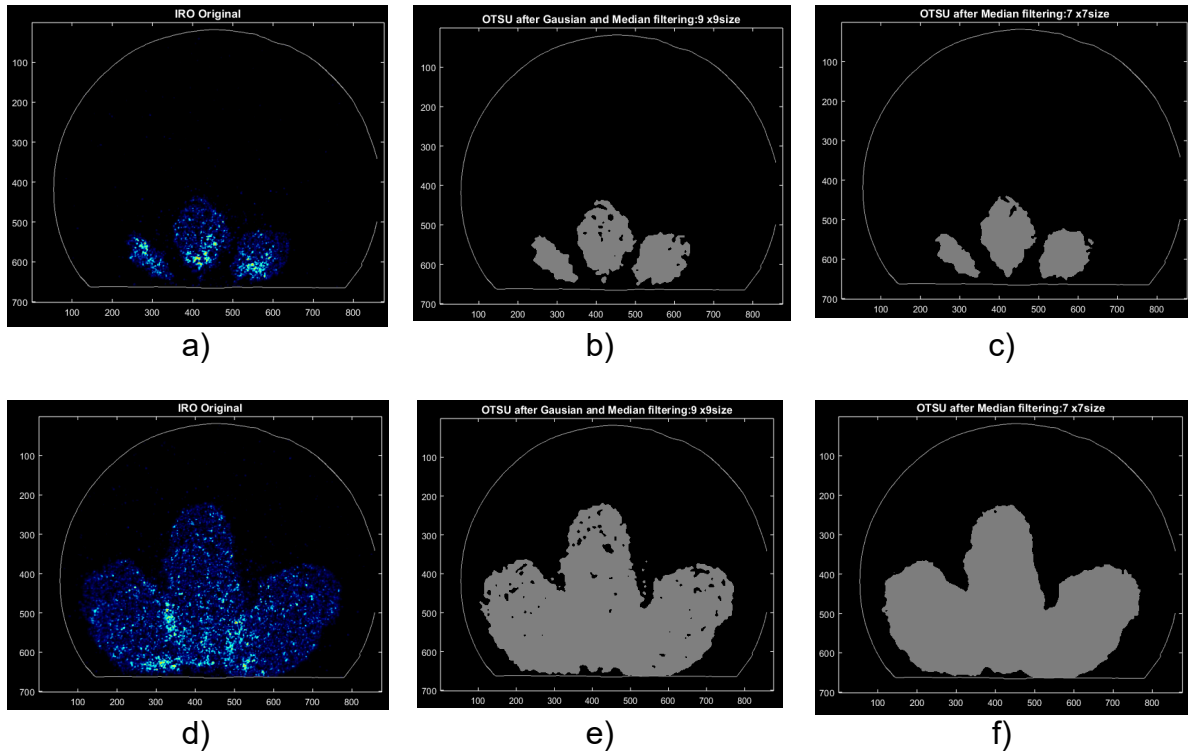
Figure 2.2: Comparison of image processing method (Gaussian filtering b-c, Median filtering e-f) prior to Otsu threshold for different timings with the original OH* chemiluminescence images (a,d)
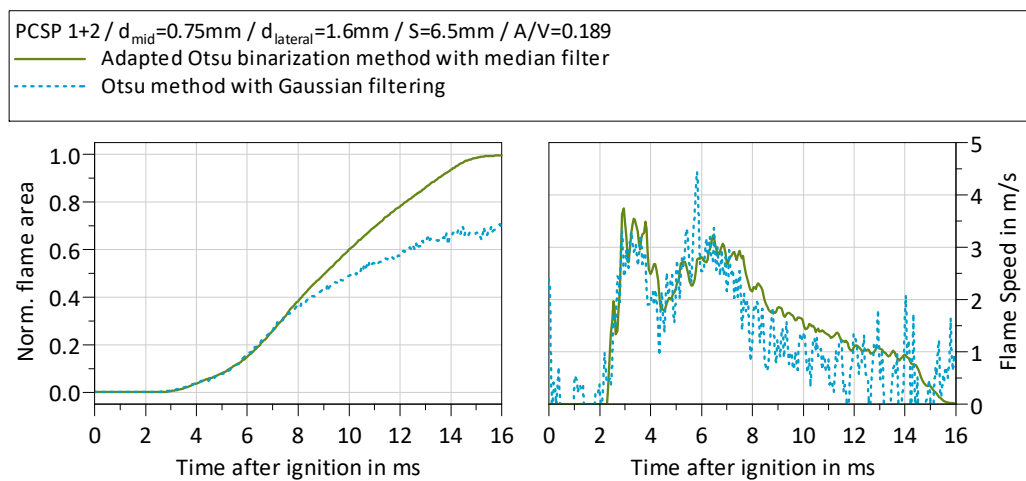
Figure 2.3: Comparison of normalized flame speed and flame area calculation for the mentioned different morphological image binarization algorithm

The penetration depth of the turbulent jets is estimated by using a different morphological image processing algorithm applied to the Schlieren pictures. After the ignition in the Pre-Chamber, hot gas jets penetrate into the main chamber through the overflow channels connecting the two chambers. For the analysis of different Pre-Chamber geometries it is important to estimate the jet penetration, as it provides information about gas and flame propagation, which is indirectly related to engine phenomena like inflammation reliability, knock tendency and burn duration.

a) Original image   *b) Processed image*
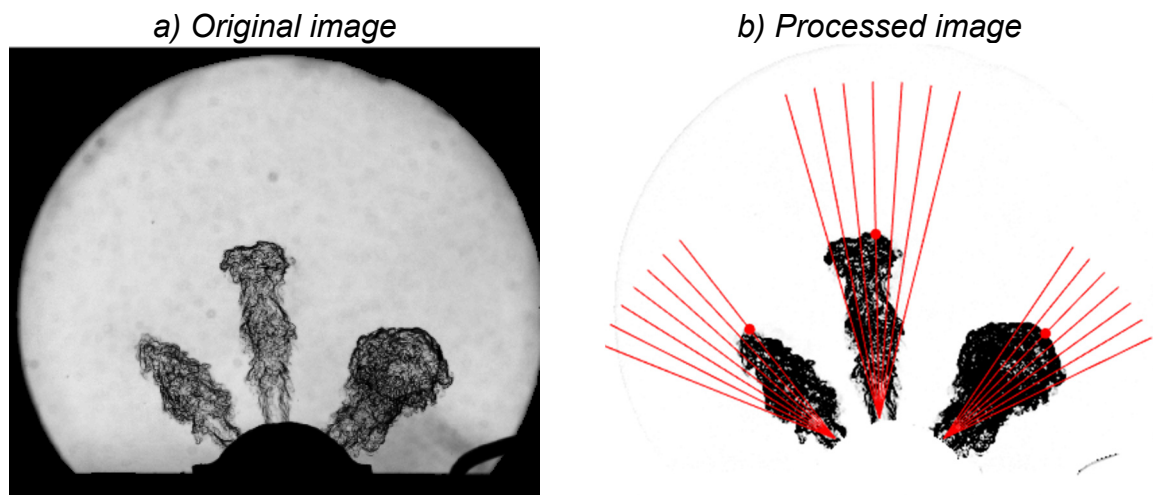
Figure 2.3: Determination of jet tip penetration inside the combustion chamber

The jet tip penetration is determined based on the Schlieren images inside the main chamber (see Figure. 3a). The background noise caused by camera CMOS chip is removed by a simple threshold method. In a second step, the recent Schlieren image is divided by the first image and normalized to enhance the contrast of the jet's front and to remove any dirt from the pictures. A quick and effective way to determine the jet penetration, is to evaluate the intensity of the pixels along a line orientated in jet direction. Since the jet can deviate when entering the main chamber, several lines with different angle but same origin (overflow-channel) are drawn, creating an array of lines (see Figure. 2.3b). The resolution can be changed by modifying the number of lines and the angle of the array. The maximal penetration is calculated for each line of the array and only the line with the highest penetration is retained. The position is tagged with a dot on the corresponding line in Figure 2.3b. This penetration is determined for each jet at each time step and exported to a data file.

3   Results

The development of well-adapted Pre-Chamber ignition systems requires the detailed technical understanding of the impact of Pre-Chamber geometry parameters to the basic mechanisms of fuel-air mixture inflammation and early flame propagation in the main combustion chamber under different thermodynamic boundary conditions. In order to examine the impacts without side effects, such as residual exhaust gas and charge motion, IAV has conducted a parameter study on a high-pressure combustion vessel. Limited by the mechanical durability of the chamber and the available power of the electrical heating device, the combustion cell enables the adjustment of chamber conditions at ignition timing of up to 18 bar and 398 K. Especially high load and catalyst heating operating points differ quite significantly from these conditions under real engine operation.

Nevertheless, it was tried to define operating points for the combustion vessel with best relevance for real engine operation. A simple approach for the comparability of boundary conditions is the correlation of the unburned gas density. The lower temperature inside the combustion bomb would be compensated by corresponding lower pressures in order to match the gas density. However, pressure and temperature do also have a significant impact to the laminar flame speed of the mixture.
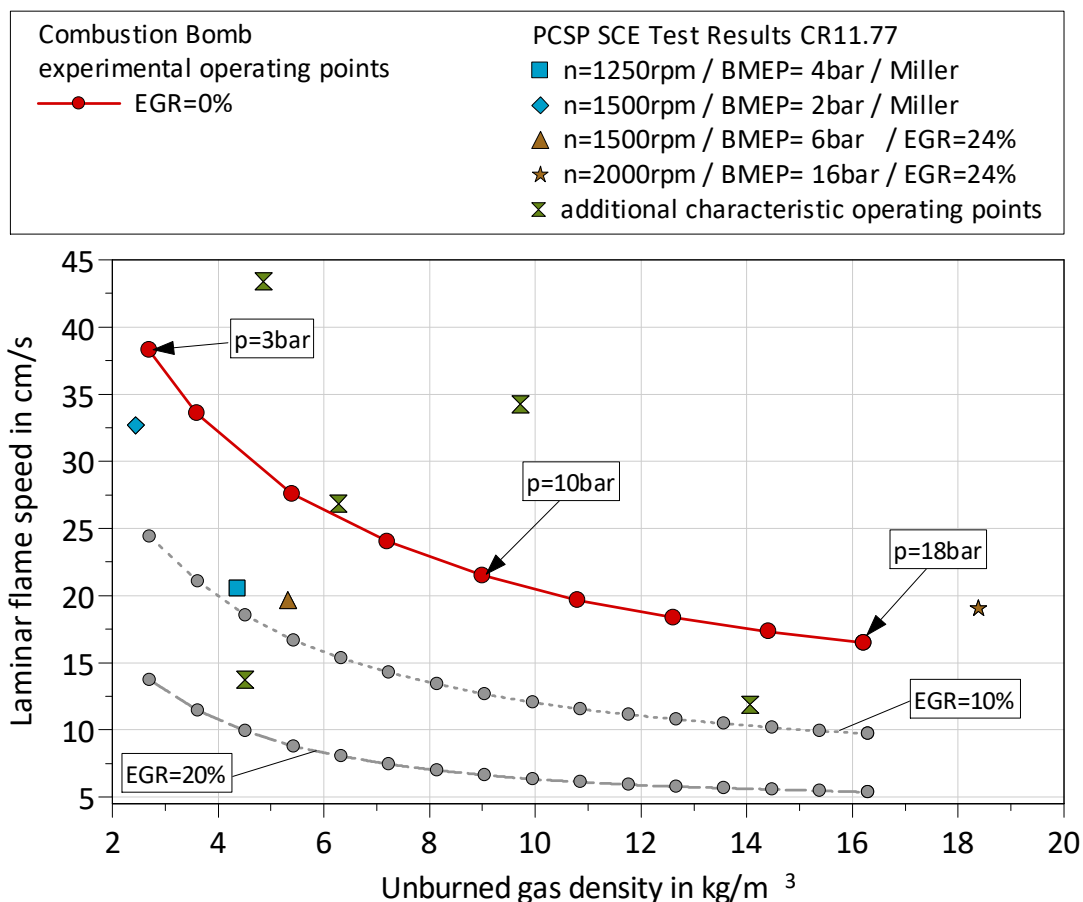
Figure 3.1: Laminar flame speed for a stoichiometric methane air mixture for different pressures and unburned gas temperatures inside the high pressure combustion cell. Comparison with typical engine operating points in consideration of its specific thermodynamic properties (temperature, pressure and residual gas rate)

A main scope of this work is the visualization and analysis of the flame / hot gas jets passing over from the Pre-Chamber to the main chamber (after the initial ignition inside the Pre-Chamber) as well as the early flame propagation inside the main chamber. From this perspective, the laminar flame speed is considered the most important parameter for the correlation of the operating points of combustion vessel and single cylinder engine. Figure 3.1 illustrates the laminar flame speed for a stoichiometric methane air mixture for different pressures and unburned gas temperatures inside the high pressure combustion bomb in comparison to different characteristic engine operating points – considering the specific thermodynamic and chemical properties (gas composition, temperature and pressure). The calculations have been conducted with the chemistry solver of CONVERGE by Convergent Science based on the GRI3.0 reaction mechanism with 53 species [23].

Referring to these preliminary considerations, three main operating points have been defined for a comprehensive parameter study in the combustion bomb – 3, 10 and 18 bar chamber pressure at ignition timing. These points can be set in relatively good correlation to characteristic single cylinder engine operating points – based on comparable laminar flame speed. 18 bar chamber pressure (at 398 K chamber temperature) represents in good approximation the medium high load operation of the single cylinder ICE (2000 rpm / 16 bar BMEP), 10 bar chamber pressure the part load map area (1500 rpm / 6 bar BMEP) and 3 bar chamber pressure the critical low load / catalyst heating operation (1250 rpm / 2 bar BEMP). In addition to those main operating points also other chamber pressures have been investigated with selected PCSP configurations.

Table 3.1 summarizes the experimental space of the geometric Pre-Chamber parameters and thermodynamic boundary conditions investigated inside the combustion vessel.

Table 3.1: Experimental space of geometric PCSP parameters and thermodynamic boundary conditions

Parameter	Unit	Range	Description
Number of bores	-	3 – 7	total
Bore layout	-	1+2 / 1+5 / 1+6	central + lateral
Central bore diameter	mm	1.0 – 3.5	
Lateral bore diameter	mm	1.0 – 1.9	
Spark location	mm	3.5 / 10 / 16.5	
PC Volume	cm³	1.27 / 1.65 / 2.02	spark location low / middle / high
A/V	-	0.012 – 0.173	bore area to PC volume ratio
Spark plug size	-	M10	mass production, 2 electrodes
Gas temperature	°C	115 – 128	
Gas pressure at ignition	bar	3 – 18	
Lambda	-	0.95 – 1.5	

Figure 3.2 shows examples of the investigated PCSP variants. The two right 1+2 bore designs have been defined in order to achieve best visualization of the Pre-Chamber jets without disturbing interferences of the single streamers within the experimental setup of the combustion bomb. Thus most investigations have been conducted with those bore layouts. The two left 1+5 and 1+6 bore designs were expected to create interferences of the different jets and thus to complicate the result analysis, however, have been tested in brief measurements in order to have the best possible overlap to the PCSP designs investigated inside the single cylinder engine.

Figure 3.2: Examples of investigated PCSP variants

3.1   Measurement repeatability and mixture homogeneity

In order to validate the repeatability of the high-pressure cell investigations, a series of repeated measurements has been conducted at the beginning of the test campaign. Figure 3.3 shows the repeatability of 3 to 5 measurements for one exemplary Pre-Chamber configuration at three different equivalence ratios.
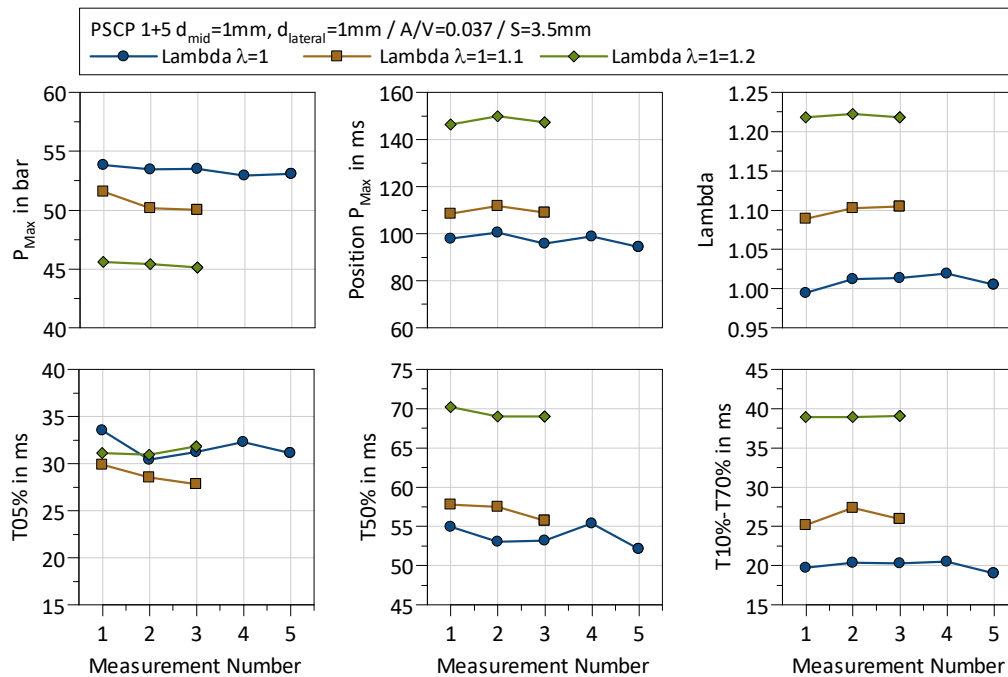
Figure 3.3: Evaluation of the measurement repeatability for one exemplarily Pre-Chamber spark plug with a spark location S=3.5mm for 10 bar ignition pressure and different equivalence-ratios.

Overall, there is a very good repeatability and thus validity of the measurement results. For the subsequent test campaign, each configuration has been measured twice. If the results have been within an acceptable deviation, they were averaged for further analysis. In case of bad repeatability, a third measurement has been conducted to identify measurement outliers. Figure 3.4 illustrates the flame front development of the standard spark plug ignition system at a system pressure of 3 bar. The flame front propagates spherical after the ignition process. This indicates a highly homogenous mixture in terms of equivalence-ratio and temperature distribution inside the combustion chamber and is in accordance to the laminar flame propagation theory inside a combustion chamber.
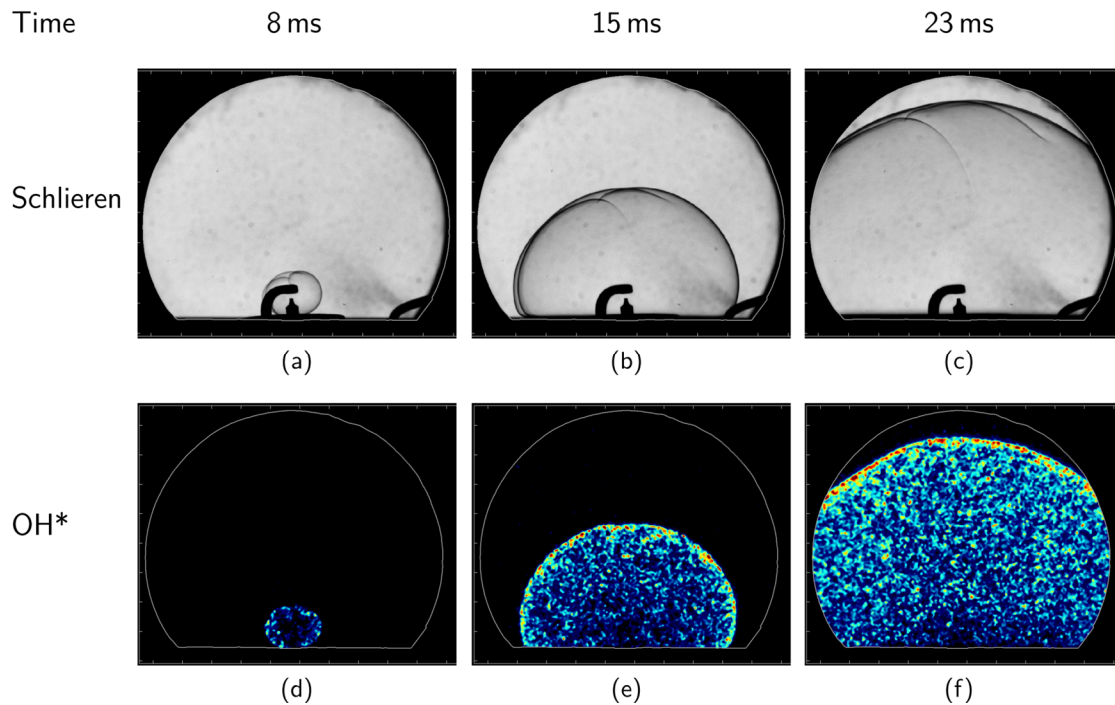
Figure 3.4: Evaluation of the flame front for the standard spark plug ignition system at 3 bar ignition pressure. Top Row: Schlieren images. Bottom Row: OH*-Chemiluminescence images at different times. Ignition timing is at 5.5ms.

3.2   Dependency of Pre-Chamber geometry and pressure on inflammation process in the main chamber

As known from previous single cylinder investigations [1, 24] the PCSP geometry might have a very positive impact on knock resistance, while the low load performance is quite challenging to improve to a level known from conventional ignition systems.
It was found, that a small A/V-ratio could have a very positive impact to knock mitigation. However, for low engine loads a different PCSP design with for example higher A/V-ratio and adapted bore layout is rather beneficial. Therefore an optimal Pre-Chamber spark plug design has to solve the trade-off between a high knock resistance and reliable inflammation at poor ignition conditions. Figure 3.5 illustrates the early heat release and the flame propagation as a function of the ignition pressure for three different PCSP geometries and the conventional spark plug ignition system. An increasing ignition pressure is achieved by a higher mixture mass and thus leads to the trivial result of an increasing maximum pressure of up 100 bar inside the main chamber. The mechanical durability of the combustion vessel limits the peak pressure to 100 bar.
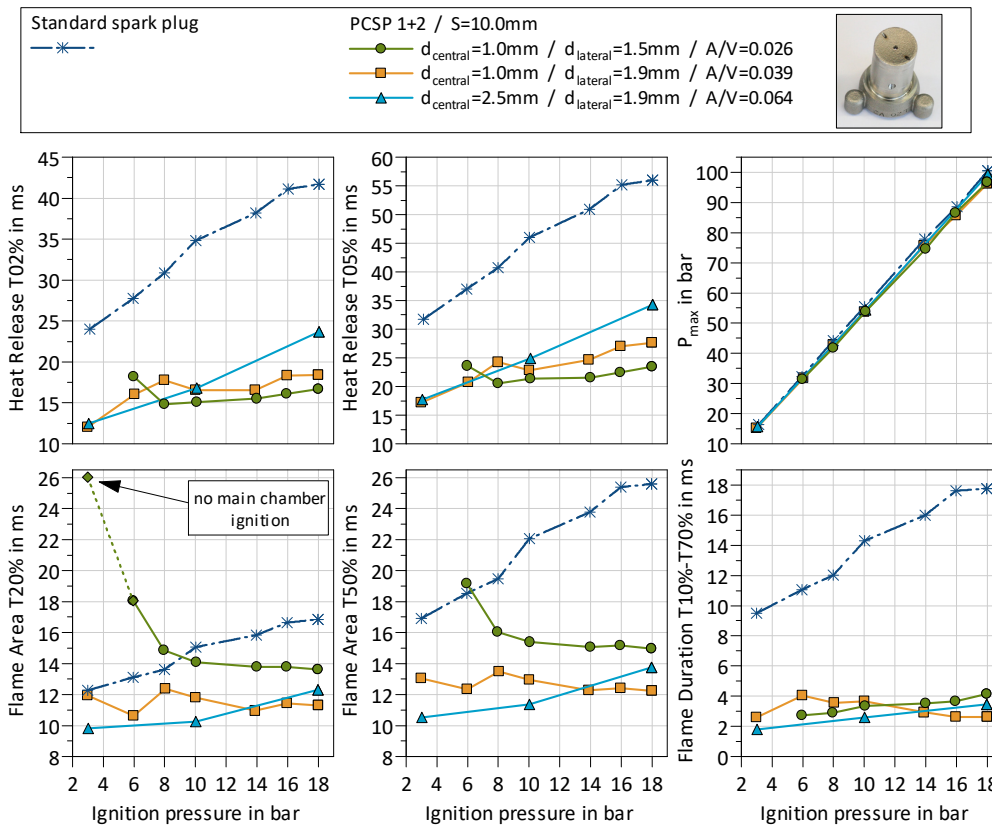
Figure 3.5: Effect of different central overflow channel diameter sizes on flame propagation and heat release for distinct ignition pressures. Equivalence-ratio ϕ=1.

A higher mixture mass as a consequence of an increased pressure results in a prolongation of the heat release. This is caused by a reduced laminar flame speed for higher pressure as shown in figure 3.1. The standard spark plug ignition system shows, as expected, the longest period of heat release. Schlieren images indicate a largely laminar flame expansion during the first phase of combustion. Later on cellular flame instabilities (Darrieus-Landau and thermo-diffusive instabilities, for more information refer to [7]) could be observed, which are a typical phenomenon of a spherically expanding flame in the case of the standard spark plug ignition system. These instabilities and

the curvature of the expanding flame increase the laminar flame velocity estimated by the image analysis process. That is comparable to the physical phenomenon of a turbulent flame propagation. The calculated flame speed for the standard spark plug ignition system is overestimated in these cases. The image analysis procedure also assumes that the flame area is equal to a circle. The flame speed calculation is based on the temporal derivation of the circle radius and thus leads to several inaccuracies for the absolute flame speed values, because the three dimensional flame surface is projected to a two dimensional image recorded by the camera. As well, the flame formation for the PCSP has a completely different shape compared to a circle. Nevertheless this methodology allows a quantitative comparison within the measurement campaign between the conventional spark plug ignition system and different Pre-Chamber geometries.

The standard spark plug shows a significantly increasing flame duration (Flame duration T10%-T70%) for an elevated ignition pressure. The dependency for the PCSP variants is nearly one order of magnitude smaller than for the spark plug. The Pre-Chamber with an A/V-ratio of 0.064 and a central bore diameter of 2.5 mm shows a similar behavior to the conventional ignition system. It can be stated that a large bore diameter is beneficial for low load conditions and disadvantageous at high ignition pressures for achieving reliable inflammation and short inflammation delays. A very small central bore diameter in combination with a small A/V-ratio of 0.026 prevents an inflammation at 3 bar and leads to a significant prolongation of the inflammation delay (Flame Area T20%) and the early heat release. The smaller bore diameter increases the jet mean velocity, the fluctuation speed and reduces the characteristic size of the turbulent eddies. For a stoichiometric methane mixture at 3 bar, the laminar flame thickness is in the order of 0.25mm. For an orifice diameter of d=1.0mm it can be assumed, that the tiniest turbulent eddies are smaller than the flame thickness and can therefore rip the flame front inside the overflow channel. Furthermore the highly turbulent jets lead to a rapid mixing and thus an increased heat loss to the preheat zone. The flame extinguishes and avoids a stable inflammation at low pressure and temperature conditions. A higher ignition pressure increases the mixture mass inside the Pre-Chamber. The heat release is intensified and the laminar flame thickness is reduced to approx. 0.07 mm. This leads to a reduced flame quenching probability for higher ignition pressures. The flame ignition mechanism becomes more prevalent [7, 27, 32]. Figure 3.6 illustrates the jet structure and the OH* intensity for the above mentioned Pre-Chamber geometries at three characteristic ignition pressures. The investigated PCSP variants show increasing density gradients for elevated pressures. This characteristic can be explained by the higher mass burnt inside the Pre-Chamber, which leads to an intensified energy input into the main chamber. In general it can be stated, that the inflammation is always induced by the bore with the largest diameter. The highest OH* intensities are observed for the PCSP with A/V ratio of 0.039, which seems to be in the optimal range for a reliable inflammation at low and high loads. The structure of the central jet changes from a typical open jet characteristic to mushroom-shaped jets for a bore diameter of 2.5 mm.

Overall, it can be claimed, that there is an optimal cross section area to volume ratio with a least one larger bore diameter, to enable a reliable inflammation at low loads and only a minor flame speed prolongation for higher ignition pressures. If the A/V-ratio becomes too small, the inflammation delay (flame area T20%) and the early flame formation period (flame area T50%) increase, especially for high loads.
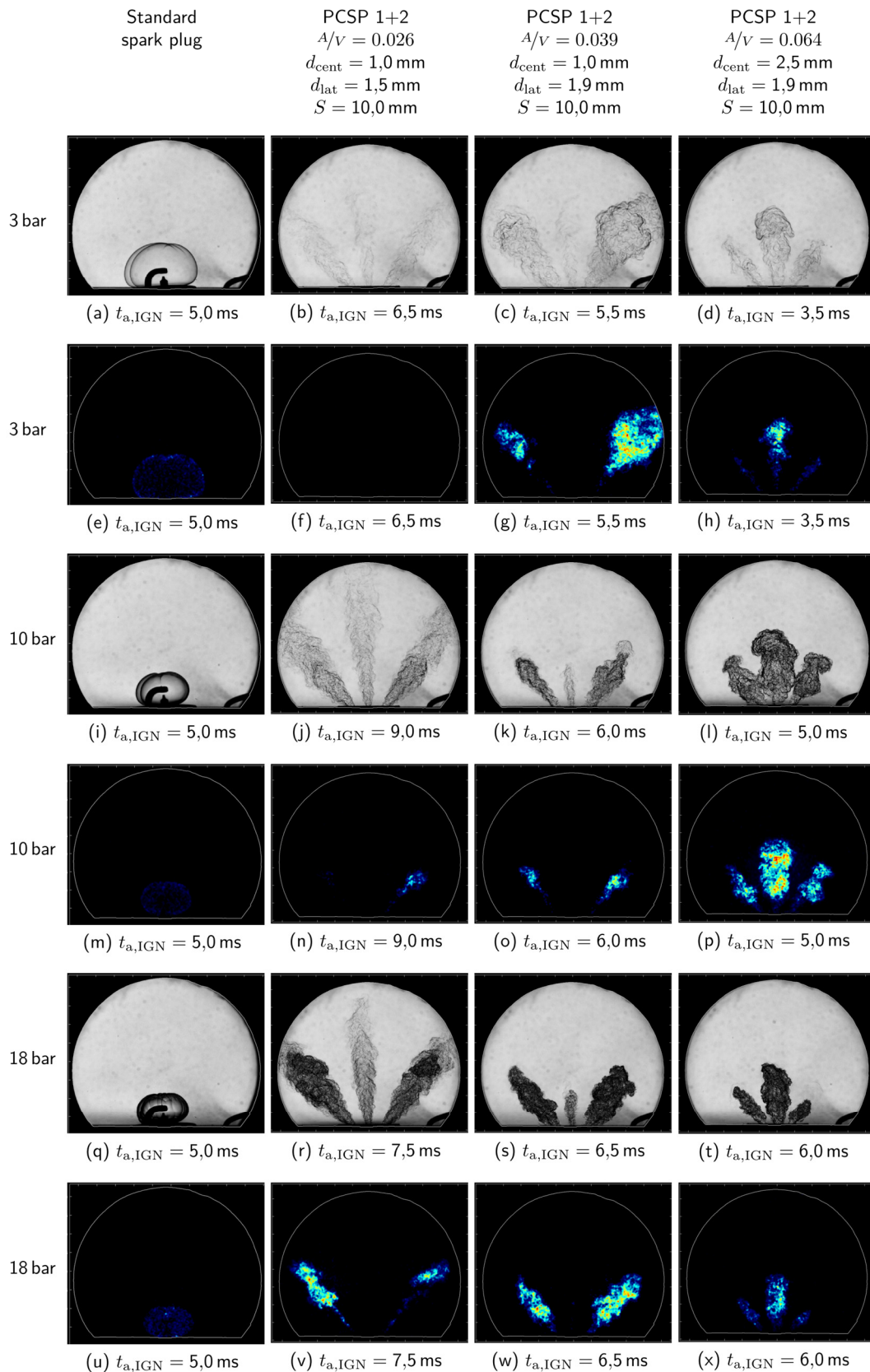
Figure 3.6: Effect of different central overflow channel diameter sizes on the flame jet structure and the OH* intensity. Ignition pressure p=3 bar. Equivalence-ratio φ=1.

3.3   Dependency of Pre-Chamber geometry on the flame formation under low pressure and low temperature conditions

In [1] and [24] it was found at a single cylinder research engine, that low load and low temperature conditions cause small pressure differences between the Pre-Chamber and the main chamber and thus resulting in low jet velocities. Consequently, this weak jet is rather unlikely to ignite the mixture in the main combustion chamber. Based on these previous findings it might be reasonable to assume that low wall temperatures and small overflow channel diameters increase the resistance for the flame to propagate from the Pre-Chamber into the main chamber. The strong and highly turbulent flow field inside the bores leads to an intensive flame stretching and in addition with a large surface contact area to the colder walls to an in tendency increasing flame quenching. In [24] it was stated, that a PCSP with an increased cross section to volume ratio in combination with a larger central bore diameter enhances the ignitibility and combustion stability at a typical catalyst heating operating point.

Figure 3.7 illustrates the impact of the overflow channel cross section area to the Pre-Chamber volume (A/V) with identical spark locations at an ignition pressure of 3 bar. The pressure difference between the Pre-Chamber and the main combustion chamber increases for smaller A/V-ratios, due to a higher flow resistance of the overflow channels. Comparing the excess pressure for the different geometric PCSP layouts with the tiniest A/V-ratio, it can be expected, that there is an A/V-ratio lower limit for a proper ignition of the mixture inside the main chamber. The PCSP layout with the smallest A/V-ratio and only three overflow channels generates overly weak flame jets with only marginal OH* luminescence detected, which in turn could not ignite the main mixture inside the combustion bomb. The 1+5 PCSP layout with smaller bore diameters does not show any OH* radical concentration at all (see Figure 3.8). This fact is a strong indicator, that the flame extinction is mainly induced by the too small bore diameter. The heat transfer from the reacting fluid to the cold walls, the strong flow field inside the overflow channels and the flame stretching are assumed to be the main causes for this characteristic at low loads. Increasing the A/V ratio leads to a reduction of the period for flame formation and thus to faster heat release in the early stage of combustion prior to an energy conversion up to 10%.
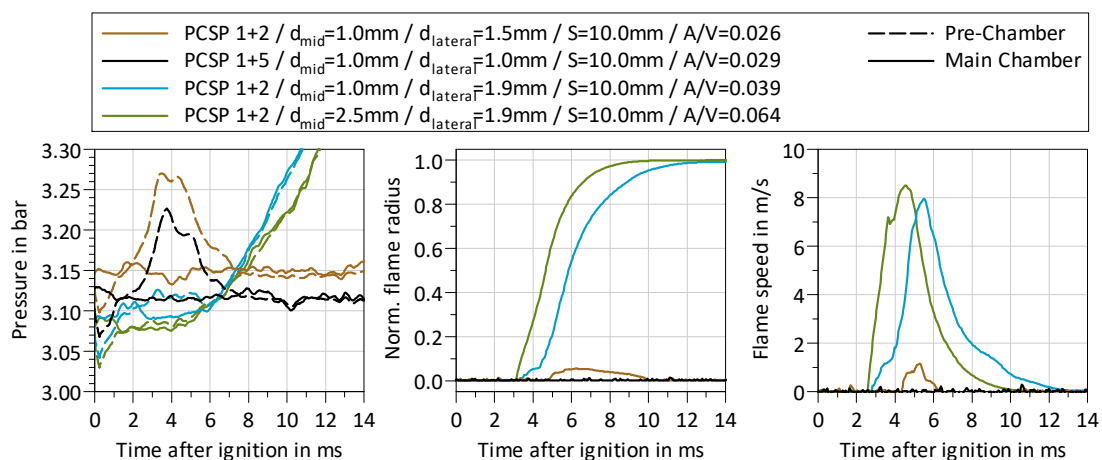
Figure 3.7: Impact of the overflow channel cross section area on the flammability of the main chamber mixture. Ignition pressure 3 bar and equivalence-ratio ϕ=1.

PCSP 1+5	PCSP 1+2	PCSP 1+2	PCSP 1+2
$A/V = 0.029$	$A/V = 0.026$	$A/V = 0.039$	$A/V = 0.064$
$d_{\text{cent}} = 1{,}0\,\text{mm},$	$d_{\text{cent}} = 1{,}0\,\text{mm}$	$d_{\text{cent}} = 1{,}0\,\text{mm}$	$d_{\text{cent}} = 2{,}5\,\text{mm}$
$d_{\text{lat}} = 1{,}0\,\text{mm}$	$d_{\text{lat}} = 1{,}5\,\text{mm}$	$d_{\text{lat}} = 1{,}9\,\text{mm}$	$d_{\text{lat}} = 1{,}9\,\text{mm}$

(a) $t_{\text{aIGN}} = 3{,}5\,\text{ms}$ (b) $t_{\text{aIGN}} = 3{,}5\,\text{ms}$ (c) $t_{\text{aIGN}} = 3{,}5\,\text{ms}$ (d) $t_{\text{aIGN}} = 3{,}5\,\text{ms}$

(e) $t_{\text{aIGN}} = 3{,}5\,\text{ms}$ (f) $t_{\text{aIGN}} = 3{,}5\,\text{ms}$ (g) $t_{\text{aIGN}} = 3{,}5\,\text{ms}$ (h) $t_{\text{aIGN}} = 3{,}5\,\text{ms}$

(i) $t_{\text{aIGN}} = 4{,}5\,\text{ms}$ (j) $t_{\text{aIGN}} = 4{,}5\,\text{ms}$ (k) $t_{\text{aIGN}} = 4{,}5\,\text{ms}$ (l) $t_{\text{aIGN}} = 4{,}5\,\text{ms}$

(m) $t_{\text{aIGN}} = 4{,}5\,\text{ms}$ (n) $t_{\text{aIGN}} = 4{,}5\,\text{ms}$ (o) $t_{\text{aIGN}} = 4{,}5\,\text{ms}$ (p) $t_{\text{aIGN}} = 4{,}5\,\text{ms}$

(q) $t_{\text{aIGN}} = 5{,}5\,\text{ms}$ (r) $t_{\text{aIGN}} = 5{,}5\,\text{ms}$ (s) $t_{\text{aIGN}} = 5{,}5\,\text{ms}$ (t) $t_{\text{aIGN}} = 5{,}5\,\text{ms}$

(u) $t_{\text{aIGN}} = 5{,}5\,\text{ms}$ (v) $t_{\text{aIGN}} = 5{,}5\,\text{ms}$ (w) $t_{\text{aIGN}} = 5{,}5\,\text{ms}$ (x) $t_{\text{aIGN}} = 5{,}5\,\text{ms}$
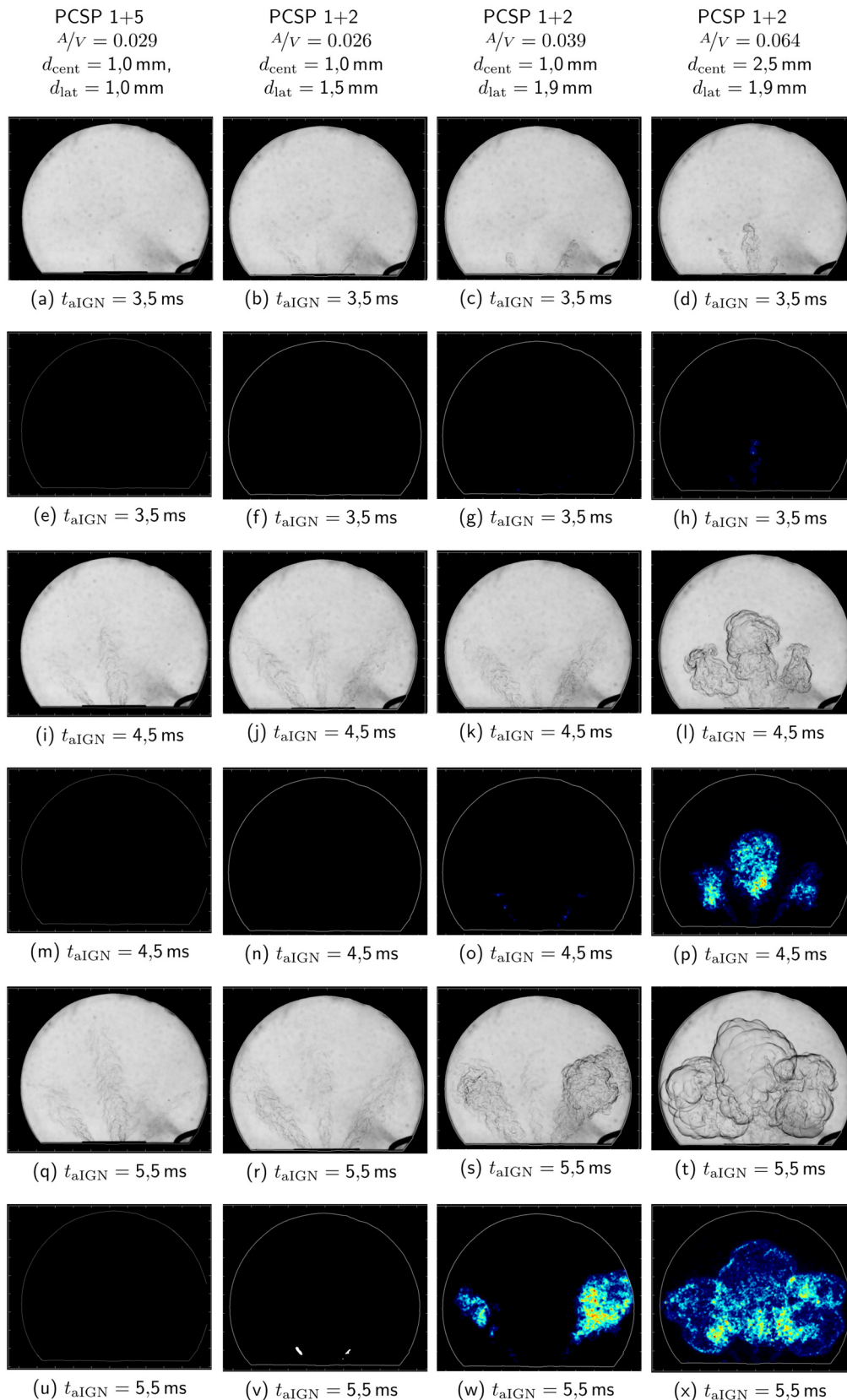
Figure 3.8: Impact of the overflow channel cross section area on flame propagation for different PCSP configurations visualized by Schlieren and OH* intensity images ((v) shows binarized flame image for a better visualization, due to very weak intensity). Ignition pressure p=3 bar. Equivalence-ratio ϕ=1.

Figure 3.8 illustrates the jet penetration (Schlieren images) and the OH* chemiluminescence intensity for the mentioned PCSP configurations at different timings after ignition. The 1+5 PCSP with A/V=0.029 shows weak non reacting hot jets entering the main chamber. The 1+2 PCSP with the smallest A/V=0.026 with a lateral bore diameter $d_{lateral}$=1.5 mm shows weak lateral flame jets exiting the Pre-Chamber 6.5 ms after the ignition. This indicates that the bore diameter is the major factor for the flame quenching during the overflow process of the flame from the PC to the main chamber. It can be assumed that the larger diameter of the lateral bores avoids an extreme flame wrinkling and thus prevents the flame from quenching inside the overflow channels compared to the smaller central bore with a diameter of $d_{central}$=1.0 mm. The ignition energy of the lateral flame jets is too small to ignite the main chamber mixture. The third PCSP configuration is achieved by an enlargement of the lateral bore diameter to $d_{lateral}$=1.9 mm. The ignition occurs in the core area of the lateral jets. After the inflammation of the main chamber mixture, the flame propagation is mainly driven by the motion of the turbulent shear layer of the jet. The last PCSP configuration with a central bore diameter of 2.5 mm and lateral bore diameters of 1.9 mm supports the thesis, that the flame is first transported by the potential core of the hot jet exiting the overflow channel with largest cross section area. The lateral overflow channels leads to additional retarded ignition sources with smaller OH* intensity. If the ignition delay is defined as the appearance of the first OH* radicals inside the main chamber, then a higher A/V-ratio shortens the ignition delay. In contrast, the robust inflammation by a flame jet is directly dependent on the overflow channel diameter and thus only indirectly influenced by the A/V-ratio for low load and temperature conditions.

Figure 3.9 shows the impact of the PCSP geometry, the spark location and the A/V-ratio on characteristic energy conversion timings and the relative visible area covered by the flame. The two PCSP geometry variants differ in the size of the central and lateral bore diameters and in the structure of the shape towards the main chamber. The PCSP variant with a convex shape is termed as Thimble. The PCSP leads in general to a faster energy conversion compared to the standard spark plug ignition system. The early detection of the 20% flame area for the conventional spark could be explained by a fast grow of the initial flame kernel inside the main chamber. In case of the PCSP configurations the initial flame kernel is generated inside the exterior Pre-Chamber volume and thus leads to minor or no advantages in terms of the early flame propagation inside the main chamber. As explained above, it could be found a lower limit of the A/V-ratio in the range of 0.021 to 0.026, which limits the ignition probability inside the main chamber. An elevated spark location S=16.4 mm can extend the lower limit. The larger Pre-Chamber volume with a higher mixture mass increases the energy release and therefore the energy input of the hot jets into the main chamber gases. The convex Thimble Pre-Chamber designs show in general advantages for the speed of heat release and flame development. The only explanation for such a characteristic is the different coverage angle between the central and the lateral jets. The central and lateral jets enables a faster flame expansion, because there is a delayed interaction of the flame front from the three jets. The jet interferences occur later for Thimble PCSP configurations and decelerate the combustion process.
The lower spark location S=3.5 mm and an increasing A/V-ratio lead to a deceleration of the combustion and early flame expansion speed. The larger the cross section area, the more the flame propagation characteristic become similar to the performance of a conventional spark plug. The intermediate spark location S=10.0 mm results in the fastest heat release and flame duration T10%-T70%. The biggest advantage in energy

conversion is achieved with an intermediate cross section to Pre-Chamber volume ratio in the range of 0.04 to 0.052. The convex PCSP with a high spark location S=16.4 mm shows a minor temporal benefit for the 10% of energy conversion. This indicates, that a larger Pre-Chamber volume generates more reactive and turbulent jets. The more turbulent flow field and reaction energy sustain the highly turbulent combustion character for a longer period and thus improve the combustion speed in large cylinder volumes.
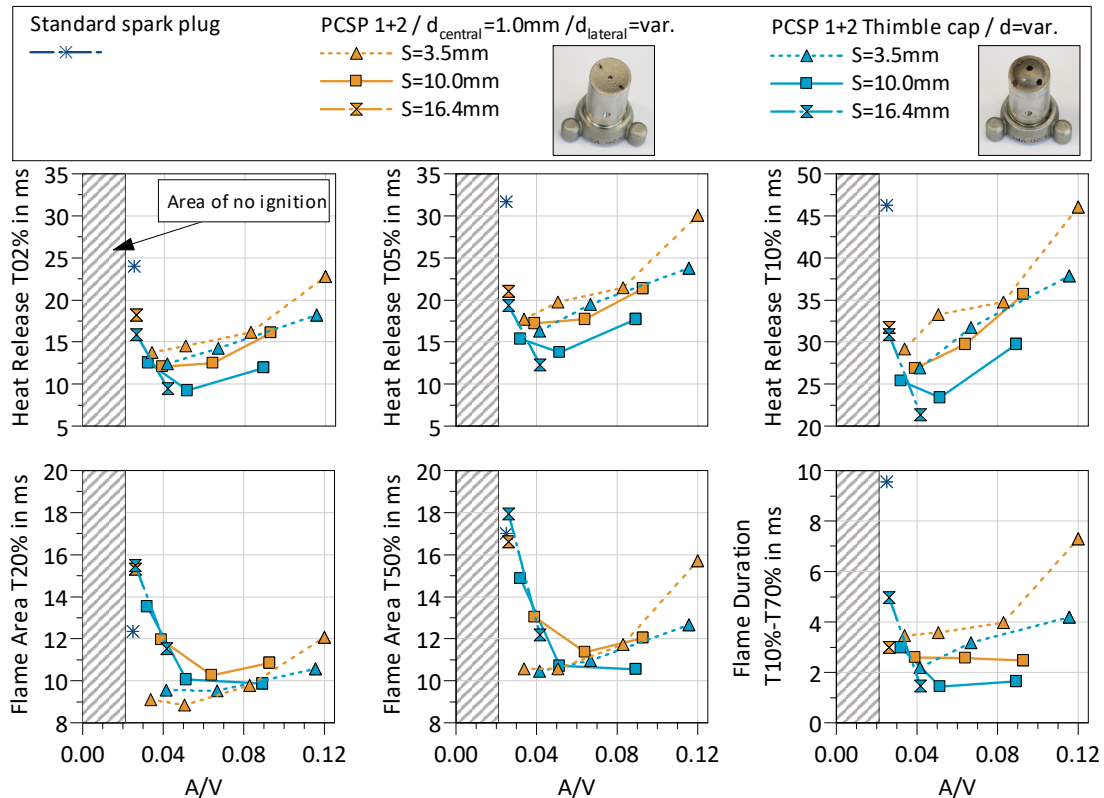
Figure 3.9: Impact of the overflow channel cross section area and spark location on the thermodynamic heat release and the flame propagation for different PCSP configurations in comparison to the standard spark plug ignition system. Ignition pressure p=3 bar. Equivalence-ratio ϕ=1

Figure 3.10 compares the jet penetration and the inflammation process for three different Pre-Chamber layouts with the standard spark plug ignition system. The 1+6 PCSP (right) is a more typical ICE design, that is used to create multiple spatial distributed ignition sources in order to enable a short burn duration and to capture a large volume in the vicinity of the combustion chamber roof. The PCSP layout with an identical A/V-ratio but a different number of overflow channels (1+2 vs. 1+6) and larger bore diameters (1.9 mm vs. 1.25 mm) shows a significant reduction of the inflammation delay in the main chamber after ignition onset in the Pre-Chamber. The 1+2 PCSP layout with a smaller A/V-ratio of 0.032 (bore diameter 1.5 mm vs. 1.9 mm) leads to a comparable inflammation delay to the Pre-Chamber with seven holes. This suggests that the bore diameter is the relevant parameter for a short ignition delay and a robust inflammation inside the main chamber.

Standard spark plug	PCSP 1+2 $A/V = 0.032$ $d_{cent} = 1.5\,mm$ $d_{lat} = 1.5\,mm$ $S = 10.0\,mm$	PCSP 1+2 $A/V = 0.052$ $d_{cent} = 1.9\,mm$ $d_{lat} = 1.9\,mm$ $S = 10.0\,mm$	PCSP 1+6 $A/V = 0.052$ $d_{cent} = 1.25\,mm$ $d_{lat} = 1.25\,mm$ $S = 10.0\,mm$

(a) $t_{a,IGN} = 4.5\,ms$ (b) $t_{a,IGN} = 4.5\,ms$ (c) $t_{a,IGN} = 4.5\,ms$ (d) $t_{a,IGN} = 4.5\,ms$

(e) $t_{a,IGN} = 4.5\,ms$ (f) $t_{a,IGN} = 4.5\,ms$ (g) $t_{a,IGN} = 4.5\,ms$ (h) $t_{a,IGN} = 4.5\,ms$

(i) $t_{a,IGN} = 5.5\,ms$ (j) $t_{a,IGN} = 5.5\,ms$ (k) $t_{a,IGN} = 5.5\,ms$ (l) $t_{a,IGN} = 5.5\,ms$

(m) $t_{a,IGN} = 5.5\,ms$ (n) $t_{a,IGN} = 5.5\,ms$ (o) $t_{a,IGN} = 5.5\,ms$ (p) $t_{a,IGN} = 5.5\,ms$

(q) $t_{a,IGN} = 7.0\,ms$ (r) $t_{a,IGN} = 7.0\,ms$ (s) $t_{a,IGN} = 7.0\,ms$ (t) $t_{a,IGN} = 7.0\,ms$

(u) $t_{a,IGN} = 7.0\,ms$ (v) $t_{a,IGN} = 7.0\,ms$ (w) $t_{a,IGN} = 7.0\,ms$ (x) $t_{a,IGN} = 7.0\,ms$

Figure 3.10: Impact of the overflow channel diameter on flame propagation for different PCSP configurations visualized by Schlieren and OH* intensity images. Ignition pressure p=3 bar. Equivalence-ratio ϕ=1. Spark location S=10.0 mm.
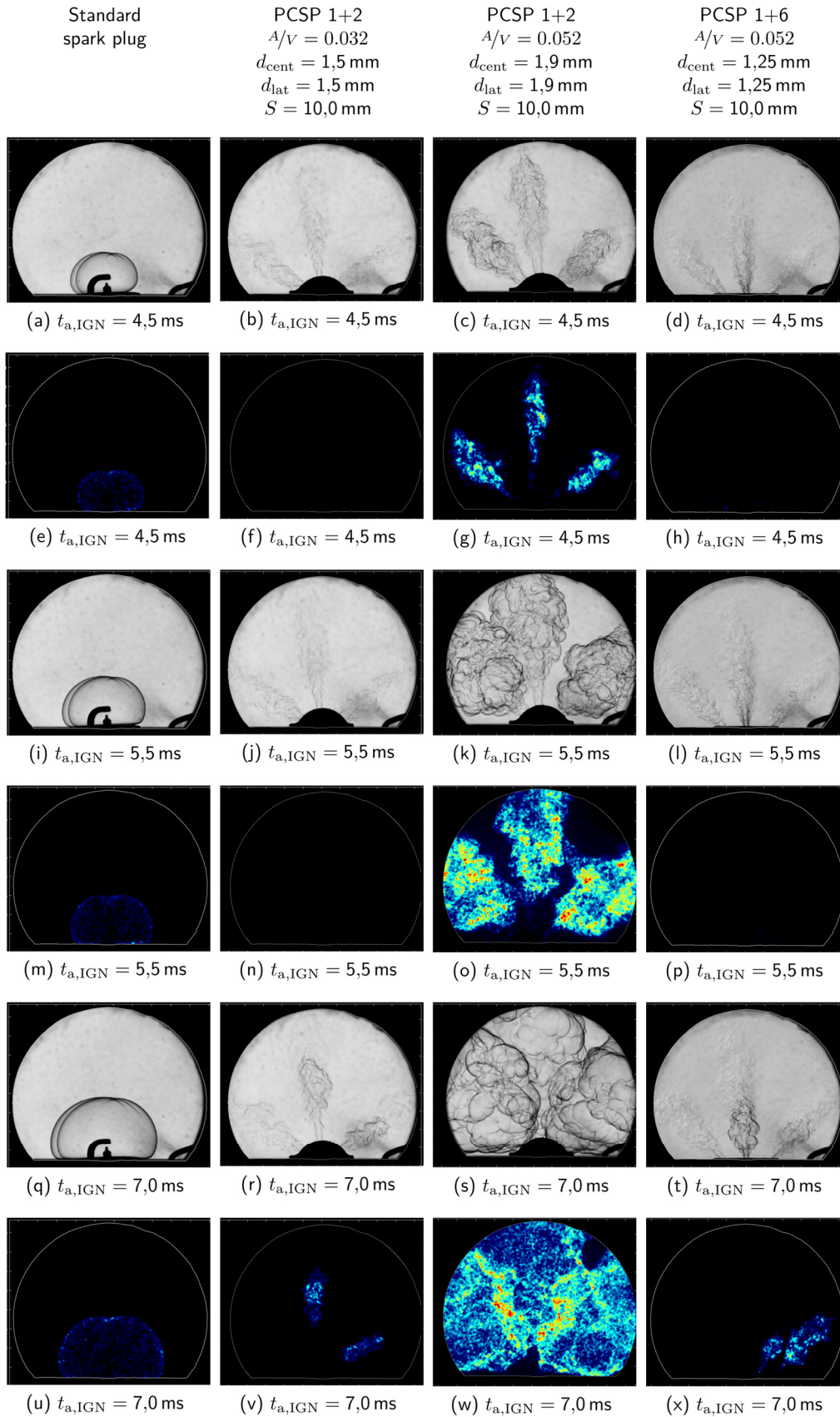
The inflammation inside the main chamber for the 1+6 PCSP design and the 1+2 layout with an orifice diameter of 1.5 mm occurs only at two jets. Without an optical access to the flame propagation inside the Pre-Chamber, shaped like a pipe with small openings, it can just be assumed that the flame formation inside the cylindrical Pre-Chamber is comparable to a tulip flame. A tulip shaped flame front can often be observed in closed or half-open ducts. The evolution of such a shape can be described by the following phases. At first the flame kernel expands spherical with the laminar flame velocity until the flame front reaches the side walls. The wall contact leads to rapid reduction of the flame surface area and a deceleration of the propagation speed. When the flame extinguishes near the walls, the curvature of the flame front is inverted, because the unburnt gases are reflected into the middle of the tube. Depending of the tube geometric sizes (diameter, length, cross section area of the opening) the flame front near the centerline can move backwards. In some cases there were observed oscillating propagations of the tulip flame that causes pressure oscillations. Considering the inflammation preferred to individual jets, it is an indication for a distorted tulip shape flame formation inside the Pre-Chamber. For a better understanding of the inflammation process in the main chamber, it is necessary to investigate the flame evolution with optical methods inside the small Pre-Chamber volume. [28, 29, 30]

Figure 3.11 shows the pressure difference between the Pre-Chamber and the main chamber, the flame radius and the jet penetration depth for these PCSP configurations. The Pre-Chamber variants with an identical geometric A/V-ratio causes a comparable pressure rise inside the Pre-Chamber, but leads to a complete different flame formation and penetration of the central jet. It can be assumed, that the pressure difference between the Pre-Chamber is mainly a function of the geometric A/V-ratio and independent of the number and the diameter of orifices.
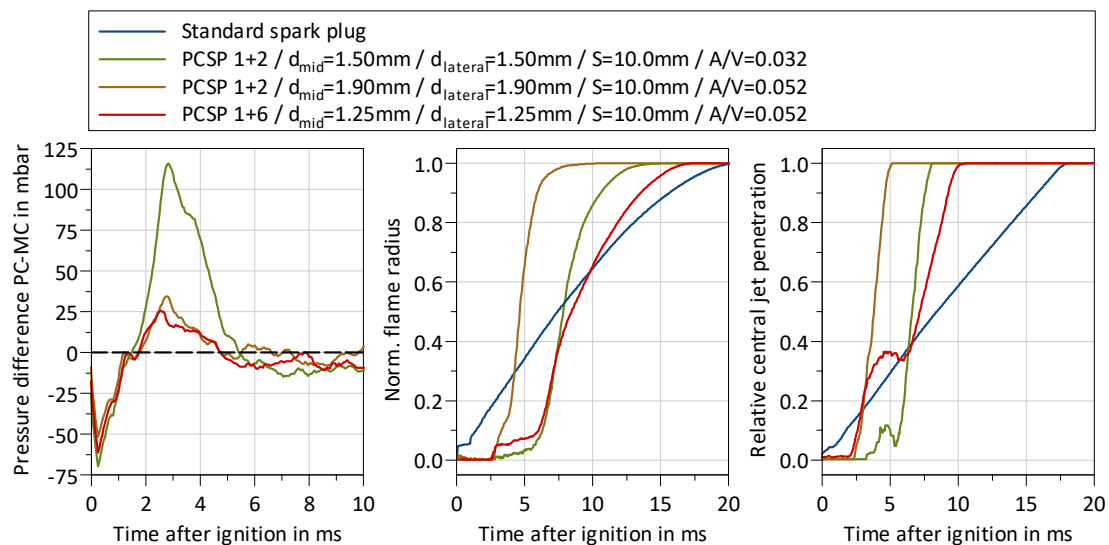

Figure 3.11: Impact of A/V-ratio on pressure rise in the Pre-Chamber, flame radius and the jet penetration. Ignition pressure p=3 bar. Equivalence-ratio ϕ=1. Spark location S=10.0 mm.

Figure 3.12 and Figure 3.13 illustrate the impact of the central orifice diameter on the inflammation and the jet penetration into the main chamber for a spark location S=10.0 mm. The first flame occurs in general at the orifice with the largest diameter. The shortest inflammation delay in combination with the highest OH* intensity is achieved by an intermediate geometric A/V-ratio. A further increase of that geometric parameter leads to a deceleration of the inflammation process. The increase of the central bore diameter reduces the flow restriction between the Pre-Chamber and main chamber. As discussed above, the pressure rise decreases and induces a reduction of the flow velocity in the overflow channels. Consequently the turbulence intensity decreases and the characteristic turbulence length scale becomes larger. The Schlieren images illustrate, that the shape of the middle jet changes significantly for an orifice diameter larger than 2 mm from a characteristic open jet shape to a mushroom-shaped flow structure. This mushroom-shaped structure grows much faster perpendicular to the jet longitudinal axis and thus enables a faster capture of the unburnt gases. A closer look at the PCSP configuration with a central orifice diameter of 2.5 mm suggests, that a specific diameter ratio among the large and the smaller orifices leads to the fastest flame area evolution under poor ignition conditions.

Figure 3.12 supports this hypothesis, showing that a central orifice diameter of 2.5 mm achieves the fastest jet penetration and the shortest flame evolution period. The first temporal rise inside the Pre-Chamber characterizes the early inflammation phase in the visible spatial range of the observation windows and correlates well with onset of the first flame inside the main chamber. The higher the pressure rise, the later the beginning of the flame formation.

The steep gradient in the pressure difference occurs first on the Pre-Chamber pressure transducer signal. It may be expected, that this behavior is induced by the strong temperature rise in the Pre-Chamber caused by the gas ionization after the ignition. The pressure transducer is located only a few millimeters away from the spark plug. This signal trace is typical for a thermal shock of a pressure transducer. [31]

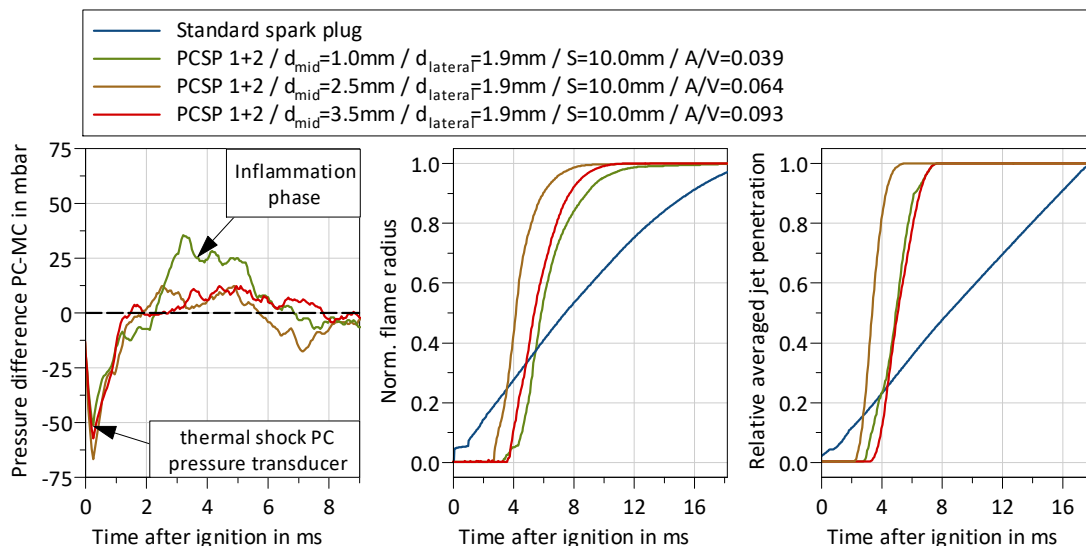*Figure 3.12: Impact of the central orifice diameter on flame evolution, averaged penetration of the three jets and pressure rise inside the Pre-Chamber. Ignition pressure p=3 bar. Equivalence-ratio ϕ=1. Spark location S=10.0 mm.*
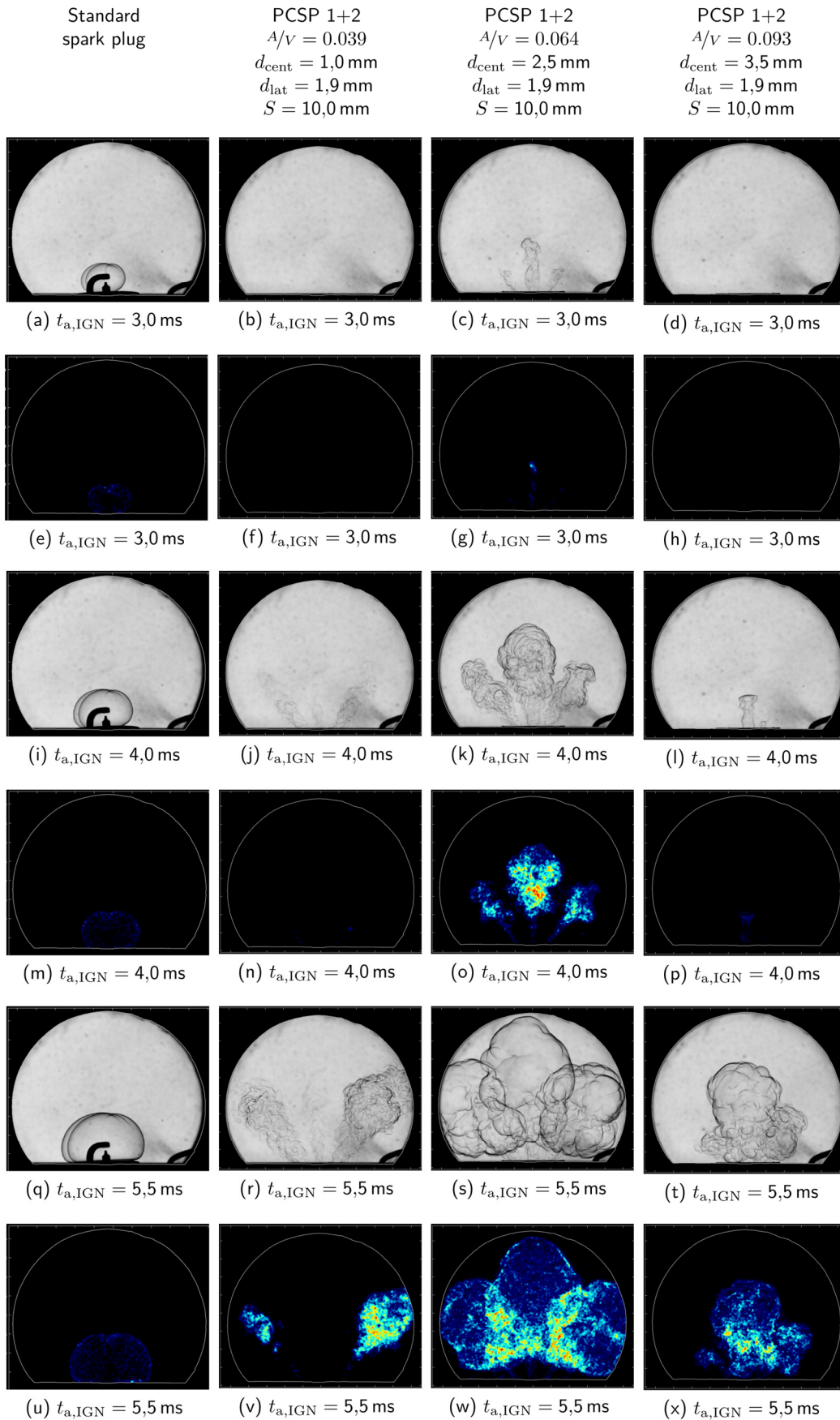
Figure 3.13: Impact of the central bore diameter on flame propagation and jet structure. Ignition pressure p=3 bar. Equivalence-ratio φ=1. Spark location S=10.0 mm.

3.4   Dependency of Pre-Chamber geometry on the flame formation under high pressure conditions

In [1] and [24] was found that a PCSP ignition system has a noticeable potential for knock mitigation. The characteristic is caused by the creation of multiple spatial ignition sources, a high turbulence production through the flame jets and thus a reduced burn duration. As mentioned in chapter 1.2, the potential is dependent on the geometric layout, the material and the system integration. This section discusses the impact of the geometric layout of the Pre-Chamber on the inflammation and early heat release under high pressure conditions. An engine load of 16 bar BMEP at an engine speed of 2000 rpm is a largely comparable knock limited operating point.

Figure 3.14 illustrates the dependency of the flame duration, the inflammation delay and the heat release on the geometric A/V-ratio. Discussed are the already known Pre-Chamber configurations (for academic purposes) coming with different shapes and spark locations. With a spark location of S=3.5 mm, the combustion is decelerated with an increasing orifice cross section area. The optimal A/V-ratio for a fast heat release is shifted to a lower A/V-ratio range from 0.025 to 0.04 compared to low pressure and temperature conditions, which was discussed in chapter 3.3. For elevated spark locations (S=10.0 mm and S=16.4 mm) the flame duration T10%-T70% reaches its minimum in the same A/V range 0.04 to 0.06. This is in accordance with the findings in chapter 3.3 for low pressure ignition conditions. It might be expected, that the turbulence production by the reacting jets during the inflammation and early flame propagating phase is independent of the ignition pressure. The main causes for the turbulence production are the orifice cross section area, the Pre-Chamber volume and indirectly the spark location. An increased Pre-Chamber volume produces a higher PC pressure rise and thus energy-richer and more persistent jets entering the main chamber. This enables short flame durations for elevated spark locations.
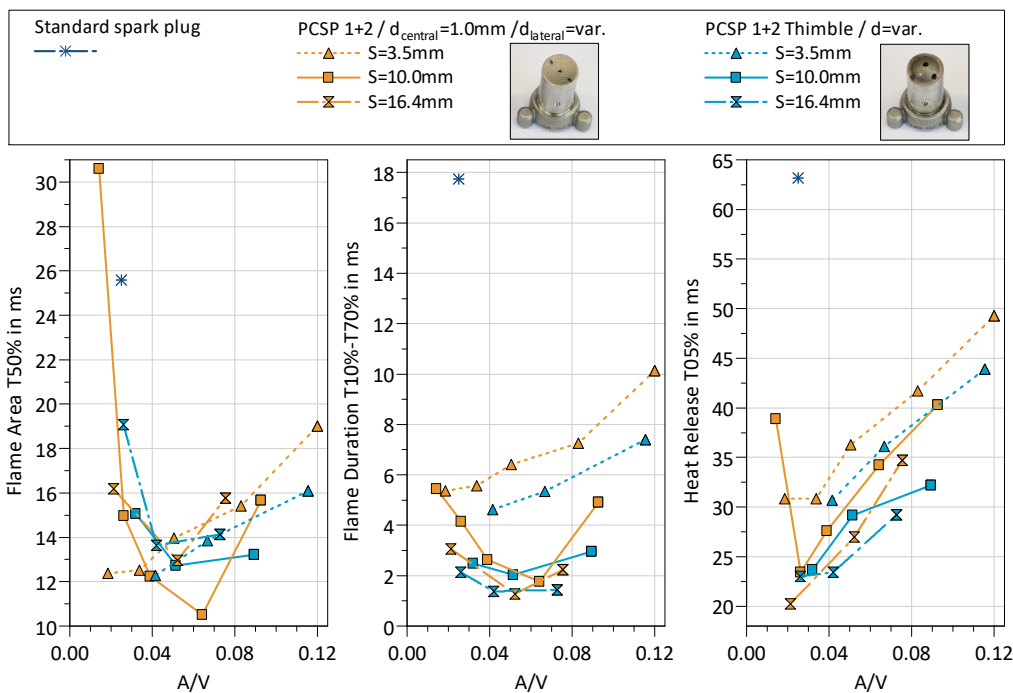

Figure 3.14: Impact of the overflow channel cross section area and spark location on the thermodynamic heat release and the flame propagation for different PCSP configurations in comparison to the standard spark plug ignition system. Ignition pressure p=18 bar. Equivalence-ratio ϕ=1.

The shortest inflammation delay (Flame at T50%) is achieved by an intermediate spark location S=10.0 mm in combination with a central orifice diameter $d_{central}$=2.5 mm. An extremely small A/V=0.014 in combination with tiny bore diameters d=1.0 mm increases the inflammation delay significantly and thus decelerates the speed of combustion. The inflammation probability for this particular design is smaller than 50%. Figure 3.15 illustrates the influence of the orifice layout on the flame formation, the jet penetration and the heat release. In general, an increase of the orifice cross section area reduces the pressure rise inside the Pre-Chamber and decelerates the heat release in the main chamber. A reduction of A/V-ratio leads to an extremely elongated inflammation delay, but to a relatively fast heat release, caused by the jet ignition characteristics inside the main chamber. The two PCSP configurations, one with a large A/V=0.0093 (red line) and another one with a small A/V=0.026 (dark blue line) shows a comparable slope for the flame evolution, but causes a large temporal difference for the 5% of energy conversion. The smaller cross section area accelerates the main chamber heat release by 39%. In the single cylinder engine results in the previously published articles by Sens et al. [1, 24] it was stated, that a large orifice cross section area is disadvantageous in terms of high knock mitigation. A large area leads to a deceleration of the speed of combustion and thus to a retarded center of combustion with a reduced indicated efficiency. It can be concluded, that an optimal PCSP design for high engine loads requires an optimization of the cross section area and orifice diameter to solve the trade-off between a reliable inflammation, an acceptable ignition delay and a fast heat release.
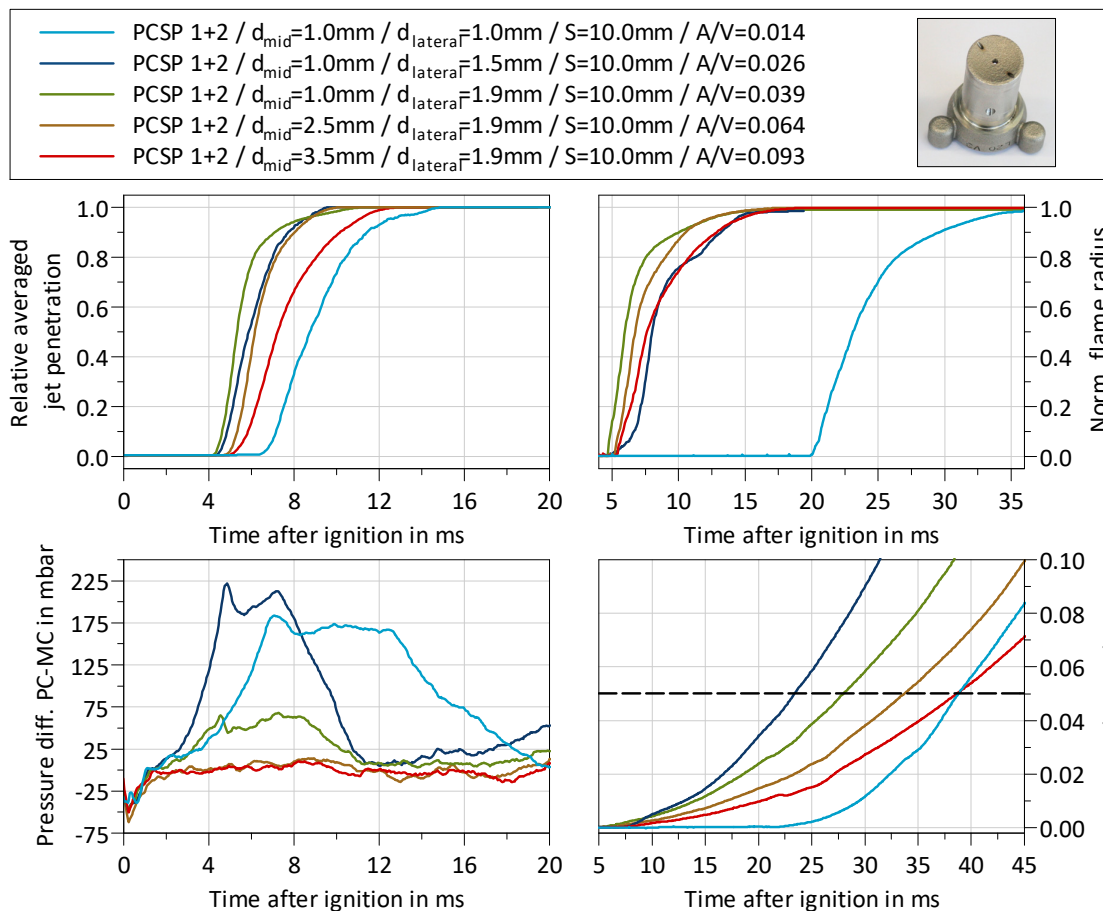

Figure 3.15: Impact of the geometric A/V-ratio on the flame evolution, jet penetration and heat release for 18 bar ignition pressure and an equivalence-ratio ϕ=1.

Figure 3.16 illustrates the influence of different bore layouts on the jet evolution and the inflammation inside the main chamber. The jet structure changes with an increasing central orifice diameter and cross section area from a typical open jet structure to a mushroom-shaped jet type. This corresponds to the findings in chapter 3.3 for low pressure ignition conditions. After the main chamber mixture has ignited and the flame propagates through the visible volume, the mushroom-shaped jet shows a reduced OH* intensity, which also correlates with the speed of heat release. Furthermore the flame ignition is initiated by the orifice with largest diameter. The OH* radicals and further combustion products stream into the main chamber and ignite the mixture in the vicinity of the jets centerline. This flame re-ignition process takes place in this region, because the early flame kernel development needs relative low turbulence intensities. Otherwise the developing flame will be distorted by the turbulent eddies, that enter into the flame structure. This characteristic reduces the turbulent mixing and thus minimizes the heat transport into the colder bulk gas. The pre-heat zone in front of the flame is small and supports the development of a self-sustainable flame front. For more details refer to the Borghi-Peters flame regime diagram in [32].

At lager stages, the highest OH* intensities are located at the significantly more turbulent shear layers, which enables a fast turbulent combustion process. A qualitative examination of the interaction of the jets shows that a larger overflow channel diameter causes larger spatial jet structures, which interact at earlier timings with each other. The turbulence level in these shear areas increases and retard locally the flame front development. It is expected, that a greater jet separation by wider overflow channel angles could improve the spatial inflammation and speed up the flame propagation.

The jet ignition process by hot gases away from the orifice could be observed for the PCSP configuration with the smallest cross section area. The flame extinguishes completely when passing the overflow channels. There is no detection of any OH* radicals exiting the orifices. The inflammation is significantly retarded. This finding is in accordance to the results of Biswas et al. [25]

In contrast to the flame ignition process, the formation of the flame front occurs first at the high turbulent shear layer as island shaped flame kernels at the left jet. The retarded ignition of the middle jet shows the same characteristic. The jet ignition can be described as a self-ignition inside the bulk gas, due to sufficient local thermodynamic and fast chemical pre-reactions. The measurement methodology does not allow to identify the specific reason for the local inflammation phenomenon in a reliable way. It is suggested, that the heat transport provides enough activation energy for starting chain branching reactions. An additional explanation is, that intermediate combustion products transported by the hot jets support the pre-reactions and thus the initiation of the heat release.

It was found that a strict separation in flame jet ignition or hot gas jet ignition regime might be difficult in some cases. The ignition process of the PCSP with an A/V=0.026 suggests, that the inflammation is very likely to be a combination of both processes. Beginning at 6.5 ms after ignition, very weak OH* radical intensities are observed at the larger lateral orifices. The radical emissions occur arbitrary and with random intensities at the exit of the lateral orifices. Later on, the OH* radicals capture a growing space along the center axis of the jet and produce spatially distributed inflammation kernels, which grow into the jet shear layer and accelerate the flame propagation accompanied by high OH* radical intensities.

PCSP 1+2	PCSP 1+2	PCSP 1+2	PCSP 1+2	PCSP 1+2
$A/V = 0.014$	$A/V = 0.026$	$A/V = 0.039$	$A/V = 0.064$	$A/V = 0.093$
$d_{\mathrm{cent}} = 1{,}0\,\mathrm{mm}$	$d_{\mathrm{cent}} = 1{,}0\,\mathrm{mm}$	$d_{\mathrm{cent}} = 1{,}0\,\mathrm{mm}$	$d_{\mathrm{cent}} = 2{,}5\,\mathrm{mm}$	$d_{\mathrm{cent}} = 3{,}5\,\mathrm{mm}$
$d_{\mathrm{lat}} = 1{,}0\,\mathrm{mm}$	$d_{\mathrm{lat}} = 1{,}5\,\mathrm{mm}$	$d_{\mathrm{lat}} = 1{,}9\,\mathrm{mm}$	$d_{\mathrm{lat}} = 1{,}9\,\mathrm{mm}$	$d_{\mathrm{lat}} = 1{,}9\,\mathrm{mm}$
$S = 10{,}0\,\mathrm{mm}$	$S = 10{,}0\,\mathrm{mm}$	$S = 10{,}0\,\mathrm{mm}$	$S = 10{,}0\,\mathrm{mm}$	$S = 10{,}0\,\mathrm{mm}$

(1) $t_{\mathrm{a,IGN}} = 20{,}5\,\mathrm{ms}$ (2) $t_{\mathrm{a,IGN}} = 5{,}5\,\mathrm{ms}$ (3) $t_{\mathrm{a,IGN}} = 5{,}5\,\mathrm{ms}$ (4) $t_{\mathrm{a,IGN}} = 5{,}5\,\mathrm{ms}$ (5) $t_{\mathrm{a,IGN}} = 5{,}5\,\mathrm{ms}$

(6) $t_{\mathrm{a,IGN}} = 20{,}5\,\mathrm{ms}$ (7) $t_{\mathrm{a,IGN}} = 5{,}5\,\mathrm{ms}$ (8) $t_{\mathrm{a,IGN}} = 5{,}5\,\mathrm{ms}$ (9) $t_{\mathrm{a,IGN}} = 5{,}5\,\mathrm{ms}$ (10) $t_{\mathrm{a,IGN}} = 5{,}5\,\mathrm{ms}$

(11) $t_{\mathrm{a,IGN}} = 20{,}9\,\mathrm{ms}$ (12) $t_{\mathrm{a,IGN}} = 6{,}5\,\mathrm{ms}$ (13) $t_{\mathrm{a,IGN}} = 6{,}5\,\mathrm{ms}$ (14) $t_{\mathrm{a,IGN}} = 6{,}5\,\mathrm{ms}$ (15) $t_{\mathrm{a,IGN}} = 6{,}5\,\mathrm{ms}$

(16) $t_{\mathrm{a,IGN}} = 20{,}9\,\mathrm{ms}$ (17) $t_{\mathrm{a,IGN}} = 6{,}5\,\mathrm{ms}$ (18) $t_{\mathrm{a,IGN}} = 6{,}5\,\mathrm{ms}$ (19) $t_{\mathrm{a,IGN}} = 6{,}5\,\mathrm{ms}$ (20) $t_{\mathrm{a,IGN}} = 6{,}5\,\mathrm{ms}$

(21) $t_{\mathrm{a,IGN}} = 22{,}9\,\mathrm{ms}$ (22) $t_{\mathrm{a,IGN}} = 8{,}0\,\mathrm{ms}$ (23) $t_{\mathrm{a,IGN}} = 8{,}0\,\mathrm{ms}$ (24) $t_{\mathrm{a,IGN}} = 8{,}0\,\mathrm{ms}$ (25) $t_{\mathrm{a,IGN}} = 8{,}0\,\mathrm{ms}$

(26) $t_{\mathrm{a,IGN}} = 22{,}9\,\mathrm{ms}$ (27) $t_{\mathrm{a,IGN}} = 8{,}0\,\mathrm{ms}$ (28) $t_{\mathrm{a,IGN}} = 8{,}0\,\mathrm{ms}$ (29) $t_{\mathrm{a,IGN}} = 8{,}0\,\mathrm{ms}$ (30) $t_{\mathrm{a,IGN}} = 8{,}0\,\mathrm{ms}$
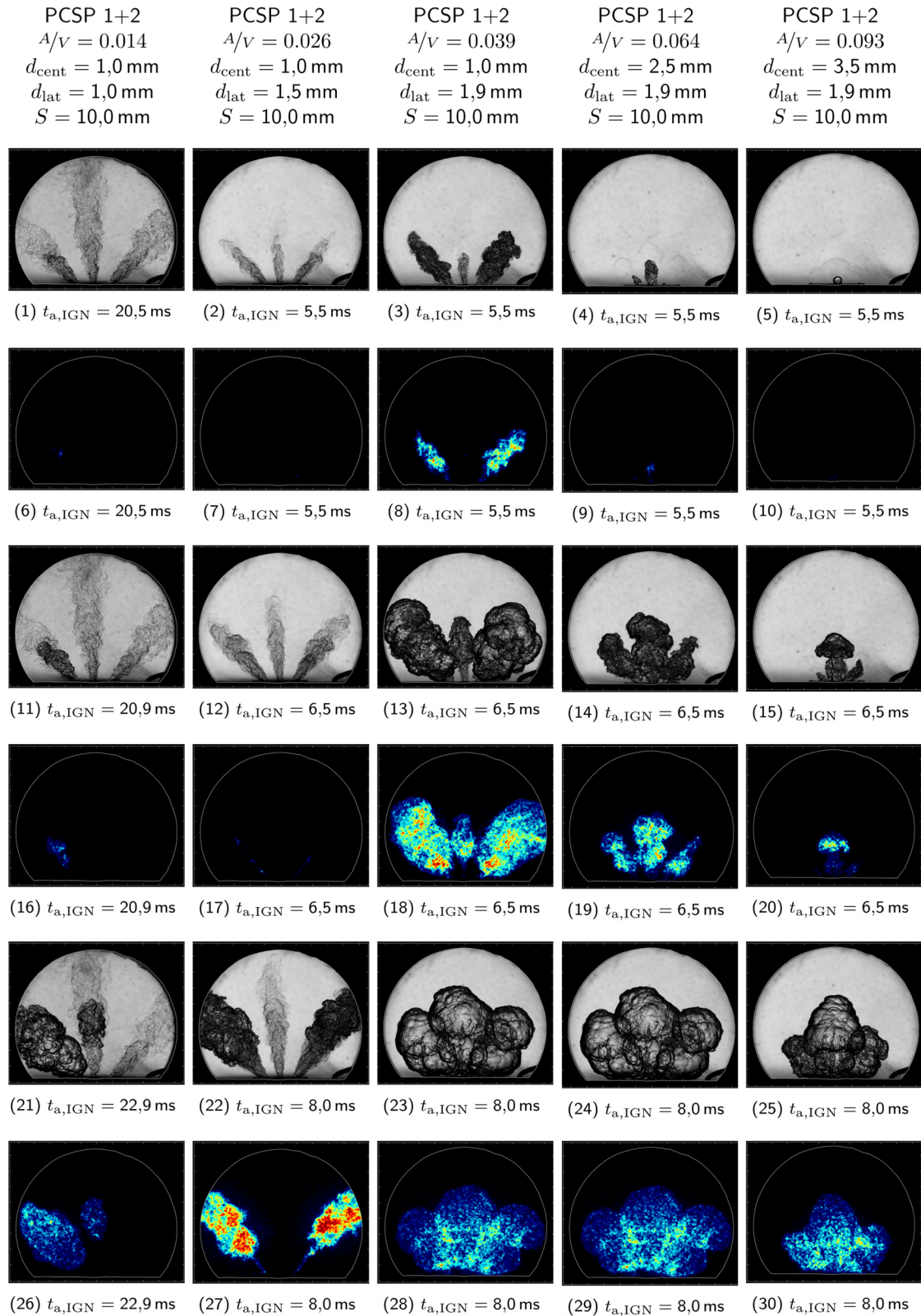
Figure 3.16: Impact of the overflow channel cross section area on the flame propagation for different PCSP configurations. Ignition pressure p=18 bar. Equivalence-ratio φ=1.

4   Conclusion and next steps

In order to build a deep understanding of Pre-Chamber based inflammation mechanisms, experiments in a combustion vessel with methane/air mixtures were carried out in varying boundary conditions in terms of chamber pressure, equivalence-ratio and geometrical design parameters of the Pre-Chamber. In order to quantify and compare the combustion characteristics with differing boundaries, both pressure measurements within the Pre-Chamber and main chamber as well as simultaneous Schlieren and OH* chemiluminescence measurements were performed and analyzed by means of morphological image analysis.

Here is a summary of the most vital findings:

- Based on the measurement principle of simultaneous Schlieren and OH* chemiluminescence, three different ignition mechanisms inside the main chamber could be observed: ignition by a reacted jet ("hot gas jet ignition"), ignition by a reacting jet ("flame jet ignition") as well as a combination of both.

- The vast majority of combustion events inside the main chamber can be attributed to a flame jet ignition, while only two cases at lowest vessel pressure of 3 bar and smallest orifice diameter indicate the presence of a pure hot gas jet. One of the two hot jet cases fails to ignite the main chamber at 3 bar.

- There is only one case at 18 bar showing a distinct hot gas jet ignition at 18 bar vessel pressure. This case is characterized again by minimum orifice diameter and absolute minimum A/V ratio and leads to an overly long inflammation delay. However, the initial heat release is very fast, which can be attributed to the nature of auto-ignition like combustion progress for the hot gas jet ignition.

- The pressure dependency of flame propagation / combustion speed is drastically reduced in the quiescent vessel conditions with the Pre-Chamber spark plug compared to conventional ignition. This is mainly due to the deep and fast penetration of the jets which consequently results in a spatial inflammation inside the main chamber. Above this, the high jet velocity induces a high level of turbulence by its own, which both temporally and spatially serves perfectly for an additionally accelerated flame propagation. It needs to be stated though, that if local turbulence gets too high in additionally poor mixture conditions, specifically the hot gas jet regime might lead to misfire in the main chamber. Nevertheless, these PCSP inherent features of spatial ignition and self-generated turbulence make the PCSP a particularly good match for high engine load and knock mitigation.

Based on these fundamental investigations, findings from previous single cylinder engine experiments are supported and understood in more detail. The single impact, importance and interference of the varied parameters and their effect onto combustion is widely understood, which is a necessity for the dedicated layout of the Pre-Chamber. The work described in this publication is then also the point of departure for setting up a detailed combustion model in 3D CFD, which needs to be capable of predicting the phenomena discussed within this paper in order to efficiently design the optimum compromise layout and address properly all the challenges for the PCSP in rather poor ignition conditions such as low mixture temperature and low cylinder pressure.

5 Literature

[1] SENS, M., E. BINDER, A. BENZ, et al: *Pre-Chamber Ignition as a Key Technology for Highly Efficient SI Engines - New Approaches and Operating Strategies,* 39th International Vienna Motor Symposium, Vienna, 2018.

[2] GUETHE, F., D. GUYOT, G. SINGLA, N. NOIRAY, B. SCHUERMANS: *Chemiluminescence as diagnostic tool in the development of gas turbines*, Applied Physics, 2012.

[3] JENS, E.T., V.A. MILLER, B.J. CANTWELL: *Schlieren and OH* chemiluminescence imaging of combustion in a turbulent boundary layer over a solid fuel*, Experiments in Fluids 57(3):39, 2016.

[4] SOID, S.N., Z.A. ZAINAL: *Spray and combustion characterization for internal combustion engines using optical measuring techniques – A review*, Energy, Elsevier, vol. 36(2):724-741, 2011.

[5] LAUER, M., T. SATTELMAYER: *On the Adequacy of Chemiluminescence as a Measure for Heat Release in Turbulent Flames With Mixture Gradients,* Proceedings of the ASME Turbo Expo, Orlando, 2009.

[6] JIPPA, K.-N.: *Onlinefähige, thermodynamikbasierte Ansätze für die Auswertung von Zylinderdruckverläufen*, Schriftenreihe des Instituts für Verbrennungsmotoren und Kraftfahrwesen der Universität Stuttgart, Expert Verlag, 2004.

[7] WARNATZ, J., U. MAAS, R.W. DIBBLE: *Combustion: Physical and chemical fundamentals, modeling and simulation, experiments, pollutant formation,* 4th ed., Springer, Berlin, 2006.

[8] ALEIFERIS, P.G., A.M.K.P. TAYLOR, J.H. WHITELAW, K. ISHII, Y. URATA: *Cyclic Variations of Initial Flame Kernel Growth in a Honda VTEC-E Lean-Burn Spark-Ignition Engine*, SAE Paper 2000-01-1207, 2000.

[9] ALEIFERIS, P.G., A.M.K.P. TAYLOR, J.H. WHITELAW, K. ISHII, Y. URATA: *The nature of early flame development in a lean-burn stratified-charge spark-ignition engine*, Combustion and Flame, 136(3), 283-302, 2004.

[10] BADAWY, T., X. BAO, H. XU: *Impact of spark plug gap on flame kernel propagation and engine performance*, Applied Energy, 191, 311-327, 2017.

[11] GOSCHÜTZ, M., M.S. MOHD SHAWAL, M. SCHILD, C. SCHULZ, S. KAISER: *Comparison of flame-front visualization in internal combustion engines using different imaging systems via endoscopic and full optical access*, 7th European Combustion Meeting, Budapest, 2015.

[12] GOSCHÜTZ, M., C. SCHULZ, S. KAISER: *Endoscopic Imaging of Early Flame Propagation in a Near-Production Engine*, SAE International Journal of Engines, 2014.

[13] SHAWAL, S., M. GOSCHÜTZ, M. SCHILD, S. KAISER, M. NEUROHR, J. PFEIL, T. KOCH: *High-Speed Imaging of Early Flame Growth in Spark-Ignited Engines Using Different Imaging Systems via Endoscopic and Full Optical Access*, SAE Int. J. Engines, 9, 704-718, 2016.

[14] ABU-GHARABIEH, R., G. HAMARNEH, T. GUSTAVSSON, C.F. KAMINSKI: *Flame front tracking by laser induced fluorescence spectroscopy and advanced image analysis,* Optics Express, 8(5), 278, 2001.

[15] ABU-GHARABIEH, R., C. KAMINSKI, T. GUSTAVSSON, G. HAMARNEH: *Flame front matching and tracking in PLIF images using geodesic paths and level sets*, IEEE Workshop on Variational and Level Set Methods in Computer Vision, Proceedings, Vancouver, Canada, 13 July 2001.

[16] MALM, H., G. SPARR, J. HULT, C.F. KAMINSKI: *Nonlinear diffusion filtering of images obtained by planar laser-induced fluorescence spectroscopy*, Journal of the Optical Society of America A, 17(12), 2148, 2000.

[17] PARK, D.J., A.R. GREEN, Y.C. CHEN: *Analysis of Local Flame Propagation in Gas Explosions with Multiple Obstacles*, 15th Australasian Fluid Mechanics Conference.

[18] PARSINEJAD, F., J.C. KECK, H. METGHALCHI: *On the location of flame edge in Shadowgraph pictures of spherical flames - A theoretical and experimental study*, Experiments in Fluids, 43(6), 887-894, 2007.

[19] SILJAN, E., M. LYSAKER, S. MAHARJAN: *Wave Front Tracking using Template Matching and Segmented Regression*, Linköping University Electronic Press, S. 326-331, 2017.

[20] YANG, X., X. SHEN, J. LONG, H. CHEN: *An Improved Median-based Otsu Image Thresholding Algorithm*, AASRI Procedia, 3, 468-473, 2012.

[21] OTSU, N.: *A Threshold Selection Method from Gray-Level Histograms*, IEEE Transactions on Systems, Man, and Cybernetics, 9(1), 62-66, 1979.

[22] SETTLES, G.S.: *Schlieren and Shadowgraph Techniques: Visualizing Phenomena in a Transparent Media*, Berlin Heidelberg, Springer-Verlag, 2001.

[23] SMITH, G.P., D.M. GOLDEN, M. FRENKLACH, N.W. MORIARTY, B. EITENEER, M. GOLDENBERG, C.T. BOWMAN, R.K. HANSON, S. SONG, W.C. GARDINER, V.V. LISSIANSKI, Z. QIN: http://www.me.berkeley.edu/gri_mech/

[24] SENS, M., E. BINDER, P.B. REINICKE, M. RIEß, M. WÖBKE: *Pre-Chamber ignition and promising complementary technologies*, 27th Aachen Colloquium Automobile and Engine Technology, Aachen, 2018.

[25] BISWAS, S., S. TANVIR, H. WANG, L. QIAO: *On ignition mechanisms of premixed CH_4/air and H_2/air using a hot turbulent jet generated by pre-chamber combustion*, Applied Thermal Engineering, Volume 106, 2016.

[26] SUCKART, D., D. LINSE, E. SCHUTTING, H. EICHLSEDER: *Experimental and simulative investigation of flame–wall interactions and quenching in spark-ignition engines*, Automotive and Engine Technology, 2(1), 25-38, 2017.

[27] HASSE, C., M. BOLLIG, N. PETERS: *Quenching of laminar iso-octane flames at cold walls*, Combust. Flame 122, 117–129, 2000.

[28] XIAO, H., R.W. HOUIM, E.S. ORAN: *Formation and evolution of distorted tulip flames*. Combustion and Flame, 162(11), 4084-4101, 2015.

[29] XIAO, H., Q. WANG, X. SHEN, S. GUO, J. SUN: *An experimental study of distorted tulip flame formation in a closed duct*, Combustion and Flame, 160(9), 1725-1728, 2013.

[30] PONIZY, B., A. CLAVERIE, B. VEYSSIÈRE: *Tulip flame - the mechanism of flame front inversion*, Combustion and Flame, 161(12), 3051-3062, 2014.

[31] LEE, S., C. BAE, R. PRUCKA, G. FERNANDES, Z. FILIPI, D.N. ASSANIS: *Quantification of Thermal Shock in a Piezoelectric Pressure Transducer*, SAE International, 2005.

[32] PETERS, N.: *Combustion Theory*, CEFRC Summer School, 184-194, Princeton, 2010

6   Abbreviations and formula symbols

A/V	Ratio of Pre-Chamber orifice cross section area to volume
BMEP	Brake mean effective pressure
CA	Crank Angle
CA50	Center of heat release
CFD	Computational Fluid Dynamics
CH_4	Methane
CO_2	Carbon dioxide
CR	Geometric compression ratio
d	Bore diameter
d_{cent} / $d_{central}$	Diameter of the central bore
d_{lat} / $d_{lateral}$	Diameter of the lateral bore
ECU	Engine control unit
EGR	Exhaust gas recirculation
EIVC	Early intake valve closure
fps	Frames per second
GRI3.0	Reaction mechanism with 53 species
HEV	Hybrid Electric Vehicle
ICE	Internal combustion engines
IGN	Ignition timing
MBT	Maximum Break Torque

NIST	National Institute of Standards and Technology
N_2	Nitrogen
O_2	Oxygen
OH / OH*	Hydroxide (exited)
PC	Pre-Chamber
PCSP	Pre-Chamber spark plug
PHEV	Plug-in Hybrid Electric Vehicle
RPM	Revolutions per minute
S	Spark gap location inside the PCSP
T10%/T50%/T70%	Time where flame area covers 10%/50%/70% of visual field
$t_{a,IGN}$	Time after ignition
TDC	Top dead center
UV	Ultra violet
xHEV	Hybrid Electric Vehicle with light electrification

Acknowledgement

8.2 Experimental Research on Pre-chamber Jet Ignition in Rapid Compression Machine and Natural Gas Engine

Boyuan Wang, Zhi Wang

Abstract

Pre-chamber jet ignition is a promising technology for spark ignition engines. In this paper, classical pre-chamber jet ignition and a new pre-chamber jet ignition method named flame accelerated ignition are investigated.

Utilizing the connecting nozzles to generate the jets is the classical form of pre-chamber jet ignition. Two combustion modes were found by the RCM experiments with optical method: double stage combustion and single stage combustion. Double stage combustion mode takes place in the condition with relatively small nozzle dimension, showing long ignition delay and extremely short combustion duration. The jets cannot ignite the mixture directly. Instead, ignition happens at a central position in the main chamber after a lag time followed by the rapid development of the flame with similar speed in each direction. However, the double stage combustion mode has poor combustion stability due to the high randomness of the ignition process inside the main chamber. With single stage combustion mode, the ignition delay and the combustion duration can be shortened simultaneously with satisfying combustion stability. The combustion processes inside the pre-chamber and the main chamber take place continuously. The flame jet develops from the nozzle, composed of thin fire near the nozzle and approximately conical fire in the tip. The speed of flame jet exceeds 15 times than that of conventional flame propagation.

According to the concept of pre-chamber jet ignition and the phenomenon of flame acceleration in tunnel, a new ignition method named flame accelerated ignition (FAI) is proposed. The flame acceleration tunnel can be regarded as a pre-chamber, where flame acceleration happens. Then the combustion in the main-chamber can be induced by the flame jet rushed out of the tunnel. The RCM experiments indicated that the combustion could be evidently enhanced by FAI. The flame jet maintains nearly cylindrical with favorable speed characteristic. Higher indicated thermal efficiency is gained by applying FAI compared to conventional spark ignition in the natural gas engine. In addition, introducing residual gas cavity into the flame acceleration tunnel could expand the misfire limit and improve the defect of FAI mode in lean-burn conditions.

1   Introduction

Spark ignition (SI) engines are widely used as automotive power. However, the thermal efficiency of conventional SI engines is not comparable to that of compression ignition engines due to its relatively low combustion velocity, resulting from the combustion mode composed of single-point ignition and flame propagation. Due to increasingly stringent regulations in automotive fuel economy, the combustion process of SI engines needs to be further optimized to gain higher thermal efficiency.

Pre-chamber jet ignition is proposed as a potential approach to improve the performance of SI engines. In this mode, a pre-chamber is introduced into the combustion chamber with spark plug set inside. The pre-chamber serves as an ignition source for the main chamber, providing flame jets spatially distributed inside the main chamber. Meanwhile, the turbulent intensity in the combustion chamber is evidently enhanced. As a result, the combustion velocity is increased, providing the capacity to improve the thermal efficiency [1].

1.1   Classical pre-chamber jet ignition

In order to differentiate from the undermentioned new pre-chamber jet ignition method, in this paper, the extensively studied ignition method which utilizes the connecting nozzles to generate the jets is called classical pre-chamber jet ignition.

Classical pre-chamber jet ignition has a long history of development and investigation. Recent years, it has become a hot research topic with the characteristics of relatively small pre-chamber volume and multiple connecting nozzles. The effects of accelerating combustion process has been proved in the engine tests [2-3]. Benefiting from the accelerated combustion velocity, the compression ratio of SI engines with pre-chamber jet ignition system could be increased by 2~3 due to the expanded knock limit [4-5].

To further explore the potential of pre-chamber jet ignition, auxiliary fuel system is introduced into the pre-chamber in order to form a rich mixture condition inside. In this case, the jet could ignite extremely lean mixture (λ=2.1 for gasoline engine [6] and λ=2.9 for natural gas engine [7]) in the main chamber, leading to higher thermal efficiency.

Although it is proved that the performance of SI engines could be improved by using pre-chamber jet ignition, the combustion process is the result of comprehensive effects of thermal effect, chemical reaction and turbulent flow, which is rather complicated. In order to investigate the mechanism of pre-chamber jet ignition, fundamental researches based on optical and numerical methods have been conducted to investigate the structure of flame and jet [8-9], effects of pre-chamber geometric conditions [10-11], and detailed process of combustion and flow [12-14] in recent years. However, considering the complexity of pre-chamber jet ignition, it still needs to be further recognized.

In this paper, Different pre-chamber nozzle configurations were investigated on rapid compression machine with full optical accessibility to study the ignition and combustion process of classical pre-chamber jet ignition.

1.2   Flame accelerated ignition

Relatively slow combustion velocity is one of the bottlenecks which limits the thermal efficiency of SI engines. Therefore, increased flame speed is required to improve the combustion characteristics of SI engines. In fundamental research field on combustion, the phenomenon of flame acceleration has been widely studied. It was found that the

flame would be accelerated while travelling in either a smooth or an obstructed tunnel. The phenomenon results from the effect of gas flow and turbulence [15]. However, flame acceleration is more obvious in an obstructed tunnel because the obstacles are effective to enhance the gas flow and increase the flame surface [16]. As a result, the flame can be suddenly accelerated when passing by the obstacles [17].

Flame acceleration inside a tunnel is an attractive phenomenon but rarely associate with automotive piston engines. However, the phenomenon exactly meets the demand of improving combustion characteristics for SI engines. Therefore, a new ignition mode which combines the concept of flame acceleration in tunnel and pre-chamber jet ignition was proposed by the authors, called Flame Acceleration Ignition (FAI) [18]. An FAI system is composed of a spark plug and a flame acceleration tunnel with small dimensions. The spark plug is set on one side of the tunnel and the other side is connected with the main combustion chamber. Obstacles are set inside the tunnel to achieve better acceleration effect in a relatively short tunnel. Considering that annulus is the most common and classical shape for the obstacles in flame acceleration researches, it was selected for the experiments in this paper. In general, the FAI system occupies a small proportion of the combustion volume so that it can be regarded as a pre-chamber. However, the exit of the FAI system is widely opened, which is different from classical pre-chamber designs characterized by relatively small nozzle dimensions.

In FAI mode, the flame kernel is formed by the spark plug on the top end and then the flame is accelerated through the tunnel. Subsequently, the mixture in the main chamber can be rapidly ignited by the flame jet rushed out of the tunnel. Therefore, the combustion in the main chamber can be enhanced and accelerated, which is beneficial to improving the thermal efficiency.

2 Experimental Setups

2.1 Rapid compression machine

In this study, Tsinghua University Rapid Compression Machine (TU RCM) [19] was utilized to study the combustion process of both classical pre-chamber jet ignition and flame accelerated ignition. TU RCM consists of high pressure gas tank, driver section, hydraulic section, compression section, and combustion chamber. The compression stroke and combustion chamber bore are 495 mm and 50.8 mm, respectively. The compression ratio is adjustable by varying the length of combustion chamber. In this study, the compression ratio was fixed at 9.5.

At the end of combustion chamber, the metal cover can be replaced by the quartz window with the same bore as the chamber to provide optical access. High speed photography was accomplished by camera Photron SA-X2 coupled with a 180 mm lens Nikon AF Micro f/4D, which was set in the axial direction to record the combustion images. The f3.5 aperture was chosen. The shutter time and the frame rate were set as 1/12661 s and 12500 fps, respectively. Each image had an original resolution of 896*896 and was processed to a circular shape with the diameter of 700 pixels, corresponding to the range of the combustion chamber.

The pre-chamber jet ignition system was set on the circumferential edge of the combustion chamber. A hemispherical design was used for the classical pre-chamber jet ignition investigation, which is shown in Figure 1(a). The pre-chamber occupied 1.25% of the total combustion volume, multiple nozzle configurations were tested. As shown in Figure 1(b), in FAI experiments, a 3-obstacle FAI system was used. The length and the diameter of the tunnel were 27 mm and 7 mm, respectively. The blockage ratio of

the annular obstacles was 0.36, i.e. the cross-section diameter of the obstacles was 80% of that of the tunnel. Note that the FAI system did not occupy the original combustion volume, there would be slight reduction in compression ratio (9.4).

As shown in Figure 1, a pressure sensor Kistler 6125C was set on the opposite side of the ignition system, measuring the pressure inside the main chamber at a sampling rate of 100 kHz. To transform the signal to the voltage version, a charge amplifier Kistler 5018A was used.

Synchronous trigger signal was produced by a pulse generator DG645. The TTL trigger signal would be generated within 2 ms after the piston reached the top dead center, according to the in-cylinder pressure. Therefore, the spark plug and the high-speed camera could action at the same time when zero time (t=0) was marked. Both pressure signal and trigger signal were acquired by National Instrument chassis cDAQ-9178 and analog input module cDAQ-9223.

The mixture of methane, oxygen and nitrogen was used in this study. Methane is the major component of natural gas. Oxygen and nitrogen were used to simulate air. Stoichiometric combustion condition was investigated so that the volumetric ratio between methane, oxygen and nitrogen was 1:2:7.52. The mixture was prepared according to Dalton's Law of Partial Pressure.

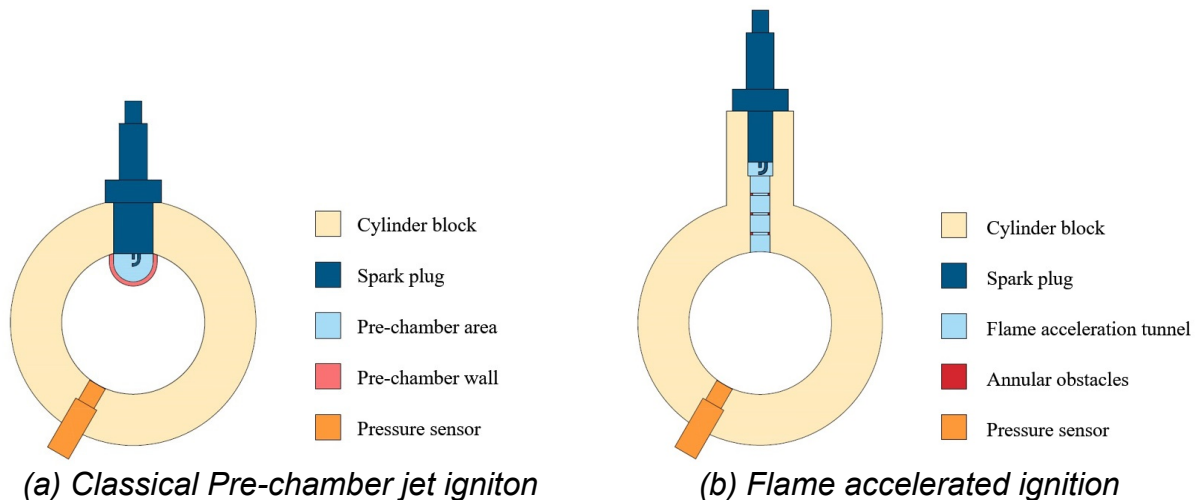(a) Classical Pre-chamber jet igniton   (b) Flame accelerated ignition

Figure 1: Cross-section view of the RCM combustion chamber

2.2 Natural gas engine

In this study, FAI was further tested in a single cylinder natural gas engine with the displacement of 1.85 L after the RCM experiments. The original compression ratio of the engine was 10.5. A dynamometer Horiba LI250 was connected to the engine. The natural gas was port injected at a pressure of 0.5 MPa. The intake air was controlled by a 6-channel sonic nozzle system. A pressure sensor AVL GU22C coupled with a charge amplifier Kistler 5011 was used to measure the in-cylinder pressure. Moreover, engine control, online combustion analysis and high-speed data acquisition were conducted by a LabVIEW system composed of National Instrument real-time system, FPGA and driven modules.

Figure 2 shows the schematic of the engine assembled with an FAI system. Compared with the original engine, the position of spark plug assembly was replaced by the FAI system. Detailed configuration of FAI systems will be discussed in Results and Discussions. The compression ratio would be reduced due to the introduction of the extra

combustion space. However, considering that the volume occupied by flame acceleration tunnel was very little in comparison with the main chamber, in this study, the compression ratio was still no lower than 10.4 in FAI mode.

During the experiment, the engine speed was fixed at 1000 r/min. And the engine was operated at the load with the indicated mean effective pressure (IMEP) of 0.65 MPa. Combustion with different mixture condition (excess air ratio, λ) was conducted to compare the performance and characteristics of FAI mode and conventional spark ignition (CSI) mode.
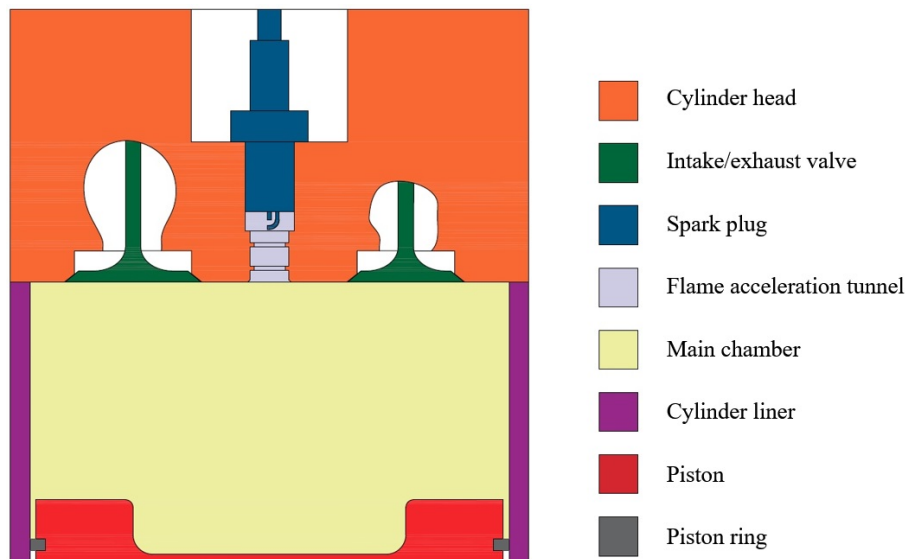
Figure 2: Schematic of the engine assembled with FAI system

3 Results and Discussions

3.1 Classical pre-chamber jet ignition investigations on RCM

Firstly, a series of 4-nozzle classical pre-chamber designs were chosen for the RCM experiments. The nozzles are symmetrically distributed. And the angle between the axis of each nozzle and the centerline of the pre-chamber was fixed at 45°. The sole difference between the designs was the nozzle size. The diameter of the nozzles varied from 1.0 mm to 2.0 mm.

Figure 3 shows the pressure inside the main chamber of each designs. Conventional spark ignition case is also shown for comparison. It can be seen that all of 5 pre-chamber jet ignition cases have remarkably earlier pressure increase in comparison to CSI case, indicating that the combustion is effectively accelerated and enhanced by utilizing pre-chamber jet ignition. Pre-chamber jet ignition cases with the nozzle diameter of 1.1 mm, 1.2 mm, 1.6 mm, and 2.0 mm show similar pressure characteristic. The pressure rise of 4×Φ1.2 mm case is slightly faster and that of 4×Φ2.0 mm case is slightly slower than others. However, 4×Φ1.0 mm case appears disparate combustion pressure trace. The pressure inside the main chamber keeps nearly unchanged for quite a long time after discharge of the spark plug. During this period, the pressure is even lower than that of the CSI case, indicating that the combustion inside the main chamber does not initiate. However, the pressure of the main chamber starts to rapidly

rise with a higher slope after the lag, which means the 4×Φ1.0 mm case possesses the fastest combustion duration in the main chamber among all tested cases.

There is little difference of nozzle size between 4×Φ1.0 mm case and 4×Φ1.1 mm case. However, the disparity of combustion pressure is significant. To analyze the cause, the partial enlarged pressure traces of the main chamber, together with corresponding heat release rates and their derivate are shown in Figure 4. Both pressure traces decrease slightly in 0~1.8 ms due to the wall heat transfer and turn to increase then. However, the degree of increase is rather different. The main chamber pressure of 4×Φ1.1 mm case appears sharp increase, corresponding to obvious heat release. It can be inferred that the combustion inside the main chamber is initiated since t=1.8 ms. In contrast, for 4×Φ1.0 mm case, the increase amplitude is only 0.01 MPa and the increase trend terminates at t=3.8 ms. During this period, the heat release is tiny. It is apparent that the slight increase of main chamber pressure results from the combustion inside the pre-chamber. Some of the hot gas enters the main chamber through nozzles driven by the pressure difference, which slightly boosts the pressure inside the main chamber. With the end of pre-chamber combustion, the pressure inside the main chamber turns to decrease without any heat release. At t=4.4 ms, the pressure begins to rise again, which marks the initiation of the combustion in the main chamber. Therefore, in 4×Φ1.1 mm case, the combustion inside the pre-chamber and the main chamber is continuous. While in 4×Φ1.0 mm case, the combustion in the two chambers is obviously interrupted. In this paper, the former one is called single stage combustion mode and the latter one is called double stage combustion mode. Heat release rate and its derivate can be used as the criterion to distinguish the combustion mode. Single stage mode is characterized by monotonicity of the combustion pressure increase and the heat release rate increase. However, double stage mode does not possess the feature. Therefore, once the derivate of the heat release rate appears negative, the combustion can be determined as the double stage mode.
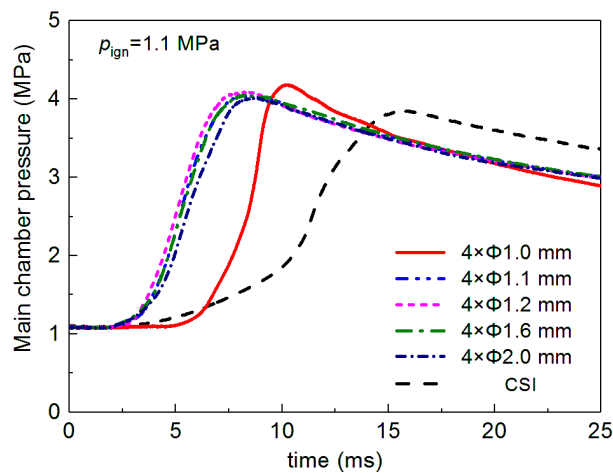

Figure 3: Main chamber pressure of pre-chamber jet ignition with different nozzle size (1.1 MPa at spark timing)

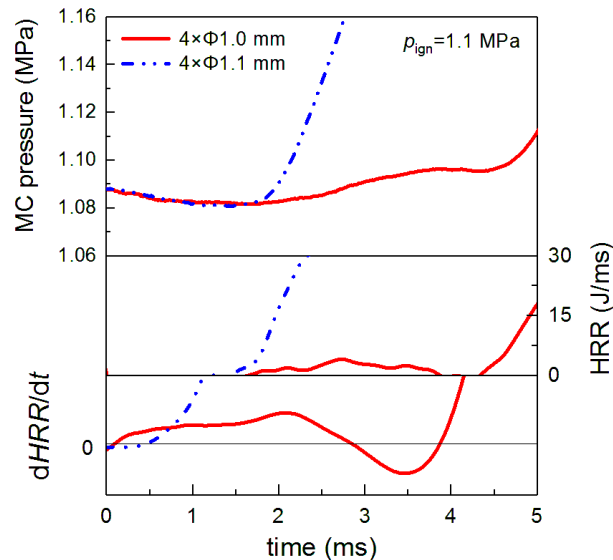*Figure 4: comparison of main-chamber pressures, heat release rates and their derivative of 4×Φ1.0 mm case and 4×Φ1.1 mm case (1.1 MPa at spark timing)*

Figure 5 shows the ignition delay (defined as the time interval between spark and 10% heat release) and the combustion duration (defined as the time interval between 10% heat release and 90% heat release) of tested cases. It can be clearly found that the ignition delay and the combustion duration among all single stage combusted pre-chamber jet ignition cases are respectively similar, although the total cross-sectional area of nozzles was tripled from the 4×Φ1.1 mm case to the 4×Φ2.0 mm case. Compared with the CSI case, the ignition delay and combustion duration of single stage combusted pre-chamber jet ignition are shortened by 45% and 55%, respectively. Double stage combusted pre-chamber jet ignition (i.e. 4×Φ1.0 mm case) shows different characteristics on combustion parameters. The ignition delay is obviously longer than that of single stage mode and even comparable to that of CSI due to the lag of the second stage combustion. However, the combustion duration of double stage mode is manifestly shorter than that of any other cases.
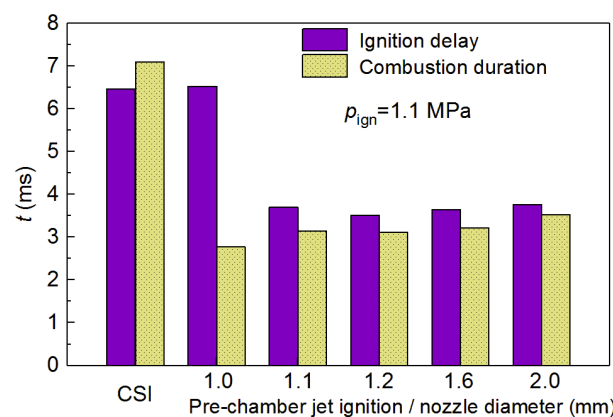

Figure 5: ignition delay and combustion duration of tested cases (1.1 MPa at spark timing)

Except for 4-nozzle cases, multiple pre-chamber configurations including single-nozzle designs and double-nozzle designs with various diameter were tested. The results are shown in Figure 6. It can be concluded that misfire occurs in the main chamber when

430

the nozzle dimension is below a certain threshold. With the increase of nozzle dimension, the mixture inside the main chamber could be indirectly ignited by the jet and the combustion is double-staged. However, the range of nozzle configuration led to double stage combustion is limited. As the nozzles are further enlarged, the combustion transforms to the single stage mode. It can be also found in Figure 6 that total cross-sectional area of nozzles is not the exclusive factor which affect the combustion mode at a certain pressure and temperature condition. Besides, the number of nozzles is also a minor factor because the increase of the nozzle number means the increase of contact surface area between the jets and the nozzle walls, resulting in more heat transfer.
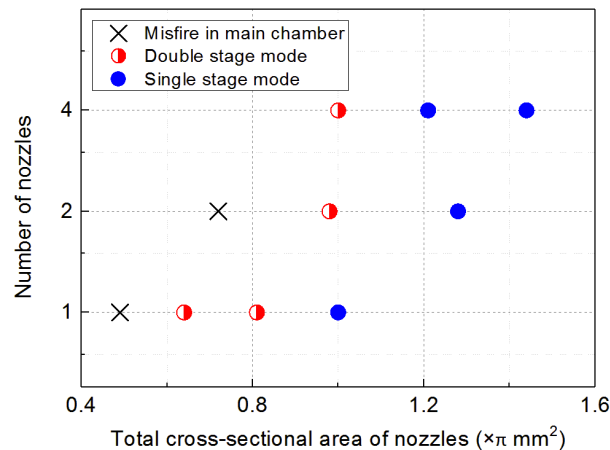

Figure 6: relationship between nozzle configuration and combustion mode (1.1 MPa at spark timing)

Figure 7 and Figure 8 display the ignition and combustion process (the contrast of images is improved) in the main chamber of single stage mode and double stage mode, respectively, corresponding to single-nozzle designs with the diameter of 3.0 mm (1×Φ3.0 mm case) and 1.6 mm (1×Φ1.6 mm case).

According to Figure 7, in the single stage case, the flame jet first appears in the main chamber at 1.12 ms after spark, indicating that the combustion inside the pre-chamber has already finished at that time. The flame jet generates from the nozzle and develops rapidly through the main chamber until it reaches the opposite side at approximately 2 ms. It means that the flame jet penetrates the main chamber in less than 1 ms. It can be calculated that the average propagation speed along the axial direction of the jet is over 50 m/s, exceeding 15 times than that of conventional flame propagation (approx. 3 m/s at the same condition). During the developing process, the flame is composed of thin fire near the nozzle and approximately conical fire in the tip.

As shown in Figure 8, in the double stage case, there is not any visible flame until 6.40 ms after spark. Compared with synchronous phenomenon of single stage mode, it can be concluded that the flame is quenched through the small dimension nozzle. The intense heat transfer cools the jet formed in the main chamber which cannot ignite the mixture directly. However, the jet composed of combusted and intermediate products still possess appropriate temperature to drive low temperature reaction, resulting in the ignition after a period of lag time. It can be clearly observed that the ignition occurs in the position far away from the nozzle, which is absolutely different from the single stage mode. Moreover, the flame develops evenly along each direction, with a high speed near 100 m/s. As a result, the 2D projection of the flame keeps approximately circular throughout the combustion process. It can be inferred that the jet preheats the mixture

and improve the reactivity in the main chamber during the lag period so that the following combustion is markedly enhanced.
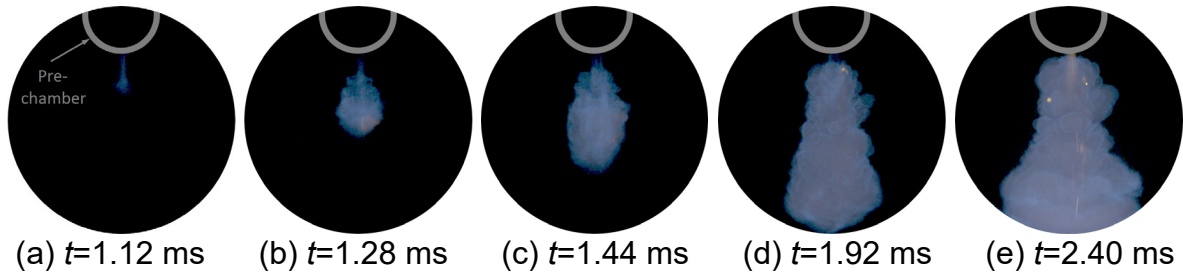
(a) t=1.12 ms   (b) t=1.28 ms   (c) t=1.44 ms   (d) t=1.92 ms   (e) t=2.40 ms

Figure 7: ignition and combustion process in main chamber of single stage mode (1×Φ3.0 mm case, 1.4 MPa at spark timing, contrast improved)

(a) t=6.40 ms   (b) t=6.56 ms   (c) t=6.72 ms   (d) t=7.20 ms   (e) t=7.68 ms

Figure 8: ignition and combustion process in main chamber of double stage mode (1×Φ1.6 mm case, 1.4 MPa at spark timing, contrast improved)

Figure 9 and Figure 10 display the repeated test results of a single stage case and a double stage case, respectively. Pressure traces of single stage combustion appear good repeatability. On the contrary, those of double stage mode are dispersed. In double stage mode, the ignition inside the main chamber has relatively high randomness, leading to instability of ignition delay and combustion phase, which is unsatisfying in engine applications.
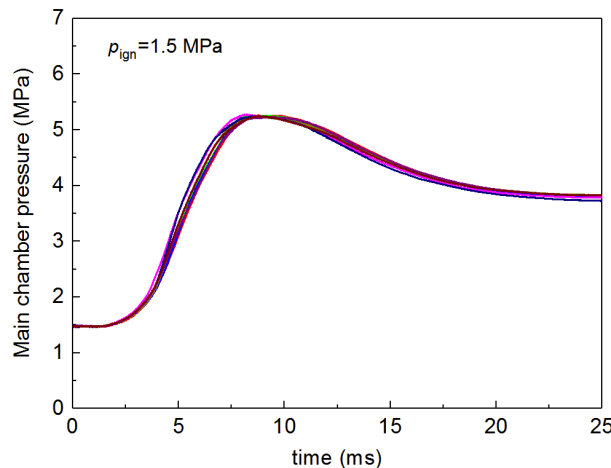

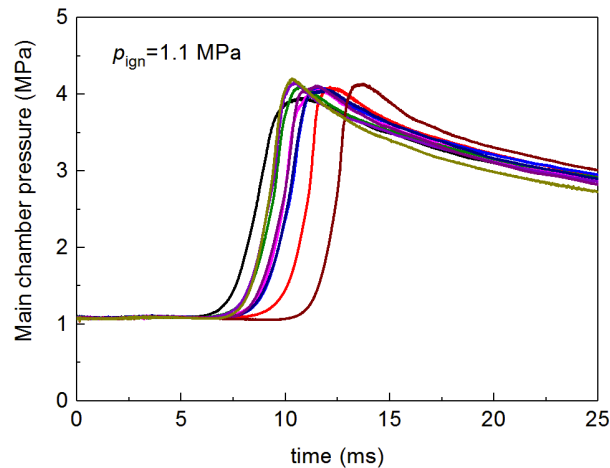*Figure 9: repeated test results of a single stage case*

Figure 10: repeated test results of a double stage case

3.2 Flame acceleration ignition investigations on RCM and natural gas engine

Figure 11 shows the comparison of in-cylinder pressure and heat release rate between FAI and CSI in RCM. The effect of accelerating combustion process achieved by FAI can be apparently recognized. Compared with CSI, the heat release peak of FAI comes 10 ms earlier with 20% higher value. The combustion process can be shortened by 40%, indicating the potential to improve combustion characteristics of SI engines.

Figure 12 records the combustion process (the contrast and brightness of images are improved) in the main chamber of FAI. The flame is generated and accelerates inside the tunnel until 1.92 ms after spark when it rushes into the main chamber (see Figure 12(a)). And then the flame curls outwards near the tunnel exit soon (see Figure 12(b)) which extends the radial width of the flame jet. After the initial period, the flame develops mainly along the axial direction at an average speed over 20 m/s. During the process, the flame jet maintains nearly cylindrical, igniting the surrounding mixture. As a result, the radial dimension of the flame also keeps growing at a speed faster than conventional flame propagation.
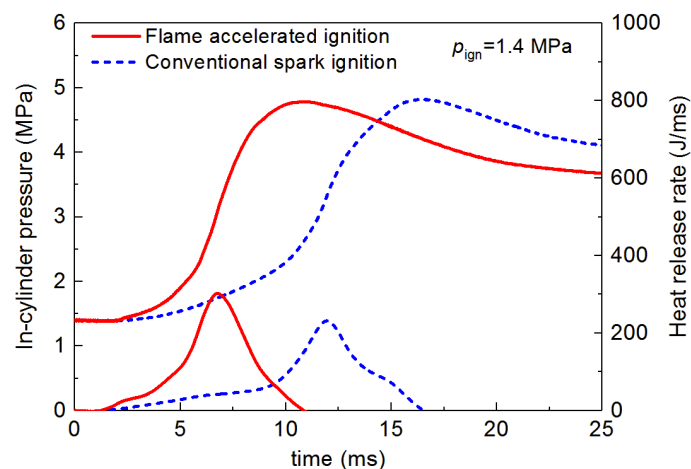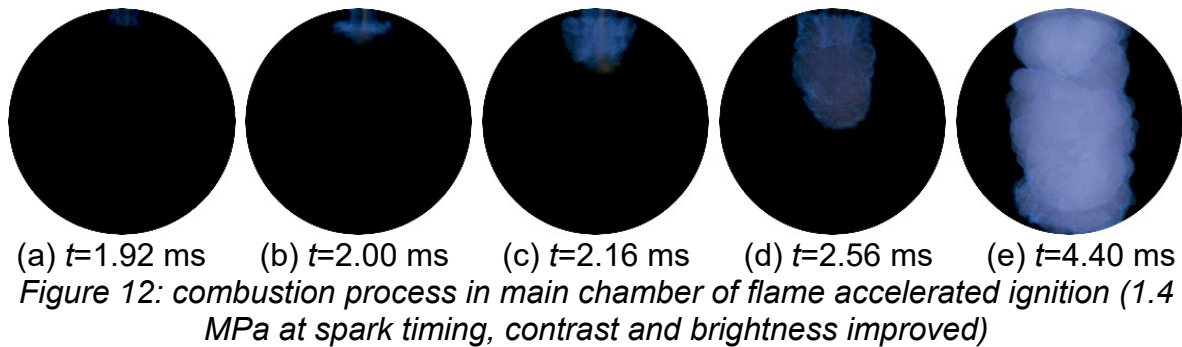

Figure 11: comparison of in-cylinder pressure and heat release rate between FAI and CSI in RCM (1.4 MPa at spark timing)

(a) *t*=1.92 ms   (b) *t*=2.00 ms   (c) *t*=2.16 ms   (d) *t*=2.56 ms   (e) *t*=4.40 ms

Figure 12: combustion process in main chamber of flame accelerated ignition (1.4 MPa at spark timing, contrast and brightness improved)

The RCM experiments indicated that the combustion could be evidently enhanced by FAI. On this basis, FAI is further tested in the natural gas engine. A 2-obstacle FAI system was assembled. The length and the diameter of the tunnel were 14 mm and 10 mm, respectively. The blockage ratio of the annular obstacles was 0.36, which was the same as that in RCM experiment.

Figure 13 shows the in-cylinder pressure and heat release rate of FAI under different mixture conditions. Corresponding CSI cases are also included for comparison. After spark, the response of pressure rise induced by FAI is slower than that of CSI, which means the heat release of FAI acts later. However, the heat release rate of FAI boosts to an evidently higher level subsequently, indicating that FAI induced combustion is faster and more centralized. Both cases with different mixture condition displayed in Figure 13 follow the characteristic. But the advantage of enhancing combustion is weakened with the introduction of excess air.
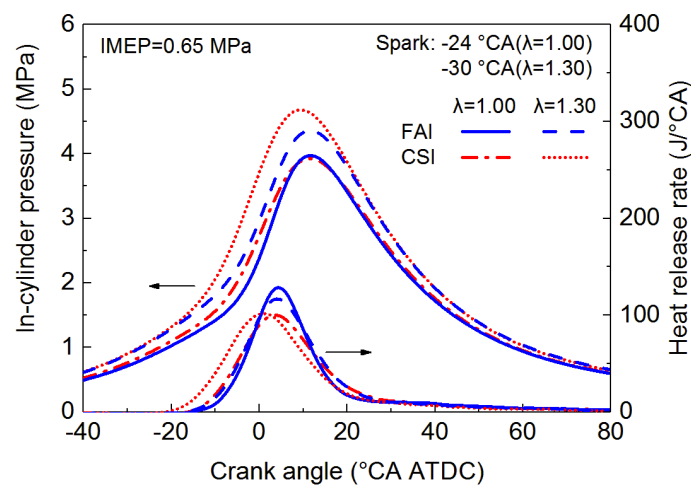

Figure 13: In-cylinder pressure and heat release rate of FAI in engine, compared with CSI

Figure 14 compares the ignition delay between FAI and CSI under different conditions. During the experiment, the spark timing was swept in order to cover the maximum output point. It can be primarily found from Figure 14 that misfire occurs in FAI mode when spark takes place at a relative early timing. It is clear that there is residual gas trapped in the tunnel after a combusted cycle. The fresh mixture has not been fully compressed into the tunnel to form an ignitable atmosphere in the position of spark plug at the early timing, resulting in misfire. With the increase of lean level, the range of optional spark timing becomes narrower.

The difference of ignition delay between FAI and CSI is notable that the former one is obviously longer than the latter one. In lean-burn conditions, the gap is further widened.

The characteristic can be ascribed to the adverse mixture atmosphere caused by residual gas inside the tunnel in FAI mode. With the addition of excess air, the natural gas concentration at spark position is further reduced, which prolongs the process of flame kernel formation and its initial development.
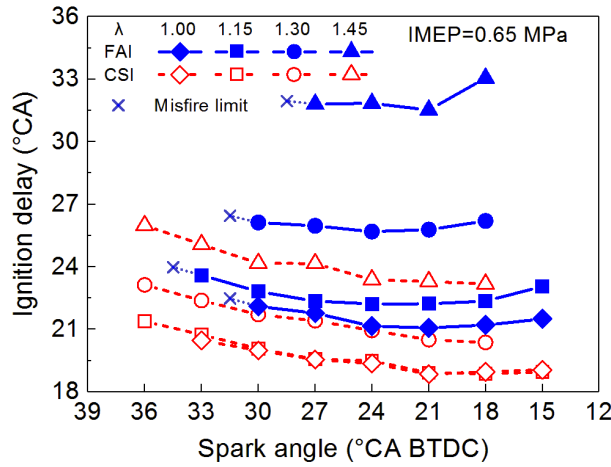

Figure 14: comparison of ignition delay between FAI and CSI

Figure 15 displays the CA10-CA50 duration. FAI mode shows advantage in this parameter when λ is less than 1.45. The effect of enhancing combustion by FAI can be directly proved according to the characteristic. FAI possesses the capacity to accelerate the first-half combustion. More importantly, the process of first-half combustion takes place around the top dead center, where the impact of heat release on the thermal efficiency is quite sensitive and significant. Hence, the feature of FAI is beneficial to improving the thermal efficiency. However, as λ increases, the advantage on CA10-CA50 fades gradually. When λ reaches 1.45, the benefit no longer exists at late spark timing.
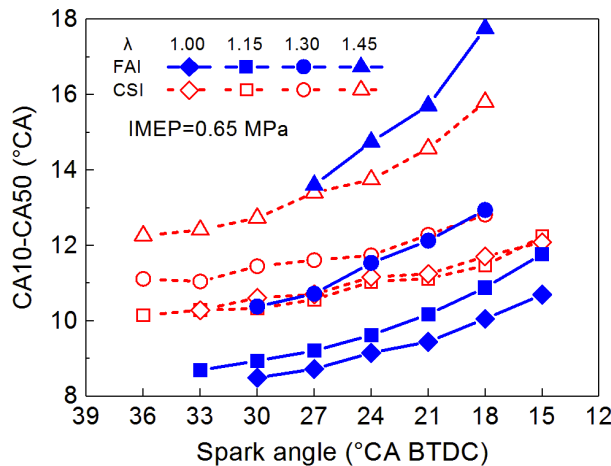

Figure 15: comparison of CA10-CA50 duration between FAI and CSI

CA50 is shown in Figure 16, which is the comprehensive result of ignition delay and CA10-CA50 duration. When the combustion takes place at stoichiometric condition or lean-burn condition with relative low λ ($\leqslant$1.15), the CA50 of FAI is comparable to that of CSI, because the accelerated CA10-CA50 duration of FAI erases the difference of ignition delay between two modes, which means that FAI possesses the capacity to

realize similar CA50 with less negative work at certain mixture conditions. Nevertheless, as the mixture becomes much leaner, the difference of CA50 between two modes gets larger as the advantage of CA10-CA50 duration achieved by FAI is narrowed while the disadvantage of ignition delay is sharply widened. Under the circumstance, the spark timing has to be advanced to adjust the combustion phase. However, the optional spark timing is limited by misfire.
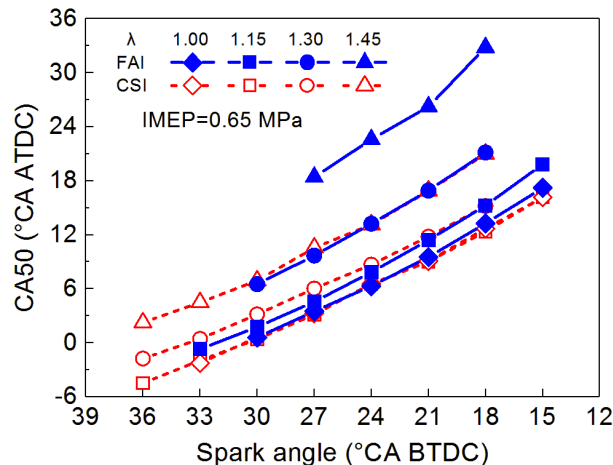

Figure 16: comparison of CA50 between FAI and CSI

Figure 17 compares the indicated thermal efficiency (ITE) of FAI and CSI under different conditions. FAI achieves higher efficiency than CSI due to the beneficial of reduced negative work and accelerated combustion process except for λ=1.45 condition. The best ITE improves 0.6, 0.5 and 0.2 percent when λ is 1.00, 1.15 and 1.30, respectively. It is clear that the biggest advantage of FAI appears at stoichiometric condition. For λ=1.45 condition, the suitable combustion phase cannot be attained which is restricted by misfire, resulting in unsatisfying ITE.
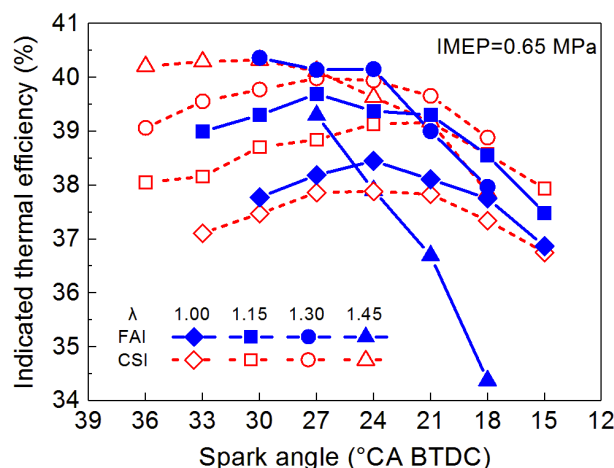

Figure 17: comparison of indicated thermal efficiency between FAI and CSI

Combustion stability is compared in Figure 18 using the coefficient of variation (COV) calculated by IMEP of consecutive cycles. Except for the leanest condition, the COV is comparable and all of them is under 3%. However, the COV of FAI under λ=1.45 condition is unacceptably high, reflecting that the stability of FAI with lean combustion needs to be improved.
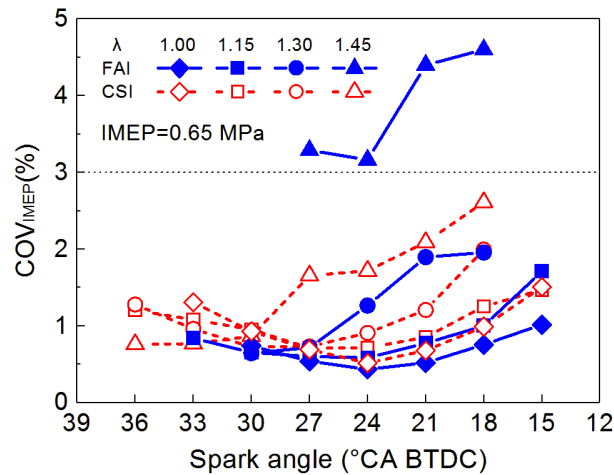
Figure 18: comparison of coefficient of variation between FAI and CSI

It can be concluded from the above engine test results that the performance of FAI under lean-burn condition is limited by misfire due to residual gas trapped in the tunnel. In order to solve the problem, the FAI system is modified by introducing a space by the side of spark position, named residual gas cavity, as shown in Figure 19. The residual gas cavity is off-centered, serving for storage of the residual gas. During the compression stroke, the residual gas which has not been exchanged outside the tunnel will be compressed to the cavity space instead of remained at the spark position in the effect of piston motion. Thus the ignition inside the tunnel can be ensured. The tunnel length and diameter of the modified design were 15 mm and 6 mm, respectively. The number and blockage ratio of the annular obstacles were kept the same with the original design.
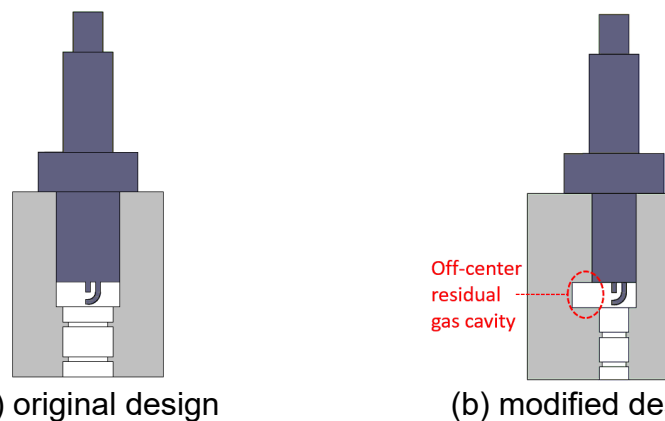
(a) original design (b) modified design

Figure 19: the original design and modified design (with residual gas cavity) of FAI system assembled in the engine

Figure 20 shows the in-cylinder pressure and heat release rate of modified FAI. The characteristics of late pressure response and centralized heat release remain.
Ignition delay is shown in Figure 21. Although FAI still behaves longer ignition delay, the gap is effectively narrowed, indicating that the ignition and combustion process inside the tunnel is improved. More importantly, attributing to the introduction of residual gas cavity, misfire limit has been eliminated which provides the capacity to adjust combustion phase flexibly.
The indicated thermal efficiency and coefficient of variation are displayed in Figure 22 and Figure 23, respectively. On account of above improvement, modified FAI gains higher ITE than CSI with acceptable combustion stability under all mixture conditions.

As a result, the lean-burned FAI performance is effectively enhanced by the modification with residual gas cavity.
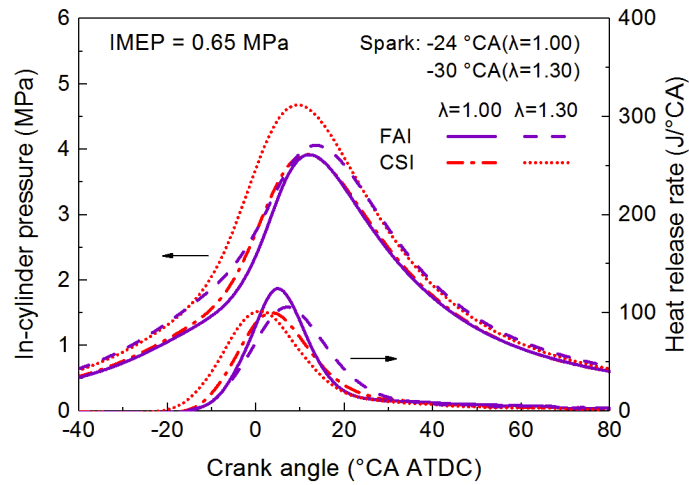

Figure 20: In-cylinder pressure and heat release rate of modified FAI with residual gas cavity in engine, compared with CSI
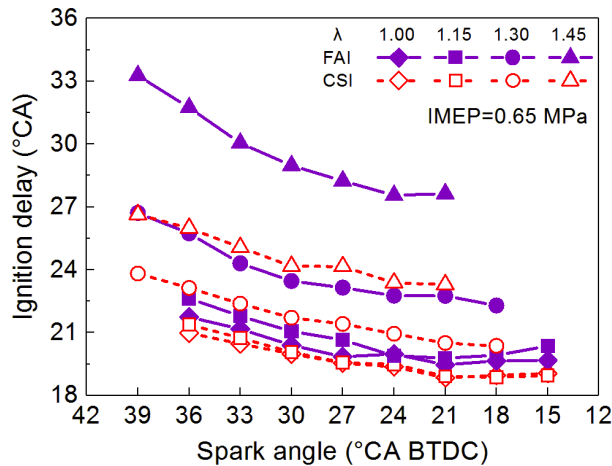

Figure 21: comparison of ignition delay between modified FAI with residual gas cavity and CSI
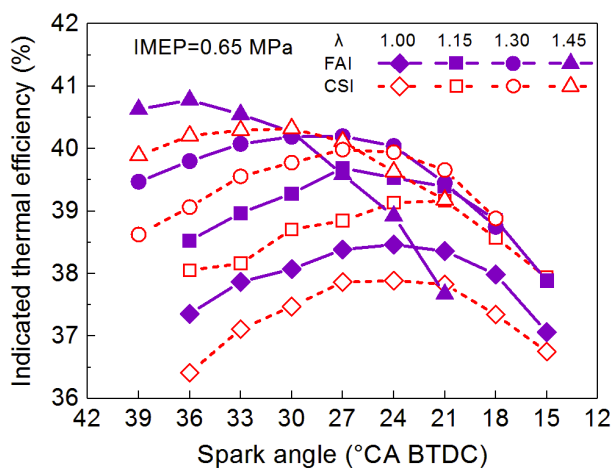

Figure 22: comparison of indicated thermal efficiency between modified FAI with residual gas cavity and CSI
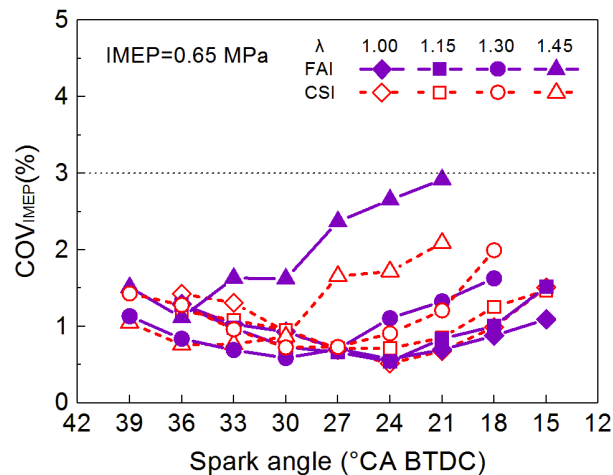
Figure 23: comparison of coefficient of variation between modified FAI with residual gas cavity and CSI

4 Conclusions

In this paper, classical pre-chamber jet ignition and a new pre-chamber jet ignition method called flame accelerated ignition were investigated. Optical RCM was used to detailed study the ignition and combustion process of both methods. Moreover, the newly proposed flame accelerated ignition was tested in a single cylinder natural gas engine. The conclusions are summarized as following:

(1) The classical pre-chamber jet ignition is classified as two modes: double stage combustion and single stage combustion. Under a certain pressure and temperature condition, nozzle configuration is the key factor affecting the combustion mode.

(2) Double stage combustion mode takes place in the condition with relatively small nozzle dimension. The jet cannot ignite the mixture in the main chamber directly due to the quenching effect. Ignition inside the main chamber occurs away from the nozzle after a lag time, initiating the speedy second-stage combustion. Therefore, double stage combustion shows long ignition delay and extremely short combustion duration. Due to the randomness of ignition in the main chamber, the combustion stability of double stage mode is unsatisfying. Moreover, the range of nozzle configuration led to double stage combustion is narrow.

(3) With the increase of nozzle dimension, combustion switches to the single stage mode. The mixture in the main chamber is directly ignited by the flame jet developing from the nozzle. Hence the combustion inside the pre-chamber and the main chamber takes place continuously, showing single-stage characteristic. In this mode, the ignition delay and the combustion duration can be shortened simultaneously with satisfying combustion stability. The flame jet consists of thin fire near the nozzle and approximately conical fire in the tip, expanding rapidly with axial speed over 15 times than that of conventional flame propagation.

(4) According to the concept of flame acceleration in tunnel and pre-chamber jet ignition, flame accelerated ignition is realized by a flame acceleration tunnel set between the spark plug and the main chamber. RCM experiment proved the effect of enhancing combustion achieved by FAI. The mixtures in the main chamber can be rapidly ignited by the cylindrical flame jet rushed out of the tunnel.

(5) According to the engine test results, FAI possesses the capacity to reduce negative work and accelerate combustion, leading to higher thermal efficiency than conventional spark ignition. The best performance takes place at stoichiometric condition. With the increase of excess air ratio, the advantages are weakened and the combustion phase is restricted by misfire due to the residual gas trapped in the tunnel. The introduction of residual gas cavity eliminates the misfire and guarantees the performance of FAI under all mixture conditions.

Literatures:

[1] Toulson E, Schock H J, Attard W P. A review of pre-chamber initiated jet ignition combustion systems[J]. SAE Technical Paper 2010-01-2263, 2010.

[2] Shah A, Tunestal P, Johansson B. Investigation of performance and emission characteristics of a heavy duty natural gas engine operated with pre-chamber spark plug and dilution with excess air and EGR[J]. SAE International Journal of Engines, 2012, 5(4):1790-1801.

[3] Takashima Y, Tanaka H, Sako T, et al. Evaluation of engine performance and combustion in natural gas engine with pre-chamber plug under lean burn conditions[J]. SAE International Journal of Engines, 2014, 8(1):221-229.

[4] Attard W P, Blaxill H, Anderson E K, et al. Knock limit extension with a gasoline fueled pre-chamber jet igniter in a modern vehicle powertrain[J]. SAE International Journal of Engines, 2012, 5(3):1201-1215.

[5] Anderson E K, Attard W P, Brown A, et al. Experimental study of a pre-chamber jet igniter in a turbocharged rotax 914 aircraft engine[J]. SAE Technical Paper 2013-01-1629, 2013.

[6] Attard W P, Fraser N, Parsons P, et al. A turbulent jet ignition pre-chamber combustion system for large fuel economy improvements in a modern vehicle powertrain[J]. SAE International Journal of Engines, 2010, 3(2):20-37.

[7] Shah A, Tunestal P, Johansson B. Effect of relative mixture strength on performance of divided chamber 'avalanche activated combustion' ignition technique in a heavy duty natural gas engine[J]. SAE Technical Paper 2014-01-1327, 2014.

[8] Gentz G, Thelen B, Litke P, et al. Combustion visualization, performance, and cfd modeling of a pre-chamber turbulent jet ignition system in a rapid compression machine[J]. SAE International Journal of Engines, 2015, 8(2):538-546.

[9] Thelen B C, Gentz G, Toulson E. Computational study of a turbulent jet ignition system for lean burn operation in a rapid compression machine[J]. SAE Technical Paper 2015-01-0396, 2015.

[10] Gentz G, Thelen B, Gholamisheeri M, et al. A study of the influence of orifice diameter on a turbulent jet ignition system through combustion visualization and

performance characterization in a rapid compression machine[J]. Applied Thermal Engineering, 2015, 81:399-411.

[11] Gentz G, Gholamisheeri M, Toulson E. A study of a turbulent jet ignition system fueled with iso-octane: Pressure trace analysis and combustion visualization[J]. Applied Energy, 2017, 189:385-394.

[12] Gholamisheeri M, Thelen B C, Gentz G R, et al. Rapid compression machine study of a premixed, variable inlet density and flow rate, confined turbulent jet[J]. Combustion and Flame, 2016, 169:321-332.

[13] Thelen B C, Toulson E. A computational study of the effects of spark location on the performance of a turbulent jet ignition system[J]. SAE Technical Paper 2016-01-0608, 2016.

[14] Validi A A, Schock H, Jaberi F. Turbulent jet ignition assisted combustion in a rapid compression machine[J]. Combustion and Flame, 2017, 186:65-82.

[15] Dorofeev S B. Hydrogen flames in tubes: Critical run-up distances[J]. International Journal of Hydrogen Energy, 2009, 34(14):5832-5837.

[16] Silvestrini M, Genova B, Parisi G, et al. Flame acceleration and DDT run-up distance for smooth and obstacles filled tubes[J]. Journal of Loss Prevention in the Process Industries, 2008, 21(5):555-562.

[17] Ciccarelli G, Dorofeev S. Flame acceleration and transition to detonation in ducts[J]. Progress in Energy & Combustion Science, 2008, 34(4):499-550.

[18] Wang B, Wang Z, Liu C, et al. Experimental study of flame accelerated ignition on rapid compression machine and heavy duty engine[J]. SAE Technical Paper 2017-01-2242, 2017.

[19] Di H, He X, Zhang P, et al. Effects of buffer gas composition on low temperature ignition of iso-octane and n-heptane[J]. Combustion and Flame, 2014, 161(10):2531–2538.

8.3 Transferability of Insights from Fundamental Investigations into Practical Applications of Prechamber Combustion Systems

Panagiotis Kyrtatos, Konstantinos Bardis, Michele Bolla, Alexey Denisov, Yuri Wright, Kai Herrmann, Konstantinos Boulouchos

Abstract

Efforts to reduce CO_2 emissions from spark ignition engines have driven engine development to lean-burn or high-dilution operation, which results in high combustion variability as well as increased unburned hydrocarbon emissions. A widely used technology to reduce these issues are prechamber ignition systems, in which the external ignition source is located in a separate small volume, connected to the main chamber via small orifices. This setup allows for design of favourable ignition conditions near the ignition source, which results in fast and repeatable early flame propagation. The pressure increase resulting from combustion taking place inside the prechamber leads to the ejection of jets containing hot combustion products and possibly active radicals into the main chamber, which ignite the lean or diluted mixture; this process is often dubbed turbulent jet ignition or TJI. The use of TJI systems in engines allows the combustion of very lean/diluted mixtures, resulting in higher efficiencies and lower NOx emissions.

In this work we shed light into the importance of quenching for practical applications involving turbulent jet ignition. This is achieved through optical investigations in a generic, constant volume test-rig, combined with zero-dimensional (0-D) model calculations. The 0-D model is applied to the generic setup and in real engine applications under varying operating conditions, in order to highlight the relative importance of quenching under the various thermochemical conditions encountered. The results indicate that thermal quenching in the nozzle should not be expected due to the small flame thickness under high pressure encountered in internal combustion engines. Nevertheless, under the jet mixing conditions expected in engines, hydrodynamic quenching due to mixing of burned products with unburned (cold) main chamber mixture can be expected. In most engine conditions, the re-ignition process of the initially quenched jet after their exit from the prechamber is expected to be so fast, that quenching will not be apparent in most measurements.

1   Introduction

Efforts to reduce CO_2 emissions from internal combustion engines have led to the use of natural gas as a fuel in lean-burn spark ignition engines. Lean-burn, or alternatively high-dilution combustion concepts, are employed to keep engine efficiency high by minimizing thermal losses, while simultaneously ensuring NOx emissions below legislated limits. Under high-dilution conditions, operation is limited by high cyclic variability as well as increased unburned hydrocarbon emissions [1, 2]. In order to address these

limitations, external ignition engines require high ignition energy and distributed ignition sources in order to ignite and consume the lean/diluted premixed main charge [1, 3].

A technology widely used in these engines is the prechamber ignition system, in which the external ignition source is located in a separate small volume, connected to the main chamber via small orifices [1, 2]. This setup allows for design of favorable conditions near the ignition source, in particular controlled flow properties (absence of large scale bulk motion) and turbulence levels, which result in fast and repeatable early flame propagation. The pressure difference resulting from combustion taking place inside the prechamber pushes jets containing active radicals and/or hot combustion products into the main chamber, which ignite the lean or diluted mixture; this process is often dubbed turbulent jet ignition or TJI. The use of TJI systems in engines allows the combustion of very lean/diluted mixtures, resulting in higher efficiencies and lower NOx emissions. Research in the field of prechamber combustion has been extensive in the past years, aiming to increase our understanding of turbulent jet ignition systems. These studies have ranged from fundamental investigations of turbulent jet ignition under atmospheric conditions [4-7], to optical experiments [8-12] and simulations [8, 12-16] in engine or engine-like setups.

Biswas et al. [4] studied TJI in a generic single-hole prechamber configuration employing simultaneous high-speed Schlieren and OH*-chemiluminescence imaging. The authors identified two distinct main chamber ignition patterns depending on the ignition time and the flame morphology, which they coined "flame ignition" and "jet ignition". In addition, they introduced a "global" Damköhler number based on the relationship between laminar flame speed and turbulence at the nozzle, which they used to explain cases where no main chamber ignition was observed. Yamaguchi et al. [5] also studied ignition in a divided chamber bomb. Based on the physical and chemical characteristics of the torch jet, ignition was classified into four different types. Other researchers [6, 7, 14, 17] carried out fundamental studies of mixture ignition via a hot jet, concluding that scalar dissipation rate and flame thickness are of vital importance for the process of ignition and the resulting ignition delay. Recent studies from Mastorakos et al. [18] and Allison et al. [19] were carried out in a constant volume chamber connected to the environment via a small orifice, resembling a prechamber-main chamber setup. They reported a curvature-induced quenching at the nozzle due to the high speed jet and the limited effective nozzle diameter.

All abovementioned investigations [4-7, 14, 17-19], have been performed under thermodynamic conditions (in particular pressure) which are significantly different to conditions encountered in typical internal combustion engine. Despite the fact that relevant observations concerning the phenomenology of TJI can be made in such investigations, there is no established framework to compare the conditions as well as the phenomenology with engine conditions; i.e. the practical relevance of the observed phenomenology and conclusions can be demanding to determine.

Recent work from the current authors has focused on optical investigations in a rapid compression-expansion machine [8, 20, 21], where engine relevant conditions can be attained Optical results using simultaneous high-speed Schlieren imaging and OH* chemiluminescense showed that the appearance of a reactive flame (non-negligible signal in the OH* chemiluminescense images) was observable near the prechamber nozzle exit, and was concurrent with the exiting of hot jets from the prechamber. This

indicates that under engine-relevant conditions, prechamber flame does not completely quench as it passes through the nozzles, and thus the use of a level-set combustion model TJI and the combustion process is justified.

In traditional spark ignition engines, flame quenching is rarely very important, since conditions typically encountered do not lead to quenching. For this reason, flame quenching is often completely neglected in spark ignition simulations, or accounted for in a very simplified way. Nevertheless, flame quenching mechanisms constitute a topic of fundamental interest, with relevance in many practical applications.

In the present study, we aim to shed light into the importance of quenching for practical applications involving turbulent jet ignition. This is achieved through optical investigations in a generic, constant volume test-rig, combined with 0-D model calculations (previously presented in [22]) in the generic setup and in real engine applications under varying operating conditions. Through this investigation we aim to highlight the relative importance of quenching under different conditions in fundamental test rigs and practical applications. This information will aid to evaluate the errors induced by neglecting quenching in TJI setups depending on the operating conditions. In the future, this information can possibly lead to improvements in the level-set methods (such methods, the most common of which is the G-equation model, have inherent limitations in simulating flame total or partial quenching) currently used for most simulations in an industrial context, as well as encourage the use of more physically accurate flame models in TJI simulation applications.

2   Flame quenching and re-ignition mechanisms

Quenching in a turbulent reacting jet passing through a nozzle into a chamber with unburned (cold) mixture can occur due to two distinct mechanisms. One is thermal quenching, whereby the heat losses towards the nozzle wall exceed the heat release of the flame. The second mechanism, named hydrodynamic quenching, is caused by the intense mixing of the products of combustion emanating from the prechamber with the cold unburned mixture found in the main chamber. Both mechanisms are depicted schematically in Figure 1.

Thermal quenching caused by wall heat losses may be relevant in TJI applications due to the large surface-to-volume ratio within the nozzle and the strong interaction with the nozzle walls during the passage of the flame front through it. The phenomenon of wall quenching refers to the inability of a flame to sustain wall heat losses below a certain distance from the wall. The critical distance below which flame quenches (δ_q) over the flame thickness (l_f), is referred to as the Peclet number (Pe).

$$Pe = \frac{\delta_q}{l_f} \approx 10 \ \text{ (side wall quenching, according to [23])} \tag{1}$$

The equation above indicates that quenching will be more probable when the flame thickness is high (low chamber pressure) or the nozzle is very narrow.
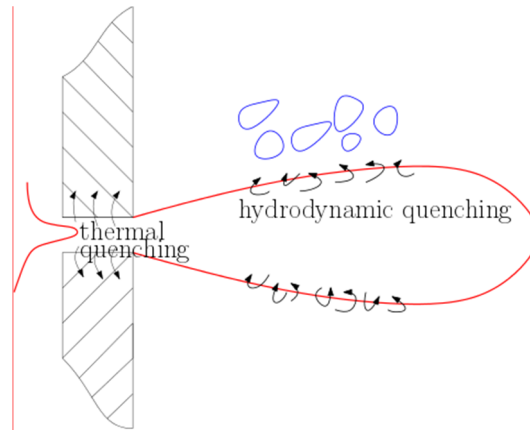
Figure 1: Schematic of the different quenching mechanisms encountered in turbulent jet ignition applications

Hydrodynamic quenching is the process whereby the flame quenches due to reduced temperature from strong mixing with the cold unburned gases. To determine the propensity of quenching by mixing we evaluate:

$$Da = \frac{\tau_{mix}}{\tau_{fl}} = \frac{\frac{l_I}{u'}}{\frac{l_f}{S_l}} \tag{2}$$

which is the non-dimensional Damköhler number (Da) of the relative chemical reactions intensity compared to mixing. Due to the time and space-varying nature of turbulence within a jet, the evaluation of a single Damköhler number is not straightforward for such a case. For the present investigation we choose to evaluate Da sufficiently downstream the nozzle exit (five nozzle diameters), where turbulence has already developed [24].

In detail, the integral length scale (l_I) is evaluated based on the nozzle diameter for a steady state jet, while the turbulent intensity (u') is based on the nozzle velocity. The two estimates provided here are derived from [24] and [25] respectively:

$$l_I = 0.2 \, d_{noz} \tag{3}$$

And

$$u' = 0.1 \, u_{noz} \tag{4}$$

Hydrodynamic quenching takes place, irrespective of the specific thermochemical conditions and fuel properties, if the aforementioned number drops below a critical threshold $Da_{cr} \approx 0.5$. This assumption for the critical Da is based on previously published results in similar configurations [4] and [26]. Although this evaluation of Da and Da_{cr} does not provide a solid indication of quenching, it can serve as a basis for comparison of different setups and operating conditions.

While the abovementioned criteria for flame quenching give an indication of the quenching probability, they do not offer insights into whether or not the mixture will ignite – and if so, how fast – once quenched. This information would be important to

judge whether quenching, if it occurs, can actually have a profound effect on the combustion, or whether it can be neglected. In cases where reactivity is very high and re-ignition is imminent, the assumption of no quenching might adequately depict reality, and can possibly be used in 3D CFD and 0-D simulations without introducing significant error. In this perspective, a simplified ignition delay time for a homogeneous mixture consisting of unburned and burned gases can be computed, which can serve as a proxy for eventual ignition processes:

$$\tau_{ign} = f(p, Tu, Tb) \tag{5}$$

This quantity can be calculated using perfectly stirred reactors (PSR) with a presumed mixture of burned and unburned gases. Having calculated the reactant temperature for the products of combustion, the PSR initial temperature is given as a function of unburned mixture fraction (ξ) assuming adiabatic mixing of the burned and unburned gases. This allows the calculation of the ignition delay for different ξ, which will tend to zero at $\xi=1$ (fully burned products). This simplified approach neglects the effect of combustion radicals coming from the prechamber on main chamber ignition; these effects can only be taken into account using significantly more complex physicochemical modelling, which is beyond the scope of this work.

A small ignition delay indicates that re-ignition is likely to occur under the given thermochemical conditions. In contrast, a mixture with high ignition delay will most likely not reignite before the temperature of the burned gases drops significantly by the action of heat losses and mixing.

3   Zero Dimensional Simulations

To address the questions presented above and to further enhance the understanding of the experimentally observed combustion modes, simulations have been performed using a zero dimensional model. Another objective for the use of the 0-D model is to enable the comparison of the fundamental experiments with engine conditions, through the comparison of the TJI characteristics in a typical engine. This will allow the determination of the transferability of findings obtained from fundamental investigations to practical applications.

Although the complete formulation of the 0-D model is beyond the scope of the present publication, some basic information regarding the model will be given for completeness. The 0-D model assumes that the PC mixture is separated into two zones; a burned zone behind the flame front position and an unburned zone ahead of the flame front. A simplified description of the pre chamber geometry as well as of the flame front is adopted to reduce complexity, while, still, preserving the main features of the pre chamber.

A coupled system of differential equations is solved to obtain the thermodynamic variables, such as pre and main chamber pressure and temperature. The heat release rate is modelled based on the active flame front area and a turbulent flame speed. Turbulence intensity inside the pre chamber, which is relevant only for the engine ap-

plication, is modelled using a refined 0-D turbulence sub-model obtained via a reduc-tion of the well established CFD k-ε model. The latter model has been extensively validated with 3D-CFD simulations in a previous publication [22].
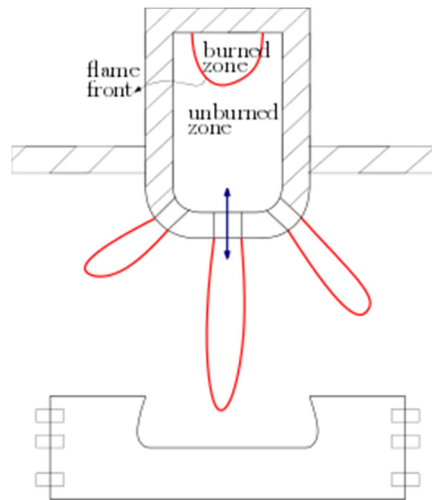

Figure 2: Schematic of the 0-D model zones in the pre and main chambers

The present publication focuses on the determination of the conditions near the nozzle exit and during the early phase of main chamber combustion, when the main chamber heat release rate does not significantly change the conditions in the main chamber; therefore, only the pressure difference between the pre and main chamber is of inter-est. In addition, the physical parameters that involve the computation of the flame speed and flame thickness are evaluated with respect to the unburned zone and, con-sequently, the main chamber burned zone properties are not of interest.

4   Experimental Setup and Operating Conditions

A newly developed, constant volume divided combustion chamber, named the optically accessible prechamber (OPC), has been designed and built to allow the study of TJI under different operating conditions. The test-rig contains two volumes, which are con-nected through a single interchangeable orifice. The smaller of the two volumes, (iden-tified as the prechamber), contains an ignition source (sparkplug), which allows the ignition of the mixture. The orifice connecting the prechamber to the main chamber can be changed in shape and diameter, and can fit a nozzle with a maximum diameter of 4 mm. In the configuration used in this investigation, the volume of the main chamber is 186'988 mm^3, whereas the prechamber is 3'602mm^3 (~1.9% of the total volume).

Both chambers have windows to allow optical access into the respective volumes, which enable optical measurements during the combustion event. The prechamber is fitted with two opposing windows, which allow optical access through the complete prechamber volume. The main chamber also has two opposing windows, allowing op-tical access from the nozzle exit to the bottom of the chamber. A removable opposing wall is placed 40 mm away from the nozzle exit.

The operation and control sequences of the OPC allow the accurate setting of condi-tions in both chambers prior to ignition, cf. Table 1 unterhalb. The charge air pressure and temperature is feedback controlled through an intake and leakage valve system,

and an electrical heating system. The fuel in the main chamber is injected using a hollow-cone piezo injector, and the mixture composition is determined using the pressure signal and a partial pressure calculation. An external mixing tank is used to prepare the mixture for the prechamber, allowing the separate setting of composition in the two chambers. The premixed mixture is injected directly into the prechamber prior to ignition. The fuel used in this study is pure methane (N45, ≥ 99,995 mol %).
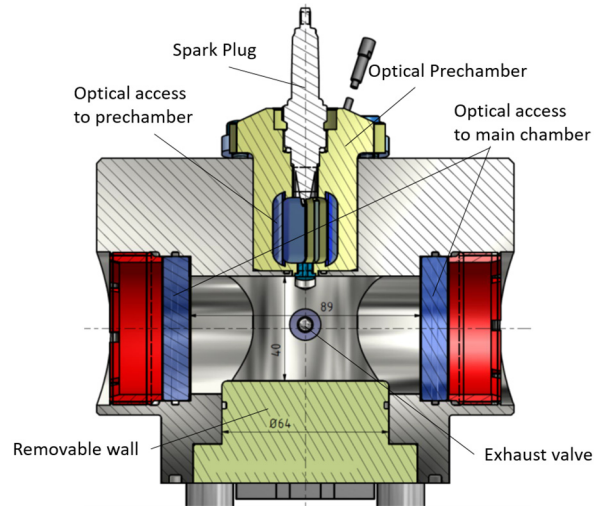

Figure 3: Schematic of the Optical Prechamber, showing the main parts

The operating conditions possible for the current setup are presented in Table 1.

Table 1. Operating conditions possible in the OPC

Parameter	Unit	Value
Initial Pressure	bar	1…20
Initial Temperature	K	300…450
Φ Prechamber		0…>5
Φ Main Chamber		0…>5

Information about the combustion characteristics of the turbulent jet emanating into the main chamber was recorded using a simultaneous high-speed Schlieren and 2D OH* chemiluminescence imaging setup. For this purpose, two LaVision HSSX high-speed cameras were used, set at a frame rate of 20 kHz. For OH* an image intensifier was fitted to the camera, in addition to a bandpass filter for a wavelength of 306 nm.

For the comparison of the OPC fundamental TJI investigations with practical engine conditions, results from a near-production Liebherr full metal test engine were used. The engine is a lean burn, medium-speed engine, equipped with chamber sparkplugs with five nozzles, of which four are peripheral and one axial. The axial nozzle is mainly applied for efficient scavenging and convection of the swirl vortex towards the spark plug. Additional information concerning the engine and experimental conditions used can be found in [15, 22].

5   Results

The present section contains the experimental results from the optical prechamber, followed by the simulations of the OPC and engine conditions. The experimental results include a brief description of the 0-D model validation. The 0-D model is used in both experimental setups in order to obtain the relative time scales and non-dimensional numbers, which allow the comparison of the two setups.

5.1   Optical Prechamber

The optically accessible prechamber constant volume setup is used in order to evaluate the propensity of jet flame quenching and re-ignition. Three distinct operating conditions were chosen in order to highlight the effect of jet mixing and thermodynamic conditions on flame quenching and the subsequent re-ignition.

The operating conditions chosen for the investigation are summarized in Table 2. The conditions differ in terms of nozzle diameter (d_{noz}=4 mm for case 1, 2 mm for cases 2 and 3) and initial charge temperature (T_{in}=~300 K for cases 1 and 2, ~430 K for case 3), with constant initial pressure (P_{in}=~5 bar), as well as prechamber and main chamber compositions (Φ_{PC}=~1 and Φ_{MC}=~0.75, respectively). The values stated are the average of the individual repetitions recorded for each operating condition (5 for case 1, 7 for cases 2 and 3). Temperature is expected to affect significantly the mixture reactivity and consequently the flame speed and ignition propensity. Higher mixture reactivity results in increased nozzle velocity and, therefore, temperature influences both terms of the Damköhler number. The different nozzle diameters significantly modify the mixing Damköhler number through changes in jet velocity.

Table 2. Operating conditions used for the investigation in the OPC

| Case No.	P_{in} (bar)	T_{in} (K)	d_{noz} (mm)	Φ_{MC}	Φ_{PC}	No. of Repetitions
1	5.67	302	4	0.75	0.97	5
2	5.13	299	2	0.75	0.92	7
3	5.16	434	2	0.74	0.94	7

The experimental results are presented in the figures below. Figure 4 shows the measured main chamber pressure (blue, left axis), along with the pressure difference between main chamber and prechamber (red, right axis), plotted against time after ignition for the three OPC cases. All repetitions are plotted for each case, showing good repeatability of the conditions.

Figure 5 shows the Schlieren images (in green/black) from the main chamber, with the OH* chemiluminescence overlaid, for significant time-instances for the same three cases. The images are taken from a representative repetition of the experiment, chosen as the cycle with pressure closest to the average of all cycles at the same conditions. Note that the different images do not correspond to the same time instances for the different cases, since the timings of the hot jet exit and subsequent ignition differ significantly between different conditions. Also note that the OH* is only shown as a binary value above a certain arbitrary threshold, which is chosen to remove signal

noise. This binary value allows comparison of the locations of significant OH* luminos-ity, permitting the determination of reaction zones and enabling identification of flame quenching and re-ignition.

In case 1, minimal pressure increase is observed in the prechamber, while the main chamber ignition happens very quickly after the hot jet exit. The burned products are first observed in the main chamber at 5.5 ms after ignition (see Figure 5), with some OH* visible immediately. The hot jet then propagates through the main chamber and hits the opposing wall, with the tip of the jet showing no OH* signal, indicating flame quenching due to mixing. The main chamber pressure shows significant increase only after 7.2ms, which is also where a broader OH* signal is observed.
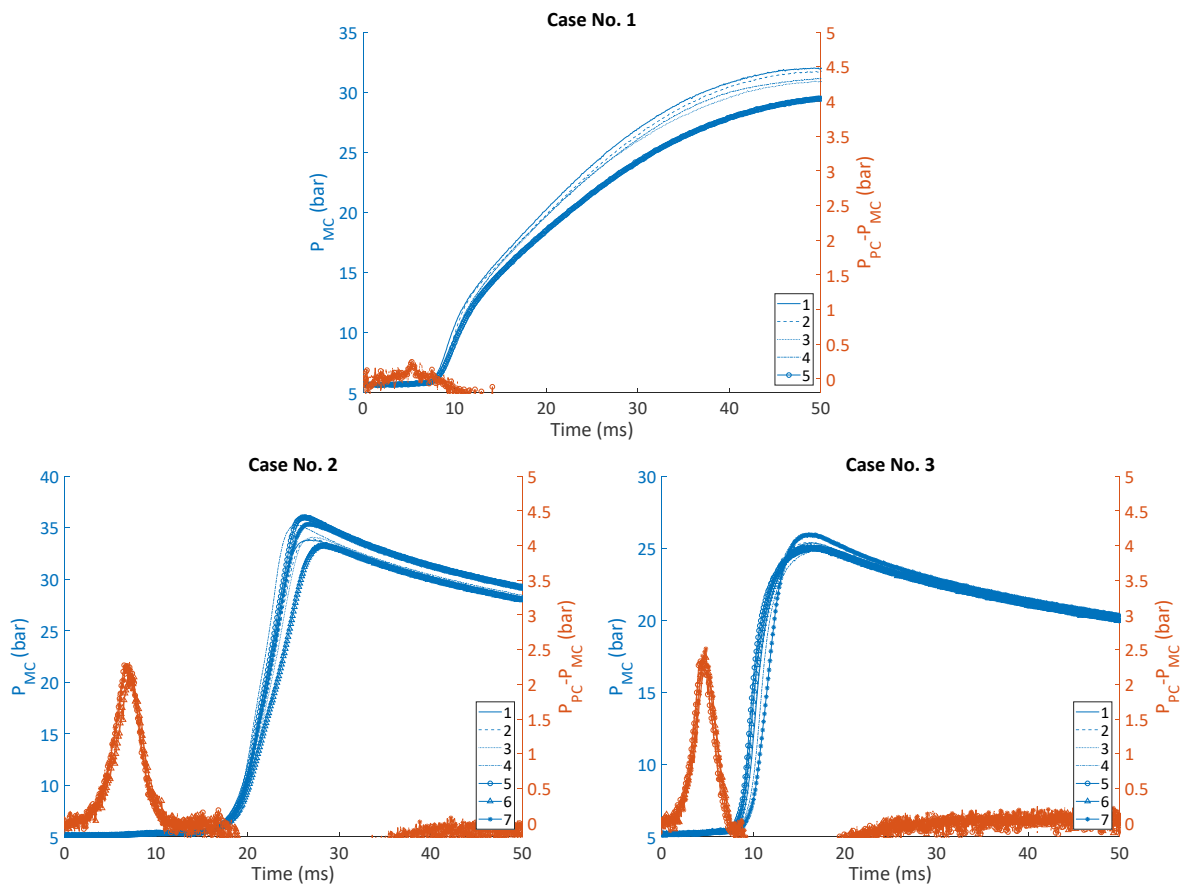
Figure 4: Measured main chamber pressure (blue, left axis) and prechamber minus main chamber pressure difference (red, right axis) plotted over time after ignition for all repetitions of the OPC cases 1-3

In cases 2 and 3 the pressure increase in the prechamber is much sharper, due to the lower cross-sectional area of the nozzle (D_{noz}=2 mm). In case 2 the PC pressure peak is delayed due to the less reactive mixture conditions compared to case 3 ($T_{in,2}$=300 K vs $T_{in,3}$=430 K). The main chamber ignition is also delayed for the same reasons. In both cases, the initial hot jet exit does not show any OH*, indicating complete flame quenching within the nozzle or in the main chamber.

In case 2 the hot jet is first observed in the main chamber 5.95 ms after ignition, with the jet penetrating fast in the main chamber and hitting the opposing wall. Early pene-tration Schlieren images (e.g. at 6.3 ms) show very low Schlieren signal near the jet

tip, indicating very low temperature gradients and thus very strong mixing at that loca-tion. The fist OH* signal is observed at the jet core near the nozzle after 9.65 ms, which is when the pressure difference between the two chambers and thus the jet velocity falls to very low values. The OH* signal then completely disappears before significant signal is observed again at around 13 ms at different locations along the jet. Significant main chamber pressure increase indicating heat release and widespread OH* signal are only observed after 15 ms, resulting in a total ignition delay between hot jet exit and widespread ignition of ~9 ms.
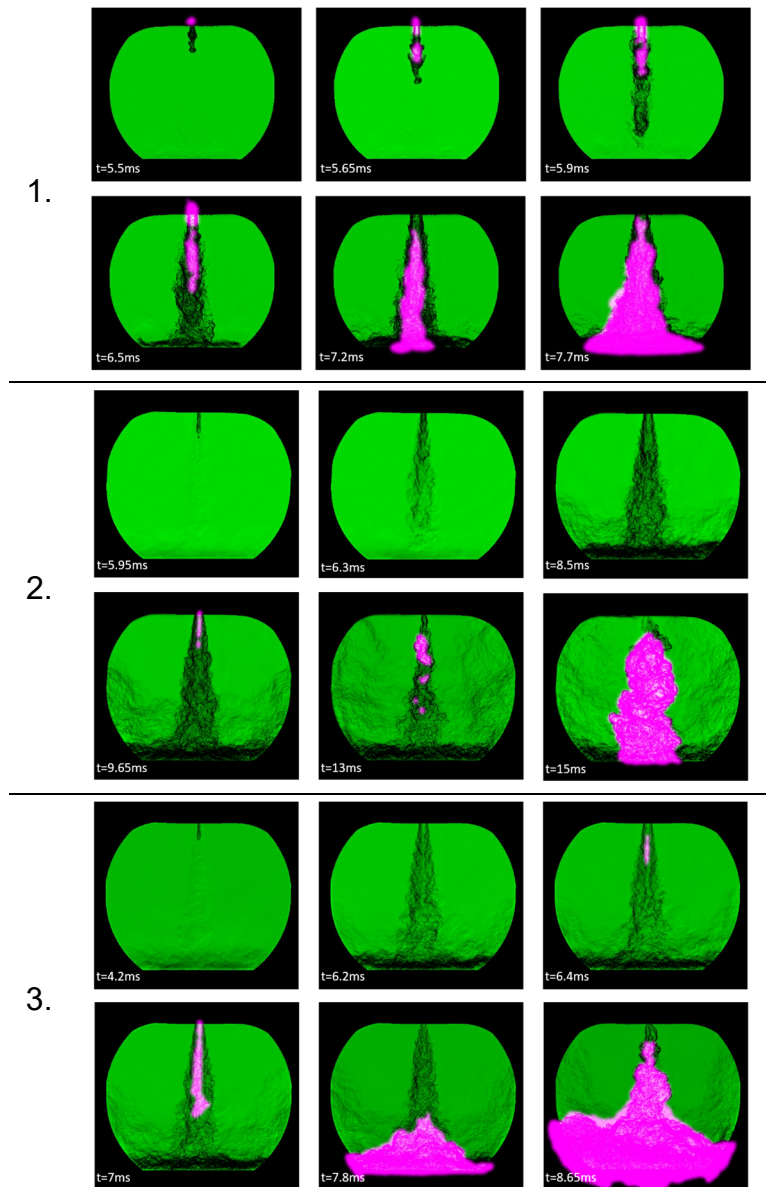

Figure 5: Optical images of the main chamber, showing the Schlieren image (green/black) with superimposed OH (pink) for one repetition of the OPC cases 1 (upper), 2 (middle) and 3 (lower series)*

The jet in case 3 shows a similar behavior to case 2, but with an accelerated sequence of events. The hot jet exit is observed at 4.2 ms, followed by the first OH* signal at 6.4 ms near the nozzle exit. The OH* area then expands and is finally convected to-wards the wall, before widespread ignition and main chamber pressure increase after 8.3 ms. The ID in this case is shorter than case 2, and is ~4 ms.

Overall, what we observe is that in case 1, there still exists a reaction zone at the nozzle exit, as indicated by the OH* signal, suggesting no complete quenching within the nozzle. The flame is nevertheless quenched downstream of the nozzle, when the hot products mix sufficiently with the cold unburned gases in the main chamber, suggesting quenching due to mixing. In cases 2 and 3 we observe complete quenching either in the nozzle or directly at its exit, while the pressure difference between the two chambers, and thus the jet velocity, are high. When the pressure difference reduces we observe a reactive jet exiting the nozzle, which quenches downstream, again indicating quenching through mixing. Finally, despite similar phenomenology, case 3 re-ignites faster than case 2, highlighting the effect of temperature on the re-ignition propensity of the burned/unburned mixture created.

Using the 0-D model described previously, we are able to compare the different cases. To do this, the 0-D model was tuned in order to match the pressure difference over time between the two chambers. Figure 6 shows the average (dashed-dotted red line) and variation (red area) experimental pressure difference for cases 1 and 3, while the modelled pressure difference is shown in blue. Although in case1 the pressure difference is of the order of the pressure sensor noise, it can still be seen that a peak is obtained around 5.5 ms after spark timing, and that the 0-D model prediction is close to this value. In both cases very good agreement of the maximum pressure difference both in terms of peak and timing is obtained. It should be mentioned that for all the simulations performed, the model parameters were fixed to their optimum value, and no case-to-case tuning was performed.
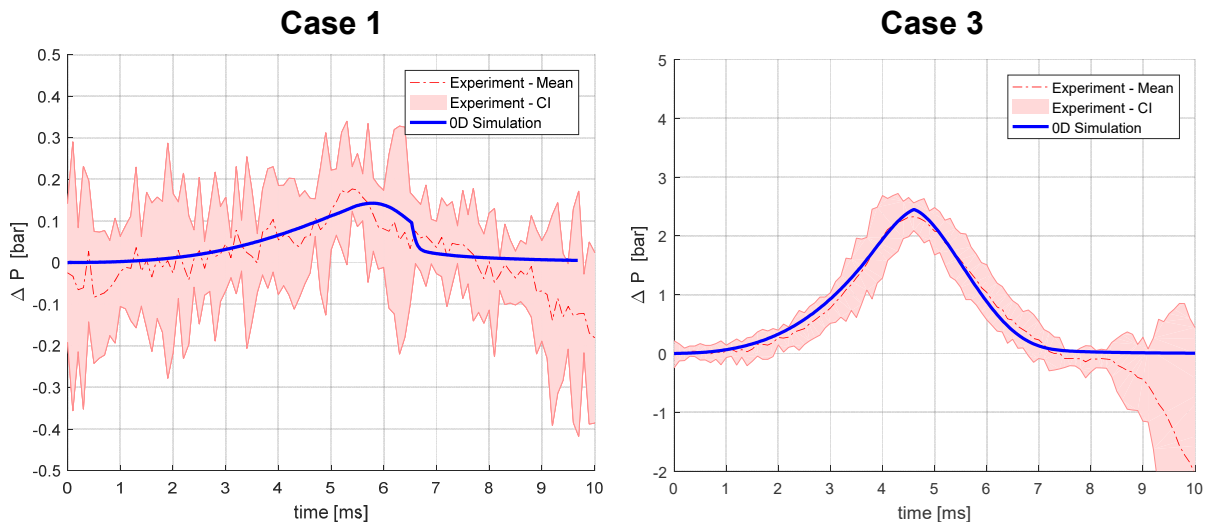

Figure 6: Exemplary comparison of experimental and simulated pressure difference between the pre- and main chambers for the OPC cases 1 and 3

Using the conditions estimated by the 0-D model, it is possible to evaluate the flame thickness for the OPC cases. The quenching distance is then:

$$\delta_q \approx 10\, l_f \approx 0.4\, mm, \text{ for case 1 and 2}$$

And

$$\delta_q \approx 10\, l_f \approx 0.35\, mm, \text{ for case 3}$$

In all cases the quenching distance is much smaller than the nozzle diameter (D_{noz}=4 mm in case 1 and 2 mm in cases 2 and 3). This means that based in this simplistic evaluation, under these thermochemical conditions thermal quenching is not expected.

The 0-D model can also be used to evaluate the evolution of the Damköhler number in time for a fixed jet position (five nozzle-diameters downstream nozzle exit). Figure 7 shows the evolution of the mixing state (blue, solid) and the flame reactivity (blue, dashed) timescales, as well as the resulting flame Damköhler number (red). In all cases the mixing timescale and thus the resulting Damköhler number starts from low values and then increases due to a reduction of the jet velocity, and thus turbulent intensity. For the larger nozzle in case 1, the initial Damköhler number is higher than in the other two cases ($Da_{fl,1}$=0.5, $Da_{fl,2}$=0.075, $Da_{fl,3}$=0.1), indicating lower quenching propensity. The lower Da_{fl} in case 2 compared to case 3 is due to the lower reactivity of the mixture, as a result of the lower temperature. Interestingly, in cases 2 and 3 the experiments show an appearance of the OH* signal when the Da_{fl} reaches a value of ~0.15. In all, the combination of the analysis using the 0-D model and the experiments indicate that at Da~0.5 the flame downstream of the nozzle is quenched, which means that a subsequent re-ignition is necessary.
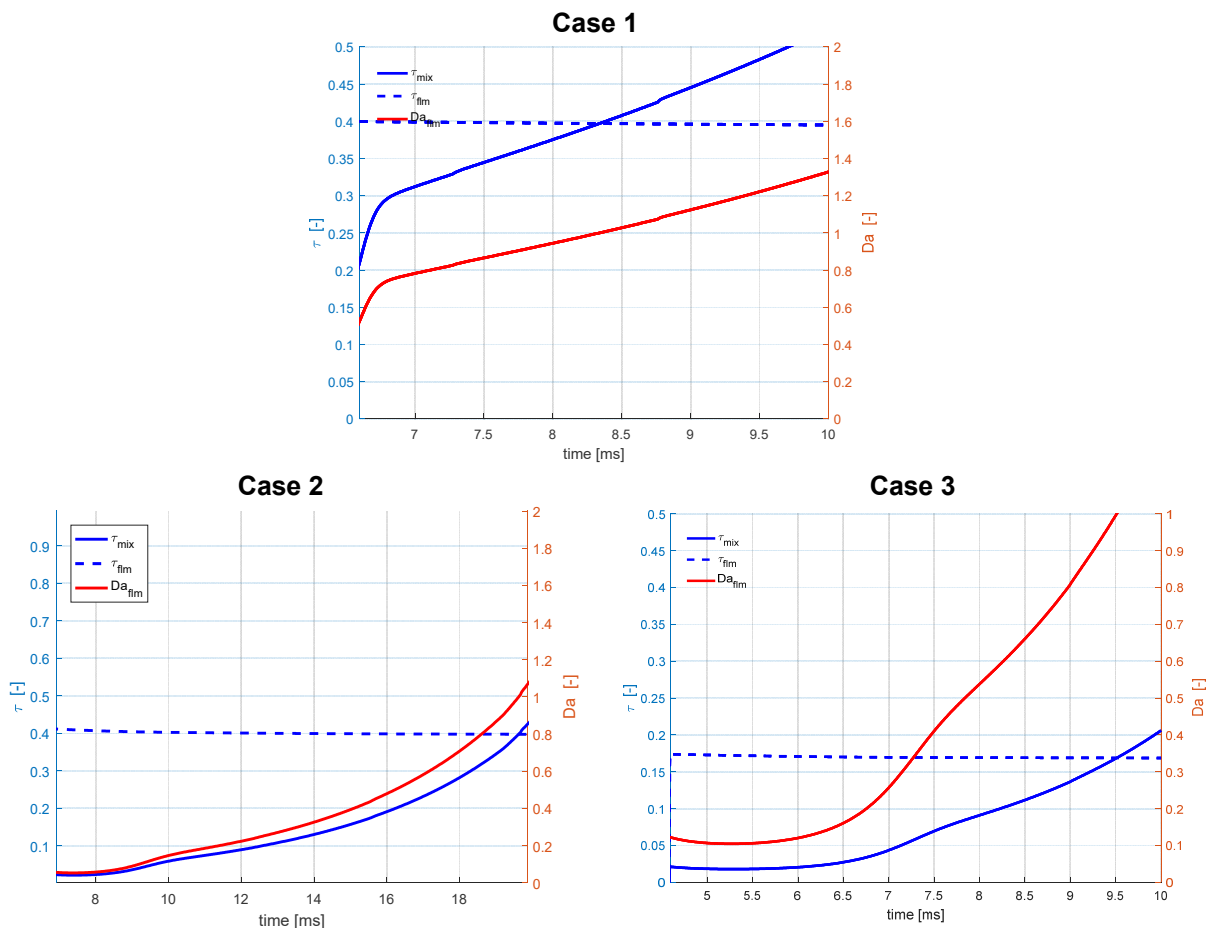

Figure 7: Evolution of mixing (blue, solid) and flame reactivity (blue, dashed) time-scales, and the resulting flame Damköhler number (red) for the OPC cases 1-3

In order to study the re-ignition process, the perfectly stirred reactor calculations for various burned/unburned mixture compositions were used. The results are presented

in *Figure 8*. The plot clearly shows the combined effect of mixing (movement towards lower mixture fractions) and mixture reactivity (unburned gas temperature). In case 1, lower mixing rates are expected to result in higher mixture fractions, resulting in shorter ignition delays, as observed. In cases 2 and 3, similar mixing is observed, but the difference in the ignition delay observed (~9 vs ~4 ms after jet exit) is the result of the nearly half-order of magnitude difference in ignition delay at a constant mixture fraction. *Figure 8* also includes the ignition delay for the case of lean composition in the prechamber ($\Phi_{MC}=\Phi_{MC}=0.75$); this shows the effect of differences in the temperature of the prechamber products on ignition.
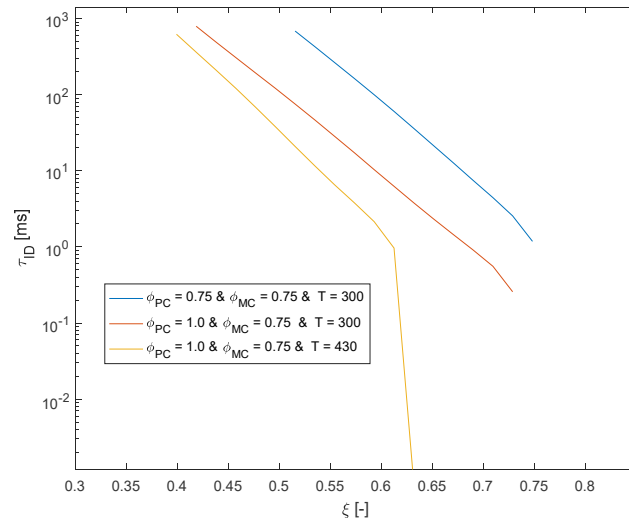
Figure 8: Ignition delay calculated using perfectly stirred reactors at different states of mixing between unburned mixture from the main chamber ($\xi=0$) and burned products from the prechamber ($\xi=1$), for different pre- and main chamber compositions and unburned temperatures

5.2   Engine application

The same analysis which was conducted for the optical prechamber can also be performed for engine applications. This will allow the estimation of the propensity for flame quenching due to thermal losses or mixing, and provide an estimate for re-ignition in cases where quenching might be present. Using the tuned 0-D engine model for the Liebherr engine, the parameters relevant for thermal and mixing-induced quenching were calculated, and are included in Table 3. The operating conditions chosen were a reference condition at high load, a condition where a prechamber with higher nozzle area (A_{noz}) to prechamber volume (V_{pc}) ratio was used, and a point at low load operation.

Table 3. Operating conditions and quenching parameter results for a typical un-scavenged prechamber lean-burn engine

Operating condition	P_{sp} (bar)	T_u (K)	λ	l_f (mm)	δ_q (mm)	τ_{mix} (ms)	τ_{fl} (ms)	Da_{fl}
Reference	76	814	1.7	0.016	0.16	0.032	0.16	0.2
High A_{noz}/V_{pc}	63	813	1.7	0.016	0.16	0.075	0.15	0.5
Low load	38	810	1.7	0.023	0.23	0.036	0.16	0.225

The engine results show smaller flame thicknesses compared to the OPC, as expected from the significantly higher pressure. This results in low tendency to quench due to thermal losses in the nozzle, since the resulting quenching distance is significantly lower than the nozzle dimension. In fact, for most engine applications the pressure at ignition is expected to be significantly above the conditions tested in the OPC, which means that barring very small prechamber nozzles, thermal quenching should not be expected. At lower loads the tendency for thermal quenching will increase, but it is expected to not be important.

In terms of the calculated flame Damköhler number, in all cases simulated here the values are similar to the OPC. As expected, with higher A_{noz}/V_{pc}, the Da_{fl} reduces, due to reduced jet velocity and resulting mixing. At low loads the Da_{fl} also reduces slightly, as a result of slightly lower mixing due to lower pressure difference over the nozzle. In all, the Damköhler values observed, when compared to the values from the OPC, indicate that even for this unscanvenged prechamber application flame quenching due to mixing could be expected. Considering the higher jet velocities observed from scavenged prechambers, it seems plausible to also expect high quenching tendencies due to mixing in the jet exit in such applications. With reducing load, the quenching tendency is expected to reduce, but only slightly as was observed in this study.

Considering that flame quenching is expected, it is interesting to study the expected ignition delay. Similarly to the results shown in *Figure 8* for the OPC, Figure 9 shows the calculated ignition delays for different charge pressures, for a constant composition of equal burned and unburned gas mass fractions (ξ=0.5). The different lines present reference conditions (blue, solid – T=800K, λ=1.7), different unburned gas temperatures (magenta, dotted/dashed – T=600K, λ=1.7; green, dashed – T=700K, λ=1.7) and different charge composition (red, dotted – T=700K, λ=1.0). The variation in pressure was chosen since this will be the major alteration when varying the engine load (low load: lower pressure). The changes in unburned temperature represent engine designs with lower compression ratio, or cold starts. The case with stoichiometric operation was chosen as representative for automotive/mobile applications using a 3-way catalyst.
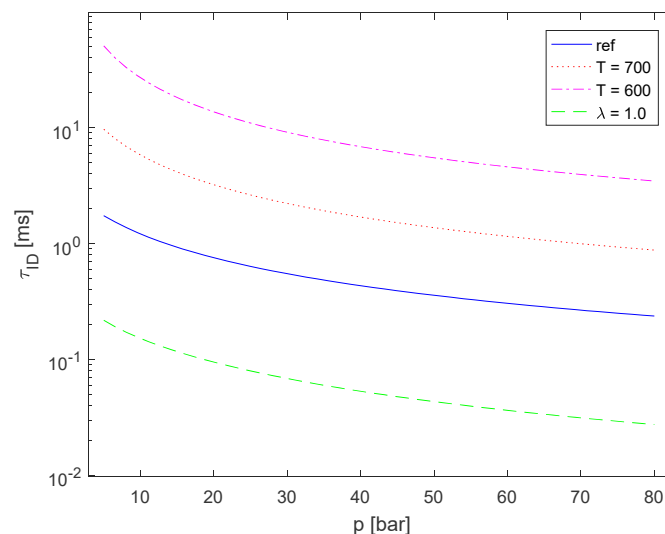
Figure 9: Ignition delay calculated using perfectly stirred reactors with equal burned/unburned mass fractions (ξ=0.5), for different mixture compositions and unburned gas temperatures. Reference T=800K, λ=1.7

The results show that the times for re-ignition are significantly shorter than observed for the OPC, as expected due to the higher temperature and pressure in the engine application. For the conditions encountered in the Liebherr engine at full load, ID for this mixture fraction is expected to be around 0.2 ms, which can be assumed to be negligible for any application, especially since the time needed to reach this level of mixing will probably be longer. Even for very low loads (10 bar, throttled operation), the ignition delay rises to around 1 ms, which is still very short compared to the OPC. This means that even if quenching takes place in such an engine application, the re-ignition will be fast enough for quenching not to be observable.

With lower charge temperatures (700 K and 600 K), the ignition delay increases significantly. This means that for engines with low compression ratios, flame quenching is expected to be more apparent. In addition, during cold start, engines with prechambers might have difficulties to ignite the main chamber mixture, depending on whether quenching is experienced and sufficient temperature and pressure is built up during compression. This provides perhaps a guideline for prechamber design, to allow engine cold-start and a wide operating range. For the stoichiometric engine application, the observed ignition delay is significantly shorter, signifying possibly reduced effect of flame quenching for such engines.

6   Conclusions

The present work uses experimental results from a generic, optically accessible prechamber test-rig, coupled to 0-D simulations of the setup as well as from a typical lean burn engine, to study the expected effect of flame quenching in prechamber applications. The generic test-rig used, called the optically accessible prechamber (OPC), allows the investigation of turbulent jet ignition under different initial pressure, temperature, composition and resulting jet velocities (through changes in the nozzle diameter). These variations enable the investigation of flame quenching and re-ignition under different thermochemical and mixing conditions. A 0-D model of the prechamber combustion and the jet formed, in combination with detailed flame and ignition chemistry calculations, allow the determination of flame quenching propensity as a result of heat losses to the nozzle wall and mixing, as well as the expected re-ignition.

The results from the OPC show that quenching is observed under all conditions presented. With a large nozzle, quenching is only observed at the tip of the hot jet, indicating quenching due to mixing of the exiting hot jet with colder reactants in the main chamber. With a smaller nozzle, resulting in very high jet velocities, no OH* signal is apparent in the hot jet, indicating quenching. In all cases flame thickness is sufficiently small and hence no flame quenching due to heat losses in the nozzle is expected. The calculated flame Damköhler number decreases with smaller nozzle diameter due to faster jet mixing, and increases with time due to the reduction of the pressure difference between pre- and main chamber, and thus the jet velocity. After some time in cases with smaller nozzle diameter, OH* appears near the nozzle, as a result of reduced mixing in that location with unburned gases. The time taken for main chamber re-ignition is strongly affected by the reactivity of the mixture, with higher temperature leading to significantly shorter ignition delay.

The application of the same methodology for quenching analysis to engine applications shows that flame quenching due to mixing can also be expected. Small flame thickness at high pressures encountered in engine do not favor flame quenching due to heat losses. For the heavy-duty/medium speed lean burn gas engine examined in this work, the flame Damköhler number was similar to the OPC, with low influence of load on the result, leading to the expectation of flame quenching due to mixing. Nevertheless, especially at conditions prevalent during high load operation and for stoichiometric engine operation (automotive/on-road applications), re-ignition in cases where quenching appears should be sufficiently fast for quenching to be not observable for most practical applications. Low-load and cold-start operation might be more demanding, due to the exponential dependency of ignition on temperature, and the resulting long ignition delays under these operating conditions. This dependency should be taken into account when prechamber engines are designed, in order to avoid ignition problems. The above analysis provides a basis to support the use of turbulent flame speed closures which do not model flame quenching, since its effect is expected to not be appreciable in most engine applications.

In all, it has been shown that the OPC is a useful test-rig for fundamental turbulent jet ignition studies. It can be used to approximate jet mixing conditions similar to those encountered in engines, and allows the study of flame quenching and re-ignition. Due to its high optical accessibility and precise setting of conditions, in addition to the lower charge ignition reactivity, this test-setup is appropriate for the study of flame quenching due to mixing, without the immediate influence of re-ignition present under high temperature and pressure conditions encountered in engines.

In terms of future work, CFD investigations, including 2D and 3D Direct Numerical Simulations, are underway in order to provide more insight into local mixing and detailed understanding of the processes observed. In addition, further experiments in the OPC are planned to expand the knowledge obtained from the investigations conducted to date.

Literature

[1]   Toulson, E., Schock, H.J., Attard, W.P., *A Review of Pre-Chamber Initiated Jet Ignition Combustion Systems.* 2010. 2010-01-2263. SAE International.

[2]   Dale, J.D., Checkel, M.D., Smy, P.R., *Application of high energy ignition systems to engines.* Progress in Energy and Combustion Science, 1997. 23(5–6): p. 379-398.

[3]   Morsy, M.H., *Review and recent developments of laser ignition for internal combustion engines applications.* Renewable and Sustainable Energy Reviews, 2012. 16(7): p. 4849-4875.

[4]   Biswas, S., et al., *On ignition mechanisms of premixed CH4/air and H2/air using a hot turbulent jet generated by pre-chamber combustion.* Applied Thermal Engineering, 2016. 106: p. 925-937.

[5]   Yamaguchi, S., Ohiwa, N., Hasegawa, T., *Ignition and burning process in a divided chamber bomb.* Combustion and Flame, 1985. 59(2): p. 177-187.

[6]   Carpio, J., et al., *Critical radius for hot-jet ignition of hydrogen–air mixtures.* International Journal of Hydrogen Energy, 2013. 38(7): p. 3105-3109.

[7]   Iglesias, I., et al., *Numerical analyses of deflagration initiation by a hot jet.* Combustion Theory and Modelling, 2012. 16(6): p. 994-1010.

[8]   Kotzagianni, M., et al., *Experimental and Computational Investigations of Prechamber Jet Ignition in a Rapid Compression Expansion Machine 10th Mediterranean Combustion Symposium.* 2017. Naples, Italy.

[9]   Toulson, E., et al., *Visualization of Propane and Natural Gas Spark Ignition and Turbulent Jet Ignition Combustion.* 2012.

[10] Schlatter, S., et al., *Comparative Study of Ignition Systems for Lean Burn Gas Engines in an Optically Accessible Rapid Compression Expansion Machine.* 2013. 2013-24-0112. SAE International.

[11] Gentz, G., et al., *A study of the influence of orifice diameter on a turbulent jet ignition system through combustion visualization and performance characterization in a rapid compression machine.* Applied Thermal Engineering, 2015. 81(Supplement C): p. 399-411.

[12] Gentz, G., et al., *Combustion Visualization, Performance, and CFD Modeling of a Pre-Chamber Turbulent Jet Ignition System in a Rapid Compression Machine.* 2015.

[13] Toulson, E., Watson, H.C., Attard, W.P., *Modeling Alternative Prechamber Fuels in Jet Assisted Ignition of Gasoline and LPG.* SAE Technical Paper 2009-01-0721, 2009.

[14] Sidey, J.,Mastorakos, E., *Pre-chamber ignition mechanism: simulations of transient autoignition in a mixing layer between reactants and partially-burnt products. 10th Mediterranean Combustion Symposium.* 2017.

[15] XU, G., et al., *Experimental and Numerical Investigation of the Engine Operational Conditions' Influences on a Small Un-Scavenged Pre-Chamber's Behavior.* SAE International Journal of Engines, 2017. 10(5).

[16] Xu, G., et al., *Characterization of combustion in a gas engine ignited using a small un-scavenged pre-chamber.* International Journal of Engine Research. 0(0): p. 1468087418798918.

[17] Sadanandan, R., et al., *Detailed investigation of ignition by hot gas jets.* Proceedings of the Combustion Institute, 2007. 31(1): p. 719-726.

[18] Mastorakos, E., et al., *Fundamental Aspects of Jet Ignition for Natural Gas Engines.* SAE Int. J. of Engines 2017-24-0097, 2017. 10(5).

[19] Allison, P., et al., *Pre-Chamber Ignition Mechanism: Experiments and Simulations on Turbulent Jet Flame Structure. 10th Mediterranean Combustion Symposium.* 2017.

[20] Xu, G., et al., *Experimental and numerical investigations of the unscavenged prechamber combustion in a rapid compression and expansion machine under engine-like conditions.* Combustion and Flame, under review.

[21] Kotzagianni, M., et al., *Optical investigations of prechamber turbulent jet ignition in a rapid compression expansion machine: Influence of geometrical characteristics and conditions on cycle-to-cycle variability.* Applied Thermal Engineering, in preparation.

[22] Bardis, K., et al., *Development of a Zero Dimensional Turbulence and Heat Transfer Phenomenological Model for Pre-Chamber Gas Engines.* 2018. SAE Technical Paper 2018-01-1453.

[23] Boust, B., et al., *A thermal formulation for single-wall quenching of transient laminar flames.* Combustion and Flame, 2007. 149(3): p. 286-294.

[24] Lockwood, F.C.,Naguib, A.S., *The prediction of the fluctuations in the properties of free, round-jet, turbulent, diffusion flames.* Combustion and Flame, 1975. 24: p. 109-124.

[25] Uzun, A.,Hussaini, M.Y., *Investigation of high frequency noise generation in the near-nozzle region of a jet using large eddy simulation.* Theoretical and Computational Fluid Dynamics, 2007. 21(4): p. 291-321.

[26] Wang, N., et al., *A numerical study of the combustion and jet characteristics of a hydrogen fueled turbulent hot-jet ignition (THJI) chamber.* International Journal of Hydrogen Energy, 2018.

Acknowledgements

The Authors

Michael Günther
IAV GmbH
Berlin

Dr Irufan Ahmed
Ricardo Software,
Shoreham Technical Centre
Shoreham by Sea, UK

Yoshihiko Akagi
Hitachi Automotive Systems, Ltd.
Hitachinaka-shi
Japan

Ph.D. Terry Alger
Southwest Research Institute
Powertrain Engineering Division
San Antonio, Texas

Dipl. -Ing. Muhammed Alp
Combustion System Engineering
Robert Bosch GmbH
Schwieberdingen

Prof. Dr.-Ing. Peter Awakowicz
Institute for Electrical Engineering
and Plasma Technology
Ruhr University Bochum
Bochum, Germany

Prof. Dr. Choongsik Bae
Department of Mechanical
Engineering
Korea Advanced Institute of
Science and Technology (KAIST)
Daejeon, Republic of Korea

Konstantinos Bardis
ETH Zurich
Zurich, Switzerland

Marc Sens
IAV GmbH
Berlin

Dr. Sayan Biswas
Sandia National Laboratories
Livermore, CA, USA

Dipl. -Ing. Matthias Blankmeister
Spark Plug Development
Robert Bosch GmbH
Stuttgart-Feuerbach

Dr. Davide Bleiner
Empa, Swiss Federal Laboratories
for Materials Science and
Technology
Dübendorf, Switzerland

Dr. Michele Bolla
ETH Zurich
Zurich, Switzerland

Prof. Dr. Konstantinos Boulouchos
ETH Zurich
Switzerland

Dr. Douglas Breden
Esgee Technologies
Austin, TX, USA

Dr. John Burrows
Federal-Mogul Tenneco
Manchester, England, UK

Guangyun Chen
Zhuzhou Torch Spark Plug Co.,
LTD

Marcel van Delden, M.Sc.
Institute of Electronic Circuits
Ruhr University Bochum
Bochum, Germany

Dr. Alexey Denisov
FHNW
Switzerland

Prof. Dr.-Ing. Wolfgang Eifler
Internal Combustion Engines
Ruhr University Bochum
Bochum, Germany

Dr. Isaac Ekoto
Sandia National Laboratories
Livermore, CA, USA

Stefan Essmann
Physikalisch-Technische
Bundesanstalt (PTB)
Braunschweig

Dipl.-Ing. Michael Frambourg
Volkswagen AG
Wolfsburg
Germany

Jess Gingrich, M. Sc.
formerly: Southwest Research
Institute
San Antonio, Texas

Sven Gröger, M.Sc.
Institute for Electrical Engineering
and Plasma Technology
Ruhr University Bochum
Bochum, Germany

Dr. Holger Grosshans
Physikalisch-Technische
Bundesanstalt (PTB)
Braunschweig

Dr.-Ing. Knut Habermann
Business Unit Gasoline Powertrains
FEV Europe GmbH
Aachen, Germany

Prof. Dr. Kai Herrmann
FHNW
Switzerland

Cherian A. Idicheria
General Motors Global Research
and Development
Pontiac, MI

Professor Yuji Ikeda
Imagineering, Inc.
Japan

Naohiro Ishikawa
Honda R&D Co.,Ltd
HRD Sakura
Sakura-shi
Japan

Dr.-Ing. Peter Janas
Federal-Mogul Ignition GmbH,
Powertrain
Germany

Thomas Kammermann
Empa, Swiss Federal Laboratories
for Materials Science and
Technology, Dübendorf,
Switzerland
Swiss Federal Institute of
Technology
Zurich, Switzerland

Dr. Anand Karpatne
Esgee Technologies
Austin, TX, USA

Dipl.-Ing. Dr.techn.
Constantin Kiesling
LEC GmbH
Graz, Austria

Wooyeong Kim, M.S.
Department of Mechanical
Engineering
Korea Advanced Institute of
Science and Technology (KAIST)
Daejeon, Republic of Korea

Noritaka Kimura
Honda R&D Co.,Ltd
Automobile R&D Center
Haga-machi
Japan

Sterling Kinkler, M. Sc.
formerly: Southwest Research
Institute
San Antonio, Texas

Hiroki Kobayashi
Honda R&D Co.,Ltd
Automobile R&D Center
Haga-machi
Japan

Prof. Dr. sc. techn. Thomas Koch
Institut für Kolbenmaschinen
Karlsruhe Institute of Technology
Karlsruhe, Germany

Associate Professor
Dr. Tatsuya Kuboyama
Chiba University
Japan

Kengo Kumano
Hitachi., Ltd. Research and
Development Group
Hitachinaka-shi
Japan

Johann-Robert Kummer
Physikalisch-Technische
Bundesanstalt (PTB)
Braunschweig

Dr. Panagiotis Kyrtatos
ETH Zurich & Vir2sense GmbH
Zurich, Switzerland

Liguang Li
School of Automotive Engineering,
Tongji University
Shanghai, China

Yilun Luo, M. Phil.
Southwest Research Institute
Powertrain Engineering Division
Ann Arbor, MI

Prof. Dr. rer. nat. habil. U. Maas
Karlsruhe Institute of Technology
Institute of Technical
Thermodynamics
Karlsruhe

Barrett Mangold, A.Sc.
Southwest Research Institute
Powertrain Engineering Division
San Antonio, Texas

Dr.-Ing. Detlev Markus
Physikalisch-Technische
Bundesanstalt (PTB), Braunschweig

Dr. Laura Merotto
Empa, Swiss Federal Laboratories
for Materials Science and
Technology
Dübendorf
Switzerland

Dipl.-Ing. Dr.techn. Georg Meyer
LEC GmbH
Graz, Austria

Tobias Michler, M.Sc.
Institut für Kolbenmaschinen
Karlsruhe Institute of Technology
Karlsruhe, Germany

Kristapher Mixell
Federal-Mogul Tenneco
Plymouth, Michigan, USA

Dr.-Ing. Bastian Morcinkowski
Business Unit Gasoline Powertrains
FEV Europe GmbH
Aachen, Germany

Professor Dr. Yasuo Moriyoshi
Chiba University
Inage-ku
Japan

Dipl. Ing. Christoph Müller
Institute of Combustion engines
RWTH Aachen University
Germany

Prof. Dr.-Ing. Thomas Musch
Institute of Electronic Circuits
Ruhr University Bochum
Bochum, Germany

Paul Najt
General Motors Global Research
and Development
Pontiac, MI

Shogo Namba
Hitachi Automotive Systems, Ltd.
Hitachinaka-shi
Japan

Werner Niessner
Federal-Mogul Ignition GmbH,
Powertrain
Germany

Dr. Atsushi Nishiyama
Imagineering, Inc., Japan

Gordon Notzon, M.Sc.
Institute of Electronic Circuits
Ruhr University Bochum
Bochum, Germany

Kazuhiro Oryoji
Hitachi, Ltd. Research and
Development Group
Hitachinaka-shi
Japan

Dipl.-Ing. Dr.techn. Gerhard Pirker
LEC GmbH
Graz, Austria

Dr.-Ing. Matthieu Prouvier
Volkswagen AG
Wolfsburg
Germany

Prof. Laxminarayan Raja
University at Austin Texas
Austin, TX, USA

Dipl.-Ing. Paul-Benjamin Reinicke
IAV GmbH
Berlin

Dipl.-Ing. Michael Rieß
IAV GmbH
Berlin

Lorenz von Römer, M.Sc.
IAV GmbH
Berlin

Tim Russwurm, M.Sc
Lehrstuhl für Technische
Thermodynamik
Friedrich-Alexander-Universität
Erlangen-Nürnberg, Germany

Dipl.-Ing. Dr.techn.
Sebastian Salbrechter
LEC GmbH
Graz, Austria

Dr. Riccardo Scarcelli
Argonne National Laboratory
Lemont, IL, USA

Dipl.-Ing. Christof Schernus
Business Development Research &
Innovation
FEV Europe GmbH
Aachen, Germany

Dipl.-Ing. Moritz Schumacher
Lehrstuhl für Technische
Thermodynamik
Friedrich-Alexander-Universität
Erlangen-Nürnberg, Germany

Dr. Takeshi Serizawa
Daihatsu Motor Co., Ltd
Japan

Dr Evgeniy Shapiro
Ricardo Software,
Shoreham Technical Centre
UK

Dr. Eriko Shimizu
Combustion System Engineering
Bosch Cooperation Yokohama
Japan

Dr. Patrik Soltic
Empa, Swiss Federal Laboratories
for Materials Science and
Technology
Dübendorf, Switzerland

Kevin Stark, M.Sc
Internal Combustion Engines
Ruhr University Bochum
Bochum, Germany

Kenta Suzuki
Esgee Technologies
Austin, TX, USA

Gunesh Tallu, M.Sc.
Volkswagen AG
Wolfsburg
Germany

Dipl.-Ing. Anton Tilz
Graz University of Technology
Graz, Austria

Nick Tiney
Ricardo Japan
Yokohama. Kanagawa
Japan

Jimi Tjong
Department of Mechanical
Automotive & Materials Engineering
University of Windsor
Canada

Dr.-Ing. Olaf Toedter
Institut für Kolbenmaschinen
Karlsruhe Institute of Technology
Karlsruhe, Germany

Yoshifumi Uchise
Hitachi Automotive Systems
Hanshin, Ltd.
Sanda-shi
Japan

Dr.-Ing. Tolga Uhlmann
Powertrain Engineering in the
Business Unit Gasoline Powertrains
FEV Europe GmbH
Aachen, Germany

Boyuan Wang, Master
Tsinghua University
Beijing, China

Professor Zhi Wang
Tsinghua University
Beijing, China

Dipl.-Ing. Michael Weißner
Volkswagen AG
Wolfsburg
Germany

Prof. Dr. Michael Wensing
Lehrstuhl für Technische
Thermodynamik
Friedrich-Alexander-Universität
Erlangen-Nürnberg, Germany

Ao.Univ.-Prof. Dipl.-Ing. Dr.techn.
Andreas Wimmer
Graz University of Technology
and LEC GmbH
Graz, Austria

Dipl.-Ing. Axel Winkler
Volkswagen AG
Wolfsburg
Germany

Marcus Wöbke; M.Sc.
IAV GmbH
Berlin

Dr. Yuri M. Wright
ETH Zurich & Combustion and Flow
Solutions GmbH
Switzerland

Zhenyi Yang
Department of Mechanical
Automotive & Materials Engineering
University of Windsor
Canada

Shui Yu
Department of Mechanical
Automotive & Materials Engineering
University of Windsor
Canada

Xiao Yu
Department of Mechanical
Automotive & Materials Engineering
University of Windsor
Canada

Hanho Yun
General Motors Global Research
and Development
Pontiac, MI

Prof. Ming Zheng
Department of Mechanical
Automotive & Materials Engineering
University of Windsor
Canada

**Dr.-Ing. Karsten Röpke,
Prof. Dr.-Ing. Clemens Gühmann (Ed.)
and 88 co-authors**

Design of Experiments (DoE) in Powertrain Development

2017, 369 S., 267 Fig. and 33 Tab., 68,00 €, 81,00 CHF
(Reihe Technik) **ISBN 978-3-8169-3381-6**

Zum Buch:

The book will expand on the topics discussed in the precursors entitled "DoE in Powertrain Development" with the related areas of "machine learning" and "big data". Now it its ninth outing, it will thus be a forum on which to critically engage with the future challenges of the digital revolution.
Real driving emissions (RDE), worldwide harmonized light-duty test procedures (WLTP) and the next round of CO_2 guidelines all demand ongoing technical refinement of the drive train. The combination of changed environmental requirements, stricter limit values and new measurement techniques additionally require changes to existing processes and the development of new methods.

To reduce costs, many OEMs are scaling down the size of their engine ranges. A small number of standard engines are then installed in numerous vehicle models with minor hardware modifications. The result is an increased focus on the use of derivatives and the systematic validation of an application.
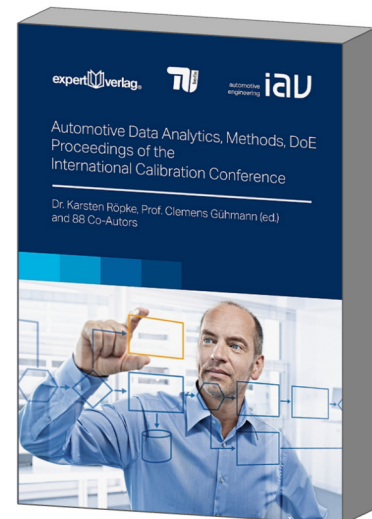
Target group:

Development and application engineers from automotive manufacturers and supply industry as well as universities

*Blätterbare Leseprobe
und einfache Bestellung unter:
www.expertverlag.de/3316*

The Editors:

Dr.-Ing. Karsten Röpke is Head of Department Development Methods at IAV.

Prof. Dr.-Ing. Clemens Gühmann is Head of the Chair of Electronic Measurement and Diagnostic Technology at TU Berlin

In addition to increasing electrification, forecasts show a worldwide increase in the number of gasoline engines being produced. Rising industrialization will likely lead to 120 million new registrations, at least 75% of them for vehicles based on combustion engines, by the year 2030. Ambitious climate targets will remain a chimera as long as the gasoline engine is not adapted to help significantly reduce carbon emissions. In addition to the requirements of the established markets, we must be prepared for new challenges in emerging economic regions in particular. Engines require greater optimization while remaining sufficiently robust to meet the demands of use all around the world. In addition to the Miller combustion cycle, the industry needs engines that employ strongly charge-diluted combustion to achieve efficiencies significantly above 40%. Instrumental in this will be ignition processes with great potential to shift ignition limits.

The Editors:
Michael Günther, IAV GmbH
Department Manager Advanced Development – Thermodynamics SI Engines Gas Exchange/Combustion

Marc Sens, IAV GmbH
Senior Vice President Advanced Development – Thermodynamic/Powertrain Concepts

expert ›

9 783816 934493